Universidad Miguel Hernández de Elche

Programa de Doctorado en Biología Molecular y Celular

Small extracellular vesicles as a potential clinical tool for *hard-to-treat cancer* therapy

Lourdes Salomé Araujo Abad

Directora de tesis

Dra. María del Pilar García Morales

Codirectora de tesis

Dra. Meuri del Camino de Juan Romero

Elche, 2023

UNIVERSITAS
Miguel Hernández

La presente Tesis Doctoral, titulada "Small extracellular vesicles as a potential clinical tool for *hard-to-treat cancer* therapy", se presenta bajo la modalidad de **tesis por compendio** de las siguientes **publicaciones**:

- **Araujo-Abad, S**.; Saceda, M.; de Juan Romero, C. Biomedical Application of Small Extracellular Vesicles in Cancer Treatment. Adv Drug Deliv Rev 2022, 182, 114117, doi:10.1016/J.ADDR.2022.114117. **IF (2022): 16.1 Q1**.
- **Araujo-Abad, S**.; Manresa-Manresa, A.; Rodríguez-Cañas, E.; Fuentes-Baile, M.; García-Morales, P.; Mallavia, R.; Saceda, M.; de Juan Romero, C. Glioblastoma-Derived Small Extracellular Vesicles: Nanoparticles for Glioma Treatment. International Journal of Molecular Sciences 2023, Vol. 24, Page 5910 2023, 24, 5910, doi:10.3390/IJMS24065910. **IF (2022): 5.6 Q1**.
- **Araujo-Abad, S.**; Manresa-Manresa, A.; Rodríguez-Cañas, E.; Fuentes- Baile, M.; García-Morales, P.; Mallavia, R.; Saceda, M.; de Juan Romero, C. New Therapy for Pancreatic Cancer Based on Extracellular Vesicles. Biomedicine & Pharmacotherapy 2023, 162, 114657, doi:10.1016/J.BIOPHA.2023.114657. **IF (2022): 7.5 Q1**.
- Neira, J.L.; **Araujo-Abad, S.**; Cámara-Artigas, A.; Rizzuti, B.; Abian, O.; Giudici, A.M.; Velazquez-Campoy, A.; de Juan Romero, C. Biochemical and Biophysical Characterization of PADI4 Supports Its Involvement in Cancer. Arch Biochem Biophys 2022, 717, 109125, doi:10.1016/J.ABB.2022.109125. **IF (2022): 3.9 Q1**.
- **Araujo-Abad, S.**; Neira, J.L.; Rizzuti, B.; García-Morales, P.; de Juan Romero, C.; Santofimia-Castaño, P.; Iovanna, J. Intrinsically Disordered Chromatin Protein NUPR1 Binds to the Enzyme PADI4. J Mol Biol 2023, 435, doi:10.1016/J.JMB.2023.168033. **IF (2022): 5.6 Q1**.
- **Araujo-Abad, S**.; Rizzuti, B.; Villamarín-Ortiz, A.; Pantoja-Uceda, D., M.; Moreno-Gonzalez, C.M; Abian, O.; Velazquez-Campoy, A.; Neira, J.L..; de Juan Romero, C. New insights into cancer: MDM2 binds to the citrullinating enzyme PADI4. Protein Sci.2023, 717, 109125, doi:10.1002/PRO.4723. **IF (2022): 8 Q1**.

Durante la Tesis Doctoral, titulada “Small extracellular vesicles as a potential clinical tool for *hard-to-treat cancer* therapy”, se publicaron otros artículos no incluidos en este compendio, presentados en el Anexo.

- Neira, J.L.; Rizzuti, B.; **Araujo-Abad, S**.; Abian, O.; Fárez-Vidal, M.E.; Velazquez-Campoy, A.; de Juan Romero, C. The armadillo-repeat domain of Plakophilin 1 binds to human enzyme PADI4. Biochim Biophys *Acta Proteins Proteom*. **2022** Nov 11;1871(2):140868. doi: 10.1016/j.bbapap.2022.140868. Epub ahead of print. PMID: 36372391. **IF (2022): 3.2 Q1**.
- Neira, J.L.; Rizzuti B.; Abián, O., **Araujo-Abad, S.**, Velázquez-Campoy, A., de Juan Romero, C. Human Enzyme PADI4 Binds to the Nuclear Carrier Importin α3. *Cells*. **2022** Jul 11;11(14):2166. doi: 10.3390/cells11142166. **IF (2022): 6.0 Q1**.

UNIVERSITAS
Miguel Hernández

La Dra. *María del Pilar García Morales*, directora, y la Dra. *Meuri del Camino de Juan Romero*, codirectora de la tesis doctoral titulada **“**Small extracellular vesicles as a potential clinical tool for *hard-to-treat cancer* therapy”**.**

INFORMAN:

Que Dña. *Lourdes Salomé Araujo Abad* ha realizado bajo nuestra supervisión el trabajo titulado **“**Small extracellular vesicles as a potential clinical tool for *hard-to-treat cancer* therapy**”** conforme a los términos y condiciones definidos en su Plan de Investigación y de acuerdo al Código de Buenas Prácticas de la Universidad Miguel Hernández de Elche, cumpliendo los objetivos previstos de forma satisfactoria para su defensa pública como tesis doctoral.

Lo que firmamos para los efectos oportunos, en Elche a 26 de julio de 2023.

Directora de la tesis	**Codirectora de la tesis**
Dra. María del Pilar García Morales	*Dra. Meuri del Camino de Juan Romero*

UNIVERSITAS
Miguel Hernández

La Dra. *Asia Fernández Carvajal*, Catedrática en Bioquímica y Biología Molecular y coordinadora del Programa de Doctorado en Biología Molecular y Celular del Instituto de Investigación, Desarrollo e Innovación en Biotecnología Sanitaria de Elche (IDiBE) de la Universidad Miguel Hernández de Elche,

INFORMA:

Que Dña. *Lourdes Salomé Araujo Abad* ha realizado bajo la supervisión de nuestro Programa de Doctorado el trabajo titulado **“**Small extracellular vesicles as a potential clinical tool for *hard-to-treat cancer* therapy**”** conforme a los términos y condiciones definidos en su Plan de Investigación y de acuerdo al Código de Buenas Prácticas de la Universidad Miguel Hernández de Elche, cumpliendo los objetivos previstos de forma satisfactoria para su defensa pública como tesis doctoral.

Lo que firmo para los efectos oportunos, en Elche a 26 de julio de 2023.

Dra. Asia Fernández Carvajal
Coordinadora del Programa de Doctorado en Biología Molecular y Celular

La presente Tesis doctoral ha sido realizada gracias a la beca predoctoral “**Fundación Carolina 2020**” en la que participan la Universidad Nacional de Loja (Ecuador) y la Universidad Miguel Hernández de Elche (España). Además, para una estancia internacional en el Instituto Nacional de Investigación en Salud y Medicina de Francia (INSERM) fue recibida la beca *The Company of Biologists: Travelling Fellowship* (DMMTF2110601).

La Tesis doctoral ha sido financiada por los proyectos: “*Identification of new therapeutic targets for the prognosis and treatment improvement of Glioblastoma multiforme*” (CP19/00095) Programa Miguel Servet e “Identificación de nuevas dianas terapéuticas para el pronóstico y la mejora del tratamiento del glioblastoma” (PI22/00824) del Instituto de Salud Carlos III, “El estudio metabolómico y el aislamiento de exosomas como fuente de biomarcadores y dianas terapéuticas en glioblastoma” (UGP-20-291) de FISABIO y “Nuevas estrategias contra el cáncer: inhibición de las interacciones moleculares de las proteínas deiminasas de arginina” Consellería de Innovación, Universidades, Ciencia y Sociedad Digital (Generalitat Valenciana) (CAICO 2021/0135).

AGRADECIMIENTOS

Llevar a cabo la presente Tesis doctoral no habría sido posible sin el apoyo y consejos de muchas personas. Primero quiero agradecer a mis padres **Eduardo** y **Lourdes**, a mi hermano **Eduardo José** y, a mi abuelita **Ena**, que son los pilares fundamentales de mi vida.

Estoy muy agradecida con el grupo de investigación liderado por **Camino**, que ha sido la mejor guía en estos años, ha depositado su confianza en mi para realizar este trabajo y me ha acogido de la mejor forma. A **Pilar** y **Miguel**, que han sido un apoyo en todo momento con sus consejos tanto académicos como personales, por estar siempre pendientes y presentes. A todos mis compañeros de laboratorio que estuvieron o están ahora mismo. Agradecimiento especial a los que se han convertido en grandes amigos, **Laura** y **Raquel**, que llegaron a alegrarme los días con sus ocurrencias y sus granas de aprender, siempre las echo de menos. A **Antonio** por su ayuda en todo momento no solo en el laboratorio sino en el día a día, aprendimos muchas cosas juntos. A **Montse** que fue un apoyo en la pandemia y con la que compartimos el gusto por viajar. A **María** que siempre ha estado para ayudarme y escucharme. A **Rocío** que ha celebrando conmigo mis pequeños logros y siempre ha estado para mi.

Además, quiero agradecer a **José Luis Neira**, que ha sido parte principal de este trabajo, me ha llenado de satisfacción coincidir con su enorme gusto por la ciencia que me motiva cada día a seguir en este camino. A **Ricardo Mallavia** quién ha sido parte importante para conseguir algunos resultados de esta Tesis y por involucrarse en este proyecto.

Quisiera agradecer a todos los que conforman la Unidad de Investigación del Hospital General Universitario de Elche, en especial a **Víctor Barberá** que ha sido un apoyo increíble en todo este tiempo, con su buen humor y consejos ha hecho que cada estancia en el hospital sea llevadera.

Agradezco al Grupo de Investigación U1068 del INSERM liderado por **Juan Iovanna** por haberme acogido durante mi estancia en su laboratorio de Marsella. Gracias a **Patricia**, por su tiempo y dedicación enseñándome el laboratorio. A **Xi**, **Scarlett** y **David** que hicieron que mi estancia fuera más divertida y haberme hecho sentir como en casa.

Finalmente, quiero agradecer al rector de la Universidad Nacional de Loja-Ecuador, **Nikolay Aguirre**, a todos quienes conforman la **Fundación Carolina,** Universidad Miguel Hernández y al Instituto de Investigación, Desarrollo e Investigación en Biotecnología Sanitaria de Elche (**IDiBE**) por otorgarme la beca que me ha permitido llegar hasta aquí.

Gracias a todos.

“Era como si se me abriera un mundo nuevo,el mundo de la ciencia,

que por fin se me permitía conocer con toda libertad”

Marie Curie

A mi familia

INDEX

ABBREVIATIONS & ACRONYMS

2-HG	2-hydroxyglutarate
BBB	Blood-Brain Barrier
bFGF	Basic Fibroblast Growth Factor
BMI	Body Mass Index
CAFs	Cancer-Associated Fibroblasts
CAR	Chimeric Antigen Receptor
CD	Circular Dichroism
CL	Classical
CNS	Central Nervous System
DMEM-HG	Dulbecco's Modified Eagle's Medium: High Glucose
DKK3	Dickkopf WNT signaling pathway inhibitor 3
DLS	Dynamic Light Scattering
DMEM F-12	Dulbecco's Modified Eagle's Medium: Nutrient Mixture F-12
DMSO	Dimethyl Sulfoxide
DNA	Deoxyribonucleic Acid
Dox	Doxorubicin
DSC	Difference Scanning Calorimetry
EDX	Energy Dispersive X-ray
EGFR	Epidermal Growth Factor Receptor
Elk1	ETS-domain containing protein
EMC	Extracellular Matrix
EMT	Epithelial-to-mesenchymal Transition
ESCRT	Endosomal Sorting Complexes Required for Transport
EVs	Extracellular Vesicles
FAMMM	Familial Atypical Multiple Mole Melanoma Syndrome
FAP	Familial Adenomatous Polyposis
far-uV CD	Far-Ultraviolet Circular Dichroism
FBS	Fetal Bovine Serum
FESEM	Field Emission Scanning Electron Microscope
FGF	Fibroblast Growth Factor
GBM	Glioblastoma
GEM	Gemcitabine
gETL NPs	Exosomes-thermosensitive liposomes hybrid NPs
GM-CSF	Colony-Stimulating Factor
GNP	Gold Nanoparticles
GSK3β	Glycogen Synthase Kinase 3 Beta
HBOC	Hereditary Breast and Ovarian Cancer syndrome
HIPEC	Hyperthermic Intraperitoneal Chemotherapy
HMGB1	High Mobility Group Box 1

HNPCC	Hereditary Non-Polyposic Colorectal Cancer Or Lynch Syndrome
HPLC	High-Performance Liquid Chromatography
Hsp	Heat Shock Protein
IC_{50}	Half Maximal Inhibitory Concentration
iCAF	Inflammatory Cancer Associated Fibroblast
ICC	Immunocytochemistry
IDH	Isocitrate Dehydrogenase
IF	Immunofluorescence
IL-8	Interleukin-8
ILV	Intraluminal Vesicle
ING4	Inhibitor of Growth 4
IPMN	Intraductal Papillary Mucinous Neoplasm
IR	Irradiation
ISEV	International Society for Extracellular Vesicles
lncRNAs	Long non-coding Rnas
MCN	Mucinous Cystic Neoplasm
MD	Molecular Dynamics
MDM2	Murine Double Minute 2 Homolog
ME	Mesenchymal
MGMT	O6-methylguanine-DNA methyltransferase
MHC	Major histocompatibility complex
miRNAs	MicroRNA
MISEV	Minimal Information for Studies of Extracellular Vesicles
mRNA	Messenger RNA
MSC	Mesenchymal stroma/stem-like cells
MTT	Methylthiazolyldiphenyl-tetrazolium bromide
MV	Microvesicle
MVB	Multivesicular Bodies
myCAF	Myofibroblastic cancer-associated fibroblast
NETs	Neutrophil Extracellular Traps
NIH	National Institutes of Health
NL	Neural
NLS	Nuclear Localization Signal
NMR	Magnetic Resonance Spectroscopy
NSCLC	Non-Small Cell Lung Cancer
NTA	Nanoparticle Tracking Analysis
PADIs	Peptidyl-Arginine Deiminases
PanIN	Pancreatic Intraepithelial Neoplasia
PaSC	Pancreatic Stellate Cells
PDAC	Pancreatic Ductal Adenocarcinoma
PDGF	Platelet-Derived Growth Factor
PDGFRA	Platelet-Derived Growth Factor Receptor A

PFA	Paraformaldehyde
PJS	Peutz–Jeghers Syndrome
PM	Plasma Membrane
PN	Proneural
PRMT5	Arginine Methyltransferase-5
PTEN	Phosphatase and Tensin Homolog
PTM	Post-translational modification
RNA	Ribonucleic Acid
SAM	Sterile alpha motif
SD	Standard Deviation
SEC	Size Exclusion Chromatography
SVZ	Subventricular Zone
TDEs	Tumor-Derived Exosomes
Teff	Effector T Cell
TEM	Transmission Electron Microscope
TERT	Telomerase Reverse Transcriptase
TGF	Transforming Growth Factor
TLR9	Toll-Like Receptor 9
TLS	Thermosensitive Liposomes
TME	Tumor Microenvironment
TMZ	Temozolomide
TNBC	Triple-Negative Breast Cancer
TNF	Tumor Necrosis Factor
Treg	Regulatory T Cell
TSG	Tumor Susceptibility Gene
VEGF	Vascular Endothelial Growth Factor
WB	Western blot
WHO	World Health Organization

ABSTRACT

Hard-to-treat cancers such as glioblastoma (GBM) and pancreatic ductal adenocarcinoma (PDAC), are characterized by their aggressive nature and resistance to conventional therapies. Despite the standard of care, which includes tumor resection followed by chemotherapy and radiotherapy, patients have a poor prognosis. Therefore, the development of novel therapeutic approaches is necessary. In this sense, the use of small extracellular vesicles (EVs) as delivery systems has become a promising tool for cancer treatment. This system can deliver anticancer drugs directly to tumor cells, improving the efficacy of treatment. In this work, we used small EVs loaded with different drugs to prove their target specificity towards their parental cells and evaluate their potential as an effective treatment for cancer. In addition, we studied the PADI4 interactome and citrullination capacity, its relationship with cancer progression, and its role as a target for cancer therapy. This doctoral thesis is structured as a compendium of six articles published in high-impact journals (Q1) that correspond to each chapter, with an additional chapter of the data pending publication.

In Chapter 1, we discussed how small EVs play a crucial role in intercellular communication and have emerged as potential biomarkers and therapeutic tools, particularly in cancer. Additionally, we reviewed the significance of small EVs as biomarkers in various cancer types. Furthermore, we explored the development of chimeric EVs that can be conjugated with nanoparticles, biomolecules, and anti-cancer drugs, showing their potential for targeted cancer therapy. The review also provides an overview of ongoing clinical trials utilizing EVs to improve the prognosis of different cancer types, emphasizing the potential of EV-based therapies to combat these challenging diseases.

In Chapter 2, we performed the isolation and characterization of small EVs derived from GBM patient cell lines. We loaded these EVs with temozolomide (TMZ) and EPZ015666 drugs and observed that a minimal amount of the drug is sufficient to affect tumor cells when it is loaded into small EVs. Additionally, GBM-derived small EVs loaded with the drugs showed the potential to induce an antiproliferative effect in pancreatic cancer cells. These findings support the use of GBM-derived small EVs as a promising drug delivery tool for further preclinical and clinical development of GBM treatments.

In Chapter 3, we isolated and characterized small EVs derived from a PDAC cell line named RWP-1. We loaded these small EVs with two chemotherapeutic drugs, TMZ and EPZ015666 by the direct incubation method, which proved to be the most effective loading method, requiring minimal drug dosage to affect tumor cells. The antiproliferative effect was tested on different cancer cell lines, revealing greater efficacy of RWP-1 small EVs^{TMZ} compared to

RWP-1 small EVs^{EPZ015666}. These findings highlight the potential of RWP-1-derived small EVs as a promising drug delivery tool for PDAC treatment.

In Chapter 4, we identified the expression and localization of PADI4, a Ca^{2+}-dependent protein involved in the conversion of arginine to citrulline, in several cancer cell lines, including GBM (GB-39), and pancreatic cancer (RWP-1). Additionally, we studied its relationship with p53. The characterization by immunofluorescence (IF) revealed different subcellular localizations of PADI4 depending on the cancer cell line. In the Westen Blot (WB) we observed different patterns of protein, revealing the possibility that PADI4 might experience alternative splicing. These findings shed light on the functional role of PADI4 in cancer development.

In Chapter 5, we performed WB to identify the expression of PADI4 in GBM cell lines. Additionally, we investigated if GSK484, a well-known PADI4 inhibitor, could have an effect on GBM and PDAC cell proliferation. Finally, we tested if GSK484 loaded into small EVs had a higher effect on cell proliferation than the administration of the drug alone. Our results indicated that PADI4 expression was different among several cancer cell lines. Besides, GSK484 effectively decreases the proliferation of GBM and PDAC cell lines when it was loaded into small EVs, with a minimum concentration of the drug.

In Chapter 6, we analyzed the interaction between NUPR1 and PADI4 in GBM cell lines. *In vitro* and *in cellulo* experiments revealed a strong binding affinity between NUPR1 and PADI4 in the nucleus, suggesting that the NUPR1/PADI4 complex may be essential in DNA repair, metastasis promotion, or citrullination of other proteins. These results highlight the importance of their interaction and their role as a potential target for cancer therapy.

Finally, in Chapter 7, we identified the interaction between PADI4 and MDM2. In this work, the PADI4/MDM2 complex was found in the nucleus and cytoplasm of different cancer cell lines. Additionally, we found that their treatment with GSK484 impeded the nuclear binding of these two proteins, suggesting that MDM2 binds to the active site of PADI4. The interaction between MDM2 and PADI4 may lead to MDM2 citrullination, which could be a therapeutic target for cancer treatment.

This Thesis revealed the potential use of small EVs derived from hard-to-treat cancer cells as a novel therapeutic approach for the treatment of GBM and PDAC. By loading these EVs with therapeutic drugs, such as TMZ, EPZ015666, and GSK484, we enhanced the drug delivery efficiency, which could reduce the side effects associated with conventional therapies. Furthermore, we explored the role of PADI4 in GBM and PDAC. By elucidating the interactions between PADI4 and its partners, we uncovered potential mechanisms involved in cancer progression and identified new avenues for targeted therapies. This work settles the basis of future personalized medical approaches and provides valuable insights into EVs biology to develop innovative strategies for the treatment of GBM and PDAC based on them as drug delivery systems.

RESUMEN

Los cánceres difíciles de tratar, como el glioblastoma (GBM) y el adenocarcinoma ductal pancreático (PDAC), se caracterizan por su agresividad y su resistencia a las terapias convencionales. A pesar del tratamiento estándar, que incluye la resección del tumor seguida de quimioterapia y radioterapia, los pacientes tienen un mal pronóstico. Por lo tanto, es necesario desarrollar nuevos enfoques terapéuticos. En este sentido, el uso de vesículas extracelulares pequeñas como sistemas de administración se ha convertido en una herramienta prometedora para el tratamiento del cáncer. Este sistema puede administrar fármacos anticancerígenos directamente a las células tumorales, mejorando la eficacia del tratamiento. En este trabajo, utilizamos pequeñas vesículas extracelulares cargadas con fármacos para inverstigar su especificidad sobre sus células progenitoras y, si son adecuadas para el tratamiento del cáncer. Además, estudiamos el interactoma de PADI4 y su capacidad de citrulinación, su relación con la progresión del cáncer y su papel como diana para la terapia del cáncer. La presente tesis doctoral, se estructura como un compendio de seis artículos publicados en revistas de alto impacto (Q1) que se corresponden con cada capítulo y, un capítulo de datos pendientes de publicación.

En el Capítulo 1, analizamos cómo las EVs desempeñan un papel crucial en la comunicación intercelular y han surgido como posibles biomarcadores y herramientas terapéuticas, especialmente en el cáncer. Además, revisamos la importancia de las EVs como biomarcadores en varios tipos de cáncer. Exploramos igualmente el desarrollo de EVs quiméricas que pueden conjugarse con nanopartículas, biomoléculas y fármacos contra el cáncer, mostrando su potencial para la terapia dirigida del cáncer. La revisión también ofrece una visión general de los ensayos clínicos en curso que utilizan EVs para mejorar el pronóstico de diferentes tipos de cáncer, haciendo hincapié en el potencial de las terapias basadas en EV para combatir estas enfermedades difíciles de tratar.

En el Capítulo 2, realizamos el aislamiento y la caracterización de EVs derivadas de líneas celulares de pacientes con GBM. Cargamos estas EVs con los fármacos temozolomida (TMZ) y EPZ015666 y observamos que una cantidad mínima del fármaco es suficiente para afectar a las células tumorales cuando se carga en EVs. Además, las EVs derivadas de GBM cargadas con los fármacos mostraron potencial para inducir un efecto antiproliferativo en células de cáncer de páncreas. Estos resultados apoyan el uso de EVs derivadas de GBM como una prometedora herramienta de administración de fármacos para el desarrollo preclínico y clínico de tratamientos contra el GBM.

En el Capítulo 3, aislamos y caracterizamos EVs derivadas de una línea celular de PDAC denominada RWP-1. Cargamos estas EVs con dos fármacos quimioterapéuticos, TMZ y

EPZ015666 mediante el método de incubación directa, que demostró ser el método de carga más eficaz, requiriendo una dosis mínima de fármaco para afectar a las células tumorales. El efecto antiproliferativo se probó en diferentes líneas celulares de cáncer, revelando una mayor eficacia de RWP-1 *small* EVs^{TMZ} en comparación con RWP-1 *small* $EVs^{EPZ015666}$. Estos resultados ponen de manifiesto el potencial de las EVs derivadas de RWP-1 como un sistema prometedor de administración de fármacos para el tratamiento del PDAC.

En el Capítulo 4, identificamos la expresión y localización de PADI4, una proteína dependiente de Ca^{2+} implicada en la conversión de arginina en citrulina, en varias líneas celulares de cáncer, incluyendo GBM (GB-39), y cáncer de páncreas (RWP-1). Además, estudiamos su relación con p53. La caracterización mediante inmunofluorescencia (IF) reveló diferentes localizaciones subcelulares de PADI4 en función de la línea celular. En el Westen Blot (WB) observamos diferentes patrones de la proteína, revelando la posibilidad de que PADI4 pudiera experimentar splicing alternativo. Estos hallazgos arrojan luz sobre el papel funcional de PADI4 en el desarrollo del cáncer.

En el Capítulo 5, identificamos la expresión de PADI4 en líneas celulares de GBM mediante WB. Además, investigamos si GSK484, un conocido inhibidor de PADI4, podría tener un efecto sobre la proliferación de células de GBM y PDAC. Por último, probamos si GSK484 cargado en EVs tenía un mayor efecto sobre la proliferación celular que la administración del fármaco solo. Nuestros resultados indicaron que la expresión de PADI4 era diferente entre varias líneas celulares cancerosas. Además, GSK484 disminuyó eficazmente la proliferación de las líneas celulares de GBM y PDAC cuando se cargó en EVs, con una concentración mínima del fármaco.

En el Capítulo 6, analizamos la interacción entre NUPR1 y PADI4 en líneas celulares de GBM. Los experimentos *in vitro* e *in cellulo* revelaron una fuerte afinidad de unión entre NUPR1 y PADI4 en el núcleo, lo que sugiere que el complejo NUPR1/PADI4 puede ser esencial en la reparación del ADN, la promoción de metástasis o la citrulinación de otras proteínas. Estos resultados ponen de manifiesto la importancia de su interacción y su papel como posible diana para la terapia del cáncer.

Por último, en el Capítulo 7, identificamos la interacción entre PADI4 y MDM2. En este trabajo, el complejo PADI4/MDM2 se encontró en el núcleo y en el citoplasma de diferentes líneas celulares de cáncer. Además, el tratamiento con GSK484 impidió la unión de estas dos proteínas, lo que sugiere que MDM2 se une al sitio activo de PADI4. La interacción entre MDM2 y PADI4 puede conducir a la citrulinación de MDM2, que podría ser una diana terapéutica para el tratamiento del cáncer.

Esta tesis ha expuesto el uso potencial de las EVs derivadas de células cancerosas de tumores difíciles de tratar como un nuevo enfoque terapéutico para el tratamiento de GBM y PDAC. Al cargar estas EVs con fármacos terapéuticos, como TMZ, EPZ015666 y GSK484, mejoramos la eficiencia de administración del fármaco, lo que podría reducir los efectos secundarios asociados a las terapias convencionales. Además, exploramos el papel de PADI4 en GBM y PDAC. Al dilucidar las interacciones entre PADI4 y otras proteínas, descubrimos posibles mecanismos implicados en la progresión del cáncer e identificamos nuevas vías para el desarrollo de terapias dirigidas. Este trabajo sienta las bases de futuros enfoques médicos personalizados y proporciona información valiosa sobre la biología de las EVs para desarrollar estrategias innovadoras en el tratamiento de GBM y PDAC basadas en estas como sistemas de administración de fármacos.

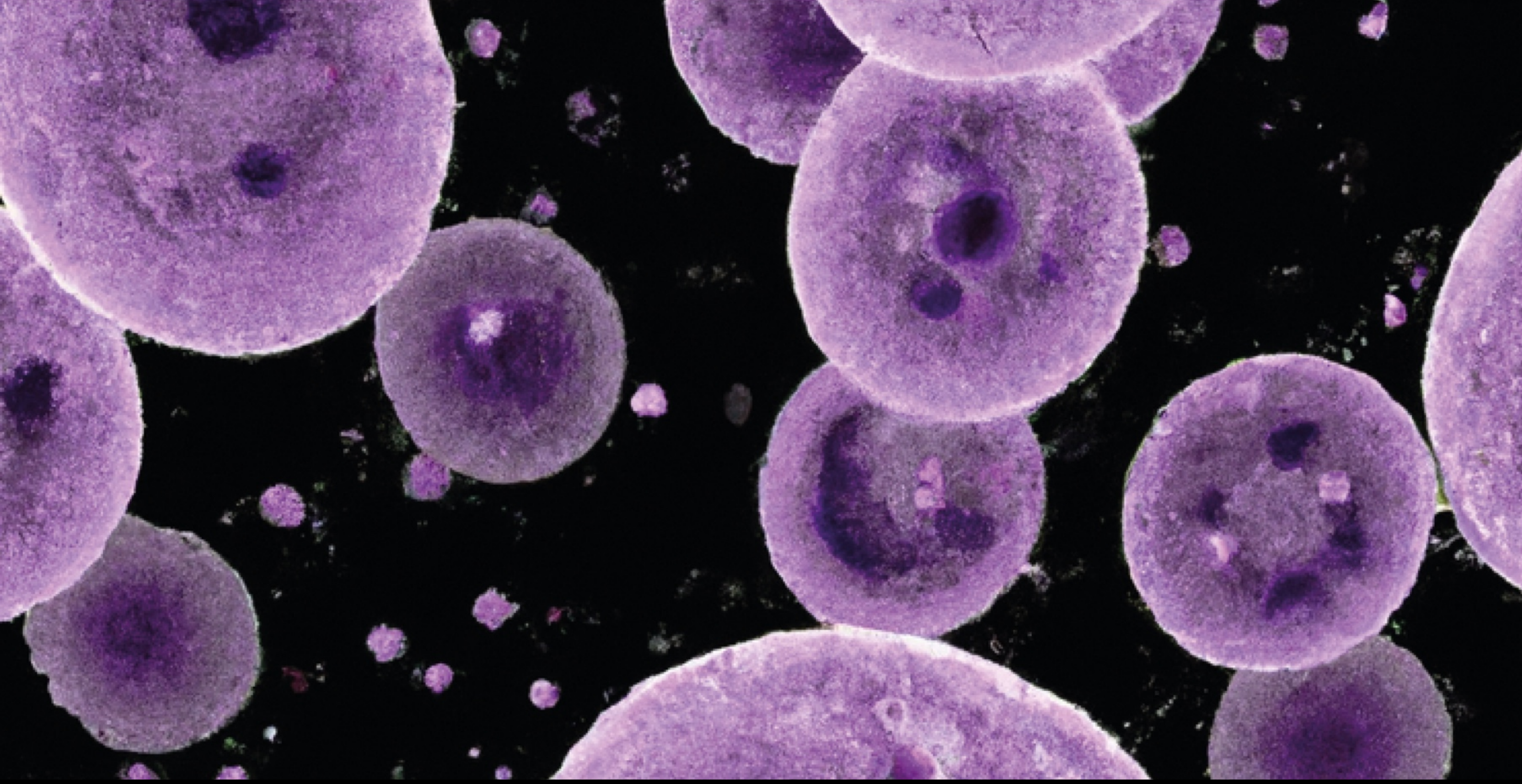

INTRODUCTION

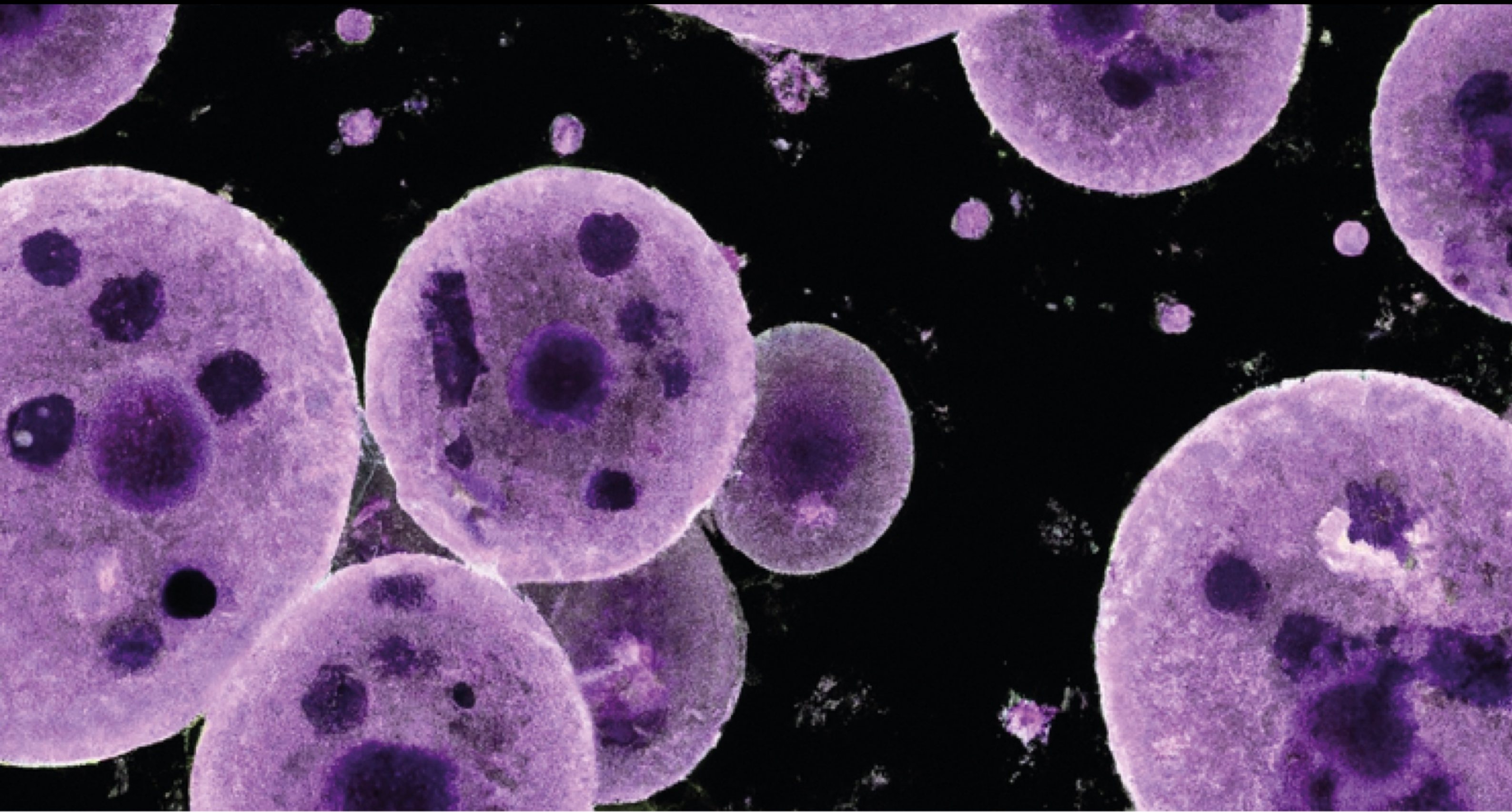

1. Introduction

1.1 Cancer

1.1.1 Definition and Epidemiology

A malignant neoplasm or cancer is described by Willis (1960) as “an abnormal mass of tissue, the growth of which exceeds and is uncoordinated with that of the surrounding normal tissues, and persists in the same excessive manner after cessation of the stimuli which caused the change” [1]. The term "cancer" refers to a collection of diseases that develop when the body's aberrant cells multiply and spread out of control, frequently producing tumors or invading other tissues. These cells can also metastasize, or spread to other parts of the body via the bloodstream or lymphatic system, causing further damage and potentially life-threatening complications [2]. Cancer can affect any part of the body and may be caused by a variety of factors, including genetic mutations, environmental exposures, and lifestyle choices. In 2011, Hanahan, D., & Weinberg published the hallmarks of cancer that include, autonomous cell proliferation, insensitivity to antiproliferative signals, evasion of destruction by the immune system, stimulation of inflammation, resistance to cell death, replicative immortality, induction of angiogenesis, activation of tissue invasion and metastasis, reprogramming of energy metabolism, and genomic instability and mutation (Figure 1) [3]. These common characteristics of cancer disease make it a severe pathology that encourages the development of novel anti-cancer treatments.

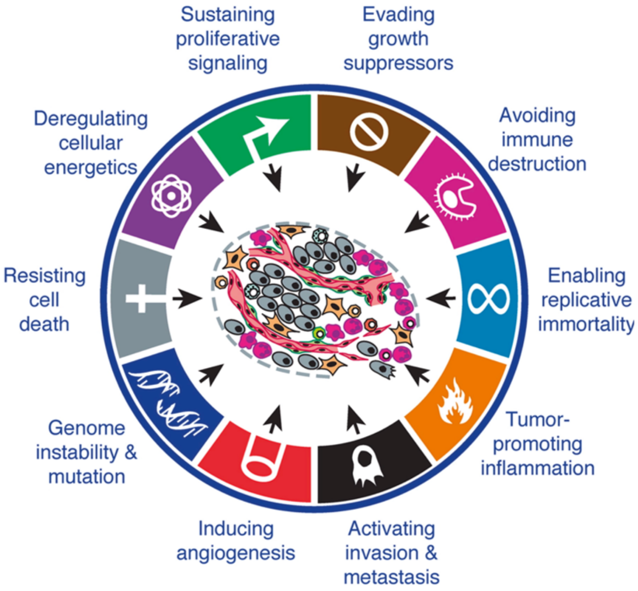

Figure 1. Hallmarks of cancer. Adapted from Hanahan, D., & Weinberg (2011) [3].

In general, the different types of cancers are named by the organ where they originated. According to the National Institutes of Health (NIH), the types of cancer are: **carcinoma**, neoplasm of epithelial origin, 80-90 % of cancer cases; **sarcoma**, malignant tumor originating in connective tissues, including bones, cartilage, fat, muscles, tendons, and bones; **myeloma**, starts in the bone marrow's plasma cells; **leukemia** or "blood cancers" also originated in the bone marrow and correlated with an overproduction of immature white blood cells; and **lymphoma**, grows in the lymphatic system's glands or nodes [4].

In 2021, Sung *et al.* resumed the GLOBOCAN statistics which estimated 19.3 million new cancer cases and almost 10.0 million cancer deaths. With an expected 2.3 million new cases (11.7 %), female breast cancer has surpassed lung cancer as the most often diagnosed malignancy. Lung (11.4 %), colorectal (10.0 %), prostate (7.3 %), and stomach (5.6 %) cancers are next in line (Figure 2A). With an expected 1.8 million deaths (18 %), lung cancer remained the most common type of cancer death. It was followed by colorectal (9.4 %), liver (8.3 %), stomach (7.7 %), and female breast (6.9 %) cancers (Figure 2B) [5].

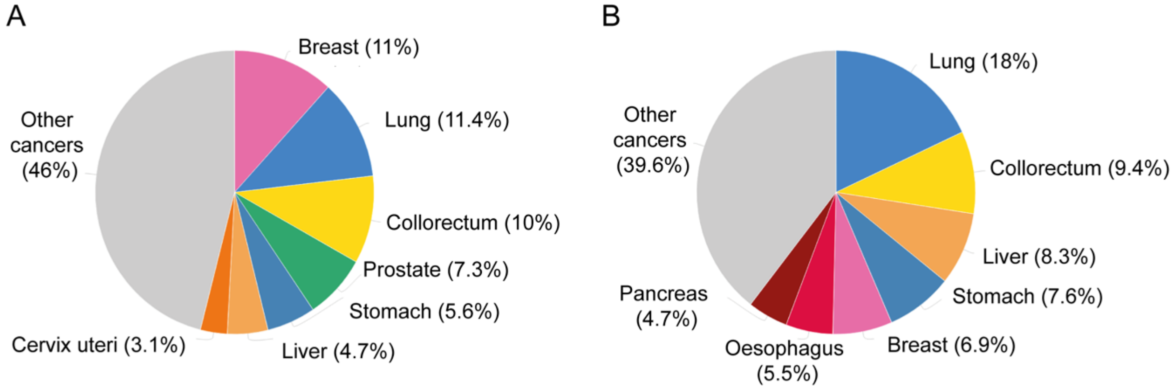

Figure 2. Epidemiology of cancer in the World. (A) New cases reported. (B) Mortality rate. Source GLOBOCAN (2020) [6].

In Spain, colorectal cancer (14.3 %) was the most common cancer, followed by prostate (12.3 %), breast (12.1 %), lung (10.3 %), bladder (6.6 %), kidney (3 %), and pancreatic (2.9 %) cancer (Figure 3A). Besides, the type of cancer causing the highest rate of death was lung cancer (18 %), followed by colorectal (14.6 %), pancreas (6.7 %), breast (5.8 %), prostate (5.1 %), liver and bladder (4.9 %), stomach (4.7 %), leukemia (3.3 %) and brain and central nervous system (CNS) cancers (2.9 %) (Figure 3B). It is important to mention that despite the fact that brain and CNS cancers appear within the statistics of mortality rate, they are not in the graph of new cases reported, and this is because they are considered in the "other cancers" category.

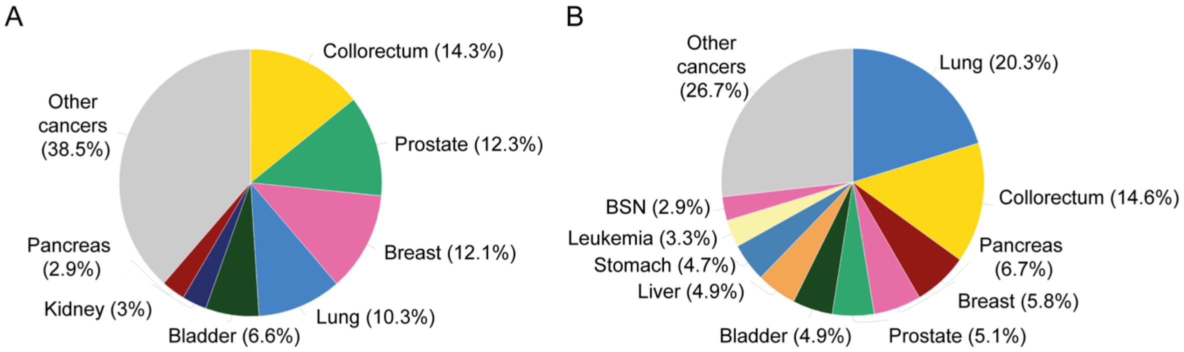

Figure 3. Epidemiology of cancer in Spain. (A) New cases reported. (B) Mortality rate. Source GLOBOCAN (2020) [6].

1.1.2 Hard-to-treat cancers

The term "hard-to-treat cancers" is not a formal scientific term, but sometimes is used by researchers to refer to cancers that are particularly challenging to manage or treat due to their resistance to standard therapies or other unique characteristics. However, it is important to note that different cancer types can have diverse characteristics and responses to treatments, so the term "hard-to-treat" can be somewhat subjective and variable depending on the specific cancer type and patient population.

The most common types of cancer that are englobed under this term are pancreatic ductal adenocarcinoma (PDAC) and glioblastoma (GBM). Additionally, malignant pleural mesothelioma, gallbladder, oesophagus, liver and bile ducts, lung and bronchus, colorectal, and gastric cancer are also been included. All these cancer types are very resistant to therapy, have aggressive growth, and show late-stage diagnoses. These cancers often have a poor prognosis and require more intensive or specialized treatments than other types of cancer [7–9]. As it is mentioned in Table 1, the 5-year survival rate for GBM is 5.7 %, and for PDAC 10.9 %, having GBM the worst rate. Besides, over the years, there hasn't been much improvement in the survival rate.

Table 1. The hard-to-treat cancers survival rate

Cancer type	5-year survival rate (2017) %	Average absolute change (2006-2017)
Glioblastoma	5.7	0.1
Pancreatic	10.9	0.6
Pleural mesothelioma	11.5	0.3
Gallbladder	19.4	0.4
Oesophagus	19.9	0.4
Liver and bile ducts	20.3	0.7
Lung and bronchus	21.7	0.5

Source https://seer.cancer.gov/

In addition to the features mentioned above, it is important to point out that surgical resection of GBM is difficult because of its ill-defined borders and the blood-brain barrier prevents drugs from reaching the tumor. Their fibrous outer layers make difficult the pass/penetration of the drugs in pancreatic and mesothelioma cancers.

The term "hard-to-treat cancers" is going to be used throughout this work to refer to GBM and PDAC types and the unique difficulties associated with their treatment. This thesis also discusses new as well as potential therapeutic approaches for these challenging cancers.

1.2 Glioblastoma

1.2.1 Epidemiology

GBM is the most aggressive cancer of brain origin, representing 14.5 % of all malignancies in the CNS [10]. According to GLOBOCAN, 308 102 new cases of brain and CNS cancers were diagnosed and 251 329 deaths occurred in 2020 (Figure 4), being only 15 months the median overall survival for GBM patients [11], which is probably attributed to late diagnosis and treatment limitations.

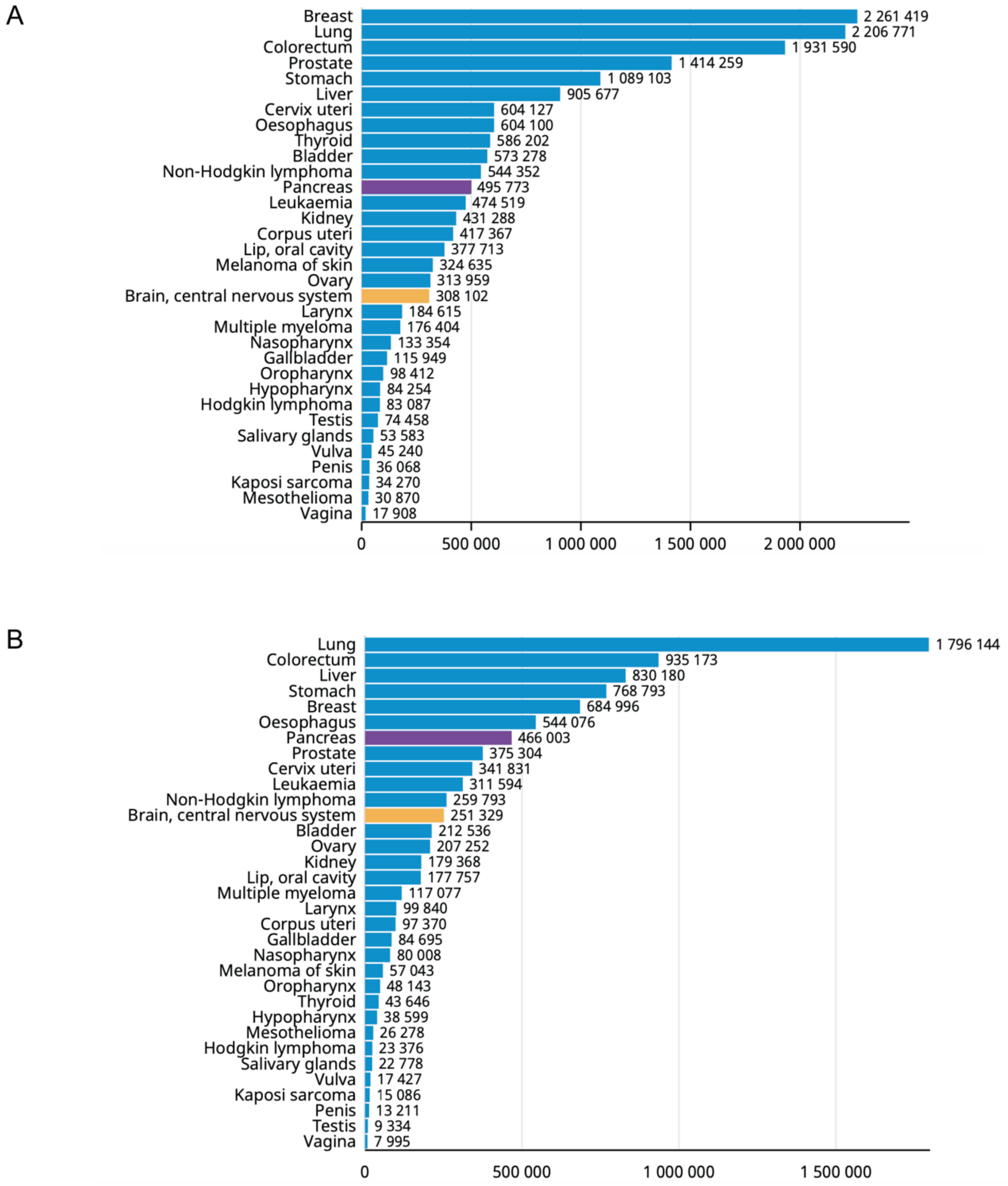

Figure 4. Number of worldwide cases of different types of cancer. (A) Number of new cases in 2020 regarding both sexes and all age ranges. (B) Number of deaths in 2020 regarding both sexes and all range ages. The yellow bar highlights the brain and central nervous system, and the purple bar highlights the pancreas data. Source GLOBOCAN (2020) [6].

According to the World Health Organization (WHO), GBM corresponds to isocitrate dehydrogenase (IDH)-wildtype grade 4 and is mainly present in adults [12]. The 2021 new classification WHO of gliomas, represented in Figure 5, includes the key proteins and genes that are analyzed for diagnostic CNS alterations using molecular diagnostics.

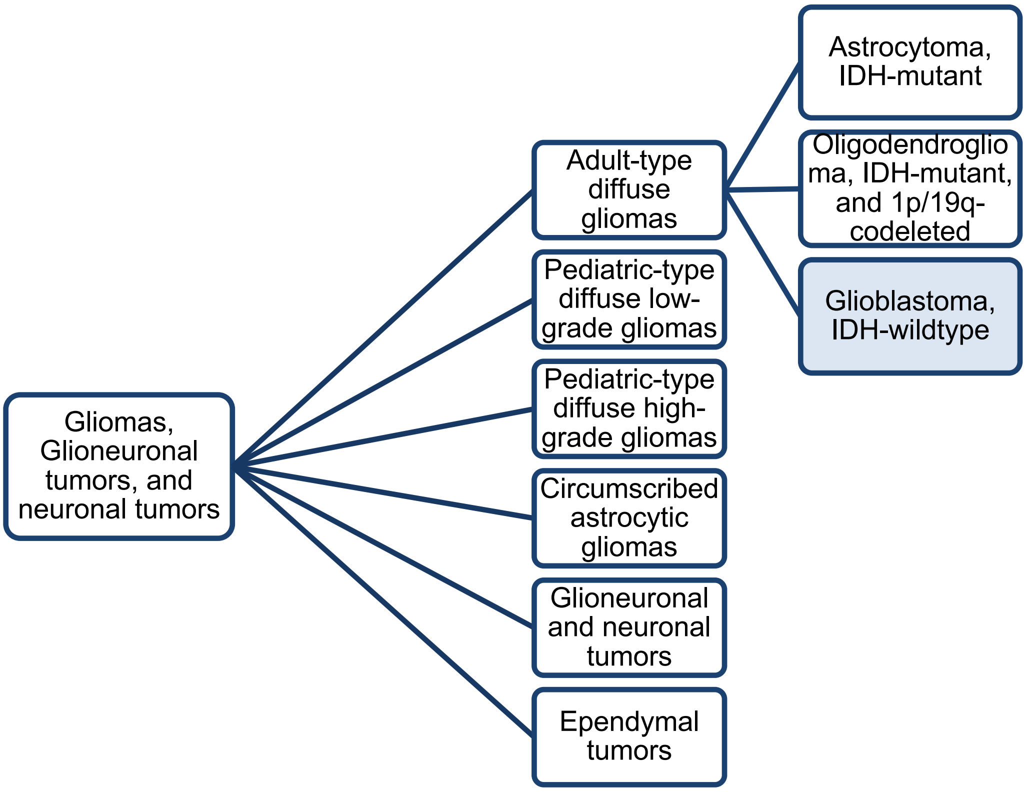

Figure 5. Gliomas classification from WHO 2021 [12].

The genetic characteristics that are analyzed for GBM diagnosis and required for its integration in CNS tumor classification are IDH-wildtype, telomerase reverse transcriptase (TERT) promoter mutation, +7/−10 chromosome copy number changes, and epidermal growth factor receptor (EGFR) gene amplification [12]. Additionally, to these criteria, histopathological grading, microvascular proliferation or necrosis, and any one of the five conditions previously described must be included in order to classify an IDH-wildtype diffuse astrocytic glioma as GBM [13,14]. GBM can be also divided into four subtypes based on their molecular signatures: proneural (PN), neural (NL), classical (CL), and mesenchymal (ME) [15].

1.2.2 Anatomy of the brain and GBM

The CNS is composed of the brain and spinal cord. The brain is the most complex organ in the human body. This organ controls all body functions, being the center of intelligence, the translator of the senses, the starter of bodily motion, and the behavior controller. The brain consists of three main parts: the cerebrum, cerebellum, and brainstem. In humans, the cerebrum is divided into four sections called lobes, that control specific functions: frontal lobe, parietal lobe, temporal lobe, and occipital lobe (Figure 6A).

The majority of GBMs spread into the subventricular zone (SVZ) surrounding the white matter of the brain (Figure 6B). Recently, the presence of certain biomarkers such as O^6-methylguanine-DNA methyltransferase (MGMT), phosphatase and tensin homolog (PTEN), isocitrate dehydrogenase 1 (IDH1), and EGFR, has been correlated with tumor localization. Therefore, in young patients, it has been shown that tumors with MGMT promoter methylation occur in the left temporal lobe, and tumors with PTEN loss occur most frequently in the frontal lobe. The left frontal lobe is where most tumors with MGMT methylation and IDH1 mutation were found. In the left temporal lobe, most of the tumors with amplified EGFR and EGFR variant 3 were located. A positive response to radiotherapy and improved survival were correlated to the left temporal lobe. In Figure 6B, the representation of the stratification of GBM tumor location by age shows a high incidence in the frontal lobe in younger patients (a) in contrast to the high incidence in more posterior regions in older patients (b) [16].

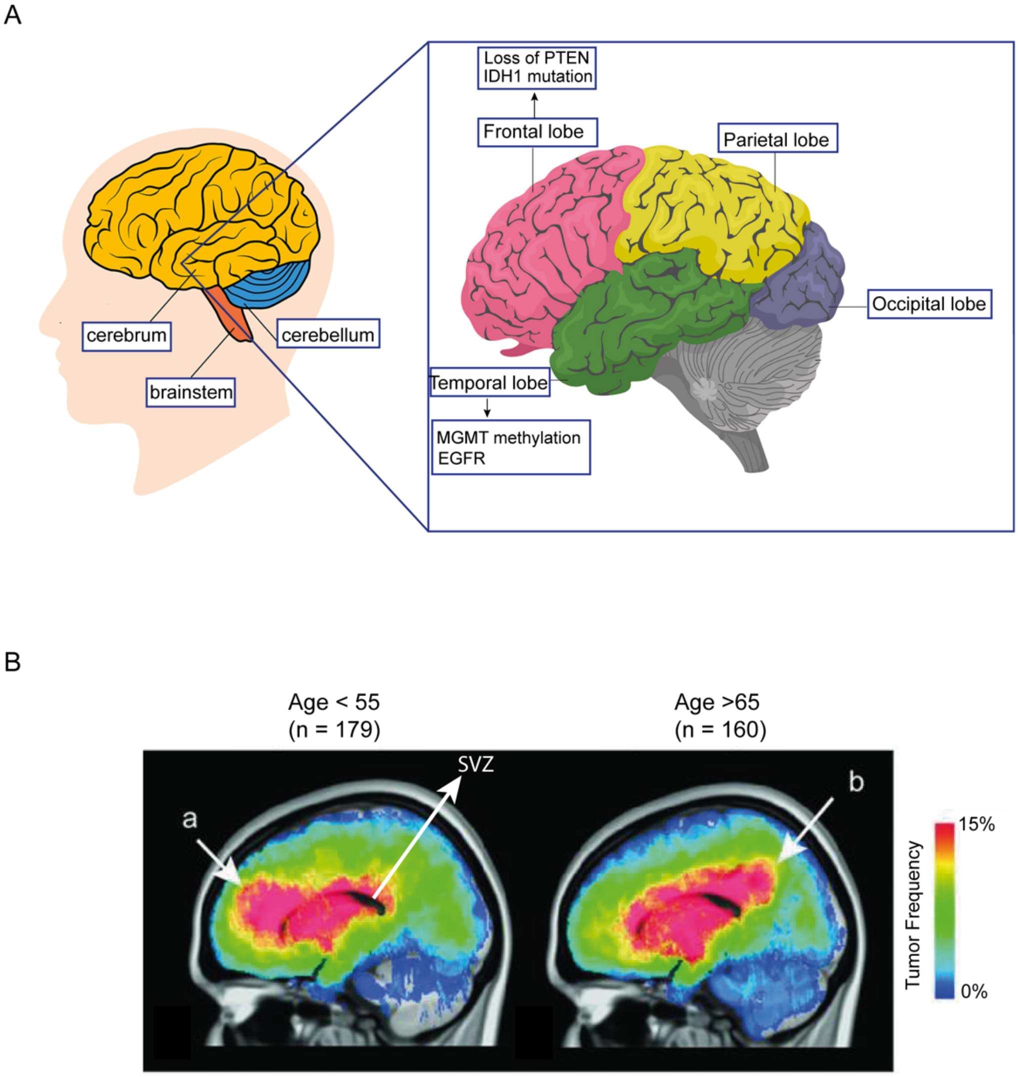

Figure 6. Anatomy of the brain and GBM localization. (A) Anatomy of the brain and localization of prevalent biomarkers. Adapted from Johns Hopkins Medicine (2023) [17]. (B) GBM location by patient age. MGMT, O^6-methylguanine-DNA methyltransferase; PTEN, phosphatase and tensin homolog; IDH1, isocitrate dehydrogenase 1; EFGR, epidermal growth factor receptor; SVZ, subventricular zone. Source Ellingson *et al.* (2013) [16].

1.2.3 Risk factors

The most commonly affected population by GBM is older adults over 50 years old. Familial gliomas are reported in only 5 % of the cases while the majority of cases occur in people who have no family history of the disease [18,19]. Retinoblastoma protein activity and cancer stem cell function variations are related to the higher incidence of GBM in men [20]. Although gender does not influence the incidence of IDH1 mutation in GBM, several studies indicated that in men with GBM, the TERT promoter mutation was increased [21–23]. As mentioned before, age is a risk factor, and it is related to IDH mutation. Young GBM patients (18 to 45) have IDH1 mutations more frequently than older patients (age ≥ 70), and p53 mutation is more frequent in older patients [24]. In addition, obesity is associated as a risk factor for many cancers, including endometrial, kidney, and esophageal cancer [25]. It has been established that having an abnormally high body mass index (BMI) at the age of 18, increases the incidence of developing GBM later in life [26]. A BMI > 30 increased the incidence of GBM, each extra kilogram of weight in the overweight raised the chance of glioma by 4 % [27]. Besides, several studies demonstrate that the incidence of GBM is correlated with growth, one of the studies revealed that for every 5 cm of height additional in men, the risk of GBM increased by 8 %, but only by 4 % in women [28].

1.2.4 GBM biomarkers

The most significant molecular biomarkers related to GBM are platelet-derived growth factor receptor A (PDGFRA) amplification, IDH mutation, MGMT promoter methylation, EGFR, neurofibromin 1 (NF1) mutation, vascular endothelial growth factor (VEGF), murine double minute 2 homolog (MDM2) amplification, TERT promoter mutation, p53 mutation, and PTEN mutation, among others [29–31]. The main objective of the study of these biomarkers is to identify potential strategies for tumor growth prevention and disease treatment. The most representative GBM biomarkers are described in Table 2.

Table 2. GBM biomarkers and functional significance

Biomarker	Source and Importance	Functional Significance
IDH	Source: tissue biopsy Diagnostic and prognostic biomarker	IDH modifications produce oncometabolite, 2-hydroxyglutarate (2-HG), leading to DNA hypermethylation. Consequently, tumorigenesis occurs.
EGFR	Source: tissue biopsy Diagnostic and prognostic biomarker	GBM tumor cells are altered by EGFR overexpression and mutation via the RTK/RAS/PI3K, SOX9, or FOXG1 pathways.
p53	Source: tissue biopsy Prognostic biomarker	Promote tumorigenesis by controlling isoprenoid or mevalonate pathways. Inactivated and degraded by MDM2.
MGMT	Source: biopsy by taking sample of non-necrotic GBM tissue. Prognostic and predictive biomarker	In comparison to nonmethylated MGMT promoter, methylated MGMT promoter provides better prognostic outcomes when combined with therapy (chemotherapy with TMZ and radiotherapy).
Loss of 10q	Source: tissue biopsy Prognostic biomarker	It leads to the deletion of tumor suppressor genes such as p53, NF1, and PTEN.
Circulating tumor cells	Source: body fluids such as blood Prognostic biomarker	It facilitates the distinction of the GBM molecular subtypes.
PDGFRA	Source: tissue biopsy Prognostic biomarker	GBM treatment is supported by an increase and modification of PDGFRA. Also facilitates the distinction of the GBM molecular subtypes.
NF1	Source: tissue biopsy Diagnostic biomarker	GBM mesenchymal subtype contained the most frequent number of mutations in NF1 [32].
VEGF	Source: blood Potentially prognostic biomarker	Potential indicator of therapy response for anti-angiogenetics [33].
MDM2	Source: tissue biopsy Potentially prognostic biomarker	Amplification and overexpression of MDM2 may be an alternative molecular mechanism by which a subset of human malignant gliomas escapes from p53-regulated growth control [34].
TERT	Source: blood Diagnostic and prognostic biomarker	Mutations in the TERT promoter have been associated with decreased overall survival [35].
PTEN	Source: tissue biopsy and plasma. Prognostic biomarker	PTEN loss or inactivity has been associated with the resistance of GBM to targeted EGFR inhibitors, and it is considered to be the main oncogenic factor causing GBM [36].

Adapted from Jadoon *et al.* (2022) [37].

1.2.5 GBM treatment

The standard therapeutic approach for GBM patients is tumor resection followed by radiotherapy and coadjuvant chemotherapy with TMZ (3,4-dihydro-3-methyl-4-oxoimidazo-[5,1-d]-astetrazine-8-carboxamide), usually known as Stupp protocol [38,39]. TMZ is a DNA alkylating compound that acts on the methylation of guanine and adenine bases, breaking double-stranded DNA, inducing cell cycle arrest and apoptosis [40]. TMZ treatment has some limitations such as a short half-life, the need of high doses to reach therapeutic levels, and a significant number of side effects like headache, fatigue, loss of appetite, opportunistic infections, thrombocytopenia, moderate to severe lymphopenia, and abnormal low levels of white blood cells [41–44]. Furthermore, only 20 % of TMZ administered systemically reaches the brain [45].

Due to the disadvantages of TMZ against new therapeutic targets, other novel compounds had been studied for cancer treatment. Recently, an arginine methyltransferase-5 (PRMT5) inhibitor has been identified as a potential target in cancer therapy. It catalyzes the transfer of two methyl groups to arginine residues, modulating the biological function of target proteins and, maintaining homeostasis in both healthy and cancer cells [46,47]. Since PRMT5 is overexpressed in GBM and other malignancies [48], and this overexpression has been correlated with poor patient prognosis [47], we have studied a specific inhibitor (EPZ015666) in this work. EPZ015666 competes with the substrate-binding pocket of the PRMT5 peptide to prevent its interaction and posterior methylation, therefore it acts as a PRMT5 inhibitor [49].

GBM tumor microenvironment (TME) is composed of normal non-cancerous cells such as immune cells, astrocytes, endothelial cells, glioma stem-like cells, and other non-cellular components like the extracellular matrix [52]. The complexity of this TME, together with the recurrence of the tumor, its capacity to be resistant to chemotherapy, and the difficulty to reach the tumor zone, leads to the development of new therapeutic approaches to improve GBM treatment. In this sense, several biomaterials such as hydrogels, nanoparticles, microfibers, flexible patches, liposomes, and, small extracellular vesicles (EVs), had also been proposed to enhance the delivery of drugs for GBM therapy (Figure 7) [50]. Small EVs had been proposed not only as a biomarker but also as a drug delivery vehicle for GBM treatment [51]. In this work, we focus on small EVs as a drug delivery system for hard-to-treat cancer therapy.

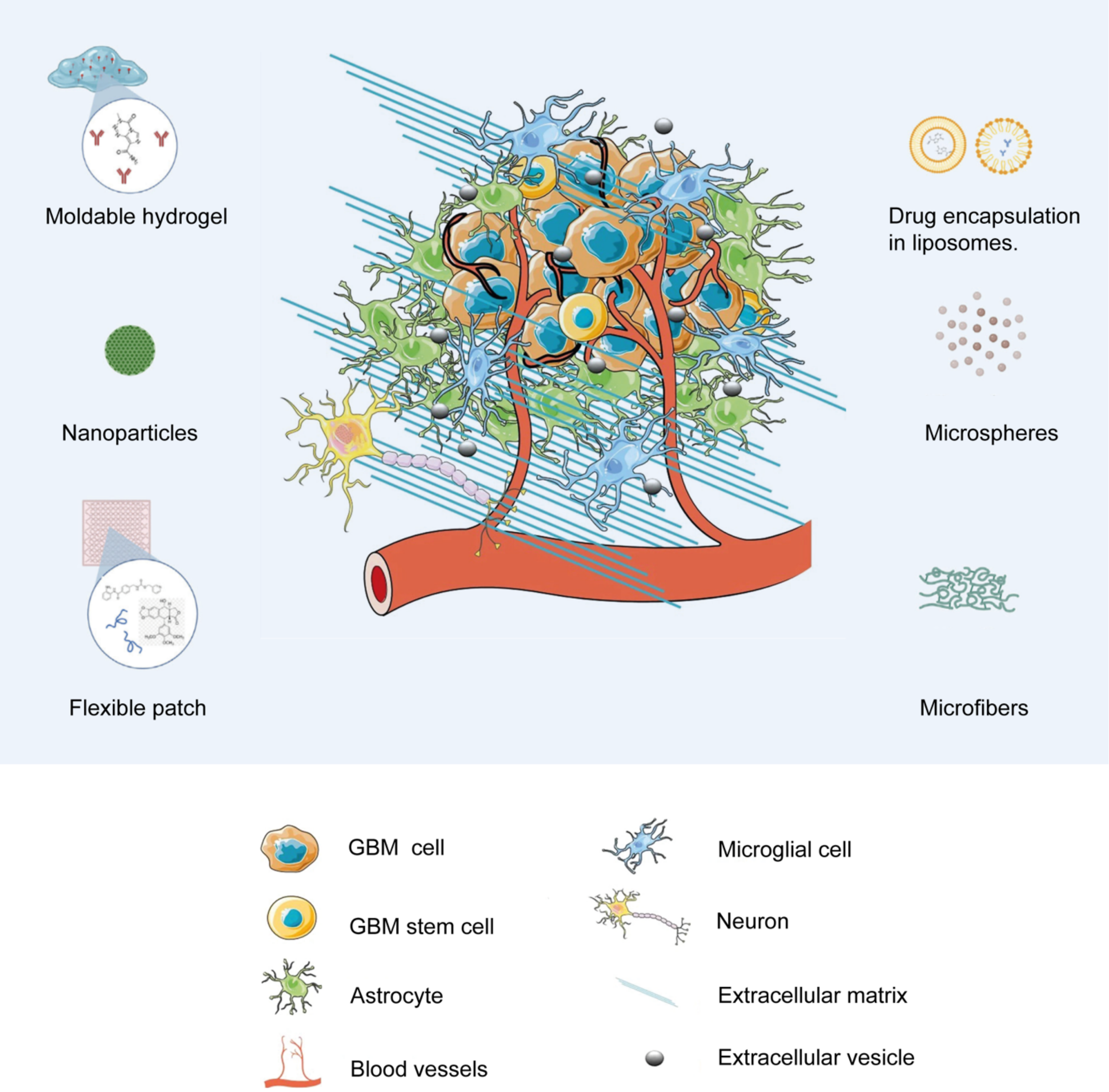

Figure 7. New treatment approaches for GBM. Biomaterials such as hydrogels, nanoparticles, microfibers, flexible patches, liposomes, and, small EVs can enhance the delivery of drugs for GBM treatment in the TME. GBM, Glioblastoma. Adapted from Aguilera-Márquez *et al*. (2022) and Simon *et al*. (2020) [50,51].

1.3 Pancreatic cancer

1.3.1 Epidemiology

The most frequent and aggressive type of cancer in the pancreas is PDAC, which constitutes more than 90 % of all pancreatic tumors. This type of cancer, which develops in the exocrine compartment, is highly aggressive and lethal [53], with a 5-year survival rate of less than 10 % of the cases. By 2025, it is expected to become the third cause of cancer-associated mortality. People over the age of 70 have the highest incidence of pancreatic cancer [5].

According to GLOBOCAN, in 2020, 495 773 new cases of pancreatic cancer were diagnosed and 466 003 deaths occurred (Figure 4). The incidence is higher in men than in women and represents the seventh leading cause of cancer death in both sexes. Europe, North America, and Australia/New Zealand have the biggest incidence rates of this cancer [5].

Pancreatic cancer can be divided into two groups according to the pancreatic component that is affected, exocrine pancreatic cancer and neuroendocrine pancreatic cancer. Exocrine pancreatic cancer is divided into **ductal adenocarcinoma**, squamous cell carcinoma, adenosquamous carcinoma, and colloid carcinoma. According to the WHO Classification of Tumors of the Digestive System (2019), it can be also classified as represented in Figure 8 [54].

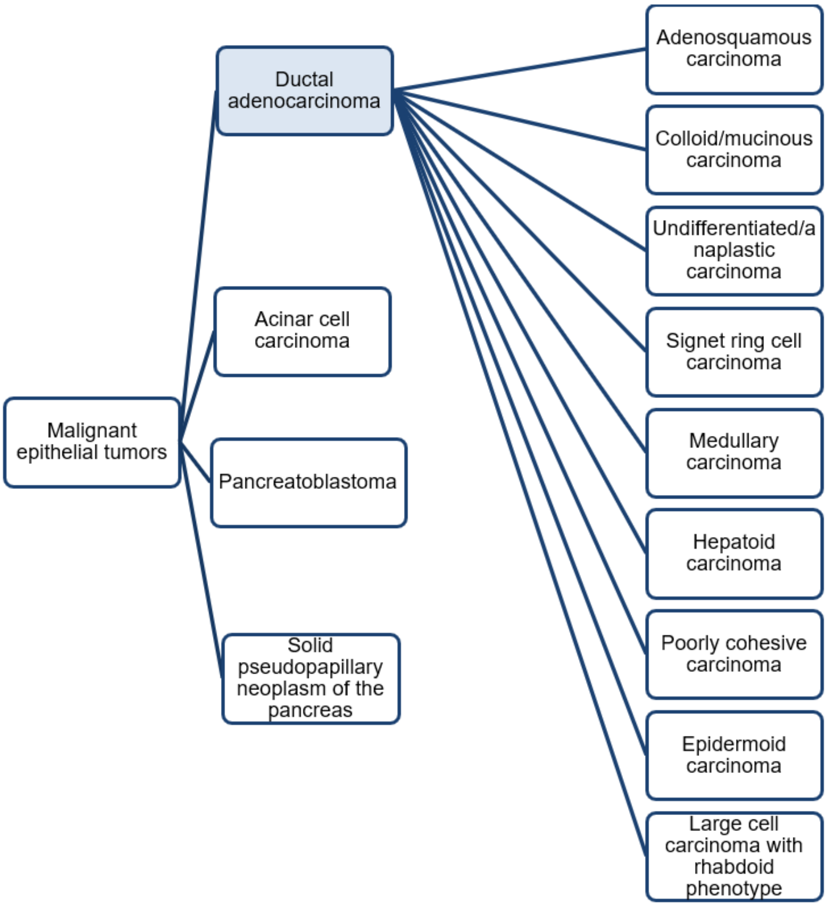

Figure 8. Pancreatic cancer classification from WHO (2019) [54]

1.3.2 Anatomy of the pancreas and PDAC

The pancreas is a long, tapering organ that lies across the back of the stomach. It is divided into four parts: head, neck, body, and tail (Figure 9A), and has two types of glands, exocrine and endocrine. The exocrine pancreas secretes digestive enzymes into the ducts that join the main pancreatic duct. The endocrine pancreatic system is formed by the islets of Langerhans, which produce hormones that are released into the bloodstream [55].

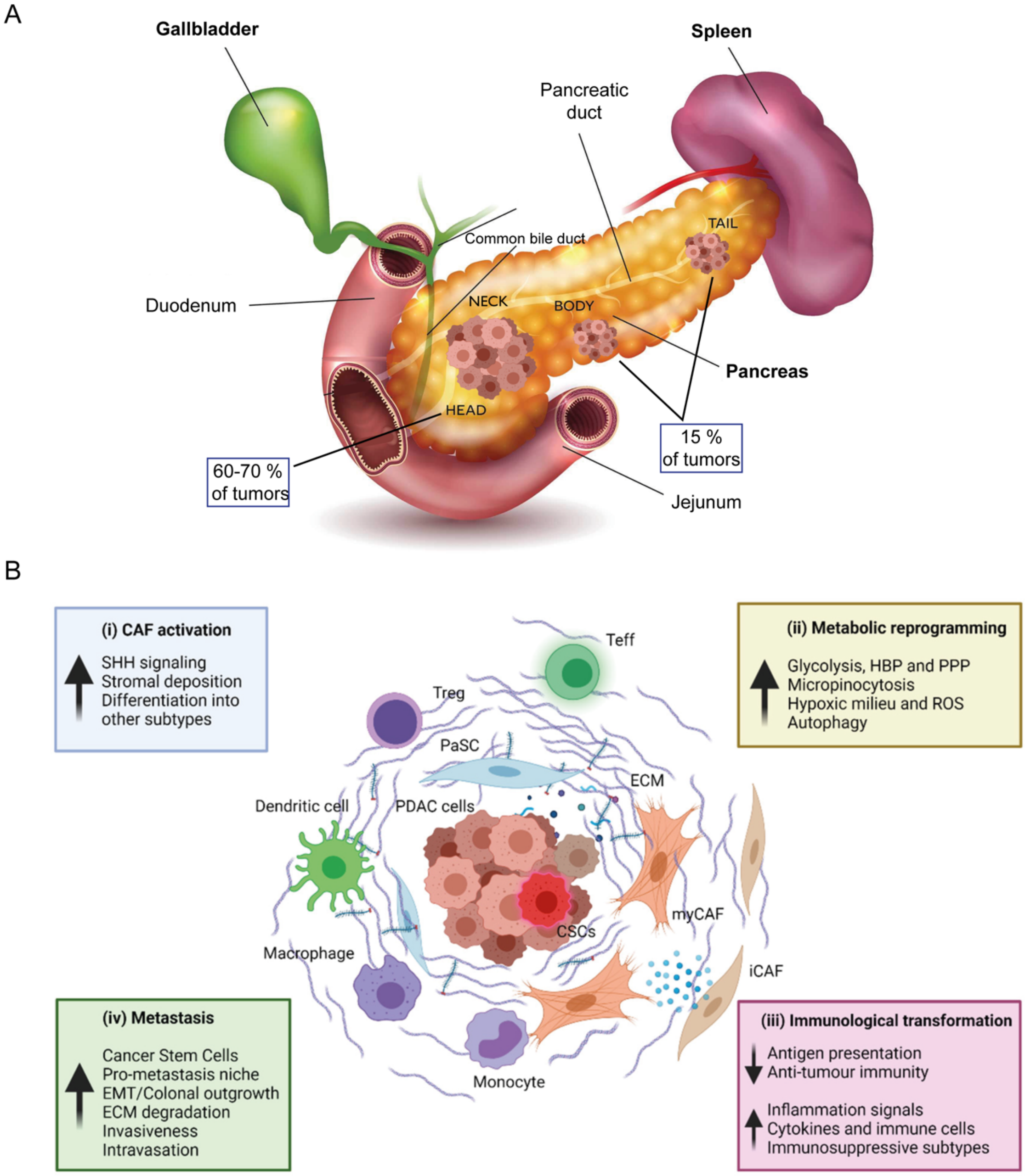

Figure 9. Pancreas and PDAC biology. (A). Pancreas anatomy and PDAC localization. Adapted from Johns Hopkins Medicine (2023) [56]. (B) PDAC microenvironment. Source Truong *et al*. (2021) [57]. Treg, regulatory T cell; Teff, effector T cell; PaSC, pancreatic stellate cells; PDAC, pancreatic ductal adenocarcinoma; EMC; extracellular matrix; myCAF, myofibroblastic cancer-associated fibroblast; iCAF, inflammatory cancer-associated fibroblast.

The development of PDAC begins when ductal or acinar cells go through metaplasia, dysplasia, and atypia after a driver mutation, often KRAS (95 %), is acquired. The development of further mutations such as p53 (60–70 %), CDKN2 (30–50 %), SMAD4 (20–50 %); BRCA 1–2 (4–7 %), ATM (2.3 %) and BRAF (1.4-3 %) leads to the expansion of invasive carcinoma and eventual metastasis, a process that could take up to 20 years [58]. There are several lesions that can develop into PDAC through the acquisition of additional mutations, including pancreatic intraepithelial neoplasia (PanIN), mucinous cystic neoplasm (MCN), and intraductal papillary mucinous neoplasm (IPMN). IPMNs are more frequently seen in the head of the pancreas and typically affect older men; MCNs are more commonly found in the body and tail of the pancreas, and frequently affect middle-aged women [59].

PDAC tumors are often localized in the head of the pancreas (60-70 %), and the most common symptoms are jaundice, cholangitis, and steatorrhoea. In the body and tail, the percentage is lower with 15 % of the cases, the most common symptoms are epigastric and back pain (Figure 9A). The prognosis of patients with body and tail PDAC is worse than for patients with head PDAC tumors [59,60].

As mentioned before, PDAC is a highly heterogeneous disease and its TME is composed of a variety of cells. The mutation/gene expression profiles of the tumor cells themselves vary, affecting the fibroblasts and immune cells in the surrounding tissue. In turn, the TME elements are involved in pro-tumor support interactions with tumor cells and their surrounding cells. The primary interactions in PDAC are (i) activation of cancer-associated fibroblasts (CAFs), (ii) metabolic reprogramming, (iii) immunological change, and (iv) metastasis-initiating events in the early stages of tumor development (Figure 9B) [57].

1.3.3 Risk factors

The evidence for risk factors for PDAC is weak and insufficient to explain its occurrence, therefore in about only 40 % of cases is possible to identify risk factors [61]. The main non-hereditary risk factors for pancreatic cancer are smoking, alcohol abuse, chronic pancreatitis, age (higher incidence in the range of 60-80 years old), obesity, and diabetes mellitus (being responsible for the development of approximately 30 % of the cases). On the other hand, several syndromes constitute hereditary risk factors: HBOC (hereditary breast and ovarian cancer syndrome), HNPCC (hereditary non-polyposic colorectal cancer or Lynch syndrome), FAP (familial adenomatous polyposis), PJS (Peutz–Jeghers syndrome), FAMMM (familial atypical multiple mole melanoma syndrome), hereditary pancreatitis and cystic fibrosis [61,62]. Besides, a diet too rich in animal fatty acids and carbohydrates raises the risk of PDAC development [63].

PDAC can be considered to be familial in approximately 10 % of the cases if two or more first-degree relatives have previously been diagnosed with the disease. Only a small percentage

(20 %) of familial PDAC cases have been connected to a known genetic syndrome or gene mutation [64]. Hereditary syndromes associated with familial pancreatic cancer include FAMMM related to the CDKN2A gene, hereditary breast, and ovarian cancer associated with BRCA1/BRCA2 (5 %), PJS with STK11 gene, PRSS1 gene of hereditary pancreatitis and HNPCC with MMR gene [65,66].

1.3.4 PDAC treatment

The standard therapeutic approach for PDAC patients is tumor resection (Whipple procedure) and adjuvant chemotherapy with Gemcitabine (Gem), however, the patient's health gets worse because of delayed diagnosis and a poor therapy response [67].

There are few chemotherapeutic choices available following tumor resection, especially in advanced stages, and only a small percentage of PDAC patients who have surgery can benefit from adjuvant chemotherapy. Gem is the first option treatment, then other drugs such as 5-fluorouracil with a median survival improvement of only a few weeks [68], or the combination of drugs such as leucovorin, irinotecan, oxaliplatin, and fluorouracil (FOLFIRINOX), also shows low efficacy in clinical trials [69–72]. Despite adjuvant therapy, recurrence rates are still high, with 69 to 75% of patients experiencing a relapse within two years [72].

As mentioned before, TMZ is a good alternative for treating a great number of solid tumors, including gliomas, GBMs, neuroendocrine tumors, melanoma, and sarcomas [73–80]. Nevertheless, due to its high cytotoxicity and minimal impact on patients, TMZ has not been considered a standard of care when used in a phase II study for advanced untreated pancreatic cancer [80]. On the other hand, the PRMT5 inhibitor EPZ01666 has been widely utilized to treat many cancers [49,81] and has been proved to control the splicing of detained introns in proliferation-associated genes in GBM [82]. Recent studies have revealed that in pancreatic cancer, PRMT5 is also a promising target whose inhibition sensitizes PDAC cells to Gem [83].

The limitations of PDAC therapy highlight the need for search of new therapeutic approaches that include, either more effective medicines, or more efficient drug delivery systems to reduce side effects. In order to improve the efficiency of chemotherapy and therefore the patient's condition, this work has investigated the improvement of drug therapy based on the use of small EVs and non-standard drugs.

1.4 Small Extracellular Vesicles

1.4.1 Definition and Types of small EVs

In 1946, Chargaff and West reported for the first time a “particulate fraction”, which was sedimented at 31 000 x *g* and had high clotting potential like a ‘thromboplastic protein’ [84]. However the first description of the presence of vesicles surrounding cells in mammalian tissues or fluids was observed in the late 1960s [85,86]. Since then, several groups reported the presence of vesicles first as "waste disposal" and then referred to them in cell-to-cell communication [87]. However, it was only in 2011 that the term "extracellular vesicles" (EVs) was suggested as a general term to describe all extracellular structures enclosed by lipid bilayers, coinciding with the establishment of the International Society for Extracellular Vesicles (ISEV) in the same year [88] (Figure 10A).

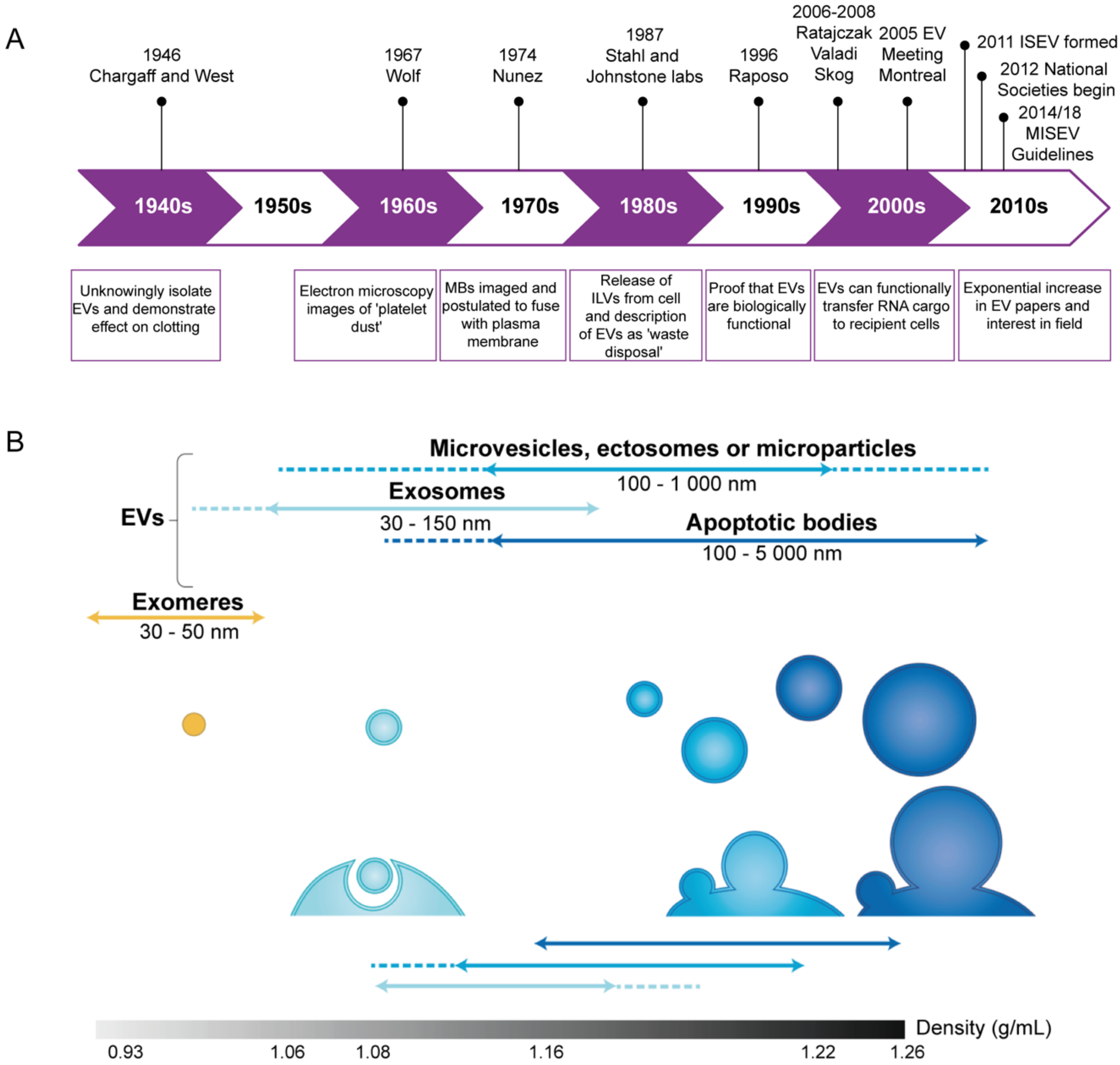

Figure 10. Timeline and physical features of the different EV subtypes. (A) Timeline of the more representative events in the EV field. Adapted from Couch *et al*. (2021) [87]. (B) Microvesicles, ectosomes, or microparticles have diameters between 100 - 1000 nm. Apoptotic bodies have a diameter of 100 - 5000 nm, overlapping with exosomes that have a size ranging from 30 to 150 nm. Exomeres are the smallest with 30 to 50 nm. EVs, extracellular vesicles. Adapted from Mathieu *et al*. (2019) [89].

EVs are mainly classified as exosomes (30–150 nm), microvesicles, ectosomes, or microparticles (MVs, 50–1000 nm), and apoptotic bodies (1–5 μm) (Figure 10B) [89]. The term “exosome” was first used by Johnstone *et al.* (1987), to describe that during reticulocyte maturation, the transferrin receptor was lost via the release of vesicles (exosomes) [90]. Nowadays, exosomes are defined as nanovesicles secreted by different cell types into the extracellular medium and formed in the endocytic compartments, the so-called multivesicular bodies (MVBs), during endosome maturation by inward budding of their membrane [91].

Nevertheless, the consensus recommendation of MISEV 2018 is that "exosomes" and other particles naturally released from the cell that is delimited by a lipid bilayer and cannot replicate, must be referred to as "small extracellular vesicles" because to date it is not possible to separate the smallest fraction of vesicles, and there is no consensus on specific markers for EV subtypes [92].

MISEV 2018 also provides the parameters for small EVs characterization, these may include two different but complementary techniques such as electron or atomic force microscopy and single particle analyzers (not electron microscope-based) [92]. The widely used techniques are Western blot (WB) to identify membrane proteins; Dynamic Light Scattering (DLS) or Nanoparticle Tracking Analysis (NTA), to measure small EV diameter; Field Emission Scanning Electron Microscope (FESEM) or Transmission Electron Microscope (TEM), to visualize its integrity, shape, and aggregation [93–96].

1.4.2 Biogenesis and secretion

The small EVs biogenesis is probably directly related to their physiological function and/or to the physiopathological state of the parent cell [89]. This biogenesis consists of four steps: cargo sorting to MVBs, MVB formation, transport of MVBs, and MVB-plasma membrane fusion. The MVBs formation is key in small EVs biogenesis, especially the intraluminal vesicles (ILVs) generation and the membrane budding [97,98]. Several mechanisms were proposed for ILVs generation, but the general mechanisms consist of the endosomal sorting complex required for transport (ESCRT)-dependent and ESCRT-independent pathways (Figure 11) [98].

The ESCRT-dependent pathway involves the generation of ILVs through the action of the ESCRT complexes (ESCRT-0, -I, -II, -III) [99]. These complexes mediate the inward budding of the endosomal membrane, leading to the formation of ILVs within MVBs, which are eventually released as small EVs upon the fusion of MVBs with the plasma membrane [100].

In the ESCRT-independent pathway, the tetraspanins and lipids play a crucial role. Small EVs are often enriched with cholesterol, sphingolipids, phosphatidylserine, and ceramide, a composition similar to that of lipid rafts of the membrane. Additionally, some small EVs proteins like flotillins, caveolins, and tetraspanins, are also components of the lipid rafts [101,102]. These lipid rafts have some functions in protein sorting, membrane curvature, and vesicle budding, so there is evidence that are related to small EVs formation and release [98].

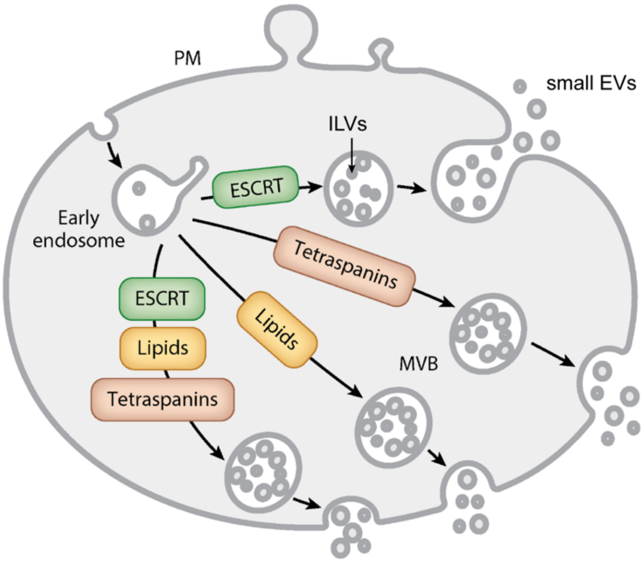

Figure 11. Small EVs biogenesis. The formation of ILVs of MVBs, and therefore small EVs, involves multiple pathways. Tetraspanins, ESCRT components, and lipids have all been identified; however, it is unknown if they can all act on the same MVB at the same time or whether some of them act in distinct MVBs. ILVs, intraluminal vesicles; MVBs, multivesicular bodies; ESCRT, endosomal sorting complex required for transport; PM, plasma membrane; EVs, extracellular vesicles. Adapted from Colombo *et al.* (2014) [103].

1.4.3 Small EVs cargo and function

Small EVs composition and cargo are directly related to their parental cell. They are surrounded by a phospholipid bilayer and contain messenger RNA (mRNA), microRNA (miRNA), long non-coding RNA (lncRNA), DNA fragments, and metabolites from their parental cells in addition to proteins, and lipids (Figure 12) [104–106]. The ExoCarta exosome database (http://www.exocarta.org/) currently contains 9 769 proteins, 3 408 mRNAs, 2 838 miRNAs, and 1 116 lipids that have been discovered in small EVs from different cell types and organisms.

Although small EVs contain a variety of proteins, Alix, TSG101 (involved in small EVs biogenesis from endosomes), RAB, other small GTPase families, flotillins, annexins, CD9, CD63, and CD81 are the most frequently employed proteins in small EVs characterization [107]. Tetraspanins (CD9, CD37, CD82, CD81, and CD63) are the most numerous small EVs components and are primarily responsible for recipient cell motility control, invasion, adhesion, and fusion. They are mainly present on the membrane surface and are often used as EV biomarkers [108,109]. CD63 and CD81 are considered classical markers in small EVs.

Small EVs also are enriched with large amounts of mRNAs, miRNAs, mitochondrial DNA, piRNAs, lncRNAs, ribosomal RNAs, snRNAs, and tRNAs among other types of nucleic acids.

Even though the nucleic acids contained in small EVs are broken down into fragments of about 200 bp, they can still affect the recipient cell [110]. Additionally, cholesterol, phospholipids, phosphatidylethanolamines, polyglycerols, and diglycerides are lipids found in small EVs membranes. These lipid molecules are involved not only in the morphology maintenance of small EVs but also in many other biological processes [110,111], such as cancer metastasis because of high lipids presence [111].

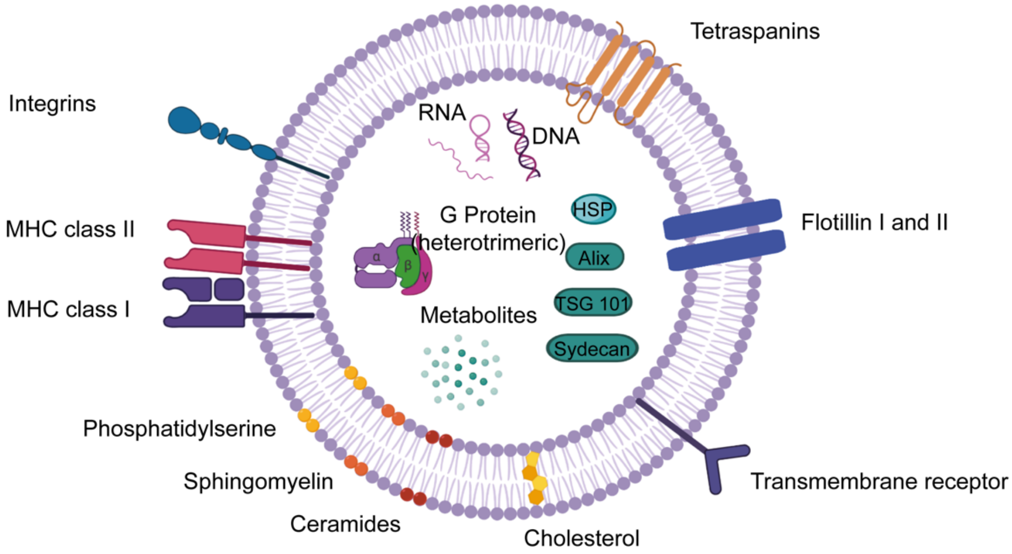

Figure 12. Small EVs composition. Small EV surrounded by a phospholipid bilayer, contains proteins, such as integrins; tetraspanins for cell targeting; other proteins, such as Alix and TSG101, that are involved in exosomal biogenesis from endosomes; Flotillin I and II; HSP, heat shock protein; MHC I and II, major histocompatibility complex; DNA, deoxyribonucleic acid, RNA, ribonucleic acid; and G protein. Adapted from Araujo-Abad, Saceda and de Juan (2022) [107].

1.4.4 Small EVs isolation methods

Since small EVs have enormous research potential in the biomedical field, several research projects are focused on the separation techniques of small EVs from a variety of cell fragments and interfering substances. Different methods can be used to isolate small EVs from body fluids or cell cultures depending on the source and size of the exosomes [108]. They are divided into: centrifugation, size-based, immunoaffinity capture, polymer precipitation, and microfluidics techniques [112], as shown in Table 3.

The most used method is ultracentrifugation [113], consisting of several centrifugation steps: first at low speed (300 *x g*) increasing it to finally at high-speed centrifugations (100 000 - 150 000 *x g*), to obtain the small EVs [108,114]. Ultrafiltration and size exclusion chromatography (SEC) are size-based isolation techniques that are based on the isolation of small EVs passing through physical barriers depending on the size of the particle [115,116]. The immunoaffinity chromatography approach is based on the affinity between proteins and their antibodies, for this purpose, antibodies are mounted on matrices such as magnetic beads [117]. The polymer precipitation method is focused on the use of polyethylene glycol and it is often sold in isolation kits [118]. Finally, microfluidic chip techniques are novel methods based on the difference between the biochemical and physical properties of small EVs. They are mainly classified into three categories (a) immune-affinity approach, (b) sieving (nanoporous membranes), and (c) trapping exosomes into porous structures (nanowire-on-micropillars) [119].

For greater accuracy in small EVs isolation, authors usually combined two methods. As an example of this, it has been reported that in order to obtain a higher purity of urine EVs is necessary the use of ultracentrifugation followed by the SEC method [107].

Table 3. Small EVs isolation techniques

Isolation method		Principle	Advantages	Disadvantages	Reference
Centrifugation	Ultrahigh-speed centrifugation	Small EVs are separated based on density and size using several centrifugation processes.	Economic and most used.	Low purity in some preparations. Time-consuming.	[114]
	Density gradient centrifugation	Small EVs are separated based on density using several centrifugation steps.	High reproducibility.	Time-consuming. Complicated operation.	[120]
Size-based	Ultrafiltration	Both only depend on the variations in diameter between small EVs and other components.	Size uniformity	Protein contamination. Blocked filter.	[115]
	Size exclusion chromatography		Non-destructive, preserves integrity.	Complex procedure. Incomplete recovery of small EVs.	[116,121]
Immunoaffinity capture	Magnetic beads and immunoaffinity	Uses specific antibodies combined with specific small EVs membrane proteins.	High purity.	Limited method. Specific small EVs population.	[122,123]
Polymer precipitation	Commercial kits	PEG-based small EVs extraction kits.	Fast and convenient. Preserves integrity.	Expensive. Sample contamination.	[118,124]
Microfluidics-derived chip	-Size and immunoaffinity -Dynamic microfluidics	It is based on small EVs' biochemical and physical characteristics, such as density, size, and immunoaffinity.	Fast small EVs obtention. High sensitivity. Small sample demand.	Complex procedure. Low yield.	[108,125]

Adapted from Yang *et al*. (2019) [108].

1.4.5 Small EVs in cancer

Small EVs produced by tumors (called tumor-derived exosomes, or TDEs) have a role in the development and progression of numerous cancer-related processes, such as TME remodeling, angiogenesis, invasion, metastasis, and treatment resistance [126]. Intercellular communication mediated by small EVs plays a significant role in the transport of information between tumor cells, TME, and healthy cells triggering those processes [127,128]. It has been demonstrated that small EVs generated by malignant tumor cells, which carry mRNAs involved in migration and metastasis, are picked up by less aggressive malignant cells both inside the same tumor and in more distant metastases, which changes cell behavior [129].

Angiogenesis in tumors is the development of fresh blood vessels, required to expand, grow, and metastasize [130]. This process is enhanced by TDEs, major angiogenic stimulatory factors carried by TDEs include VEGF, fibroblast growth factor (FGF), platelet-derived growth factor (PDGF), basic fibroblast growth factor (bFGF), transforming growth factor (TGF), tumor necrosis factor (TNF), and interleukin-8 (IL-8) [131]. GBM is an angiogenic tumor type, and it was reported that GBM derived- small EVs include high levels of miR-221, proteoglycans glypican-1, and syndecan-4, which promote the growth of endothelial cells and the development of tubules, which in turn promotes angiogenesis [132]. Small EVs also have a role in migration, invasion, and metastasis. Furthermore, it has been reported that EVs from cervical carcinomas and breast cancer cells are enriched in MALAT1*,* a long-non-coding RNA related to tumor metastasis and invasion in lung cancer and hepatocellular carcinoma [133,134].

Additionally, small EVs are involved in the acquisition of drug resistance. This happens because drug-resistant cancer cells have the capacity to transport chemotherapy agents outside of the tumor cell, packaged in small EVs, and delivered to sensitive cells [135]. This has been demonstrated by Yoshida *et. al*, who reported that miRNAs like miR-25-3p suppress the Dickkopf WNT signaling pathway inhibitor 3 (DKK3) gene in osteosarcoma cells, promoting cancer growth *in vitro* and enhancing resistance to various chemotherapy drugs (methotrexate, cisplatin, doxorubicin, and docetaxel) [136].

However, small EVs are not always related to negative effects. Several research projects confirmed that exosomes could have a potential role as biomarkers for cancer diagnosis or monitoring at each stage of the disease [107]. And also, they can be used as drug delivery systems to treat cancer tumors such as in GBM and PDAC [67,137], among others.

1.4.6 Small EVs as a delivery system

Small EVs have been proved to be an effective drug delivery method in cancer treatment, as they have several advantages compared to other delivery methods like nanoparticles or liposomes [138]. Small EVs are non-toxic, biocompatible, can transport hydrophilic or hydrophobic biomolecules, have the ability to cross the Blood-Brain Barrier (BBB) [139,140], have tropism for their parental cell [141], and minimize cytotoxicity and immunogenicity [142]. In this sense, to improve small EVs BBB penetration and its ability to target tumors, is important to modify and optimize their physicochemical properties, these are called engineer or chimeric exosomes. These types of small EVs, for example, combine the advantages of nanoparticles and exosomes for a better therapeutic outcome against cancer (Figure 13) [107].

In 2016, Srivastava *et al*. designed and proved the "nanosomes" (Exo-GNP-Dox) for lung cancer treatment. Nanosomes consisted of gold nanoparticles (GNP) conjugated with Doxorubicin (Dox) through a pH-cleavable bond and loaded into exosomes derived from lung cancer cells and normal lung fibroblasts (Figure 13A). In this way, they could stop the immunological reaction, aggregation, and fast elimination of the nanoparticles alone. According to this study's findings, nanosomes were efficiently transported and caused a cytotoxic effect on cancer cells but not on healthy cells [143]. Another example of engineered exosomes is the exosomes-thermosensitive liposomes hybrid NPs (gETL NPs) that in combination with hyperthermic intraperitoneal chemotherapy (HIPEC), were used to treat peritoneal carcinoma (Figure 13B). These gETL NPs were obtained from fibroblast-derived exosomes that express CD-47 protein and were combined with heat-sensitive liposomes. The conclusion of this study was that gETL NPs loaded with granulocyte-macrophage colony-stimulating factor and docetaxel, conducted to an inhibition of tumor progression, and its efficacy was increased with HIPEC [144]. Kamerkar *et al*. (2017), have designed them as iExosomes. Small EVs are produced by normal fibroblast-like mesenchymal cells that have siRNA or shRNA targeted against the oncogenic KRAS^{G12D}, which is generally mutated in pancreatic cancer (Figure 13C). Pancreatic cancer mouse models KPC (Pdx1$^{cre/+}$; LSL-Kras$^{G12D/+}$; LSL-Trp53$^{R172H/+}$) and KTC (Ptf1a$^{cre/+}$; LSL-Kras$^{G12D/+}$; Tgfbr2$^{lox/lox}$) treated with iExosomes both suppressed tumor development and decreased KRAS^{G12D} expression, which conducted to a higher survival rate of these models. Furthermore, this study confirmed that iExosomes target KRAS more effectively than liposomes [145]. Another type of engineered exosome is AMSC-Exo-199a, these types of small EVs are derived from adipose mesenchymal stroma/stem-like cells (MSC) and contain miR-199-a (Figure 13D). Although miR-199a is one of the most abundant miRNAs in healthy liver tissue, it is downregulated in hepatocellular carcinoma, and as a result, its reduction correlates with poor prognosis. The study findings support that AMSC-Exo-199a can deliver miR-199a to hepatocarcinoma cells and sensitize cancer cells to chemotherapeutic drugs through mTOR pathway inhibition [146]. Furthermore, Exo-CD19 CAR exosomes express CD19 Chimeric Antigen Receptor to cause cell death in malignant CD19 positive leukemia B cells without cytotoxicity in CD19 negative cells (Figure 13E). They would also not have the negative side effects that are associated with standard CAR-T cell therapy [147].

The engineer exosomes mentioned before are only a few examples of all the possible combinations with these small EVs. These highly improve the effectiveness of treatment and open up new possibilities for cancer patients.

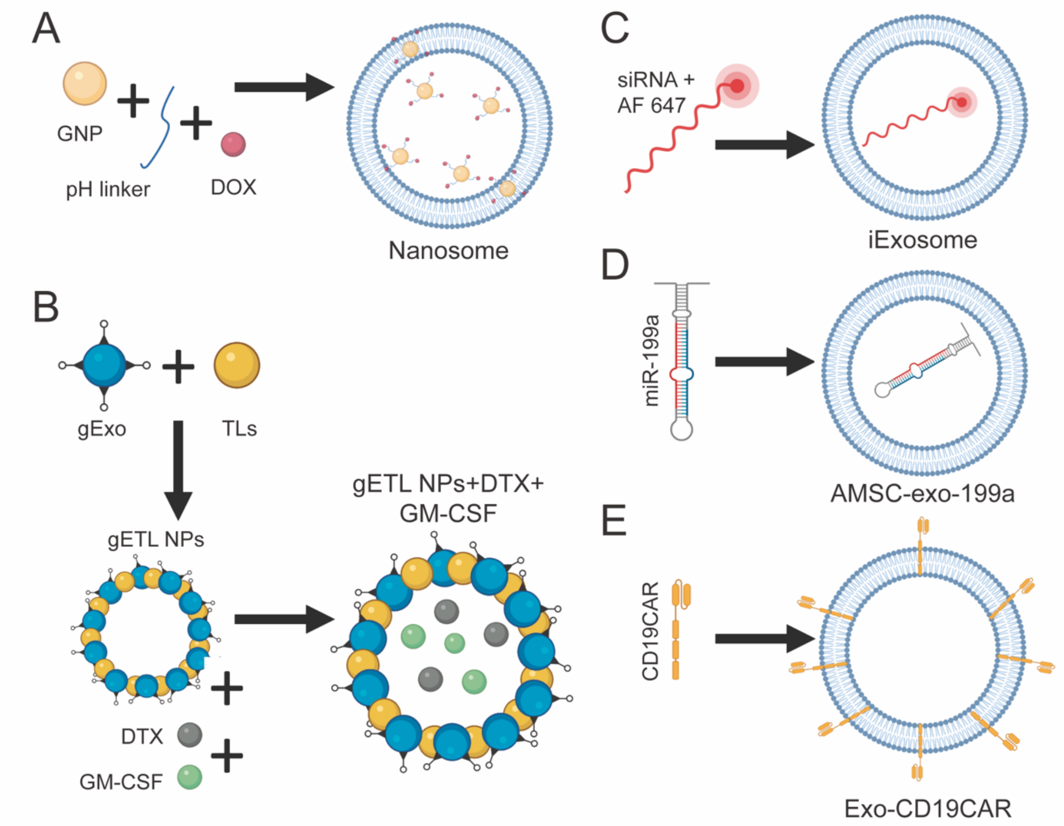

Figure 13. Engineer exosomes. (A) Nanosomes engineered from exosome harvest from normal lung fibroblast cells bonded to Gold Nanoparticles (GNP), pH linker, and Doxorubicin (Dox), for lung cancer treatment. (B) gETL NPS +DTX+GM-CSF made up of fibroblast exosomes overexpressing CD27 (gExo), thermosensitive liposomes (TLS), and loaded with colony-stimulating factor (GM-CSF) and docetaxel (DTX), for peritoneal carcinoma treatment. (C) iExosomes (siRNA+AF647), engineered by exosomes derived from normal fibroblast-like mesenchymal cells carrying specific siRNA for oncogenic KRASG12D, used to treat pancreatic cancer. (D) AMSC-exo-199a, exosomes from adipose tissue-derived MSCs (AMSCs) modified with miR-199-a, for hepatocellular carcinoma treatment. (E) ExoCD19-CAR, exosomes that express CD19 Chimeric Antigen Receptor (CD19 CAR) used for leukemia treatment. AF, Alexa Fluor; siRNA, small interfering RNA; miR, micro RNA. Source Araujo-Abad, Saceda and de Juan (2022) [107].

1.4.7 Small EVs loading methods

Several loading methods can be used in order to transform small EVs, such as incubation, sonication, electroporation, transfection, extrusion, freeze-thaw cycles, thermal shock, saponin-assisted loading, pH gradient method, and hypotonic dialysis. The following table (Table 4) describes the principal loading approaches.

Table 4. Small EVs loading methods

Loading Method	Advantages	Disadvantages	Reference
Direct Incubation	Do not affect the small EVs structure and stability.	Low encapsulation rate, depending on the polarity of the drug.	[67,137,148]
Indirect Incubation	Do not affect the small EVs structure and stability.	Low encapsulation rate.	[148–150]
Sonication	Highly efficient.	Small EV aggregation.	[151]
Electroporation	Efficient method to encapsulate miRNAs.	RNA precipitation and small EVs aggregation.	[148,152,153]
Transfection	Stable and efficient method.	Transfection reagents may cause changes in gene expression in donor cells. As a result, small EVs cargo and biological activities may be affected.	[154,155]
Extrusion	Efficient drug loading method.	The mechanical force employed may change the properties of small EVs membrane.	[156]
Freeze-thaw cycle	Simple and don't alter drugs or bioactive substances	May induce small EV aggregation and low encapsulation rate.	[157,158]
Thermal shock	Improve small EVs immunogenicity.	Altered cargo stability.	[159]
Saponin-assisted	Efficient drug loading method.	Saponins can enhance exosome membrane permeability, cytotoxicity, and hemolysis.	[160]
pH gradient method	Don't alter drug stability.	Affect total protein cargo of Small EVs.	[161]
Hypotonic dialysis	Efficient and simple loading method.	Causes a shift in the size distribution and peak broadening of Small EVs. Better results in combination with co-incubation.	[162]

Adapted from Xi *et al*. (2021) [156].

All methods described in Table 4, confirmed that small EVs could be easily modified to improve their drug delivery characteristics. Incubation methods are the simplest of all approaches, producing a very modest drug loading rate. Moreover, incubation methods are inexpensive and extremely safe since they do not compromise the stability of the small EV membranes. Increasing the drug concentration and stirring during incubation may be useful to improve the poor drug-loading rate. The incubation approach has several potential uses in medicine, such as therapy and drug delivery [156].

1.4.8 Clinical applications

There are several ongoing clinical trials in humans in which small EVs are used as a therapy for cancer treatment or potential biomarkers. Small EVs and anticancer drugs are frequently used in combination in early-phase clinical trials. The table below (Table 5) summarizes and describes an update of the clinical trials published on ClinicalTrials.gov.

Table 5. Clinical trials of Small EVs-based treatments

Disease	Year, patient, Status	Intervention (exosome treatment)	Outcome	Reference
Colon cancer	February 2011, n=35, Ongoing.	Curcumin conjugated with plant exosomes.	Deliver Curcumin to Normal and colon cancer tissue using plant exosomes.	NCT01294072
Malignant Ascites and Pleural Effusion	May 2013, n=30, Ongoing.	Drug-packaging microparticles with chemotherapeutic drugs.	Tumor cell-derived microparticles packaging chemotherapeutic drugs are useful to treat malignant ascites and pleural effusion.	NCT01854866
Malignant Pleural Effusion	January 2016, n=90, Ongoing.	Exosomes loaded with methotrexate.	Control tumor growth *in vivo* effectively and induced pleural adhesion.	NCT02657460
Pancreatic cancer	August 2018, n=28, Ongoing.	Mesenchymal Stromal Cells-derived Exosomes with KRAS^{G12D} siRNA. iExosomes	Progression-free survival (Time Frame: Up to 1 year)	[145] NCT03608631
	December 2022, n=1000, Ongoing	ExoLuminate Study for Early Detection of PDAC.	Develop a non-invasive blood test ("liquid biopsy") that can identify early-stage disease	[163] NCT05625529
Rectal cancer	February 2018, n=30, Ongoing.	Exosomal as Correlative Biomarker.	Compare rates of exosomal expression before during and after chemoradiation.	NCT03874559
Hepatocellular carcinoma **Gastric cancer** **Colon cancer**	June 2022, n=30, Ongoing.	exoASO-STAT6 (CDK-004) for treatment.	Characterize the safety and tolerability of CDK-004.	NCT05375604
Gastric cancer	May 2022, n=700, Ongoing.	Circulating Exosomal lncRNA-GC1.	Detection of levels of circulating exosomal lncRNA-GC1.	NCT05397548
Melanoma	2005, n=15, Completed.	Dendritic exosomes with tumor antigenic peptides.	Proof of feasibility and safety.	[164]
	2009, n=15, Completed.	Human dendritic exosomes with NKG2D ligands.	Proof of feasibility and safety.	[165]
Non-small lung cancer	2005, n=13, Completed.	Dendritic exosomes with tumor antigenic peptides.	Proof of feasibility and safety.	[166]
Colon cancer	2008, n=40, Completed.	Autologous ascites exosomes.	Proof of feasibility and safety.	[167]
Advanced Non- small cell lung cancer	July 2010, n=41, Completed.	Dendritic exosomes with tumor antigenic peptides (Dex).	Stabilization and antitumor immunity.	[168] NCT01159288

*Green color highlights ongoing clinical trials while red color are completed trials. Updated from Araujo-Abad, Saceda and de Juan (2022) [107].

These clinical trials confirm the effectiveness of novel exosome-based anticancer treatment strategies and highlight the relevance of further research in clinical application.

1.5 Citrullination in cancer

Citrullination, or deamination, is a type of post-translational modification (PTM) that is carried out by enzymes called peptidyl-arginine deiminases, or PADIs (EC 3.5.3.15, L-arginine iminohydrolases). In this process, peptidyl arginine is converted into peptidyl citrulline [169]. Additionally, as a consequence of citrullination, the protein loses its positive charge, which may affect both its structure and function [170]. Five human PADI protein-encoding genes have so far been identified: PADI1, PADI2, PADI3, PADI4, and PADI6 [171]. PADIs have specific tissue expression and substrates as shown in Table 6.

Table 6. PADIs tissue expression and substrates

PADI	Expression	Target
PADI1	Epidermis, hair follicles, keratinocytes, arrector pili muscles, sweat glands.	Keratins
PADI2	Epidermis, keratinocytes, lymphocytes, macrophages, monocytes, neutrophils, oligodendrocytes, Schwann cells.	Histone H3, vimentin, enolase, MBP, tubulin.
PADI3	Epidermis, hair follicles, hair cuticles, keratinocytes, neutrophils, Schwann cells.	Keratins, S100A3.
PADI4	Bone marrow, CD34+ cells, granulocytes, HL-60, lymphocytes, macrophages, monocytes, adenocarcinomas.	Histone H3/H4, OKL38.
PADI6	Embryo, oocyte, testicles.	Unknown

Adapted from Modal and Thompson (2019) [172].

While there are several PADI substrates, histones are the most extensively studied. Histones PTMs play an important role in tumorigenesis and cancer [173]. All PADIs are found only in the cytoplasm, except PADI4, which has been detected in both the cytoplasm and the nucleus, and PADI2, which is also found in the nucleus under some stress conditions [171,174,175]. The nuclear localization signal (NLS) of PADI4 allows it to enter the nucleus [171,176]. Additionally, all PADIs are Ca^{2+}-dependent enzymes because it is necessary for PADI-driven citrullination. Actually, under physiological conditions when the Ca^{2+} concentration is low, PADIs remain inactive; their activation is therefore caused by the entry of extracellular Ca^{2+} or the release of Ca^{2+} from intracellular calcium stores [177,178].

In this work, we focused on PADI4, also known as protein L-arginine iminohydrolase 4. As mentioned in Table 6, PADI4 is present in macrophages, monocytes, granulocytes, and a variety of adenocarcinomas [178]. At the patient level, it has been demonstrated that after tumor removal, plasma PADI4 levels in patients with malignancies are reduced, indicating that PADI4 circulating in the blood may be used for the tumor diagnosis [176].

In this Thesis, we emphasize how its expression is altered in hard-to-treat cancer cells, the effect of its inhibitor in cell proliferation, and its relationship with small EVs.

1.5.1 PADI4 and its role in cancer

Citrullination mediated by PADI4 contributes to the development of cancer through several different processes (Figure 14A).

Firstly, histones citrullination with the removal of the methylation tag, has a significant impact on key physiological processes like cell differentiation and apoptosis. As a consequence, the Wnt and androgen receptor signaling pathways are affected, which are directly involved in the development of cancer [179]. It has been studied that PADI4 citrullinates histone H3 on arginine 2, 17, and 26, while histones H2A and H4 can be citrullinated on arginine 3 [180–182]. Furthermore, H3 citrullination at the p21 promoter site by PADI4 appears to function as a p53 co-repressor, inhibiting downstream gene transcription [183]. Consequently, if PADI4 serves as a p53 co-repressor, inhibitors of this enzyme may therefore be used for cancer treatment [178]. As an example, in osteosarcoma and breast cancer cells, inhibition of PADIs by Cl-amidine inhibitor leads to the expression of the OKL38 gene. The overexpression of this gene in cell culture caused apoptosis and structural abnormalities in the mitochondria, as well as the release of cytochrome c [184].

Another substrate of PADI4 is a tumor suppressor protein, the inhibitor of growth 4 (ING4). Regardless of the presence of calcium, PADI4 citrullinates and binds ING4. Citrullination of ING4 by PADI4 in the NLS prevents p53 from binding to ING4, suppressing p53 acetylation, and consequently decreasing p21 production downstream. When ING4 is citrullinated, it stimulates its degradation and the growth, invasion, and migration of tumors [185].

Finally, another PADI4 target is the transcription factor glycogen synthase kinase 3 beta (GSK3β). This regulates the epithelial-to-mesenchymal transition (EMT) [186]. EMT is a biological process that consists of the loss of epithelial polarity, cell-to-cell, and cell–matrix adhesion properties, which facilitates tumor metastasis and drug resistance [187]. GSK3β maintains the epithelial phenotype through the citrullination of arginine residue at the N-terminal, which is regulated by PADI4. This process inhibits the TGF-β pathway and therefore EMT. As an example, in breast cancer, the knockdown of PADI4 in MCF-7 cells led to a decrease in nuclear GSK3β, the stabilization of Smad4, and the activation of the TGF-β signaling pathway, reducing E-cadherin and promoting vimentin, ultimately stimulating tumor migration and invasion [186]. In other types of cancer such as non-small cell lung cancer (NSCLC), the inhibition of PADI4 increases ETS-domain containing protein (Elk1) expression, which in turn induced EMT and gefitinib (EGFR inhibitor used in breast, lung, and other types of cancer) resistance, while PADI4 upregulation has the opposite effect [188]. In colon cancer, when the EMC is citrullinated by PADI4 it promotes the EMT and therefore cancer progression [189] (Figure 14A).

On the other hand, PADI4 is also related to neutrophil extracellular traps (NETs) (Figure 14B). NETs have been detected in multiple human cancer types, and several studies have suggested that they can contribute to cancer development by facilitating tumor growth and metastasis via multiple mechanisms [190–194]. These mechanisms involve circulating cancer cells being trapped in distant sites; the activation of dormant cells by cleaved laminin peptides; and the high mobility group box 1 (HMGB1) protein release, which stimulated the growth of cancer cells by activating the toll-like receptor 9 (TLR9) signaling pathway. In addition, cell-free DNA and serum levels of citrullinated peptides associated with NETs were proposed as potential biomarkers of solid tumors, which seems consistent with the evidence that many malignancies have higher intratumoral levels of PADI4 [179].

Additionally, PADI4 inhibitors such as Cl-amidine and GSK484 were used to decrease the growth of cancer cells without having an impact on healthy cells [195]. It is important to mention that Cl-amidine is an inhibitor of all PADIs while GSK484 is specific for PADI4 [196,197]. Therefore in this work we used GSK484 [(3S,4R)-3-amino-4-hydroxy-1-piperidinyl][2-[1-(cyclopropylmethyl)-1H-indol-2-yl]-7-methoxy-1-methyl-1H-benzimidazol-5-yl] methanone inhibitor. This new drug prevents the citrullination of PADI4-targeted proteins in neutrophils, inhibits the formation of NETs, and also decreases the release of dsDNA [198]. Although research on the role of GSK484 in cancer is limited, this drug has already been used as a pretreatment in triple-negative breast cancer (TNBC). Moreover, it was seen that it enhanced irradiation (IR), and induced inhibitory effects on cell proliferation, migration, and invasion. Additionally, *in vivo* experiments also showed that, in contrast to IR-alone or GSK484-alone treatment, the combined treatment of IR and GSK484 exhibited a decrease in tumor growth [196].

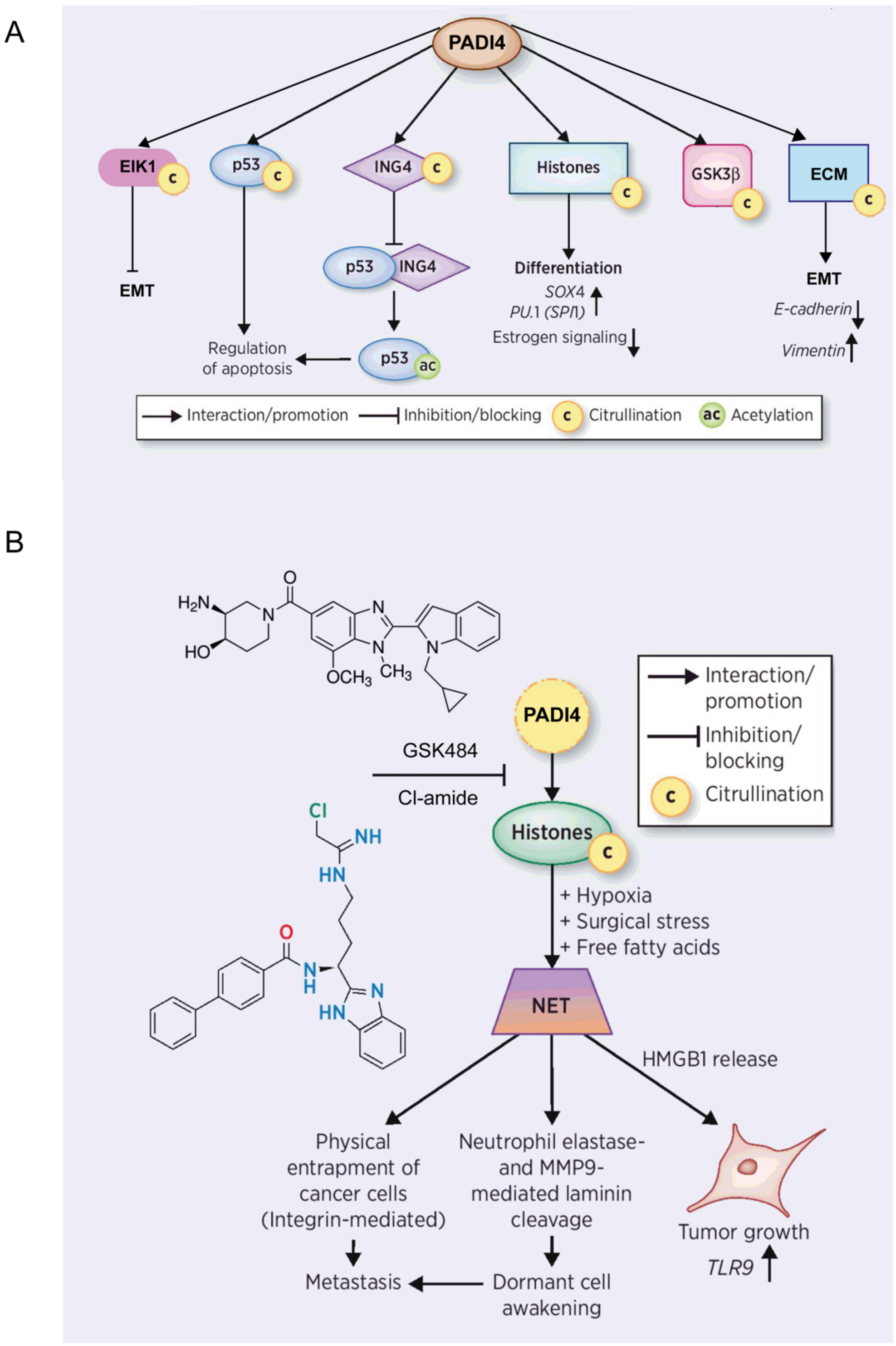

Figure 14. PADI4 and pathways. (A) Through several distinct mechanisms, the citrullination of ECM, p53, ING4, histones, GSK3β, and ELK1, which is mediated by PADI4, contributes to the development of cancer. (B) Histones that have been citrullinated by PADI4 promote NET formation, facilitating tumor growth and metastasis. EMT, epithelial-mesenchymal transition; ECM, extracellular matrix; ING4, inhibitor of growth 4; GSK3β, glycogen synthase kinase 3 beta; ELK1, ETS-domain containing protein; NET, neutrophil extracellular traps. Adapted from Yuzhalin (2019) [179].

1.5.2 Effect of citrullination in small EVs

As it was mentioned before, small EVs cargo is constituted of different molecules, like enzymes that can generate PTMs. PTMs (oxidation, citrullination, phosphorylation, and glycosylation) can also control the subcellular localization, selection, and EVs biogenesis [199,200]. Small EV PTMs can also contribute to disease pathogenesis by enhancing inflammation, producing neoepitopes, or carrying neoepitopes themselves [199]. A recent study has highlighted that MVs play a role in cancer progression and, it is known that PADI4 is overexpressed in tumor tissues. Both PADI4 and MVs are calcium-dependent, so they may have synergistic relationships. Therefore, it was suggested that the release of MVs and PADIs enzymes was influenced by calcium input [201].

Recently, the effects of PADI-specific inhibitors in GBM have been highlighted. These inhibitors modulated the expression of microRNA (miR21, miR126, and miR210) in small EVs cargo as well in their release. Surprisingly, PADIs isozymes inhibitors had distinct inhibitory effects, the PADI3 inhibitor had the most effective function regulating EVs in LN229 cells while the PADI2 and PADI4 inhibitors were more effective in LN18 cells [202]. Similar work has been performed on PDAC cancer cells where Panc-1 and MiaPaCa-2 cell lines were treated with pan-PADI inhibitor Cl-amidine, and PADI2, PADI3, and PADI4-specific inhibitors. Treatments using PADIs inhibitors had an impact on the EV signature profiles, reducing pro-oncogenic miR-21 and miR-221 and increasing anti-oncogenic miR-126. Inhibitors of PADI2 and PADI3 most effectively decreased Panc-1 cancer cell invasion and increased moesin expression, a protein that functions as a cross-linker between plasma membranes and actin-based cytoskeletons. [203]. These studies show the diversity of PADIs role in malignancies, which supports their possible use for cancer-specific therapies. However, further research is necessary to fully understand the relationship between cancer-derived small EVs and the PADIs proteins in the context of each cancer type.

OBJECTIVES

2. Objectives

The main objective of this work is to develop alternative therapies for tumors that show resistance to classical treatments, focusing on glioblastoma (GBM) and pancreatic cancer adenocarcinoma (PDAC). This Thesis is centered on the **study of small EVs and their potential use in clinical applications.**

In order to achieve the general objective of this work, the following specific aims were proposed:

Objective 1. To determine the sensitivity and/or resistance profile to treatments of patient-derived hard-to-treat cancer cell lines.

Objective 2. To isolate and characterize small EVs from patient-derived hard-to-treat cancer cell lines.

Objective 3. To establish the conditions for the use of small EVs as drug delivery systems.

Objective 4. To establish the therapeutic potential of cancer-derived loaded small EVs.

Objective 5. To analyze citrullination as an alternative therapeutic target in cancer.

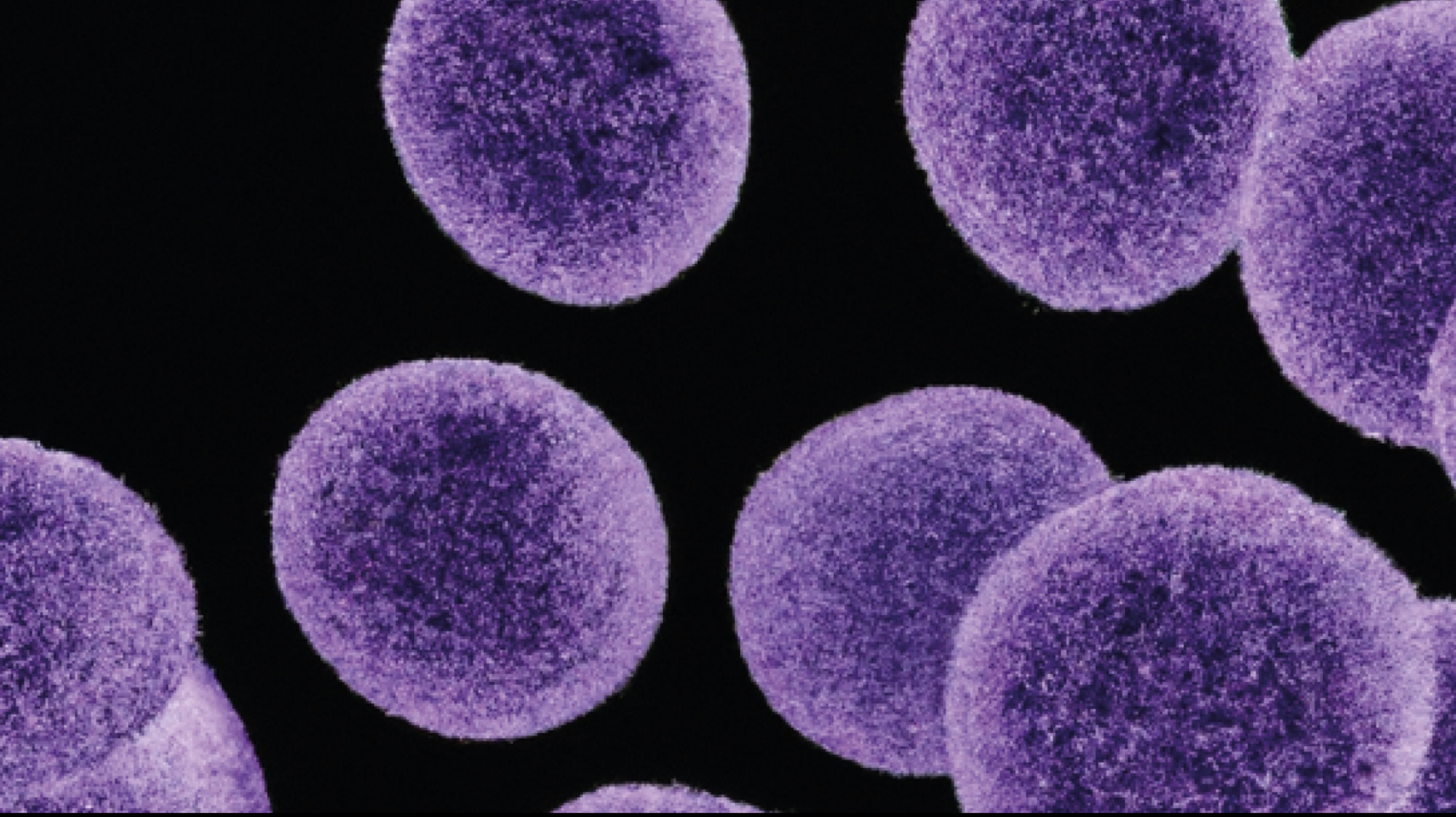

METHODS

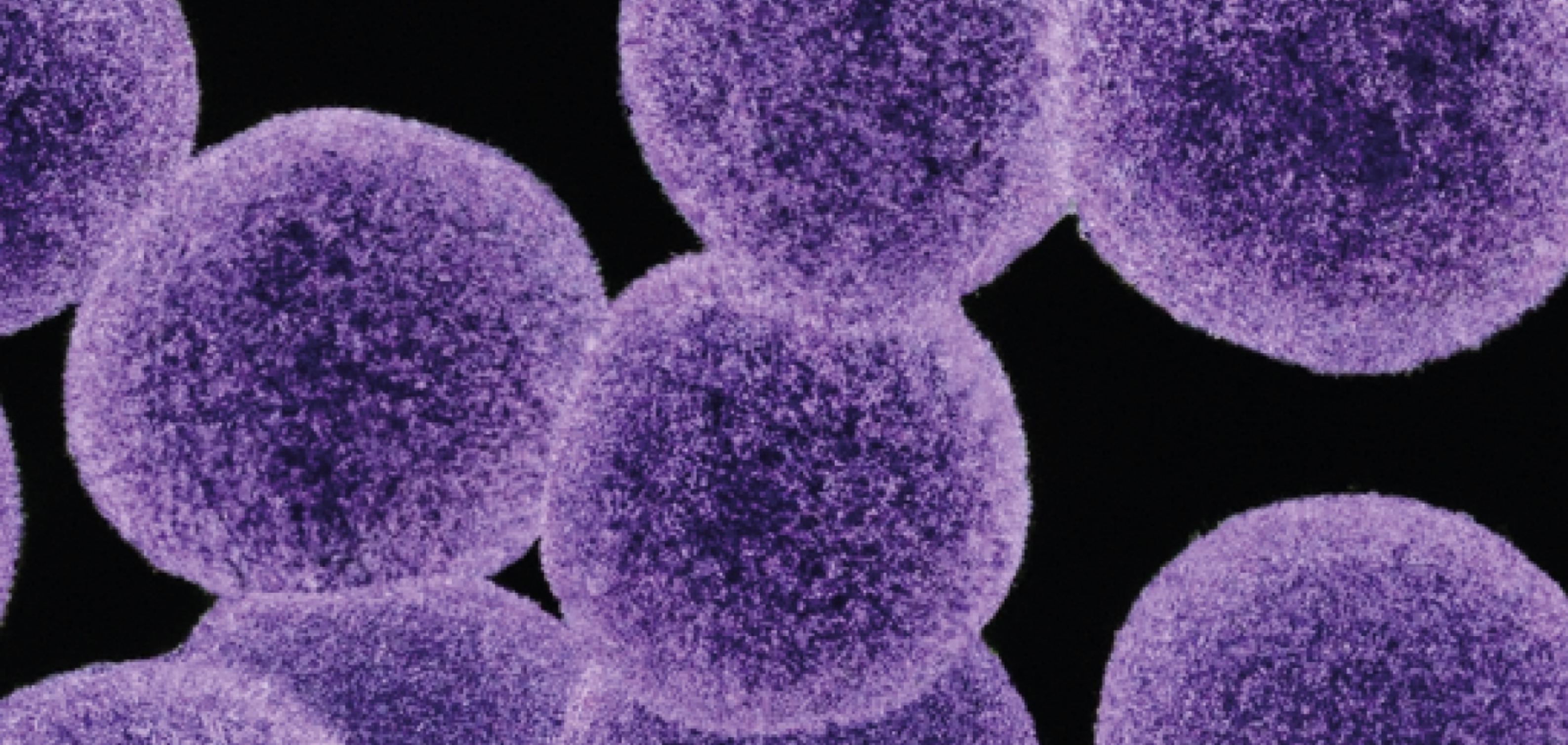

3. Methods

3.1 Chemicals and reagents

The reagents for cellular and molecular assays are listed below (Table 7):

Table 7. Reagents for cellular and molecular assays

Reagent	Function	Supplier
TMZ	Alkylating agent	Sigma-Aldrich
EPZ015666	PRMT5 inhibitor	Sigma-Aldrich
GSK484	PADI4 inhibitor	Abcam

The following antibodies were used for Western Blot (WB), Immunocytochemistry (ICC), and proximity Ligation Assay (PLA) (Table 8):

Table 8. Antibodies used for WB, ICC, and PLA

Protein	Weight (kDa)	Biological Source	Concentration (µl: µl)	Supplier	Assay
Alix	100	Mouse	1:500	Invitrogen	WB
TSG101	46-50	Mouse	1:500	Invitrogen	WB
CD63	63	Mouse	1:1 000	Invitrogen	WB
PADI4	75	Mouse	1:200	Abcam	IF/PLA
		Rabbit	1:2 000	Invitrogen	WB
NUPR1	18	Rabbit	1:100	homemade	ICC/PLA
Mdm2	~ 54	Rabbit	1:100	Invitrogen	ICC/PLA
α-tubulin	50	Mouse	1:10 000	Invitrogen	WB
HSP90-B1	90	Rabbit	1:4 000	Cusabio	WB
E-cadherin	106	Rabbit	1:100	Invitrogen	ICC
Alexa Fluor 568-labeled	--	Mouse	1:500	Invitrogen	ICC
Alexa Fluor 488-labeled	--	Rabbit	1:500	Invitrogen	ICC

3.2 Cell culture

The human GBM cell lines used in this work were isolated from surgical washes as reported previously by Ventero *et al.* [204]. PDAC (RWP-1) cell line, colon adenocarcinoma (HT-29), and (SW-480) cell lines, were donated by Instituto Municipal de Investigaciones Médicas (IMIM, Barcelona, Spain) [205]. The GBM cell lines, HGUE-GB-16, HGUE-GB-18, HGUE-GB-37, HGUE-GB-39, HGUE-GB-40, HGUE-GB-42, HGUE-GB-48 were cultured in Dulbecco's Modified Eagle's Medium: Nutrient Mixture F-12 (DMEM F-12) (Biowest, MO, USA) while RWP-1, HT-29, and SW-480 cells were cultured in Dulbecco's Modified Eagle's Medium: High Glucose (DMEM-HG) (Biowest, MO, USA), all of them were supplemented with 10% (v/v) of heat-inactivated fetal bovine serum (FBS) (Biowest, MO, USA) and 1% (v/v) penicillin/streptomycin mixture (Biowest, MO, USA). Cells were incubated at 37 ºC in a humidified 5% CO_2 atmosphere [137].

3.3 Proliferation assays

To analyze the antiproliferative effect of either the drugs and the loaded small EVs on cells, Methylthiazolyldiphenyl-tetrazolium bromide (MTT) assay was performed. Cells were seeded in 96-well standard plates (Sarstedt, Nümbrecht, Germany) at a density of 4 000 cells/well and incubated at 37 ºC and 5 % CO_2 for 24 h. Cells were then treated with either increasing concentrations of the chemotherapeutic drugs (Table 7) or with loaded small EVs, and incubated for 72 h under the same conditions. Then, 0.25 mg mL^{-1} of MTT (Sigma-Aldrich, MO, USA) was added to the cells and incubated for 3 h. Cell culture media was removed and 100 µL of dimethyl sulfoxide (DMSO) (Sigma-Aldrich, MO, USA) was added to the plate. The plate was stirred at room temperature for 20 min to dissolve the formazan crystals. Finally, the absorbance was measured on Eon^{TM} Microplate Spectrophotometer (BioTeK$^{®}$, Winooski, VT, USA) at 570 nm [137].

3.4 Small EV purification

The seven GBM and RWP-1 cell lines were incubated in 75 cm^2 cell culture flasks with DMEM F-12 or DMEM-HG conditioned media respectively, and after four days small EVs were obtained by differential ultracentrifugation method. The media samples were centrifuged at 2000 *x g* for 20 min at 4 ºC to remove cells and debris. After that, an initial ultracentrifugation step was performed using Optima L-90K Ultracentrifuge (Beckman Coulter, Brea, CA, USA) with 70.1 Ti rotor, at 25 000 x *g* for 40 min at 4 ºC to remove macrovesicles. The resulting supernatant was filtered through 0.22 µm filters (Fisher Scientific, Pittsburgh, PA, USA), and centrifuged at 110 000 x *g* for 90 min at 4 ºC to pellet small EVs. Finally, small EVs were washed in (1X) PBS at 110 000 x *g* for 90 min at 4 ºC and the final pellet was resuspended in 200 µL of (1X) PBS and then stored at -80 ºC (Figure 15) [67].

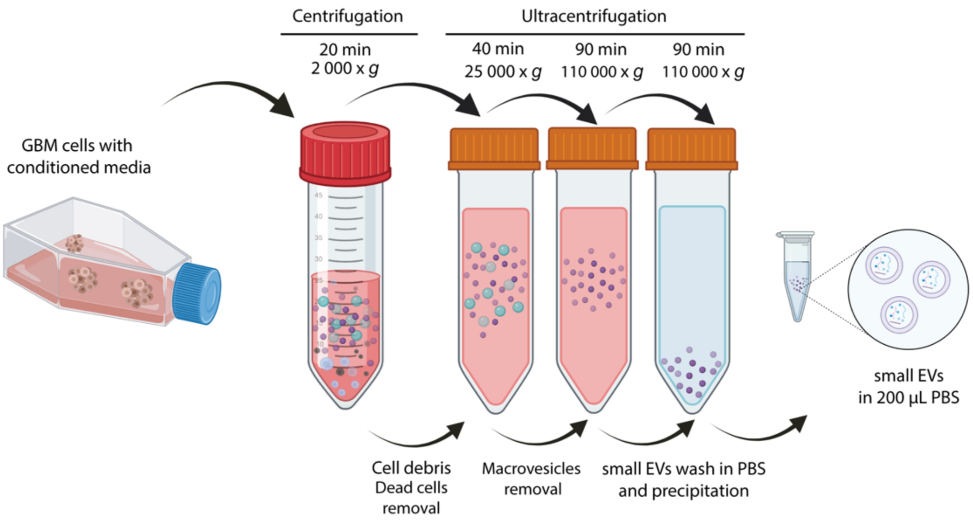

Figure 15. Scheme representing GBM-derived small EVs isolation. Sequential steps of centrifugation and ultracentrifugation were performed, as indicated on top of the arrows. GBM, glioblastoma; EVs, extracellular vesicles. Source Araujo-Abad *et al.* (2023) [137].

3.5 Western blot (WB)

An amount of 20 µg (cells) and/or 10 µg (small EVs) of total protein was solubilized with loading buffer (4x) (2-mercaptoethanol + NuPage; 1:5) and heated at 95 ºC for 5 min for reducing conditions, while for non-reducing conditions the loading buffer was used without 2-mercaptoethanol. Then, proteins were separated by SDS-PAGE using 10 % gels and transferred to a nitrocellulose membrane (Bio-Rad Laboratories Inc, California, USA) [137]. Membranes were incubated overnight at 4 ºC with primary antibodies (Table 8) followed by one-hour incubation at room temperature with ECL^{TM} Anti-mouse IgG or ECL^{TM} Anti-rabbit IgG, Horseradish Peroxidase linker (GE Healthcare, UK). The membranes were visualized with ECL^{TM} Prime Western blotting detection reagent (Amersham^{TM}) in the ChemiDoc Bio-Rad instrument [67,137].

3.6 Dynamic light scattering (DLS)

The DLS technique was used to characterize the size distribution of small EV samples, using a Zetasizer Nano ZS instrument (Malvern Panalytical). All samples were diluted in Milli-Q^{TM} water (1:10), 1 mL was dispensed in a polystyrene disposable cuvette (Zen0040), and read seven times in Zeta sizer Software. The final image with the distribution curves was used in the figures as an illustration of the medium size [67].

3.7 Field emission scanning electron microscope (FESEM)

The small EVs were fixed with paraformaldehyde (PFA) 2 %, sonicated for 5 minutes, and then diluted in serial dilutions with Milli-Q^{TM} water (1:10; 1:100; 1:1000, 1:10 000). Then, 50 μL of each sample was dropped on a silicon wafer, and once evaporated, the samples were observed using a Zeiss Sigma 300 VP Microscope (FESEM) without coating. Small EVs morphology was analyzed at low voltages around 1 kV, while higher voltages were employed to differentiate the salts from the biological sample using Energy Dispersive X-ray (EDX) [67,137].

3.8 Small EVs drug-loading

Two different techniques, direct and indirect incubation, were employed to load small EVs. For the first method, small EVs were incubated for 2 h at 37 ºC in a thermoblock with defined concentrations of a given chemotherapeutic drug (EPZ015666 15 μM or TMZ 5 mM). After incubation, they were washed with (1X) PBS and ultracentrifuged at 110 000 x *g* for 60 min at 4 ºC to pellet the loaded small EVs. The small EVs were filtered with a 0.22 μm membrane under sterile conditions and preserved at -80 ºC. On the other hand, the indirect approach involved incubation of the GBM cell culture with the desired drug (EPZ015666 15 μM or TMZ 5 mM) for 72 h. Subsequently, the flasks were treated in the same way as described previously in the small EVs purification section (Figure 16) [67].

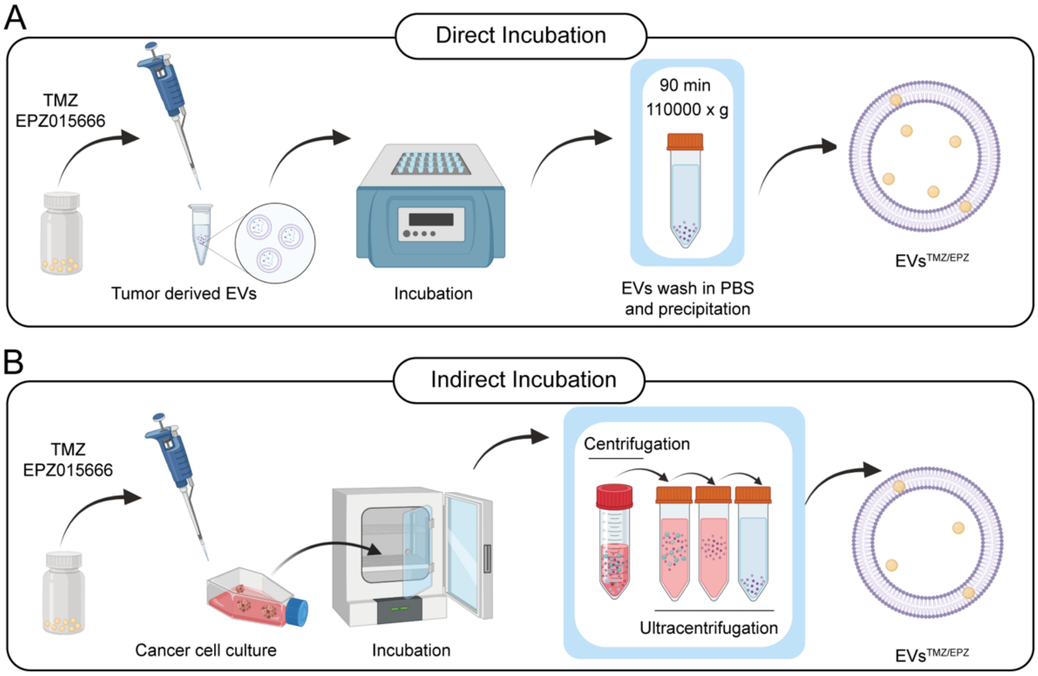

Figure 16. Drug loading of small EVs particles. (A) Scheme representing the sequential steps for small EVs loading using the direct method. (B) Scheme representing the sequential steps for small EVs loading using the indirect method. Adapted from Araujo-Abad *et al.* (2023) [67].

3.9 Quantification of TMZ and EPZ015666 by HPLC

The quantity of TMZ and EPZ015666 loaded into the small EVs was determined using the high-performance liquid chromatography (HPLC) technique. Initially, 200 μL of small EVs were placed in a Concentrator plus (Eppendorf) at 40 ºC for 2 hours to remove the solvent. Then, 100 μL of acetonitrile was added, and the mixture was vortexed, sonicated, and then centrifuged at 13 000 r.p.m (Centrifuge 5415 R, Eppendorf) for 10 min. Following centrifugation, the supernatant was collected and then transferred to HPLC vials. Next, it was injected into the UPLC-QtoF-MS/MS equipment, which utilized high-resolution flight tubes and quadrupole technology (Waters-Bruker). The detection of TMZ and EPZ015666 was optimized using a Waters I-Class system with UV detection at 330 and 254 nm respectively, as well as a QToF-MS from Bruker Daltonics, maXis impact Series model that uses positive ionization mode through Electrospray (ESI) with an ACE Excel C18-Ar column (50-3; 1.7 µm). The mobile phase consisted of water with 0.1 % v/v acetic acid (A) and methanol with 0.1% acetic acid (B). The gradient used was as follows: 0 min, 95 % A; 5.50 min, 60 % A, 8.75 min, 5 % A, with a flow rate of 0.3 mL/min, and the injection volume was 5 µL [137].

3.10 Small EVs labeling

In order to study the cellular uptake and intracellular localization of small EVs, they were labeled with the CellVue® Claret Far Red Fluorescent kit purchased from (Sigma-Aldrich, MO, USA). Specifically, 200 μL of RWP-1 small EVs were treated with the kit content according to the manufacturer's instructions. After two washes in (1X) PBS with 110 000 x *g* ultracentrifugation for 1 h, the labeled small EVs were filtered with a 0.2 μm filter, and finally, they were resuspended in (1X) PBS prior to use [67].

3.11 Immunocytochemistry (ICC)

A total of 30 000 cells from GBM, SW-480, and RWP-1 cell lines were seeded into 24-well plates on coverslips. After 24 hours, the cells were fixed with PFA at 4 % concentration and then blocked using FBS/PBS (1X) (50 μL/mL). Next, the cells were incubated with primary antibodies listed in Table 8. After washing out the first antibody with (1x) PBS, the cells were incubated with secondary antibodies. The nucleus was stained using DAPI (4′,6-diamidino-2-phenylindole) reagent from Sigma (Madrid, Spain). The coverslips were mounted in Prolong™ Gold Antifade Reagent (Invitrogen, Barcelona, Spain) and visualized using a Zeiss Axioscope 5 microscope with the LED light source Colibri 3 (Carl Zeiss, Oberkochen, Germany) [206].

3.12 Proximity ligation assay (PLA)

For this assay, 3 000 cells of GBM, SW480, and RWP-1 cell lines were seeded onto coverslips in 24-well plates. The experiments were carried out in the absence, and in the presence of GSK484 at a final concentration of 20 μM. Following a 24-hour incubation, the cells were washed twice with (1X) PBS, fixed, and washed twice again. Then, they were permeabilized in (1X) PBS with 0.2 % Triton X-100 and blocked for 30 min using a blocking solution. Immune-staining was performed using Duolink PLA Technology (Merck, Madrid, Spain), according to the manufacturer's protocol. Primary antibodies listed in Table 8 were used. The slides were processed for in situ PLA using the Duolink In Situ Detection Reagents Red, Duolink In Situ PLA Probe Anti-Mouse MINUS and Duolink In Situ PLA Probe Anti-Rabbit PLUS (Merck, Madrid, Spain) in a sequential manner. In these experiments, the red fluorescence signal indicates a PLA-positive signal, confirming that the two proteins are bound, forming a protein complex. The blue fluorescence corresponds to nuclei that were stained with DAPI. Both negative and positive control experiments were performed by omitting one of the primary antibodies. The images were acquired at ×63 magnification using an Axio Observer Z1 inverted microscope (Carl Zeiss, Oberkochen, Germany) [206,207].

3.13 Live cell imaging

To visualize the uptake of small EVs, RWP-1 cells were seeded in 96-well black plates with clear bottoms (Corning, Kennebunk, ME, USA) with a density of 16 000 cells/well and incubated at 37 ºC and 5 % CO_2 for 24 hours. Next, the cells were treated with red labeled RWP-1 small EVs^{TMZ} and incubated for 3 and 6 hours under the same conditions. After washing twice with (1X) PBS, the cells were imaged using a Cytation 3 (BioTeK®, Winooski, VT, USA) instrument. The images were exported in tiff format and analyzed using Fiji software [67].

3.14 Statistical analysis

The results are shown as the mean ± standard deviation (SD) of three independent experiments. To evaluate the normal distribution of the data, the Shapiro-Wilk statistical test was employed. The association between variables was analyzed using either Student's t-test or the Mann-Whitney U test. Differences with a *p*-value of less than 0.05 were considered statistically significant. To calculate the half-maximal inhibitory concentration (IC_{50}) values, a nonlinear regression analysis was performed. GraphPad Prism v7.0a software (GraphPad Software Inc., San Diego CA, USA) was used for statistical analysis [67,137].

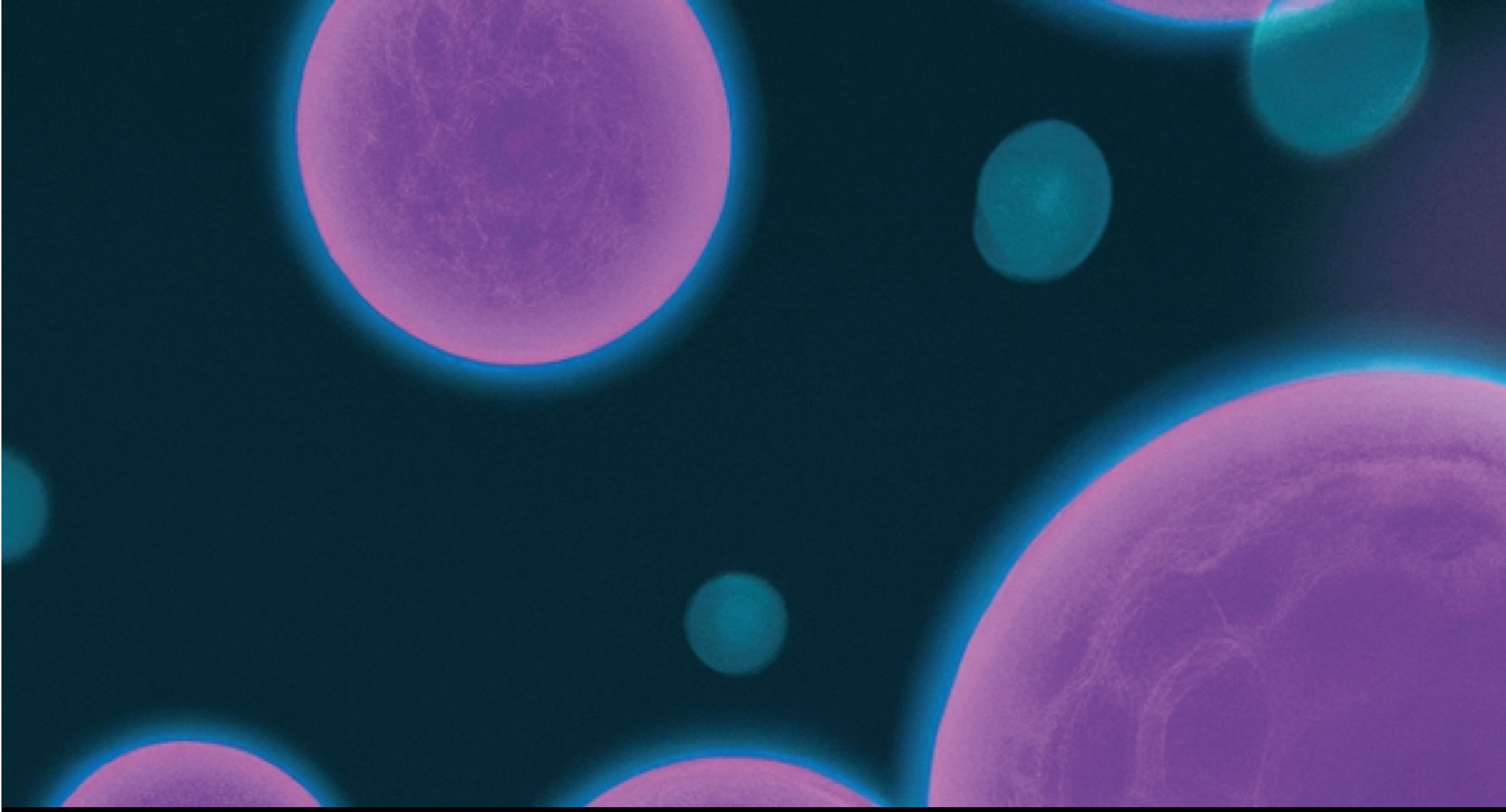

RESULTS

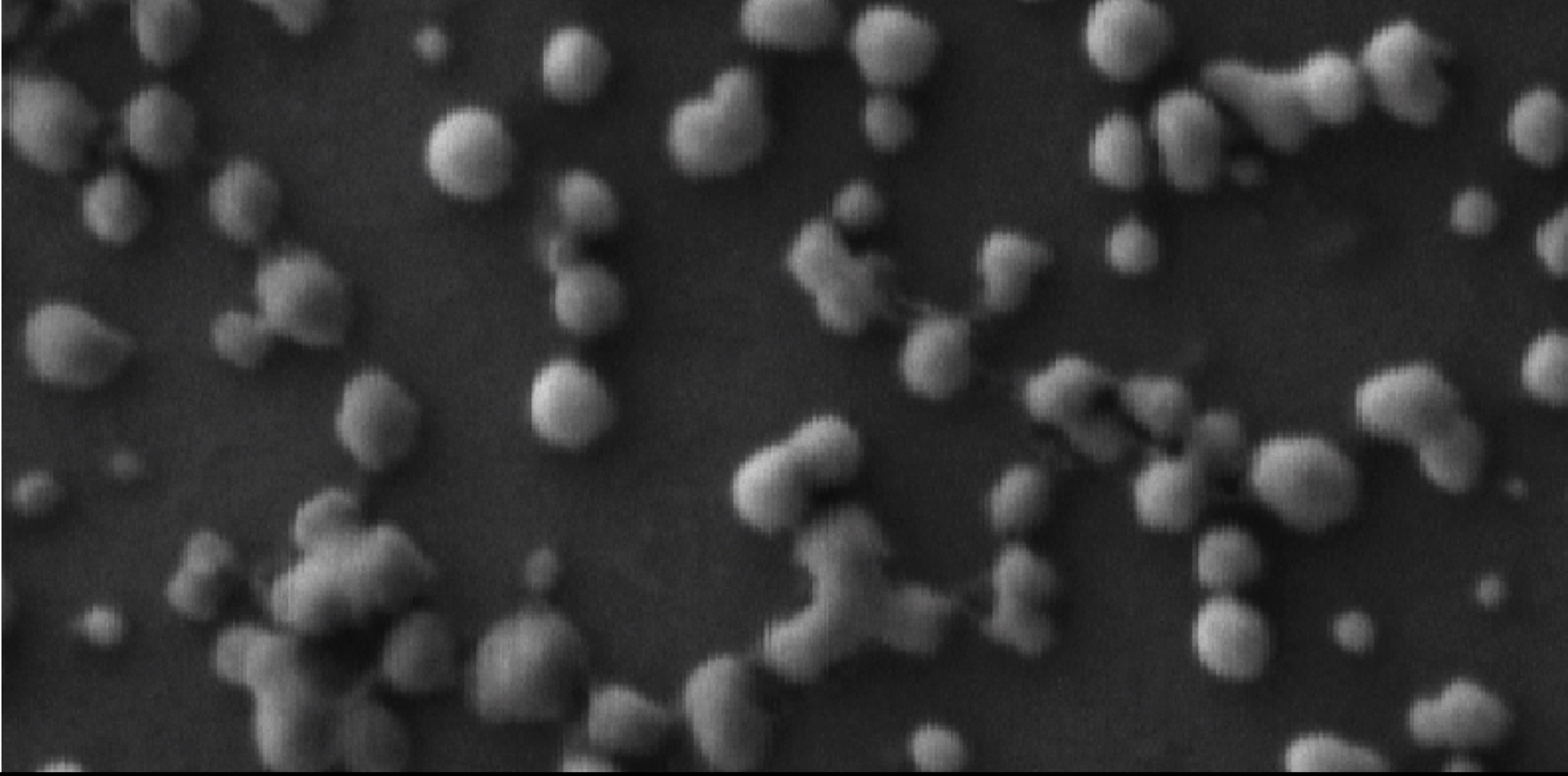

CHAPTER 1

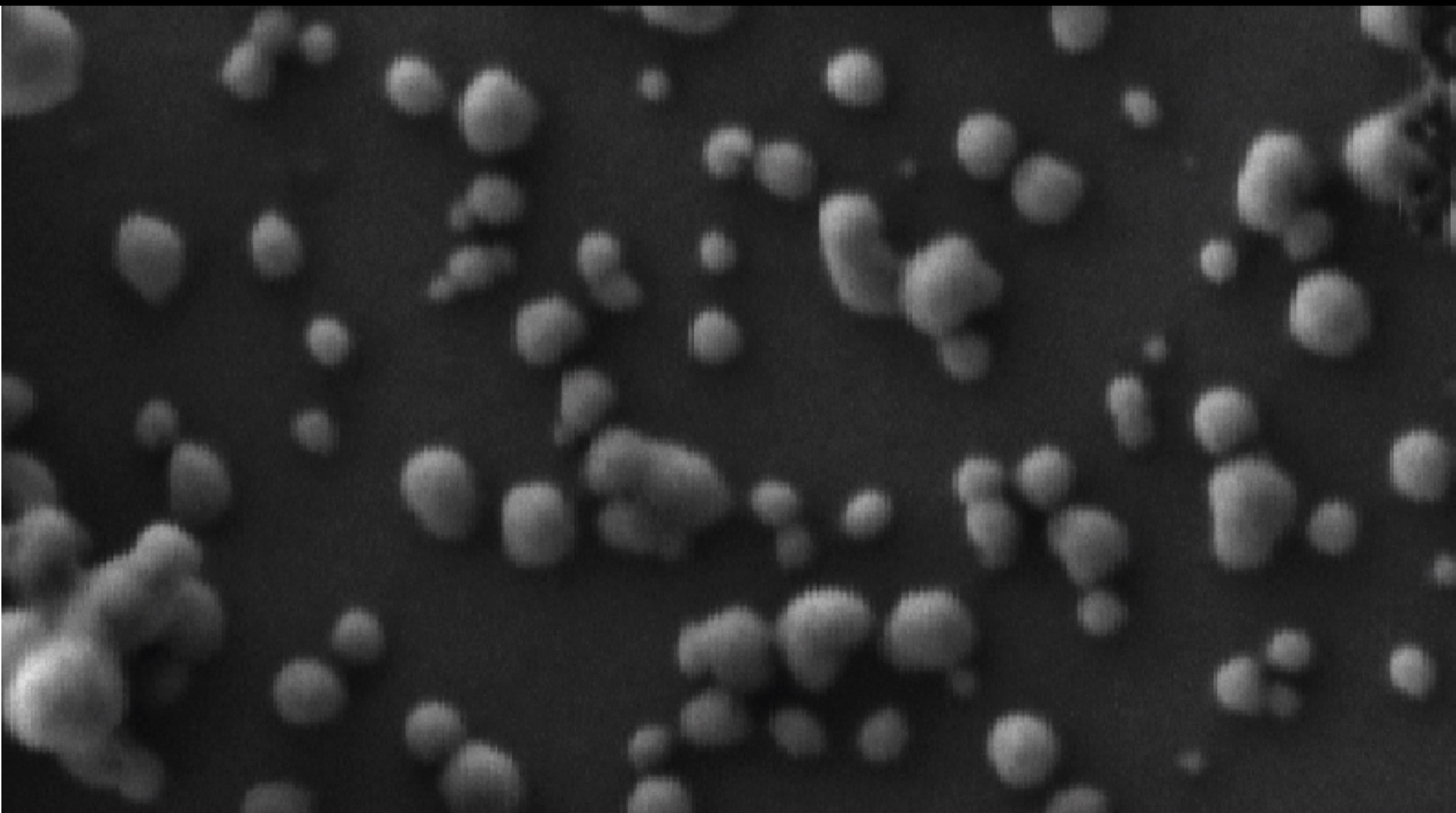

4. Results

4.1 Chapter 1. Biomedical application of small extracellular vesicles in cancer treatment

Summary of the results

This review provides an overview of the use of small EVs in cancer treatment. We describe the role of small EVs in cancer biology, including their involvement in intercellular communication, their isolation, and characterization, the potential of small EV-based therapies for cancer treatment, and preclinical and clinical trials underway to date.

Small EVs are nanovesicles between 30 and 150 nm in diameter that are produced by almost all cell types, and their biogenesis is related to the physiological function of the parent cell. Small EVs were initially known as "trash bags," but several studies have confirmed that they play an important role in cell-to-cell communication under normal conditions and in pathologies, such as cancer. These small EVs are composed of various proteins, lipids, nucleic acids, and metabolites that reflect the molecular signatures of their parent cells. The most common proteins used for small EV characterization are Alix, TSG101, RAB, small GTPases, flotillins, annexins, CD9, CD63, and CD81 [137].

Accordingly, small EVs can be useful as biomarkers in cancer, and several studies have confirmed that small EVs related to pancreatic, gastric, glioblastoma, colorectal, breast, or prostate tumors can be detected in the blood. This type of analysis of small EVs circulating in bodily fluids can provide a great deal of information about an individual’s tumor state and can be used to follow cancer and treatment progression [107].

There are several methods for isolating small EVs, such as ultracentrifugation, ultrafiltration, SEC, polymer precipitation, immunoaffinity chromatography, and microfluidic techniques. Each method is used depending on the sample origin and small EVs size, all have advantages and disadvantages, and the most used technique is ultracentrifugation [107]. The authors improved the isolation methods by combining them, e.g., by ultracentrifugation followed by SEC, to obtain urine EVs with higher purity as compared with simple ultracentrifugation or ultrafiltration.

One of the most interesting features of small EVs is their potential use as drug delivery systems, due to their ability to transport therapeutic cargo and interact with target cells. They present important advantages, such as their size, biocompatibility, ability to transport hydrophilic or hydrophobic biomolecules, ability to cross the BBB, and specific cellular tropism for the cell of origin compared to NPs. In this direction, engineering small EVs, like “nanosomes” (Exo-GNP-Dox) for lung cancer treatment, emerged. Nanosomes consisted of gold nanoparticles (GNP) conjugated to Doxorubicin (Dox) through a pH-cleavable bond and loaded into exosomes obtained from lung cancer cells and normal lung fibroblasts. These nanosomes were delivered effectively and caused a cytotoxic effect on cancer cells but not on normal cells [107].

Several preclinical models have demonstrated the potential of small EVs-based strategies to inhibit cancer progression and metastasis, and numerous ongoing human clinical trials have shown promising results. Until 2021, there were nine clinical trials in which small EVs were used as drug delivery systems. Out of them, four have already been completed, obtaining remarkable results with exosomes derived from human cells.

Engineering small EVs, iExosomes, which have been effectively used in preclinical studies, were included in the clinical trial NCT03608631.In this ongoing trial, siRNA $KRAS^{G12D}$ was loaded into exosomes derived from mesenchymal stromal cells and used as an anticancer drug in patients with metastatic pancreatic cancer [145].

Finally, small EVs were used to develop a novel treatment for COVID-19, called “EXO-CD24, which includes EVs as CD24 carriers. Some evidence suggests that the small protein CD24, which is involved in the control of T-cells proliferation, can negatively regulate inflammation. Therefore, as small EVs are involved in cell-to-cell communication, their use for CD24 protein delivery to the lungs helps to calm down the immune system [107].

Taken together, this work highlights the potential of small EVs in cancer treatment and the need for further research to fully understand their mechanisms and optimize their clinical use.

Biomedical application of small extracellular vesicles in cancer treatment

Salome Araujo-Abad [b,c], Miguel Saceda [a,b], Camino de Juan Romero [a,b,*]

[a] Unidad de Investigación, Fundación para el Fomento de la Investigación Sanitaria y Biomédica de la Comunidad Valenciana (FISABIO), Hospital General Universitario de Elche, Camí de l'Almazara 11, Elche, 03203 Alicante, Spain
[b] Instituto de Investigación, Desarrollo e Innovación en Biotecnología Sanitaria de Elche (IDiBE), Universidad Miguel Hernández, Avda, Universidad s/n, Ed. Torregaitán, Elche, 03202 Alicante, Spain
[c] Centro de Biotecnología, Universidad Nacional de Loja, Avda. Pio Jaramillo Alvarado s/n, Loja, 110111 Loja, Ecuador

ARTICLE INFO

Article history:
Received 10 September 2021
Revised 9 December 2021
Accepted 15 January 2022
Available online 19 January 2022

Keywords:
Exosomes
Cancer
Chimera
Biomarkers
Drug delivery
EXO-CD24

ABSTRACT

Extracellular vesicles (EVs) are produced by almost all cell types *in vivo* or *in vitro*. Among them, exosomes are small nanovesicles with a lipid bilayer, proteins and RNAs actively involved in cellular communication, suggesting that they may be used both as biomarkers and for therapeutic purposes in diseases such as cancer. Moreover, the idea of using them as drug delivery vehicle arises as a promising field of study. Here, we reviewed recent findings showing the importance of EVs, with special focus in exosomes as biomarkers including the most relevant proteins found in different cancer types and it is discussed the FDA approved tests which use exosomes in clinical practice. Finally, we present an overview of the different chimeric EVs developed in the last few years, demonstrating that they can be conjugate to nanoparticles, biomolecules, cancer drugs, etc., and can be developed for a specific cancer treatment. Additionally, we summarized the clinical trials where EVs are used in the treatment of several cancer types aiming to improve the prognosis of these deadly diseases.

Contents

1. Introduction

Extracellular vesicles (EVs) are mainly classified as exosomes (30–150 nm), microvesicles (MVs, 50–1000 nm) and apoptotic bodies (1–5 μm) and their mode of biogenesis is probably directly related to their physiologic function and/or to the physiopathologic state of the producing cell [1].

Exosomes are nanovesicles which are secreted from several cell types to the extracellular media and formed within the endocytic compartments called multivesicular bodies during endosome

---

* Corresponding author at: Unidad de Investigación, Fundación para el Fomento de la Investigación Sanitaria y Biomédica de la Comunidad Valenciana (FISABIO), Hospital General Universitario de Elche, Camí de l'Almazara 11, Elche, 03203 Alicante, Spain.

maturation by inward budding of their limiting membrane [2]. The word "exosome" was first used by Johnstone *et al.* (1987) [3]. It has been also suggested the existence of an association between the functions of exosomes and the plasma membrane of the mother cell. Initially, exosomes were considered as a media of removing waste proteins and other unnecessary molecules [4]. Nevertheless, diverse studies have confirmed that exosomes play an important role in cellular communication both in normal conditions and in pathologies, such as cancer [5–7].

Exosomes are made up of proteins, lipids, messenger RNA (mRNA), microRNA (miRNA), long non-coding RNA (lncRNA), DNA fragments, and metabolites from parental cells [8–10]. They are characterized by the presence of clathrin, involved in the biogenesis of MVBs and ARF6, which participate in the fusion and release of exosomes. However the most common proteins used in exosome characterization are Alix, TSG101, RAB and other families of small GTPases, flotillins, annexins, and also CD9, CD63, CD81, among others [11,12].

Research groups have investigated different types of inhibitors to target cancer cells. That includes not only chemical drugs, but also specific signal transduction pathways inhibitors, epigenetic modulators and enzymatic treatments [13] and their inhibition has successfully lead to cell death in tumor [14]. Nowadays, cancer is recognized as a plurality of different diseases highlighting the importance of the drug administration route and promoting the development of novel drug-delivery systems (DDS). Therapeutic cancer drugs present a structural diversity that affect their efficacy and toxicity profile. However, one of the main problems remain the specific targeting of the tumor cells, so that the toxic secondary effects of the cancer drugs can be reduced. Therefore, much effort has been put in the development of innovative DDS to improve bioavailability, pharmacokinetics and biodistribution profiles. The development of exosomal cargo loading approaches provides effective methods to assemble specific molecules on exosomal surface for targeted delivery. Exosomes can be equipped with ligands for specifically expressed receptors for precise targeting, although only few cell-, tissue-, and organ- specific receptors have been identified [15]. Moreover, small EVs can be guided based on newly acquired chemical or physical properties. Chemical strategy directly assembles ligands on the membrane [16,17] or is based in abnormal tissue chemical properties such as low pH microenvironment in tumors. In this way it is possible to design pH sensitive materials that confer targeting capacity to exosomes [18,19]. In physical strategy, superparamagnetic nanoparticle-equipped exosomes are guided to their targets via magnetic force [20,21]. Therefore, in recent times, there is an increasing amount of studies using small EVs as delivery systems not only for drugs but also for small molecules such as small interfering RNA (siRNAs) [22].

The fact that exosomes transport genetic cargo from parental cells to recipient cells leads to an exchange of genetic information. Cell reprogramming therapies have taken advantage of that property to engineer small EVs for clinical applications.

Interestingly, there are several proteins associated with exosomes, either as cargo or as peripheral proteins bound to the exosome surface (Table 1), that could be used as indicators of the biological state or condition of patients. For example, it has been shown that pancreatic ductal adenocarcinoma extracellular vesicles (PDAC^{EV}) signature (EGFR, EPCAM, MUC1, GPC1, WNT2) is related with pancreatic carcinoma (PC) and by looking at the expression of these proteins it is possible to differentiate between the PCs patients, healthy controls or benign pancreatic disease with an 86% sensitivity and 81% specificity [23]. Additionally, in glioblastoma, there is a positive correlation between polymerase I and transcript release factor (PTRF) expression present both in tumor tissues and blood exosomes harvested from glioma patients with tumor grade and malignancy [24].

This is why the use of exosomes as biomarkers has been largely investigated from various bodily fluids and analyzed for tumor-relevant mutations. Thus, exosomes provide an alternative to current methods of tumor detection. In the past few decades, a growing number of studies are reporting that exosomes can regulate biological functions and be used as biomarkers in pathologies for diagnosis and therapy [25,26].

Table 1

Potential biomarkers found in exosomes from different cancer types. Several proteins have been identified as exosome biomarkers in different types of cancer, in blood, urine, plasma samples, etc. Which may mean a less aggressive option for cancer diagnosis. Adapted from Zhu *et al.* (2020) [26].

Cancer type	Protein	Sample	Biological effect/clinical significance	Reference
Pancreatic	ZIP4	Serum	Promote cancer growth.	[99]
	CKAP4	Serum	Promote cell proliferation and migration.	[100]
	Eps8	Serum	Correlated with migratory cell potential. Metastatic biomarker.	[101]
	PDAC^{EV} signature (EGFR, EPCAM, MUC1, GPC1, WNT2)	Plasma	86% sensitivity and 81% specificity for differentiation between PCs, healthy controls or benign pancreatic disease.	[23]
	MIF	Plasma	Prognostic marker of PDAC liver metastasis.	[102]
	c-met, PD-L1	serum	High levels are considered negative prognostic factor.	[103]
Colorectal	CPNE3	Plasma	Lower levels are correlated with better disease-free survival.	[104]
	TMEM 180	Supernatant	Uptaking or metabolizing glutamine and arginine in tumor growth and proliferation.	[105]
	HSP60	Blood	Involved in tumorigenesis.	[106]
Breast	AnxA2	Serum	Promotes angiogenesis and metastasis.	[107,108]
	CD82	Serum/plasma	Inhibits tumor cells metastasis.	[109]
	HSP70	Blood	Promotes tumor progression	[110]
	MTA1	Serum	Promotes cancer progression and increased metastatic potential.	[111]
	TRPC5	Blood	Promotes tumor chemoresistance in metastatic patients.	[112,113]
Glioblastoma	PTRF	Serum	Associated with malignancy grade and poor prognosis.	[24]
Gastric	GKN1	Serum	Maintains mucosal homeostasis and regulates cell proliferation and differentiation.	[114]
	PSMA3, PSMA6	Serum	Promotes tumor metastasis.	[115]
	TRIM3	Serum	Inhibit tumor growth and metastasis.	[116]
Prostate	EphrinA2	Serum	Regulates tumor invasiveness and tumorigenesis.	[117]
	avβ3	Blood	Promotes cell migration and metastatic phenotype.	[118]
Lung	ADAM10	Blood	Mediates tumor progression, invasion and metastasis.	[119]
Thyroid	Thyroglo-bulin	Urine	Implicate in the probable recurrence of thyroid cancer.	[120]
	SRC, TLN1, ITGB2, CAPNS1	Serum	Tumor metastasis.	[121]

Few clinical trials using human-derived small EVs are defined as completed whereas others are still ongoing, including those with plant-derived exosomes. In this review we discuss the potential clinical application of small EVs ranging from biomarkers to therapeutic agents in the context of cancer treatments and the challenges related to its clinical translation. It is hoped that exosome-based approaches and diagnosis open up new perspectives in the fight against cancer.

2. Exosomes biomarkers in different cancer types

Our understanding of the relationship between small EVs cancer cells and mechanisms that promote cancer development has significantly advanced during the last 20 years [7]. Exosomes have been shown to be actively related to processes such as angiogenesis, migration and invasion, metastasis, modulation of the immune response, drug resistance, and adaptation to hypoxia that further facilitates angiogenesis and metastasis [27]. This is possible due to the important role of exosomes in cellular communication by transferring information between tumor cells and normal cells [1,6]. It has been shown that exosomes released by malignant tumor cells, which contain mRNAs involved in migration and metastasis, are not only taken up by less aggressive malignant cells within the same tumor but also in more distant metastasis, which alters cell behavior [28].

As mentioned before, exosomes carry different types of cargo like proteins, metabolites and nucleic acids important in the progress of cancer as a disease. Thus, this cargo can provide important information about the patient's tumor status and act as biomarkers in liquid biopsies (Table 1), which allows the identification and treatment of different cancer types [26]. Although invasive biopsies have been the most common way of detecting cancer, there are cancers, for example epithelial ovarian cancer, where surgery is necessary for a definitive diagnosis. Furthermore, liquid biopsies which are less invasive and can yield results for early detection, have gained attention in clinical-oncology practice [29].

Small EVs, and more concretely exosomes, can be extracted from bodily fluids. Depending on the tumor type, the more informative exosomes are more likely to come from a certain kind of fluid. Accordingly, exosome biomarkers for pancreatic, gastric, glioblastoma, colorectal, breast or prostate tumors can be detected in blood (Table1). Moreover, the analysis of exosomes circulating in bodily fluids can provide a great deal of information about an individual's tumor state and be used to follow cancer and treatment progression. For example, serum or plasma derived exosomes can contain DNA carrying genetic mutations and deletions, that provides information about cancer-specific mutations present in parental tumor cells [30].

A lot of effort has been put in finding biomarkers for the different types of cancer. The exosome research field has helped a lot by increasingly adding candidates for that purpose. Several transmembrane and Heat Shock proteins, growth factor receptor or solute carriers among others, can be used for cancer detection and consideration of clinical outcomes in cancer patients (Table 1). Different exosome-based diagnostic tests are already available on the market for different types of cancer detection. In 2014, Yoshikota *et al.* developed "ExoScreen", an analytical technique for early detection of colorectal cancer, based on the fact that from raw blood samples from patients, EVs are trapped by CD147 (colorectal cancer specific antibody) and CD9 (exosomal membrane marker) and detected by photosensitizing beads [31]. Along this line, in 2016, McKiernan *et al.* developed the "ExoDx Prostate (Intelliscore) EPI test" for the detection of prostate cancer, which is approved for clinical use by the Food and Drug Administration (FDA). This is based on the isolation of exosomal mRNA and the detection of PCA3 and ERG genes in a urine sample from the patient [32]. Both tests are simple, non-invasive and commonly used in clinical practice, to avoid unnecessary and undesired biopsies.

These examples illustrate the potential capability of exosomes to be used for diagnosis, prognosis, prediction, surveillance and as biomarkers in cancer progression. Despite their low concentration, exosomes in biofluids are robustly and systemically distributed and provide important molecular information about their parental tumors. However, the amount of exosome content that can be isolated from them may constitute a limitation for their clinical use. Therefore, it is necessary to improve the sampling and isolation methods in order to translate and adapt them for clinical use.

3. Sampling and isolation techniques

There are various approaches to isolate small EVs from biological fluids and cell culture supernatants for clinical applications [33]. Isolation of pure population of EVs is a challenge, and there are different procedures to achieve it: Ultracentrifugation, ultrafiltration, size exclusion chromatography (SEC), polymer precipitation, immunoaffinity chromatography and microfluidic techniques [11,27]. Each method is used for clinical applications in cancer depending of the sample origin and small EVs size. The advantages and disadvantages of their use in experimental biology and medicine has been reviewed by Salmond *et al.* [33] and Konoshenko *et al.* [34].

Ultracentrifugation is the most used technique [35]. Briefly, it consists in different centrifugation steps with increasing force: first, a low speed centrifugation (300 × *g*) to remove cell debris and cells; then, a second round of centrifugation (10,000–20,000 × *g*) in order to remove MVs and organelles; the final step consists in a high speed centrifugation (100,000–150,000 × *g*) to pellet exosomes [35–37]. Ultracentrifugation is quite expensive, time consuming and a large amount of sample is needed [36]. Ultrafiltration and size exclusion chromatography (SEC) are size-based isolation techniques, both consist of the isolation of small EVs passing through physical barriers depending on the size of the particle. Ultrafiltration is a simple procedure allowing to process several samples using nanomembranes with different cutoff molecular weight [38], but small EVs obtained by this method could result in protein contamination, low purity of EVs proteins, loss of sample or depending on the nature of the sample the filter could be blocked by protein accumulation [39,40]. On the other hand, by using SEC there is no risk of small EVs aggregation, is reproducibly and preserves small EVs integrity [41] but is a laborious method, this technique exhibits an incomplete recovery of small EVs because nonspecific adherence to the agarose chromatography column or the dilution into a multiple fractions [42]. Polymer precipitation, using polyethylene glycol is a simple, fast and inexpensive technique that preserve small EVs integrity [43]. The major issue for the extensive use of this method is contamination of small EVs samples and retention of the polymer [44]. Immunoaffinity chromatography is a method based on the affinity of proteins and their antibodies. For this purpose, antibodies are fixed on magnetic beads or other matrices [45]. Surface proteins that are present in small EVs such as CD63, CD81, CD82, CD9, Alix, annexin, EpCAM, and Rab5, can be employed as specific molecular markers for isolation. This is a very limiting method, only appropriate for the separation of exosomes with the same membrane protein expression [46,47]. Finally, microfluidic chip techniques, refers to methods based on the difference between the biochemical and physical properties of exosomes. They are classified into three categories (a) immune-affinity approach, (b) sieving (nanoporous membranes) and (c) trapping exosomes into porous structures

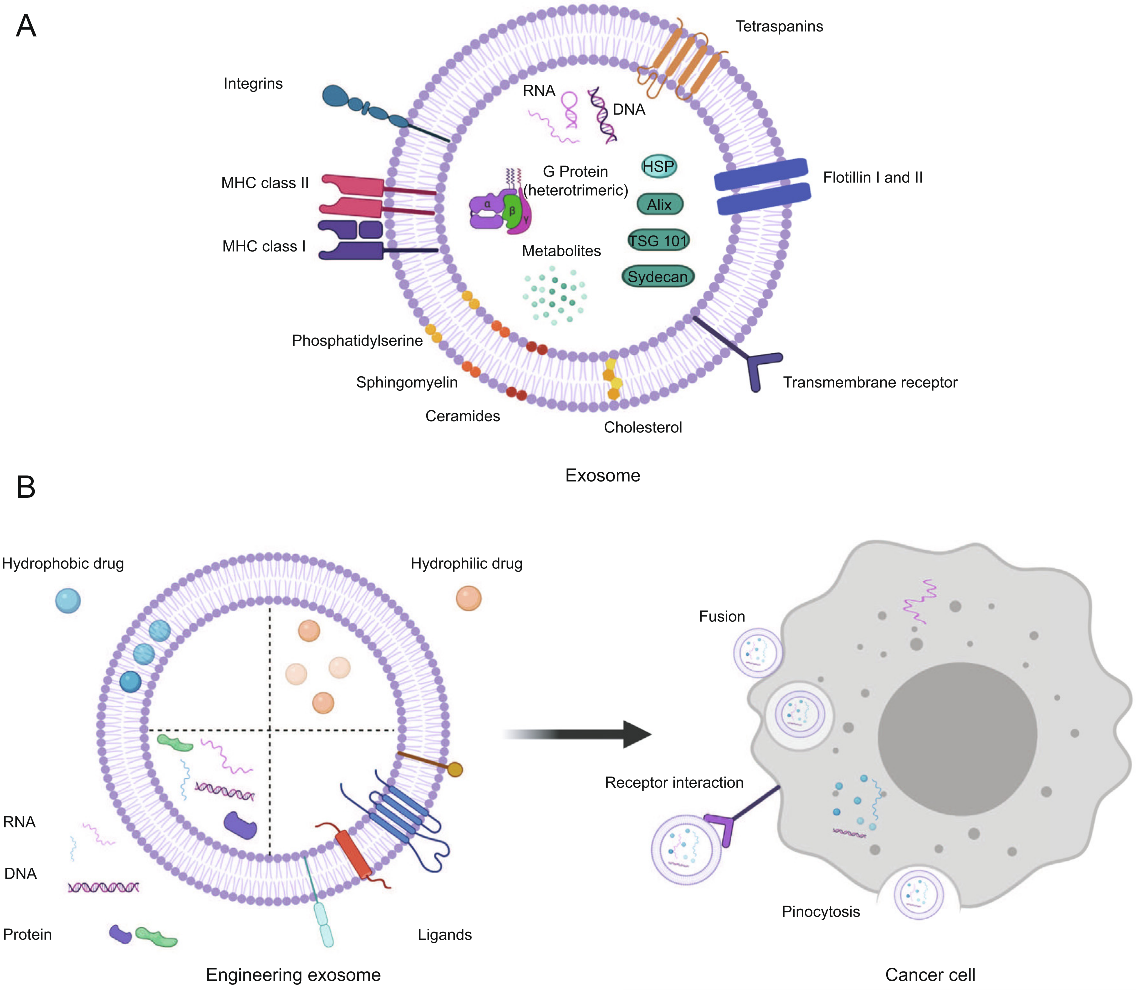

Fig. 1. Exosomes as drug vehicle. (A) Structure of exosomes, surrounded by a phospholipid bilayer, and contain proteins, such as integrins; tetraspanins for cell targeting; and other proteins, such as Alix and TSG101, that are involved in exosomal biogenesis from endosomes; Flotillin I and II; HSP, heat shock protein; MHC I and II, major histocompatibility complex; DNA, deoxyribonucleic acid, RNA, ribonucleic acid; G protein. **(B)** The aqueous space and the lipid bilayer can incorporate hydrophobic or/and hydrophilic drugs, also can be used to delivery DNA, RNA and proteins, besides, ligands can be added to the exosome surface. The exosomes with the anticancer drug or cargo, act on the target cell or on cancer stem cell (CSC) pathways to prevent tumor development. The delivery of the exosomal cargo to the recipient cell can occur by ligand–receptor interaction, pinocytosis or fusion with the cell membrane. Created in BioRender.com.

(nanowire-on-micropillars) [48]. Although the advantages of microfluidic chip techniques are high sensitivity, fast speed, small sample demand [49], the sample processing is quick and low cost. These techniques have a low yield, so larger amounts of raw materials are required to improve them [36].

In order to improve isolation techniques, authors combine them. For example, urine EVs obtained by ultracentrifugation followed by SEC, display higher purity than simple ultracentrifugation or ultrafiltration [39,50].

4. Use of small EVs as drug delivery vehicles

For years, the administration of anticancer drugs via nanoparticles (NPs) has been studied. The use of liposomes, micelles, dendrimers, mesoporous silica nanoparticles, gold nanoparticles, superparamagnetic iron oxide nanoparticles (SPION), carbon nanotubes and quantum dots has achieved good results [51–53]. However, the use of NPs have drawbacks such as early elimination, bioincompatibility, long-term toxicity, and undesired biological effects [54,55]. Those problems appear when blood proteins interact with NPs to form a dynamic ‘‘nanoparticle-protein corona” [56].

Exosomes are considered also as NPs that can transfer their cargo to the receptor cells and, given their involvement in cellular communication, their use as carriers for drug delivery has been broadly studied (Fig. 1). They present important advantages such as their size, biocompatibility, facility of transporting hydrophilic or hydrophobic biomolecules, ability to cross the Blood-brain Barrier (BBB) [57,58] and specific cellular tropism for the cell of origin compared to NPs [59,60]. Moreover, it has been shown that they minimize cytotoxicity and immunogenicity [61], which makes them more suitable for cancer therapy.

In the last few years, some research has been carried out in cancer models both *in vitro* and *in vivo*, using exosomes as drug delivery vehicles. In 2015, Yang *et al.* used exosomes derived from brain endothelial cells bEND.3, brain neuronal glioblastoma-astrocytoma U-87 MG, neuroectodermal tumor PFSK-1, and glioblastoma A-172 cell lines. They loaded 2 mg/mL of rhodamine 123, paclitaxel, or doxorubicin into the exosomes and tested them not only on cell cultures, but also on a brain cancer model in Zebrafish (*Danio rerio)* [62]. They concluded that brain endothelial cell derived exosomes could potentially be used as drug delivery vehicles of anticancer drug for the treatment of brain cancer. Interestingly, they found that exosomes have the particularity to deliver anticancer drugs across the BBB. In 2017, a study was performed in which the researchers tested whether brain endothelial cell-derived exosomes could deliver siRNA across the BBB in zebrafish [63]. Exosomes were isolated from bEND.3 cell culture, and loaded with vascular endothelial growth factor (VEGF) siRNA. Knockdown of the VEGF RNA expression and reduction in protein levels were observed in U-87 MG cells upon treatment with exosome-delivered siRNAs. In the zebrafish tumor model, exosome-delivered VEGF siRNAs were able to inhibit aggregation of xenotransplanted cancer cells [63]. Taken together, an increasing amount of evidence has been obtained indicating that the exosome use enhances the efficiency for both drug and siRNA transport *in vitro* and *in vivo.* The observation of a series of effects on cancer cells provides a strong rationale for the development of individually tailored therapeutic strategies based in exosomes as natural nanocarriers with potential usage as a drug delivery vehicle in brain cancer disease.

Recently, Melzer *et al.* (2019) have tested the efficiency of taxol loaded exosomes. Taxol is a chemotherapy drug used for the treatment of several types of solid cancers. MSC-derived exosomes were loaded with this drug and used as delivery system for the treatment of several types of cancer including metastatic breast cancer. They applied different sublethal concentrations of taxol for 24 h to human mesenchymal stroma/stem-like cell (MSC). They isolated the exosomes produced and applied them to A549 (lung cancer), SK-OV-3 (ovarian cancer) and MDA-hyb1 (breast cancer) cell cultures. Taxol-loaded exosomes caused 80–90% more death by cytotoxicity in cancer cells compared to control exosomes without taxol. *In vivo* studies were performed where they induced the formation of highly metastatic MDA-hyb1 breast cancer tumors in NODscid mice. When taxol-loaded exosomes were applied intravenously, a 60% reduction in subcutaneous tumors together with a reduction of 50% in the number of organ distant metastases was observed. Although the results were similar to the group to which only taxol was directly applied, the concentration of taxol that was used in the loaded exosomes was substantially less by 1000 times. It has been shown that exosomes can be used with low doses of drugs without causing secondary adverse effects, and effectible reach the target organ or cell [64]. Whether this effect is observed with exosomes loaded with other drugs needs to be further investigated. However, these experiments support the application of exosomes as a viable and promising alternative for the treatment of cancer.

4.1. Chimeric exosomes

In general, exosomes are better nanocarriers than other lipidic vesicles such as liposomes because they have better targeting capacity [65,66], possess higher binding affinity [67], are more stable in bodily fluids [68] and are highly biocompatible vesicles due to their endogenous origins [69]. In addition, the engineer exosomes, are less likely to be phagocytosed by macrophages and microglia, which results in a greater biostability [70]. Moreover, modification and optimization of the exosome physicochemical properties are important to increase tumor target abilities or even to enhance the BBB penetration. Therefore, the possibility of combining the advantages of exosomes and NPs for a better therapeutic result against cancer has been studied in depth. Srivastava *et al.* 2016, developed and tested the chimera called “nanosomes” (Exo-GNP-Dox) for the treatment of lung cancer. Nanosomes, consisted in gold nanoparticles (GNP) conjugated with Doxorubicin (Dox) through a pH-cleavable bond and loaded into exosomes obtained from lung cancer cells and normal lung fibroblasts (Fig. 2A). In this way they could prevent the immune response, aggregation and rapid elimination of the NPs. The efficacy of the nanosomes was tested on lung cancer cells (H129, A549), normal lung fibroblasts (MRC9) and, Dox-sensitive human coronary artery smooth muscle cells (HCASM). The researchers concluded that the nanosomes were delivered effectively and caused a cytotoxic effect on cancer cells but not on non-cancer cells [71]. Additionally, Lv *et al.* (2020) designed and tested the efficacy of engineered exosomes-thermosensitive liposomes hybrid NPs (gETL NPs) in conjunction with hyperthermic intraperitoneal chemotherapy (HIPEC), for peritoneal carcinoma (mPC) treatment (Fig. 2B). The gETL NPs were designed from CD47-expressing fibroblast exosomes that were fused with heat-sensitive liposomes. They determined that, after *in vivo* administration of gETL NPs loaded with granulocyte-macrophage colony-stimulating factor (GM-CSF) and docetaxel (DTX), tumor development was effectively inhibited and efficacy is increased with HIPEC [72]. Other type of chimeric exosomes, iExosomes, has been designed by Kamerkar *et al.* (2017). They are exosomes derived from normal fibroblast-like mesenchymal cells carrying siRNA or shRNA specific for oncogenic KRAS^{G12D}, which is generally mutated in pancreatic cancer (Fig. 2C). Treatment with iExosomes in KTC (Ptf1a$^{cre/+;}$ LSL-Kras$^{G12D/+;}$ Tgfbr2$^{lox/lox}$) and KPC (Pdx1$^{cre/+}$; LSL-Kras$^{G12D/+;}$ LSL-Trp53$^{R172H/+}$) mice *in vivo* models for pancreatic cancer, succeeded in suppressing tumor development, reducing KRAS^{G12D} expression which led to a significantly increased survival of these models. Additionally, they demonstrated that iExosomes target KRAS with more efficacy than liposomes. This efficacy depends on CD47 and is facilitated by macropinocytosis [73]. AMSC-Exo-199a are a type of engineered exosomes from adipose tissue-derived MSCs (AMSCs) modified with miR-199-a (Fig. 2D) [74]. miR-199a is the third most expressed miRNA in normal liver, but it is downregulated in almost all hepatocellular carcinoma (HCC), and therefore its reduction correlates with poor prognosis. These exosomes are capable of carrying miR-199a to hepatocarcinoma cells, sensitizing cancer cells to chemotherapeutic drugs by inhibiting the mTOR pathway and increasing the effect of Dox *in vivo* [74]. Other chimeric exosome that has been designed and tested is “Exo-CD19 CAR”, which are exosomes that express CD19 Chimeric Antigen Receptor (CD-19 CAR) [75]. In “Exo-CD19 CAR”, exosomes are used instead of complete CAR T-CD19 cells (Fig. 2E). These “Exo-CD19 CAR”, can induce cell death in malignant CD19 positive leukemia B cells without producing cytotoxicity in CD19 negative cells. In addition, they would not cause adverse side effects as occurs in normal CAR-T cell therapy [75].

The design and use of chimeric exosomes open a new route to improve their effect in cancer therapy. Thus, the evidence suggests that exosome-based therapies could be relevant for almost all types of cancer. Therefore, it has been suggested that chimeric exosomes, designed to target exclusively certain types of cancer, may be useful for transporting drugs, siRNA and cargo to the specific organ or cell more efficiently than only with NPs.

The key to improving therapies based in chimeric exosomes may lie in studying in deep the consequences of applying this technology in living animals and understanding how the immune system react to these combined therapies.

5. Clinical applications

It has been shown that small EVs play important roles in determining innate immune responses [76,77]. Small EVs released by antigen presenting cells (APCs) such as B-cells or dendritic cells (DC), display major histocompatibility complex (MHC) I and/or II on their surface and therefore can induce antigen-specific activation of T-cells [78–80]. This characteristic has allowed the development of exosome-based vaccines for cancer treatment or therapeutic approaches in humans [81,82]. Most of the research has been focused on loading EVs with MHC class I or MHC class

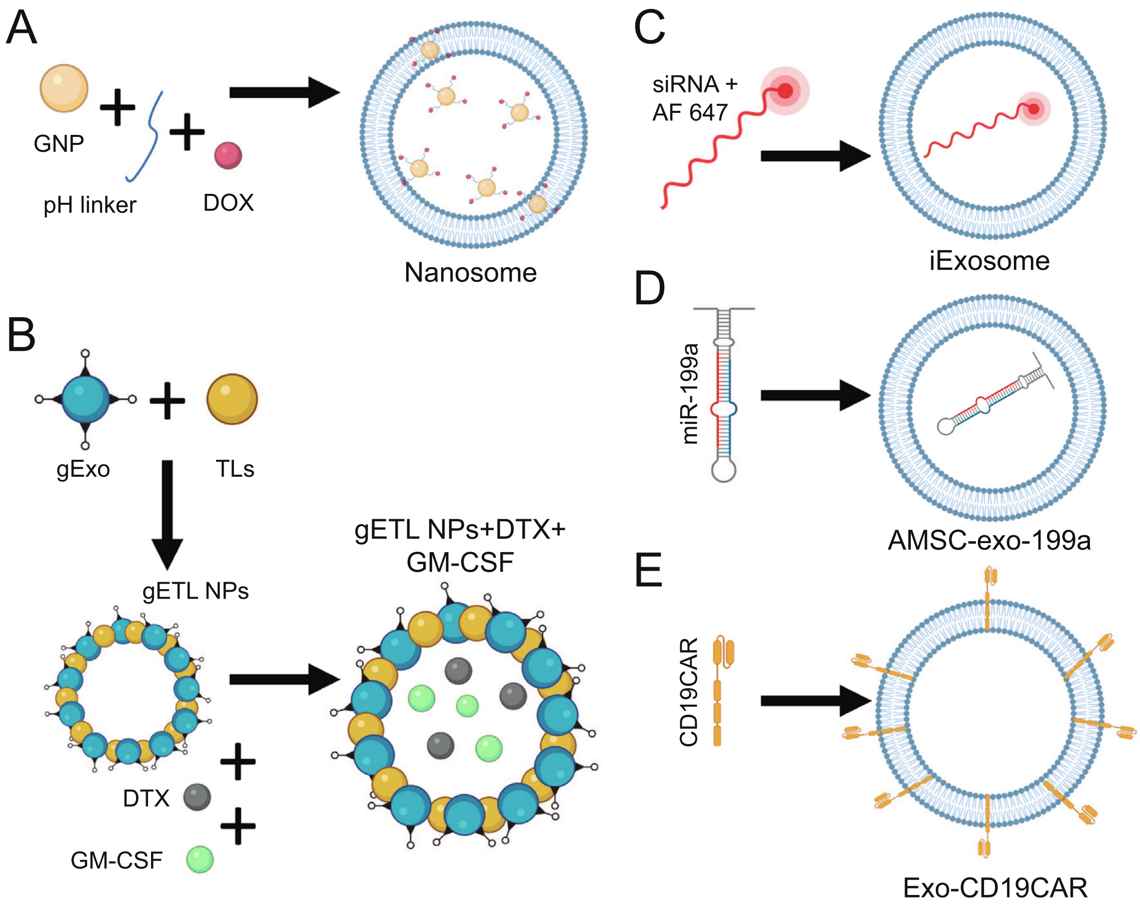

Fig. 2. Chimeric exosomes. (A) Nanosomes engineer by exosome harvest from normal lung fibroblasts cells bonded to Gold Nanoparticles (GNP), pH linker and Doxorubicin (Dox), for lung cancer treatment. **(B)** gETL NPS + DTX + GM-CSF made up of fibroblast exosomes overexpressing CD27 (gExo), thermosensitive liposomes (TLS), and loaded with colony-stimulating factor (GM-CSF) and docetaxel (DTX), for peritoneal carcinoma treatment. **(C)** iExosomes (siRNA + AF647), engineer by exosomes derived from normal fibroblast-like mesenchymal cells carrying specific siRNA for oncogenic KRAS^{G12D}, used to treat pancreatic cancer. **(D)** AMSC-*exo*-199a, exosomes from adipose tissue-derived MSCs (AMSCs) modified with miR-199-a, for hepatocellular carcinoma treatment. **(E)** ExoCD19-CAR, exosomes that express CD19 Chimeric Antigen Receptor (CD19 CAR) used for leukemia treatment. Created in BioRender.com. AF, Alexa Fluor; siRNA, small interfering RNA; miR, micro RNA.

II restricted peptides to stimulate the immune system [81], making them more effective in cancer immunotherapy.

A need to increase the exosome-induced immunity arises from the moderate T cell responses in human clinical trials. DC-derived EVs contain co-stimulatory molecules such as CD80/86 [11], and small EVs with tumor antigens are being engineered in order to improve their immunogenicity [76]. The safety of using small EVs in immunotherapy has been shown in some clinical trials using autologous, blood-derived or MSC-derived EVs [83–86] (Table 2).

Exosome-based strategies have demonstrated their potential to inhibit the progression and metastasis in diverse preclinical models and there are several clinical trials ongoing in humans with very promising results (Table 2). Such strategies may have broad implications not only for the treatment of cancer, but also for other diseases. Many early-phase clinical trials are combining the use un exosomes with cancer drug inhibitors (Table 2). Currently, there are nine clinical trials where exosomes have been used as drug delivery system. Out of them, four have already been completed, obtaining remarkable results with exosomes derived from human cells. It should be noted that one of those clinical trial performed with exosomes uses plant-derived exosomes (NCT01294072). In that trial, curcumin is loaded to plant exosomes and used as a drug delivery system in normal and colon cancer tissue. Some clinical trials (NCT01854866 and NCT02657460) used exosomes loaded with chemotherapeutic drugs, to treat patients diagnosed with malignant ascites and pleural effusion. In the preclinical study of the clinical trial NCT01854866, the use of methotrexate (MTX) and cisplatin followed by exposure to ultraviolet irradiation was reported to treat hepatocarcinoma ascites in nude mice. The results confirmed that MTX induces apoptosis and cisplatin almost completely suppressed tumor growth [87]. In NCT02657460 trial, MTX-autologous tumor derived exosomes were used with cisplatin as the comparator (Table 2).

Chimeric exosome iExosomes, that were effectively used in preclinical studies as described above Kamerkar *et al.* (2017), were included in the clinical trial NCT03608631. In this ongoing trial, siRNA Kras^{G12D} was loaded into exosomes derived from mesenchymal stromal cells and used as an anticancer drug for patients with treatment of metastatic pancreatic cancer [73].

There are other clinical trials using exosomes that has been already completed, like the one to treat melanoma patients, which finished in 2005. It consisted in an intradermal and subcutaneous application of autologous DCs derived-exosomes (Dex) loaded with MAGE 3 peptides during 4 weeks. Although no significant outcome has been observed, this phase I trial highlighted the safety of exosome administration [83] (Table 2). Later, the same research group tested in a phase I clinical trial Dex based-vaccines bearing NKG2D ligands in melanoma patients. The melanoma patients treated with the Dex vaccines had decreased NKG2D compared to healthy patients but, after inoculation of the vaccine, their values increased significantly. Therefore, those vaccines were able to increase the recirculation of NK cells in patients and restored NKG2D function

Table 2

Clinical studies of exosome-based treatments. There are four clinical trials in progress (“Ongoing”), while another five have already been completed (“Completed”) obtaining remarkable results with exosomes derived from human cells.

Disease	Year, patient, status	Intervention (exosome treatment)	Outcome	Reference
Colon cancer	February 2011, n = 35, Ongoing.	Curcumin conjugated with plant exosomes.	Deliver Curcumin to Normal and Colon Cancer Tissue using plant exosomes.	NCT01294072
Malignant ascites and pleural effusion	May 2013, n = 30, Ongoing.	Drug-packaging microparticles with chemotherapeutic drugs.	Tumor cell-derived microparticles packaging chemotherapeutic drugs are useful to treat malignant ascites and pleural effusion.	NCT01854866
Malignant pleural effusion	January 2016, n = 90, Ongoing.	Exosomes loaded with methotrexate.	Control tumor growth *in vivo* effectively and induced pleural adhesion.	NCT02657460
Pancreas cancer	August 2018, n = 28, Ongoing.	Mesenchymal Stromal Cells-derived Exosomes with KRAS^{G12D} siRNA. iExosomes	Progression-free survival (Time Frame: Up to 1 year)	[73] NCT03608631
Melanoma	2005, n = 15, Completed.	Dendritic exosomes with tumor antigenic peptides.	Proof of feasibility ad Safety.	[83]
	2009, n = 15, Completed.	Human dendritic exosomes with NKG2D ligands.	Proof of feasibility ad Safety.	[88]
Non- small lung cancer	2005, n = 13, Completed.	Dendritic exosomes with tumor antigenic peptides.	Proof of feasibility ad Safety.	[84]
Colon cancer	2008, n = 40, Completed.	Autologous ascites exosomes.	Proof of feasibility ad Safety.	[85]
Advanced non-small cell lung cancer	July 2010, n = 41, Completed.	Dendritic exosomes with tumor antigenic peptides (Dex).	Stabilization and antitumor immunity.	[86] NCT01159288

on that cells, which stimulates the NK cell pathway, that resulted in the increase of the cytotoxicity of transformed or altered cells [88]. In 2005, Morse *et al.,* also completed a phase I clinical trial for Non- Small Cell Lung Cancer (NSCLC) patient’s treatment. In this study, they tested the safety, feasibility and efficacy of autologous Dex loaded with the MAGE tumor antigens. It was shown that immune response was activated and disease progression was slowed upon Dex treatment [84].

Few years later autologous ascites exosomes (Aex) were used in combination with the granulocyte–macrophage colony-stimulating factor (GM-CSF) to treat colon cancer [85]. The clinical trial concludes that Aex plus GM-CSF but not Aex alone can induce beneficial tumor-specific antitumor cytotoxic T lymphocyte (CTL) response, indicating that this therapy was feasible and safe [85]. In a different kind of approach involving directly the immune system, IFN-γ-DC-derived extracellular vesicles were loaded with MHC class I and class II-restricted cancer antigens. This treatment used a maintenance immunotherapy in patients with inoperable NSCLC after chemotherapy induction. Dex maintains the key functions of DCs in their ability to present tumor-associated antigen and to activate their specific immune responses [89,90]. In the two phase-I trials that were conducted using the first generation of Dex (IFN-γ-free) in end-stage cancer, Dex were reported to exert natural killer (NK) cell effector functions in patients. This phase II clinical trial (Table 2), uses a second generation of Dex (IFN-γ-Dex) and it has shown that Dex are capable to stimulate NK cells of antitumor immunity. Clinical responses to Dex vaccination post-chemotherapy were evaluated and of the cohort of 22 patients recruited into the trial (95% confidence interval), 32% remained stable after nine injections and were stabilized for almost four months. Moreover, there were no treatment-related deaths and lethal events were all disease-related indicating that IFN-γ-Dex is a very well tolerated immunotherapy [86].

These results support the idea that new exosome-based antitumor therapeutic approaches are efficient and demonstrate the importance of their study in clinical practice.

5.1. Exosomes and COVID-19, new avenues for clinical application

Since early 2020, the world changed with the fast expansion of the Coronavirus disease (COVID-19). Many treatments have been employed to overcome it. However, some have been unsuccessful or have led to serious side effects [91,92]. Exosome based technology has also been used to fight this terrible pandemic and in 2021 a novel treatment for COVID-19 is being developed. NCT04747574 is a phase I study, which includes exosomes as carriers of CD24. During COVID-19, a cytokine storm takes place in the lung. That is when the immune system essentially goes into overdrive and begins attacking healthy cells. As a result, an inflammation starts, which is the principal cause of patient health deterioration and a death prognosis in COVID-19 [93]. Some evidence suggest that the small protein CD24, which is involved in the control of the T-cells proliferation [94] can negatively regulate inflammation [95]. Therefore, as exosomes are involved in cell-to-cell communication, their use for CD24 protein delivery to the lungs helps calm down the immune system.

The treatment, called “EXO-CD24”, is a biologic therapeutic agent that works inhibiting the cytokine storm. The exosomes, used as a vehicle, deliver CD24 directly to the target organ. The exosomes used in the study were isolated from T-REx™-293 cells that are designed to overexpress CD24. This treatment fights the potentially lethal overreaction of the body’s immune system to COVID-19 which is believed to be responsible for many deaths and its mechanism reduces the “required” dose and the risk of undesired events. This novel treatment is administrated to patients through an inhalation device in which the medicine EXO-CD24 is aerosolized in normal saline and inhaled for three minutes, breathing regularly, without any side effects (Table 3). The treatment achieved in its phase 1 tests more than 95% of effectiveness, helping 29 of 30 patients to quickly recover from the disease. COVID-19 patients with a moderate or severe condition were treated between three to seven days. Even if the treatment does not reduce the presence of the virus in the body, it does reduce the impact on

Table 3
EXO-CD24 treatment. Treatment using exosomes derived from T-REx™-293 cells and overexpressing CD24 were administrated to four dose escalation groups. They were aerosolized in normal saline for inhalation, via a standard hospital-grade inhalation device, for 5 days (NCT04747574).

Group	Number of patients	Doses
1	5	1x10^8 exosome particles per 2 ml saline
2	5	5x10^8 exosome particles per 2 ml saline
3	20	1x10^9 exosomes particles per 2 ml saline.
4	5	1x10^10 exosomes particles per 2 ml saline.

the lungs preventing death. This direct administration route throughout an inhalation device open new possibilities for the use of engineered exosomes as a new therapy for lung cancer treatment.

6. Conclusions and future perspectives

Since the exosome discovery as vesicles for eliminating specific proteins, research on its function in health and disease has increasingly gained interest. Recent studies have emerged indicating their major role in intercellular communication and demonstrating that exosomes are much more than simple lipidic vesicles. As they contain a lot of information about their parental cells, they are easily detectable in fluids such as blood and urine, which make them ideal to become biomarkers in cancer diagnosis. Additionally, the use of exosomes as a delivery system is an important breakthrough in targeted therapy against cancer. The fact that there are evidences that tumor cell-derived exosomes possess tropism for their parental cells opens a promising field of study [59,96]. Its tropism and ability to carry practically any cargo into a certain cell, allows the design and use of drugs for targets that were considered not achievable due to their intracellular location and difficulty in reaching them.

Although the potential of the small EVs as delivery system has been proved in preclinical models, exosome-related therapeutics are still to be approved by the U.S. FDA. To be able to use them as carriers it is necessary to gather more information about practical issues, such us their half-life in biological fluids. Moreover, there are some limitations concerning their biodistribution to specific organs that limits their therapeutic potential. The actual tendency is to use several types of lipid membranes in combination with nanoparticles of different types [97].

There has been an extensive research on small EVs as a tool in therapeutic and diagnostic settings. Here we recapitulate some ongoing clinical trials based in preclinical studies that shows their potential as biomarkers. However, we need to understand better the biology of the exosomes, the proportion of cancer derived exosomes in plasma or the insights of the packaging process among others. In addition to the evaluation of efficacy, it is of great significance to take into consideration the toxicological safety evaluation and immunological compatibility including absorption, distribution, metabolism, excretion and toxicokinetic, etc [98]. Technically, there is still room for improvement since we have to make sure that the current technologies possess the range necessary for small EVs detection. A profound understanding of small EVs will likely be essential to develop novel, more efficient small EVs -based therapeutic strategies against cancer.

Declaration of Competing Interest

The authors declare that they have no known competing financial interests or personal relationships that could have appeared to influence the work reported in this paper.

Acknowledgements

We thank E. de Juan Romero for the critical reading of manuscript. We thank A. Falcó, JL. Neira and JA. Encinar for insightful discussions. C.d.J.R. was recipient of a research "Miguel Servet Program" from predoctoral Instituto de Salud Carlos III (CP19/00095) and UGP-20-291 from FISABIO. M.S was funded by FISABIO intramural grants UGP-18-298, UGP-19-063, UGP-20-135 and UGP-20-254. S.A.A was recipient of "Carolina foundation predoctoral fellowship" 2020.

References

[1] M. Mathieu, L. Martin-Jaular, G. Lavieu, C. Théry, Specificities of secretion and uptake of exosomes and other extracellular vesicles for cell-to-cell communication, Nat. Cell Biol. 21 (1) (2019) 9–17, https://doi.org/10.1038/s41556-018-0250-9.

[2] J. Conde-Vancells, E. Rodriguez-Suarez, N. Embade, D. Gil, R. Matthiesen, M. Valle, F. Elortza, S.C. Lu, J.M. Mato, J.M. Falcon-Perez, Characterization and comprehensive proteome profiling of exosomes secreted by hepatocytes, J. Proteome Res. 7 (12) (2008) 5157–5166, https://doi.org/10.1021/pr8004887.

[3] R.M. Johnstone, M. Adam, J.R. Hammond, L. Orr, C. Turbide, Vesicle formation during reticulocyte maturation. Association of plasma membrane activities with released vesicles (exosomes), J. Biol. Chem. 262 (19) (1987) 9412–9420, https://doi.org/10.1016/S0021-9258(18)48095-7.

[4] R.M. Johnstone, Maturation of reticulocytes: formation of exosomes as a mechanism for shedding membrane proteins. The Jeanne Manery-Fisher Memorial Lecture 1991., Biochem. Cell Biol. 70 (1992) 179–190. doi: 10.1139/o92-028.

[5] J. Wolfers, A. Lozier, G. Raposo, A. Regnault, C. Théry, C. Masurier, C. Flament, S. Pouzieux, F. Faure, T. Tursz, E. Angevin, S. Amigorena, L. Zitvogel, Tumor-derived exosomes are a source of shared tumor rejection antigens for CTL cross-priming, Nat. Med. 7 (3) (2001) 297–303, https://doi.org/10.1038/85438.

[6] L. Cruz, J.A.A. Romero, R.P. Iglesia, M.H. Lopes, Extracellular vesicles: Decoding a new language for cellular communication in early embryonic development, Front. Cell Dev. Biol. 6 (2018), https://doi.org/10.3389/FCELL.2018.00094.

[7] S. Fais, L. O'Driscoll, F.E. Borras, E. Buzas, G. Camussi, F. Cappello, J. Carvalho, A. Cordeiro da Silva, H. Del Portillo, S. El Andaloussi, T. Ficko Trček, R. Furlan, A.n. Hendrix, I. Gursel, V. Kralj-Iglic, B. Kaeffer, M. Kosanovic, M.E. Lekka, G. Lipps, M. Logozzi, A. Marcilla, M. Sammar, A. Llorente, I. Nazarenko, C. Oliveira, G. Pocsfalvi, L. Rajendran, G. Raposo, E. Rohde, P. Siljander, G. van Niel, M.H. Vasconcelos, M. Yáñez-Mó, M.L. Yliperttula, N. Zarovni, A.B. Zavec, B. Giebel, Evidence-based clinical use of nanoscale extracellular vesicles in nanomedicine, ACS Nano 10 (4) (2016) 3886–3899.

[8] S. Rani, K. O'Brien, F.C. Kelleher, C. Corcoran, S. Germano, M.W. Radomski, J. Crown, L. O'Driscoll, Isolation of exosomes for subsequent mRNA, MicroRNA, and protein profiling, Methods Mol. Biol. 784 (2011) 181–195, https://doi.org/10.1007/978-1-61779-289-2_13.

[9] T. Skotland, K. Sandvig, A. Llorente, Lipids in exosomes: Current knowledge and the way forward, Prog. Lipid Res. 66 (2017) 30–41, https://doi.org/10.1016/j.plipres.2017.03.001.

[10] R. Wubbolts, R.S. Leckie, P.T.M. Veenhuizen, G. Schwarzmann, W. Möbius, J. Hoernschemeyer, J.-W. Slot, H.J. Geuze, W. Stoorvogel, Proteomic and biochemical analyses of human B cell-derived exosomes: Potential implications for their function and multivesicular body formation, J. Biol. Chem. 278 (13) (2003) 10963–10972, https://doi.org/10.1074/jbc.M207550200.

[11] S. Gurunathan, M.-H. Kang, M. Jeyaraj, M. Qasim, J.-H. Kim, Review of the isolation, characterization, biological function, and multifarious therapeutic approaches of exosomes, Cells. 8 (2019) 307, https://doi.org/10.3390/cells8040307.

[12] H. Kalra, G. Drummen, S. Mathivanan, Focus on extracellular vesicles: Introducing the next small big thing, Int. J. Mol. Sci. 17 (2) (2016) 170, https://doi.org/10.3390/ijms17020170.

[13] M. Fuentes-Baile, M.P. Ventero, J.A. Encinar, P. García-Morales, M. Poveda-Deltell, E. Pérez-Valenciano, V.M. Barberá, J. Gallego-Plazas, Á. Rodríguez-Lescure, J. Martín-Nieto, M. Saceda, Differential effects of IGF-1R small molecule tyrosine kinase inhibitors BMS-754807 and OSI-906 on human cancer cell lines, Cancers (Basel). 12 (2020) 1–18, https://doi.org/10.3390/cancers12123717.

[14] E. Carrasco-Garcia, I. Martinez-Lacaci, L. Mayor-López, E. Tristante, M. Carballo-Santana, P. García-Morales, M. Ventero Martin, M. Fuentes-Baile, Á. Rodriguez-Lescure, M. Saceda, PDGFR and IGF-1R inhibitors induce a G2/M arrest and subsequent cell death in human glioblastoma cell lines, Cells. 7 (2018) 131, https://doi.org/10.3390/cells7090131.

[15] S. Fu, Y.i. Wang, X. Xia, J.C. Zheng, Exosome engineering: Current progress in cargo loading and targeted delivery, NanoImpact. 20 (2020) 100261.

[16] S.A. Dusoswa, S.K. Horrevorts, M. Ambrosini, H. Kalay, N.J. Paauw, R. Nieuwland, M.D. Pegtel, T. Würdinger, Y. Van Kooyk, J.J. Garcia-Vallejo, Glycan modification of glioblastoma-derived extracellular vesicles enhances

receptor-mediated targeting of dendritic cells, J. Extracell. Vesicles. 8 (1) (2019) 1648995, https://doi.org/10.1080/20013078.2019.1648995.

[17] E.S. Choi, J. Song, Y.Y. Kang, H. Mok, Mannose-modified serum exosomes for the elevated uptake to murine dendritic cells and lymphatic accumulation, Macromol. Biosci. 19 (2019) 1900042, https://doi.org/10.1002/MABI.201900042.

[18] H. Lee, H. Park, G.J. Noh, E.S. Lee, pH-responsive hyaluronate-anchored extracellular vesicles to promote tumor-targeted drug delivery, Carbohydr. Polym. 202 (2018) 323–333, https://doi.org/10.1016/J.CARBPOL.2018.08.141.

[19] J.Y. Kim, J. Song, H. Jung, H. Mok, I-motif-coated exosomes as a pH-sensitive carrier for anticancer drugs, Appl. Biol. Chem. 61 (6) (2018) 599–606.

[20] M. Zhuang, X. Chen, D. Du, J. Shi, M. Deng, Q. Long, X. Yin, Y. Wang, L. Rao, SPION decorated exosome delivery of TNF-α to cancer cell membranes through magnetism, Nanoscale. 12 (1) (2020) 173–188, https://doi.org/10.1039/C9NR05865F.

[21] M. Zhuang, D. Du, L. Pu, H. Song, M. Deng, Q. Long, X. Yin, Y. Wang, L. Rao, SPION-decorated exosome delivered BAY55-9837 targeting the pancreas through magnetism to improve the blood GLC response, Small. 15 (52) (2019) 1903135.

[22] L. Alvarez-Erviti, Y. Seow, HaiFang Yin, C. Betts, S. Lakhal, M.J.A. Wood, Delivery of siRNA to the mouse brain by systemic injection of targeted exosomes, Nat. Biotechnol. 29 (4) (2011) 341–345, https://doi.org/10.1038/nbt.1807.

[23] K.S. Yang, H. Im, S. Hong, I. Pergolini, A.F. del Castillo, R. Wang, S. Clardy, C.-H. Huang, C. Pille, S. Ferrone, R. Yang, C.M. Castro, H. Lee, C.F. del Castillo, R. Weissleder, Multiparametric plasma EV profiling facilitates diagnosis of pancreatic malignancy, Sci. Transl. Med. 9 (391) (2017), https://doi.org/10.1126/scitranslmed.aal3226.

[24] K. Huang, C. Fang, K. Yi, X. Liu, H. Qi, Y. Tan, J. Zhou, Y. Li, M. Liu, Y. Zhang, J. Yang, J. Zhang, M. Li, C. Kang, The role of PTRF/Cavin 1 as a biomarker in both glioma and serum exosomes, Theranostics. 8 (6) (2018) 1540–1557, https://doi.org/10.7150/thno.22952.

[25] T. Soares Martins, J. Catita, I. Martins Rosa, O. A. B. da Cruz e Silva, A.G. Henriques, G.-C. Fan, Exosome isolation from distinct biofluids using precipitation and column-based approaches, PLoS ONE 13 (6) (2018) e0198820, https://doi.org/10.1371/journal.pone.0198820.

[26] L.e. Zhu, H.-T. Sun, S. Wang, S.-L. Huang, Y. Zheng, C.-Q. Wang, B.-Y. Hu, W. Qin, T.-T. Zou, Y. Fu, X.-T. Shen, W.-W. Zhu, Y. Geng, L.u. Lu, H.-L. Jia, L.-X. Qin, Q.-Z. Dong, Isolation and characterization of exosomes for cancer research, J. Hematol. Oncol. 13 (1) (2020), https://doi.org/10.1186/s13045-020-00987-y.

[27] M. Tschuschke, I. Kocherova, A. Bryja, P. Mozdziak, A. Angelova Volponi, K. Janowicz, R. Sibiak, H. Piotrowska-Kempisty, D. Iżycki, D. Bukowska, P. Antosik, J.A. Shibli, M. Dyszkiewicz-Konwińska, B. Kempisty, Inclusion biogenesis, methods of isolation and clinical application of human cellular exosomes, J Clin. Med. 9 (2020) 436, https://doi.org/10.3390/jcm9020436.

[28] A. Zomer, C. Maynard, F.J. Verweij, A. Kamermans, R. Schäfer, E. Beerling, R.M. Schiffelers, E. De Wit, J. Berenguer, S.I.J. Ellenbroek, T. Wurdinger, D.M. Pegtel, J. Van Rheenen, In vivo imaging reveals extracellular vesicle-mediated phenocopying of metastatic behavior, Cell 161 (2015) 1046–1057, https://doi.org/10.1016/j.cell.2015.04.042.

[29] C.V. Trinidad, A.L. Tetlow, L.E. Bantis, A.K. Godwin, Reducing ovarian cancer mortality through early detection: Approaches using circulating biomarkers, Cancer Prev. Res. 13 (3) (2020) 241–252, https://doi.org/10.1158/1940-6207.CAPR-19-0184.

[30] B.K. Thakur, H. Zhang, A. Becker, I. Matei, Y. Huang, B. Costa-Silva, Y. Zheng, A. Hoshino, H. Brazier, J. Xiang, C. Williams, R. Rodriguez-Barrueco, J.M. Silva, W. Zhang, S. Hearn, O. Elemento, N. Paknejad, K. Manova-Todorova, K. Welte, J. Bromberg, H. Peinado, D. Lyden, Double-stranded DNA in exosomes: A novel biomarker in cancer detection, Cell Res. 24 (6) (2014) 766–769, https://doi.org/10.1038/cr.2014.44.

[31] Y. Yoshioka, N. Kosaka, Y. Konishi, H. Ohta, H. Okamoto, H. Sonoda, R. Nonaka, H. Yamamoto, H. Ishii, M. Mori, K. Furuta, T. Nakajima, H. Hayashi, H. Sugisaki, H. Higashimoto, T. Kato, F. Takeshita, T. Ochiya, Ultra-sensitive liquid biopsy of circulating extracellular vesicles using ExoScreen, Nat. Commun. 5 (2014) 3591, https://doi.org/10.1038/ncomms4591.

[32] J. McKiernan, M.J. Donovan, V. O'Neill, S. Bentink, M. Noerholm, S. Belzer, J. Skog, M.W. Kattan, A. Partin, G. Andriole, G. Brown, J.T. Wei, I.M. Thompson, P. Carroll, A novel urine exosome gene expression assay to predict high-grade prostate cancer at initial biopsy, JAMA Oncol. 2 (7) (2016) 882, https://doi.org/10.1001/jamaoncol.2016.0097.

[33] N. Salmond, K.C. Williams, Williams, Isolation and characterization of extracellular vesicles for clinical applications in cancer – time for standardization?, Nanoscale Adv 3 (7) (2021) 1830–1852, https://doi.org/10.1039/D0NA00676A.

[34] M.Y. Konoshenko, E.A. Lekchnov, A.V. Vlassov, P.P. Laktionov, Isolation of extracellular vesicles: General methodologies and latest trends, Biomed Res. Int. 2018 (2018) 1–27, https://doi.org/10.1155/2018/8545347.

[35] C. Théry, S. Amigorena, G. Raposo, A. Clayton, Isolation and characterization of exosomes from cell culture supernatants and biological fluids, Curr. Protoc. Cell Biol. 30 (2006) 3.22.1-3.22.29. doi: 10.1002/0471143030.CB0322S30.

[36] X.X. Yang, C. Sun, L. Wang, X.L. Guo, New insight into isolation, identification techniques and medical applications of exosomes, J. Control. Release. 308 (2019) 119–129, https://doi.org/10.1016/J.JCONREL.2019.07.021.

[37] K.W. Witwer, E.I. Buzás, L.T. Bemis, A. Bora, C. Lässer, J. Lötvall, E.N. Nolte-'t Hoen, M.G. Piper, S. Sivaraman, J. Skog, C. Théry, M.H. Wauben, F. Hochberg, Standardization of sample collection, isolation and analysis methods in extracellular vesicle research, J. Extracell. Vesicles. 2 (1) (2013) 20360.

[38] A. Cheruvanky, H. Zhou, T. Pisitkun, J.B. Kopp, M.A. Knepper, P.S.T. Yuen, R.A. Star, Rapid isolation of urinary exosomal biomarkers using a nanomembrane ultrafiltration concentrator, Am. J. Physiol. Renal Physiol. 292 (5) (2007) F1657–F1661.

[39] M. Salih, R. Zietse, E.J. Hoorn, Urinary extracellular vesicles and the kidney: biomarkers and beyond, Am. J. Physiol. Renal Physiol. 306 (11) (2014) F1251–F1259.

[40] D.D. Taylor, S. Shah, Methods of isolating extracellular vesicles impact downstream analyses of their cargoes, Methods 87 (2015) 3–10, https://doi.org/10.1016/J.YMETH.2015.02.019.

[41] A.N. Böing, E. van der Pol, A.E. Grootemaat, F.A.W. Coumans, A. Sturk, R. Nieuwland, Single-step isolation of extracellular vesicles by size-exclusion chromatography, J. Extracell. Vesicles. 3 (1) (2014) 23430.

[42] D.D. Taylor, W. Zacharias, C. Gercel-Taylor, Exosome isolation for proteomic analyses and RNA profiling, Methods Mol. Biol. 728 (2011) 235–246, https://doi.org/10.1007/978-1-61779-068-3_15.

[43] M.A. Rider, S.N. Hurwitz, D.G. Meckes, ExtraPEG: A polyethylene glycol-based method for enrichment of extracellular vesicles, Sci. Rep. 6 (2016) 1–14, https://doi.org/10.1038/srep23978.

[44] A. Gámez-Valero, M. Monguió-Tortajada, L. Carreras-Planella, M. Franquesa, K. Beyer, F.E. Borràs, Size-exclusion chromatography-based isolation minimally alters extracellular vesicles' characteristics compared to precipitating agents, Sci. Rep. 6 (1) (2016).

[45] J. Fitzgerald, P. Leonard, E. Darcy, S. Sharma, R. O'Kennedy, Immunoaffinity chromatography: Concepts and applications, Methods Mol. Biol. 1485 (2017) 27–51, https://doi.org/10.1007/978-1-4939-6412-3_3.

[46] D.W. Greening, R. Xu, H. Ji, B.J. Tauro, R.J. Simpson, A protocol for exosome isolation and characterization: Evaluation of ultracentrifugation, density-gradient separation, and immunoaffinity capture methods, Methods Mol. Biol. 1295 (2015) 179–209, https://doi.org/10.1007/978-1-4939-2550-6_15.

[47] B.J. Tauro, D.W. Greening, R.A. Mathias, H. Ji, S. Mathivanan, A.M. Scott, R.J. Simpson, Comparison of ultracentrifugation, density gradient separation, and immunoaffinity capture methods for isolating human colon cancer cell line LIM1863-derived exosomes, Methods 56 (2) (2012) 293–304.

[48] A. Liga, A.D.B. Vliegenthart, W. Oosthuyzen, J.W. Dear, M. Kersaudy-Kerhoas, Exosome isolation: a microfluidic road-map, Lab Chip. 15 (11) (2015) 2388–2394, https://doi.org/10.1039/C5LC00240K.

[49] M. He, J. Crow, M. Roth, Y. Zeng, A.K. Godwin, Integrated immunoisolation and protein analysis of circulating exosomes using microfluidic technology, Lab Chip. 14 (19) (2014) 3773, https://doi.org/10.1039/C4LC00662C.

[50] I.M. Rood, J.K.J. Deegens, M.L. Merchant, W.P.M. Tamboer, D.W. Wilkey, J.F.M. Wetzels, J.B. Klein, Comparison of three methods for isolation of urinary microvesicles to identify biomarkers of nephrotic syndrome, Kidney Int. 78 (8) (2010) 810–816.

[51] M. Fuentes-Baile, D. Bello-Gil, E. Pérez-Valenciano, J.M. Sanz, P. García-Morales, B. Maestro, M.P. Ventero, C. Alenda, V.M. Barberá, M. Saceda, CLytA-DAAO, free and immobilized in magnetic nanoparticles, induces cell death in human cancer cells, Biomolecules. 10 (2020) 222, https://doi.org/10.3390/biom10020222.

[52] M. Fuentes-Baile, P. García-Morales, E. Pérez-Valenciano, M.P. Ventero, J.M. Sanz, C.d.J. Romero, V.M. Barberá, C. Alenda, M. Saceda, Cell death mechanisms induced by CLytA-DAAO chimeric enzyme in human tumor cell lines, Int. J. Mol. Sci. 21 (22) (2020) 8522, https://doi.org/10.3390/ijms21228522.

[53] M. Fuentes-Baile, E. Pérez-Valenciano, P. García-Morales, C. de Juan Romero, D. Bello-Gil, V.M. Barberá, Á. Rodríguez-Lescure, J.M. Sanz, C. Alenda, M. Saceda, Clyta-daao chimeric enzyme bound to magnetic nanoparticles. A new therapeutical approach for cancer patients?, Int J. Mol. Sci. 22 (3) (2021) 1477, https://doi.org/10.3390/ijms22031477.

[54] M.J. Mitchell, M.M. Billingsley, R.M. Haley, M.E. Wechsler, N.A. Peppas, R. Langer, Engineering precision nanoparticles for drug delivery, Nat. Rev. Drug Discov. 20 (2) (2021) 101–124, https://doi.org/10.1038/s41573-020-0090-8.

[55] H. Parhiz, M. Khoshnejad, J.W. Myerson, E. Hood, P.N. Patel, J.S. Brenner, V.R. Muzykantov, Unintended effects of drug carriers: Big issues of small particles, Adv. Drug Deliv. Rev. 130 (2018) 90–112, https://doi.org/10.1016/j.addr.2018.06.023.

[56] Y.-F. Zhang, J.-B. Shi, C. Li, Small extracellular vesicle loading systems in cancer therapy: Current status and the way forward, Cytotherapy. 21 (11) (2019) 1122–1136, https://doi.org/10.1016/j.jcyt.2019.10.002.

[57] X. Luan, K. Sansanaphongpricha, I. Myers, H. Chen, H. Yuan, D. Sun, Engineering exosomes as refined biological nanoplatforms for drug delivery, Acta Pharmacol. Sin. 38 (6) (2017) 754–763, https://doi.org/10.1038/aps.2017.12.

[58] E.V. Batrakova, M.S. Kim, Using exosomes, naturally-equipped nanocarriers, for drug delivery, J. Control. Release. 219 (2015) 396–405, https://doi.org/10.1016/j.jconrel.2015.07.030.

[59] L.i. Qiao, S. Hu, K.e. Huang, T. Su, Z. Li, A. Vandergriff, J. Cores, P.-U. Dinh, T. Allen, D. Shen, H. Liang, Y. Li, K.e. Cheng, Tumor cell-derived exosomes home to their cells of origin and can be used as trojan horses to deliver cancer drugs, Theranostics. 10 (8) (2020) 3474–3487, https://doi.org/10.7150/thno.39434.

[60] S. Barua, S. Mitragotri, Challenges associated with penetration of nanoparticles across cell and tissue barriers: A review of current status and

future prospects, Nano Today 9 (2) (2014) 223–243, https://doi.org/10.1016/j.nantod.2014.04.008.

[61] J. Dai, Y. Su, S. Zhong, L. Cong, B. Liu, J. Yang, Y. Tao, Z. He, C. Chen, Y. Jiang, Exosomes: key players in cancer and potential therapeutic strategy, Signal Transduct. Target. Ther. 5 (2020) 145, https://doi.org/10.1038/s41392-020-00261-0.

[62] T. Yang, P. Martin, B. Fogarty, A. Brown, K. Schurman, R. Phipps, V.P. Yin, P. Lockman, S. Bai, Exosome delivered anticancer drugs across the blood-brain barrier for brain cancer therapy in Danio Rerio, Pharm. Res. 32 (6) (2015) 2003–2014, https://doi.org/10.1007/s11095-014-1593-y.

[63] T. Yang, B. Fogarty, B. LaForge, S. Aziz, T. Pham, L. Lai, S. Bai, Delivery of small interfering RNA to inhibit vascular endothelial growth factor in zebrafish using natural brain endothelia cell-secreted exosome nanovesicles for the treatment of brain cancer, AAPS J. 19 (2) (2017) 475–486, https://doi.org/10.1208/s12248-016-0015-y.

[64] C. Melzer, V. Rehn, Y. Yang, H. Bähre, J. von der Ohe, R. Hass, Taxol-loaded MSC-Derived exosomes provide a therapeutic vehicle to target metastatic breast cancer and other carcinoma cells, Cancers (Basel). 11 (2019) 798, https://doi.org/10.3390/cancers11060798.

[65] C.K. Das, B.C. Jena, I. Banerjee, S. Das, A. Parekh, S.K. Bhutia, M. Mandal, Exosome as a novel shuttle for delivery of therapeutics across biological barriers, Mol. Pharm. 16 (1) (2019) 24–40.

[66] S. EL Andaloussi, S. Lakhal, I. Mäger, M.J.A. Wood, Exosomes for targeted siRNA delivery across biological barriers, Adv. Drug Deliv. Rev. 65 (3) (2013) 391–397.

[67] G. Kibria, E.K. Ramos, Y. Wan, D.R. Gius, H. Liu, Exosomes as a drug delivery system in cancer therapy: Potential and challenges, Mol. Pharm. 15 (9) (2018) 3625–3633.

[68] F. Soltani, H. Parhiz, A. Mokhtarzadeh, M. Ramezani, Synthetic and biological vesicular nano-carriers designed for gene delivery, Curr. Pharm. Des. 21 (2015) 6214–6235, https://doi.org/10.2174/1381612821666151027153410.

[69] T.L. Whiteside, Immune modulation of T-cell and NK (natural killer) cell activities by TEXs (tumour-derived exosomes), Biochem. Soc. Trans. 41 (2013) 251, https://doi.org/10.1042/BST20120265.

[70] E. Koh, E.J. Lee, G.H. Nam, Y. Hong, E. Cho, Y. Yang, I.S. Kim, Exosome-SIRPα, a CD47 blockade increases cancer cell phagocytosis, Biomaterials 121 (2017) 121–129, https://doi.org/10.1016/J.BIOMATERIALS.2017.01.004.

[71] A. Srivastava, N. Amreddy, A. Babu, J. Panneerselvam, M. Mehta, R. Muralidharan, A. Chen, Y.D. Zhao, M. Razaq, N. Riedinger, H. Kim, S. Liu, S. Wu, A.B. Abdel-Mageed, A. Munshi, R. Ramesh, Nanosomes carrying doxorubicin exhibit potent anticancer activity against human lung cancer cells, Nature 6 (2016) 1–15, https://doi.org/10.1038/srep38541.

[72] Q. Lv, L. Cheng, Y. Lu, X. Zhang, Y. Wang, J. Deng, J. Zhou, B.o. Liu, J. Liu, Thermosensitive exosome–liposome hybrid nanoparticle-mediated chemoimmunotherapy for improved treatment of metastatic peritoneal cancer, Adv. Sci. 7 (18) (2020) 2000515, https://doi.org/10.1002/advs.202000515.

[73] S. Kamerkar, V.S. LeBleu, H. Sugimoto, S. Yang, C.F. Ruivo, S.A. Melo, J.J. Lee, R. Kalluri, Exosomes facilitate therapeutic targeting of oncogenic KRAS in pancreatic cancer, Nature 546 (7659) (2017) 498–503, https://doi.org/10.1038/nature22341.

[74] G. Lou, L. Chen, C. Xia, W. Wang, J. Qi, A. Li, L. Zhao, Z. Chen, M. Zheng, Y. Liu, MiR-199a-modified exosomes from adipose tissue-derived mesenchymal stem cells improve hepatocellular carcinoma chemosensitivity through mTOR pathway, J. Exp. Clin. Cancer Res. 39 (1) (2020), https://doi.org/10.1186/s13046-019-1512-5.

[75] S. Haque, S.R. Vaiselbuh, CD19 Chimeric antigen receptor-exosome targets CD19 positive B-lineage acute lymphocytic leukemia and induces cytotoxicity, Cancers (Basel). 13 (6) (2021) 1401, https://doi.org/10.3390/cancers13061401.

[76] X. Zhou, F. Xie, L. Wang, L. Zhang, S. Zhang, M. Fang, F. Zhou, The function and clinical application of extracellular vesicles in innate immune regulation, Cell. Mol. Immunol. 17 (4) (2020) 323–334, https://doi.org/10.1038/s41423-020-0391-1.

[77] P. Kurywchak, J. Tavormina, R. Kalluri, The emerging roles of exosomes in the modulation of immune responses in cancer, Genome Med. 10 (2018), https://doi.org/10.1186/S13073-018-0535-4/FIGURES/1.

[78] G. Raposo, H.W. Nijman, W. Stoorvogel, R. Leijendekker, C.V. Harding, C.J.M. Melief, H.J. Geuze, B lymphocytes secrete antigen-presenting vesicles, J. Exp. Med. 183 (1996) 1172, https://doi.org/10.1084/JEM.183.3.1161.

[79] M.F.S. Lindenbergh, W. Stoorvogel, Antigen presentation by extracellular vesicles from professional antigen-presenting cells, Annu. Rev. Immunol. 36 (1) (2018) 435–459.

[80] H. Schwarzenbach, P.B. Gahan, Exosomes in immune regulation, Non-Coding RNA. 7 (1) (2021) 4.

[81] S. Hiltbrunner, P. Larssen, M. Eldh, M.-J. Martinez-Bravo, A.K. Wagner, M.C.I. Karlsson, S. Gabrielsson, Exosomal cancer immunotherapy is independent of MHC molecules on exosomes, Oncotarget. 7 (25) (2016) 38707–38717.

[82] S. Hong, S. Ruan, Z. Greenberg, M. He, J.L. McGill, Development of surface engineered antigenic exosomes as vaccines for respiratory syncytial virus, Sci. Rep. 11 (1) (2021), https://doi.org/10.1038/s41598-021-00765-x.

[83] B. Escudier, T. Dorval, N. Chaput, F. André, M.P. Caby, S. Novault, C. Flament, C. Leboulaire, C. Borg, S. Amigorena, C. Boccaccio, C. Bonnerot, O. Dhellin, M. Movassagh, S. Piperno, C. Robert, V. Serra, N. Valente, J.B. Le Pecq, A. Spatz, O. Lantz, T. Tursz, E. Angevin, L. Zitvogel, Vaccination of metastatic melanoma patients with autologous dendritic cell (DC) derived-exosomes: Results of the first phase 1 clinical trial, J. Transl. Med. 3 (2005) 1–13, https://doi.org/10.1186/1479-5876-3-10.

[84] M.A. Morse, J. Garst, T. Osada, S. Khan, A. Hobeika, T.M. Clay, N. Valente, R. Shreeniwas, M.A. Sutton, A. Delcayre, D.H. Hsu, J.B. Le Pecq, H.K. Lyerly, A phase I study of dexosome immunotherapy in patients with advanced non-small cell lung cancer, J. Transl. Med. 3 (2005) 1–8, https://doi.org/10.1186/1479-5876-3-9.

[85] S. Dai, D. Wei, Z. Wu, X. Zhou, X. Wei, H. Huang, G. Li, Phase I clinical trial of autologous ascites-derived exosomes combined with GM-CSF for colorectal cancer, Mol. Ther. 16 (4) (2008) 782–790, https://doi.org/10.1038/mt.2008.1.

[86] B. Besse, M. Charrier, V. Lapierre, E. Dansin, O. Lantz, D. Planchard, T. Le Chevalier, A. Livartoski, F. Barlesi, A. Laplanche, S. Ploix, N. Vimond, I. Peguillet, C. Théry, L. Lacroix, I. Zoernig, K. Dhodapkar, M. Dhodapkar, S. Viaud, J.-C. Soria, K.S. Reiners, E. Pogge von Strandmann, F. Vély, S. Rusakiewicz, A. Eggermont, J.M. Pitt, L. Zitvogel, N. Chaput, Dendritic cell-derived exosomes as maintenance immunotherapy after first line chemotherapy in NSCLC, Oncoimmunology. 5 (4) (2016) e1071008, https://doi.org/10.1080/2162402X.2015.1071008.

[87] K. Tang, Y. Zhang, H. Zhang, P. Xu, J. Liu, J. Ma, M. Lv, D. Li, F. Katirai, G.X. Shen, G. Zhang, Z.H. Feng, D. Ye, B. Huang, Delivery of chemotherapeutic drugs in tumour cell-derived microparticles, Nat. Commun. 3 (2012) 1–11, https://doi.org/10.1038/ncomms2282.

[88] S. Viaud, M. Terme, C. Flament, J. Taieb, F. André, S. Novault, B. Escudier, C. Robert, S. Caillat-Zucman, T. Tursz, L. Zitvogel, N. Chaput, Dendritic cell-derived exosomes promote natural killer cell activation and proliferation: a role for NKG2D ligands and IL-15Ralpha, PLoS ONE 4 (2009), https://doi.org/10.1371/JOURNAL.PONE.0004942.

[89] J.M. Pitt, M. Charrier, S. Viaud, F. André, B. Besse, N. Chaput, L. Zitvogel, Dendritic cell–derived exosomes as immunotherapies in the fight against cancer, J. Immunol. 193 (3) (2014) 1006–1011, https://doi.org/10.4049/jimmunol.1400703.

[90] P.D. Robbins, A.E. Morelli, Regulation of immune responses by extracellular vesicles, Nat. Rev. Immunol. 14 (3) (2014) 195–208, https://doi.org/10.1038/nri3622.

[91] İ. Aygün, M. Kaya, R. Alhajj, Identifying side effects of commonly used drugs in the treatment of Covid 19, Sci. Rep. 10 (2020) 1–14, https://doi.org/10.1038/s41598-020-78697-1.

[92] L.i. Zou, L. Dai, X. Zhang, Z. Zhang, Z. Zhang, Hydroxychloroquine and chloroquine: a potential and controversial treatment for COVID-19, Arch. Pharm. Res. 43 (8) (2020) 765–772, https://doi.org/10.1007/s12272-020-01258-7.

[93] Q. Ye, B. Wang, J. Mao, The pathogenesis and treatment of the 'cytokine storm'' in COVID-19', J. Infect. 80 (6) (2020) 607–613, https://doi.org/10.1016/j.jinf.2020.03.037.

[94] O. Li, P. Zheng, Y. Liu, CD24 expression on T cells is required for optimal T cell proliferation in lymphopenic host, J. Exp. Med. 200 (2004) 1083–1089, https://doi.org/10.1084/jem.20040779.

[95] J. Lee, P. Smeriglio, J. Dragoo, W.J. Maloney, N. Bhutani, CD24 enrichment protects while its loss increases susceptibility of juvenile chondrocytes towards inflammation, Arthritis Res. Ther. 18 (2016) 292, https://doi.org/10.1186/s13075-016-1183-y.

[96] S.E. Emam, A.S. Abu Lila, N.E. Elsadek, H. Ando, T. Shimizu, K. Okuhira, Y.u. Ishima, M.A. Mahdy, F.-E. Ghazy, T. Ishida, Cancer cell-type tropism is one of crucial determinants for the efficient systemic delivery of cancer cell-derived exosomes to tumor tissues, Eur. J. Pharm. Biopharm. 145 (2019) 27–34.

[97] J. Shen, J. Karges, K. Xiong, Y.u. Chen, L. Ji, H. Chao, Cancer cell membrane camouflaged iridium complexes functionalized black-titanium nanoparticles for hierarchical-targeted synergistic NIR-II photothermal and sonodynamic therapy, Biomaterials 275 (2021) 120979, https://doi.org/10.1016/j.biomaterials.2021.120979.

[98] X. Liu, I. Tang, Z.A. Wainberg, H. Meng, Safety considerations of cancer nanomedicine – A key step towards translation, Small. 16 (2020), https://doi.org/10.1002/SMLL.202000673 e2000673.

[99] H. Jin, P. Liu, Y. Wu, X. Meng, M. Wu, J. Han, X. Tan, Exosomal zinc transporter ZIP4 promotes cancer growth and is a novel diagnostic biomarker for pancreatic cancer, Cancer Sci. 109 (9) (2018) 2946–2956, https://doi.org/10.1111/cas.13737.

[100] H. Kimura, H. Yamamoto, T. Harada, K. Fumoto, Y. Osugi, R. Sada, N. Maehara, H. Hikita, S. Mori, H. Eguchi, M. Ikawa, T. Takehara, A. Kikuchi, CKAP4, a DKK1 receptor, is a biomarker in exosomes derived from pancreatic cancer and a molecular target for therapy, Clin. Cancer Res. 25 (6) (2019) 1936–1947, https://doi.org/10.1158/1078-0432.CCR-18-2124.

[101] K. Ohshima, K. Hatakeyama, K. Kanto, T. Ide, Y. Watanabe, S. Moromizato, K. Wakabayashi-Nakao, N. Sakura, K. Yamaguchi, T. Mochizuki, Comparative proteomic analysis identifies exosomal Eps8 protein as a potential metastatic biomarker for pancreatic cancer, Oncol. Rep. 41 (2019) 1019–1034, https://doi.org/10.3892/or.2018.6869.

[102] B. Costa-Silva, N.M. Aiello, A.J. Ocean, S. Singh, H. Zhang, B. Thakur, A. Becker, A. Hoshino, M.T. Mark, H. Molina, J. Xiang, T. Zhang, T.-M. Theilen, G. García-Santos, C. Williams, Y. Ararso, Y. Huang, G. Rodrigues, T.-L. Shen, K.J. Labori, I. M.B. Lothe, E.H. Kure, J. Hernandez, A. Doussot, S.H. Ebbesen, P. Grandgenett, M. Hollingsworth, M. Jain, K. Mallya, S.K. Batra, W. Jarnagin, R. Schwartz, I. Matei, H. Peinado, B.Z. Stanger, J. Bromberg, D. Lyden, Pancreatic cancer exosomes initiate pre-metastatic niche formation in the liver, Nat. Cell Biol. 17 (6) (2015) 816–826, https://doi.org/10.1038/ncb3169.

[103] A. Lux, C. Kahlert, R. Grützmann, C. Pilarsky, c-Met and PD-l1 on circulating exosomes as diagnostic and prognostic markers for pancreatic cancer, Int. J. Mol. Sci. 20 (2019) 3305, https://doi.org/10.3390/ijms20133305.

[104] B.o. Sun, Y. Li, Y. Zhou, T.K. Ng, C. Zhao, Q. Gan, X. Gu, J. Xiang, Circulating exosomal CPNE3 as a diagnostic and prognostic biomarker for colorectal cancer, J. Cell. Physiol. 234 (2) (2019) 1416–1425, https://doi.org/10.1002/jcp.26936.

[105] M. Yasunaga, S. Saijou, S. Hanaoka, T. Anzai, R. Tsumura, Y. Matsumura, Significant antitumor effect of an antibody against TMEM180, a new colorectal cancer-specific molecule, Cancer Sci. 110 (2) (2019) 761–770, https://doi.org/10.1111/cas.13907.

[106] C. Campanella, F. Rappa, C. Sciumè, A. Marino Gammazza, R. Barone, F. Bucchieri, S. David, G. Curcurù, C. Caruso Bavisotto, A. Pitruzzella, G. Geraci, G. Modica, F. Farina, G. Zummo, S. Fais, E. Conway de Macario, A.J.L. Macario, F. Cappello, Heat shock protein 60 levels in tissue and circulating exosomes in human large bowel cancer before and after ablative surgery, Cancer 121 (18) (2015) 3230–3239, https://doi.org/10.1002/cncr.29499.

[107] S. Maji, P. Chaudhary, I. Akopova, P.M. Nguyen, R.J. Hare, I. Gryczynski, J.K. Vishwanatha, Exosomal annexin II promotes angiogenesis and breast cancer metastasis, Mol. Cancer Res. 15 (1) (2017) 93–105, https://doi.org/10.1158/1541-7786.MCR-16-0163.

[108] P. Chaudhary, L.D. Gibbs, S. Maji, C.M. Lewis, S. Suzuki, J.K. Vishwanatha, Serum exosomal-annexin a2 is associated with african-American triple-negative breast cancer and promotes angiogenesis, Breast Cancer Res. 22 (2020) 1–15, https://doi.org/10.1186/s13058-020-1251-8.

[109] X. Wang, W. Zhong, J. Bu, Y. Li, R. Li, R. Nie, C. Xiao, K. Ma, X. Huang, Y. Li, Exosomal protein CD82 as a diagnostic biomarker for precision medicine for breast cancer, Mol. Carcinog. 58 (5) (2019) 674–685, https://doi.org/10.1002/mc.22960.

[110] G. Chanteloup, M. Cordonnier, N. Isambert, A. Bertaut, A. Hervieu, A. Hennequin, M. Luu, S. Zanetta, B. Coudert, L. Bengrine, I. Desmoulins, L. Favier, A. Lagrange, P.-B. Pages, I. Gutierrez, J. Lherminier, L. Avoscan, C. Jankowski, C. Rébé, A. Chevriaux, M.-M. Padeano, C. Coutant, S. Ladoire, S. Causeret, L. Arnould, C. Charon-Barra, V. Cottet, J. Blanc, C. Binquet, M. Bardou, C. Garrido, J. Gobbo, Monitoring HSP70 exosomes in cancer patients' follow up: a clinical prospective pilot study, J. Extracell. Vesicles. 9 (1) (2020) 1766192, https://doi.org/10.1080/20013078.2020.1766192.

[111] B.N. Hannafon, A.L. Gin, Y.-F. Xu, M. Bruns, C.L. Calloway, W.-Q. Ding, Metastasis-associated protein 1 (MTA1) is transferred by exosomes and contributes to the regulation of hypoxia and estrogen signaling in breast cancer cells, Cell Commun. Signal. 17 (2019) 13, https://doi.org/10.1186/s12964-019-0325-7.

[112] X. Ma, Z. Chen, D. Hua, D. He, L. Wang, P. Zhang, J. Wang, Y. Cai, C. Gao, X. Zhang, F. Zhang, T. Wang, T. Hong, L. Jin, X. Qi, S. Chen, X. Gu, D. Yang, Q. Pan, Y. Zhu, Y. Chen, D. Chen, L. Jiang, X. Han, Y. Zhang, J. Jin, X. Yao, Essential role for TrpC5-containing extracellular vesicles in breast cancer with chemotherapeutic resistance, Proc. Natl. Acad. Sci. U. S. A. 111 (17) (2014) 6389–6394, https://doi.org/10.1073/pnas.1400272111.

[113] T. Wang, K. Ning, T.-X. Lu, X.u. Sun, L. Jin, X. Qi, J. Jin, D. Hua, Increasing circulating exosomes-carrying TRPC5 predicts chemoresistance in metastatic breast cancer patients, Cancer Sci. 108 (3) (2017) 448–454, https://doi.org/10.1111/cas.13150.

[114] J.H. Yoon, I.-H. Ham, O. Kim, H. Ashktorab, D.T. Smoot, S.W. Nam, J.Y. Lee, H. Hur, W.S. Park, Gastrokine 1 protein is a potential theragnostic target for gastric cancer, Gastric Cancer 21 (6) (2018) 956–967, https://doi.org/10.1007/s10120-018-0828-8.

[115] X.Q. Ding, Z.Y. Wang, D. Xia, R.X. Wang, X.R. Pan, J.H. Tong, Proteomic profiling of serum exosomes from patients with metastatic gastric cancer, Front. Oncol. 10 (2020) 1113, https://doi.org/10.3389/fonc.2020.01113.

[116] H. Fu, H. Yang, X. Zhang, B. Wang, J. Mao, X. Li, M. Wang, B. Zhang, Z. Sun, H. Qian, W. Xu, Exosomal TRIM3 is a novel marker and therapy target for gastric cancer, J. Exp. Clin. Cancer Res. 37 (2018) 162, https://doi.org/10.1186/s13046-018-0825-0.

[117] S. Li, Y. Zhao, W. Chen, L. Yin, J. Zhu, H. Zhang, C. Cai, P. Li, L. Huang, P. Ma, Exosomal ephrinA2 derived from serum as a potential biomarker for prostate cancer, J. Cancer. 9 (15) (2018) 2659–2665, https://doi.org/10.7150/jca.25201.

[118] A. Singh, C. Fedele, H. Lu, M.T. Nevalainen, J.H. Keen, L.R. Languino, Exosome-mediated transfer of αvβ3 integrin from tumorigenic to nontumorigenic cells promotes a migratory phenotype, Mol. Cancer Res. 14 (11) (2016) 1136–1146, https://doi.org/10.1158/1541-7786.MCR-16-0058.

[119] T. Yoneyama, M. Gorry, A. Sobo-Vujanovic, Y. Lin, L. Vujanovic, A. Gaither-Davis, M.L. Moss, M.A. Miller, L.G. Griffith, D.A. Lauffenburger, L.P. Stabile, J. Herman, N.L. Vujanovic, ADAM10 sheddase activity is a potential lung-cancer biomarker, J. Cancer. 9 (14) (2018) 2559–2570, https://doi.org/10.7150/jca.24601.

[120] T.Y. Huang, C.Y. Wang, K.Y. Chen, L.T. Huang, Urinary exosomal thyroglobulin in thyroid cancer patients with post-ablative therapy: A new biomarker in thyroid cancer, Front. Endocrinol. (Lausanne). 11 (2020) 382, https://doi.org/10.3389/fendo.2020.00382.

[121] D. Luo, S. Zhan, W. Xia, L. Huang, W. Ge, T. Wang, Proteomics study of serum exosomes from papillary thyroid cancer patients, Endocr. Relat. Cancer. 25 (2018) 879–891, https://doi.org/10.1530/ERC-17-0547.

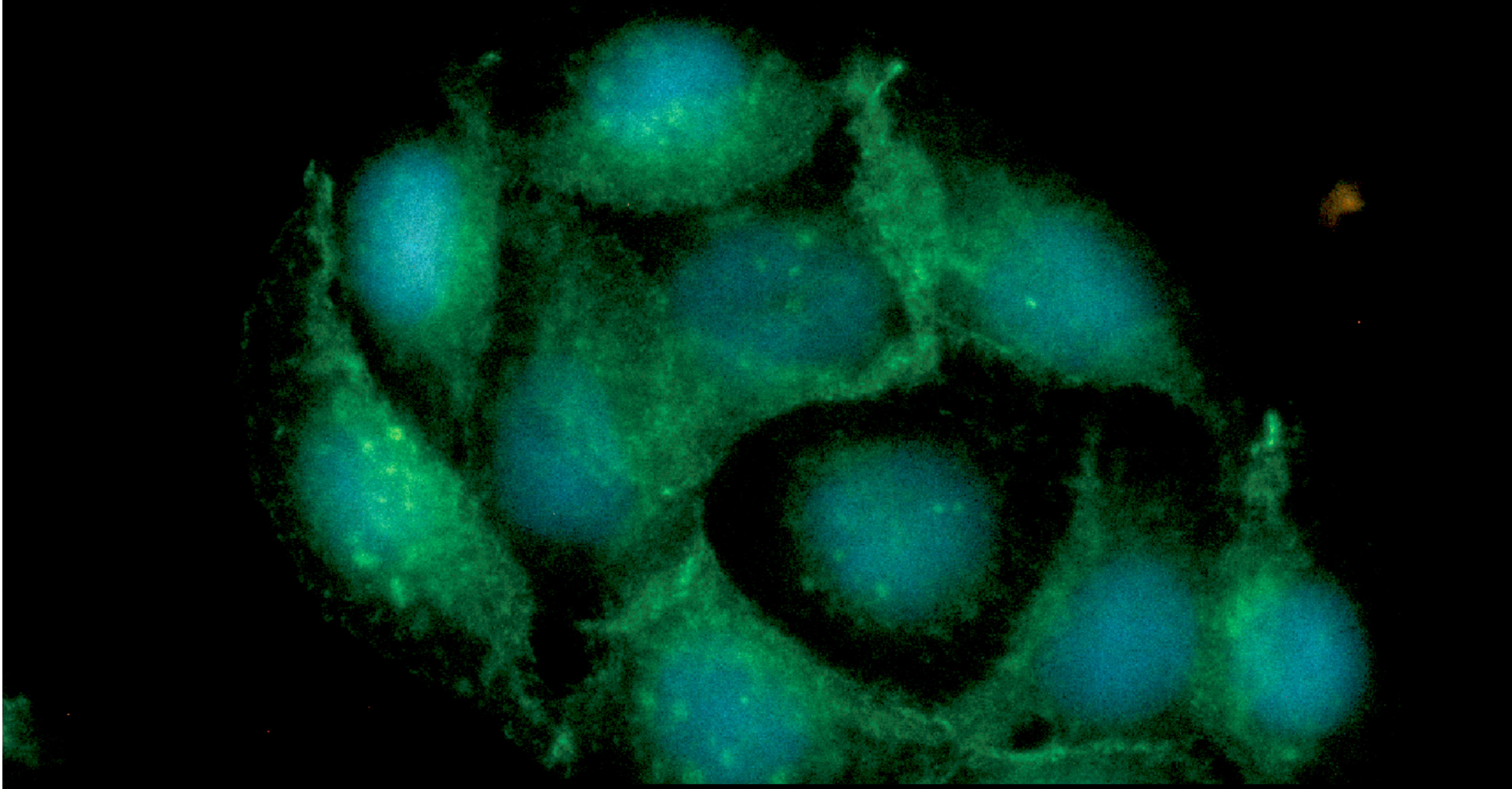

CHAPTER 2

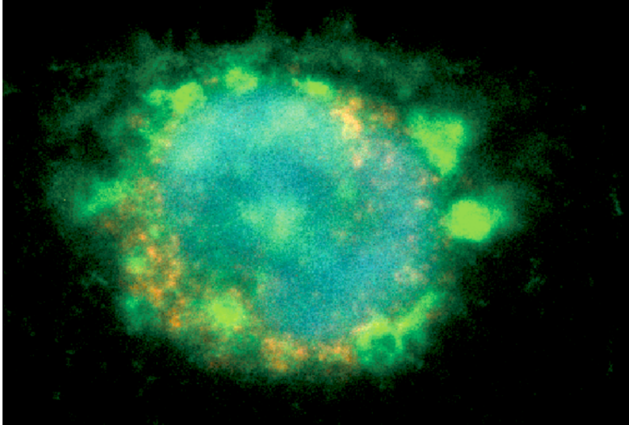

4.2 Chapter 2. Glioblastoma derived small EVs: Nanoparticles for glioma treatment

Summary of the results

Small EVs have emerged as a promising tool for biomarker identification and drug delivery systems, particularly in cancer. This article describes a method for small EVs isolation from patient-derived GBM cell cultures (HGUE-GB-16, HGUE-GB-18, HGUE-GB-37, HGUE-GB-39, HGUE-GB-40, HGUE-GB-42, and HGUE-GB-48), their in-depth characterization using biochemical and biophysical approaches, and their applicability as drug delivery systems.

First, we characterized the sensitivity/resistance profile of the seven GBM cell cultures to treatments and found that all cells were sensitive to TMZ and partially sensitive to EPZ015666. TMZ is an alkylating agent, characterized as a good treatment for many solid tumors such as GBM, sarcomas, melanoma, etc. EPZ015666 is a novel compound, which inhibits PRMT5 and correlates with poor patient prognosis. This was the first study testing the effect of EPZ015666 on cell cultures from GBM patients.

We used the differential ultracentrifugation method (Figure 15) to isolate GBM small EVs, and WB, DLS, and FESEM were used for characterization. Subsequently, we investigated the potential use of small EVs in GBM treatment by loading them with two different chemotherapeutic drugs (TMZ and EPZ015666) using direct and indirect incubation methods (Figure 16). An HPLC protocol was used to measure the uptake of small EVs, which revealed that the direct incubation method was better for treatment. The resultant amounts of TMZ loaded into GBM small EVs were 25 µM and 0.04 µM for EPZ015666.

We conducted proliferation assays to evaluate the efficacy of small EVs loaded with these drugs for GBM treatment (GB-39 EVs^{TMZ} and GB-39 EVs^{EPZ015666}). When GB-39 EVs^{TMZ} were applied to the GBM cell lines (HGUE-GB-39, HGUE-GB-48) and an unrelated pancreatic tumor cell line (RWP-1), a significant effect was obtained compared to the same concentration when the drug alone was used. Similarly, when GB-39 EVs^{EPZ015666} were applied to HGUE-GB-39, HGUE-GB-42, and RWP-1 a more significant effect was reached than the drug alone at the same concentrations, being the effect in RWP-1 not dosage dependent. These experiments showed that small EVs loaded with TMZ and EPZ015666 significantly inhibited the growth of GBM cells compared with unloaded small EVs or free drugs alone.

To test whether or not EVs exhibit tropism to their parent cell, we used three GBM cell lines (HGUE-GB-39 and HGUE-GB-42 or HGUE-GB-48) and RWP-1. We observed that small EVs exhibit tropism for the same type of tumor but not at the patient level, which makes them a good vehicle for drug delivery.

Our findings also indicate that the small EVs derived from GBM are effective in RWP-1 cells, although with lower efficiency, suggesting their potential application to treat other secondary metastases. These results highlight the potential of using GBM-derived small EVs not only for liquid biopsies, but also as a drug delivery system for GBM treatment, and therefore novel therapies can be developed based on these vesicles. However, further research is needed to optimize small EV-based drug delivery systems and to understand the mechanisms underlying their therapeutic effects.

International Journal of
Molecular Sciences

Article

Glioblastoma-Derived Small Extracellular Vesicles: Nanoparticles for Glioma Treatment

Salomé Araujo-Abad [1,2,3], Antonio Manresa-Manresa [3], Enrique Rodríguez-Cañas [1], María Fuentes-Baile [3], Pilar García-Morales [1], Ricardo Mallavia [1], Miguel Saceda [1,3] and Camino de Juan Romero [1,3,*]

[1] Instituto de Investigación, Desarrollo e Innovación en Biotecnología Sanitaria de Elche (IDiBE), Universidad Miguel Hernández de Elche, 03202 Alicante, Spain
[2] Centro de Biotecnología, Universidad Nacional de Loja, Loja 110111, Ecuador
[3] Fundación para el Fomento de la Investigación Sanitaria y Biomédica de la Comunidad Valenciana (FISABIO), Hospital General Universitario de Elche, Unidad de Investigación, 03203 Alicante, Spain
* Correspondence: m.juan@umh.es

Abstract: Glioblastoma (GBM), characterized by fast growth and invasion into adjacent tissue, is the most aggressive cancer of brain origin. Current protocols, which include cytotoxic chemotherapeutic agents, effectively treat localized disease; however, these aggressive therapies present side effects due to the high doses administered. Therefore, more efficient ways of drug delivery have been studied to reduce the therapeutic exposure of the patients. We have isolated and fully characterized small extracellular vesicles (EVs) from seven patient-derived GBM cell lines. After loading them with two different drugs, Temozolomide (TMZ) and EPZ015666, we observed a reduction in the total amount of drugs needed to trigger an effect on tumor cells. Moreover, we observed that GBM-derived small EVs, although with lower target specificity, can induce an effect on pancreatic cancer cell death. These results suggest that GBM-derived small EVs represent a promising drug delivery tool for further preclinical studies and potentially for the clinical development of GBM treatments.

Keywords: glioblastoma; small EVs; nanocarriers; temozolomide; EPZ015666; FESEM

check for updates

Citation: Araujo-Abad, S.; Manresa-Manresa, A.; Rodríguez-Cañas, E.; Fuentes-Baile, M.; García-Morales, P.; Mallavia, R.; Saceda, M.; de Juan Romero, C. Glioblastoma-Derived Small Extracellular Vesicles: Nanoparticles for Glioma Treatment. *Int. J. Mol. Sci.* **2023**, *24*, 5910. https://doi.org/10.3390/ijms24065910

Academic Editor: Paola Manini

Received: 9 March 2023
Revised: 14 March 2023
Accepted: 15 March 2023
Published: 21 March 2023

1. Introduction

Glioblastoma (GBM) is the most aggressive primary malignant tumor of the central nervous system. According to the World Health Organization (WHO), it corresponds to IDH-wildtype grade 4 and is mainly present in adults, with a median survival up to 15 months [1,2]. This short survival rate can be attributed to treatment limitations. The standard of care for GBM patients is the combination of radiotherapy and chemotherapy with temozolomide (TMZ) (3,4-dihydro-3-methyl-4-oxoimidazo-[5,1-d]-astetrazine-8-carboxamide) after tumor resection [3,4]. TMZ is a DNA alkylating agent that acts over the methylation of guanine and adenine bases, breaking double-stranded DNA and causing cell cycle arrest and cell death by apoptosis [5]. Despite its mighty effect on GBM, there are some disadvantages associated with TMZ treatment, such as its short half-life, the requirement of high doses to achieve therapeutic levels, and a great number of side effects [6], among them, headache, fatigue, loss of appetite, opportunistic infections, thrombocytopenia, moderate to severe lymphopenia, and abnormally low levels of white blood cells [7–9]. More importantly, only 20% of TMZ, with respect to a systemic dose, reaches the brain [10].

Recently, arginine methyltransferase-5 (PRMT5) has been described as a potential target for cancer treatment. PRMT5 modulates the biological function of target proteins, catalyzing the transference of two methyl groups to arginine residues, and is essential to maintain homeostasis in both normal and malignant cells [11,12]. This enzyme is involved in tumorigenesis, and it has been found overexpressed in a variety of cancers, including melanoma, multiple myeloma, lung, gastric, prostate, ovarian, colorectal cancers, and GBM [13]. Moreover, the overexpression of this protein has been correlated with poor patient prognosis [12].

EPZ015666 is a small molecule that competes with the substrate-binding pocket of the PRMT5 peptide to deny its interaction and posterior methylation; therefore, it has been considered a PRMT5 inhibitor [14].

The delivery of therapeutic agents to brain tumors is particularly challenging, with no improvement in outcomes observed over the last 20 years, since the Stupp protocol was shown to extend the life span of patients for just several months [3]. This is in contrast to the cancer of other organs that have undergone huge therapeutic improvements over the last decade. Among the new therapies, a novel alternative is the use of exosomes as drug carriers that can contribute to increasing the efficiency of treatments and enhancing brain targeting. Exosomes are small extracellular vesicles (EVs) that were first identified as "trash bags", a system in which waste cellular products were disposed of [15]. However, diverse studies have confirmed that small EVs play a major role in cell–cell communication, both in normal conditions and in pathologies, such as cancer [16]. Small EVs can be used as nanocarriers with some advantages, such as specific tropism for cell origin, non-cytotoxic effect, biocompatibility, facility of transporting hydrophilic or hydrophobic biomolecules, and facility to cross the blood–brain barrier (BBB) [16–19]. Small EVs have a diameter of 30–150 nm and a lipid bilayer membrane with the same characteristics as the donor cell, and their cargo is made up of proteins, messenger RNA (mRNA), microRNA (miRNA), long non-coding RNA (lncRNA), DNA fragments, and metabolites from the donor cell [16,20–22]. Small EVs can be characterized by the presence of proteins, such as Alix, TSG101, RAB, small GTPases, flotillins, annexins, and CD9, CD63, and CD81. The presence or absence of these is closely related to the cell from which the small EVs originated [23–25].

In the present study, we focused on small EVs released from previously isolated, patient-derived GBM cells [26]. We described an efficient method of small-EV purification from those GBM cell lines that we used, and the purity of the small EVs population in our samples has been ensured by performing several characterization methods. We have used those small EVs to overcome the present challenges of drug delivery in GBM and to improve the delivery system by testing two procedures in order to load them with chemotherapeutic drugs, TMZ and EPZ015666. We demonstrate that small EVs loaded with each drug inhibit the proliferation of GBM more efficiently than the drug alone. Therefore, GBM-derived small EVs are not only valuable as a prognostic marker for GBM, but also as delivery systems for the development of new therapeutic strategies.

2. Results

2.1. Sensitivity and/or Resistance Profile to Treatments of Patient-Derived GBM Cell Lines

The GBM cell lines used in this work were obtained by our research group, as described previously, by surgical washes of resection surgery from patients older than 18 years diagnosed with GBM, and all of them IDH wt. They were denominated "Hospital General Universitario de Elche" (HGUE), Glioblastoma (GB), and the number of the patient (Figure 1A) [26]. Thus, seven cell lines were established: HGUE-GB-16, HGUE-GB-18, HGUE-GB-37, HGUE-GB-39, HGUE-GB-40, HGUE-GB-42, and HGUE-GB-48 (indicated in the Figures as GB-patient number).

We performed a proliferation assay that showed an important decrease in proliferation as a response to TMZ treatment by all GBM cell lines (Figure S1). TMZ was the most effective treatment, together with EPZ015666, which also showed a significant response in the GBM cell lines (Figure S2).

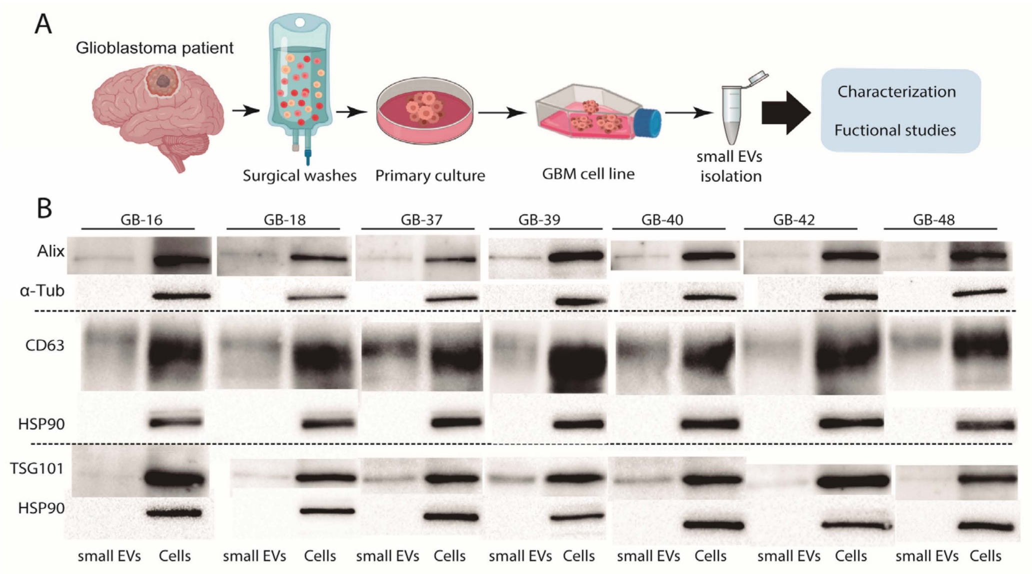

Figure 1. Small EVs isolation and biochemical characterization. (**A**) Scheme of the GBM cell line obtention, followed by small EVs isolation and functional studies. (**B**) Expression by WB of Alix, CD63, and TSG 101 in isolated small EVs and corresponding cell protein extracts. α-Tub and HSP-90 were used as control. Of note, HSP-90 in GBM is not a biomarker and has been used as a marker of small EVs isolation (negative control). GBM, glioblastoma; EVs, extracellular vesicles.

Those were the only treatments to which no GBM cell line showed resistance. Regarding the GBM cell lines, the most sensitive to all treatments was HGUE-GB-42, whereas HGUE-GB-39 was the most resistant, together with HGUE-GB-16. The different sensitivity/resistance profiles of the cell lines derived from several patients suffering from the same type of tumor highlights the importance of better analysis and understanding of the tumor features in order to find common properties and, therefore, overcome GBM therapy limitations (Table 1).

Table 1. Sensitivity and/or resistance classification of GBM lines to treatments. GBM cell lines classification according to their sensitivity and/or resistance to EPZ015666, TMZ, Carmustine (BCNU), and radiotherapy treatments. Cells were treated with different concentrations of the chemotherapeutic agents EPZ015666 and TMZ. Classification of BCNU and radiotherapy data was performed based on data previously reported by our research group [26]. Classification of those treatments is based on the IC_{50} of each one. The resistant cell lines of each treatment are highlighted in red and the sensitive ones are highlighted in light green. GBM, glioblastoma; TMZ, Temozolomide.

Treatment **Cell Line**	**EPZ015666**	**TMZ**	**BCNU**	**Radiotherapy**
HGUE-GB-16	Partially sensitive	Sensitive	Resistant	Sensitive
HGUE-GB-18	Partially sensitive	Sensitive	Partially sensitive	Partially sensitive
HGUE-GB-37	Partially sensitive	Sensitive	Partially sensitive	Sensitive
HGUE-GB-39	Sensitive	Sensitive	Partially sensitive	Resistant
HGUE-GB-40	Partially sensitive	Sensitive	Partially sensitive	Partially sensitive
HGUE-GB-42	Sensitive	Sensitive	Sensitive	Sensitive
HGUE-GB-48	Partially sensitive	Sensitive	Partially sensitive	Partially sensitive

2.2. Small EVs Isolation and Biochemical Characterization of Small EVs from Patient-Derived GBM Cell Lines

There are many procedures for small EVs isolation based on different biophysical and biochemical properties of EVs, such as size, mass density, shape, charge, or antigen exposure [23,27].

In order to isolate small EVs from GBM cell lines, the protocol was adapted according to the small EVs' origin and experiment type. In this study, we used the ultracentrifugation approach for small EVs isolation (Figure 2).

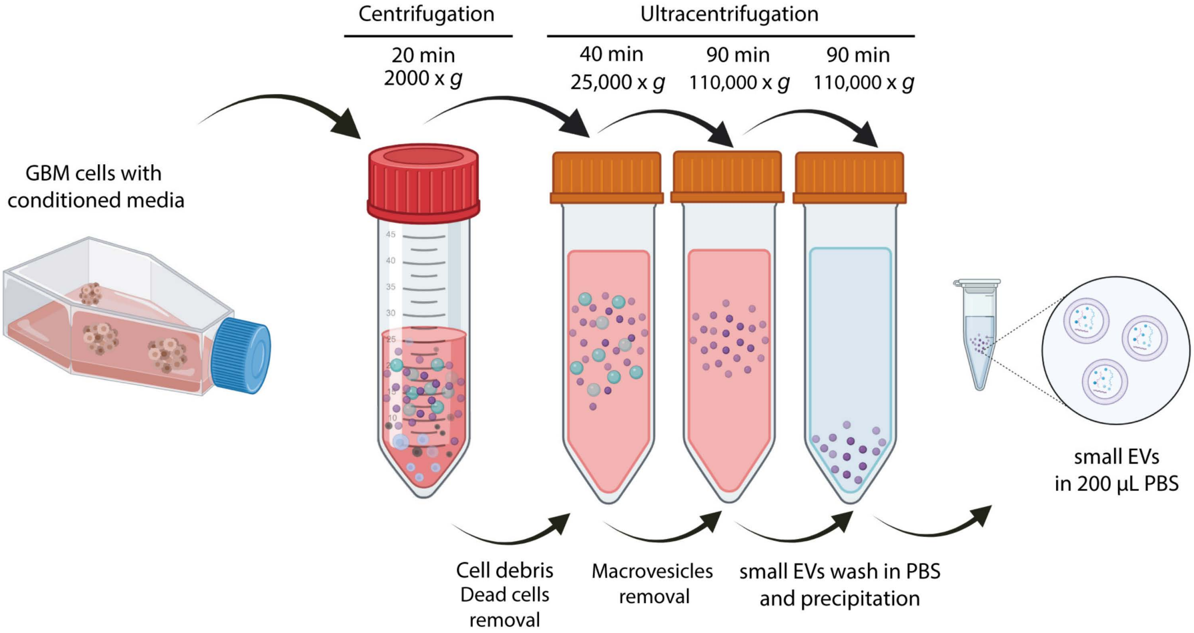

Figure 2. Scheme representing GBM-derived small EVs isolation. Sequential steps of centrifuge and ultracentrifuge were performed, as indicated on top of the arrows. GBM, glioblastoma; EVs, extracellular vesicles.

Small EVs can mirror their cellular origin and, therefore, can provide us with critical information associated with the physiological state of their parental cell [28].

The standardization of small EVs characterization is an essential step for reliable and reproducible results from assays and other downstream applications. In order to characterize our samples, we used Western Blot (WB) as an analytical technique, with antibodies against the main proteins present in small EVs. Our results showed the presence of typical small EVs proteins, such as Alix (Invitrogen), TSG101 (Invitrogen), and CD63 (Invitrogen), while α-Tubulin (Invitrogen) and HSP-90 (CUSABIO) were only found in cell lysates (Figure 1B), in contrast to other results obtained with small EVs purified from breast or prostate cancer cells [29,30]. Furthermore, the absence of tubulin was reported as a characteristic of small EVs purity, indicating the absence of cell contaminants in the sample [31]. Altogether, our results established the purity of the small EVs samples. Moreover, we could identify the expression of HSP-90 in the GBM cell lines, but not in the GBM-derived small EVs samples, which differs from small EVs of different origin.

2.3. Morphological Characterization of GBM-Derived Small EVs

Characterization of isolated GBM-derived small EVs was completed by Dynamic light scattering (DLS) (Figure 3) and showed that the isolated particles from the seven patients' samples were consistently within the expected size range for small EVs (Figure 3). Analysis revealed different diameter means according to each group of cell-line-derived small EVs: HGUE-GB-16 (93 nm ± 7), HGUE-GB-18 (126 nm ± 3), HGUE-GB-37 (117 nm ± 5), HGUE-GB-39 (129 nm ± 1), HGUE-GB-40 (118 nm ± 6), HGUE-GB-42 (110 nm ± 6), and HGUE-GB-48 (126 nm ± 3).

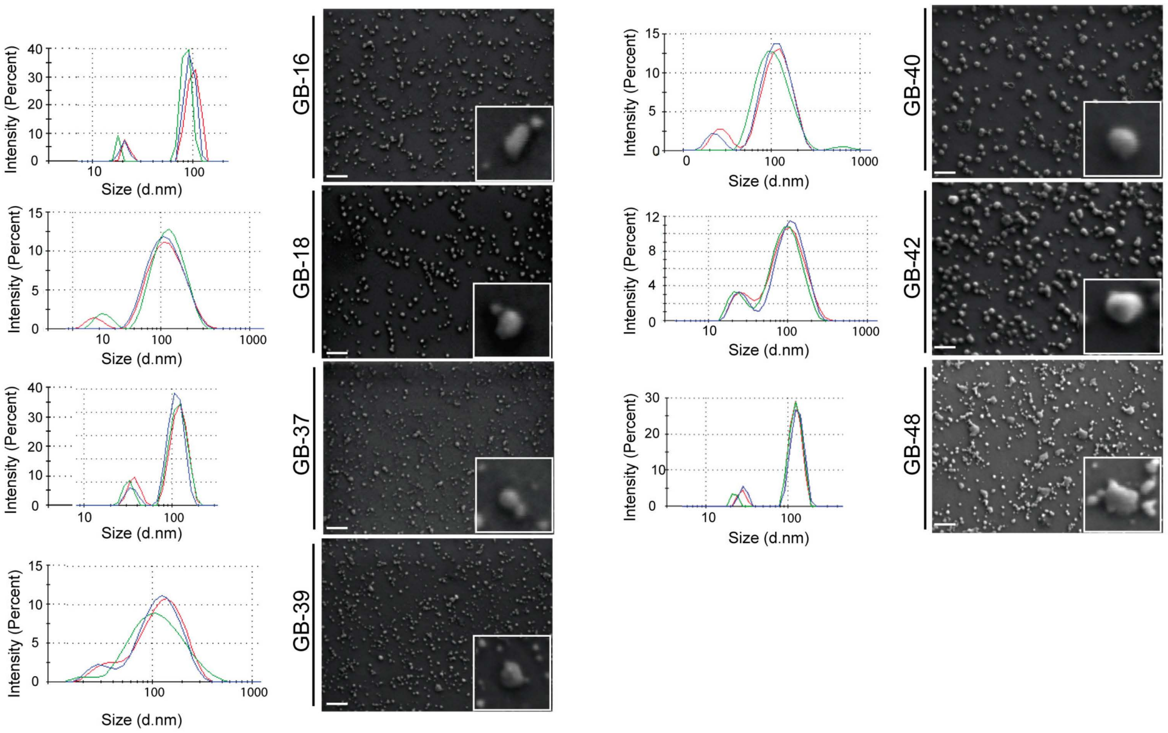

Figure 3. Size characterization of small EVs particles. Size and morphology of the seven GBM cell lines' small EVs were visualized by using Dynamic Light Scattering (DLS) and Field Emission Scanning Electron Microscopy (FESEM). White boxes show an optical magnification of a representative small EV. Scale bars 200 nm. GBM, glioblastoma; EVs, extracellular vesicles.

We further examined the size and morphology of GBM-derived small EVs by performing field emission scanning electron microscopy (FESEM) analyses (Figure 3). FESEM images indicated the presence of a homogeneous population of small EVs, with a mean diameter between 100 and 150 nm. Small EVs appeared almost exclusively as round or cup-shaped vesicles. In some cases, we could identify multiple small EVs clusters of about 200 nm in diameter.

To rule out that the structures visualized by FESEM could be an artifact of the isolation or fixation process, we performed an exhaustive analysis of the samples. Energy dispersive X-ray (EDX) analysis was performed with the X-ray detector in a FESEM microscope on a HGUE-GB-48-derived small EVs sample (Figure S3). As expected, the studied sample was a mixture of biological samples and salts. The spectrum of the rounded, small EVs-like areas confirmed their biological origin. Taken together, DLS and FESEM imaging confirmed the purity of the GBM-derived small EVs in our preparations and are in line with similar studies uncovering small EVs characteristics derived from cells of diverse origins [32]. Moreover, for the first time, EDX analysis was performed to allow the discrimination of small EVs structures from salts by establishing the biological nature of the samples (Figure S3).

2.4. Effect of GBM-Derived Small EVs Directly Loaded on Glioma Cells

The current standard-of-care treatment for GBM relies on a multidisciplinary approach combining surgery, chemotherapy, and radiation therapy. TMZ has been used as a first-line treatment for GBM. On the other hand, chemoresistance has become the main barrier to treatment success, and therefore, other drugs have been developed to treat GBM patients [3]. Our data showed that patient-derived GBM cell lines were mostly sensitive to TMZ and EPZ015666; thus, we decided to test both drugs. EPZ015666 is an inhibitor of PRMT5 that has been shown to regulate the splicing of detained introns in proliferation-associated genes in GBM [33]. PRMT5 has a nuclear localization, and its expression correlates with poor survival in several types of cancers. This makes PRMT5 a good candidate for cancer therapy, and consequently, many compounds have been screened to find the required specificity and efficacy for GBM treatment [34]. One of them is EPZ015666, which has been broadly used in several other types of cancer [14,35]. In this study, we tested the effect of EPZ015666 on GBM cell survival.

In order to test whether or not GBM-derived small EVs can be used as a drug delivery system for cancer treatment, we first loaded them by two incubation methods [36]. The first method has been broadly used to load small EVs and consists in the treatment of the cells for at least 48 h with high doses of a certain drug, followed by small EVs isolation from the medium [19]. From now on, we will call this method "indirect incubation" [37]. In the second one, called "direct incubation", small EVs are first isolated from the cell line and then incubated in a medium containing a low dosage of the drug [38].

To test the loading efficiency of small EVs, the small EVs were loaded by direct and indirect incubation, and the amount of TMZ was measured by HPLC (Figure S4). Small EVs isolated from the GBM cell line HGUE-GB-39 were isolated (Figure 2), and the drug was encapsulated by direct incubation in 5 mM TMZ. Our HPLC measurements showed higher amounts of TMZ being loaded into the small EVs by direct incubation; therefore, we decided to continue the experiments with this loading method (Figure S4).

Small EVs have been proposed to tend to fuse preferentially with their parent cancer cells [17]. To test this idea, we included in our experiment not only the parental cell HGUE-GB-39, but also another GBM cell line and the unrelated pancreatic cancer cell line RWP-1. The second GBM cell line was chosen based on its sensitivity/resistance profile against each drug (Figure S1). The HGUE-GB-48 GBM cell line was used for TMZ treatment, whereas EPZ015666 was applied to HGUE-GB-42, since they were the most sensitive lines against those drugs, according to our data (Table 1). The above-mentioned three cancer cell lines were treated with small EVs derived from the GB-39 GBM cell line that was loaded by the direct incubation method, and the effect on cell proliferation was measured. When applying the loaded small EVs in the same or in another GBM cell line, direct incubation showed a significant effect, as indicated by the decrease in cell proliferation, especially at higher concentrations (Figures 4, S5 and S6). Surprisingly, RWP-1 also responded to drug-loaded small EVs. This may be explained by the fact that RWP-1 is very sensitive to both of the tested drugs, even at low doses, as shown in the direct exposure to both drugs (Figures 4–6, S5, S6, S9, and S10).

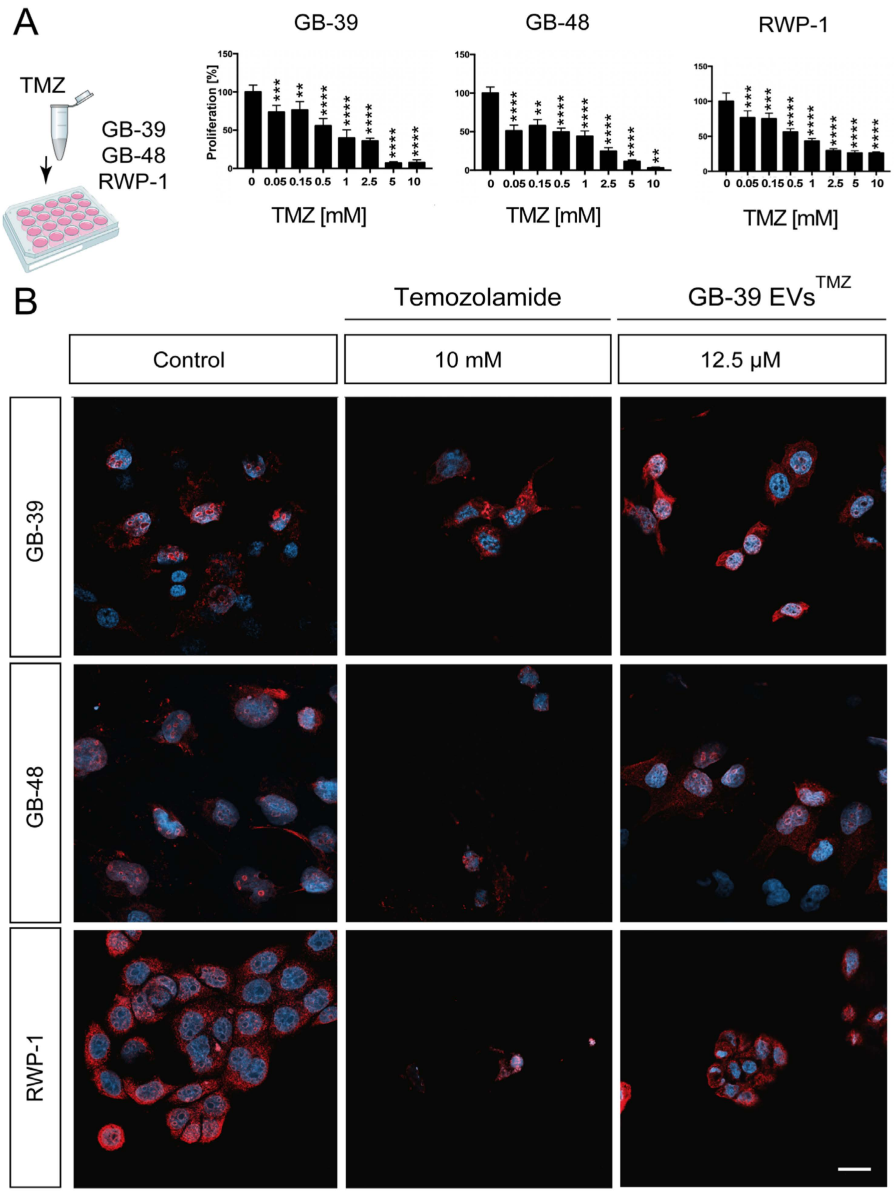

Figure 4. Cell proliferation effect of TMZ in cancer cell lines. (**A**) Cancer cells were treated with increasing concentrations of TMZ, and their proliferation was measured. (**B**) Confocal images showing the expression of a proliferative marker and the decrease in cell density due to the TMZ and GB-39 EVs^{TMZ} effect. Asterisks indicate the statistical significance of the results (** $p < 0.01$, *** $p < 0.001$, **** $p < 0.0001$). Scale bar B, 20 µm. TMZ, Temozolomide; EVs, extracellular vesicles.

2.5. TMZ-Loaded GBM-Derived Small EVs Barely Affect Cancer Cells

The effect of TMZ treatment on proliferation was assessed using an increasing concentration of the drug. We used three cancer cell lines, two of GBM and one of pancreatic cancer, to evaluate cell tropism later. A range of concentrations between 0.05 mM and 10 mM was evaluated. Our analyses revealed that treatment of the GBM cell lines HGUE-GB-39 and HGUE-GB-48 with TMZ resulted in more than 90% decreased proliferation, together with an IC_{50} of 1.088 ± 0.082 and 0.2264 ± 0.195 mM, respectively (Figures 4, S5 and S6). Interestingly, the pancreatic cancer cell line RWP-1 was also affected by the TMZ administration, with only 20% of proliferating cells at 10 mM concentrations and an IC_{50} of 0.7301 ± 0.066 mM (Figures 4, S5 and S6).

We then tested the second loading method by directly incubating GB-39-derived small EVs in 5 mM TMZ (GB-39 EVs^{TMZ}). It has been described that this kind of incubation results in a very low encapsulation rate of the administered drug dose within the small EVs [36]. In order to know the precise amount of drug contained in the small EVs, we performed HPLC analysis, followed by drug identification with a mass spectrometer (Figure S4). Our quantifications showed that GB-39 EVs^{TMZ} contained 25 µM of the drug. Isolated GB-39 EVs^{TMZ} were applied to the cells in serial dilutions ranging from 50% to 5% of the original stock. Since the amount of drug applied to the cultures through the GB-39 EVs^{TMZ} corresponds to a range of 12.5 µM to 1.25 µM, we tested the direct exposure of the GBM cell lines to TMZ at these low concentrations to compare both effects (Figures 5, S5 and S6).

The maximum concentration applied was 12.5 µM of TMZ, corresponding to 50% GB-39 EVs^{TMZ}, and the minimum was 1.25 µM at 5% of TMZ. GB-39 EVs^{TMZ} treatment resulted in a very subtle reduction in cancer cell proliferation. Interestingly, the total amount of TMZ used for this treatment was up to 1000 times less than the direct application of TMZ in cells (Figure 5B) already starting at a 6 µM concentration.

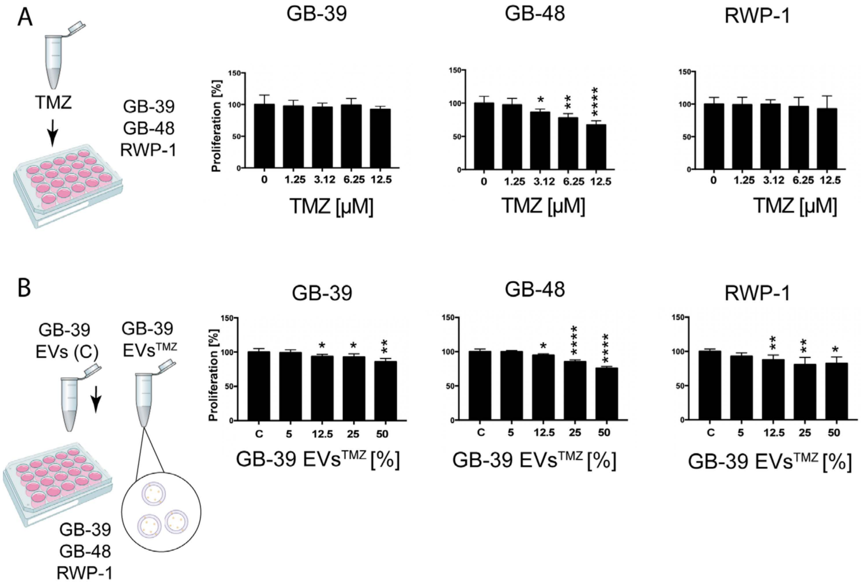

Figure 5. Cell proliferation effect at low concentrations of TMZ in cancer cell lines. (**A**) Cancer cells were treated with low concentrations of TMZ, similar to the calculated concentrations present in GB-39 EVs^{TMZ}, and their proliferation was measured. (**B**) GB-39 EVs^{TMZ} were loaded directly with a 5 mM concentration of TMZ. Small EVs alone (Control, C) or serial dilutions of the loaded small EVs were applied to different cancer cell lines, and their effect on proliferation was measured. Asterisks indicate the statistical significance of the results (* $p < 0.05$, ** $p < 0.01$, **** $p < 0.0001$). TMZ, Temozolomide; EVs, extracellular vesicles; C, control.

Moreover, our HPLC data indicated that the amount of drug loaded into isolated GB-39 EVs^{TMZ} (Figure S4) was 200 times less than the concentration they were exposed to while being incubated by the direct method (Figure S4). On the other hand, less amount of drug was loaded into GB-39 EVs^{TMZ} by indirect incubation, since it was 600 times less than the original exposure. Altogether, our results revealed that direct incubation is more efficient than the indirect method (Figure S4).

2.6. EPZ015666-Loaded GBM-Derived Small EVs Have a Similar effect on Cancer Cells

PRMT5 has recently emerged as a promising therapeutic target in GBM treatment. According to the UALCAN database, a web portal for gene expression and survival analysis in different types of tumors, PRMT5 was upregulated in most of the tumors (Figure S7A). This database, which uses data extracted from "The Cancer Genome Atlas" project, showed significant upregulation of PRMT5 in GBM samples (p-value 1.62×10^{-12}) (Figure S7B) [39]. Moreover, its expression has been related to a high grade of malignancy in GBM, while its inhibition correlates with survival [40,41]. One of the PRMT5 inhibitors that have been successfully developed is EPZ015666 [14].

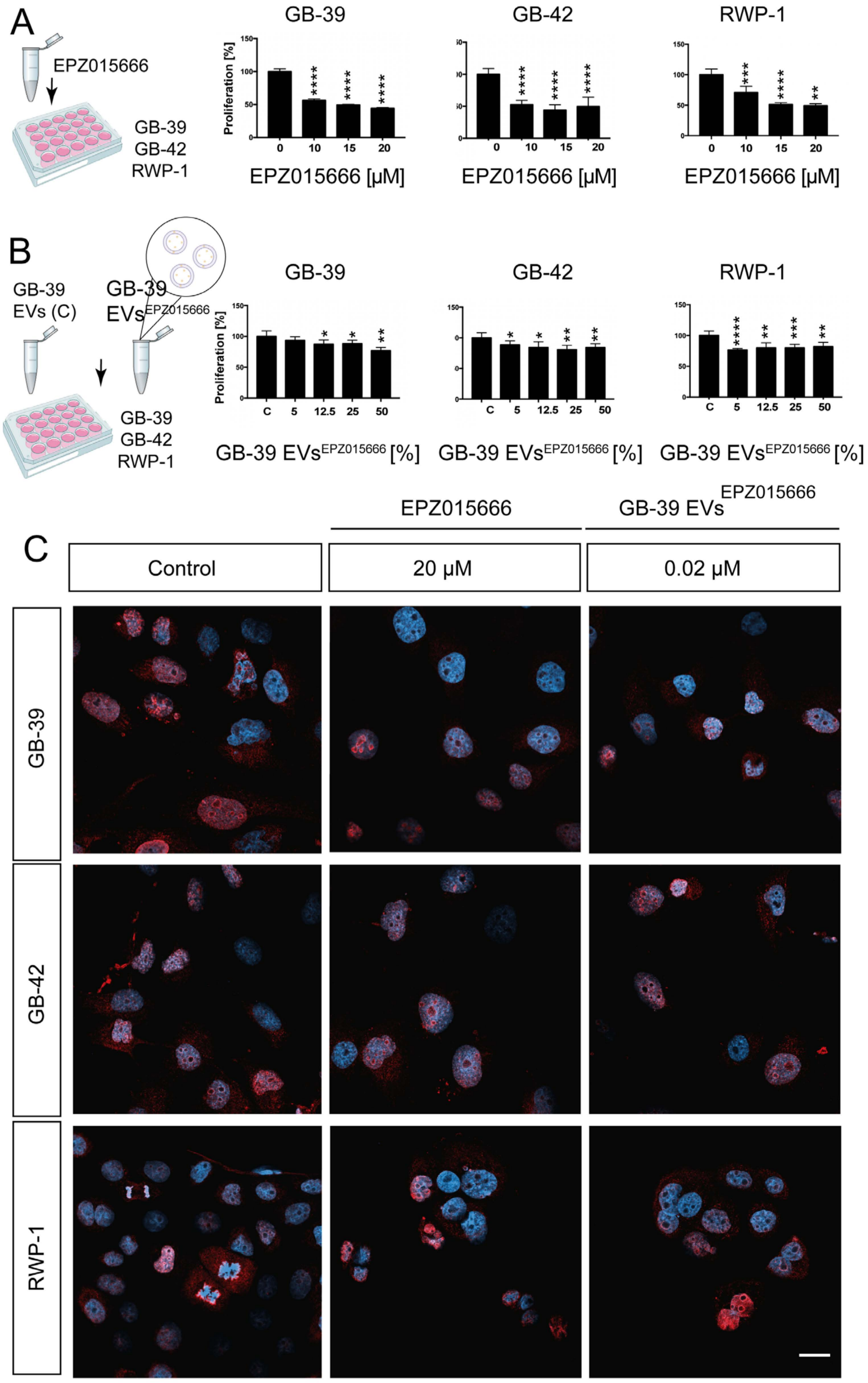

Figure 6. Cell proliferation effect of EPZ015666 in cancer cell lines. (**A**) Cancer cells were treated with increasing concentrations of EPZ015666, and their proliferation was measured. (**B**) Small EVs of GB-39 were loaded directly with a 15 μM concentration of EPZ015666. Small EVs alone or serial dilutions of the loaded small EVs were applied to different cancer cell lines, and their effect on proliferation was measured. (**C**) Confocal images showing the expression of a proliferative marker and the decrease in cell density due to the EPZ015666 and GB-39 EVs^{EPZ015666} effect. Asterisks indicate the statistical significance of the results (* $p < 0.05$, ** $p < 0.01$, *** $p < 0.001$, **** $p < 0.0001$). Scale bar C, 20 μm. EVs, extracellular vesicles.

We wondered if small EVs could have a different target efficacy based on the loaded drugs. Along this line, different drugs with different mechanisms of action and chemical properties could be more suitable for small EVs drug delivery. To test the effect of EPZ015666 treatment on proliferation, an increasing concentration of the drug was used. A range of concentrations between 5 µM and 20 µM were applied to 3 cancer cell lines (Figure 6A,C). For this experiment, and to assess the effect in another GBM cell line, HGUE-GB-42 was used. Our analyses showed a nearly 50% decrease in proliferation in the GBM cell lines and a slightly higher reduction in RWP-1 (IC_{50}) after EPZ015666 treatment (Figure 6A,C).

Small EVs were loaded by direct incubation in 15 µM EPZ015666 (GB-39 $EVs^{EPZ015666}$). Similar to the previous experiments, HPLC analysis, followed by drug identification with a mass spectrometer, was performed (Figure S8). Our quantifications showed a 0.04 µM concentration in the small GB-39 $EVs^{EPZ015666}$ by direct incubation. Therefore, those samples were loaded with a concentration that was 400 times less than the original 15 µM. Isolated small GB-39 $EVs^{EPZ015666}$ were applied to the cells in serial dilutions ranging from 50% to 5% of the original stock. Consequently, the maximum concentration was 0.02 µM, corresponding to 50% small EVs, and the minimum was 0.002 µM when 5% of $EVs^{EPZ015666}$ was applied. GB39-$EVs^{EPZ015666}$ treatment resulted in a reduction in significant cancer cell proliferation. Confirming the tested idea, the higher decrease in proliferation took place in HGUE-GB-39, the cell line where the small EVs were obtained. An average of a 20.54% reduction in proliferation was seen in the RWP-1 cell line, regardless of the small EVs concentration (Figure 6B,C). These results indicate that even if this cell line does not have a specific affinity for this type of small EVs, the amount of EPZ015666 that reaches the cell is sufficient to induce an effect.

In accordance with our previous observations with GB-39 EVs^{TMZ}, our HPLC data indicated that the amount of drug loaded into isolated GB39-$EVs^{EPZ015666}$ (Figure S8) was much less than the concentration they were exposed to while being incubated by the direct method (Figure S8). Therefore, it confirms that direct incubation is the most efficient method to load GB39-$EVs^{EPZ015666}$ (Figure S8).

3. Discussion

Glioblastoma patients with metastatic or relapsed disease have poor outcomes, despite intense and aggressive multimodal treatment strategies, including high-dose chemotherapy regimens. Current therapies are insufficient, with nearly universal recurrence, mostly due to the difficulty of delivering therapeutic agents to the brain. Since the BBB limits the entry of systematically administered drugs to the brain, efforts are underway to develop methods to deliver treatments behind the BBB, such as the implantation of a drug-eluting material into the brain tissue. Along this line, controlled release systems for direct delivery of chemotherapy to brain tumors were first approved by the FDA in 1996 [42,43]. The intensification of preclinical discovery efforts has led to the identification of novel drug delivery systems that are currently being investigated in clinical trials; however, the efficacy, and more importantly, the direct pharmacological targeting of tumor cells remains elusive [25]. Of note, while there are an increasing number of drug delivery systems that are currently being developed and tested in preclinical studies, only a few of them advance to clinical testing due to inherent limitations, such as toxicity to normal cells [44].

Recently, small EVs are being investigated and manipulated to be used as delivery vehicles for anticancer drugs and molecules [25]. Their nanosize, structure, and origin, together with the presence of several adhesion proteins on the surface that enhance fusion with recipient cells, make small EVs very good candidates to deliver therapeutics with increased efficiency and specificity to tumor cells [45,46]. Given the pressing need in GBM therapy for testing new drug delivery systems that are safe, exhibit preferential toxicity to tumor cells, and spare normal cells, we decided to investigate the possible application of small EVs in cancer, with a special focus on GBM. Hence, we performed a deep characterization of seven patient-derived GBM cell lines and their small EVs.

Small EVs have been tested as natural drug delivery vehicles for cancer treatment by loading them with a drug or molecule through several methods, including sonication, electroporation, or by transfecting the cells with the molecules of interest and then isolating the small EVs loaded with those molecules from the transfected cells [47–49]. Since methods such as electroporation and sonication are likely to produce structural or physiological changes in the small EVs, we loaded our small EVs by incubation methods with two drugs: TMZ and EPZ015666 [50,51].

The current standard-of-care treatment for GBM includes maximum safe surgical resection and radiotherapy with concomitant TMZ, followed by adjuvant TMZ. In most of the experiments performed, this drug was dissolved in DMSO, which is cytotoxic by itself [52]. Therefore, it is important to mention that in the experiments reported in this article, TMZ was dissolved in Milli-Q^{TM} water, as other authors have tested it [53]. Consequently, the effects on cell proliferation that we have described are solely relative to TMZ.

In the past few years, PRMT5 has been proposed as a possible therapeutic target for some cancers [12,13]. Not only is it dysregulated in several cancer types, but its expression has also been correlated with cancer patient survival. A detailed analysis of TCGA atlas samples with the internet tool cBioPortal (https://www.cbioportal.org/ accessed on 30 March 2022) shows that of the four GBM subtypes, PRMT5 is mostly upregulated in Classical GBM (Figure S7C) [54]. This is important, because the classical subtype shows a significant reduction in mortality with aggressive radiotherapy and chemotherapy [55]. In this article, we have shown for the first time the effect of the PRMT5 inhibitor, EPZ015666, on patient-derived GBM cell lines. More importantly, we have seen that EPZ015666 affects GBM cell proliferation more than TMZ already by direct application of the drug (Figures S1 and S2).

When we exposed GB-39 EVs to TMZ or EPZ015666, by direct or indirect incubation, we observed that both methods could load the small EVs. However, direct incubation with any of the drugs was more efficient in GBM patient-derived small EVs, as shown with the HPLC (Figures S4 and S8). Moreover, we observed that in the direct incubation method, a higher loading efficiency is obtained, depending on the hydrophobicity of the tested drugs, since they have a better interaction with the lipid bilayer of the small EVs membranes, as previously reported for other compounds (Figures S4 and S8) [56–58].

Interestingly, in vitro proliferation analysis led to the observation that drug-loaded small EVs of GBM cell lines affect GBM cells, regardless of the patient from whom they came. The alternative GBM cell line, which was very sensitive to both treatments being used, was also affected by GB-39 drug-loaded small EVs. Very low levels of those drugs already have an effect in that cell line, which can explain the effect of the loaded small EVs on its proliferation. In any case, we could rule out that the uptake of the GBM small EVs was specific since the effect on RWP-1 was not dosage-dependent.

GBM has an isocitrate dehydrogenase-wt phenotype (IDH wt), and it is considered as a grade 4 astrocytoma, according to WHO classification. On the other side, WHO 2021 classification indicates that IDH-wt LGG shows a molecular resemblance to GBM, and now it is also classified as such. Finally, there is another group that can also reach a grade 4, according to WHO classification, which is the Astrocytoma IDH-mutant that was previously considered as GBM, IDH-mutant [1]. The effect on the proliferation of this pancreatic cell line suggests that this delivery system could be used to target secondary metastasis [59]. Moreover, extracranial metastases of GBM are rare due to the short survival experienced by the patients, but they exist. These cases can benefit from the observation that GBM-derived small EVs can also affect other tumor cells; however, more analysis should be done to explore this possibility.

Several active efforts to re-evaluate existing or investigate new anti-GBM agents are ongoing, and our results expand the possibilities of investigating other combinatorial therapies. Another important aspect of GBM treatment includes the fact that chemotherapeutic regimens are largely non-selective and cytotoxic in nature, and despite all the efforts, almost all patients experience tumor progression, with nearly universal mortality and a median survival of less than 15 months, depending on several risk factors [60]. There is a need to optimize the balance between effectiveness and toxicity, and the use of small EVs may help to reduce the amount of drug given to a patient in order to reach the same effect. In this work, we measured the amount of drug loaded into the small EVs by HPLC to compare it with the direct application of those drugs. Specific studies are necessary to assess the therapeutic efficiency of the current drugs since, as we have shown, each drug has different loading properties. Importantly, this is the first work showing a detailed protocol to measure the EPZ015666 concentration by HPLC that can be applied to small EVs. HPLC analysis of loaded GBM small EVs has shown that very low amounts of EPZ015666 are more lethal than TMZ to cancer cells (Figures S1, S2, S4, and S8). Altogether, this work showed that small EVs can be loaded with an amount of at least 200 times less TMZ and an amount of 400 times less EPZ015666 and still be very efficient. This work opens a venue to work with GBM small EVs as drug delivery systems for GBM treatment.

4. Materials and Methods

4.1. Cell Culture

Isolation of primary human GBM cells was performed from surgical washes, as reported previously by Ventero and colleagues, and the cells were recently used to get some insight into GBM development [26,61]. The pancreatic adenocarcinoma (RWP-1) cell line was donated by Instituto Municipal de Investigaciones Médicas (IMIM, Barcelona, Spain), and it was recently used to understand not only the mechanism of cancer progression, but also to develop new delivery systems for cancer therapy [61,62]. Cells from the GBM cell lines HGUE-GB-16, HGUE-GB-18, HGUE-GB-37, HGUE-GB-39, HGUE-GB-40, HGUE-GB-42, and HGUE-GB-48 were cultured in Dulbecco’s Modified Eagle’s Medium: Nutrient Mixture F-12 (DMEM F-12) (Biowest, Riverside, MO, USA), whereas the RWP-1 cells were cultured in Dulbecco’s Modified Eagle’s Medium: High Glucose (DEMEM-HG) (Biowest, Riverside, MO, USA), and both were supplemented with 10% (*v*/*v*) of heat-inactivated fetal bovine serum (FBS) (Biowest, MO, USA) and 1% (*v*/*v*) of a penicillin/streptomycin mixture (Biowest, Riverside, MO, USA). The cells were incubated at 37 °C in a humidified 5% CO_2 atmosphere.

4.2. Proliferation Assays

BCNU is a common treatment for GBM patients, together with radiotherapy. Therefore, we established a classification that includes not only TMZ and EPZ015666, but also BCNU and radiotherapy. We characterized the seven GBM cell lines according to their sensitivity and/or resistance to different chemotherapeutic drugs into three categories—Sensitive, Partially Sensitive, and Resistant—based on the IC_{50} calculated from the results obtained after cell exposure to drugs or X-ray radiation [26]. We performed a series of MTT experiments with EPZ015666 and TMZ, while previous data were analyzed to evaluate BCNU and radiotherapy resistance, according to this classification [26]. (Table 1, Figures S1 and S2).

Cells were seeded in 96-well standard plates (Sarstedt, Nümbrecht, Germany) with a density of 4000 cells/well and incubated at 37 °C and 5% CO_2 for 24 h. After that, cells were treated with different and crescent concentrations of the chemotherapeutic drugs or loaded small EVs and incubated for 72 h under the same conditions. Then, 0.25 mg mL^{-1} of methylthiazolyldiphenyl-tetrazolium bromide (MTT) (Sigma-Aldrich, St. Louis, MO, USA) was added and incubated for 3 h, media were carefully removed, and 100 µL of dimethyl sulfoxide (DMSO) (Sigma-Aldrich, St. Louis, MO, USA) was added. The plate was vigorously shaken at room temperature for 20 min to dissolve the formazan crystals. Finally, the absorbance was measured on an Eon^{TM} Microplate Spectrophotometer (BioTeK®, Winooski, VT, USA) at 570 nm.

4.3. Small EVs Purification for Characterization

Confluent populations of the seven GBM cell lines were incubated in 75 cm^2 cell culture flasks with DMEM F-12 conditioned media, and after 96 h without a medium change, small EVs were obtained by the differential ultracentrifugation method (Figure 2). The media samples were centrifuged at 2000× *g* for 20 min at 4 °C to eliminate cells and debris, followed by an initial ultracentrifugation using an Optima L-90K Ultracentrifuge (Beckman Coulter, Brea, CA, USA) with 70.1 Ti rotor at 25,000× *g* for 40 min at 4 °C to remove macrovesicles, and then the supernatant was filtered through 0.22 μm filters (Fisher Scientific, Pittsburgh, PA,USA). The resultant filtrate was centrifuged at 110,000× *g* for 90 min at 4 °C to pellet small EVs. Small EVs were washed in PBS at 110,000× *g* for 90 min at 4 °C, and the final pellet was resuspended in 200 μL of 1X PBS and then stored at −80 °C.

4.4. Western Blot

Protein samples were solubilized with a loading buffer (4×) (2-mercaptoethanol + NuPage; 1:5) and heated at 95 °C for 5 min for reducing conditions, and for non-reducing conditions, the loading buffer was used without 2-mercaptoethanol. Then, proteins were separated by SDS-PAGE using 10% acrylamide gels and transferred to a nitrocellulose membrane (Bio-Rad Laboratories Inc., Hercules, CA, USA). Membranes were incubated overnight at 4 °C with the primary antibodies anti-CD63 (mouse,1:1000, Clone Ts63, Invitrogen, Waltham, MA, USA), anti-ALIX (mouse,1:500, Clone 3A9, Invitrogen), anti-TSG101 (mouse,1:500, Clone 4A10, Invitrogen), anti-α-tubulin (mouse, 1:10,000, Clone DM1A, Invitrogen), and anti-HSP90-B1 (rabbit,1:4000, CUSABIO), followed by one hour of incubation at room temperature with ECL™ Anti-mouse IgG and ECL™ Anti-rabbit IgG, Horseradish Peroxidase linker (GE Healthcare, Chalfont St Giles, UK). The membranes were visualized with ECL™ Prime Western blotting detection reagent (Amersham™) in the ChemiDoc Bio-Rad instrument (Hercules, CA, USA).

4.5. Dynamic Light Scattering (DLS)

Small EVs samples were analyzed using a Zetasizer Nano ZS instrument (Malvern Panalytical, Worcestershire, UK). In order to characterize the size distribution, each sample was diluted in Milli-Q™ water (1:10), and 1 mL was dispensed in a polystyrene disposable cuvette (Zen0040) and read seven times in Zeta sizer Software. The final image with the distribution curves was used in the Figures as illustrative of the medium size (Figure 3).

4.6. Field Emission Scanning Electron Microscope (FESEM)

Small EVs were vortex and fixed with paraformaldehyde 2%. The fixed small EVs were sonicated for 5 min and then diluted in serial dilutions with Milli-Q™ water (1:10; 1:100; 1:1000, 1:10,000). A 50 μL sample droplet was deposited on a silicon wafer, and, once evaporated, the samples were observed using a Zeiss Sigma 300 VP Field Emission Scanning Electron Microscope (FESEM, Carl Zeiss, Oberkochen, Germany) without coating. The EVs morphology was analyzed at low voltages around 1 kV, while higher voltages were employed to differentiate the salts from the biological sample by using Energy Dispersive X-ray (EDX).

4.7. Small EVs Drug Loading

Small EVs, obtained as described in the small EVs purification for characterization section, were loaded by direct incubation. Small EVs were incubated for 2 h at 37 °C in a thermoblock with defined concentrations of a given chemotherapeutic drug (EPZ015666 15 μM or TMZ 5 mM). Then, they were washed with PBS 1X and ultracentrifuged at 110,000× *g* for 60 min at 4 °C to pellet loaded small EVs. Finally, they were filtered with a 0.22 μm membrane under sterile conditions and stored at −80 °C. For the indirect procedure, confluent populations of GBM cells were seeded, and after 24 h, they were treated with the drug of interest (EPZ015666 15 μM or TMZ 5 mM) for 72 h. Then, the small EVs were purified as described in the small EVs purification for characterization section.

4.8. Quantification of TMZ and EPZ015666 by HPLC

The amount of TMZ and EPZ015666 loaded into the small EVs was measured by the high-performance liquid chromatography (HPLC) method. Briefly, 200 µL of small EVs were placed in a Concentrator plus (Eppendorf, Germany) at 40 °C for 2 h to evaporate the solvent. Then, 100 µL volume of acetonitrile was added, and the mixture was vortexed, sonicated, and then centrifuged at 13,000 r.p.m (Centrifuge 5415 R, Eppendorf, Germany) for 10 min. After centrifugation, the supernatant was taken, transferred into HPLC vials, and injected into the UPLC-QtoF-MS/MS equipment with a high-resolution flight tube and quadrupole technology (Waters-Bruker). Detection of TMZ and EPZ015666 was optimized with a Waters I-Class with UV detection at 330 and 254 nm, respectively, and also a QToF-MS de Bruker Daltonics, model maXis impact Series, in the mode positive ionization by Electrospray (ESI) with column ACE Excel C18-Ar (50-3; 1.7 µm). The mobile phase used was (A) water with 0.1% (v/v) acetic acid and (B) methanol with 0.1% acetic acid. The gradient was set with the following conditions: 0 min, 95%A; 5.50 min, 60%A, 8.75 min, 5%A, with a flow rate of 0.3 mL/min and an injection volume of 5 µL.

4.9. Immunocytochemistry

HGUE-GB-39, HGUE-GB42, HGUE-GB-48, and RWP-1 cells were seeded on coverslips in 24-well plates (30,000 cells/well) and incubated at 37 °C and 5% CO_2. After 24 h, cells were treated with crescent concentrations of the chemotherapeutic drugs or loaded small EVs and incubated for 72 h under the same conditions. Cells were fixed with paraformaldehyde 4% and blocked with FBS/PBS (1×) (50 µL/mL), followed by incubation with anti-ki67 (1:100, mouse; Invitrogen) primary antibody. After washing out the first antibody, cells were incubated with Alexa Fluor 568-labeled anti-mouse (1:500) secondary antibody (Invitrogen, Barcelona, Spain) and DAPI (4′,6-diamidino-2-phenylindole, Sigma) to stain the nucleus. Coverslips were mounted in Prolong™ Gold Antifade reagent (Invitrogen, OR, USA) and analyzed using a confocal microscope, LSM 900 (Carl Zeiss, Germany).

4.10. Statistical Analysis

Results are shown as the mean ± standard deviation (SD) of three independent experiments. In order to evaluate the normal distribution of the data, the Shapiro–Wilk statistical test was used, and the Student's t-test or the Mann–Whitney U test was used to analyze the association between variables. Differences were considered to be statistically significant with a p-value of less than 0.05. To calculate the IC_{50} values, a nonlinear regression analysis was performed. Statistical analysis was performed with GraphPad Prism v7.0a software (GraphPad Software Inc., San Diego CA, USA).

5. Conclusions

In summary, we have demonstrated that TMZ and EPZ015666 inhibit the growth of GBM cells in vitro by less exposure to the drug when this is loaded in small EVs. In this work, EPZ015666 content was measured by HPLC for the first time in EVs, and our results showed that direct incubation was a better loading method for small EVs. We challenged the hypothesis that small EVs tend to fuse with their own mother cell, and, accordingly, we observed a dose-dependent proliferation effect in GBM cell lines, but not in the pancreatic cancer cell line. The fact that other cancer cells can be affected, although to a lesser extent, by drug-loaded GBM EVs entails their possible application to secondary metastasis. Collectively, these results suggest a potential use of GBM-derived small EVs in drug delivery to obtain the maximum therapeutic effect with minimal toxicity in the treatment of GBM patients.

Supplementary Materials: The following supporting information can be downloaded at: https://www.mdpi.com/article/10.3390/ijms24065910/s1.

Author Contributions: C.d.J.R. participated in conceptualization, funding acquisition, supervision, and project administration. S.A.-A. participated in conceptualization, investigation, and methodology. E.R.-C., A.M.-M., and M.F.-B. participated in methodology. C.d.J.R., S.A.-A., and R.M. participated in validation and formal analysis of data presented in this article. C.d.J.R. and S.A.-A. participated in writing the original draft. C.d.J.R., S.A.-A., P.G.-M., and M.S. participated in reviewing and editing. All authors have read and agreed to the published version of the manuscript.

Funding: This study has been funded by Instituto de Salud Carlos III through the project "CP19/00095" (Co-funded by European Social Fund "Investing in your future"). and Consellería de Innovación, Universidades, Ciencia y Sociedad Digital from Generalitat Valenciana (CIAICO/2021/135) given to C. d J.R. This study was also funded by Instituto de Salud Carlos III (ISCIII) through the project (PI22/00824) and co-funded by the European Union (FEDER) granted to M.S. and C.d.J.R. FISABIO intramural grants UGP-20-135 and UGP-20-254 also supported this work. S.A.-A. was the recipient of the "Carolina foundation predoctoral fellowship" 2020. R.M. was funded by the Spanish Ministry of Economy and Competitiveness (PID2021-123253OB-C21). E.R.C was financed by the Spanish Ministry of Science, Innovation and Universities PTA2018-015394-I. The FESEM equipment used in this work was funded by the Generalitat Valenciana (Spain) and co-financed with the ERDF funds (OP ERDF of Comunitat Valenciana, Spain) GVA-IDIFEDER_2018/020, "Una forma de hacer Europa". Figures were created in BioRender.com.

Institutional Review Board Statement: The study was conducted according to the guidelines of the Declaration of Helsinki and approved by the Ethics Committee of the Health Department of the University General Hospital of Alicante (protocol code PI 110/2022).

Informed Consent Statement: Informed consent was obtained from all subjects involved in the study.

Data Availability Statement: The data that support the findings of this study are available from the corresponding author, C.d.J.R., upon reasonable request.

Acknowledgments: The authors thank Ignacio Pachón for assistance with cell culture and Enrique Yuste for the HPLC experiments. We thank Ramón Martínez Máñez and Carmen Martínez Bisbal for their project support and Reyes Mateo for sharing reagents.

Conflicts of Interest: The authors declare that the research was conducted in the absence of any commercial or financial relationships that could be construed as a potential conflict of interest.

References

1. Louis, D.N.; Perry, A.; Wesseling, P.; Brat, D.J.; Cree, I.A.; Figarella-Branger, D.; Hawkins, C.; Ng, H.K.; Pfister, S.M.; Reifenberger, G.; et al. The 2021 WHO Classification of Tumors of the Central Nervous System: A summary. *Neuro. Oncol.* **2021**, *23*, 1251. [CrossRef] [PubMed]
2. Thakkar, J.P.; Dolecek, T.A.; Horbinski, C.; Ostrom, Q.T.; Lightner, D.D.; Barnholtz-Sloan, J.S.; Villano, J.L. Epidemiologic and molecular prognostic review of Glioblastoma. *Cancer Epidemiol. Biomark. Prev.* **2014**, *23*, 1985–1996. [CrossRef] [PubMed]
3. Stupp, R.; Mason, W.P.; van den Bent, M.J.; Weller, M.; Fisher, B.; Taphoorn, M.J.B.; Belanger, K.; Brandes, A.A.; Marosi, C.; Bogdahn, U.; et al. Radiotherapy plus concomitant and adjuvant temozolomide for glioblastoma. *N. Engl. J. Med.* **2005**, *352*, 987–996. [CrossRef] [PubMed]
4. Davis, M.E. Glioblastoma: Overview of disease and treatment. *Clin. J. Oncol. Nurs.* **2016**, *20*, S2–S8. [CrossRef]
5. Fang, C.; Wang, K.; Stephen, Z.R.; Mu, Q.; Kievit, F.M.; Chiu, D.T.; Press, O.W.; Zhang, M. Temozolomide nanoparticles for targeted glioblastoma therapy. *ACS Appl. Mater. Interfaces* **2015**, *7*, 6682. [CrossRef]
6. Ostermann, S.; Csajka, C.; Buclin, T.; Leyvraz, S.; Lejeune, F.; Decosterd, L.A.; Stupp, R. Plasma and cerebrospinal fluid population pharmacokinetics of temozolomide in malignant glioma patients. *Clin. Cancer Res.* **2004**, *10*, 3728–3736. [CrossRef]
7. Sengupta, S.; Marrinan, J.; Frishman, C.; Sampath, P. Impact of temozolomide on immune response during malignant glioma chemotherapy. *Clin. Dev. Immunol.* **2012**, *2012*, 831090. [CrossRef]
8. Chamberlain, M.C. Temozolomide: Therapeutic limitations in the treatment of adult high-grade gliomas. *Expert Rev. Neurother.* **2014**, *10*, 1537–1544. [CrossRef]
9. Trinh, V.A.; Patel, S.P.; Hwu, W.-J. The safety of temozolomide in the treatment of malignancies. *Expert Opin. Drug Saf.* **2009**, *8*, 493–499. [CrossRef]
10. Khan, A.; Imam, S.S.; Aqil, M.; Ahad, A.; Sultana, Y.; Ali, A.; Khan, K. Brain targeting of temozolomide via the intranasal route using lipid-based nanoparticles: Brain pharmacokinetic and scintigraphic analyses. *Mol. Pharm.* **2016**, *13*, 3773–3782. [CrossRef]
11. Gullà, A.; Hideshima, T.; Bianchi, G.; Fulciniti, M.; Samur, M.K.; Qi, J.; Tai, Y.-T.; Harada, T.; Morelli, E.; Amodio, N.; et al. Protein Arginine Methyltransferase 5 (PRMT5) has prognostic relevance and is a druggable target in Multiple Myeloma. *Leukemia* **2018**, *32*, 1002. [CrossRef]

12. Stopa, N.; Krebs, J.E.; Shechter, D. The PRMT5 arginine methyltransferase: Many roles in development, cancer and beyond. *Cell. Mol. Life Sci.* **2015**, *72*, 2059. [CrossRef]
13. Vinet, M.; Suresh, S.; Maire, V.; Monchecourt, C.; Némati, F.; Lesage, L.; Pierre, F.; Ye, M.; Lescure, A.; Brisson, A.; et al. Protein arginine methyltransferase 5: A novel therapeutic target for triple-negative breast cancers. *Cancer Med.* **2019**, *8*, 2428. [CrossRef]
14. Chan-Penebre, E.; Kuplast, K.G.; Majer, C.R.; Boriack-Sjodin, P.A.; Wigle, T.J.; Johnston, L.D.; Rioux, N.; Munchhof, M.J.; Jin, L.; Jacques, S.L.; et al. A selective inhibitor of PRMT5 with in vivo and in vitro potency in MCL models. *Nat. Chem. Biol.* **2015**, *11*, 432–437. [CrossRef]
15. Zhu, L.; Sun, H.T.; Wang, S.; Huang, S.L.; Zheng, Y.; Wang, C.Q.; Hu, B.Y.; Qin, W.; Zou, T.T.; Fu, Y.; et al. Isolation and characterization of exosomes for cancer research. *J. Hematol. Oncol.* **2020**, *13*, 152. [CrossRef]
16. Singh, A.; Fedele, C.; Lu, H.; Nevalainen, M.T.; Keen, J.H.; Languino, L.R. Exosome-mediated transfer of $\alpha v\beta 3$ integrin from tumorigenic to nontumorigenic cells promotes a migratory phenotype. *Mol. Cancer Res.* **2016**, *14*, 1136–1146. [CrossRef]
17. Qiao, L.; Hu, S.; Huang, K.; Su, T.; Li, Z.; Vandergriff, A.; Cores, J.; Dinh, P.U.; Allen, T.; Shen, D.; et al. Tumor cell-derived exosomes home to their cells of origin and can be used as trojan horses to deliver cancer drugs. *Theranostics* **2020**, *10*, 3474–3487. [CrossRef]
18. Batrakova, E.V.; Kim, M.S. Using exosomes, naturally-equipped nanocarriers, for drug delivery. *J. Control Release* **2015**, *219*, 396–405. [CrossRef]
19. Luan, X.; Sansanaphongpricha, K.; Myers, I.; Chen, H.; Yuan, H.; Sun, D. Engineering exosomes as refined biological nanoplatforms for drug delivery. *Acta Pharmacol. Sin.* **2017**, *38*, 754–763. [CrossRef]
20. Colombo, M.; Raposo, G.; Théry, C. Biogenesis, secretion, and intercellular interactions of exosomes and other extracellular vesicles. *Annu. Rev. Cell Dev. Biol.* **2014**, *30*, 255–289. [CrossRef]
21. Wang, X.; Zhong, W.; Bu, J.; Li, Y.; Li, R.; Nie, R.; Xiao, C.; Ma, K.; Huang, X.; Li, Y. Exosomal protein CD82 as a diagnostic biomarker for precision medicine for breast cancer. *Mol. Carcinog.* **2019**, *58*, 674–685. [CrossRef] [PubMed]
22. Rani, S.; O'Brien, K.; Kelleher, F.C.; Corcoran, C.; Germano, S.; Radomski, M.W.; Crown, J.; O'Driscoll, L. Isolation of exosomes for subsequent mRNA, MicroRNA, and protein profiling. *Methods Mol. Biol.* **2011**, *784*, 181–195. [CrossRef] [PubMed]
23. Gurunathan, S.; Kang, M.-H.; Jeyaraj, M.; Qasim, M.; Kim, J.-H. Review of the isolation, characterization, biological function, and multifarious therapeutic approaches of exosomes. *Cells* **2019**, *8*, 307. [CrossRef] [PubMed]
24. Kalra, H.; Drummen, G.P.C.; Mathivanan, S. Focus on extracellular vesicles: Introducing the next small big thing. *Int. J. Mol. Sci.* **2016**, *17*, 170. [CrossRef]
25. Araujo-Abad, S.; Saceda, M.; de Juan Romero, C. Biomedical application of small extracellular vesicles in cancer treatment. *Adv. Drug Deliv. Rev.* **2022**, *182*, 114117. [CrossRef]
26. Ventero, M.P.; Fuentes-Baile, M.; Quereda, C.; Perez-Valeciano, E.; Alenda, C.; Garcia-Morales, P.; Esposito, D.; Dorado, P.; Barbera, V.M.; Saceda, M. Radiotherapy resistance acquisition in glioblastoma. Role of SOCS1 and SOCS3. *PLoS ONE* **2019**, *14*, e0212581. [CrossRef]
27. Tschuschke, M.; Kocherova, I.; Bryja, A.; Mozdziak, P.; Angelova Volponi, A.; Janowicz, K.; Sibiak, R.; Piotrowska-Kempisty, H.; Iżycki, D.; Bukowska, D.; et al. Inclusion biogenesis, methods of isolation and clinical application of human cellular exosomes. *J. Clin. Med.* **2020**, *9*, 436. [CrossRef]
28. Zhang, Y.; Liu, Y.; Liu, H.; Tang, W.H. Exosomes: Biogenesis, biologic function and clinical potential. *Cell Biosci.* **2019**, *9*, 19. [CrossRef]
29. Hosseini-Beheshti, E.; Pham, S.; Adomat, H.; Li, N.; Guns, E.S.T. Exosomes as biomarker enriched microvesicles: Characterization of exosomal proteins derived from a panel of prostate cell lines with distinct AR phenotypes. *Mol. Cell. Proteom.* **2012**, *11*, 885. [CrossRef]
30. Kavanagh, E.L.; Lindsay, S.; Halasz, M.; Gubbins, L.C.; Weiner-Gorzel, K.; Guang, M.H.Z.; McGoldrick, A.; Collins, E.; Henry, M.; Blanco-Fernández, A.; et al. Protein and chemotherapy profiling of extracellular vesicles harvested from therapeutic induced senescent triple negative breast cancer cells. *Oncogenesis* **2017**, *6*, e388. [CrossRef]
31. La Shu, S.; Yang, Y.; Allen, C.L.; Hurley, E.; Tung, K.H.; Minderman, H.; Wu, Y.; Ernstoff, M.S. Purity and yield of melanoma exosomes are dependent on isolation method. *J. Extracell. Vesicles* **2020**, *9*, 1692401. [CrossRef]
32. Sokolova, V.; Ludwig, A.K.; Hornung, S.; Rotan, O.; Horn, P.A.; Epple, M.; Giebel, B. Characterisation of exosomes derived from human cells by nanoparticle tracking analysis and scanning electron microscopy. *Colloids Surf. B Biointerfaces* **2011**, *87*, 146–150. [CrossRef]
33. Braun, C.J.; Stanciu, M.; Boutz, P.L.; Patterson, J.C.; Calligaris, D.; Higuchi, F.; Neupane, R.; Fenoglio, S.; Cahill, D.P.; Wakimoto, H.; et al. Coordinated splicing of regulatory detained introns within oncogenic transcripts creates an exploitable vulnerability in malignant glioma. *Cancer Cell* **2017**, *32*, 411–426.e11. [CrossRef]
34. Banasavadi-Siddegowda, Y.K.; Welker, A.M.; An, M.; Yang, X.; Zhou, W.; Shi, G.; Imitola, J.; Li, C.; Hsu, S.; Wang, J.; et al. PRMT5 as a druggable target for glioblastoma therapy. *Neuro. Oncol.* **2018**, *20*, 753–763. [CrossRef]
35. Liu, X.; He, J.Z.; Mao, L.; Zhang, Y.; Cui, W.W.; Duan, S.; Jiang, A.; Gao, Y.; Sang, Y.; Huang, G. EPZ015666, a selective protein arginine methyltransferase 5 (PRMT5) inhibitor with an antitumour effect in retinoblastoma. *Exp. Eye Res.* **2021**, *202*, 108286. [CrossRef]
36. Xi, X.-M.; Xia, S.-J.; Lu, R. Drug loading techniques for exosome-based drug delivery systems. *Pharmazie* **2021**, *76*, 61–67. [CrossRef]

37. Zhao, Y.; Liu, P.; Tan, H.; Chen, X.; Wang, Q.; Chen, T. Exosomes as smart nanoplatforms for diagnosis and therapy of cancer. *Front. Oncol.* **2021**, *11*, 3364. [CrossRef]
38. Yang, T.; Martin, P.; Fogarty, B.; Brown, A.; Schurman, K.; Phipps, R.; Yin, V.P.; Lockman, P.; Bai, S. Exosome delivered anticancer drugs across the blood-brain barrier for brain cancer therapy in Danio Rerio. *Pharm. Res.* **2015**, *32*, 2003–2014. [CrossRef] [PubMed]
39. Chandrashekar, D.S.; Bashel, B.; Balasubramanya, S.A.H.; Creighton, C.J.; Ponce-Rodriguez, I.; Chakravarthi, B.V.S.K.; Varambally, S. UALCAN: A portal for facilitating tumor subgroup gene expression and survival analyses. *Neoplasia* **2017**, *19*, 649–658. [CrossRef]
40. Yan, F.; Alinari, L.; Lustberg, M.E.; Martin, L.K.; Cordero-Nieves, H.M.; Banasavadi-Siddegowda, Y.; Virk, S.; Barnholtz-Sloan, J.; Bell, E.H.; Wojton, J.; et al. Genetic validation of the protein arginine methyltransferase PRMT5 as a candidate therapeutic target in glioblastoma. *Cancer Res.* **2014**, *74*, 1752–1765. [CrossRef]
41. Han, X.; Li, R.; Zhang, W.; Yang, X.; Wheeler, C.G.; Friedman, G.K.; Province, P.; Ding, Q.; You, Z.; Fathallah-Shaykh, H.M.; et al. Expression of PRMT5 correlates with malignant grade in gliomas and plays a pivotal role in tumor growth in vitro. *J. Neurooncol.* **2014**, *118*, 61–72. [CrossRef]
42. Fleming, A.B.; Saltzman, W.M. Pharmacokinetics of the carmustine implant. *Clin. Pharmacokinet.* **2002**, *41*, 403–419. [CrossRef] [PubMed]
43. Sawyer, A.J.; Piepmeier, J.M.; Saltzman, W.M. Cancer issue: New methods for direct delivery of chemotherapy for treating brain tumors. *Yale J. Biol. Med.* **2007**, *79*, 141.
44. Vargason, A.M.; Anselmo, A.C.; Mitragotri, S. The evolution of commercial drug delivery technologies. *Nat. Biomed. Eng.* **2021**, *5*, 951–967. [CrossRef]
45. Parolini, I.; Federici, C.; Raggi, C.; Lugini, L.; Palleschi, S.; De Milito, A.; Coscia, C.; Iessi, E.; Logozzi, M.; Molinari, A.; et al. Microenvironmental pH is a key factor for exosome traffic in tumor cells. *J. Biol. Chem.* **2009**, *284*, 34211. [CrossRef] [PubMed]
46. Clayton, A.; Turkes, A.; Dewitt, S.; Steadman, R.; Mason, M.D.; Hallett, M.B. Adhesion and signaling by B cell-derived exosomes: The role of integrins. *FASEB J.* **2004**, *18*, 977–979. [CrossRef]
47. Kim, M.S.; Haney, M.J.; Zhao, Y.; Mahajan, V.; Deygen, I.; Klyachko, N.L.; Inskoe, E.; Piroyan, A.; Sokolsky, M.; Okolie, O.; et al. Development of exosome-encapsulated paclitaxel to overcome MDR in cancer cells. *Nanomedicine* **2016**, *12*, 655–664. [CrossRef]
48. Pascucci, L.; Coccè, V.; Bonomi, A.; Ami, D.; Ceccarelli, P.; Ciusani, E.; Viganò, L.; Locatelli, A.; Sisto, F.; Doglia, S.M.; et al. Paclitaxel is incorporated by mesenchymal stromal cells and released in exosomes that inhibit in vitro tumor growth: A new approach for drug delivery. *J. Control Release* **2014**, *192*, 262–270. [CrossRef]
49. Alvarez-Erviti, L.; Seow, Y.; Yin, H.; Betts, C.; Lakhal, S.; Wood, M.J.A. Delivery of siRNA to the mouse brain by systemic injection of targeted exosomes. *Nat. Biotechnol.* **2011**, *29*, 341–345. [CrossRef]
50. Hung, M.E.; Leonard, J.N. Stabilization of exosome-targeting peptides via engineered glycosylation. *J. Biol. Chem.* **2015**, *290*, 8166–8172. [CrossRef]
51. Hood, J.L.; Scott, M.J.; Wickline, S.A. Maximizing exosome colloidal stability following electroporation. *Anal. Biochem.* **2014**, *448*, 49. [CrossRef]
52. Barciszewska, A.M.; Gurda, D.; Głodowicz, P.; Nowak, S.; Naskręt-Barciszewska, M.Z. A new epigenetic mechanism of temozolomide action in glioma cells. *PLoS ONE* **2015**, *10*, e0136669. [CrossRef]
53. Rubio-Camacho, M.; Encinar, J.A.; Martínez-Tomé, M.J.; Esquembre, R.; Mateo, C.R. The interaction of temozolomide with blood components suggests the potential use of human serum albumin as a biomimetic carrier for the drug. *Biomolecules* **2020**, *10*, 1015. [CrossRef]
54. Verhaak, R.G.W.; Hoadley, K.A.; Purdom, E.; Wang, V.; Qi, Y.; Wilkerson, M.D.; Miller, C.R.; Ding, L.; Golub, T.; Mesirov, J.P.; et al. An integrated genomic analysis identifies clinically relevant subtypes of glioblastoma characterized by abnormalities in PDGFRA, IDH1, EGFR and NF1. *Cancer Cell* **2010**, *17*, 98. [CrossRef]
55. Zhang, P.; Xia, Q.; Liu, L.; Li, S.; Dong, L. Current opinion on molecular characterization for GBM classification in guiding clinical diagnosis, prognosis, and therapy. *Front. Mol. Biosci.* **2020**, *7*, 562798. [CrossRef]
56. Yang, X.; Shi, G.; Guo, J.; Wang, C.; He, Y. Exosome-encapsulated antibiotic against intracellular infections of methicillin-resistant *Staphylococcus aureus*. *Int. J. Nanomed.* **2018**, *13*, 8095. [CrossRef]
57. Li, X.Q.; Liu, J.T.; Fan, L.L.; Liu, Y.; Cheng, L.; Wang, F.; Yu, H.Q.; Gao, J.; Wei, W.; Wang, H.; et al. Exosomes derived from gefitinib-treated EGFR-mutant lung cancer cells alter cisplatin sensitivity via up-regulating autophagy. *Oncotarget* **2016**, *7*, 24585. [CrossRef]
58. Sun, D.; Zhuang, X.; Xiang, X.; Liu, Y.; Zhang, S.; Liu, C.; Barnes, S.; Grizzle, W.; Miller, D.; Zhang, H.G. A novel nanoparticle drug delivery system: The anti-inflammatory activity of curcumin is enhanced when encapsulated in exosomes. *Mol. Ther.* **2010**, *18*, 1606. [CrossRef]
59. Labuschagne, J.J.; Chetty, D. Glioblastoma multiforme as a secondary malignancy following stereotactic radiosurgery of a meningioma: Case report. *J. Neurosurg.* **2019**, *46*, E11. [CrossRef]
60. Orasanu, C.I.; Aschie, M.; Deacu, M.; Bosoteanu, M.; Vamesu, S.; Enciu, M.; Băl̦țătescu, G.I.; Cozaru, G.C.; Mitroi, A.F.; Voda, R.I. Implications of Cellular Immaturity in Necrosis and Microvascularization in Glioblastomas IDH-Wild-Type. *Clin. Pract.* **2022**, *12*, 1054–1068. [CrossRef]

61. Neira, J.L.; Araujo-Abad, S.; Cámara-Artigas, A.; Rizzuti, B.; Abian, O.; Giudici, A.M.; Velazquez-Campoy, A.; de Juan Romero, C. Biochemical and biophysical characterization of PADI4 supports its involvement in cancer. *Arch. Biochem. Biophys.* **2022**, *717*, 109125. [CrossRef] [PubMed]
62. Fuentes-Baile, M.; Bello-Gil, D.; Pérez-Valenciano, E.; Sanz, J.M.; García-Morales, P.; Maestro, B.; Ventero, M.P.; Alenda, C.; Barberá, V.M.; Saceda, M. CLyta-DAAO, free and immobilized in magnetic nanoparticles, induces cell death in human cancer cells. *Biomolecules* **2020**, *10*, 222. [CrossRef] [PubMed]

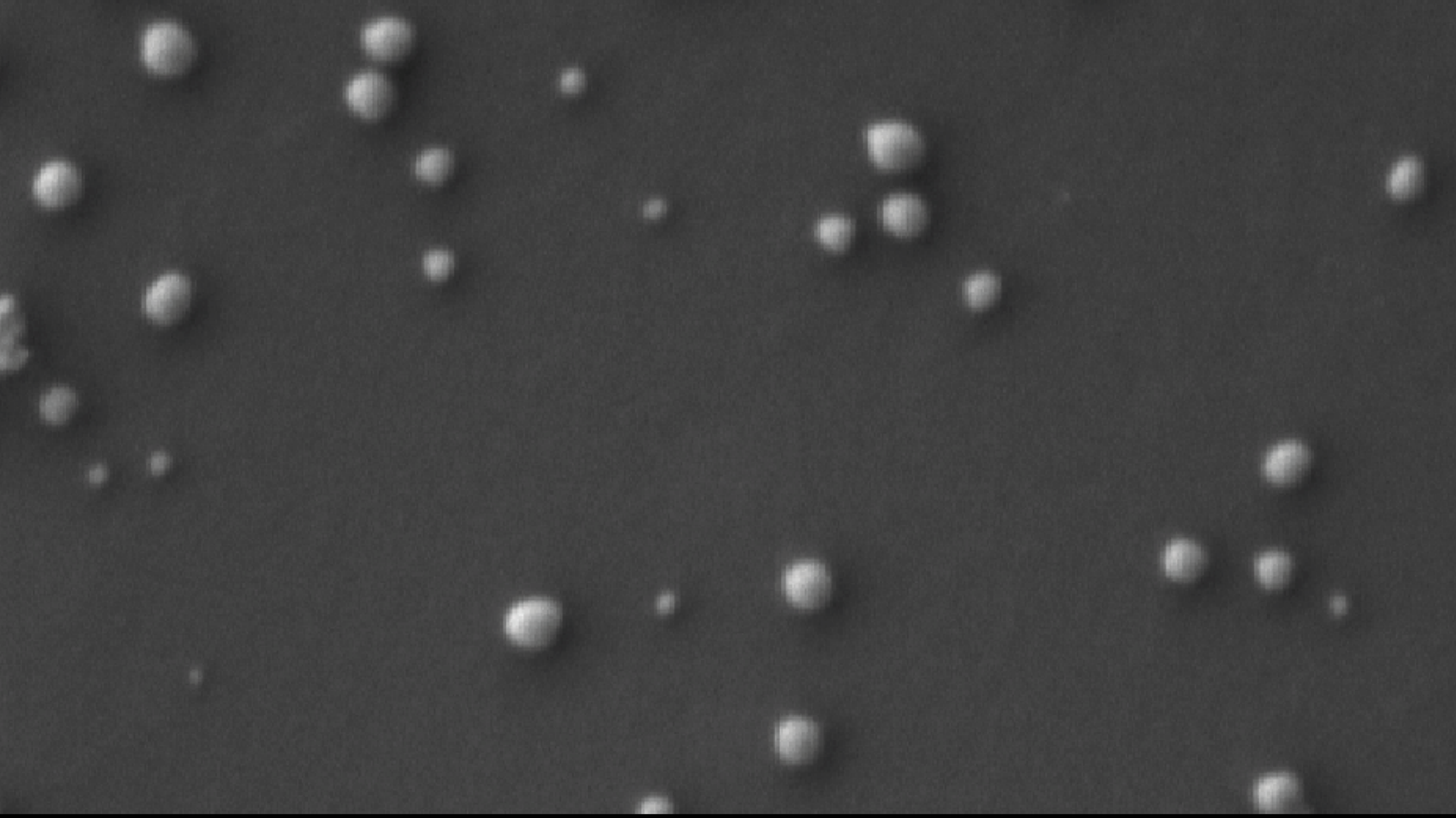

CHAPTER 3

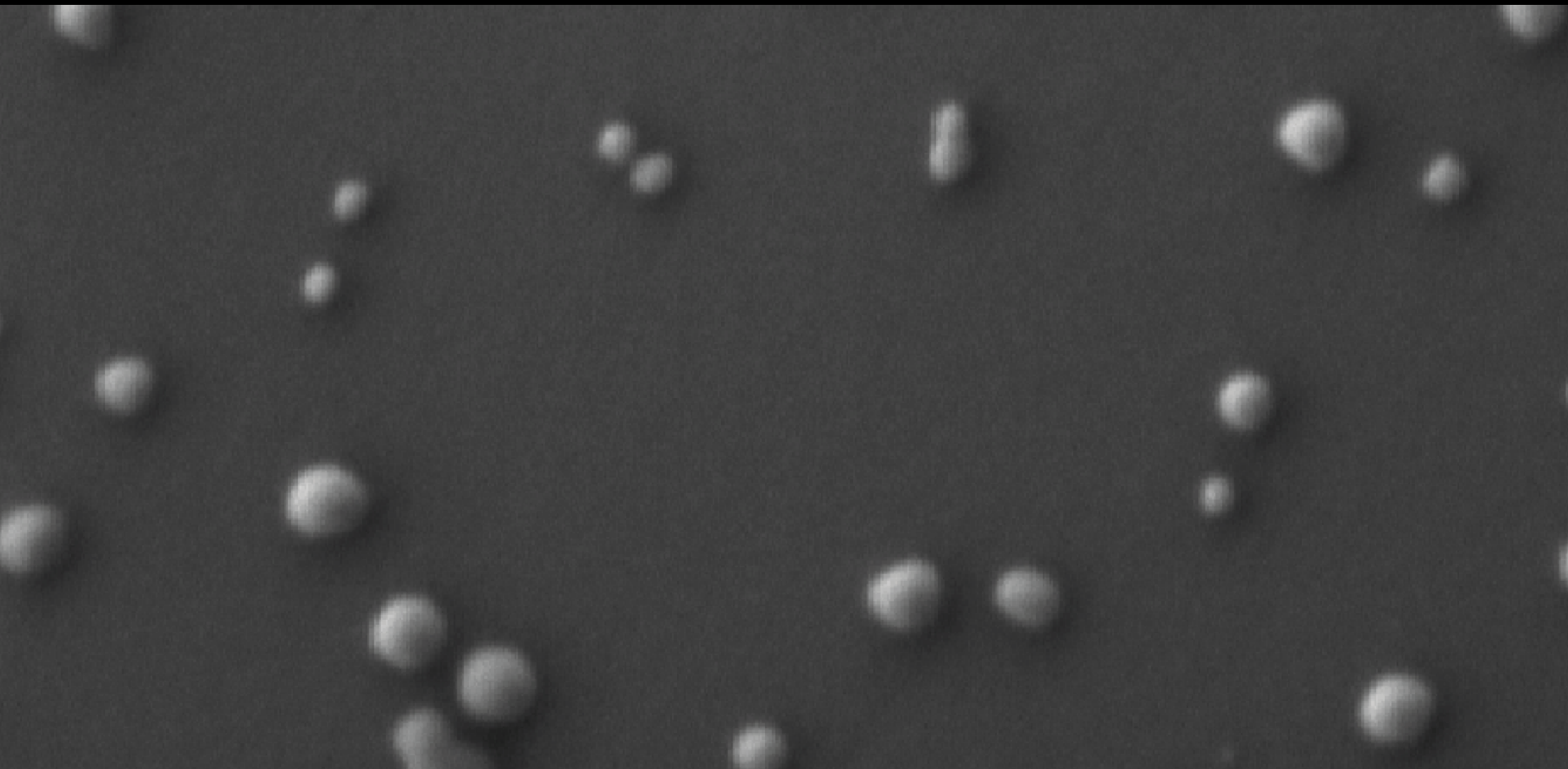

4.3 Chapter 3. New therapy for pancreatic cancer based on extracellular vesicles

Summary of the results

PDAC is the most common aggressive pancreatic cancer, with a very poor prognosis, mainly due to a limited response to treatment. This article describes how small EVs derived from RWP-1, a pancreatic cancer cell line, are good drug carriers for PDAC treatment, and how they provide more efficiency than direct administration at very low doses [67].

First, we isolated RWP-1-derived small EVs with the ultracentrifugation method and characterized them with WB, DLS, and FESEM. Then, we evaluated the drug resistance profile of the RWP-1 cell line to two chemotherapeutic drugs, TMZ and EPZ015666. Both drugs had a significant effect on cell proliferation; where TMZ resulted in more than 75 % decreased proliferation, and EPZ015666 resulted in approximately 60 %.

Next, we tested direct and indirect incubation EVs loading methods (Figure 16). RWP-1 small EVs were incubated with 5 mM of TMZ and 15 μM of EPZ015666 and, the resultant amount of drug loaded into RWP-1 small EVs was assessed with HPLC obtaining 7.2 μM for TMZ, and 0.05 μM when loaded with EPZ015666. Based on HPLC and proliferation assay results, we concluded that the most efficient treatment method was direct incubation.

After that, we performed proliferation assays with RWP-1 EVs^{TMZ} and RWP-1 $\text{EVs}^{\text{EPZ015666}}$ and the drug alone. We observed that when TMZ was applied to the cells directly, at the same RWP-1 EVs^{TMZ} treatment concentrations, it had no significant effect on cell proliferation, but when we treated cells with RWP-1 EVs^{TMZ}, a statistically significant decrease in proliferation was observed. Similarly, when RWP-1 $\text{EVs}^{\text{EPZ015666}}$ were applied to the cells in a concentration of 50% that corresponds with 0.02 μM of EPZ015666, they lead to a slight decrease in cell proliferation. Taken together, our data indicated that RWP-1 EVs^{TMZ} were more efficient than RWP-1 $\text{EVs}^{\text{EPZ015666}}$, suggesting that TMZ had a better interaction with the lipid bilayer [67].

We also tested the stability of RWP-1 EVs^{TMZ} and RWP-1 $\text{EVs}^{\text{EPZ015666}}$ over long-term storage. After storing the EVs at -80 ºC for two years, we performed the same experiments and found that the efficacy of TMZ decreased by only 4%, while EPZ015666 efficiency decreased by 10% with respect to the freshly obtained EVs. These results confirmed the suitability of EVs storage at -80 ºC; although their stability was slightly affected by the drugs.

Finally, we tracked the RWP-1 small EVs incorporation by their parental cells into living cells. We noted that after 6 h of treatment, RWP-1 small EVs^{TMZ} (red labeled) was incorporated mainly in the nucleus, and the number of small EVs/cell significantly increased.

In this work, we demonstrated the target-specific properties of small EVs and their strong effect on proliferation when derived from the same type of tumor cells. We observed that the effectiveness of small EVs as a drug delivery system depended on the chemical structure of the drug and its interaction with the extravesicular membrane. In this sense, our data indicated that RWP-1 EVs^{TMZ} had higher efficiency than RWP-1 EVs^{EPZ015666}, suggesting a better interaction of TMZ with the lipid bilayer [67]. This opens a new avenue to investigate the drugs that are more suitable for loading into small EVs. Overall, this work highlights the potential of RWP-1-derived small EVs as a promising drug delivery system for PDAC treatment, which can be further explored in preclinical studies and clinical trials.

Biomedicine & Pharmacotherapy 162 (2023) 114657

Contents lists available at ScienceDirect

Biomedicine & Pharmacotherapy

journal homepage: www.elsevier.com/locate/biopha

New therapy for pancreatic cancer based on extracellular vesicles

Salomé Araujo-Abad [a,b,c], Antonio Manresa-Manresa [a], Enrique Rodríguez-Cañas [b], María Fuentes- Baile [a], Pilar García-Morales [b], Ricardo Mallavia [b], Miguel Saceda [a,b], Camino de Juan Romero [a,b,*,1]

[a] Unidad de Investigación, Fundación para el Fomento de la Investigación Sanitaria y Biomédica de la Comunidad Valenciana (FISABIO), Hospital General Universitario de Elche, Camí de l'Almazara 11, Elche, 03203 Alicante, Spain

[b] Instituto de Investigación, Desarrollo e Innovación en Biotecnología Sanitaria de Elche (IDiBE), Universidad Miguel Hernández, Avda, Universidad s/n, Ed. Torregaitán, Elche, 03202 Alicante, Spain

[c] Centro de Biotecnología, Universidad Nacional de Loja, Avda. Pio Jaramillo Alvarado s/n, Loja, 110111 Loja, Ecuador

ARTICLE INFO

Keywords:
Pancreatic ductal adenocarcinoma
Small EVs
Nanocarriers
Chemotherapy
FESEM

ABSTRACT

Pancreatic Ductal Adenocarcinoma (PDAC), is the most common aggressive cancer of the pancreas. The standard care of PDAC includes tumor resection and chemotherapy, but the lack of early diagnosis and the limited response to the treatment worsens the patient's condition. In order to improve the efficiency of chemotherapy, we look for more efficient systems of drug delivery. We isolated and fully characterized small Extracellular Vesicles (EVs) from the RWP-1 cell line. Our study indicates that the direct incubation method was the most efficient loading protocol and that a minimum total amount of drug triggers an effect on tumor cells. Therefore, we loaded the small EVs with two chemotherapeutic drugs (Temozolomide and EPZ015666) by direct incubation method and the amount of drug loaded was measured by high-performance liquid chromatography (HPLC). Finally, we tested their antiproliferative effect on different cancer cell lines. Moreover, the system is highly dependent on the drug structure and therefore RWP-1 small EVs^{TMZ} were more efficient than RWP-1 small EVs^{EPZ015666}. RWP-1 derived small EVs represent a promising drug delivery tool that can be further investigated in preclinical studies and its combination with PRMT5 inhibitor can be potentially developed in clinical trials for the treatment of PDAC.

1. Introduction

Pancreatic ductal adenocarcinoma (PDAC) is a highly aggressive lethal malignancy and the most prevalent type of pancreatic neoplasm. This type of cancer, that develops in the exocrine compartment, accounts for more than 90% of pancreatic cancer cases [1]. It has an average 5-year survival rate of less than 10% and is anticipated to become the third leading cause of cancer–related mortality by 2025 [2], mostly due to the lack of early diagnosis and limited response to treatments [3].

Only a small fraction of PDAC patients can benefit from adjuvant chemotherapy and, especially in advanced stages after tumor resection, chemotherapeutic options are limited, with gemcitabine (Gem) being the first drug treatment or other drugs as 5- fluorouracil with a median survival improvement of only a few weeks [4]. PDAC treatment limitations reinforce the importance of looking for new methodologies, more efficient drugs or drug delivery to be explored and investigated, for the development of novel treatment options.

Temozolomide (TMZ) (3,4-dihydro-3-methyl-4-oxoimidazo-[5,1-d]-astetrazine-8-carboxamide) is a DNA alkylating agent that acts over the methylation of guanine and adenine bases, breaking double-stranded DNA and causing cell cycle arrest and cell death by apoptosis [5]. It has been used to treat glioma, glioblastoma neuroendocrine tumors, melanoma, and sarcomas [6–13] but TMZ treatment has a short half-life

---

Abbreviations: PDAC,, Pancreatic Ductal Adenocarcinoma; *TMZ,*, temozolomide; *GEM*, gemcitabine; *EVs,*, extracellular vesicles; *BBB,*, blood-brain barrier; *DMEM F-12,*, Dulbecco's Modified Eagle's Medium: Nutrient Mixture F-12; *FBS,*, fetal bovine serum; *MTT,*, methylthiazolyldiphenyl-tetrazolium bromide; FESEM, Field Emission Scanning Electron Microscope; DLS, Dynamic Light Scattering.

[*] Corresponding author at: Unidad de Investigación, Fundación para el Fomento de la Investigación Sanitaria y Biomédica de la Comunidad Valenciana (FISABIO), Hospital General Universitario de Elche, Camí de l'Almazara 11, Elche, 03203 Alicante, Spain.

E-mail address: m.juan@umh.es (C. de Juan Romero).

[1] ORCID: 0000–0001-7890–8447

https://doi.org/10.1016/j.biopha.2023.114657
Received 24 February 2023; Received in revised form 29 March 2023; Accepted 3 April 2023

[14] and, to achieve therapeutic levels, high doses are required, with the subsequent appearance of a great number of side effects [15–17].

EPZ015666, is a small-molecule considered a protein arginine methyltransferase-5 (PRMT5) inhibitor. It competes with the substrate binding pocket of PRMT5 peptide to deny its interaction and posterior methylation [18]. PRMT5, which modulates the biological function of target proteins catalyzing the transference of two methyl groups to arginine residues, is essential to maintain homeostasis in both normal and malignant cells [19] and plays an important role in cell development and adult hematopoiesis [20]. PRMT5 is a novel target that has recently emerged for cancer treatment. This enzyme is involved in tumorigenesis and it has been found overexpressed in a variety of cancers including melanoma, multiple myeloma, lung, gastric, prostate, ovarian, colorectal cancers, and glioblastoma [21] and is associated with poor prognosis [19].

Small EVs, that are being secreted from cells into the extracellular space, play an important role in both physiological and pathological processes through interaction with their neighbors and the extracellular environment [22]. Small EVs have a diameter of 30–150 nm [22–24], and a lipid bilayer membrane with the same characteristics of the donor cell [25]. EVs contain mostly RNA, DNA, and proteomic material [25]. Importantly, while the proteins and genetic material may reflect the properties of the parent cells, EVs are generally not mirrored images of the cellular membrane. This suggests that EVs are derived from specific subcellular locations, and their contents are likely intended for a defined function in the extracellular space.

One of the most important characteristics to be explored of small EVs is their use as drug delivery carriers. Small EVs have some advantages over synthetic systems (liposomes, dendrimers, nanoparticles, etc.), like, specific tropism for cell origin [26], non-cytotoxic effect, biocompatibility, facility of transporting either hydrophilic or hydrophobic biomolecules and facility to cross the blood-brain barrier (BBB) [27,28]. These novel nanocarriers can contribute to increasing the efficiency of PDAC treatment.

The advanced age of most PDAC patients explains the lack of satisfactory results, as postoperative systemic therapy may not be ideal for these individuals. The patient's systemic contact with chemotherapeutics at high concentrations exposes them to an increased risk of systemic toxicities, affecting their overall well-being [29]. Localized interventions, however, retain cytotoxic agents at a specific site, thus reducing drug exposure and decreasing toxicity while maximizing treatment efficacy. In recent years, there has been considerable interest in the use of localized drug delivery systems to perform localized interventions as alternatives to systemic therapy [30].

In the present study, we focused on small EVs released from RWP-1 cells. We described an efficient and reproducible method of small EVs purification, performing as well several characterization methods in order to ensure its purity. We have used those small EVs to overcome the present challenges of treatment and drug delivery in PDAC. We have used TMZ and EPZ015666 to demonstrate that small EVs derived from RWP-1 have target specificity, and that those drugs loaded into small EVs inhibit the proliferation of PDAC cells in vitro at less concentration exposure than when they are directly applied. Therefore, RWP-1-derived small EVs could be used as a nanocarrier for the development of new therapeutic strategies.

2. Materials and methods

2.1. Cell culture

Pancreatic adenocarcinoma cell line (RWP-1), was donated by Instituto Municipal de Investigaciones Médicas (IMIM, Barcelona, Spain) [31]. Isolation of primary human GBM cell line (HGUE-GB-39) was performed from surgical washes as previously reported [32,33]. The GBM cell line, HGUE-GB-39 and RWP-1 were cultured as previously described [31–33].

2.2. Proliferation assays

Methylthiazolyldiphenyl-tetrazolium bromide (MTT) assays were performed to analyze the antiproliferative effect of the drugs and the EVs. Cells were seeded in 96-well standard plates (Sarstedt, Nümbrecht, Germany) with a density of 4000 cells/well and incubated at 37 ºC and 5% CO_2 for 24 h. Then, cells were either treated with different and increasing concentrations of the TMZ, EPZ or loaded small EVs and incubated for 72 h under the same conditions. After that, 0.25 mg mL^{-1} of MTT (Sigma-Aldrich, MO, USA) was added and incubated for 3 h, media was carefully removed and 100 µL of dimethyl sulfoxide (DMSO) (Sigma-Aldrich, MO, USA) was added. To dissolve the formazan crystals, the plates were vigorously shaken at room temperature for 20 min. Finally, the absorbance was measured on an Eon™ Microplate Spectrophotometer (BioTeK®, Winooski, VT, USA) at 570 nm.

2.3. Small EVs purification

Confluent populations of RWP-1 and HGUE-GB-39 cell lines were incubated in T75 flasks with DMEM-HG and DMEM F-12 conditioned media respectively. After 4 days small EVs were obtained by differential ultracentrifugation method. The media samples were centrifuged at 2000 x *g* for 20 min at 4 ºC to eliminate cells and debris followed by an initial ultracentrifugation using Optima L-90 K Ultracentrifuge (Beckman Coulter) with 70.1 Ti rotor at 25,000 x *g* for 40 min at 4 ºC to remove macrovesicles then the supernatant was filtered through 0.22 µm filters (Fisher Scientific). The resultant filtrate was centrifuged at 110,000 x *g* for 90 min at 4 ºC to pellet small EVs that were then washed in PBS at 110,000 x *g* for 90 min at 4 ºC and the final pellet was resuspended in 200 µL of 1X PBS and then stored at − 80 ºC.

2.4. Western blot

An amount of 10 µg of total protein was solubilized with loading buffer (4x) (2-mercaptoethanol + NuPage; 1:5) and heated at 95 ºC for 5 min for reducing conditions and without 2-mercaptoethanol for non-reducing conditions. Then, proteins were separated by SDS-PAGE using 10% gels and transferred to a Nitrocellulose membrane (Bio-Rad Laboratories Inc, California, USA). Membranes were incubated overnight at 4 ºC with primary antibodies: anti-CD63 (mouse,1:1000, Invitrogen), anti-ALIX (mouse,1:500, Invitrogen), anti-TSG101 (mouse,1:500, Invitrogen), anti-α-tubulin (mouse, 1:10000, Invitrogen) and anti-HSP90-B1 (rabbit,1:4000, CUSABIO) followed by one hour incubation at room temperature with ECL™ Anti-mouse IgG and ECL™ Anti-rabbit IgG, Horseradish Peroxidase linker (GE Healthcare, UK). The membranes were visualized with ECL™ Prime Western blotting detection reagent (Amersham™) in the ChemiDoc Bio-Rad instrument [33].

2.5. Dynamic light scattering (DLS)

To characterize size distribution, RWP-1 small EVs samples were analyzed using a Zetasizer Nano ZS instrument (Malvern Panalytical). Each sample was diluted in Milli-Q™ water (1:10), 1 mL was dispensed in a polystyrene disposable cuvette (Zen0040) and read at least seven times in Zeta sizer Software. The final image with the distribution curves was used in the figures as an illustrative example of the medium size (Fig. 1B).

2.6. Field emission scanning electron microscope (FESEM)

RWP-1 small EVs were fixed with Paraformaldehyde 2%, sonicated for 5 min and diluted in serial dilutions with Milli-Q™ water (1:10; 1:100; 1:1000, 1:10000). A 50 µL sample droplet was deposited on a silicon wafer and, once evaporated, the samples were observed using a Zeiss Sigma 300 VP Field Emission Scanning Electron Microscope (FESEM) without coating (Fig. 1C). EVs morphology was analyzed at

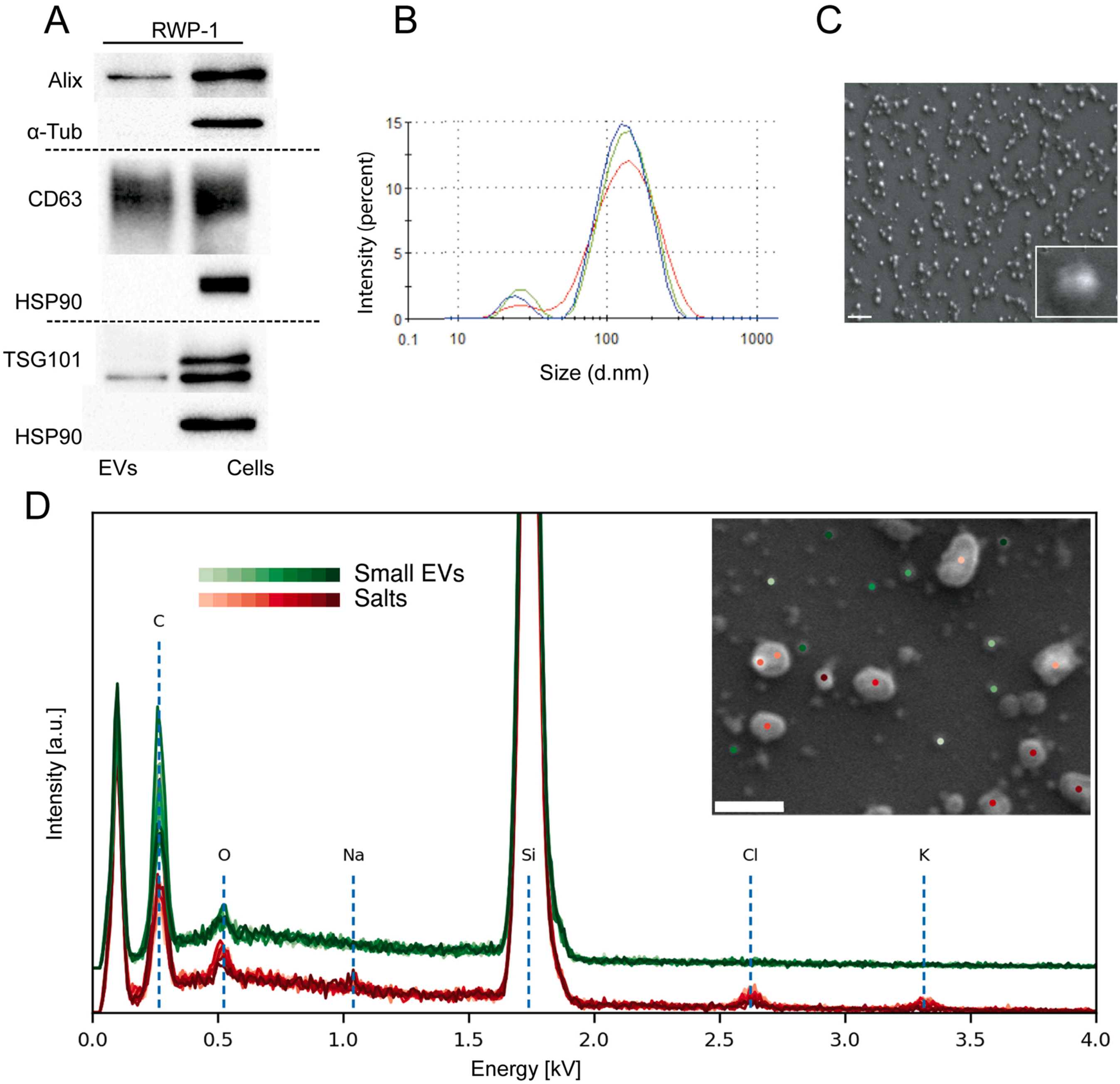

Fig. 1. Biochemical and biophysical characterization. **A** Expression by WB of Alix, CD63, and TSG101 in small EVs and RWP-1 cell line. α-Tub and HSP-90 were used as control. **B** Size and morphology of the RWP-1 cell line derived small EVs were visualized using Dynamic light scattering (DLS) and (**c**) Field Emission Scanning Electron Microscopy (FESEM). **C** Energy dispersive X-ray (EDX) analysis was performed with the X-ray detector in a FESEM microscope on one of the EVs samples. The studied samples were a mixture of biological samples and salts. Green color indicates the location of the EVs analysis and red color salts. The spectrum of each of the areas was done at 3.5 kV in order to maximize the contribution of the EVs and minimize the contribution of the silica peak (Si) which corresponds to the substrate and is present in both samples. Blue chopped lines point at different inorganic elements present in salt crystals but not in the EVs. Scale bar 0.5 µm. EVs, extracellular vesicles; FESEM, Field Emission Scanning Electron Microscope White boxes show an optical magnification of a representative small EV. Scale bars 200 nm.). EVs, extracellular vesicles.

low voltages around 1 kV while higher voltages were employed to differentiate the salts from the biological sample using Energy Dispersive X-ray (EDX) (Fig. 1D).

2.7. *Small EVs labelling*

The CellVue® Claret Far Red Fluorescent kit (Sigma-Aldrich, MO, USA) was used to label small EVs. 200 µL of RWP-1 small EVs, were treated with the kit content following manufacturer's instructions. After being washed twice in PBS with 110,000 x *g* centrifugation, the labeled small EVs were filtered with 0.2 µm and resuspended in PBS prior to be used.

2.8. *Immunocytochemistry (ICC)*

An amount of 35,000 cells of RWP-1 cell line were seeded into twenty-four-well plates on coverslips. After, cells were treated for 6 h with red labeled RWP-1 small EVs, fixed with paraformaldehyde at 4% concentration, and blocked with FBS/PBS (1X) (50 µL/mL). Then, cells were incubated with anti-E-cadherin (1:100, rabbit, Invitrogen, Barcelona, Spain) primary antibody. After washing out the first antibody, cells were incubated with Alexa Fluor 488-labeled anti-rabbit (1:500) secondary antibody (Invitrogen, Barcelona, Spain); the DAPI (4′,6-diamidino-2-phenylindole) reagent from Sigma (Madrid, Spain) was used to stain the nucleus. Coverslips were mounted in Prolong™ Gold Antifade Reagent (Invitrogen, Barcelona, Spain) and analyzed using a Zeiss Axioscope 5 microscope with the LED light source Colibri 3 (Carl Zeiss, Oberkochen, Germany).

2.9. *Small EVs drug-loading*

RWP-1 small EVs were loaded with two different procedures, direct and indirect incubation. For the first method, small EVs were incubated for 2 h at 37 ºC in a thermoblock with defined concentrations of a given chemotherapeutic drug (EPZ015666 15 μM or TMZ 5 mM). Then, they were washed with PBS 1X and ultracentrifuged at 110,000 x *g* for 60 min at 4 ºC to pellet the loaded small EVs. Finally, they were filtered with a 0.22 μm membrane under sterile conditions and stored at − 80 ºC. The indirect procedure consisted in the incubation of GBM cell culture with the drug of interest (EPZ015666 15 μM or TMZ 5 mM) for 72 h. Then, the flasks were treated as previously described in the small EVs purification section.

2.10. *Quantification of TMZ and EPZ015666 by HPLC*

The amount of TMZ and EPZ015666 loaded into the small EVs was determined by the high-performance liquid chromatography (HPLC) method. Briefly, 200 μL of small EVs were placed in a Concentrator plus (Eppendorf, Germany) at 40ºC for 2 h to evaporate the solvent. Then, 100 μL volume of acetonitrile was added, and the mixture was vortexed, sonicated and then centrifuged at 13,200 x *g* (Centrifuge 5415 R, Eppendorf) for 10 min. After centrifugation, the supernatant was transferred into HPLC vials and injected into the UPLC-QtoF-MS/MS equipment with a high-resolution flight tube and quadrupole technology (Waters- Bruker). Detection of TMZ and EPZ015666 were optimized with a Waters I-Class with UV detection at 330 and 254 nm respectively, followed by the use of QToF-MS de Bruker Daltonics, maXis impact Series model in positive ionization mode by Electrospray (ESI) with column ACE Excel C18-Ar (50–3; 1.7 μm). The mobile phase used was: A) Water with 0.1%v/v acetic acid and B) Methanol with 0.1% acetic acid. Gradient: 0 min, 95% A; 5.50 min, 60% A, 8.75 min, 5% A, with a flow rate of 0.3 mL/min and an injection volume of 5 μL.

2.11. *Live cell imaging*

For live imaging of small EVs uptake, RWP-1 cells were seeded in 96-well black plates with clear bottoms (Corning, Kennebunk, ME, USA) with a density of 16000 cells/well and incubated at 37ºC and 5% CO_2 for 24 h. Then, cells were treated with red labeled RWP-1 small EVs^{TMZ} and incubated for 3 and 6 h under the same conditions. After that, cells were rinsed with (1X) PBS twice and then placed in a Cytation 3 (BioTeK®, Winooski, VT, USA) instrument to take the images. Images were exported as a tiff file format for further analysis in Fiji software.

2.12. *Statistical analysis*

Results were expressed as mean ± standard deviation (SD) of three independent experiments. In order to evaluate the normal distribution of the data, Shapiro-Wilk statistical test was used, and the statistical significance was determined by Student's t-test or the Mann-Whitney U test. Differences were considered to be statistically significant with a *p*-value of less than 0.05. Statistical analysis was performed with GraphPad Prism v7.0a software (GraphPad Software Inc., San Diego CA, USA).

3. Results

3.1. *Small EVs isolation and biochemical characterization from a pancreatic cancer cell line*

In order to study the role of tumor derived small EVs, we have used one of the two human pancreatic cancer lines, RWP-1 and RWP-2, that were established from patients with primary pancreatic cancer metastatic to the liver [34]. In this work, we are using RWP-1, which has moderately well differentiated ductal cell adenocarcinoma features, and has been used as a model cell line for pancreatic ductal adenocarcinoma in several studies [34–38]. If an effect is observed in this PDAC cell line, we will check if it is specific to this cancer type. Therefore, we also used the radioresistant GBM, GB-39 cell line, obtained from a patient's primary culture [32].

We isolated a small EVs sample from RWP-1 by ultracentrifugation protocol for further biochemical and biophysical characterization. RWP-1 and GB-39 small EVs were used in functional studies. Characterization of small EVs derived from RWP-1 has been standardized for reliable and reproducible results from assays and other downstream applications. We have used Western Blot (WB) as an analytical technique to detect specific proteins in a sample of small EVs, as well as a semi-quantitative estimation of the protein content. We have identified the presence and expression level of Alix, CD63, and TSG101, the most commonly used proteins in small EVs characterization. Our results showed their presence in small EVs derived from RWP1, while α-Tubulin and HSP-90 were only found in cell lysates (Fig. 1A). Given that the proteins and genetic material inside the small EVs may reflect properties of the parent cells [39], our results established a high purity of the RWP-1-derived small EVs samples that will be used in functional experiments.

3.2. *Morphological and physical characterization of RWP-1-derived small EVs*

DLS was used on RWP-1-derived small EVs (Fig. 1B) to analyze the size of the isolated vesicle population. Our results showed that the isolated particles had a medium size of: 141.5 ± 4.4, consistently within the expected size range for small EVs (Fig. 1B). We further examined the size and morphology of RWP-1-derived small EVs by performing FESEM analyses (Fig. 1C). FESEM images indicated the presence of a homogeneous population of small EVs with diameters of 100–150 nm, with a round or cup shaped morphology. To rule out that the structures visualized by FESEM could be an artifact of the isolation or fixation process, we performed an energy dispersive X-ray (EDX) analysis. The X-ray detector in a FESEM microscope was used on RWP-1-derived small EVs sample (Fig. 1D) for 10 times. The X-ray detector was placed on several structures of the sample, confirming that the studied sample was a mixture of organic samples and salts. All the samples showed a silica peak corresponding with the substrate. The spectrum of the rounded small EVs like areas, showed a high content in carbon and oxygen confirming their organic origin. Areas corresponding to salts presented a chloride and potassium content. In line with similar studies uncovering small EVs characteristics, DLS and FESEM imaging confirmed the presence and purity of RWP-1-derived small EVs in our preparations [40]. Moreover, the EDX analysis established the organic nature of RWP-1 derived small EVs samples (Fig. 1D). Finally, since the small EVs will be loaded with different drugs, it was interesting to see that they keep their round shape after isolation (Fig. 1B) and that they have a considerable and well established size (Fig. 1C) that can be reproducible.

3.3. *RWP-1 drug resistance profile*

PDAC is one of the most lethal diseases, mostly because the majority of patients have unresectable, locally advanced, or metastatic disease at the time of diagnosis. Unfortunately, traditional treatments such as surgery, chemotherapy and radiation lead to modest improvements in postoperative survival due to the high prevalence of drug-resistant phenotypes [41]. Moreover, since chemotherapy is all too often associated with toxicity, many patients elect for palliative care [42]. At the moment the standard of care is the use of Gem alone or in combination with other drugs such as 5-Fluorouracil, Leucovorin, Irinotecan, and Oxaliplatin, although it shows marginal efficacy in clinical trials [43–45]. Since there is currently no effective treatment for PDAC, it is essential to find new alternative drugs and new delivery systems that enhance drug efficacy and extend patient survival while improving quality of life.

The alkylating agent TMZ is a treatment option for several solid tumors such as glioma, glioblastoma, neuroendocrine tumors, melanoma, and sarcomas [6–13]. However, when TMZ has been used in an advanced untreated pancreatic cancer phase II study, it is not a standard of care due to its high cytotoxicity and low effect on patients [13]. We hypothesize that if it could reduce the side effects of systemic exposure to TMZ, this drug could also be a therapeutic option for PDAC patients. The effect of TMZ treatment on proliferation was assessed using an increasing concentration of the drug. We evaluated a range of concentrations between 0.05 mM and 10 mM. Our analyses revealed that treatment of the RWP-1 with TMZ resulted in more than 75% decreased proliferation, together with an IC_{50} of 0.7301 ± 0.066 (Fig. 2A).

As mentioned before, Gem has been used since 1983, constituting the first-line chemotherapy for most PDAC patients and forming the backbone of several drug combinations [46]. Recent studies have revealed that protein arginine methyltransferase gene 5 (PRMT5) is a promising druggable candidate whose inhibition creates synergistic vulnerability of PDAC cells to Gem [47]. EPZ01666 is the inhibitor of PRMT5, which has been shown to regulate the splicing of detained introns in proliferation-associated genes in GBM[48] and has been broadly used in several types of cancer [18,49]. In this study, we are testing the effect of both treatments, TMZ but also new therapies like EPZ015666, on the RWP-1 cell line.

The effect of the EPZ015666 treatment on proliferation was assessed using an increasing concentration of the drug. We evaluated a range of concentrations between 10 μM to 60 μM. Our analyses revealed that treatment of the RWP-1 with EPZ015666 resulted in more than 60% decreased proliferation, together with an IC_{50} of 23.31 ± 0.064 (Fig. 2B).

3.4. Loaded GBM derived small EVs decrease RWP-1 cell proliferation

In order to test which incubation method is better for drug loading, GB-39 derived small EVs were loaded by two incubation methods [50]. For indirect incubation, the GB-39 cell line was treated for 72 h with high doses of TMZ or EPZ015666 and small EVs were isolated from the medium (Fig. 3B). For direct incubation protocol, small EVs were first isolated from GB-39 and then incubated in a medium containing a low dose of either of the proposed drugs (Fig. 3A).

Small EVs were loaded by direct and indirect incubation with 5 mM of TMZ, and the loading efficiency of GBM derived small EVs was determined by measuring the amount of TMZ within the EVs by HPLC. Our HPLC measurements showed a higher amount of TMZ being loaded into the small GBM derived EVs by direct incubation (data not shown).

Next, we wonder if small EVs can be used as a drug delivery system for PDAC cancer treatment. When applying the TMZ loaded small EVs on the RWP-1 cell line, direct incubation showed no significant differences as compared with indirect incubation, although both incubation methods have a mild effect on tumor pancreatic cells (Fig. 3C). However, EPZ015666 has a significant effect in RWP-1 cells, direct incubation being the most effective loading method (Fig. 3D). This reduction in proliferation is very important since the small EVs were loaded with only 0.04 μM and they were applied in concentrations that range from 0.002 to 0.02 μM.

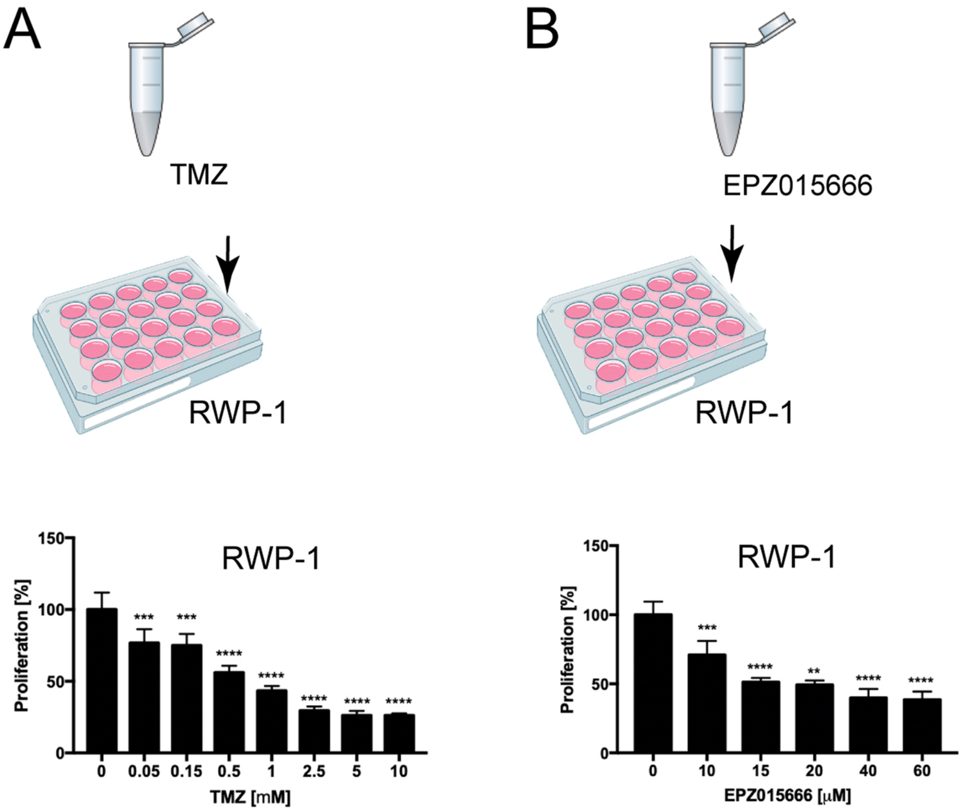

Fig. 2. Cell proliferation effect of TMZ and EPZ015666 in RWP-1 cell line. (**A**) Cancer cells were treated with increasing concentrations of TMZ and (**B**) EPZ015666 and their effect over cell proliferation was measured. Asterisks indicate the statistical significance of the results (** $p < 0.01$, *** $p < 0.001$, **** $p < 0.0001$). TMZ, Temozolomide.

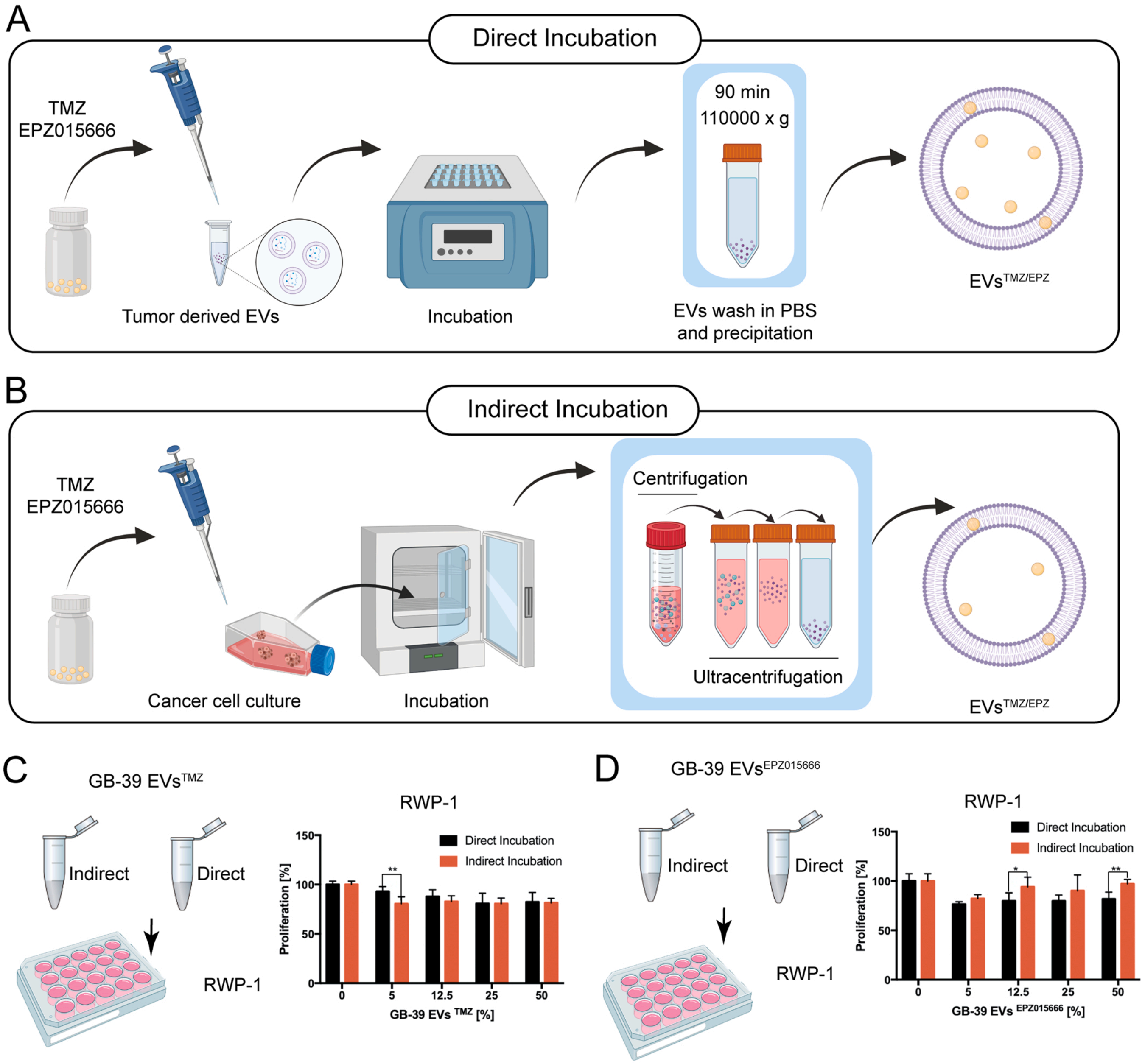

Fig. 3. Drug loading of small EVs particles. A Scheme representing the sequential steps for small EVs loading using the direct method. **B** Scheme representing the sequential steps for small EVs loading using the indirect method. **C** Comparison of the effect on cell proliferation of GB-39^{TMZ} small EVs using direct (black bars) and indirect (red bars) loading methods. **D** Comparison of the effect on cell proliferation of GB-39^{EPZ015666} small EVs using direct (black bars) and indirect (red bars) loading methods. Asterisks indicate the statistical significance of the results (* $p < 0.05$, ** $p < 0.01$).

Taken together, direct incubation was a better method to load the small EVS (Fig. 1C-D) and, for the first time, the effect of PRMT5 drug inhibitor has been tested on a cancer cell line derived from a patient with pancreatic adenocarcinoma. Our results show not only the potential therapeutic effect of EPZ05666, but also the increase in the efficacy of both drugs as indicated by the decrease in cell proliferation at very low doses (Fig. 3C-D).

3.5. TMZ shows more efficiency when loaded in RWP-1-derived small EVs

It has been proposed that small EVs have directionality toward their mother cell [26]. Therefore, we speculate that small EVs derived from RWP-1 may have a higher effect on their cells of origin, than the GBM derived small EVS. To test this idea, we used the isolated small EVs from the RWP-1 cell line to load them with the proposed drugs. We used the direct incubation method in our experiment to load the vesicles, using a concentration of 5 mM for TMZ (RWP-1 EVs^{TMZ}) and 15 μM for EPZ015666 (RWP-1 EVs^{EPZ015666}) for the incubation.

In order to know the precise amount of drug contained in the small EVs, we performed an HPLC analysis followed by drug identification with a mass spectrometer (Fig. 4A). Our quantifications showed that RWP-1 EVs^{TMZ} were loaded with 7.2 μM. Isolated RWP-1 EVs^{TMZ} were applied to the cells in serial dilutions ranging from 50% to 5% of the original stock. Since the amount of drug applied to the cultures throughout the RWP-1 EVs^{TMZ} corresponds to a range that goes from 3.6 μM to 0.36 μM, we tested the direct exposure of the RWP-1 cell line to TMZ at these low concentrations to compare both effects (Fig. 4C). The maximum concentration applied was 3.6 μM of TMZ corresponding to 50% of RWP-1 EVs^{TMZ} and the minimum was 0.36 μM at 5% of TMZ.

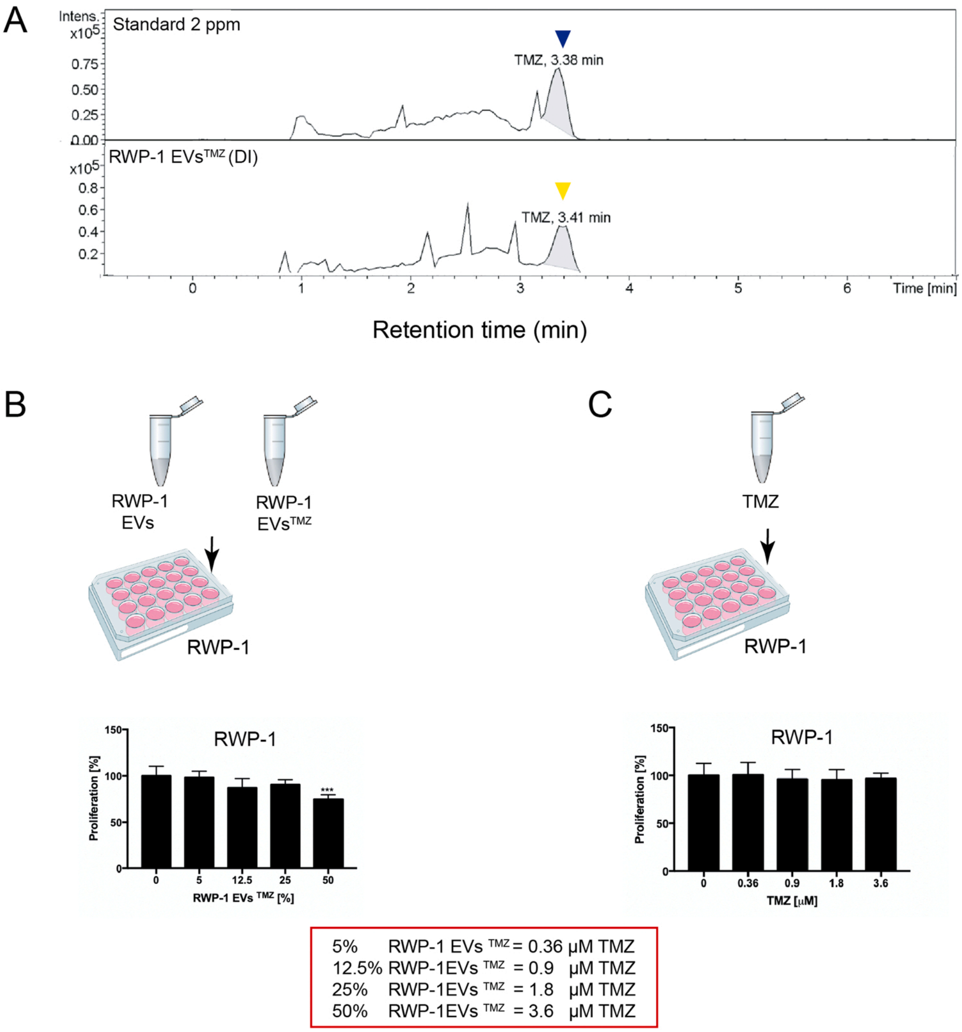

Fig. 4. HPLC-MS analysis of small EVs sample RWP-1 EVs^{TMZ} and cell proliferation effect. A The amount of TMZ incorporated into small EVs was quantified by HPLC. The dark blue arrow indicates the standard TMZ (2 ppm) at 3.38 min retention time. The yellow arrow indicates the RWP-1 EVs^{TMZ} sample (Direct Incubation) (1.405 μg/mL) at a retention time of 3.41 min **B** Small EVs of RWP-1 were loaded directly with a 5 mM concentration of TMZ (RWP-1 EVs^{TMZ}). Small EVs alone or serial dilutions of RWP-1 EVs^{TMZ} were applied to RWP-1 cell line and their effect on proliferation was measured. **C** Cancer cells were treated with increasing concentrations of TMZ and their proliferation was measured. The red box indicates the equivalence of concentrations. Asterisks indicate the statistical significance of the results (*** $p < 0.001$). TMZ, Temozolomide; EVs, extracellular vesicles.

RWP-1 EVs^{TMZ} treatment resulted in a dose dependent reduction in cancer cell proliferation. Interestingly, the application of the drug using RWP-1 EVs^{TMZ} resulted in a more significant effect on RWP-1 cell proliferation with 25.6% than the reduction produced by GB-39 EVs^{TMZ} by only 17.7% (Fig. 3C, Fig. 4B), supporting the idea that small EVs have tumor tropism to their mother cell.

It has been shown that the best way to maintain the structure and functionality of the EVs is to keep them at − 80 °C [51]. Therefore, we also analyzed the stability of the drug loaded EVs over long term storage. We repeated the same experiments after two years of keeping EVs^{TMZ} under − 80 °C conditions and we observed only a decrease of 4% efficiency in the case of TMZ and 10% decrease in EPZ015666 (Fig. S4), These results corroborate that the storage at − 80 °C is appropriate but the stability also depends on the drug.

Our results indicate that the total amount of TMZ used for the treatment with EVs was up to a hundred and fifty times lower than the direct application of TMZ in cells (Fig. 2A, Fig. 4B). This is very important because when TMZ was applied to the cells directly, at the very same RWP-1 EVs^{TMZ} treatment concentrations, it had no significant effect in cell proliferation (Fig. 4C). All these data indicate that RWP-1 EVs^{TMZ} treatment not only increases the target directionality but also the efficiency of the drug.

3.6. Small EVs incorporation by their mother cell

It has been shown that small EVs have tropism for their mother cell [26,38]. In order to see how the loaded small EVs were incorporated into RWP-1, we treated this cell line with red labeled RWP-1 small EVs^{TMZ} in unfixed cells, for 3 and 6 h. As shown in the figure (Fig. 5A) small EVs ^{TMZ} tend to aggregate in the cytoplasm but mostly in the nucleus after 6 h of treatment. Besides, after 6 h of incubation, the number of small EVs/ cell significatively increases (Fig. 5B). At 6 h of treatment, immunocytochemistry showed that the internalized small EVs were in the cytoplasm, aggregated around the nucleus, as shown by DAPI and E-Cad staining (Fig. S2).

3.7. EPZ015666-loaded RWP-1-derived small EVs have a similar effect on cancer cells

Given that PDAC patients' median survival rate is only 6 months, and more than 93% of patients die within the first 5 years [52], many efforts have been made to find novel drug combinations that will synergistically increase Gem's therapeutic effects. Using a multiplex CRISPR gene KO screening technology with a library of sgRNAs to screen chromatin regulators whose depletion may create conditional lethality with Gem, Wei and colleagues have recently shown that PRMT5 is a significant therapeutic target in PDAC patients who mostly receive Gem as a chemotherapeutic agent [47].

To test the effect of the EPZ015666 treatment on proliferation, increasing concentrations of the drug were used. Small EVs were loaded by direct incubation in 15 μM EPZ015666 (RWP-1 EVs^{EPZ015666}). Similar to the previous experiments, the HPLC analysis followed by drug

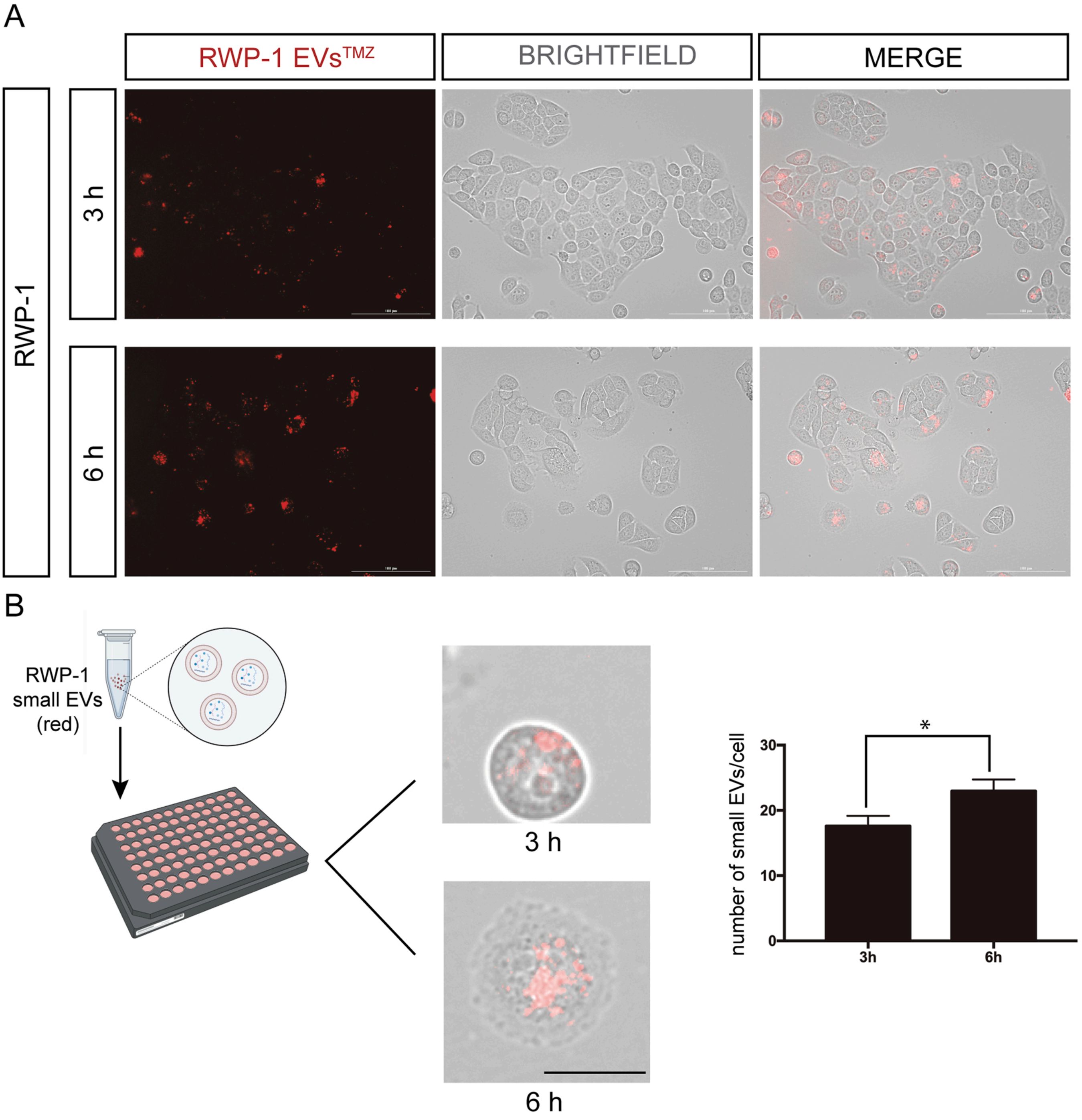

Fig. 5. RWP-1 small EVs internalization in living cells. A RWP-1 cells (Brightfield) were incubated with RWP-1 small EVs^{TMZ} (red) at 3 and 6 h. A representative experiment is shown ($n = 6$). **B** Scheme representing the treatment with RWP-1 small EVs (red). The Fiji software was used to account for the number of small EVs (red dots). Data represent mean ± SEM, Student's 2-tailed unpaired t-test was used, $*p < 0.05$. Scale bars: A,1000 µm; B, 20 µm.

identification with a mass spectrometer was performed (Fig. 6A). Our quantifications showed a 0.05 µM concentration in the small RWP-1 EVs^{EPZ015666} by direct incubation. Therefore, those samples were loaded with a concentration that was three hundred times lower than the original 15 µM. We wonder if EPZ015666 could have different target efficacy based on the cell origin of the small EVs. Therefore, isolated small RWP-1 EVs^{EPZ015666} were applied to the RWP1 and GB-39 cells in serial dilutions ranging from 50% to 5% of the original stock (Fig. 5B, Fig. S1). Consequently, the maximum concentration was 0.02 µM corresponding to 50% small EVs and the minimum was 0.002 µM when 5% of EVs^{EPZ015666} were applied (Fig. 6B). Direct administration of the drug showed a nearly 60% decrease in proliferation in RWP-1 at high doses (60 µM) (Fig. 2B) however, at the low concentration corresponding to the amount loaded inside the small EVs, EPZ015666 didn't have any effect (Fig. 5C).

RWP-1 EVs^{EPZ015666} application resulted in an average of 16% reduction in proliferation on the RWP-1 cell line. Contrary to the RWP-1 EVs^{TMZ} effect, this reduction was observed regardless of the small EVs concentration (Fig. 6B). It has been shown that different drugs with different mechanisms of action and chemical properties could be more suitable for small EVs drug delivery. We could observe that TMZ-loaded in RWP-1 EVs was more efficient than EPZ015666, indicating that TMZ

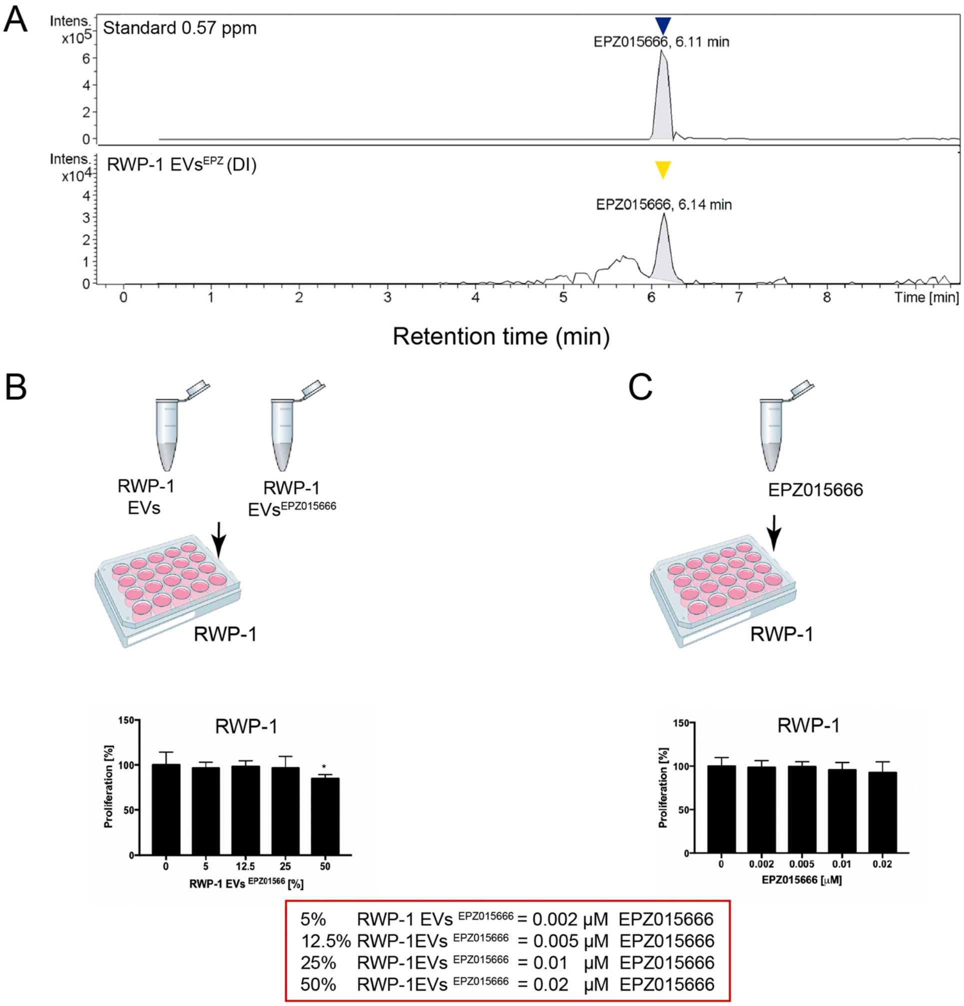

Fig. 6. HPLC-MS analysis of small EVs sample RWP-1 EVs^{EPZ015666} and cell proliferation effect. A The amount of EPZ015666 incorporated into small EVs was quantified by HPLC. The dark blue arrow indicates the standard EPZ015666 (0.57 ppm) at a 6.11 min retention time. Yellow arrow indicates the RWP-1 EVs^{EPZ015666} sample (Direct Incubation) (0.02 µg/mL) at 6.14 min retention time. **B** Small EVs of RWP-1 were loaded directly with a 15 µM concentration of EPZ015666 (RWP-1 EVs^{EPZ015666}). Small EVs alone or serial dilutions of RWP-1 EVs^{EPZ015666} were applied to RWP-1 cell line and their effect on proliferation was measured. **C** Cancer cells were treated with increasing concentrations of EPZ015666 and their proliferation was measured. The red box indicates the equivalence of concentrations. Asterisks indicate the statistical significance of the results (*** $p < 0.001$). EVs, extracellular vesicles.

has better interaction with the lipid bilayer of the small EVs membrane as previously reported for other compounds [53]. Therefore, our results indicate that even if the amount of EPZ015666 that reaches the cell is sufficient to induce an effect, RWP-1 derived small EVs are not suitable to be loaded with EPZ015666 for PDAC therapy.

4. Discussion

Endocrine pancreatic cancers are generally more indolent tumors with a more favorable prognosis as compared with exocrine cell tumors, most commonly pancreatic ductal adenocarcinomas. Since PDAC constitutes approximately 95% of pancreatic cancers, the fundamental challenges that underlie the high mortality of this type of cancer are: 1) Pancreas location. As the pancreas is situated deep within the upper abdomen and only 15–20% can undergo surgical resection. As the pancreas is located between the aorta and its major upper abdominal branches, it is difficult to visualize growing tumors and cancer often grows around the vessels, wrapping them. 2) Early metastasis. More than 50% of PDAC patients develop distant metastasis and the majority of patients who undergo resection will develop metastases within 4 years of surgery [54–57]. 3) Wasting syndrome. At diagnosis, 80% of patients with PDAC, have a reduced ability to withstand aggressive treatment due to the physiologic effects of PDAC [58]. The poor treatment tolerance is evidenced by decreased survival of those patients after pancreatectomy or chemotherapy [59–63]. In order to improve the treatment of these patients it is necessary to find not only new treatments but also new delivery approaches to reduce the side effects.

In this study, we used several sources of small EVs and presented evidence that direct incubation was a better method to load the small EVS (Fig. 1C-D). Thus, when RWP-1 pancreatic tumor cell line is exposed to GB-39 EVs loaded with TMZ or EPZ015666, it undergoes a lower decrease in proliferation than when loaded RWP-1 EVs are applied. This data supports the idea that small EVs derived from RWP-1 are a more efficient drug carrier than GB-39 EVs.

In this study, we demonstrated that EVs derived from RWP-1 are good drug carriers for PDAC treatment, providing more efficiency than direct administration at very low doses. Moreover, in this work we have shown that small EVs have target specificity, having a higher impact on proliferation when they are isolated from the same type of tumor cell.

The uptake of the RWP-1 EVs^{EPZ015666} by the pancreatic tumor cells was not dose-dependent, indicating that RWP-1 small EVs were not a good carrier for this drug. The fact that the direct application of EPZ015666 has a great impact on RWP-1 suggests that it could be a good therapy for PDAC, although it should be mobilized by other means such as nanoparticles (Fig. 2B).

Several groups have extensively studied how the storage conditions affect the morphology and functionality of the EVs [51,64–66]. We have observed that both tested drugs not only behave differently and have different loading capacities, but also present different long-term stability.

The fact that the benefit associated with the use of this natural nanocarrier depends on the type of the used drug, probably relies on the different interactions between the chemical structure of the drug and the extravesicular membrane, and this interaction will define its internalization. Along this line, our data indicate that RWP-1 EVs$^{\mathrm{TMZ}}$ was more efficient than RWP-1 EVs$^{\mathrm{EPZ015666}}$, suggesting that TMZ has better interaction with the lipid bilayer. This opens a new field of study, to investigate which drugs can be better loaded into small EVs. Taken together, this work provides evidence that RWP-1 derived small EVs represent a promising drug delivery tool that can be further investigated in preclinical studies and in clinical trials for the treatment of PDAC.

5. Conclusions

In summary, we have demonstrated that TMZ and EPZ015666 inhibit the growth of RWP-1 cells in vitro by less exposure to the drug when this is loaded in small EVs. Interestingly, we observed that the benefit associated with the use of this natural nanocarrier, depends on the type of the used drug, probably due to the different interactions between the chemical structure of the drug and the extravesicular membrane and this interaction will define its internalization. In this context, our results suggest that TMZ has a better interaction with the lipid bilayer than EPZ015666. Altogether, these results suggest a potential use of RWP-1 derived small EVs as a drug delivery system to obtain the maximum therapeutic effect with minimal toxicity for PDAC patients' treatment.

Funding sources

This study has been funded by Instituto de Salud Carlos III through the project "CP19/00095" (Co-funded by European Social Fund "Investing in your future") and Consellería de Innovación, Universidades, Ciencia y Sociedad Digital from Generalitat Valenciana (CIAICO/2021/135) given to C. d J.R. This study was also funded by Instituto de Salud Carlos III (ISCIII) through the project (PI22/00824) and co-funded by the European Union (FEDER) granted to M.S. and C.d. J.R. FISABIO intramural grants UGP-20–135 also supported this work. S. A.-A. was the recipient of the "Carolina foundation predoctoral fellowship" 2020. R.M. was funded by the Spanish Ministry of Economy and Competitiveness (PID2021–123253OB-C21). E.R.C was financed by the Spanish Ministry of Science, Innovation and Universities PTA2018–015394-I. The FESEM equipment used in this work was funded by the Generalitat Valenciana (Spain) and co-financed with the ERDF funds (OP ERDF of Comunitat Valenciana, Spain) GVA-IDI-FEDER_2018/020, "Una forma de hacer Europa". Figures were created in BioRender.com.

CRediT authorship contribution statement

Salomé Araujo-Abad: Conceptualization, Investigation, Methodology, Validation, Formal analysis of data presented in this article, Writing – original draft, Writing – review & editing. **Antonio Manresa-Manresa**: Methodology. **Enrique Rodríguez-Cañas**: Methodology. **María Fuentes- Baile**: Methodology. **Pilar García-Morales**: Writing – review & editing. **Ricardo Mallavia**: Validation, Formal analysis of data presented in this article. **Miguel Saceda**: Writing – review & editing. Camino de Juan Romero: Conceptualization, Funding acquisition, Supervision, Project administration, Validation, Formal analysis of data presented in this article, Writing – original draft, Writing – review & editing. All authors have read and agreed to the published version of the manuscript.

Conflict of Interest Statement

The authors declare that the research was conducted in the absence of any commercial or financial relationships that could be construed as a potential conflict of interest.

Data Availability

Data will be made available on request.

Acknowledgments

The authors thank Ignacio Pachón for assistance with cell culture and Enrique Yuste for the HPLC experiments. We thank Reyes Mateo for sharing reagents. We also thank Maria Irene De La Encarnación Boronat for the English editing of the manuscript.

Appendix A. Supporting information

Supplementary data associated with this article can be found in the online version at doi:10.1016/j.biopha.2023.114657.

References

[1] K.D. Miller, R.L. Siegel, C.C. Lin, A.B. Mariotto, J.L. Kramer, J.H. Rowland, K. D. Stein, R. Alteri, A. Jemal, Cancer treatment and survivorship statistics, 2016, CA Cancer J. Clin. 66 (2016) 271–289, https://doi.org/10.3322/CAAC.21349.

[2] H. Sung, J. Ferlay, R.L. Siegel, M. Laversanne, I. Soerjomataram, A. Jemal, F. Bray, Global cancer statistics 2020: GLOBOCAN estimates of incidence and mortality worldwide for 36 cancers in 185 countries, CA Cancer J. Clin. 71 (2021) 209–249, https://doi.org/10.3322/CAAC.21660.

[3] A. Adamska, A. Domenichini, M. Falasca, Pancreatic ductal adenocarcinoma: current and evolving therapies, Int. J. Mol. Sci. (2017) *18*, https://doi.org/10.3390/IJMS18071338.

[4] J.L. Abbruzzese, Adjuvant therapy for surgically resected pancreatic adenocarcinoma, JAMA 299 (2008) 1066–1067, https://doi.org/10.1001/JAMA.299.9.1066.

[5] C. Fang, K. Wang, Z.R. Stephen, Q. Mu, F.M. Kievit, D.T. Chiu, O.W. Press, M. Zhang, Temozolomide nanoparticles for targeted glioblastoma therapy, ACS Appl. Mater. Interfaces 7 (2015) 6682, https://doi.org/10.1021/AM5092165.

[6] A. Gronchi, A.B. Miah, A.P. Dei Tos, N. Abecassis, J. Bajpai, S. Bauer, R. Biagini, S. Bielack, J.Y. Blay, S. Bolle, et al., Soft tissue and visceral sarcomas: ESMO-EURACAN-GENTURIS clinical practice guidelines for diagnosis, treatment and follow-up, Ann. Oncol. Off. J. Eur. Soc. Med. Oncol. 32 (2021) 1348–1365, https://doi.org/10.1016/J.ANNONC.2021.07.006.

[7] P.G. Casali, S. Bielack, N. Abecassis, H.T. Aro, S. Bauer, R. Biagini, S. Bonvalot, I. Boukovinas, J.V.M.G. Bovee, B. Brennan, et al., Bone sarcomas: ESMO-PaedCan-EURACAN clinical practice guidelines for diagnosis, treatment and follow-up, Ann. Oncol. 29 (2018) iv79–iv95, https://doi.org/10.1093/ANNONC/MDY310.

[8] L.B. Nabors, J. Portnow, M. Ahluwalia, J. Baehring, H. Brem, S. Brem, N. Butowski, J.L. Campian, S.W. Clark, A.J. Fabiano, et al., Central nervous system cancers, version 3.2020, NCCN clinical practice guidelines in oncology, J. Natl. Compr. Canc. Netw. 18 (2020) 1537–1570, https://doi.org/10.6004/JNCCN.2020.0052.

[9] M. von Mehren, J.M. Kane, M.M. Bui, E. Choy, M. Connelly, S. Dry, K.N. Ganjoo, S. George, R.J. Gonzalez, M.J. Heslin, et al., NCCN guidelines insights: soft tissue sarcoma, Version 1.2021, J. Natl. Compr. Cancer Netw. 18 (2020) 1605–1612, https://doi.org/10.6004/JNCCN.2020.0058.

[10] S.M. Swetter, J.A. Thompson, M.R. Albertini, C.A. Barker, J. Baumgartner, G. Boland, B. Chmielowski, D. DiMaio, A. Durham, R.C. Fields, et al., NCCN Guidelines® insights: melanoma: cutaneous, version 2.2021, J. Natl. Compr. Cancer Netw. 19 (2021) 364–376, https://doi.org/10.6004/JNCCN.2021.0018.

[11] M. Pavel, K. Öberg, M. Falconi, E.P. Krenning, A. Sundin, A. Perren, A. Berruti, Gastroenteropancreatic neuroendocrine neoplasms: ESMO clinical practice guidelines for diagnosis, treatment and follow-up, Ann. Oncol. 31 (2020) 844–860, https://doi.org/10.1016/J.ANNONC.2020.03.304.

[12] R. Stupp, M. Brada, M.J. van den Bent, J.C. Tonn, G. Pentheroudakis, High-grade glioma: ESMO clinical practice guidelines for diagnosis, treatment and follow-up, Ann. Oncol. 25 (2014) iii93–iii101, https://doi.org/10.1093/ANNONC/MDU050.

[13] M.J. Moore, R. Feld, D. Hedley, A. Oza, L.L. Siu, A phase II study of temozolomide in advanced untreated pancreatic cancer, Invest. N. Drugs 16 (1998) 77–79, https://doi.org/10.1023/A:1006043332368.

[14] S. Ostermann, C. Csajka, T. Buclin, S. Leyvraz, F. Lejeune, L.A. Decosterd, R. Stupp, Plasma and cerebrospinal fluid population pharmacokinetics of temozolomide in malignant glioma patients, Clin. Cancer Res. 10 (2004) 3728–3736, https://doi.org/10.1158/1078-0432.CCR-03-0807.

[15] S. Sengupta, J. Marrinan, C. Frishman, P. Sampath, Impact of temozolomide on immune response during malignant glioma chemotherapy, Clin. Dev. Immunol. 2012 (2012), 831090, https://doi.org/10.1155/2012/831090.

[16] M.C. Chamberlain, Temozolomide: therapeutic limitations in the treatment of adult high-grade gliomas, Expert Rev. Neurother. 10 (2014) 1537–1544, https://doi.org/10.1586/ERN.10.32.

[17] V.A. Trinh, S.P. Patel, W.-J. Hwu, The safety of temozolomide in the treatment of malignancies, Expert Opin. Drug Saf. 8 (2009) 493–499, https://doi.org/10.1517/14740330902918281.

[18] E. Chan-Penebre, K.G. Kuplast, C.R. Majer, P.A. Boriack-Sjodin, T.J. Wigle, L. D. Johnston, N. Rioux, M.J. Munchhof, L. Jin, S.L. Jacques, et al., A selective

inhibitor of PRMT5 with in vivo and in vitro potency in MCL models, Nat. Chem. Biol. 11 (2015) 432–437, https://doi.org/10.1038/nchembio.1810.

[19] N. Stopa, J.E. Krebs, D. Shechter, The PRMT5 arginine methyltransferase: many roles in development, cancer and beyond, Cell. Mol. life Sci. 72 (2015) 2059, https://doi.org/10.1007/S00018-015-1847-9.

[20] Y. Wang, W. Hu, Y. Yuan, Protein arginine methyltransferase 5 (PRMT5) as an anticancer target and its inhibitor discovery, J. Med. Chem. 61 (2018) 9429–9441, https://doi.org/10.1021/ACS.JMEDCHEM.8B00598/ASSET/IMAGES/LARGE/JM-2018-00598Z_0009.JPEG.

[21] M. Vinet, S. Suresh, V. Maire, C. Monchecourt, F. Némati, L. Lesage, F. Pierre, M. Ye, A. Lescure, A. Brisson, et al., Protein arginine methyltransferase 5: a novel therapeutic target for triple-negative breast cancers, Cancer Med 8 (2019) 2428, https://doi.org/10.1002/CAM4.2114.

[22] A. Singh, C. Fedele, H. Lu, M.T. Nevalainen, J.H. Keen, L.R. Languino, Exosome-mediated transfer of Avβ3 integrin from tumorigenic to nontumorigenic cells promotes a migratory phenotype, Mol. Cancer Res. 14 (2016) 1136–1146, https://doi.org/10.1158/1541-7786.MCR-16-0058.

[23] M. Colombo, G. Raposo, C. Théry, Biogenesis, secretion, and intercellular interactions of exosomes and other extracellular vesicles, Annu. Rev. Cell Dev. Biol. 30 (2014) 255–289, https://doi.org/10.1146/ANNUREV-CELLBIO-101512-122326.

[24] X. Wang, W. Zhong, J. Bu, Y. Li, R. Li, R. Nie, C. Xiao, K. Ma, X. Huang, Y. Li, Exosomal protein CD82 as a diagnostic biomarker for precision medicine for breast cancer, Mol. Carcinog. 58 (2019) 674–685, https://doi.org/10.1002/mc.22960.

[25] S. Araujo-Abad, M. Saceda, C. de Juan Romero, Biomedical application of small extracellular vesicles in cancer treatment, Adv. Drug Deliv. Rev. 182 (2022), 114117, https://doi.org/10.1016/J.ADDR.2022.114117.

[26] L. Qiao, S. Hu, K. Huang, T. Su, Z. Li, A. Vandergriff, J. Cores, P.U. Dinh, T. Allen, D. Shen, et al., Tumor cell-derived exosomes home to their cells of origin and can be used as trojan horses to deliver cancer drugs, Theranostics 10 (2020) 3474–3487, https://doi.org/10.7150/thno.39434.

[27] E.V. Batrakova, M.S. Kim, Using exosomes, naturally-equipped nanocarriers, for drug delivery, J. Control. Release 219 (2015) 396–405, https://doi.org/10.1016/j.jconrel.2015.07.030.

[28] Y. Tian, S. Li, J. Song, T. Ji, M. Zhu, G.J. Anderson, J. Wei, G. Nie, A doxorubicin delivery platform using engineered natural membrane vesicle exosomes for targeted tumor therapy, Biomaterials 35 (2014) 2383–2390, https://doi.org/10.1016/J.BIOMATERIALS.2013.11.083.

[29] L. Nam, C. Coll, L.C.S. Erthal, C. de la Torre, D. Serrano, R. Martínez-Máñez, M. J. Santos-Martínez, E. Ruiz-Hernández, Drug delivery nanosystems for the localized treatment of glioblastoma multiforme, Mater. (Basel) (2018) *11*, https://doi.org/10.3390/MA11050779.

[30] Bazeed, A.Y.; Day, C.M.; Garg, S. Pancreatic Cancer: Challenges and Opportunities in Locoregional Therapies. Cancers 2022, Vol. 14, Page 4257 2022, 14, 4257, doi: 10.3390/CANCERS14174257.

[31] M. Fuentes-Baile, D. Bello-Gil, E. Pérez-Valenciano, J.M. Sanz, P. García-Morales, B. Maestro, M.P. Ventero, C. Alenda, V.M. Barberá, M. Saceda, CLyta-DAAO, free and immobilized in magnetic nanoparticles, induces cell death in human cancer cells, Biomolecules 10 (2020) 222, https://doi.org/10.3390/biom10020222.

[32] M.P. Ventero, M. Fuentes-Baile, C. Quereda, E. Perez-Valeciano, C. Alenda, P. Garcia-Morales, D. Esposito, P. Dorado, V.M. Barbera, M. Saceda, Radiotherapy resistance acquisition in glioblastoma. Role of SOCS1 and SOCS3, PLoS One 14 (2019), e0212581, https://doi.org/10.1371/journal.pone.0212581.

[33] J.L. Neira, S. Araujo-Abad, A. Cámara-Artigas, B. Rizzuti, O. Abian, A.M. Giudici, A. Velazquez-Campoy, C. de Juan Romero, Biochemical and biophysical characterization of PADI4 supports its involvement in cancer, Arch. Biochem. Biophys. 717 (2022), 109125, https://doi.org/10.1016/J.ABB.2022.109125.

[34] D.L. Dexter, G.M. Matook, P.A. Meitner, H.A. Bogaars, G.A. Jolly, M.D. Turner, P. Calabresi, Establishment and characterization of two human pancreatic cancer cell lines tumorigenic in athymic mice, Cancer Res. 42 (1982) 2705–2714.

[35] M. Fuentes-Baile, M.P. Ventero, J.A. Encinar, P. García-Morales, M. Poveda-Deltell, E. Pérez-Valenciano, V.M. Barberá, J. Gallego-Plazas, Á. Rodríguez-Lescure, J. Martín-Nieto, et al., Differential effects of IGF-1R small molecule tyrosine kinase inhibitors BMS-754807 and OSI-906 on human cancer cell lines, Cancers (Basel) 12 (2020) 1–18, https://doi.org/10.3390/cancers12123717.

[36] M. Fuentes-Baile, E. Pérez-Valenciano, P. García-Morales, C. Romero, J. de, D. Bello-Gil, V.M. Barberá, Á. Rodríguez-Lescure, J.M. Sanz, C. Alenda, M. Saceda, Clyta-daao chimeric enzyme bound to magnetic nanoparticles. A new therapeutical approach for cancer patients? Int. J. Mol. Sci. 22 (2021) 1–24, https://doi.org/10.3390/ijms22031477.

[37] M. Fuentes-baile, P. García-morales, E. Pérez-valenciano, M.P. Ventero, J.M. Sanz, C. Romero, J. de, V.M. Barberá, C. Alenda, M. Saceda, Cell death mechanisms induced by CLytA-DAAO chimeric enzyme in human tumor cell lines, Int. J. Mol. Sci. 21 (2020) 1–25, https://doi.org/10.3390/ijms21228522.

[38] Araujo-Abad, S.; Manresa-Manresa, A.; Rodríguez-Cañas, E.; Fuentes-Baile, M.; García-Morales, P.; Mallavia, R.; Saceda, M.; De, C.; Romero, J. Glioblastoma-Derived Small Extracellular Vesicles: Nanoparticles for Glioma Treatment. Int. J. Mol. Sci. 2023, Vol. 24, Page 5910 2023, 24, 5910, doi:10.3390/IJMS24065910.

[39] Y. Zhang, Y. Liu, H. Liu, W.H. Tang, Exosomes: biogenesis, biologic function and clinical potential, Cell Biosci. 9 (2019) 1–18, https://doi.org/10.1186/S13578-019-0282-2.

[40] V. Sokolova, A.K. Ludwig, S. Hornung, O. Rotan, P.A. Horn, M. Epple, B. Giebel, Characterisation of exosomes derived from human cells by nanoparticle tracking analysis and scanning electron microscopy, Colloids Surf. B Biointerfaces 87 (2011) 146–150, https://doi.org/10.1016/J.COLSURFB.2011.05.013.

[41] P. Sarantis, E. Koustas, A. Papadimitropoulou, A.G. Papavassiliou, M. V. Karamouzis, Pancreatic ductal adenocarcinoma: treatment hurdles, tumor microenvironment and immunotherapy, World J. Gastrointest. Oncol. 12 (2020) 173–181, https://doi.org/10.4251/WJGO.V12.I2.173.

[42] D.R. Principe, P.W. Underwood, M. Korc, J.G. Trevino, H.G. Munshi, A. Rana, The current treatment paradigm for pancreatic ductal adenocarcinoma and barriers to therapeutic efficacy, Front. Oncol. 11 (2021) 2773, https://doi.org/10.3389/FONC.2021.688377/BIBTEX.

[43] E.S. Casper, M.R. Green, D.P. Kelsen, R.T. Heelan, T.D. Brown, C.D. Flombaum, B. Trochanowski, P.G. Tarassoff, Phase II trial of gemcitabine (2,2`-difluorodeoxycytidine) in patients with adenocarcinoma of the pancreas, Invest. N. Drugs 12 (1994) 29–34, https://doi.org/10.1007/BF00873232.

[44] J. Carmichael, U. Fink, R.C.G. Russell, M.F. Spittle, A.L. Harris, G. Spiessi, J. Blatter, Phase II study of gemcitabine in patients with advanced pancreatic cancer, Br. J. Cancer 73 (1996) 101–105, https://doi.org/10.1038/BJC.1996.18.

[45] M. Moore, Activity of gemcitabine in patients with advanced pancreatic carcinoma a review BACKGROUND. In early phase I1 trials in advanced pancreatic cancer, Gemcitabine. Cancer 78 (1996) 633–638, https://doi.org/10.1002/(SICI)1097-0142(19960801)78:3<633::AID-CNCR44>3.0.CO;2-X.

[46] J. Robertson, R. Barr, L.N. Shulman, G.B. Forte, N. Magrini, Essential medicines for cancer: WHO recommendations and national priorities, Bull. World Health Organ 94 (2016) 742, https://doi.org/10.2471/BLT.15.163998.

[47] X. Wei, J. Yang, S.J. Adair, H. Ozturk, C. Kuscu, K.Y. Lee, W.J. Kane, P.E. O'Hara, D. Liu, Y.M. Demirlenk, et al., Targeted CRISPR screening identifies PRMT5 as synthetic lethality combinatorial target with gemcitabine in pancreatic cancer cells, Proc. Natl. Acad. Sci. U. S. A. 117 (2020) 28068–28079, https://doi.org/10.1073/PNAS.2009899117/-/DCSUPPLEMENTAL.

[48] C.J. Braun, M. Stanciu, P.L. Boutz, J.C. Patterson, D. Calligaris, F. Higuchi, R. Neupane, S. Fenoglio, D.P. Cahill, H. Wakimoto, et al., Coordinated splicing of regulatory detained introns within oncogenic transcripts creates an exploitable vulnerability in malignant glioma, Cancer Cell 32 (2017) 411–426, https://doi.org/10.1016/J.CCELL.2017.08.018, e11.

[49] X. Liu, J.Z. He, L. Mao, Y. Zhang, W.W. Cui, S. Duan, A. Jiang, Y. Gao, Y. Sang, G. Huang, EPZ015666, a selective protein arginine methyltransferase 5 (PRMT5) inhibitor with an antitumour effect in retinoblastoma, Exp. Eye Res. 202 (2021), 108286, https://doi.org/10.1016/J.EXER.2020.108286.

[50] X.-M. Xi, S.-J. Xia, R. Lu, Drug loading techniques for exosome-based drug delivery systems, Pharmazie 76 (2021) 61–67, https://doi.org/10.1691/ph.2021.0128.

[51] J.Y. Wu, Y.J. Li, X. Hu, Bin, S. Huang, D.X. Xiang, Preservation of small extracellular vesicles for functional analysis and therapeutic applications: a comparative evaluation of storage conditions, Drug Deliv. 28 (2021) 162–170, https://doi.org/10.1080/10717544.2020.1869866/SUPPL_FILE/IDRD_A_1869866_SM9282.DOCX.

[52] R.L. Siegel, K.D. Miller, A. Jemal, Cancer Statistics, 2016, CA Cancer J. Clin. 66 (2016) 7–30, https://doi.org/10.3322/CAAC.21332.

[53] X.Q. Li, J.T. Liu, L.L. Fan, Y. Liu, L. Cheng, F. Wang, H.Q. Yu, J. Gao, W. Wei, H. Wang, et al., Exosomes derived from gefitinib-treated EGFR-mutant lung cancer cells alter cisplatin sensitivity via up-regulating autophagy, Oncotarget 7 (2016) 24585, https://doi.org/10.18632/ONCOTARGET.8358.

[54] Howlader, N.; Noone, A.; Krapcho, M. SEER Cancer Statistics Review (CSR) 1975–2017. National Cancer Institute Available online: https://seer.cancer.gov/archive/csr/1975_2017/ (accessed on 30 September 2022).

[55] National Cancer Institute Surveillance, Epidemiology, and End Results (SEER) Program Available online: https://seer.cancer.gov/statfacts/html/pancreas.html (accessed on 30 September 2022).

[56] T. Conroy, P. Hammel, M. Hebbar, M. Ben Abdelghani, A.C. Wei, J.-L. Raoul, L. Choné, E. Francois, P. Artru, J.J. Biagi, et al., FOLFIRINOX or gemcitabine as adjuvant therapy for pancreatic cancer, N. Engl. J. Med. 379 (2018) 2395–2406, https://doi.org/10.1056/NEJMOA1809775/SUPPL_FILE/NEJMOA1809775_DATA-SHARING.PDF.

[57] J.P. Neoptolemos, D.D. Stocken, H. Friess, C. Bassi, J.A. Dunn, H. Hickey, H. Beger, L. Fernandez-Cruz, C. Dervenis, F. Lacaine, et al., A randomized trial of chemoradiotherapy and chemotherapy after resection of pancreatic cancer, N. Engl. J. Med. 350 (2004) 1200–1210, https://doi.org/10.1056/NEJMOA032295.

[58] A. Laviano, M.M. Meguid, A. Inui, M. Muscaritoli, F. Rossi-Fanelli, Therapy insight: cancer anorexia-cachexia syndrome–when all you can eat is yourself, Nat. Clin. Pract. Oncol. 2 (2005) 158–165, https://doi.org/10.1038/NCPONC0112.

[59] A.J. Grossberg, L.C. Chu, C.R. Deig, E.K. Fishman, W.L. Hwang, A. Maitra, D. L. Marks, A. Mehta, N. Nabavizadeh, D.M. Simeone, et al., Multidisciplinary standards of care and recent progress in pancreatic ductal adenocarcinoma, Ca. Cancer J. Clin. 70 (2020) 375, https://doi.org/10.3322/CAAC.21626.

[60] A. Babic, M.H. Rosenthal, W.R. Bamlet, N. Takahashi, M. Sugimoto, L.V. Danai, V. Morales-Oyarvide, N. Khalaf, R.F. Dunne, L.K. Brais, et al., Post diagnosis loss of skeletal muscle, but not adipose tissue, is associated with shorter survival of patients with advanced pancreatic cancer, Cancer Epidemiol. Biomark. Prev. 28 (2019) 2062, https://doi.org/10.1158/1055-9965.EPI-19-0370.

[61] J.K. Kays, S. Shahda, M. Stanley, T.M. Bell, B.H. O'Neill, M.D. Kohli, M.E. Couch, L. G. Koniaris, T.A. Zimmers, Three cachexia phenotypes and the impact of fat-only loss on survival in FOLFIRINOX therapy for pancreatic cancer, J. Cachex. Sarcopenia Muscle 9 (2018) 673, https://doi.org/10.1002/JCSM.12307.

[62] J. Bachmann, M. Heiligensetzer, H. Krakowski-Roosen, M.W. Büchler, H. Friess, M. E. Martignoni, Cachexia worsens prognosis in patients with resectable pancreatic cancer, J. Gastrointest. Surg. 12 (2008) 1193–1201, https://doi.org/10.1007/S11605-008-0505-Z/TABLES/6.

[63] A. Hendifar, A. Osipov, J. Khanuja, N. Nissen, J. Naziri, W. Yang, Q. Li, R. Tuli, Influence of body mass index and albumin on perioperative morbidity and clinical outcomes in resected pancreatic adenocarcinoma, PLoS One 11 (2016), 152172, https://doi.org/10.1371/JOURNAL.PONE.0152172.

[64] A. Görgens, G. Corso, D.W. Hagey, R. Jawad Wiklander, M.O. Gustafsson, U. Felldin, Y. Lee, R.B. Bostancioglu, H. Sork, X. Liang, et al., Identification of storage conditions stabilizing extracellular vesicles preparations, J. Extracell. Vesicles 11 (2022), e12238, https://doi.org/10.1002/JEV2.12238.

[65] A. Sivanantham, Y. Jin, Impact of storage conditions on EV integrity/surface markers and cargos, Life 12 (2022) 697, https://doi.org/10.3390/LIFE12050697.

[66] Y. Zhang, J. Bi, J. Huang, Y. Tang, S. Du, P. Li, Exosome: a review of its classification, isolation techniques, storage, diagnostic and targeted therapy applications, Int. J. Nanomed. 15 (2020) 6917, https://doi.org/10.2147/IJN.S264498.

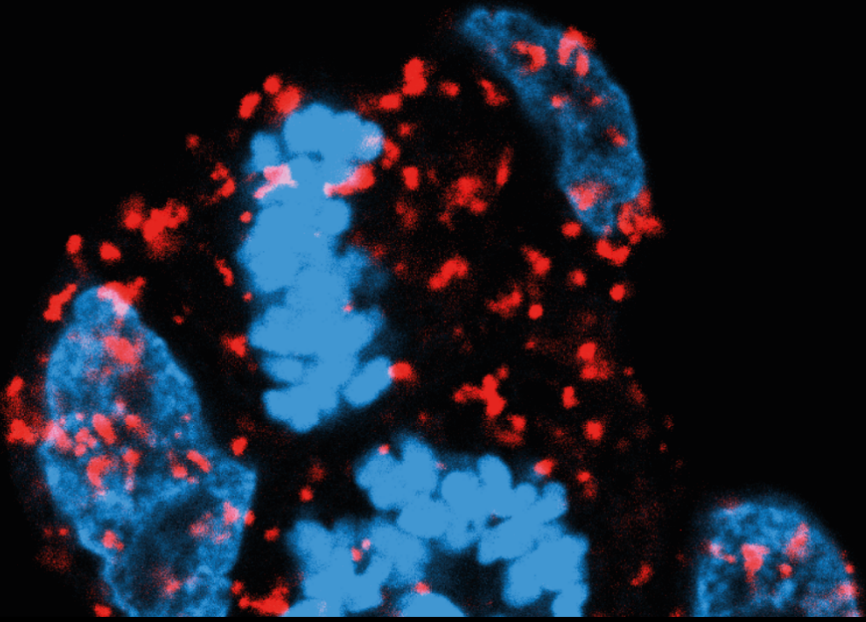

CHAPTER 4

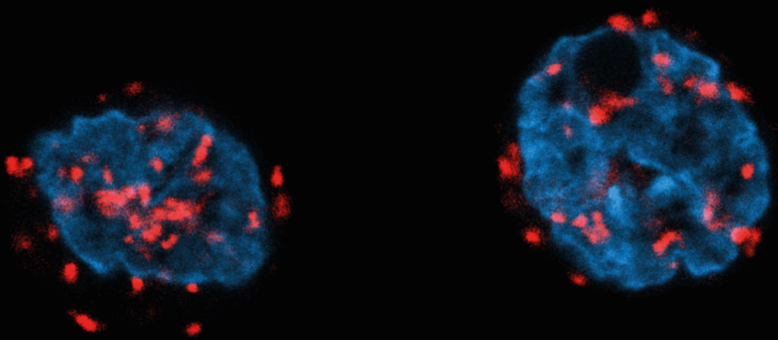

4.4 Chapter 4. Biochemical and biophysical characterization of PADI4 supports its involvement in cancer

Summary of the results

PADI4, also known as protein L-arginine iminohydrolase 4, is a member of the protein arginine deiminase family of Ca^{2+}-dependent enzymes that catalyzes the conversion of arginine to citrulline, well known as citrullination. PADI4 is present in macrophages, monocytes, granulocytes, and a variety of adenocarcinomas. In this manuscript, we focused on how its expression is altered in cancer cells [178] .

To confirm the expression and localization of PADI4 in different cell lines, including GBM (GB-39), PDAC (RWP-1), and colorectal cancer (HT-29), WB and IF assays were performed. GB-39 exhibited higher expression of PADI4 than HT-29, and RWP-1 showed the lowest expression of PADI4 among the three cell lines. Besides, p53 expression was only detected in HT-29 cells and it was absent in GB-39 and RWP-1 cells. Then, the IF for PADI4 was mainly detected in the nucleus of HT-29 cells, GB-39 showed both nuclear and cytoplasmic expression, and it was mostly cytoplasmic and diffuse in RWP-1. These results are consistent with its role as a chromatin modifier and suggest that PADI4 plays a major role in tumorigenesis by upregulating p53 expression in certain cancer cell lines [178].

To study the structure and conformational preferences of PADI4, we used several biophysical techniques, namely, fluorescence, far-ultraviolet circular dichroism (far-uV CD) spectroscopy, difference scanning calorimetry (DSC), and DLS [178,208]. In agreement with its function in histones, *in silico* experiments showed that the structure of PADI4 is strongly pH-dependent, with a narrow pH range (6.5-8.0), where it acquires a native structure. Fluorescence and CD studies in the presence of the Ca^{2+} indicated that it did not affect the protein's quaternary structure, and there were only changes around some of the tryptophans of the protein, as shown by the X-ray structure of the protein. Folding studies in the presence of the denaturant guanidinium chloride or using heat in DSC experiments indicated the presence of several partially folded species.

Overall, this manuscript provides valuable data on the biochemical and biophysical properties of PADI4 and its molecular mechanisms, which may contribute to the understanding of its role in cancer and the development of new cancer therapies. Furthermore, it sets the basis to understand the conformational stability of PADI4 to be used in future studies describing the binding to different molecular partners.

Archives of Biochemistry and Biophysics 717 (2022) 109125

Contents lists available at ScienceDirect

Archives of Biochemistry and Biophysics

journal homepage: www.elsevier.com/locate/yabbi

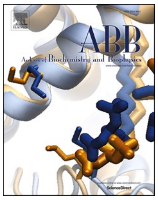

Biochemical and biophysical characterization of PADI4 supports its involvement in cancer

José L. Neira [a,b,*], Salomé Araujo-Abad [a,c], Ana Cámara-Artigas [d], Bruno Rizzuti [b,e], Olga Abian [b,f,g,h], Ana Marcela Giudici [a], Adrian Velazquez-Campoy [b,f,g,h], Camino de Juan Romero [a,i,**]

[a] IDIBE, Universidad Miguel Hernández, 03202, Elche, (Alicante), Spain
[b] Instituto de Biocomputación y Física de Sistemas Complejos, Universidad de Zaragoza, 50009, Zaragoza, Spain
[c] Centro de Biotecnología, Universidad Nacional de Loja, Avda. Pio Jaramillo Alvarado s/n, 110111, Loja, Ecuador
[d] Departamento de Química y Física, Research Center CIAIMBITAL, Universidad de Almería, CeiA3, 04120, Almería, Spain
[e] CNR-NANOTEC, SS Rende (CS), Department of Physics, University of Calabria, 87036, Rende, Italy
[f] Instituto de Investigación Sanitaria Aragón (IIS Aragón), Zaragoza, Spain
[g] Centro de Investigación Biomédica en Red en el Área Temática de Enfermedades Hepáticas y Digestivas (CIBERehd), Madrid, Spain
[h] Departamento de Bioquímica y Biología Molecular y Celular, Universidad de Zaragoza, 50009, Zaragoza, Spain
[i] Unidad de Investigación, Fundación para el Fomento de la Investigación Sanitaria y Biomédica de la Comunidad Valenciana (FISABIO), Hospital General Universitario de Elche, Camí de l'Almazara 11, 03203, Elche, (Alicante), Spain

ARTICLE INFO

Keywords:
Cancer
Circular dichroism
Calorimetry
Fluorescence
Protein stability
Western blot

ABSTRACT

PADI4 (protein-arginine deiminase, also known as protein L-arginine iminohydrolase) is one of the human isoforms of a family of Ca^{2+}-dependent proteins catalyzing the conversion of arginine to citrulline. Although the consequences of this process, known as citrullination, are not fully understood, all PADIs have been suggested to play essential roles in development and cell differentiation. They have been found in a wide range of cells and tissues and, among them, PADI4 is present in macrophages, monocytes, granulocytes and cancer cells. In this work, we focused on the biophysical features of PADI4 and, more importantly, how its expression was altered in cancer cells. Firstly, we described the different expression patterns of PADI4 in various cancer cell lines and its colocalization with the tumor-related protein p53. Secondly, we carried out a biophysical characterization of PADI4, by using a combination of biophysical techniques and *in silico* molecular dynamics simulations. Our biochemical results suggest the presence of several forms of PADI4 with different subcellular localizations, depending on the cancer cell line. Furthermore, PADI4 could have a major role in tumorigenesis by regulating p53 expression in certain cancer cell lines. On the other hand, the native structure of PADI4 was strongly pH-dependent both in the absence or presence of Ca^{2+}, and showed two pH-titrations at basic and acidic pH values. Thus, there was a narrow pH range (from 6.5 to 8.0) where the protein was dimeric and had a native structure, supporting its role in histones citrullination. Thermal denaturations were always two-state, but guanidinium-induced ones showed that PADI4 unfolded through at least one intermediate. Our simulation results suggest that the thermal melting of PADI4 structure was rather homogenous throughout its sequence. The overall results are discussed in terms of the functional role of PADI4 in the development of cancer.

1. Introduction

Citrullination, or deamination, is a post-translational modification (PTM) catalyzed by peptidyl-arginine deiminases also known as L-arginine iminohydrolases (EC 3.5.3.15, PADIs). Although the full consequences of the modification of the positive charge of the guanidino group of arginine to the neutral ureido group of citrulline are unknown, it is thought that such PTM induces local protein unfolding, impairing the formation of functional tertiary structures [1,2]. PADIs have key

---

* Corresponding author. IDIBE, Edificio Torregaitán, Universidad Miguel Hernández, Avda. del Ferrocarril s/n, 03202, Elche, (Alicante), Spain.
** Corresponding author. Unidad de Investigación, Fundación para el Fomento de la Investigación Sanitaria y Biomédica de la Comunidad Valenciana (FISABIO), Hospital General Universitario de Elche, Camí de l'Almazara 11, 03203, Elche, (Alicante), Spain.
E-mail addresses: jlneira@umh.es (J.L. Neira), m.juan@umh.es (C. de Juan Romero).

https://doi.org/10.1016/j.abb.2022.109125
Received 21 December 2021; Received in revised form 14 January 2022; Accepted 17 January 2022
Available online 23 January 2022

Abbreviations

ANS	1-anilino-8-naphtalene sulfonate
AUC	analytical ultracentrifugation
BSA	bovine serum albumin
CD	circular dichroism
COAD	colon adenocarcinoma
DAPI	4′, 6′ Diamidin-2-phenylindol
DLS	dynamic light scattering
DSC	differential scanning calorimetry
DSF	differential scanning fluorimetry
FBS	foetal bovine serum
GBM	glioblastoma
GdmCl	guanidinium hydrochloride
IPTG	isopropyl-β-D-1-tiogalactopyranoside
LB	Luria Bertani
MD	molecular dynamics
NLS	nuclear localization signal
PAAD	pancreatic adenocarcinoma
PADI	peptidyl-arginine deiminase
PBS	phosphate buffer solution
PDB	Protein Data Bank
SDS-PAGE	sodium dodecyl sulphate polyacrylamide gel electrophoresis
PTM	protein translational modification
RMSF	root mean square fluctuations
TCEP	Tris(2-carboxyethyl)phosphine
UV	ultraviolet;
WB	western blot

roles in nerve growth, onset of inflammation states, embryonic development, tissue aging, epithelial terminal differentiation, trauma apoptosis and transcriptional regulation of gene expression and regulation [3–10]. Furthermore, several human diseases such as Alzheimer's disease, rheumatoid arthritis, multiple sclerosis, psoriasis and different types of cancers are associated with the presence of PADIs and their citrullinated targets [9,11–13].

To date, five human genes encoding PADI proteins have been found, PADI1, PADI2, PADI3, PADI4 and PADI6 [14–20]. Each enzyme type has a tissue-specific expression, including the uterus and epidermis (PADI1); brain, secretory glands, inflammatory cells, and several cancer cell lines (PADI2); hair follicles and keratinocytes (PADI3); cancer cells, macrophages, monocytes and granulocytes (PADI4); and embryos and oocytes during embryonic development (PADI6), although this latter isoform is a pseudo-enzyme with no detectable catalytic activity. PADI3 displays the highest specificity for synthetic and natural substrates among all the PADIs, and it also modulates cell growth by affecting apoptosis-induced factor-mediated cell death [21,22]. Apoptosis enhanced through the mitochondrial pathway seems to be associated with an increase of enzyme activity of some PADI4 mutants [23]. Furthermore, PADI4 is involved in p53 gene expression, as well as the expression of other p53 target-genes [24,25]. Thus, PADI4 functions as a p53 co-repressor, and therefore, inhibitors of this enzyme could be considered potential treatments of cancer.

All PADIs are found in the cytoplasm, except PADI4, which has been detected in both the cytoplasm and the nucleus, and PADI2, which is also found in the nucleus under some stress conditions [2,26,27]. Moreover, all PADIs are Ca^{2+}-dependent enzymes, as PADI-driven citrullination requires supraphysiological levels of such cation [2,11]. In fact, PADIs are inactive at normal physiological conditions when Ca^{2+} concentration is low, and their activity is triggered by the influx of extracellular calcium, or its release from intracellular calcium stores [11].

PADI4 can convert Arg and monomethyl-Arg to citrulline, thereby regulating histone arginine-methylation catalyzed by members of the protein Arg methyltransferase family [8,10,28]. This PADI4-mediated demethylimination and citrullination of histones have been found to play a role in transcriptional repression of nuclear receptor target genes [3]. The involvement of PADI4 in several diseases, and the fact that is also found in the nucleus where it interacts with histones, have prompted us to study its presence in different cancer cells, and to elucidate its conformational features at different pH values, its stability in the absence and in the presence of Ca^{2+} in solution, and its unfolding properties.

This work revealed that PADI4 expression varied among different cancer cell lines, suggesting that PADI4 could have diverse functional roles depending on the tumor type. Its conformational features and stability were studied by using several biophysical and biochemical techniques, namely fluorescence and circular dichroism (CD) spectroscopic techniques, dynamic light scattering (DLS), differential scanning calorimetry (DSC), differential scanning fluorimetry (DSF) and molecular dynamics (MD) simulations. Our results showed that the protein exhibited a native structure in a narrow pH range (pH 6.5 to 8.0), where it was a dimer, either in the presence or in the absence of Ca^{2+}. Within that pH range, PADI4 had an apparent thermal denaturation midpoint of ~55 °C, as judged by thermal denaturations followed by intrinsic and extrinsic fluorescence, far-UV CD, DSF, and DSC; such value is not very high, and might facilitate protein-protein interactions with other partners by promoting PADI4 flexibility. The MD simulations results also indicated an overall flexibility of the protein that appeared to drive a rather homogeneous loss of structure throughout its sequence during the thermal denaturation. In the presence of Ca^{2+}, the shapes of the thermal and heat denaturation calorimetric curves were modified; thus, the interaction with Ca^{2+} can provide another layer for PADI4 function regulation. On the other hand, chemical unfolding occurred through at least an intermediate unfolding species, at variance with the thermal unfolding process.

2. Materials and methods

2.1. Materials

Kanamycin and isopropyl-β-D-1-tiogalactopyranoside (IPTG) were obtained from Apollo Scientific (Stockport, UK). Imidazole, Trizma base, 8-anilino-naphtalene-1-sulfonic acid ammonium salt (ANS) and His-Select HF nickel resin were from Sigma-Aldrich (Madrid, Spain). Triton X-100, TCEP (tris(2-carboxyethyl) phosphine) and protein marker (PAGEmark Tricolor) were from VWR (Barcelona, Spain). Ultrapure guanidinium hydrochloride (GdmCl) and urea were from Pierce (Madison, Wisconsin, USA). Amicon centrifugal devices with a cut-off molecular weight of 30 and 50 kDa were from Millipore (Barcelona, Spain). The rest of the materials used were of analytical grade. Water was deionized and purified on a Millipore system.

2.2. Protein expression and purification

The codon-optimized, N-terminal His-tagged PADI4 inserted in the vector pHTP1 (with kanamycin resistance) was synthesized and produced by NZytech (Lisbon, Portugal). Expression of PADI4 was carried out in *E. coli* BL21 (DE3) strain. The protein was expressed with a final amount of 0.8 mM of IPTG, when the absorbance at 600 nm of 1 L of LB medium reached a value in the range 0.8–1.0. After induction, cells were grown overnight at 30 °C. They were subsequently harvested by centrifugation at 5 °C for 15 min at 10,000 rpm in a JA-10 rotor (using a Beckman Coulter Avanti J26-XP Centrifuge). The cell pellet was resuspended in washing buffer (20 mM sodium phosphate (pH 8.0) with 300 mM NaCl, containing 20 mM imidazole) with an additional tablet of SIGMAFAST protease inhibitor cocktail EDTA-free, and DNase with a final concentration of 2 mg/L of LB medium (Sigma-Aldrich, Madrid, Spain). Cells were disrupted while cooled on ice by using a Branson sonicator for 10 periods (amplitude 25% of the maximum power) of 60 s, alternated with periods of 60 s on ice. The resulting lysate was centrifuged at 5 °C for 30 min at 17,000 rpm in a JA-20 rotor (Beckman Coulter, Barcelona, Spain) by using the same centrifuge as in the harvesting step. The rest of the purification protocol was the same previously described to purify other PADI isoforms [29–31], but in our case we used TCEP as a redox agent and the final concentration of glycerol was 5%. Briefly, after elution from the Ni-resin the protein was exchanged back (by using Amicon centrifugal devices with a cut-off of 30 K) to 50 mM Tris buffer (pH 7.5), 5 mM TCEP, 10 mM EDTA, 150 mM NaCl and 5% glycerol (Elution buffer). The resulting solution was loaded in a Hi-Trap Q HP column (5 mL) (GE Healthcare, Barcelona, Spain) and eluted with a gradient from the above buffer to the same buffer modified by adding 1 M NaCl in 1 h with a flow rate of 1 mL/min. The protein eluted in the range 20%–30% of 1 M NaCl. After that, the protein was also exchanged back to the Elution buffer and loaded in a gel filtration column Superdex 200 (HiLoad 16/60) (GE Healthcare), which had been previously equilibrated in the Elution buffer. Both columns were connected to an AKTA FPLC machine and the protein was detected by following the absorbance of the eluting solution at 280 nm. After expression and purification of several litres of media, we could also confirm that, after elution from the resin, by using solely an Amicon 50 K, and exchanging to Elution buffer, the protein was pure enough to carry out the biophysical studies. Protein was stored in the Elution buffer, after being flash frozen, at −20 °C until use. For the experiments in the presence of Ca^{2+}, the protein, once purified, was exchanged from the elution buffer containing 10 mM EDTA to one containing 10 mM Ca^{2+}. The protein maintained its His-tag all along the purification process, and was used as such in the experiments.

Protein concentration was determined from the absorbance at 280 nm of the 13 tyrosine and 10 tryptophan residues of each PADI4 monomer [32].

2.3. Cell lines

The human colon carcinoma (HT-29) and pancreatic adenocarcinoma (RWP-1) cell lines, were donated by Instituto Municipal de Investigaciones Médicas (IMIM, Barcelona, Spain) [33]. Isolation of primary human glioblastoma cell line (GB-39) was performed from surgical wash, as reported previously [34]. HT-29 and RWP1 cell lines were cultured in Dubelcco's Modified Eagle's Medium: High Glucose (DEMEM-HG) (Biowest, MO, USA) whereas glioblastoma (GBM) cells were cultured in Dubelcco's Modified Eagle's Medium: Nutrient Mixture F-12 (DMEM F-12) (Biowest, MO, USA). Both culture media, were supplemented with 10% (v/v) heat-inactivated foetal bovine serum (FBS) (Biowest, MO, USA) and 1% (v/v) penicillin/streptomycin mixture (Biowest, MO, USA). Cells were incubated at 37 °C in a humidified 5% CO_2 atmosphere.

2.4. Western Blot (WB)

All cell lysates were analysed for total protein concentration using the BCA protein assay kit (Pierce™, Thermo Scientific, Madrid, Spain); an amount of 20 μg of total protein was solubilized with loading buffer (4x) (2-mercaptoethanol + NuPage; (1:5)) and heated at 95 °C for 5 min. Then, they were separated by using 10% SDS-PAGE, and transferred to a nitrocellulose membrane (Bio-Rad Laboratories Inc, California, USA). Following standard protocols, membranes were incubated overnight at 4 °C with primary antibodies: anti-PADI4 (rabbit,1:2500, Invitrogen, Barcelona, Spain), anti-p53 (mouse,1:500, Calbiochem, Madrid, Spain) and anti-HSP90-B1 (rabbit,1:4000, CUSABIO, Houston, USA) followed by 1 h incubation at room temperature with ECL™ anti-mouse IgG and ECL™ anti-rabbit IgG, Horseradish Peroxidase linker (GE Healthcare, UK). The membranes were visualized with ECL™ Prime Western blotting detection reagent (Amersham™, Barcelona, Spain) in a ChemiDoc Bio-Rad (Bio-Rad) instrument.

2.5. Immunofluorescence

Cell cultures were fixed with formaldehyde for 20 min and then washed with phosphate buffer solution (PBS) (1x). Coverslips were blocked with 10% horse serum, 2% bovine serum albumin (BSA), 0.25% Triton in PBS for 1.5 h prior to staining. Primary antibodies anti-PADI4 (rabbit,1:300, Invitrogen) and anti-p53 (mouse,1:300, Calbiochem) were prepared in blocking solution and applied to samples to incubate overnight at 4 °C. Then, primary antibodies were washed with PBS (1x) and fluorescent secondary antibodies were applied (1:1000, Invitrogen) and incubated for 1.5 h at room temperature. In order to visualize the nuclei, samples were incubated for 5 min in 0.1 μg/mL DAPI (4′.6-Diamidin-2-phenylindol, Sigma). Coverslips were mounted in Vectashield H-1000 (Vector Laboratories, CA, USA) and analysed using Zeiss Axioscope 5 microscope with the LED light source Colibri 3.

2.6. Fluorescence

(a) *Steady-state fluorescence*

Fluorescence spectra were collected on a Cary Eclipse Varian spectrofluorometer (Agilent, CA, USA), interfaced with a Peltier unit. Unless it is stated otherwise, all experiments were carried out at 25 °C. Following the standard protocols used in our laboratories, the samples were prepared the day before and left overnight at 5 °C; before experiments, samples were left for 1 h at 25 °C. A 1-cm-pathlength quartz cell (Hellma, Kruibeke, Belgium) was used. Protein concentration was 1.5 μM, in protomer units. A control experiment to follow GdmCl-denaturation by measuring intrinsic fluorescence was carried out by using a final protein concentration of 10.5 μM, in protomer units. The pathlength of the cell was 1 cm.

For the pH-denaturation experiments either in the presence of Ca^{2+} (10 mM) or in its absence (10 mM EDTA), protein samples were excited at either 280 or 295 nm in the pH range from 2.0 to 12.0. Slit widths were 5 nm. The final buffer concentration was 50 mM in all cases containing 5% glycerol and 5 mM TCEP, and the corresponding salts and acids used were: pH 2.0–3.0, phosphoric acid; pH 3.0–4.0, formic acid; pH 4.0–5.5, acetic acid; pH 6.0–7.0, NaH_2PO_4; pH 7.5–9.0, Tris acid; pH 9.5–11.0, Na_2CO_3; pH 11.5–13.0, Na_3PO_4. Appropriate blank corrections were made in all spectra. The pH of each sample was measured after completion of experiments with an ultra-thin Aldrich (Madrid, Spain) electrode in a Radiometer (Copenhagen, Denmark) pH-meter.

Chemical-denaturations at pH 7.5 (in 50 mM Tris buffer, with 5% glycerol and 5 mM TCEP) either followed by intrinsic or ANS (see below) fluorescence, and far-UV CD experiments (see below) were carried out by dilution of the proper amount of a 7 M GdmCl stock solution. Experiments were carried out either in the presence of Ca^{2+} (10 mM, final concentration) or in its absence (10 mM EDTA, final concentration). Also, urea denaturations were followed at the same pH, but the stock solution of denaturant agent used to prepare the samples was 8 M. In all cases, spectra from blank solutions were subtracted from the corresponding spectra in the presence of the protein. The GdmCl or urea concentrations in the stock solutions were quantified by using refractive index measurements [35]. Both the chemical- and pH-denaturations were repeated at least three times with different samples. Variations by using the same voltage in the fluorescence photomultiplier from experiments repeated day to day were 2–5%.

(b) *Thermal-denaturations*

Experiments were performed at constant heating rates of 60 °C h^{-1} with an average time of 1 s. Thermal scans were collected at 315, 330 and 350 nm after excitation at either 280 or 295 nm, typically from 25 to 80 °C. The rest of the experimental set-up was the same described above. Thermal denaturations were irreversible; irreversibility was tested by acquiring steady-state spectra of thermally denatured proteins, and by comparing their shape and intensity with those of the spectra acquired before heating. The apparent thermal denaturation midpoint, T_m, was estimated from a two-state equilibrium equation taking into account the concentration-dependence of the unfolding (see below).

(c) *ANS binding*

The excitation wavelength was 370 nm, and emission was measured from 400 to 600 nm at 25 °C. Slit widths were 5 nm for both excitation and emission. ANS stock solution (10 mM) was prepared in water and diluted to yield a final concentration of 100 μM in each sample, with a final protein protomer concentration of 1.5 μM (both in the pH- or GdmCl-denaturation experiments at pH 7.5). The same set of buffers and their concentrations used in the steady-state intrinsic fluorescence experiments (see above) were utilized for the pH-denaturations followed by ANS. Experiments were carried out either in the presence of Ca^{2+} (10 mM, final concentration) or in its absence (10 mM EDTA, final concentration). Spectra from blank solutions were subtracted from the corresponding spectra. In the pH-denaturations, the pH of each sample was measured after completion of titration with an ultra-thin Aldrich electrode in a Radiometer pH-meter.

We also used ANS to follow thermal denaturations, as it can provide information on how the different solvent-exposed hydrophobic patches change their environment upon heating [36]. The experimental set-up in these denaturations was the same used for measuring the intrinsic fluorescence of the protein, except for the excitation (370 nm) and emission (480 nm) wavelengths. Thermal denaturations were always irreversible.

(d) *Differential scanning fluorimetry (DSF)*

Experiments were acquired in a Mx3005p real-time qPCR (Agilent, Madrid, Spain) using SYPRO Orange as an extrinsic fluorescence probe, and we measured its fluorescence intensity as a function of temperature. As the protein unfolds, SYPRO Orange binds to hydrophobic patches and its quantum yield increases, indirectly reporting about the protein unfolding process. We used 50 μL of total volume with PADI4 at a concentration of 4 μM (in protomer units) and a concentration of dye of 5 x, in 50 mM Tris buffer (pH 7.5), 5 mM TCEP and 5% glycerol. We are fully aware that the pK_a of Tris is temperature-dependent, but we have preferred to use this buffer as it is the one employed at the high protein concentrations of DSC experiments (see below). Furthermore, the use of phosphate buffer could lead to precipitation of calcium in the experiments in the presence of the cation. DSF provides a signal reflecting the global unfolding of the protein, but it may overlook some unfolding steps, if present; therefore, it is usually employed as a semi-quantitative technique, mainly aimed at identifying potential ligands for a given protein target [37].

The mathematical treatment of the experimental data may rely on a simple estimation of the unfolding temperature, T_m, through identification of the temperature for maximal slope of the fluorescence signal, or the calculation of the unfolded fraction, F_U, through a well-known normalization procedure:

$$F_U(T) = \frac{S(T) - S_N(T)}{S_U(T) - S_N(T)} \quad (1)$$

where $S(T)$ is the measured signal at any temperature T, and $S_N(T)$ and $S_U(T)$ are the intrinsic signals corresponding to the native and unfolded protein states, usually considered to be linear functions of the temperature. We have used Eq. (1) to normalize the experimental data obtained by DSF, and the analyses of the thermal denaturation curves were carried out by using the equations described below (Eq. (9)), taking into account the concentration-dependence of the unfolding. A further calculation allows the estimation of the unfolding enthalpy from the temperature derivative of the unfolded fraction at T_m:

$$\Delta H(T_m) = 4RT_m^2 \left(\frac{\partial F_U(T)}{\partial T} \right)_{T=T_m} \quad (2)$$

2.7. *Circular dichroism (CD)*

The steady-state CD spectra were collected on a Jasco J810 spectropolarimeter (Jasco, Tokyo, Japan) with a thermostated cell holder, and interfaced with a Peltier unit at 25 °C. The instrument was periodically calibrated with (+)-10-camphorsulphonic acid. A cell with a path length of 0.1 cm was used (Hellma, Kruibeke, Belgium). All spectra were corrected by subtracting the corresponding baseline. Concentration of PADI4 was the same used in the fluorescence experiments (1.5 μM, in protomer units).

(a) *Far-UV spectra*

Isothermal wavelength spectra at different pH values or GdmCl concentrations were acquired at a scan speed of 50 nm min^{-1} with a response time of 2 s, a band-width of 1 nm, and averaged over six scans. Both the chemical- and pH-denaturations were repeated at least three times with new samples. Buffer concentrations for the pH- and chemical-denaturation experiments were 50 mM, and the buffers (in the absence or presence of Ca^{2+}) were the same used in the fluorescence experiments (see above). Final glycerol concentration was 5% (v/v), and that of TCEP was 5 mM. In the pH-denaturations, the pH of each sample was measured after completion of titration with an ultra-thin Aldrich electrode in a Radiometer pH-meter. Variations from day to day of with the new prepared samples were less than 2%. The samples were prepared the day before and left overnight at 5 °C to allow for equilibration. Before starting the experiments, samples were left for 1 h at 25 °C.

(b) *Thermal-denaturations*

Experiments were performed at constant heating rates of 60 °C h^{-1} and a response time of 8 s. Thermal scans were collected by following the changes in ellipticity at 222 nm, typically from 25 to 70 °C. The rest of the experimental set-up was the same described in the steady-state experiments. No difference was observed between the scans aimed at testing a drift in the spectropolarimeter signal. Thermal denaturations were always irreversible, as shown by: (i) the comparison of spectra before and after the heating; and, (ii) the changes in the voltage of the instrument detector [38]. The apparent thermal denaturation midpoint, T_m, was estimated from a two-state equilibrium denaturation equation by taking into account the concentration-dependence of the unfolding equilibrium (see below).

(c) *Near-UV spectra*

Spectra of PADI4 either in the presence of Ca^{2+} (10 mM, final concentration) or in its absence (10 mM EDTA, final concentration) were acquired between 250 and 320 nm, in a 0.5-cm-pathlength cell at pH 7.5 (20 mM, Tris buffer, 5 mM TCEP, 150 mM NaCl and 5% glycerol) and

25 °C. The spectra were collected with a scan speed of 50 nm min^{-1} with a response time of 2 s, a band-width of 1 nm, and averaged over ten scans. The spectrum of the buffer solution was subtracted from that of the protein. Final protein concentration was 60 μM (in protomer units), under both conditions.

2.8. Differential scanning calorimetry (DSC)

The thermal stability of PADI4 was evaluated by DSC. The excess partial heat capacity of the protein in solution was measured as a function of temperature in an Auto-Cap-DSC (MicroCal, Malvern-Panalytical, Malvern, UK), using a constant heating rate of 60 °C h^{-1}. Experiments were done with PADI4 at 23.5 and 26.2 μM, in protomer units, in the absence and presence of Ca^{2+}, respectively, in 20 mM Tris buffer (pH 7.5), 5 mM TCEP, 150 mM NaCl and 5% glycerol. Buffer scans were performed until complete reproducibility was attained; the last measured buffer scan was subtracted from the protein scan. A model-free analysis provides an evaluation of the complexity of the observed unfolding pathway through the comparison of the calorimetric enthalpy (ΔH_{cal}, associated with the unfolding of the protein molecule) and the van't Hoff enthalpy (ΔH_{VH}, associated with the unfolding of the cooperative unit, defined as below, and the unfolding enthalpy corresponding to a two-state process). Whereas ΔH_{cal} is directly calculated as the area under the transition profile, ΔH_{VH} is calculated as follows:

$$\Delta H_{VH} = \frac{4RT_m^2 C_{P,max}}{\Delta H_{cal}} \tag{3}$$

where R is the ideal gas constant, T_{m} is the apparent unfolding temperature, and $C_{\text{P,max}}$ is the maximum value of the excess molar heat capacity. If $\Delta H_{\text{VH}} = \Delta H_{\text{cal}}$ (within experimental error), the cooperative unit coincides with the protein molecule (e.g., a protein domain) and the two-state model would be appropriate for the data analysis; if $\Delta H_{\text{VH}} < \Delta H_{\text{cal}}$, the cooperative unit is smaller than the protein molecule and the non-two-state model would be appropriate for the data analysis; and if $\Delta H_{\text{VH}} > \Delta H_{\text{cal}}$, the cooperative unit is larger than the protein molecule (i.e., the protein molecule self-associates into oligomers) and the dissociation-two-state model (e.g., oligomer unfolding coupled to dissociation into unfolded subunits) would be appropriate for the data analysis.

According to the two-state model (N ↔ U), the equilibrium unfolding process can be described by the following set of equations:

$$\begin{aligned} K(T) &= \frac{F_U(T)}{F_N(T)} = e^{(-\Delta G(T)/RT)} \\ F_U(T) &= \frac{K(T)}{1+K(T)} \\ \Delta G(T) &= \Delta H(T_m)\left(1-\frac{T}{T_m}\right) + \Delta C_P\left(T - T_m - T\ln\frac{T}{T_m}\right) \\ \Delta H(T) &= F_U \Delta H(T) \\ \Delta C_P(T) &= \frac{\partial \Delta H(T)}{\partial T} \end{aligned} \tag{4}$$

where K is the equilibrium unfolding constant; F_{U} and F_{N} are the fraction of unfolded and native protein molecules, respectively; ΔG is the unfolding Gibbs energy; ΔH is the unfolding enthalpy; ΔC_{P} is the unfolding heat capacity; $<\Delta H>$ is the excess average molar unfolding enthalpy; and $<\Delta C_{\text{P}}>$ is the excess average molar unfolding heat capacity (the observable provided by the calorimetric signal).

According to the dissociation-two-state model, particularized for a homodimeric protein (N_2 ↔ 2U), the equilibrium unfolding process can be described by the following set of equations:

$$\begin{aligned} K(T) &= P_T\frac{(F_U(T))^2}{F_{N_2}(T)} = e^{(-2\Delta G(T)/RT)} \\ F_U(T) &= \frac{-1+\sqrt{1+8P_T/K(T)}}{4P_T/K(T)} \\ \Delta G(T) &= \Delta H(T_0)\left(1-\frac{T}{T_0}\right) + \Delta C_P\left(T - T_0 - T\ln\frac{T}{T_0}\right) \\ \Delta H(T) &= F_U \Delta H(T) \\ \Delta C_P(T) &= \frac{\partial \Delta H(T)}{\partial T} \end{aligned} \tag{5}$$

where P_{T} is the total concentration of protein, and energy-related quantities have been defined per subunit. T_0 is the temperature at which the unfolding Gibbs energy is zero. In this case, *K(T)* is the dissociation constant for the protein dimer. Contrary to what happens to the two-state model, in the case of an oligomeric protein, T_0 is different from T_{m} (temperature for maximal heat capacity) and $T_{1/2}$ (temperature for half-denaturation, $F_{\text{U}} = 0.5$).

Non-linear regression data analysis of the experimental data using Origin 7.0 (OriginLab, Northampton, MA, USA) allowed the estimation of the thermal unfolding parameters, from which the stability profile (ΔG as a function of T) can be constructed. In order to evaluate different models and establish the (statistically) most appropriate, parametric tests (e.g., F-test) and non-parametric tests (e.g., Akaike and Bayesian Information Criteria) were applied and compared.

2.9. Dynamic light scattering (DLS)

DLS measurements were performed in a Zetasizer Nano instrument (Malvern Instrument Ltd, Malvern, UK) equipped with a 10-mW helium-neon laser (λ = 632.8 nm) and a thermoelectric temperature controller. All the experiments were performed at a fixed angle (Θ = 173°) at 25 °C and the results were analysed with the Zetasizer software V7.12 (Malvern Instrument Ltd, Malvern, UK). Before each measurement, protein samples were centrifuged for 30 min at 14,000 g and filtered through a 0.2 μm cut-off Millex filter to remove big aggregates and dust. Once in the cuvette, samples were sonicated for 1 min to remove bubbles. Measurements on each sample were performed 20 times with 10 runs of 30 s each. The Z-average size was obtained by fitting the autocorrelation function with the cumulants method. The hydrodynamic radius, R_{h}, of the protein in solution was calculated by applying the Stokes-Einstein equation:

$$D = \frac{kT}{(6\,\pi\eta R_h)} \tag{6}$$

where k is the Boltzmann constant, T is the temperature and η is the solution viscosity. Experiments in the presence of 10 mM Ca^{2+} were carried out at 12 and 45 μM, in protomer units. Experiments in the absence of the cation (10 mM EDTA) were carried out at 8 and 25 μM, in protomer units. The buffer conditions were: 20 mM Tris (pH 7.5), 5 mM TCEP, 150 mM NaCl and 5% glycerol.

2.10. Fitting of pH-, chemical- and thermal-denaturations, followed by spectroscopic probes

In the fluorescence experiments, to allow for a better comparison among the different probes used (either intrinsic or ANS fluorescence), and since we can obtain information over all the spectrum, we calculated the average energy, <λ>, which is defined as [39]:

$$<\lambda> = \frac{\sum_1^n\left(\frac{1}{\lambda_i}I_i\right)}{\sum_1^n(I_i)} \tag{7}$$

The titration points for the pH-denaturation experiments were fitted to the Henderson-Hasselbalch equation:

$$X = \left(X_a + X_b 10^{(pK_a - pH)}\right) / \left(1 + 10^{(pK_a - pH)}\right) \tag{8}$$

where X is the measured property ($<\lambda>$, the fluorescence intensity or the ellipticity at 222 nm) for a particular pH; X_a is the same property at low pH; X_b is the property at high pH; and pK_a is the titration midpoint of the pH-transition. When several transitions were observed, the different pK_a values were obtained by fitting each particular transition to Eq. (8), provided we had enough experimental data (at least >4 experimentally measured pH data points for the corresponding titration).

The change in the physical property, Y (the fluorescence intensity or the ellipticity at 222 or 230 nm), for the thermal denaturations, was fit to:

$$Y = \left(Y_N + Y_D e^{(-\Delta G/RT)}\right) / \left(1 + e^{(-\Delta G/RT)}\right) \tag{9}$$

where $Y_N = \alpha_N + \beta_N[T]$ and $Y_D = \alpha_D + \beta_D[T]$ are the baselines of the folded and unfolded states, respectively, for which a linear relationship with temperature is assumed; R is the gas constant; and T is the temperature in K.

Although the thermal denaturations, either followed by fluorescence (intrinsic, ANS or SYPRO Orange) or CD were irreversible, we obtained an apparent thermal denaturation midpoint, T_m, allowing us for a rough estimate of the stability of PADI4 at the different pH values, and for a comparison with the DSC data. The T_m can be obtained from the change in free energy, ΔG, given by [40–42]:

$$\Delta G(T) = \Delta H_m \left(1 - \frac{T}{T_m}\right) - \Delta C_p \left[(T_m - T) + Tln\left(\frac{T}{T_m}\right)\right] - RT\ \ln(2C_t) \tag{10}$$

where ΔH_m is the van't Hoff unfolding enthalpy; C_t is the total concentration of protein expressed in dimer equivalents; and ΔC_p is the heat capacity change of the folding reaction. The fact that both in the numerator and denominator of Eq. (9) appears the term $\Delta G(T)$ derived from Eq. (9) avoids to impose restrictions on the value of the ΔC_p used in the fitting. The term $-RT\ \ln(2C_t)$ comes from considering the dimeric nature of the protein (see Results) and it takes into account the concentration-dependence of the unfolding equilibria (both heat or chemical, see next paragraph) [40–42]; thus, we have assumed that the main species when thermal unfolding was carried out was a dimer.

For the GdmCl-denaturations (followed by intrinsic or ANS fluorescence and ellipticity at 222 nm) the same Eq. (9) was used, but in this case the value of the ΔG follows a linear relationship with respect to the denaturant concentration: $\Delta G = m$ ([GdmCl]$_{50\%}$ - [GdmCl]) - RTln(2C_t), where m-value is the slope of the sigmoidal transition; C_t is the total concentration of protein expressed in dimer equivalents; and [GdmCl]$_{50\%}$ is the concentration of GdmCl at the midpoint of the transition [43], and the spectroscopic properties of the native and unfolded species are given by: $Y_N = \alpha_N + \beta_N$[GdmCl] and $Y_D = \alpha_D + \beta_D$[GdmCl], respectively. Chemical denaturations were always irreversible, as indicated by refolding experiments.

Fittings to Eqs. (8)–(10) were carried out by using the general curve-fit option of KaleidaGraph (Abelbeck Software, PA, USA).

2.11. Molecular simulations

The structure of PADI4 was built from the PDB entry 3APN [31], and missing atoms in some loop regions were reconstructed by using the Modeller server [44]. Classical MD simulations of the protein in explicit solvent were performed by using the GROMACS software [45], with the AMBER ff99SB-ILDN force field [46] and the TIP3P water model [47]. The dimer was solvated in a box with a dodecahedron shape, maintaining a minimum distance of 1.5 nm from each edge, and 14 Na$^+$ counterions were added to obtain an overall neutral system charge. Simulations were carried out for 10 ns at room temperature (300 K, 27 °C), as well as at a higher value (450 K, 177 °C) to probe the early stages of the unfolding pathway through an accelerated sampling. Other details of the simulation conditions (including the modelling of electrostatic and van der Waals interactions, and the parameters used for the virtual thermostat and barostat), and of the simulation protocol (energy minimization, annealing, and equilibration) were as previously described [48,49].

Although MD runs can often be performed even at greater temperatures (T = 500 and beyond) [50], in this particular case this led to simulation crashes – which is not a rare occurrence, especially for very large protein systems. Thus, all-atom MD simulations at higher temperature could not be pursued further. Due to the excessive sampling required to probe more denatured protein states, the investigation was confined to the early steps of the unfolding, and we enhanced it by using a coarse-grained model implemented in the CABS-flex algorithm [51], available as a web server [52]. The starting structure of the dimer was the same used for MD simulations, with restraints assigned to residue pairs only when both possessed a well-defined secondary structure. In this case, we used a complete flexibility of the protein chain (assigning a null 'rigidity' parameter), and a dimensionless reduced temperature with a value (T = 2.0) twice larger than the default used to sample proteins in a crystal state to speed up the process [52].

3. Results

3.1. PADI4 expression in glioblastoma, pancreatic and colon cancer cells

It is known that PADI4 is expressed in a variety of adenocarcinomas, but absent in normal healthy tissues [53]. Moreover, it has been shown that plasma PADI4 levels in patients with malignancies decreased after tumour resection, suggesting that PADI4 circulating in the blood may be used for diagnostic of tumour tissues [54]. To address the prevalence of expression of PADI4 in cancer, protein levels were analysed and compared in a panel of tumour cell lines, that had never been tested before. We used pancreatic adenocarcinoma (PAAD) (RWP-1), colon adenocarcinoma (COAD) (HT-29) and glioblastoma (GBM) (GB-39) cell lines. This GBM cell line was obtained from a surgical wash from a patient that suffered multiforme GBM [34]. Western Blot analyses confirmed that the expression of PADI4 varied among the cancer cell lines. Out of the three lines examined, the PAAD one showed the least PADI4 expression (Fig. 1 A). Moreover, PADI4 expressions in COAD and GBM cell lines were of similar intensity, but with a different pattern (i.e. there were several bands in the GBM) consistent with the existence of alternatively spliced PADI4 transcripts [55].

Although most of PADI isoforms are cytoplasmatic, PADI4 has a nuclear localization signal (NLS) that allows it to enter the nucleus [2, 54]. PADI4 first description in hematopoietic human cells shows a clear nuclear localization, however it can be also found in the cytoplasm depending on the cell line [56]. To investigate the subcellular localization of PADI4 in the above-mentioned cancer cell lines, we performed immunocytochemistry with PADI4 antibody and analysed it by fluorescence microscopy. PADI4 has an interesting nuclear localization pattern, and nuclei of the cells are characteristically stained with anti-PADI4 antibody at the nuclear edge. This distinctive signals of anti-PADI4 are usually confined to narrow diffuse DAPI-staining regions located along segmented forms of the nucleus (Fig. 1 B). Interestingly, PADI4 showed a clear nuclear localization only in HT-29 cells. PADI4 in GBM showed both a nuclear and cytoplasmatic expression; and in RWP-1, PADI4 expression was mostly cytoplasmatic and diffuse (Fig. 1 B). On the basis of these observations, together with the WB data, we hypothesize the presence of several forms of PADI4 with different subcellular localizations, depending on the cancer cell line.

The tumour suppressor p53 plays a pivotal role in regulating the cell cycle progression and apoptosis in response to various genotoxic and nongenotoxic stresses [56]. The ability of p53 to function as a sequence-specific transcription factor is critical for its tumour suppressor function [57]. It has been shown that PADI4 interacts with p53 and is

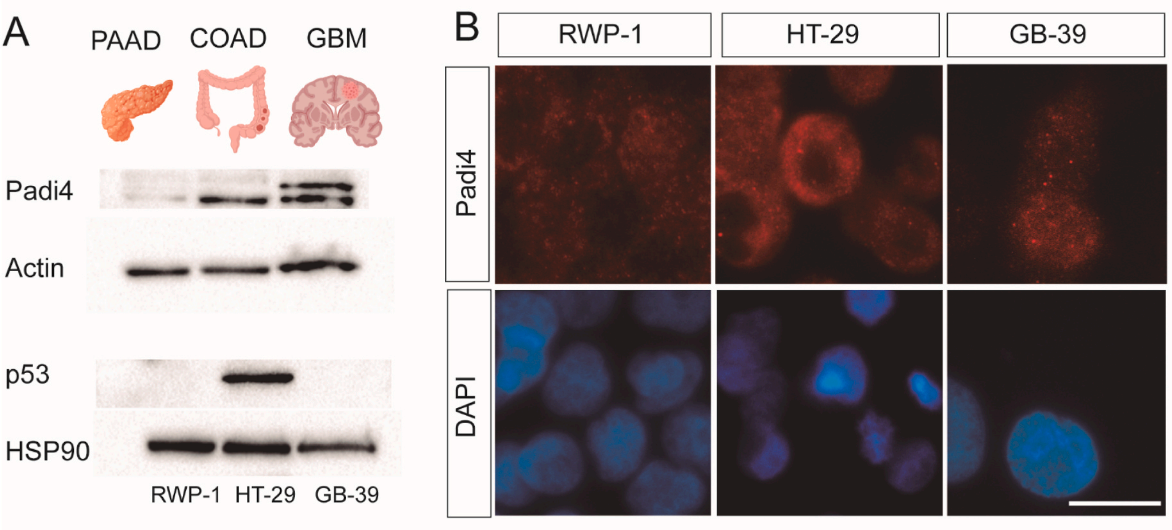

Fig. 1. PADI4 expression in cancer cells lines. (A) Western blot analysis of RWP-1, HT-29 and GB-39 cell lines for PADI4 and p53. (B) Immunocytochemistry of PADI4 (red) and DAPI (blue) in cancer cell lines. Scale bar: 20 μm. Experiments were repeated three times. (For interpretation of the references to color in this figure legend, the reader is referred to the Web version of this article.)

recruited by the p21 promoter to regulate histone arginine-methylation and citrullination to regulate gene expression [24]. Therefore, we investigated the relationship between PADI4 and p53 in the three cancer cell lines described above. We observed a large expression of p53 in HT-29, but not in the other cell lines (Fig. 1 B). Thus, based on two different lines of evidence: (i) HT-29 was the sole cell line with a clear nuclear localization of PADI4; and (ii) the distinct enzyme expression observed in the WB data, we suggest that PADI4 could have a major role in tumorigenesis by up-regulating p53 expression in certain types of cancer cell types.

3.2. *PADI4 acquired a native structure in a narrow pH range either in the absence or in the presence of Ca^{2+}*

To measure the conformational stability of PADI4, we firstly needed to determine in which pH range it had a native structure. To that end, we used several spectroscopic probes, namely intrinsic fluorescence, ANS fluorescence, and far- and near-UV CD. The use of this whole set of techniques gave us complementary information on different structural features of the polypeptide chain. We used intrinsic fluorescence to monitor the changes in the tertiary structure of PADI4, around its 13 tyrosines and 10 tryptophans. We used ANS fluorescence to follow the water accessibility of solvent-exposed hydrophobic patches and to detect the presence of partially folded species [58]. And finally, we carried out far-UV CD experiments to monitor changes in protein secondary structure, and near-UV CD to follow the changes in the asymmetry of the environment around aromatic residues at a determined pH.

3.3. *Fluorescence*

(1) *Steady-state intrinsic fluorescence and thermal denaturations*

The fluorescence emission spectrum of PADI4 showed a maximum around 338 nm at physiological pH in the absence of Ca^{2+} (Fig. S1 A). These results indicate that PADI4 fluorescence was dominated by the emission of the 10 tryptophan residues, some of which appeared, from the value of the maximum wavelength, to be partially solvent-exposed, as also shown in the X-ray structure deposited in the Protein Data Bank (PDB) as the entry 3APN [31]. A red-shift of the signal maximum in the presence of Ca^{2+} (towards 342 nm) was observed, as well as a decrease in the intensity (Fig. S1). The same changes were also observed by excitation at 295 nm, indicating that some tryptophan residues were located in the polypeptide regions involved in the binding of Ca^{2+}. This result suggests that the environment of at least some of the tryptophans and/or tyrosines were altered in the presence of Ca^{2+}, resulting in a more solvent-exposed species.

The value of $<\lambda>$ (measured either by excitation at 280 or 295 nm) in the presence of EDTA (10 mM) showed two transitions (Fig. 2 A): one appeared to end around pH 6.5, but we could not find its pK_a value due to the absence of an acidic baseline; and another one started at pH 8.0, which had a pK_a value larger than 10, but we could not assess its exact value as we could not determine a basic baseline. The same two transitions were observed by following the changes in intensity (Fig. 2 A), and a dumb-bell shape was detected on the whole pH range for the intensity variations. We followed the changes in intensity at pH 7.5 (in the middle of the interval where the protein seemed to possess a tertiary native structure: pH 6.5–8.0) by thermal denaturations; an irreversible, sigmoidal thermal transition was observed with a T_m of 57.7 ± 0.3 °C, whose value was obtained from Eq. (10) (Fig. S1 B). No sigmoidal transitions were observed outside that pH interval (data not shown).

On the other hand, the fluorescence spectra in the presence of Ca^{2+} were noisier than those in the presence of EDTA (Fig. S1 A), and therefore the pH data from the titrations were more scattered. The $<\lambda>$ (either by excitation at 280 or 295 nm) in the presence of Ca^{2+} showed two transitions as well (Fig. 2 B), starting and finishing roughly at the same pH values as the transitions found in the presence of EDTA. Similarly, the same two transitions at acidic and basic pH values were observed by following the changes in intensity (Fig. 2 B). We also performed fluorescence thermal denaturations in that pH range (6.5–8.0), as well as outside that interval. No sigmoidal transitions were observed by fluorescence (data not shown), and the irreversible transitions observed in that pH interval were less co-operative (that is, they were flatter than those observed in the presence of 10 mM of EDTA). Attempts to fit those curves to Eq. (10) yielded a T_m of 73 ± 5 °C (Fig. S1 B).

Therefore, it seems that, regardless of the absence or the presence of Ca^{2+}, the same titrating residues are determining the features of the tertiary structure around tryptophan and tyrosine residues at both extremes of pH, but the presence of Ca^{2+} changed the environment around at least some of the indole or phenol moieties.

(2) *ANS-binding*

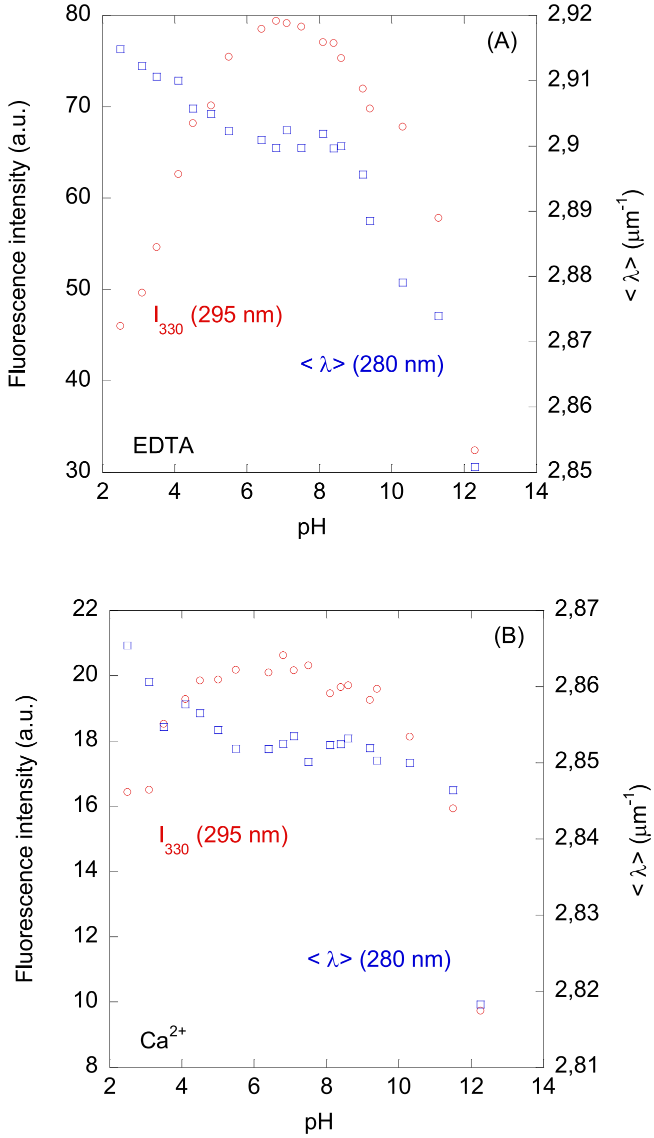

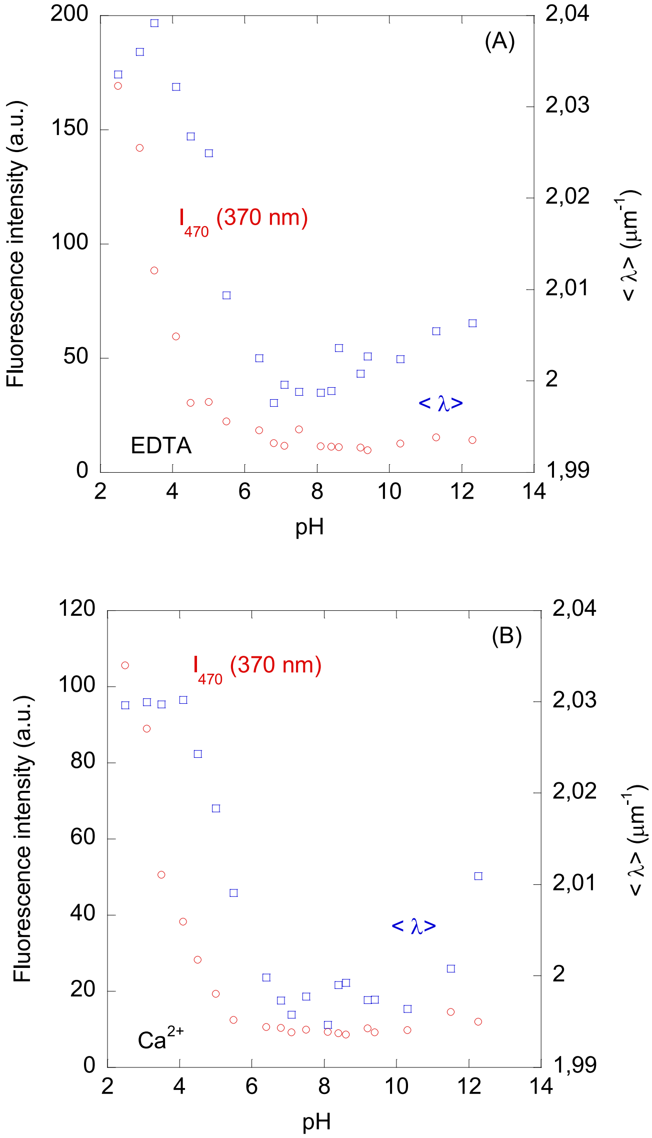

Fig. 2. pH-induced structural changes of PADI4 followed by intrinsic fluorescence: Conformational changes of PADI4 monitored by the intrinsic fluorescence at 330 nm, after excitation at 295 nm (blank, red circles) and by <λ> (average energy), after excitation at 280 nm (blank, blue squares) in the presence of EDTA (A), and in the presence of Ca^{2+} (B). (For interpretation of the references to color in this figure legend, the reader is referred to the Web version of this article.)

Fig. 3. pH-induced structural changes of PADI4 followed by ANS fluorescence: Conformational changes of PADI4 monitored by ANS fluorescence at 470 nm, after excitation at 370 nm (blank, red circles) and by <λ> (blank, blue squares) in the presence of EDTA (A), and in the presence of Ca^{2+} (B). (For interpretation of the references to color in this figure legend, the reader is referred to the Web version of this article.)

We also observed two transitions in the pH-titrations (either in the presence or absence of Ca^{2+}) followed by ANS (Fig. 3 A). In the presence of EDTA, conversely to what we had observed by following the intrinsic fluorescence of the protein, the pK_a of the acidic transition, obtained following <λ>, was 5.3 ± 0.5; in contrast, by following the intensity, we could not determine the pK_a because we did not have an acidic baseline. This acidic transition was completely finished at pH ~6.5. The basic transition, which started at pH ~8.0, was clearly observed by following <λ>, but such transition could not be monitored by following the intensity at 470 nm.

On the other hand, in the presence of Ca^{2+}, the pK_a of the acidic transition followed by <λ> was 5.9 ± 0.6 (Fig. 3 B), similar to that observed in the presence of EDTA. We could not determine the pK_a of this acidic transition from the changes in the fluorescence intensity, due to the lack of an acidic baseline. This acidic transition ended at pH ~6.5. At basic pH values, as it happened in the presence of EDTA, the transition was more clearly observed by monitoring <λ> rather than the fluorescence intensity; this transition started at pH ~8.0, but we could not determine its pK_a due to the absence of baseline.

Thermal denaturations following the ANS fluorescence, at different pH values in the presence of EDTA, showed only a single sigmoidal transition (Fig S2 A). The apparent T_m value at pH 7.5 was 56.8 ± 0.3 °C, identical to that measured by intrinsic fluorescence at the same pH. On the other hand, in the presence of Ca^{2+}, we also observed only a sigmoidal transition for pH values between 6.5 and 8.0 (Fig. S2 B); at pH 7.5, we obtained a T_m value of 52 ± 4 °C.

Therefore, we can conclude that the variation monitored by ANS in the burial of solvent-exposed hydrophobic surface occurred concomitantly to that of the acquisition of tertiary structure, monitored by the intrinsic fluorescence of tryptophans and tyrosines, during protein folding.

(3) *DSF*

We also carried out measurements in the presence of the fluorescent dye SYPRO Orange as protein unfolding reporter. Our results (Fig. S3 A) indicate that the fluorescence of this extrinsic probe was higher in the presence of EDTA than when Ca^{2+} was present, suggesting solvent-exposure of hydrophobic regions in the Ca^{2+}-free protein. Thermal denaturation experiments further suggest that the Ca^{2+}-free protein exhibited an apparent single transition centred at 57 °C (similar to the values observed by monitoring the intrinsic and ANS fluorescence, see above), whereas the Ca^{2+}-bound protein exhibited two transitions centred at 59 and 71 °C, respectively (Fig. S3 B). The former value was similar to that obtained from ANS fluorescence in the presence of Ca^{2+}, and the latter was similar to that obtained by intrinsic fluorescence (see above). An apparent unfolding enthalpy of 45 kcal mol^{-1} for the Ca^{2+}-free protein could be estimated from the derivative of the curve expressing the unfolded fraction at such T_m (Eq. (9)). This value is relatively small for a 74 kDa protein protomer suggesting: (i) a non-complete unfolding of the protein upon heating in the presence of this probe; or alternatively, (ii) a considerable level of flexibility, in agreement with the exposure of hydrophobic surface detected in the steady-state spectra (Fig. S3 A) (see Discussion). It could be argued that such small value of the apparent unfolding enthalpy might be due to a disordered nature of the protein; however, the fact that intrinsic fluorescence and far-UV CD spectra (see below) were those of a typical folded protein with buried tryptophan residues suggests that such small enthalpy value was due to any of the reasons indicated above.

Far-UV CD: The CD spectrum of PADI4 in the absence of Ca^{2+} at pH 7.5 showed minima at 210 and 222 nm (Fig. S4 A). These results indicate that the protein had mainly a helical fold, as well as a fraction of β-sheet structure, in agreement with its X-ray structure (PDB entry 3APN [31]). We estimated the percentage of helical structure by assuming that, at 222 nm, a 100% amount of fully formed helical structure determines a molar ellipticity, [Θ], of −39500 deg cm^2 $dmol^{-1}$ [59]. The $[\Theta]^{222}$ of PADI4 at pH 7.5 was −2668 deg cm^2 $dmol^{-1}$, yielding an estimated value of 7% of helical structure. The value obtained from the X-ray structure (PDB number: 3APN), where 112 residues out of 651 (per monomer) are in an α-helix conformation, was 17%. Besides uncertainties in the determination of secondary structure by using CD data, the main difference in the amount of helical structure calculated from the X-ray and from experimental far-UV CD data could be attributed to the presence of aromatic residues, which also absorb at 222 nm in the far-UV CD spectrum [60–63]. We could not acquire a good far-UV CD spectrum of PADI4 in the presence of Ca^{2+}, since its presence precluded having any meaningful information for wavelengths below 215 nm.

In the following, we shall not try to over-interpret the CD results, and we shall report on those changes which are clearly observable and are also supported, to some extent, by the results from fluorescence (either in the intrinsic or ANS experiments). In the pH-titrations followed by the raw ellipticity at 222 nm (Θ^{222}), either in the absence or presence of Ca^{2+}, we also observed two transitions (Fig. 4). We had to observe the changes in ellipticity in the presence of Ca^{2+} at 230 nm, due to the poorer signal-to-noise ratio at 222 nm (because of the presence of the salt). The first acidic transition resulted in an increase of the helicity (in absolute value) as the pH was raised, under either condition. These findings mean that the protein has lost its secondary structure, as monitored by far-UV CD, at acidic conditions. In the presence of EDTA, the first acidic transition had a pK_a of 5.1 ± 0.4 (Fig. 4 A); whereas in the presence of Ca^{2+}, the transition was at 5.6 ± 0.3 (Fig. 4 B). The two values are similar, within the fitting error to the Henderson-Hasselbalch equation (Eq. (8)), and comparable to those obtained by ANS fluorescence (see above). Under both conditions, we also observed that at basic pH values there was a decrease in the ellipticity at 222 nm (in absolute value) as the pH was raised (Fig. 4), but we could not determine the pK_a value, as we did not have a basic baseline. Therefore, to sum up, we can conclude that acquisition of secondary structure, as monitored by far-UV CD, occurred concomitantly to that of tertiary structure (intrinsic fluorescence) and the burial of solvent-exposed hydrophobic surface (ANS fluorescence) under both solution conditions (in the absence and presence of Ca^{2+}) and moving towards physiological conditions starting from either acidic or pH values. Thus, the acquisition of native structure only occurred in a narrow pH interval (Figs. 2–4).

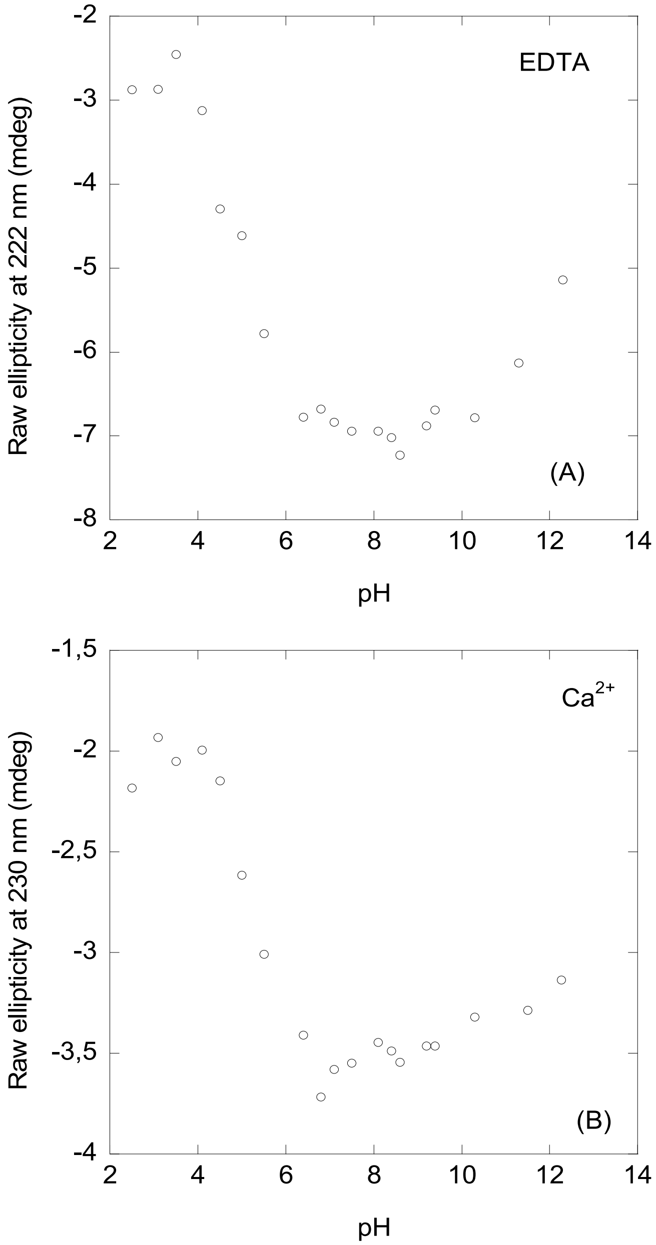

Fig. 4. pH-induced structural changes of PADI4 followed by far-UV CD: Conformational changes of PADI4 monitored by the raw ellipticity at 222 nm in the presence of EDTA (A), and in the presence of Ca^{2+} (B).

Thermal denaturations in the pH interval where PADI4 acquired a native structure were characterized, in the presence of Ca^{2+}, by a poor signal-to-noise ratio, thus precluding any reliable determination of T_m. On the other hand, in the presence of EDTA at pH 7.5 (Fig. S4 B), the irreversible, single sigmoidal denaturation curve yielded a T_m value of 52.9 ± 0.7 °C. This value was smaller than those obtained by intrinsic, ANS and SYPRO Orange fluorescence (see above); however, it was similar to that obtained for wild-type PADI4 under similar conditions reported by other laboratories [31]. These findings might suggest that secondary structure, as monitored by far-UV CD, melted before the tertiary one, in contrast of what one could expect (i.e., tertiary structure melting before the secondary one). This apparent discrepancy is due to the strong irreversibility of the thermal denaturation, and it has also been observed in thermal denaturations of other large proteins [64–66]. It could be argued that the irreversibility can either be inherent to the unfolding process (i.e., concomitant with the unfolding) or occur at high temperatures much later than the unfolding process. This can be tested by performing an unfolding experiment up to the apparent T_m, and then reheating. If the reheating recovers most of the unfolding trace, the unfolding can be considered reversible, even if maintaining the protein at higher temperatures would result in an irreversible process. Furthermore, the irreversibility can be assessed in the far UV CD experiments by monitoring the voltage as the thermal unfolding progresses [38]. If the voltage follows a linear-temperature dependence, it indicates that the unfolding is reversible; on the other hand, if it shows a sigmoidal-like behaviour (as that observed for the ellipticity) then the process is irreversible indicating aggregation. We used both procedures for PADI4: the first one by following intrinsic fluorescence of the protein and the second one by using far-UV CD. In the case of fluorescence, stopping the thermal scan at the apparent midpoint did not result in recovering neither the original fluorescence intensity of the spectrum at 25 °C (Fig. S1 A) nor a sigmoidal-like scan (Fig. S1 B) under both solution conditions. In the case of far-UV CD, we observed a sigmoidal-like behaviour in the voltage of the instrument with an apparent midpoint at 53 °C (close to the value observed by following the ellipticity at 222 nm). Then, we suggest that unfolding of PADI4 is associated with aggregation (that is, a temperature higher than the apparent T_m is not necessary to achieve self-association of the unfolded protein).

Near-UV CD: We only carried out near-UV experiments at pH 7.5 in the absence and in the presence of Ca^{2+}. PADI4 has a large number of aromatic residues (10 tryptophans, 13 tyrosines, 33 phenylalanines and 15 histidines in its sequence) and thus, the near-UV CD spectrum under both conditions had a large intensity [60–63]. The near-UV spectrum of PADI4 showed a broad maximum peak around 265 nm (Fig. S5), and a minimum at 297 nm. The normalized ellipticity was larger (in absolute value) for the spectrum in the presence of Ca^{2+} than in the presence of EDTA, thus confirming the previous findings obtained by intrinsic fluorescence, that the local environment around some of the tryptophan residues changed in the presence of the cation (Fig. S1 A).

To sum up, based on the findings obtained with the different spectroscopic probes used, we can conclude that the secondary and tertiary structures of PADI4 are lost concomitantly when moving to the two extremes values of pH. Thus, the pH range where PADI4 acquired a native structure was very narrow, encompassing an interval from 6.5 to 8.0.

3.4. PADI4 was a dimer in aqueous solution at physiological pH both in the absence and the presence of Ca^{2+}

DLS measurements of PADI4, in the absence and presence of Ca^{2+}, were performed at different concentrations ranging from 8 to 45 μM (in protomer units). The samples showed a small amount of high molecular weight aggregates: lower than 1% in the samples in the presence of the cation, and lower than 5% in the presence of EDTA. In the range of PADI4 concentrations assayed, its hydrodynamic radius (R_h) did not change in presence of Ca^{2+} when compared to that in the presence of EDTA (Fig. 5). The average R_h values of PADI4 under the different assayed conditions were: (i) in the presence of EDTA: $R_h = 5.4 \pm 1.1$ nm (8 μM) and 5.1 ± 0.6 nm (25 μM); and, (ii) in the presence of Ca^{2+}: $R_h = 5.1 \pm 1.1$ nm (12 μM) and 5.6 ± 0.6 nm (45 μM). The estimated molecular weight by using the Stokes-Einstein equation (Eq. (6)) for a protein with $R_h = 5.1$ nm is approximately 150 kDa, which indicates the presence of a dimer of PADI4 in solution under both conditions (the molecular weight of the monomer is 74.0 kDa). These results agree with previous findings obtained under slightly different conditions [67], and confirm that in solution PADI4 is a dimer as in the crystal structure [30, 31].

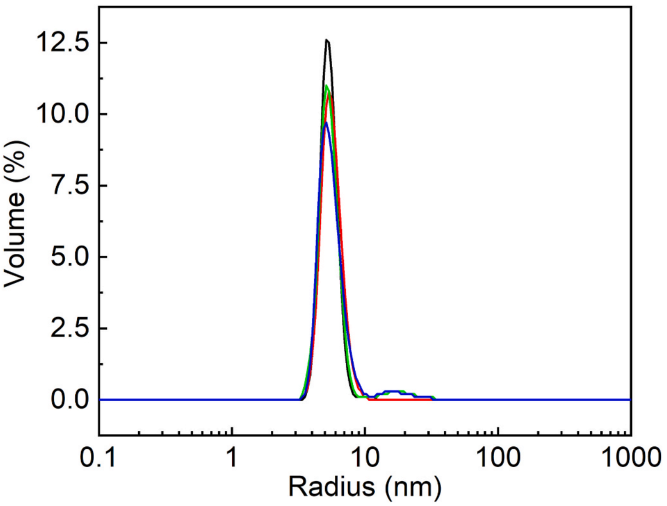

Fig. 5. DLS measurements of PADI4: The DLS volume distribution profiles of PADI4 in presence and absence of Ca^{2+}: (black line) at 12 μM in the presence of Ca^{2+}; (red line) at 45 μM in the presence of Ca^{2+}; (green line) at 8 μM in the presence of EDTA; and (blue line) at 25 μM in the presence of EDTA. (For interpretation of the references to color in this figure legend, the reader is referred to the Web version of this article.)

3.5. Conformational stability of PADI4

We proceeded to measure the conformational stability of PADI4 by using heat (*via* DSC), and chemical denaturation followed by intrinsic and ANS fluorescence and far-UV CD at pH 7.5. Our previous results indicate that thermal denaturations of PADI4 were irreversible and that stability of PADI4 at such pH in the presence of EDTA was not very high (see above). Even though the thermal denaturations seemed to be irreversible, the irreversibility may stem from additional processes different from the unfolding process (e.g., aggregation of the unfolded conformation). In that case, although the application of equilibrium models is problematic, still those models provide useful estimates of the thermal stability parameters. Furthermore, we aimed to obtain an estimate of the stability of PADI4 by using far-UV and fluorescence, either in the absence or the presence of Ca^{2+}, by using a chemical agent as denaturant.

3.5.1. A calorimetric point of view

The DSC experiments of PADI4 in the absence and presence of Ca^{2+} are shown in Fig. 6. The presence of Ca^{2+} induces a more complex unfolding behaviour; it may be possible that, because the unfolding shifts to higher temperatures, the irreversibility of the process might be more pronounced at those higher temperatures, hindering a reasonable analysis. Still, a considerable stabilization effect induced by Ca^{2+} binding could be observed: an apparent T_m value of 53.2 °C without Ca^{2+}; and two apparent T_m values of 59.6 and 72.6 °C were observed when the cation was present. The single T_m observed in the absence of Ca^{2+} and the highest T_m observed in the presence of Ca^{2+} are similar to those observed by fluorescence thermal denaturations (see above).

The model-free analysis provided apparent values for the thermal stability parameters: ΔH_{cal} value of 86 kcal mol^{-1}, and $C_{P,max}$ value of 11.1 kcal $K^{-1}\cdot mol^{-1}$, from which a ΔH_{VH} value of 109 kcal mol^{-1} could be estimated. From those figures, an enthalpy ratio of 1.27 could be calculated, which differs from unity beyond the experimental error. Importantly, the unfolding trace is slightly asymmetric, with a negative skew, as typically observed in the unfolding of homooligomeric proteins. Therefore, the most appropriate model for analysing the unfolding process of PADI4 is that of a protein dimer unfolding and dissociating simultaneously into unfolded subunits.

Fig. 6 shows the calorimetric thermal unfolding of PADI4 in the

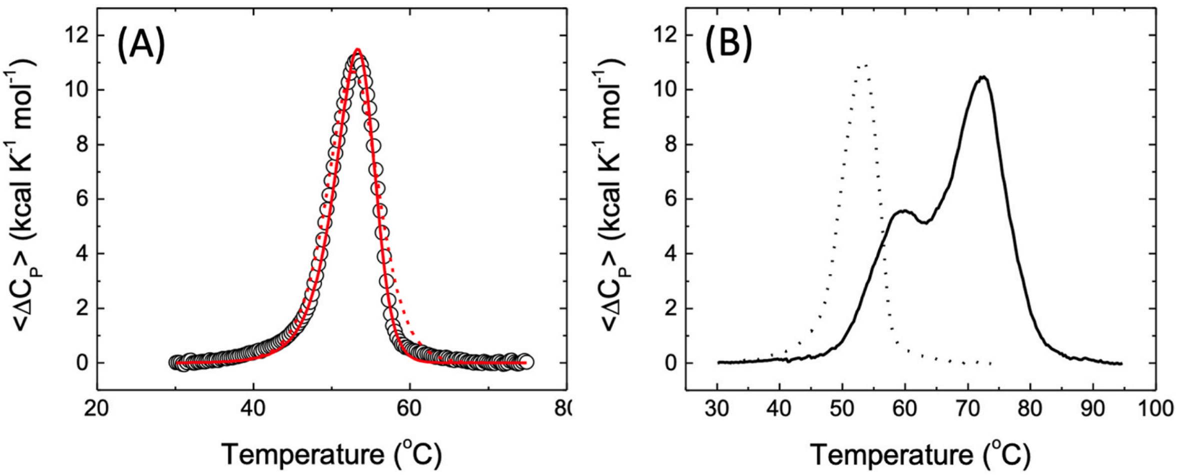

Fig. 6. DSC experiments: (A) Thermal denaturation of PADI4 in the absence of Ca^{2+}. A single apparent unfolding transition is observed. The experimental data (empty circles) were analysed according to a two-state model (dashed red line) and a two-state-unfolding-dissociation model (continuous red line). (B) Thermal denaturation of PADI4 in the presence of Ca^{2+} (continuous black line). The unfolding, in the absence of Ca^{2+} (dotted line), is shown for comparison. (For interpretation of the references to color in this figure legend, the reader is referred to the Web version of this article.)

absence of Ca^{2+} analysed with the two-state model ($T_m = 52.2 \pm 0.2$ °C, $\Delta H(T_m) = 94 \pm 2$ kcal mol^{-1}) and with the unfolding-dissociation model ($T_0 = 64.0 \pm 0.3$ °C, $\Delta H(T_m) = 117 \pm 2$ kcal mol^{-1}). It is important to note that the T_0 obtained by using the dissociation model corresponds to the temperature at which the Gibbs energy of unfolding becomes zero, which, for a dimeric protein, it is much higher than the T_m, the temperature for maximal unfolding heat capacity, which corresponds to the temperature estimated by spectroscopic measurements (see above); in fact, the apparent T_m values observed using the different techniques (spectroscopy and calorimetry) are very similar. Therefore, this finding indicates that the apparent thermal denaturation midpoint determined by spectroscopy was probably strongly affected by protein self-association. The fitting was visually much better for the unfolding dissociation model, but also statistically better considering the residual-sum-of-squares (RSS), with values of $4.9 \cdot 10^7$ and $1.1 \cdot 10^7$, for the two-state model and the unfolding-dissociation model, respectively. The thermal stability parameters were used for extrapolating the unfolding Gibbs energy and the equilibrium unfolding constant from 64 to 25 °C, and a dissociation constant for the PADI4 dimer of 0.9 ± 0.4 μM was estimated at 25 °C, a value in agreement with the one previously reported from analytical ultracentrifugation (AUC) experiments [67].

3.5.2. *A chemical-denaturation point of view*

Chemical refolding experiments using GdmCl as denaturant, indicated that unfolding of PADI4 was not reversible. Therefore, we could not obtain the free energy (ΔG) of the unfolding reaction, and we will not be able to discuss quantitatively the unfolding mechanism of PADI4.

Firstly, we tried, in the presence of EDTA, to determine whether urea or GdmCl was better suited to follow the chemical unfolding of PADI4. Experiments using urea as denaturant agent showed that, when using $\langle\lambda\rangle$ (or the intensity) of the intrinsic fluorescence as the physical quantity to follow the denaturation, no transition was observed, but rather an un-cooperative, flat transition without any native or unfolded baselines of the curve (Fig. S6). On the other hand, the ellipticity at 222 nm in the urea-denaturations showed two transitions: one occurring at low urea concentration, and the other occurring with an $[\text{urea}]_{1/2}$ of 4.1 ± 0.3 M (Fig. S6). These findings suggest that the chemical unfolding of PADI4, due to its large size, is complex. Due to the lack of a clear transition when PADI4 unfolding was monitored using urea by fluorescence, we decided to use GdmCl as a chaotropic agent.

Chemical denaturations by using GdmCl as denaturant showed, as well, a complex behaviour when the ellipticity at 222 nm was monitored, with at least three transitions (Fig. 7 A); one of them, as it happened for experiments with urea, occurring at low denaturant concentrations. Conversely, the GdmCl-denaturations followed by fluorescence (either $\langle\lambda\rangle$ or the intensity) showed a single, very broad transition, with $[\text{GdmCl}]_{1/2} = 0.9 \pm 0.5$ M and $m = 0.9 \pm 0.3$ kcal mol^{-1} M^{-1} (at 280 nm), suggesting that PADI4 was a protein with low stability. We also followed the GdmCl-denaturations by using ANS as a probe (Fig. 7 B), yielding $[\text{GdmCl}]_{1/2} = 1.52 \pm 0.09$ M and $m = 2.1 \pm 0.4$ kcal mol^{-1} M^{-1}. These values are different from those obtained by following the intrinsic fluorescence, indicating that the denaturation of PADI4 in the presence of EDTA was complex. Furthermore, as PADI4 is a dimer, we hypothesized that some of the transitions observed in the far-UV CD spectra could be due to dimer dissociation, and then, this reaction could be better observed at higher protein concentrations used during the experiments. Therefore, we carried out a chemical denaturation experiment at a protein concentration of 10.5 μM, in protomer units (Fig. S7), but even at this value we were not able to resolve the different transitions observed at low protein concentration. These results suggest that the dissociation constant of the PADI4 dimer was smaller than the lowest protein concentration (in protomer units) used in our chemical denaturation experiments; in fact, AUC experiments have shown that such constant has a value of 0.45 μM at 20 °C [67], in agreement with the value estimated from our DSC experiments (see above). The thermal stability of PADI4 seems to be much lower from the spectroscopic assays (ΔG value of 0.8 kcal mol^{-1} from tryptophan intrinsic fluorescence thermal denaturations, and a value of 3.2 kcal mol^{-1} from ANS extrinsic fluorescence thermal denaturations) compared to the value estimated from DSC experiments (ΔG value of 4.1 kcal mol^{-1}) and that estimated from AUC experiments (ΔG value of 4.3 kcal mol^{-1}). This may be due to the local nature of the protein features determining the spectroscopic signal, compared to the global nature of the DSC and AUC observable signals.

On the other hand, chemical denaturation experiments of PADI4 carried out in the presence of Ca^{2+} did not yield sigmoidal transitions (i.e., we observed a non-cooperative behaviour) when followed by fluorescence or ellipticity at 222 nm (Fig. 8 A), suggesting that the unfolding of the protein under these conditions was less co-operative than in the presence of EDTA. Furthermore, by using ANS as a probe, we obtained $[\text{GdmCl}]_{1/2} = 2.02 \pm 0.08$ M and $m = 1.9 \pm 0.4$ kcal mol^{-1} M^{-1} (Fig. 8 B), which yields an apparent ΔG value larger than that obtained in the presence of EDTA, and in agreement with the DSC data (Fig. 6), where we observed a stabilization of the protein. Therefore, the presence of Ca^{2+} induced changes in the tertiary environment around some aromatic residues (see above), as well as variations in the solvent-exposed

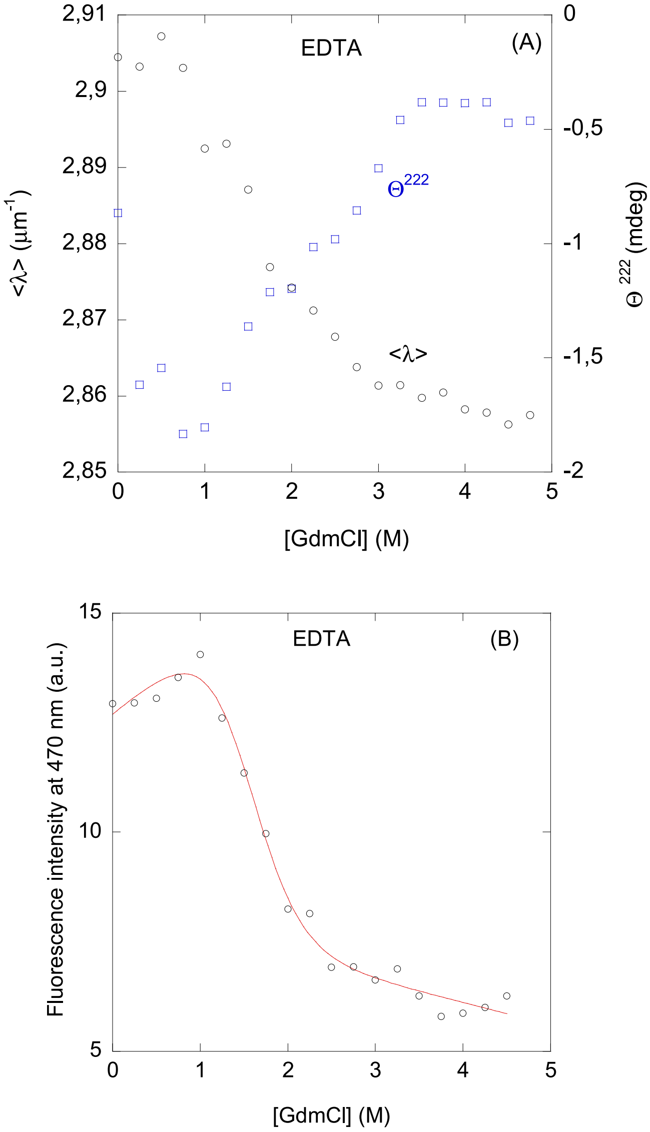

Fig. 7. Chemical denaturations of PADI4 in the presence of EDTA followed by spectroscopic techniques. (A) Conformational changes of PADI monitored by <λ>, after excitation at 280 (filled, black circles), and by the ellipticity at 222 nm (blue, blank squares). (B) Conformational changes of PADI4 monitored by the changes in the intensity at 470 nm of the ANS probe (after excitation at 370 nm). The line through the ANS fluorescence data is the fitting to a two-state model according to Eq. (9). (For interpretation of the references to color in this figure legend, the reader is referred to the Web version of this article.)

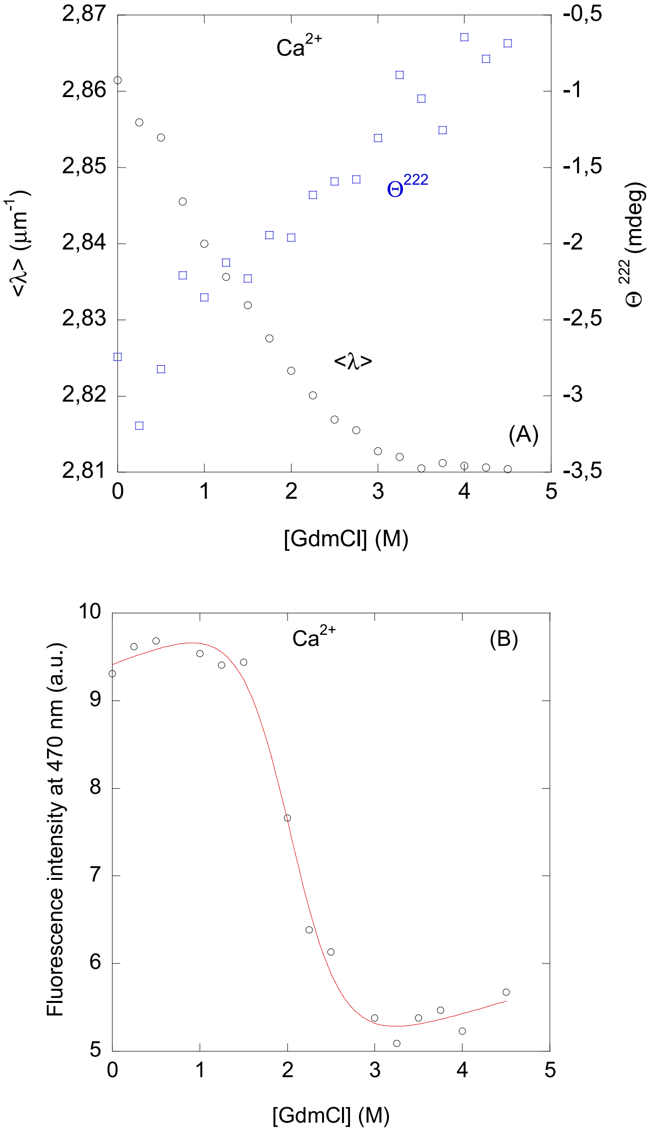

Fig. 8. Chemical denaturations of PADI4 in the presence of Ca^{2+} followed by spectroscopic techniques. (A) Conformational changes of PADI monitored by <λ>, after excitation at 280 (filled, black circles), and by the ellipticity at 222 nm (blue, blank squares). (B) Conformational changes of PADI4 monitored by the changes in the intensity at 470 nm of the ANS probe (after excitation at 370 nm). The line through the ANS fluorescence data is the fitting to a two-state model according to Eq. (9). (For interpretation of the references to color in this figure legend, the reader is referred to the Web version of this article.)

surface. These results indicate that the solvent-exposure of hydrophobic regions of PADI4 was different from that observed in the presence of EDTA. These findings are confirmed by the X-ray structures of PADI4 in the absence (PDB number: 1APN) and in the presence of Ca^{2+} (PDB number: 1WD9). Furthermore, since by AUC experiments no quaternary structure stabilization was observed in the presence of Ca^{2+} [67], we suggest that the changes in stabilization observed by chemical denaturation (Fig. 8) and DSC (Fig. 6) were due to stabilization of the secondary and/or tertiary structure within the monomer (see Discussion).

3.6. *Flexibility of the protein structure in molecular simulations*

Molecular simulations were used to elucidate the flexibility of PADI4, which was observed to have peculiar characteristics on the basis of our experimental findings (see above). A low rigidity of the protein structure could play a mechanistic role in determining its low stability and, from a functional point of view, could favor the interaction with various molecular partners. To investigate this aspect, we employed MD simulation, which is one of the most direct techniques to probe the dynamics of a protein [50]. The PADI4 dimer was observed on the time scale of 10 ns, which was adequate to equilibrate the deviations of the atomic positions with respect to the starting structure (Fig. S8, black line). The results reported in Fig. 9 show the root mean square fluctuations (RMSF) of the atomic positions of the C^{α} atoms as a function of the residue number. The data shown are averaged on the two monomers; therefore, they tend to evidence non-random, coordinated motions of relatively long (>10 residues) portions of PADI4 sequence. At room temperature (Fig. 9 A, black line), the stiffer regions of PADI4 have fluctuations of ~0.1 nm, whereas the most flexible regions can reach values up to ~0.3 nm. It is immediate noticeable that the fluctuations were almost evenly distributed on the whole sequence, despite the presence of extended protein regions with different secondary (α/β) and

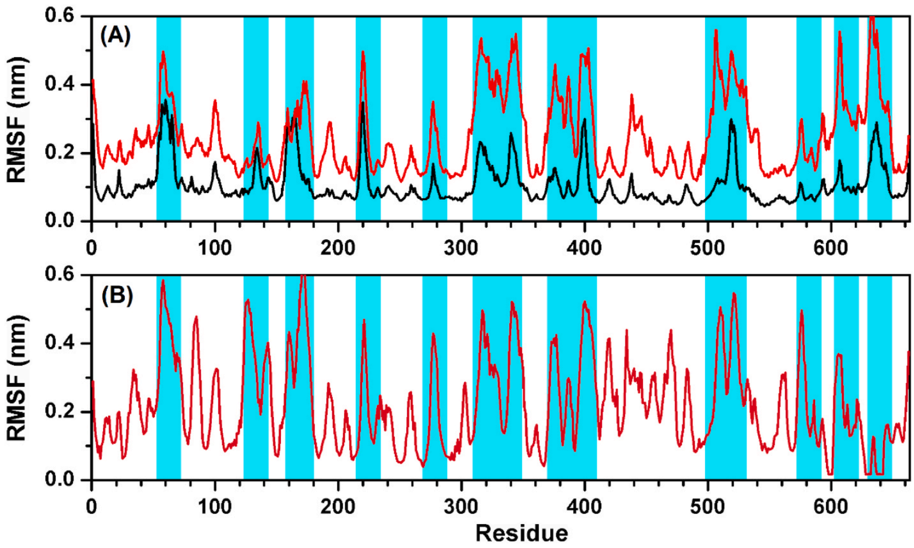

Fig. 9. Simulated average RMSF of the backbone atomic position of PADI4. (A) MD simulations at (black line) 300 K and (red line) 450 K. (B) Coarse-grained simulation using the CABS-flex model [51], with dimensionless reduced T = 2.0. Regions ≥20 residues highlighted in cyan have RMSF >0.4 and/or 0.5 nm in MD and CAB-flex modeling, respectively. Values are calculated in all cases by simulating the dimeric structure and averaging the fluctuations obtained for the two monomers. (For interpretation of the references to color in this figure legend, the reader is referred to the Web version of this article.)

tertiary structure (three distinct subdomains) [30]. High-temperature MD simulation was also used to investigate the early steps of the protein unfolding; to speed up the process, a simulation value of 450 K was used, as it is common practice [68,69]. The results (Fig. 9 A, red line) indicated that the RMSF of the atomic positions were about twice larger compared to those at room temperature, for both the most rigid and flexible protein regions. In particular, the highest fluctuation values were found in correspondence with the same regions showing relatively high motions also at room temperature. This observation confirms that the flexibility of PADI4 remained evenly distributed on the whole structure when the temperature was increased.

Besides the local unfolding of the protein structure in a few selected regions, the simulation temperature of 450 K was insufficient to observe the melting of the whole structure on a reasonable time scale (see the equilibration of atomic deviations in Fig. S8, red line), at variance with what we have found for other large proteins [66,70,71]. Thus, the effect of high temperature was further tested by using the CABS-flex algorithm [51] for mimicking protein structure flexibility, which focuses on the coarse-grained modeling of large-scale conformational transitions. In particular, we used a temperature twice larger than that typically used to reproduce the native protein state, which is usually sufficient for the complete melting of unrestrained small polypeptide chains [52]. The results shown in Fig. 9 B indicate again a high flexibility for a large number of protein regions, scattered throughout the whole sequence. The fluctuations calculated by using the CABS-flex and MD data were generally in very good agreement (see regions highlighted in cyan both in Fig. 9 A and B, each consisting of at least 20 residues), although the former tended to be higher in some N-terminal protein regions (around residue 130 and 170), and the latter in some C-terminal ones (around position 610 and 630). In any case, no indication was found of the potential presence of an unfolding intermediate in the denaturation process. Furthermore, although the contact map of the protein residues (reported in Fig. S9) showed that most of the inner interactions in the homodimer took place within each monomer (and, for both monomers, predominantly within each of their three subdomains), no indication was found of the dissociation of the two monomers. This suggests that the overall secondary, tertiary and quaternary structure of PADI4 might not be lost at very different stages during the unfolding process.

4. Discussion

Under conditions of cellular stress, some proteins can undergo several processes of PTM, such as citrullination. The conversion of arginine residues to citrulline by PADI enzymes, results in the recognition by the immune system of the citrullinated proteins; this recognition occurs in cancer and other diseases. PADI proteins are mostly cytosolic; however, PADI4 has an NLS that allows its nuclear translocation, and therefore it can citrullinate nuclear targets such as histones. Our results not only indicate that the PADI4 gene is significantly expressed in various tumour types, but further show different protein expression levels and patterns. The WB analyses showed that different tumour cell lines had levels of PADI4 protein expression that ranged from very low in PAAD to high in COAD and GBM. Moreover, protein extracts revealed multiple PADI4 protein bands that reflected the fact that PADI4 could undergo alternative splicing, and then generate protein species with or without NLS, resulting in a different subcellular localization. Immunostaining with anti-PADI4 antibody confirmed: (i) the expression of PADI4 in the above-mentioned tumours; and (ii) its tumour-dependent distribution.

The p53 gene is considered the most frequent target of genetic alteration identified in human cancers [72]. Biological functions of p53 include: G1 arrest induction, apoptosis following DNA damage or other cellular insults, genomic stability maintenance, and angiogenesis inhibition. To perform those functions, p53 binds DNA in a sequence-specific fashion [73] resulting in a transcriptional activation of downstream genes that carry out a variety of functions. Biochemical assays indicate that p53 interacts with PADI4 both in cells and when the two are combined as purified proteins [24]. Our results show that tumour cell lines differed in the levels of certain PADI4 protein forms and p53 (Fig. 1 B). Since PADI4 plays a role during tumorigenesis by antagonizing regulation of p53 to tumour suppressor genes [54], we hypothesize that PADI4 might play a different role on the cell function and development depending on the tumour origin. These results are in line with the observations made on several types of cancers, where it has been highlighted the major role of PADI4 at the onset and progression of cancer [74]. Therefore, tampering with citrullination has been proposed as a possible target for developing cancer treatments [75].

Given the important role of PADI4 in cancer, we reasoned that a first step in deciphering its protein interactome and its function was to perform its biophysical and conformational characterization. The biophysical and biochemical features described in this work will also help to understand how PADI4 mediates its interactions and its regulation with putative therapeutic agents. We found that PADI4 in solution possessed a native structure in a narrow pH range, between 6.5 and 8.0. In such pH range, the ellipticity at 222 nm showed the highest value (in absolute terms) and we could observe sigmoidal thermal denaturations. The acquisition of native secondary and tertiary structure, as well as the burial of solvent-exposed hydrophobic surface, occurred concomitantly, either starting from acidic or basic pH values. We could not explore the acquisition of native quaternary structure at low pH values, since the protein precipitated at the concentrations used in the DLS experiments. The fact that the protein species populated at low pH showed a large ANS binding suggests that they are probably molten globules [58], as we could further confirm by the absence of thermal unfolding sigmoidal curves in the fluorescence or CD experiments at low pH values (data not shown). The optimal activity for histone H3 citrullination is between pH 6.4 and 7.2 [76], close to the pH range observed for the acquisition of native secondary structure of PADI4. A similar pH range was observed for citrullination of the model compound N-α-benzoyl L-arginine ethyl ester [77]. Therefore, the pH range where PADI4 acquires a native conformation seems to be within its range for optimal activity. It has been shown that, due to the increased glucose metabolism, the production of H^+ is enhanced in cancer states, resulting in acidification of the extracellular milieu (in the range of pH from 6.5 to 6.9) and, in parallel, an alkalization of the cytoplasm environment ($pH > 7.2$) [78, 79]. We hypothesize that even these variations of pH in cancer cells do not alter the functionality of PADI4. However, in such pH range (between 6.5 and 8.0) the apparent T_m values of the protein were ~55 °C. We are fully aware, that judging protein stability based only on the value of an apparent T_m can skew our reasoning (in fact, the use of T_m to judge protein stability can be properly used when comparing similar proteins, such as in the case of mutants). However, the apparent ΔG for PADI4 is ~4 kcal mol^{-1}, which is small for a 74 kDa protein; similar values of the apparent thermal denaturation midpoints have been observed for other large proteins [65,66], where they has been associated with a low stability, which often occurs in proteins with large flexibility. Our simulation results support this latter view, as they indicate the dynamics of the protein is almost uniformly distributed on the whole sequence, in spite of being formed by distinct subdomains.

PADI enzymes are activated by millimolar concentrations of Ca^{2+} which can occur, for instance, during apoptosis. Our *in vitro* analysis showed that the presence of Ca^{2+} did not alter the quaternary structure of the protein, and PADI4 remained dimeric in the presence of the cation (Fig. 5). However, the local environment around some of the tryptophans and/or tyrosines changed when the cation was present in solution (Fig. S1), and the use of a probe such as SYPRO Orange indicates differences in the solvent-exposure of hydrophobic patches in the protein in the Ca^{2+}-free species (Fig. S3). These findings agree with results found in the X-ray structure of PADI4 in the absence of Ca^{2+}, where the regions Ile313-Ile320, Pro338-Met348, Pro371-Pro387, Pro396-Gly403 and Phe633-His644 are solvent-exposed and highly disordered [80]. All these regions become well-ordered in the presence of the cation. Furthermore, the region from Glu351 to Ala359 has a conformational change and acquires a β-strand conformation in the presence of Ca^{2+}. It is interesting to note that Tyr356, Trp547 and Tyr636 are included in some of those regions, explaining the changes in the intrinsic fluorescence observed under the two conditions (Fig. S1) and the results of SYPRO Orange (Fig. S3). In addition, the presence of Ca^{2+} induced a considerable stabilization of PADI4, as observed by DSC, although the effect may be masked by a further irreversible stage during the denaturation process.

We also found that PADI4 had a complex unfolding behaviour, as shown by our DSC findings, in the presence of Ca^{2+} and during the chemical denaturations. The far-UV CD chemical denaturation curves used to explore the folding of PADI4 showed at least two intermediates, at variance with the chemical denaturations observed by fluorescence and the MD simulations. These findings indicate that the unfolding of PADI4 was not a two-state process [81]. Furthermore, the CD and ANS results suggest the presence of nearby solvent-exposed hydrophobic patches in the structure of the protein at physiological conditions, which are disrupted by low denaturant concentrations resulting in a step-by-step increase of the ellipticity in absolute value, and then in the helicity of the protein. The increase of the fluorescence of the ANS at low GdmCl concentrations, suggests that those hydrophobic patches are close enough among them in the native structure to bind the probe, and probably to some PADI4 partners. The simulation results also suggest that the protein regions with higher flexibility at room temperature are the same that show an enhanced dynamic during the first steps of the thermal unfolding process. Furthermore, the melting of the secondary structure does not seem to be accompanied by large scale conformational transitions, neither by the loss of the protein quaternary structure.

5. Conclusions

PADI proteins are present in a large number of cell and tissue types, and have an important role in key biochemical pathways. In this work, we have performed a comprehensive biophysical analysis of PADI4, by using a variety of techniques. The results have revealed aspects of the protein stability and dynamics that could have a significant importance in the interaction with various molecular partners, for instance, in the histones citrullination. Furthermore, our biochemical characterization, performed by using different cancer cell lines, indicated the presence of PADI4 in different subcellular localizations. Our observations also support a role of this protein in regulating the expression of p53. Taken all together, the results here presented not only agree with the proposed role of PADI4 in the onset and progression of cancer, but also set the knowledge for the development of tools to study the function of PADI4. .

Author contributions and competing interests

JLN, ACA, BR, AVC and CdJ designed the experiments and the research methodology. JLN, ACA, AMG, BR, OA and SAA carried out the experiments. JLN, ACA, AMG, BR, AVC, SAA and CdJ analysed the data. JLN, OA, AVC and CdJ provided funding acquisition and project administration. All authors wrote, revised, edited and corrected the manuscript.

Declaration of competing interest

The authors declare no competing interests.

Data availability

Data will be made available on request.

Funding and Acknowledgements

This work was supported by Spanish Ministry of Economy and Competitiveness and European ERDF Funds (MCIU/AEI/FEDER, EU) [RTI2018-097991-B-I00 to JLN, BFU2016-78232-P to AVC; CP19/00095 to CdJ]; Fondo de Investigaciones Sanitarias from Instituto de Salud Carlos III, and European Union (ERDF/ESF, “Investing in your future”) [PI18/00349 to OA]; Diputación General de Aragón [“Protein targets and Bioactive Compounds group” E45-20R to AVC, and “Digestive Pathology Group” B25-20R to OA]. SAA was recipient of a “Carolina Foundation predoctoral fellowship” 2020. The funders had no role in the study design, data collection and analysis, decision to publish, or preparation of the manuscript.

We thank Dr. Miguel Saceda (IDIBE) for providing us with the tumour cell lines used in this work. We thank the two anonymous reviewers for helpful suggestions and discussions. BR acknowledges the kind use of computational resources by the European Magnetic Resonance Center (CERM), Sesto Fiorentino (Florence), Italy.

Appendix A. Supplementary data

Supplementary data to this article can be found online at https://doi.org/10.1016/j.abb.2022.109125.

References

[1] S. Mondal, P.R. Thompson, Protein arginine deiminases (PADs): Biochemistry and chemical biology of protein citrullination, Acc. Chem. Res. 52 (2019) 818–832, https://doi.org/10.1021/ACS.ACCOUNTS.9B00024.

[2] E.R. Vossenaar, A.J.W. Zendman, W.J. Van Venrooij, G.J.M. Pruijn, PAD, a growing family of citrullinating enzymes: genes, features and involvement in disease, Bioessays 25 (2003) 1106–1118, https://doi.org/10.1002/BIES.10357.

[3] G.L. Cuthbert, S. Daujat, A.W. Snowden, H. Erdjument-Bromage, T. Hagiwara, M. Yamada, R. Schneider, P.D. Gregory, P. Tempst, A.J. Bannister, T. Kouzarides, Histone deimination antagonizes arginine methylation, Cell 118 (2004) 545–553, https://doi.org/10.1016/J.CELL.2004.08.020.

[4] H. Asaga, M. Yamada, T. Senshu, Selective deimination of vimentin in calcium ionophore-induced apoptosis of mouse peritoneal macrophages, Biochem. Biophys. Res. Commun. 243 (1998) 641–646, https://doi.org/10.1006/BBRC.1998.8148.

[5] C. Assohou-Luty, R. Raijmakers, W.E. Benckhuijsen, J. Stammen-Vogelzangs, A. De Ru, P.A. Van Veelen, K.L.M.C. Franken, J.W. Drijfhout, G.J.M. Pruijn, The human peptidylarginine deiminases type 2 and type 4 have distinct substrate specificities, Biochim. Biophys. Acta 1844 (2014) 829–836, https://doi.org/10.1016/J.BBAPAP.2014.02.019.

[6] T. Senshu, K. Akiyama, A. Ishigami, K. Nomura, Studies on specificity of peptidylarginine deiminase reactions using an immunochemical probe that recognizes an enzymatically deiminated partial sequence of mouse keratin K1, J. Dermatol. Sci. 21 (1999) 113–126, https://doi.org/10.1016/S0923-1811(99)00026-2.

[7] K. Kizawa, H. Takahara, H. Troxler, P. Kleinert, U. Mochida, C.W. Heizmann, Specific citrullination causes assembly of a globular S100A3 homotetramer: a putative Ca^{2+} modulator matures human hair cuticle, J. Biol. Chem. 283 (2008) 5004–5013, https://doi.org/10.1074/JBC.M709357200/ATTACHMENT/30FDC955-973C-47BA-B803-D6787A3A216D/MMC1.PDF.

[8] Y. Wang, J. Wysocka, J. Sayegh, Y.H. Lee, J.R. Pertin, L. Leonelli, L.S. Sonbuchner, C.H. McDonald, R.G. Cook, Y. Dou, R.G. Roeder, S. Clarke, M.R. Stallcup, C.D. Allis, S.A. Coonrod, Human PAD4 regulates histone arginine methylation levels via demethylimination, Science 306 (2004) 279–283, https://doi.org/10.1126/SCIENCE.1101400/SUPPL_FILE/WANG.SOM.PDF.

[9] A. Ishigami, N. Maruyama, Importance of research on peptidylarginine deiminase and citrullinated proteins in age-related disease, Geriatr. Gerontol. Int. 10 (2010) S53–S58, https://doi.org/10.1111/J.1447-0594.2010.00593.X.

[10] R.J. Klose, Y. Zhang, Regulation of histone methylation by demethylimination and demethylation, Nat. Rev. Mol. Cell Biol. 8 (2007) 307–318, https://doi.org/10.1038/nrm2143.

[11] B. György, E. Tóth, E. Tarcsa, A. Falus, E.I. Buzás, Citrullination: a posttranslational modification in health and disease, Int. J. Biochem. Cell Biol. 38 (2006) 1662–1677, https://doi.org/10.1016/J.BIOCEL.2006.03.008.

[12] C. Anzilotti, F. Pratesi, C. Tommasi, P. Migliorini, Peptidylarginine deiminase 4 and citrullination in health and disease, Autoimmun. Rev. 9 (2010) 158–160, https://doi.org/10.1016/J.AUTREV.2009.06.002.

[13] L.L. Wang, Y.P. Song, J.H. Mi, M.L. Ding, Peptidyl arginine deiminase 4 and its potential role in Alzheimer's disease, Med. Hypotheses 146 (2021) 110466, https://doi.org/10.1016/J.MEHY.2020.110466.

[14] M. Guerrin, A. Ishigami, M.C. Méchin, R. Nachat, S. Valmary, M. Sebbag, M. Simon, T. Senshu, G. Serre, cDNA cloning, gene organization and expression analysis of human peptidylarginine deiminase type I, Biochem. J. 370 (2003) 174, https://doi.org/10.1042/BJ20020870.

[15] A. Ishigami, T. Ohsawa, H. Asaga, K. Akiyama, M. Kuramoto, N. Maruyama, Human peptidylarginine deiminase type II: molecular cloning, gene organization, and expression in human skin, Arch. Biochem. Biophys. 407 (2002) 25–31, https://doi.org/10.1016/S0003-9861(02)00516-7.

[16] T. Kanno, A. Kawada, J. Yamanouchi, C. Yosida-Noro, A. Yoshiki, M. Shiraiwa, M. Kusakabe, M. Manabe, T. Tezuka, H. Takahara, Human peptidylarginine deiminase type III: molecular cloning and nucleotide sequence of the cDNA, properties of the recombinant enzyme, and immunohistochemical localization in human skin, J. Invest. Dermatol. 115 (2000) 813–823, https://doi.org/10.1046/J.1523-1747.2000.00131.X.

[17] S. Chavanas, M.C. Méchin, H. Takahara, A. Kawada, R. Nachat, G. Serre, M. Simon, Comparative analysis of the mouse and human peptidylarginine deiminase gene clusters reveals highly conserved non-coding segments and a new human gene, PADI6, Gene 330 (2004) 19–27, https://doi.org/10.1016/J.GENE.2003.12.038.

[18] K. Nakashima, T. Hagiwara, A. Ishigami, S. Nagata, H. Asaga, M. Kuramotot, T. Senshu, M. Yamada, Molecular characterization of peptidylarginine deiminase in HL-60 cells induced by retinoic acid and 1α,25-dihydroxyvitamin D3, J. Biol. Chem. 274 (1999) 27786–27792, https://doi.org/10.1074/JBC.274.39.27786.

[19] S. Dong, T. Kanno, A. Yamaki, T. Kojima, M. Shiraiwa, A. Kawada, M.C. Méchin, S. Chavanas, G. Serre, M. Simon, H. Takahara, NF-Y and Sp1/Sp3 are involved in the transcriptional regulation of the peptidylarginine deiminase type III gene (PADI3) in human keratinocytes, Biochem. J. 397 (2006) 449–459, https://doi.org/10.1042/BJ20051939.

[20] S. Chavanas, V. Adoue, M.C. Méchin, S. Ying, S. Dong, H. Duplan, M. Charveron, H. Takahara, G. Serre, M. Simon, Long-range enhancer associated with chromatin looping allows AP-1 regulation of the peptidylarginine deiminase 3 gene in differentiated keratinocyte, PLoS One 3 (2008), e3408, https://doi.org/10.1371/JOURNAL.PONE.0003408.

[21] M.C. Méchin, M. Enji, R. Nachat, S. Chavanas, M. Charveron, A. Ishida-Yamamoto, G. Serre, H. Takahara, M. Simon, The peptidylarginine deiminases expressed in human epidermis differ in their substrate specificities and subcellular locations, Cell. Mol. Life Sci. 62 (2005) 1984–1995, https://doi.org/10.1007/S00018-005-5196-Y.

[22] K.P. U, V. Subramanian, A.P. Nicholas, P.R. Thompson, P. Ferretti, Modulation of calcium-induced cell death in human neural stem cells by the novel peptidylarginine deiminase–AIF pathway, Biochim. Biophys. Acta 1843 (2014) 1162–1171, https://doi.org/10.1016/J.BBAMCR.2014.02.018.

[23] H.C. Hung, C.Y. Lin, Y.F. Liao, P.C. Hsu, G.J. Tsay, G.Y. Liu, The functional haplotype of peptidylarginine deiminase IV (S55G, A82V and A112G) associated with susceptibility to rheumatoid arthritis dominates apoptosis of acute T leukemia Jurkat cells, Apoptosis 12 (2007) 475–487, https://doi.org/10.1007/S10495-006-0005-0/FIGURES/7.

[24] P. Li, H. Yao, Z. Zhang, M. Li, Y. Luo, P.R. Thompson, D.S. Gilmour, Y. Wang, Regulation of p53 target gene expression by peptidylarginine deiminase 4, Mol. Cell Biol. 28 (2008) 4745–4758, https://doi.org/10.1128/MCB.01747-07.

[25] P. Li, D. Wang, H. Yao, P. Doret, G. Hao, Q. Shen, H. Qiu, X. Zhang, Y. Wang, G. Chen, Y. Wang, Coordination of PAD4 and HDAC2 in the regulation of p53-target gene expression, Oncogene 29 (2010) 3153–3162, https://doi.org/10.1038/onc.2010.51.

[26] K. Nakashima, T. Hagiwara, M. Yamada, Nuclear localization of peptidylarginine deiminase V and histone deimination in granulocytes, J. Biol. Chem. 277 (2002) 49562–49568, https://doi.org/10.1074/JBC.M208795200.

[27] J.E. Jones, C.P. Causey, B. Knuckley, J.L. Slack-Noyes, P.R. Thompson, Protein arginine deiminase 4 (PAD4): current understanding and future therapeutic potential, Curr. Opin. Drug Discov. Dev 12 (2009) 627.

[28] D. Chen, M. Ma, H. Hong, S.S. Koh, S.M. Huang, B.T. Schurter, D.W. Aswad, M. R. Stallcup, Regulation of transcription by a protein methyltransferase, Science 284 (1999) 2174–2177, https://doi.org/10.1126/science.284.5423.2174.

[29] K. Funabashi, M. Sawata, A. Nagai, M. Akimoto, R. Mashimo, H. Takahara, K. Kizawa, P.R. Thompson, K. Ite, K. Kitanishi, M. Unno, Structures of human peptidylarginine deiminase type III provide insights into substrate recognition and inhibitor design, Arch. Biochem. Biophys. 708 (2021) 108911, https://doi.org/10.1016/J.ABB.2021.108911.

[30] O. Rechiche, T. Verne Lee, J. Shaun Lott, Structural characterization of human peptidyl-arginine deiminase type III by X-ray crystallography, Acta Crystallogr. F77 (2021) 334–340, https://doi.org/10.1107/S2053230X21009195.

[31] N. Horikoshi, H. Tachiwana, K. Saito, A. Osakabe, M. Sato, M. Yamada, S. Akashi, Y. Nishimura, W. Kagawa, H. Kurumizaka, Structural and biochemical analyses of the human PAD4 variant encoded by a functional haplotype gene, Acta Crystallogr. D67 (2011) 112–118, https://doi.org/10.1107/S0907444910051711.

[32] S.C. Gill, P.H. von Hippel, Calculation of protein extinction coefficients from amino acid sequence data, Anal. Biochem. 182 (1989) 319–326, https://doi.org/10.1016/0003-2697(89)90602-7.

[33] M. Fuentes-Baile, D. Bello-Gil, E. Pérez-Valenciano, J.M. Sanz, P. García-Morales, B. Maestro, M.P. Ventero, C. Alenda, V.M. Barberá, M. Saceda, CLyta-DAAO, free and immobilized in magnetic nanoparticles, induces cell death in human cancer cells, Biomolecules 10 (2020) 222, https://doi.org/10.3390/biom10020222.

[34] M.P. Ventero, M. Fuentes-Baile, C. Quereda, E. Perez-Valeciano, C. Alenda, P. Garcia-Morales, D. Esposito, P. Dorado, V.M. Barbera, M. Saceda, Radiotherapy resistance acquisition in glioblastoma. Role of SOCS1 and SOCS3, PLoS One 14 (2019), e0212581, https://doi.org/10.1371/journal.pone.0212581.

[35] Y. Nozaki, The preparation of guanidine hydrochloride, Methods Enzymol. 26 (1972) 43–50, https://doi.org/10.1016/S0076-6879(72)26005-0.

[36] P. Cimmperman, D. Matulis, Protein thermal denaturation measurements via a fluorescent dye, in: A. Podjrany, A. Dejaegere, B. Kieffer (Eds.), Biophysical Approaches Determining Ligand Binding to Biomolecular Targets: Detection, Measurement and Modelling, Royal Society of Chemistry, London, 2011, pp. 247–274, https://doi.org/10.1039/9781849732666-00247.

[37] A. Velazquez-Campoy, J. Sancho, O. Abian, S. Vega, Biophysical screening for identifying pharmacological chaperones and inhibitors against conformational and infectious diseases, Curr. Drug Targets 17 (2016) 1492–1505, https://doi.org/10.2174/1389450117666160201110449.

[38] S. Benjwal, S. Verma, K.-H. Röhm, O. Gursky, Monitoring protein aggregation during thermal unfolding in circular dichroism experiments, Protein Sci. 15 (2006) 635–639, https://doi.org/10.1110/PS.051917406.

[39] C.A. Royer, Fluorescence spectroscopy, in: N. Shirley (Ed.), Protein Stability and Folding, Humana Press, Totowa, NJ, 1995, pp. 65–89, https://doi.org/10.1385/0-89603-301-5:65.

[40] C.M. Doyle, J.A. Rumfeldt, H.R. Broom, A. Broom, P.B. Stathopulos, K.A. Vassall, J. J. Almey, E.M. Meiering, Energetics of oligomeric protein folding and association, Arch. Biochem. Biophys. 531 (2013) 44–64, https://doi.org/10.1016/J.ABB.2012.12.005.

[41] L.M. Gloss, Equilibrium and kinetic approaches for studying oligomeric protein folding, Methods Enzymol. 466 (2009) 325–357, https://doi.org/10.1016/S0076-6879(09)66014-6.

[42] J. Backmann, G. Schäfer, L. Wyns, H. Bönisch, Thermodynamics and kinetics of unfolding of the thermostable trimeric adenylate kinase from the archaeon *Sulfolobus acidocaldarius*, J. Mol. Biol. 284 (1998) 817–833, https://doi.org/10.1006/JMBI.1998.2216.

[43] J.L. Neira, F. Hornos, J. Bacarizo, A. Cámara-Artigás, J. Gómez, The monomeric species of the regulatory domain of tyrosine hydroxylase has a low conformational stability, Biochemistry 55 (2016) 3418–3431, https://doi.org/10.1021/ACS.BIOCHEM.6B00135/SUPPL_FILE/BI6B00135_SI_001.PDF.

[44] A. Šali, T.L. Blundell, Comparative protein modelling by satisfaction of spatial restraints, J. Mol. Biol. 234 (1993) 779–815, https://doi.org/10.1006/JMBI.1993.1626.

[45] M.J. Abraham, T. Murtola, R. Schulz, S. Páll, J.C. Smith, B. Hess, E. Lindah, GROMACS: high performance molecular simulations through multi-level parallelism from laptops to supercomputers, Software 1–2 (2015) 19–25, https://doi.org/10.1016/J.SOFTX.2015.06.001.

[46] K. Lindorff-Larsen, S. Piana, K. Palmo, P. Maragakis, J.L. Klepeis, R.O. Dror, D. E. Shaw, Improved side-chain torsion potentials for the Amber ff99SB protein force field, Proteins Struct. Funct. Bioinforma. 78 (2010) 1950–1958, https://doi.org/10.1002/PROT.22711.

[47] W.L. Jorgensen, J. Chandrasekhar, J.D. Madura, R.W. Impey, M.L. Klein, Comparison of simple potential functions for simulating liquid water, J. Chem. Phys. 79 (1998) 926, https://doi.org/10.1063/1.445869.

[48] J.L. Neira, B. Rizzuti, J.L. Iovanna, Determinants of the pKa values of ionizable residues in an intrinsically disordered protein, Arch. Biochem. Biophys. 598 (2016) 18–27, https://doi.org/10.1016/J.ABB.2016.03.034.

[49] S. Evoli, R. Guzzi, B. Rizzuti, Molecular simulations of β-lactoglobulin complexed with fatty acids reveal the structural basis of ligand affinity to internal and possible external binding sites, Proteins Struct. Funct. Bioinforma. 82 (2014) 2609–2619, https://doi.org/10.1002/PROT.24625.

[50] B. Rizzuti, V. Daggett, Using simulations to provide the framework for experimental protein folding studies, Arch. Biochem. Biophys. 531 (2013) 128–135, https://doi.org/10.1016/J.ABB.2012.12.015.

[51] M. Jamroz, M. Orozco, A. Kolinski, S. Kmiecik, Consistent view of protein fluctuations from all-atom molecular dynamics and coarse-grained dynamics with knowledge-based force-field, J. Chem. Theor. Comput. 9 (2013) 119–125, https://doi.org/10.1021/CT300854W/SUPPL_FILE/CT300854W_SI_002.PDF.

[52] A. Kuriata, A.M. Gierut, T. Oleniecki, M.P. Ciemny, A. Kolinski, M. Kurcinski, S. Kmiecik, CABS-flex 2.0: a web server for fast simulations of flexibility of protein structures, Nucleic Acids Res. 46 (2018) W338–W343, https://doi.org/10.1093/NAR/GKY356.

[53] X. Chang, J. Han, Expression of peptidylarginine deiminase type 4 (PAD4) in various tumors, Mol. Carcinog. 45 (2006) 183–196, https://doi.org/10.1002/MC.20169.

[54] X. Chang, J. Han, L. Pang, Y. Zhao, Y. Yang, Z. Shen, Increased PADI4 expression in blood and tissues of patients with malignant tumors, BMC Cancer 9 (2009) 40, https://doi.org/10.1186/1471-2407-9-40.

[55] N. Moshkovich, H.J. Ochoa, B. Tang, H.H. Yang, Y. Yang, J. Huang, M.P. Lee, L. M. Wakefield, Peptidylarginine deiminase IV regulates breast cancer stem cells via a novel tumor cell-autonomous suppressor role, Cancer Res. 80 (2020) 2125–2137, https://doi.org/10.1158/0008-5472.CAN-19-3018.

[56] O. Laptenko, C. Prives, Transcriptional regulation by p53: one protein, many possibilities, Cell Death Differ. 13 (2006) 951–961, https://doi.org/10.1038/SJ.CDD.4401916.

[57] B. Vogelstein, D. Lane, A.J. Levine, Surfing the p53 network, Nature 408 (2000) 307–310, https://doi.org/10.1038/35042675.

[58] O.B. Ptitsyn, Molten globule and protein folding, Adv. Protein Chem. 47 (1995) 83–229, https://doi.org/10.1016/S0065-3233(08)60546-X.

[59] Y.-H. Chen, J.T. Yang, K.H. Chau, Determination of the helix and β form of proteins in aqueous solution by circular dichroism, Biochemistry 13 (2002) 3350–3359, https://doi.org/10.1021/BI00713A027.

[60] S. Vuilleumier, J. Sancho, R. Loewenthal, A.R. Fersht, Circular dichroism studies of barnase and its mutants: characterization of the contribution of aromatic side chains, Biochemistry 32 (1993) 10303–10313.

[61] S.M. Kelly, T.J. Jess, N.C. Price, How to study proteins by circular dichroism, Biochim. Biophys. Acta Protein Proteonomics 1751 (2005) 119–139, https://doi.org/10.1016/J.BBAPAP.2005.06.005.

[62] S. Kelly, N. Price, The use of circular dichroism in the investigation of protein structure and function, Curr. Protein Pept. Sci. 1 (2000) 349–384, https://doi.org/10.2174/1389203003381315.

[63] R.W. Woody, Circular dichroism, Methods Enzymol. 246 (1995) 34–71, https://doi.org/10.1016/0076-6879(95)46006-3.

[64] J.L. Neira, S. Vega, S. Martínez-Rodríguez, A. Velázquez-Campoy, The isolated GTPase-activating-protein-related domain of neurofibromin-1 has a low conformational stability in solution, Arch. Biochem. Biophys. 700 (2021) 108767, https://doi.org/10.1016/J.ABB.2021.108767.

[65] A.M. Giudici, J.G. Hernández-Cifre, A. Cámara-Artigas, F. Hornos, S. Martínez-Rodríguez, J. Carlos Alvarez-Pérez, I. Díaz-Cano, M. Esther Fárez-Vidal, J.L. Neira, The isolated armadillo-repeat domain of Plakophilin 1 is a monomer in solution with a low conformational stability, J. Struct. Biol. 211 (2020) 107569, https://doi.org/10.1016/J.JSB.2020.107569.

[66] C. Díaz-García, F. Hornos, A.M. Giudici, A. Cámara-Artigas, J.R. Luque-Ortega, A. Arbe, B. Rizzuti, C. Alfonso, J.K. Forwood, J.L. Iovanna, J. Gómez, M. Prieto, A. Coutinho, J.L. Neira, Human importin α3 and its N-terminal truncated form, without the importin-β-binding domain, are oligomeric species with a low conformational stability in solution, Biochim. Biophys. Acta Gen. Subj. 1864 (2020) 129609, https://doi.org/10.1016/J.BBAGEN.2020.129609.

[67] Y.L. Liu, Y.H. Chiang, G.Y. Liu, H.C. Hung, Functional role of dimerization of human peptidylarginine deiminase 4 (PAD4), PLoS One 6 (2011), e21314, https://doi.org/10.1371/JOURNAL.PONE.0021314.

[68] R. Day, B.J. Bennion, S. Ham, V. Daggett, Increasing temperature accelerates protein unfolding without changing the pathway of unfolding, J. Mol. Biol. 322 (2002) 189–203, https://doi.org/10.1016/S0022-2836(02)00672-1.

[69] B. Rizzuti, V. Daggett, R. Guzzi, L. Sportelli, The early steps in the unfolding of azurin, Biochemistry 43 (2004) 15604–15609, https://doi.org/10.1021/BI048685T.

[70] L.M. Contreras, P. Sevilla, A. Cámara-Artigas, J.G. Hernández-Cifre, B. Rizzuti, F. J. Florencio, M.I. Muro-Pastor, J.G. de la Torre, J.L. Neira, The cyanobacterial ribosomal-associated protein LrtA from Synechocystis sp. PCC 6803 is an oligomeric protein in solution with chameleonic sequence properties, Int. J. Mol. Sci. 19 (2018) 1857, https://doi.org/10.3390/IJMS19071857.

[71] A. Guglielmelli, B. Rizzuti, R. Guzzi, Stereoselective and domain-specific effects of ibuprofen on the thermal stability of human serum albumin, Eur. J. Pharmaceut. Sci. 112 (2018) 122–131, https://doi.org/10.1016/J.EJPS.2017.11.013.

[72] M. Hollstein, D. Sidransky, B. Vogelstein, C.C. Harris, p53 mutations in human cancers, Science 253 (1991) 49–53, https://doi.org/10.1126/SCIENCE.1905840.

[73] S.E. Kern, J.A. Pietenpol, S. Thiagalingam, A. Seymour, K.W. Kinzler, B. Vogelstein, Oncogenic forms of p53 inhibit p53-regulated gene expression, Science 256 (1992) 827–830, https://doi.org/10.1126/SCIENCE.1589764.

[74] N. Moshkovich, H.J. Ochoa, B. Tang, H.H. Yang, Y. Yang, J. Huang, M.P. Lee, L. M. Wakefield, Peptidylarginine Deiminase IV regulates breast cancer stem cells via a novel tumor cell-autonomous suppressor role, Cancer Res. 80 (2020) 2125–2137. https://doi.org/10.1158/0008-5472.

[75] V.A. Brentville, M. Vankemmelbeke, R.L. Metheringham, L.G. Durrant, Post-translational modifications such as citrullination are excellent targets for cancer therapy, Semin. Immunol. 47 (2020) 101393. https://doi.org/10.1016/j.smim.2020.101393.

[76] Y. Zhou, N. Mittereder, G.P. Sims, Perspective on protein arginine deiminase activity—Bicarbonate is a pH-independent regulator of citrullination, Front. Immunol. 9 (2018), https://doi.org/10.3389/FIMMU.2018.00034.

[77] B. Knuckley, M. Bhatia, P.R. Thompson, Protein arginine deiminase 4: evidence for a reverse protonation mechanism, Biochemistry 46 (2007) 6578–6587. https://doi.org/10.1021/bi700095s.

[78] E. Persi, M. Duran-Frigola, M. Damaghi, W.R. Roush, P. Aloy, J.L. Cleveland, R. J. Gillies, E. Ruppin, Systems analysis of intracellular pH vulnerabilities for cancer therapy, Nat. Commun. 9 (2018) 1–11, https://doi.org/10.1038/s41467-018-05261-x.

[79] V. Estrella, T. Chen, M. Lloyd, J. Wojtkowiak, H.H. Cornnell, A. Ibrahim-Hashim, K. Bailey, Y. Balagurunathan, J.M. Rothberg, B.F. Sloane, J. Johnson, R. A. Gatenby, R.J. Gillies, Acidity generated by the tumor microenvironment drives local invasion, Cancer Res. 73 (2013) 1524–1535, https://doi.org/10.1158/0008-5472.CAN-12-2796.

[80] K. Arita, H. Hashimoto, T. Shimizu, K. Nakashima, M. Yamada, M. Sato, Structural basis for Ca^{2+}-induced activation of human PAD4, Nat. Struct. Mol. Biol. 11 (2004) 777–783, https://doi.org/10.1038/nsmb799.

[81] S.E. Jackson, How do small single-domain proteins fold? Folding Des. 3 (1998) R81–R91, https://doi.org/10.1016/S1359-0278(98)00033-9.

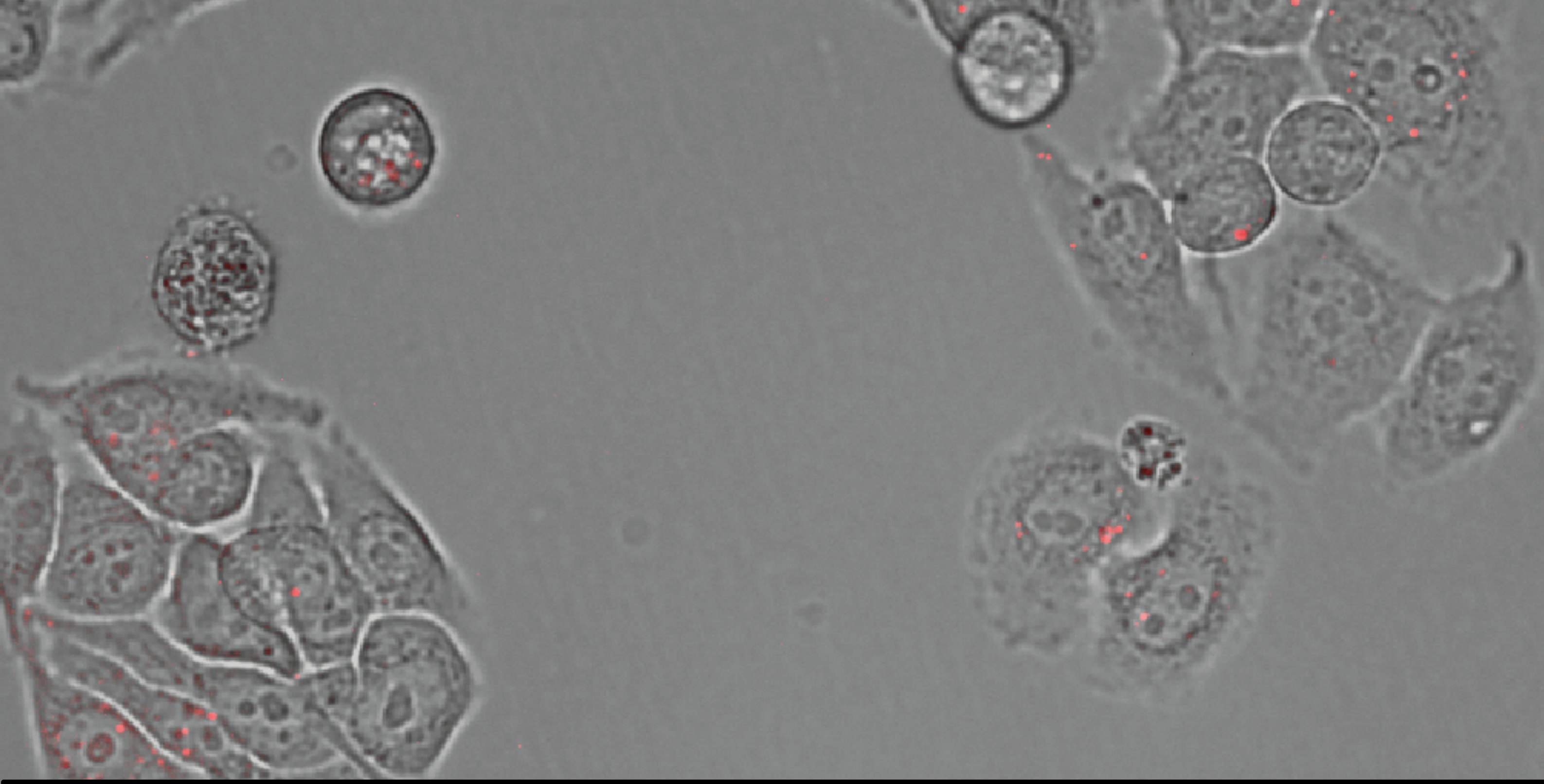

CHAPTER 5

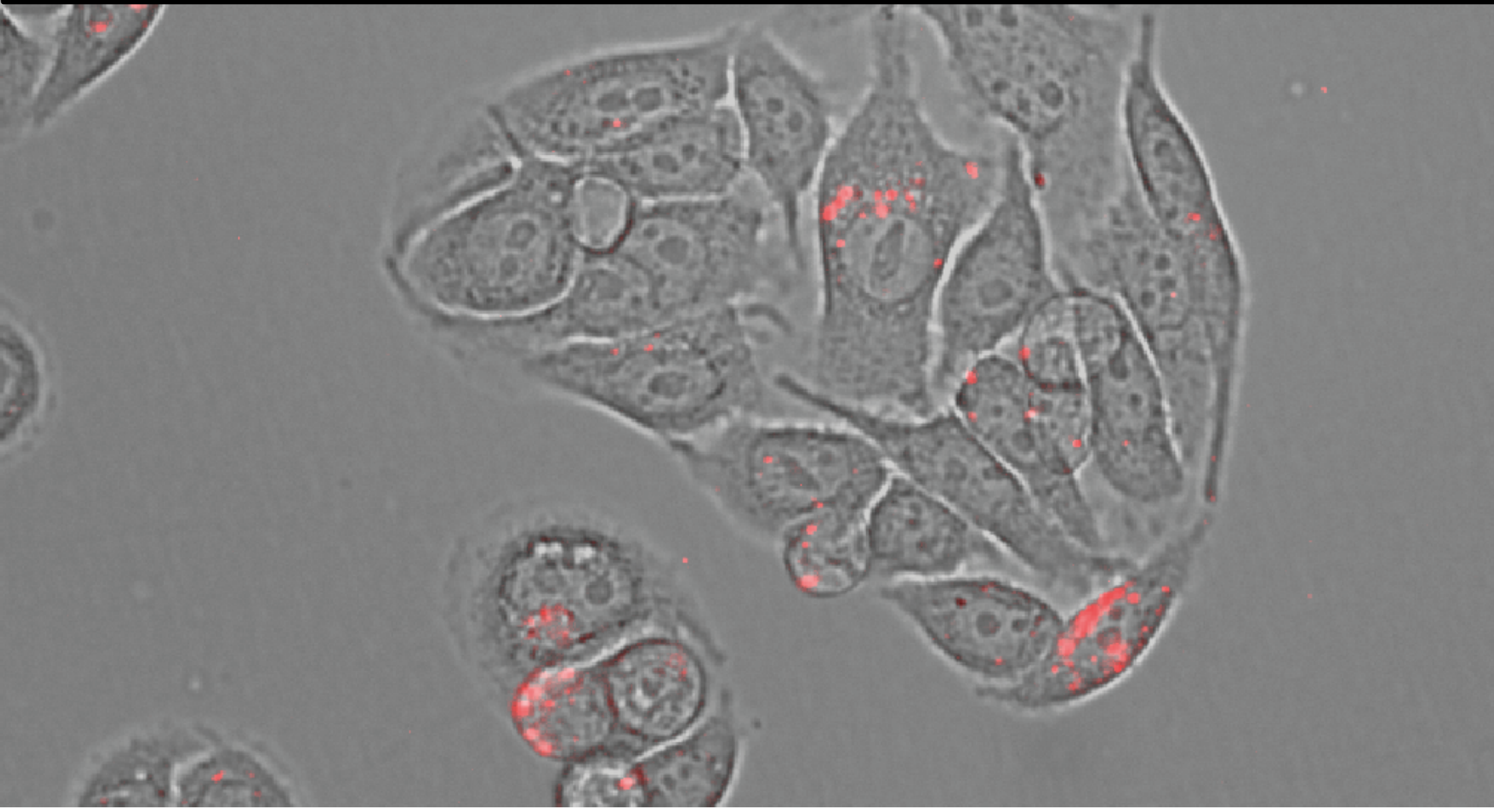

4.5 Chapter 5. PADI4 and its role in cancer progression (Unpublished Results)

As PADI4 is involved in cancer progression, we investigated whether a well-known PADI4 inhibitor, GSK484, could have an effect on GBM and PDAC cell proliferation. First, we performed a WB assay to determine the differences among the seven GBM cell lines (Figure 17).

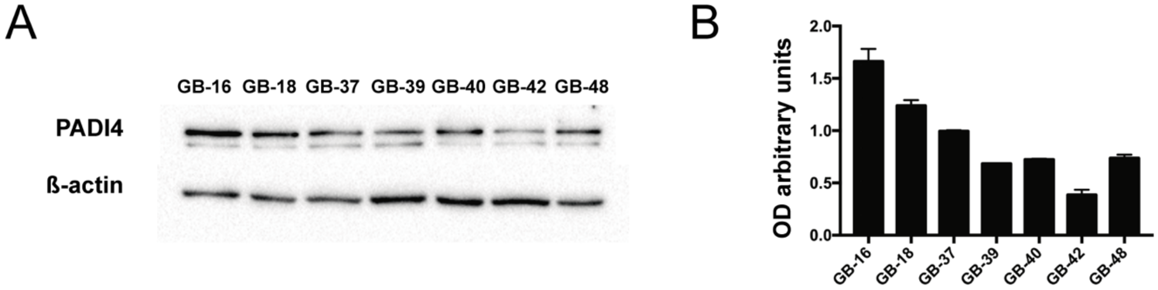

Figure 17. PADI4 expression in GBM cell lines. (A) Western Blot of seven GBM cell lines. (B) Densitometric quantifications of PADI4 protein level relative to ß-actin. A representative immunoblot is shown. Values represent the mean ± SD from three independent experiments. OD, Optical Density.

The above graph shows that GB-16 and GB18 had a higher expression of PADI4 than the other five cell lines, being the GB-42 cell line the one showing the lowest expression. Then, we measured the antiproliferative effect of GSK484 using the MTT assay. The results showed that GB-18 was the most sensitive cell line followed by GB-39, and GB-42, while GB-16, GB-37, and GB-48 were most resistant to GSK484 treatment as shown with the IC_{50} (Figure 18). On the other hand, the RWP-1 cell line was only partially sensitive to this treatment. These results were consistent with those of WB, in which GB-39 and GB-42 had the lowest expression of PADI4 and were very sensitive to treatment. Similarly, GB-16 had the highest expression of the protein and was one of the most resistant to treatment, together with GB-37 and GB-48. Surprisingly, although GB-18 had high protein expression, it was the most sensitive to the inhibitor.

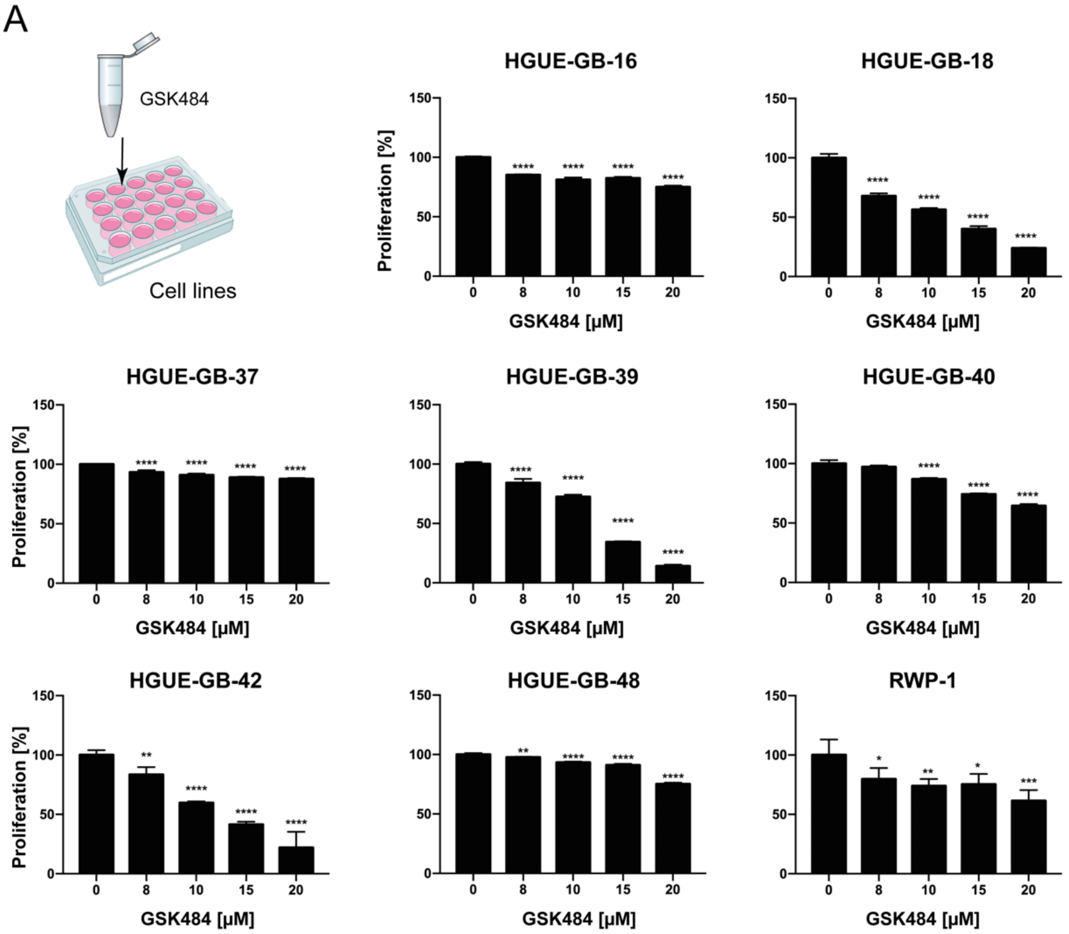

B

Cell lines	GB-16	GB-18	GB-37	GB-39	GB-40	GB-42	GB-48	RWP-1
IC_{50}	ND	11.64	ND	12.67	25.41	12.73	29.20	39.72

Figure 18. GSK484 effect on GBM and RWP-1cell lines proliferation. (A) Cancer cells were treated with increasing concentrations of GSK484. Proliferation was measured in GBM and PDAC cell lines. (B) IC_{50} for those cell lines was calculated and shown in the table. The red color represents the IC_{50}, values >20 µM, and with ND (no data), the cell lines that do not reach an IC_{50} value. Asterisks indicate the statistical significance of the results (* $p<0.05$, ** $p<0.01$, ** $p<0.01$, **** $p<0.0001$).

As previously tested for other drugs, we wondered whether GSK484 loaded in small EVs had a higher effect on cell proliferation than the administration of the drug alone. We used the direct incubation method to load GB-39 small EVs with 63 µM GSK484 (GB-39 EVs^{GSK484}). Then, we performed HPLC analysis to measure the amount of drug that finally was loaded into small EVs (0.045 µM) (Figure 19 A). As shown in Figure 19B, the use of GB-39 EV^{GSK484} at a lower concentration lead to a great decrease in GB-39 cell proliferation at every concentration ranging from 5 to 50 %; at 50 % concentration, the decrease in cell proliferation was 21 %.

This treatment had a slight effect on the GB-42 cell line, with only an 8 % antiproliferative effect at 50 % concentration, and the same effect was observed in the RWP-1 cell line, with a major effect observed at 12.5 and 25 %, with a decrease in cell proliferation of 15 % (Figure 19B). It should be noted that in GB-42 and RWP-1, the treatment was not dose-dependent, corroborating our previous observations that small EVs show target specificity for their parental cell line.

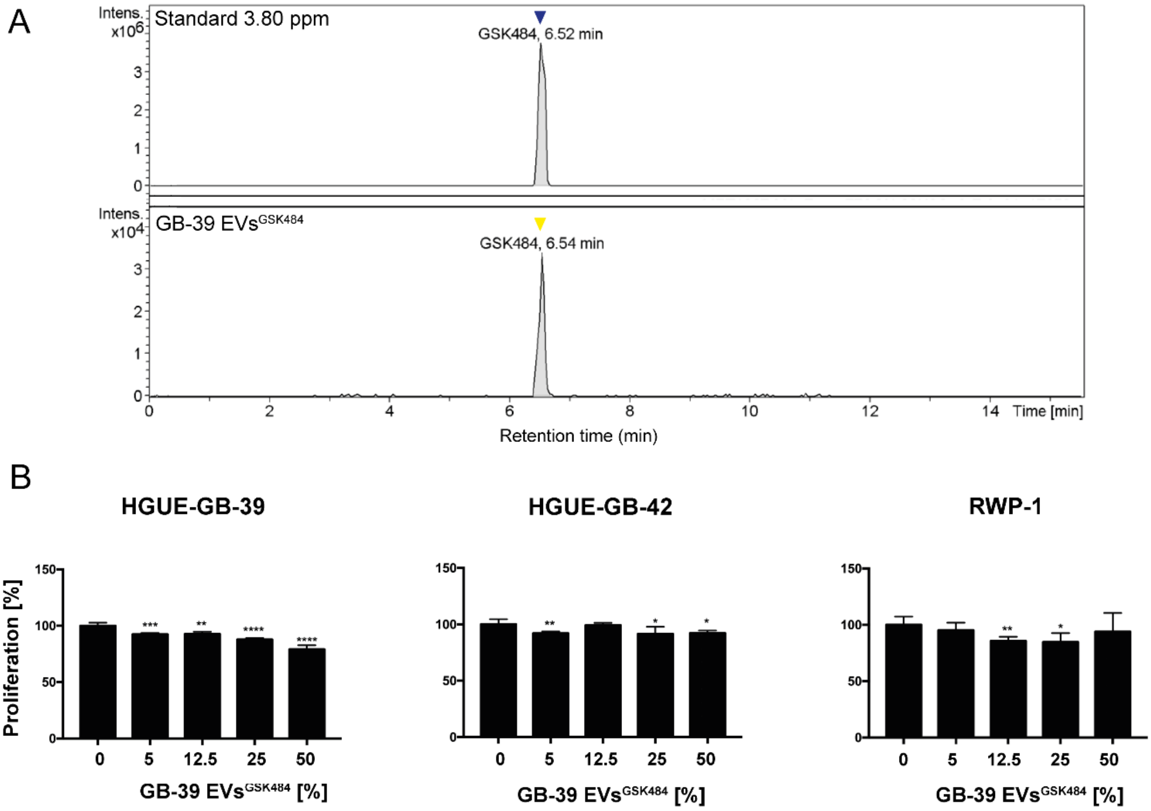

5% GB-39 EVs ^{GSK484} = 0.002 μM GSK484
12.5% GB-39 EVs ^{GSK484} = 0.005 μM GSK484
25% GB-39 EVs ^{GSK484} = 0.011 μM GSK484
50% GB-39 EVs ^{GSK484} = 0.022 μM GSK484

Figure 19. HPLC-MS analysis of small EVs sample RWP-1 EVs^{GSK484} and cell proliferation effect. (A) The amount of GSK484 incorporated into small EVs was quantified by HPLC. The dark blue arrow indicates the standard GSK484 (3.80 ppm) at 6.52 min retention time. The yellow arrow indicates the GB-39 EVs^{GSK484} sample (direct incubation) (0.023 μg/mL) at a retention time of 6.54 min. (B) Small EVs of GB-39 were loaded directly with a 63 μM concentration of GSK484 (GB-39 EVs^{GSK484}). Small EVs alone or serial dilutions of GB-39 EVs^{GSK484} were applied to the GB-39, GB-42, and RWP-1 cell lines, and their effect on proliferation was measured. The red box indicates the equivalence of concentrations. Asterisks indicate the statistical significance of the results (*p<0.05, **p<0.01, ***p<0.001, ****p<0.0001). EVs, extracellular vesicles; Intens, intensity.

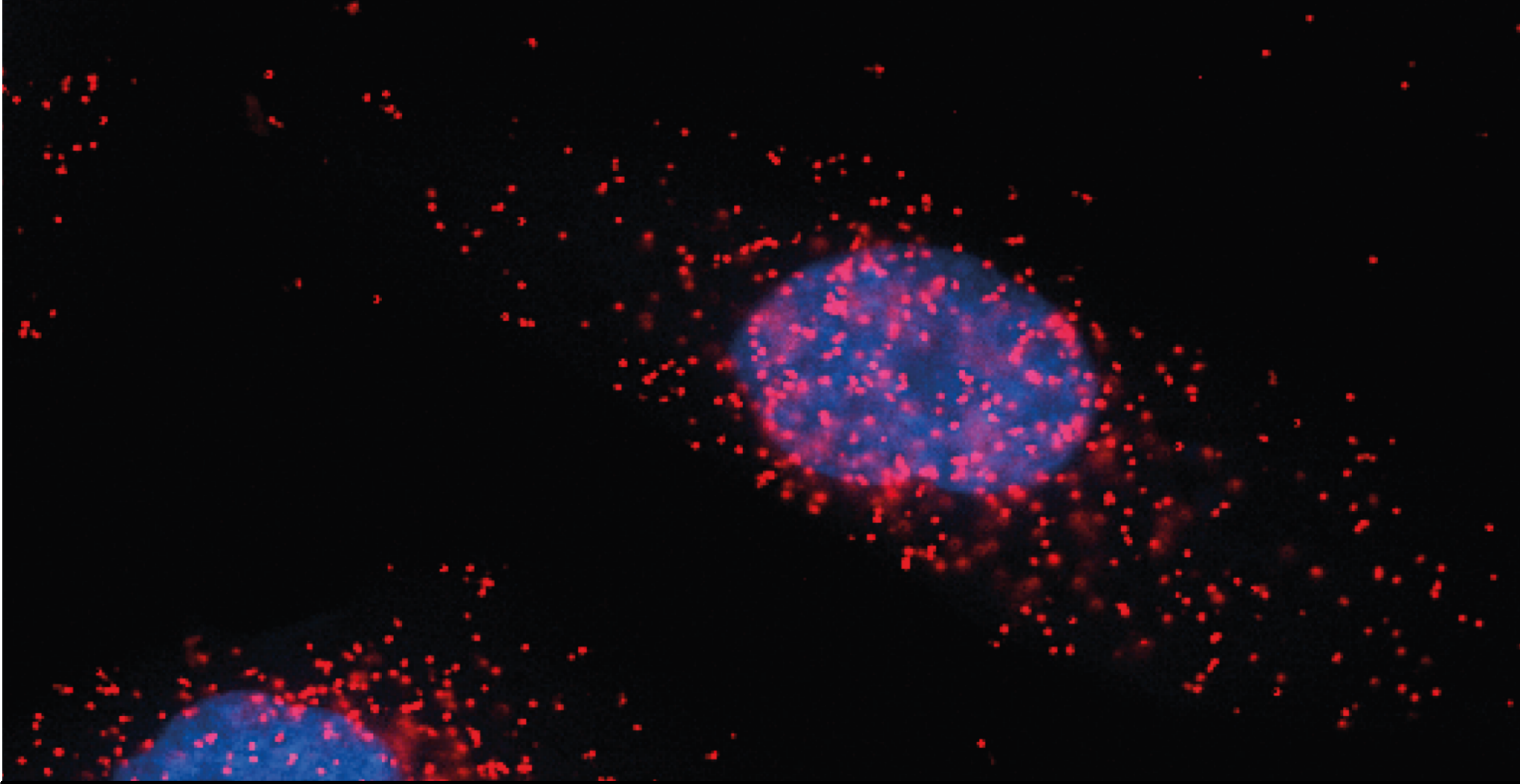

CHAPTER 6

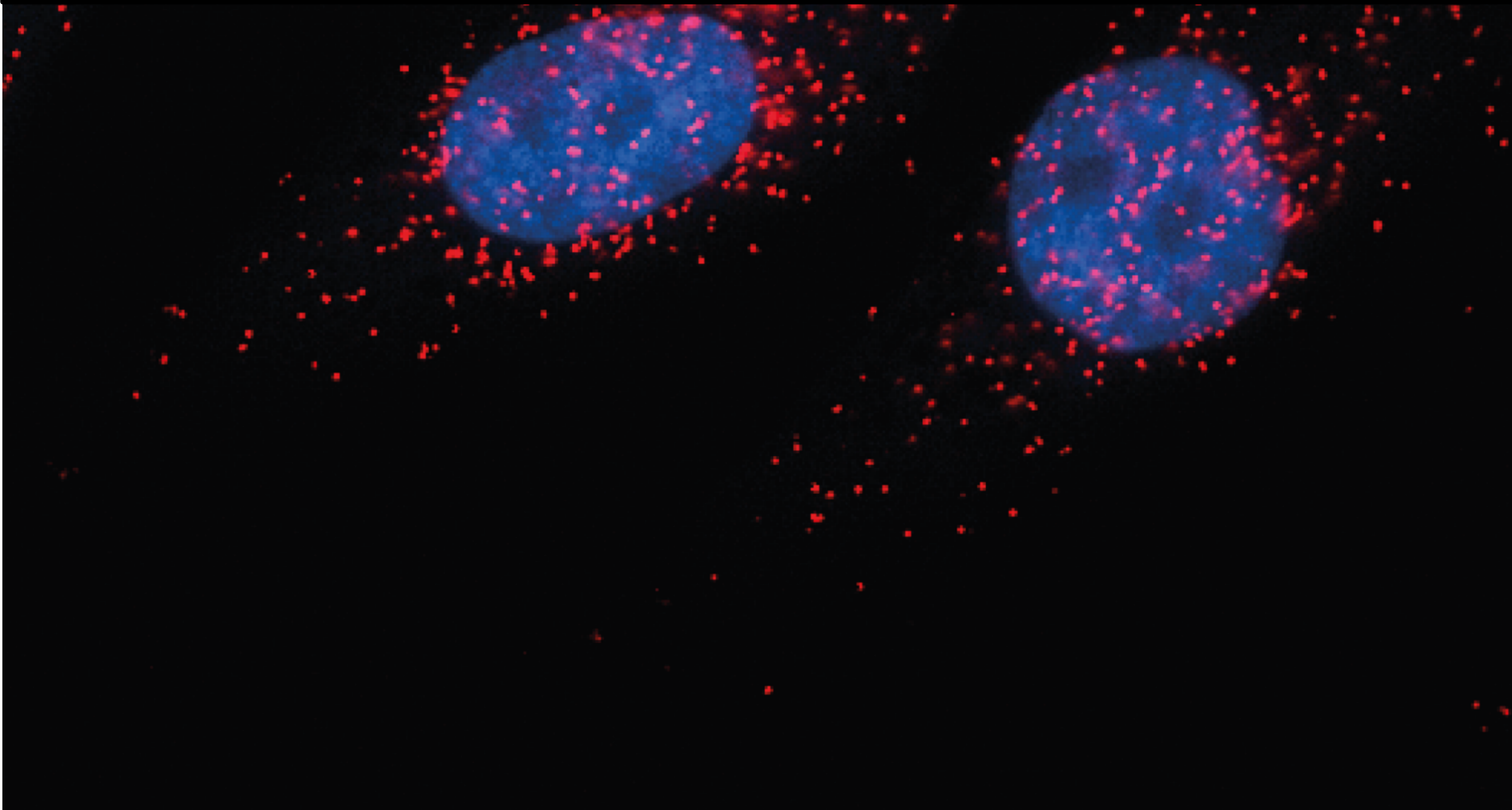

4.6 Chapter 6. Intrinsically disordered chromatin protein NUPR1 binds to the enzyme PADI4

Summary of the results

In this study, we described the interaction between NUPR1 and PADI4. NUPR1 is an 82-residue-long, intrinsically disordered protein involved in various cellular processes, including carcinogenesis. PADI4 is an enzyme that modifies proteins by citrullination, and its deregulation has been correlated with several diseases, including cancer. Citrullination is a post-translational modification converting the amino acid arginine into citrulline. In this study, we used *in cellulo*, *in vitro,* and *in silico* techniques namely, fluorescence, far-uV CD, nuclear magnetic resonance spectroscopy (NMR), molecular dynamics (MD) simulation, immunofluorescence (IF), and PLA, to investigate the interaction between NUPR1 and PADI4.

We expressed and purified recombinant NUPR1 and PADI4 proteins, then used NMR to identify the specific regions of NUPR1 that bind to PADI4, as we had the assignment of NUPR1. We found that the region around the 30s of NUPR1 was involved in binding to PADI4. Binding *in vitro* was also confirmed by fluorescence and far-uV CD. Besides, the blind molecular docking corroborates this finding, as we were able to obtain a NUPR1-PADI4 complex model.

To verify the *in cellulo* localization of the proteins, we performed IF assays with seven GBM cell lines, and the result was nuclear colocalization in every patient-derived cell line. Therefore, we used the PLA technique to investigate the interaction between NUPR1 and PADI4. This sensitive method resolves the binding of proteins that occurs at distances of less than 16 Å. It uses pairs of antibodies conjugated to complementary oligonucleotides that recognize and bind to the target proteins in close proximity. When the antibodies bind to their target proteins, the oligonucleotides are brought into close proximity and a ligation reaction occurs, producing a DNA template that can be amplified using fluorescent probes, and the interaction is visualized by fluorescence microscopy. As a result of the application of PLA, we observed red dots that confirmed a positive interaction between the two proteins, which occurred mostly in the nuclei of all GBM cell lines.

In summary, our findings indicate binding between PADI4 and NUPR1, suggesting that this interaction may have implications for cancer therapy.

Intrinsically Disordered Chromatin Protein NUPR1 Binds to the Enzyme PADI4

Salomé Araujo-Abad [1,2†], José L. Neira [1,3*†], Bruno Rizzuti [3,4], Pilar García-Morales [1], Camino de Juan Romero [1,5], Patricia Santofimia-Castaño [6*] and Juan Iovanna [6]

1 - ***IDIBE,*** *Universidad Miguel Hernández, 03202 Elche (Alicante), Spain*

2 - ***Centro de Biotecnología,*** *Universidad Nacional de Loja, Avda. Pío Jaramillo Alvarado s/n, Loja, 110111 Loja, Ecuador*

3 - ***Institute of Biocomputation and Physics of Complex Systems – Joint Unit GBsC-CSIC-BIFI,*** *Universidad de Zaragoza, 50018 Zaragoza, Spain*

4 - ***CNR-NANOTEC,*** *SS Rende (CS), Department of Physics, University of Calabria, 87036 Rende, Italy*

5 - ***Unidad de Investigación,*** *Fundación para el Fomento de la Investigación Sanitaria y Biomédica de la Comunidad Valenciana (FISABIO), Hospital General Universitario de Elche, Camí de l'Almazara 11, 03203 Elche (Alicante), Spain*

6 - ***Centre de Recherche en Cancérologie de Marseille,*** *INSERM U1068, CNRS UMR 7258, Aix-Marseille Université and Institut Paoli-Calmettes, Parc Scientifique et Technologique de Luminy, 13288 Marseille, France*

Correspondence to José L. Neira and Patricia Santofimia-Castaño: IDIBE, Edificio Torregaitán, Universidad Miguel Hernández, Avda. del Ferrocarril s/n, 03202 Elche (Alicante), Spain (J.L. Neira). Centre de Recherche en Cancérologie de Marseille, INSERM U1068, CNRS UMR 7258, Aix-Marseille Université and Institut Paoli-Calmettes, Parc Scientifique et Technologique de Luminy, 13288 Marseille, France (P. Santofimia-Castaño).*jlneira@umh.es (J. L. Neira), patricia.santofimia@inserm.fr (P. Santofimia-Castaño)*

https://doi.org/10.1016/j.jmb.2023.168033
Edited by Monika Fuxreiter

Abstract

The nuclear protein 1 (NUPR1) is an intrinsically disordered protein involved in stress-mediated cellular conditions. Its paralogue nuclear protein 1-like (NUPR1L) is p53-regulated, and its expression down-regulates that of the *NUPR1* gene. Peptidyl-arginine deiminase 4 (PADI4) is an isoform of a family of enzymes catalyzing arginine to citrulline conversion; it is also involved in stress-mediated cellular conditions. We characterized the interaction between NUPR1 and PADI4 *in vitro*, *in silico*, and *in cellulo*. The interaction of NUPR1 and PADI4 occurred with a dissociation constant of 18 ± 6 μM. The binding region of NUPR1, mapped by NMR, was a hydrophobic polypeptide patch surrounding the key residue Ala33, as pinpointed by: (i) computational results; and, (ii) site-directed mutagenesis of residues of NUPR1. The association between PADI4 and wild-type NUPR1 was also assessed *in cellulo* by using proximity ligation assays (PLAs) and immunofluorescence (IF), and it occurred mainly in the nucleus. Moreover, binding between NUPR1L and PADI4 also occurred *in vitro* with an affinity similar to that of NUPR1. Molecular modelling provided information on the binding hot spot for PADI4. This is an example of a disordered partner of PADI4, whereas its other known interacting proteins are well-folded. Altogether, our results suggest that the NUPR1/PADI4 complex could have crucial functions in modulating DNA-repair, favoring metastasis, or facilitating citrullination of other proteins.

Introduction

Peptidyl-arginine deiminases (PADI, EC 3.5.3.15), or L-arginine iminohydrolases, catalyze Ca(II)-dependent hydrolysis (deimination or citrullination) of peptidyl-arginine to peptidyl-citrulline. This post-translational modification (PTM) is irreversible and leads to the loss of a positive charge in the protein, which may cause functional alterations. The number of PADI isotypes in vertebrates increased during evolution from one in fishes and amphibians, to five human genes encoding PADI isoforms: PADI1, PADI2, PADI3, PADI4 and PADI6.[1–8] Each of these enzymes has a tissue-specific expression pattern that depends on the cell differentiation stage, and on the overall physiological or pathological conditions.[1] PADI4 was initially cloned from human myeloid leukemia HL-60 cells, after been induced by retinoic acid.[2] PADI4 is usually located in cytoplasmic granules of inflammatory cells (eosinophil, neutrophils and macrophages), mammary gland cells, stem cells, and in several tumor and metastatic tissues[9–14]; it is expressed in the cytosol and in the nucleus. Several PADI4 haplotype mutants show an increase in their enzymatic activity during apoptosis occurring *via* the mitochondrial pathway.[10] In addition, PADI4 is involved in the expression of the *p53* gene and of other *p53*-target genes,[9,15,16] as well as in p53-regulated PTMs of several proteins[17] and in p53-histone modification and alteration of the chromatin structure.[13] DNA-histone interaction is charge-dependent, and any change in the isoelectric point of a histone, including citrullination, will weaken protein–protein interactions (PPIs) involving such modified proteins.[13]

Since cancer tissues are persistently exposed to oxidative stress, activation of PADI4 in cells would possibly be related with cellular stress conditions[13]: PADI4 could work as a tumor suppressor mediating the apoptotic process in damaged cells. We have recently shown that PADI4 is a dimeric protein expressed in glioblastoma (GBM), pancreatic adenocarcinoma, and colon cancer.[18] Furthermore, PADI4 binds to importin α3 (Imp α3), a member of the armadillo (ARM) repeat-containing family of proteins, to allow its translocation into the cell nucleus,[19] and to plakophilin 1 (PKP1),[20] another protein with an ARM-repeat architecture.

NUPR1 is an 82-residue-long (8 kDa), highly basic, monomeric intrinsically disordered protein (IDP) that is overexpressed during the acute phase of pancreatitis, and in the development and regeneration of pancreas.[21] NUPR1 does not have any stable structure,[22,23] in fact, there is no evidence of transient secondary or tertiary structure along any patch in its sequence when it is isolated in solution. Furthermore, when NUPR1 binds to other macromolecules, it remains fuzzy (disordered) in the corresponding complexes.[24–27] NUPR1 binds to DNA,[24] as it happens to other chromatins, and it is involved in its repairing.[25] It is translocated into the nucleus by means of importin α3,[26,27] and possibly other importin species. It does interact with different proteins during transcription, where it is considered a crucial protein, as well as being an essential element in the stress-cell response and cell-cycle regulation, although its exact function is not known.[25,26,28–32] In all these PPIs, or in the binding to DNA, NUPR1 uses two hydrophobic regions, the so-called “hot spots”, centered around residues Ala33 and Thr68.[30,31,33] The expression of the *NUPR1* gene is down-regulated by NUPR1L, a 100-residue-long NUPR1 isoform; in turn, NUPR1L expression is p53-regulated.[34] NUPR1L translocates to the nucleus of the cell, by means of a fully characterized nuclear localization signal,[35] and there it binds to DNA.[34] Threading and homology-based modelling studies suggest that NUPR1L has properties analogous to those of members of the HMG-like family of chromatin regulators. NUPR1L is an oligomeric IDP,[36] as proven by biophysical and spectroscopic methods.[37]

It has previously been shown that both NUPR1 and PADI4 are involved in stress-cell processes, sharing several regulation routes with other proteins[25,26,38–41] and intervene in the development of several types of cancer. Moreover, they share the same localization inside the cell and have complementary isoelectric points. Therefore, we hypothesized that NUPR1 and PADI4 could interact *in cellulo*. In addition, we have recently shown that the same proteins binding to NUPR1 are also capable of interacting with NUPR1L[37]; hence, in this work, we also investigated whether there was binding between NUPR1L and PADI4. To characterize the binding between PADI4 and both NUPR1 or NUPR1L, we carried out *in cellulo*, *in vitro* and *in silico* experiments. Spectroscopic techniques complemented by molecular simulations were used, while *in cellulo* assays were carried out by means of proximity ligation assay (PLA) and immunofluorescence (IF). Our hypothesis-driven experiments showed binding between these proteins both *in cellulo* and *in vitro*, with an affinity of ∼10 μM. The binding region of NUPR1 involved a hydrophobic patch surrounding the key residue Ala33 (hereafter referred to as the “30 s region”), as shown by NMR. NUPR1 remained disordered in the complex, as it occurs when it takes part in the formation of other complexes.[24–27,42] Blind molecular docking studies carried out by using the X-ray structure of PADI4[43] in interaction with all possible polypeptide patches of NUPR1 showed that the binding region involved Ala33 and its hydrophobic surroundings, as happens with other PPIs where NUPR1 is involved.[25–27,30–33] This finding was further confirmed by protein-engineering studies: the interaction with PADI4 was fully abolished *in vitro*, when mutations at Ala33 occurred. Similarly to other protein partners of NUPR1, NUPR1L was also capable of binding to PADI4, with a dissociation constant similar to that of wild-type NUPR1, as measured by fluorescence. To the best of our knowledge, NUPR1 and NUPR1L are unconventional molecular partners of PADI4, compared to its other known interacting proteins, because of their intrinsically disordered nature. Our findings suggest that NUPR1 may play a PADI4–associated function, perhaps involving the common p53-route, which may help to explain both its gene regulatory and oncogenic functions.

Results

PADI4 and NUPR1 interacted in vitro

To test whether PADI4 could bind to NUPR1 *in vitro*, we followed an experimental approach combining fluorescence, CD, and NMR, together with the use of two mutants of NUPR1 (Thr68Gln and Ala33Gln/Thr68Gln) to define the interacting region of NUPR1 involved in the binding.

Fluorescence was used to determine whether there was a change in: (i) the value of the maximum wavelength in the emission spectrum; (ii) the fluorescence intensity observed at that maximum wavelength; or (iii) both these physical parameters, when the spectrum of the complex was compared to that obtained from the addition of the spectra of the two isolated proteins. A variation in fluorescence intensity by excitation at 280 nm was observed when the complex of PADI4 with NUPR1 was formed (Figure 1 (A)), but there were no changes in the position of the maximum wavelength. Similar variations were observed by excitation at 295 nm. These findings suggest that there was binding between the two proteins, as monitored by fluorescence.

Next, we carried out far-UV CD measurements, to elucidate whether there were changes in the intensity or the shape of the addition spectrum and that of the complex. This comparison could allow us to conclude whether secondary structural changes in any of the proteins occurred when they were mixed together. The far-UV addition spectrum was identical to that of the complex (Figure 1 (B)). Since NUPR1 is an IDP, with a much smaller size than PADI4, and a spectrum typical of a random-coil conformation, with a minimum at ∼200 nm[24,25] (Figure S1), our far-UV CD results can be rationalized by considering that the spectroscopic signal was mainly due to the native structure of the latter. The X-ray structure of PADI4 is composed of two domains: an immunoglobulin-like domain at the N terminus, and an α/β-propeller one (containing the active site) at the C-terminus.[43] Therefore, these findings suggest that NUPR1 remained disordered upon binding to PADI4.

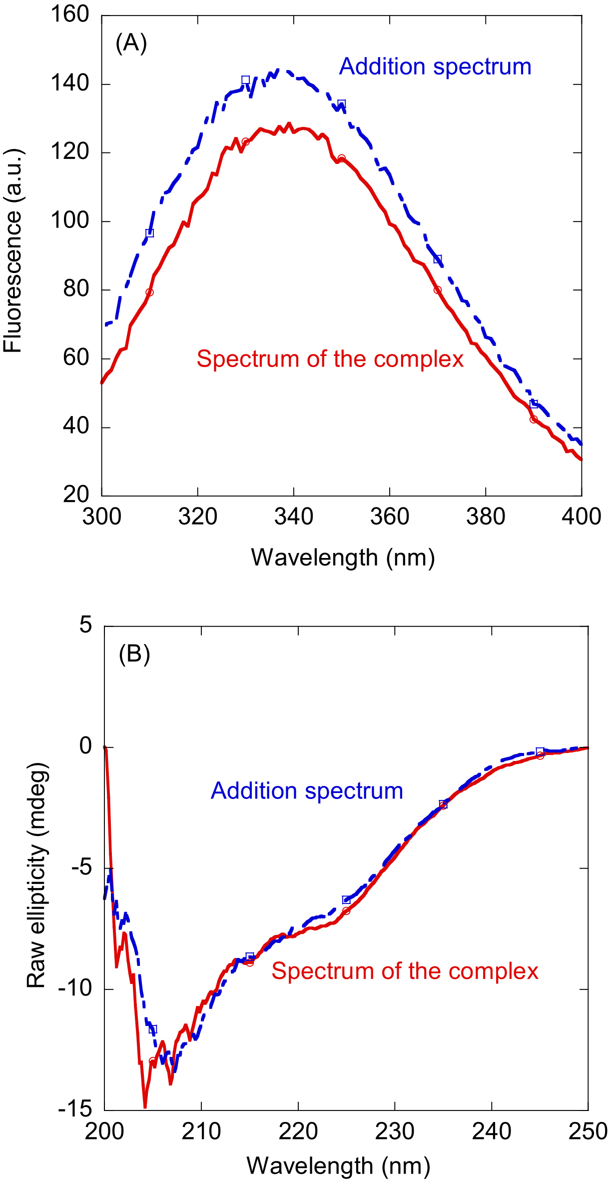

Figure 1. Binding of wild-type NUPR1 to PADI4 as monitored by spectroscopic techniques: (A) Fluorescence spectrum obtained by excitation at 280 nm of the NUPR1/PADI4 complex, and addition spectrum obtained by the sum of the spectra of the two isolated macromolecules. (B) Far-UV CD spectrum of the NUPR1/PADI4 complex, and addition spectrum obtained by the sum of the spectra of the two isolated macromolecules.

To characterize the molecular bases behind the formation of the NUPR1/PADI4 complex, we sought to determine the NUPR1 regions involved in the binding. Because we have previously reported the NMR assignment of all residues of wild-type NUPR1[25] (Biological Magnetic Resonance Data Bank entry n. 19364), we used 2D ^{1}H-^{15}N heteronuclear single quantum correlation (HSQC) spectra of wild-type NUPR1 to monitor any possible changes in chemical shifts and/or signal intensities upon PADI4 addition. We carried out the experiments at pH 7.2, a value at which PADI4 is stable and has a native structure.[18] At this pH, only the residues of wild-type NUPR1 most protected from solvent-exchange could be observed,[30] resulting in spectra with an unusually low number of detected signals for an 82-residue-long polypeptide chain (Figure 2). The additional presence of PADI4 in the solution resulted in no changes in the chemical shifts of the signals of the spectrum, but rather in a smaller signal intensity of the cross-peaks compared to those of the spectrum of isolated wild-type NUPR1 for residues Leu29, Tyr30 and Arg82. Furthermore, the signals of residues Ser31 and Ala33 disappeared in the presence of PADI4. This decrease in intensity, or even the complete disappearance of the cross-peaks, suggests a closer proximity of the NUPR1 residue to the enzyme. As there was no variation in the chemical shifts of any residue, it seems that NUPR1 remained disordered upon binding, confirming the results of the far-UV CD technique (Figure 1). Moreover, as there were changes only in the intensities of the cross-peak signals, the equilibrium exchange between the free and bound wild-type NUPR1 must be intermediate-to-slow within the NMR time-scale. It could be thought that the observed broadening of the signals is due, at least in part, by the change of medium viscosity due to the presence of PADI4 in solution,[44] or even by the typical difficulties faced when measuring peak intensities in HSQC spectra.[45] However, we did not observe broadening of signals in the spectra of NUPR1 while working at protein concentrations larger than 1 mM.[25] The fact that we observed the most severe broadening only in the above indicated cross-peaks suggests that such effect is specific and due to the binding of PADI4.

The results from NMR experiments suggest that the region around the 30 s of NUPR1 was involved in the binding to PADI4. The other ordinary hot spot region of NUPR1 in the interaction with its molecular partners is located around Thr68, and it contains the nuclear localization signal of NUPR1.[27] However, we could not figure out from the NMR experiments whether that region was also involved in the binding to PADI4, as it happens in the presence of other NUPR1 binding partners.[25,26,30] This region is more solvent-exposed than the 30 s portion of the sequence and, thus, the signals from residues belonging or close to that region disappeared at the pH value where the spectra were acquired. To test the importance of Thr68 in the binding to PADI4, we carried out fluorescence titration experiments of NUPR1 mutants, Thr68Gln and Ala33Gln/Thr68Gln, with PADI4. Whereas the fluorescence titration curve of the double mutant did not show a clear decrease of the fluorescence intensity as the mutant concentration was raised (Figure S2 (A)), the single mutant at position Thr68 did show a clear decrease of the intensity (Figure S2 (B); however, such variation could not be fit properly to Eq. (1). These findings with PADI4 suggest that Ala33 was a key residue in the binding to PADI4, whereas

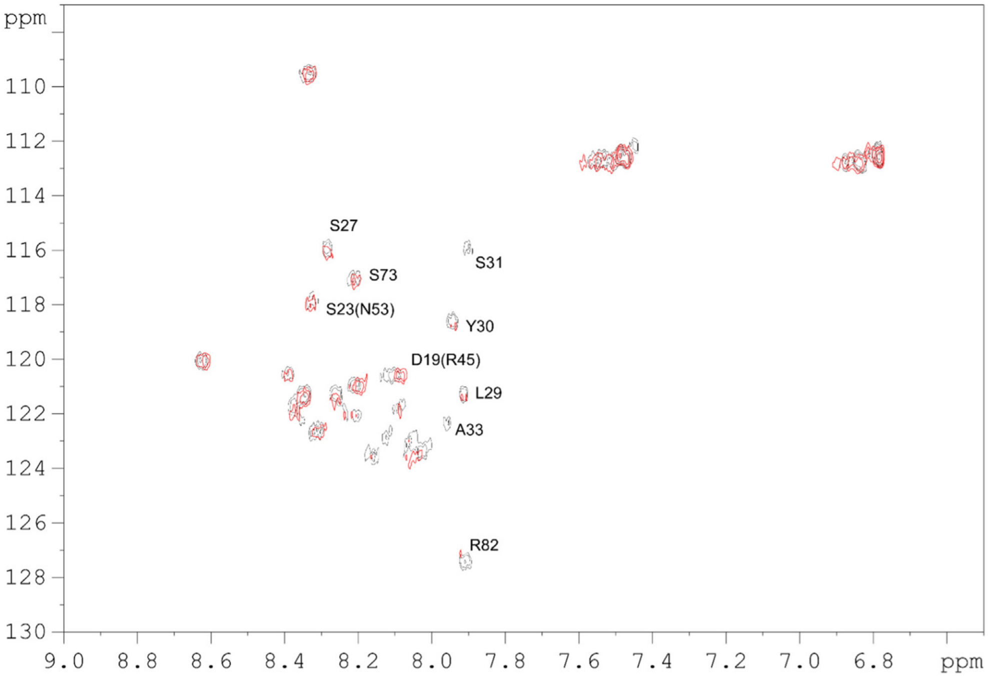

Figure 2. Interaction of wild-type NUPR1 to PADI4 mapped by 2D ^{1}H-^{15}N HSQC spectra of NUPR1: Overlay of wild-type NUPR1 spectra in the presence of 0 μM (black) and 300 μM of PADI4. Residues within parenthesis indicate signal overlapping.

removal of Thr68 resulted in a somewhat lower affinity for PADI4 than that of wild-type NUPR1 (see below), but without fully hampering the binding.

Thus, the NMR experiments further confirmed both the fluorescence and far-UV CD results, pinpointing not only the occurrence of binding, but also that such association: (i) did not alter the disordered nature of NUPR1, as shown by far-UV CD experiments; and (ii) mainly involved the 30 s region of NUPR1.

Since we observed binding between NUPR1 and PADI4, as monitored by both fluorescence and NMR, we decided to measure quantitatively such binding by using fluorescence. The titration curve yielded a dissociation constant for the complex NUPR1/PADI4 in the presence of EDTA of 18 ± 6 μM (Figure 3), and the exact same value was observed in the presence of Ca(II) (Figure S3). Thus, there were no changes in the affinity between the two proteins in the presence

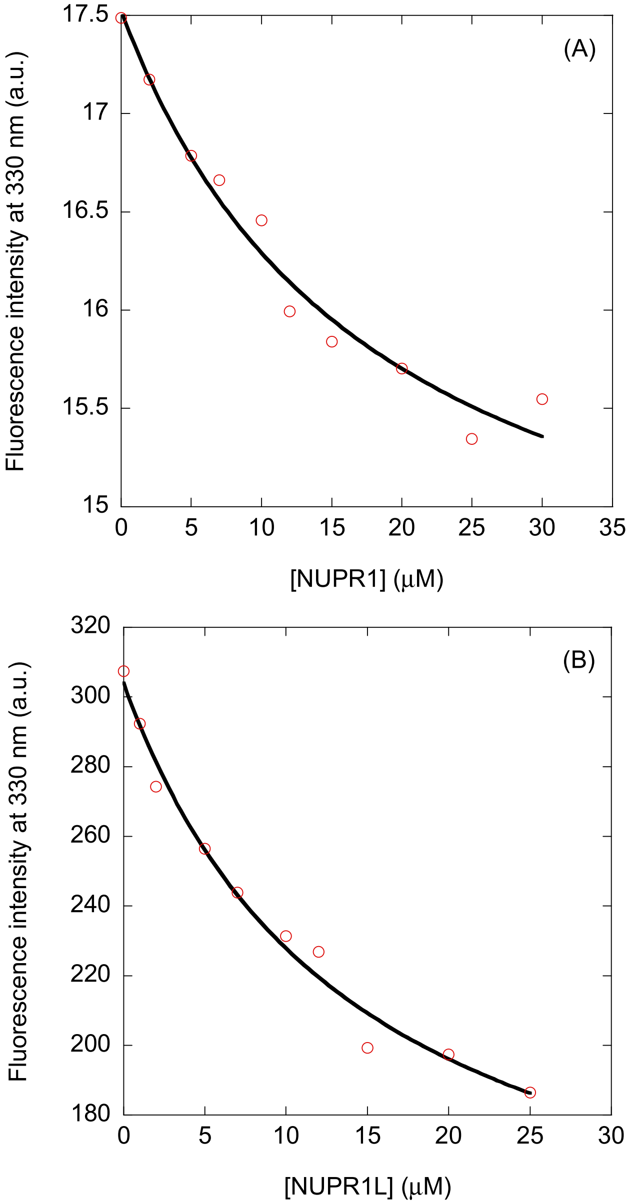

Figure 3. Measurement of the affinity of wild-type NUPR1 and NUPR1L to PADI4 as measured by fluorescence: (A) Titration curve monitoring the changes in the fluorescence at 330 nm (after excitation at 295 nm) when NUPR1 was added to PADI4 in the presence of EDTA. The fluorescence intensity is the relative signal after removal of the corresponding blank. The line through the data is the fitting to Eq. (1). (B) Titration curve monitoring the changes in the fluorescence at 330 nm (after excitation at 280 nm) when NUPR1L was added to PADI4 in the presence of EDTA. The fluorescence intensity is the relative signal after removal of the corresponding blank. The line through the data is the fitting to Eq. (2).

of the ion, and then we did not pursue any longer the investigation of the effects of Ca(II) in the binding to PADI4 of the mutants of NUPR1, or of wild-type NUPR1L. Furthermore, the binding with wild-type NUPR1 was observed to be stronger than that with the Thr68Gln mutant (Figure S2 (B)).

To sum up, NUPR1 and PADI4 interacted with an affinity constant in the low micromolar range, and the region of NUPR1 involved in the binding was mainly that around Ala33.

Computational prediction of the interaction between PADI4 and NUPR1

Molecular docking was used to obtain additional information on the binding between PADI4 and NUPR1. Because of the intrinsically unfolded structure of NUPR1, we considered the docking on the surface of PADI4 of seven-residue fragments encompassing the whole sequence of this IDP. In fact, this methodology has proved to be successful to study the binding of NUPR1 to other folded proteins[27,30,31] and to organic synthetic compounds.[46–48]

Figure 4 shows the binding affinity predicted for the various fragments, as a function of the NUPR1 sequence. The curve for wild-type NUPR1 (Figure 4, solid line) shows a global minimum in correspondence of the two seven-residue fragments centered on Asp28 and Ala33 and, therefore, overall includes the contribution of residues 25–36. The affinity was relatively favorable ($\lesssim -9$ kcal/mol), comparable to the one predicted for the association of this region to some specific binding sites of NUPR1 molecular partners, such as the basic binding patch in the groove of the armadillo-repeat domain of PKP1.[31] A less pronounced local minimum in the curve was also visible in correspondence of residues Gln13 and Glu18, and another one around Ser58. Notably, the affinity values corresponding to residues Ala33 and Thr68 in wild-type NUPR1 both dramatically reduced (by ~1 kcal/mol) upon their mutation to glutamine (Figure 4, dotted line). These results agree with our experimental findings obtained with the two NUPR1 mutants, because substitution of Ala33 fully abolished the binding to PADI4 (Figure S2 (A)), and substitution of the sole Thr68 resulted in a less favorable binding (Figure S2 (B)).

In all cases, it must be noted that the docking scores obtained in simulation should be considered as a lower limit (i.e., the affinity corresponding to the most favorable, ‘ideal’ case) for the actual binding energies of the NUPR1 fragments. In fact, the binding modes found for single NUPR1 fragments: (i) may not correspond to conformations easily accessible to each sequence segment when the intact polypeptide chain is considered; and (ii) the docking technique is more accurate in determining the enthalpic component of the binding, but does not consider the dynamics of the molecular system, which will likely tend to hamper the association in this case.

Despite the limitations of the simulation techniques discussed above, based on our findings, we could draw two simple but important conclusions. First, the simulation can correctly reproduce our experimental results, at least qualitatively, and contributes to pinpoint the region around the 30 s of NUPR1 sequence as the most important one for the binding to PADI4. This region is also the key hot spot for the interaction of NUPR1 with other molecular partners,[26,30,31] and this could be considered a further confirmation of the reliability of the simulation predictions. As a second conclusion, we point out that other regions of NUPR1 had a binding energy that almost

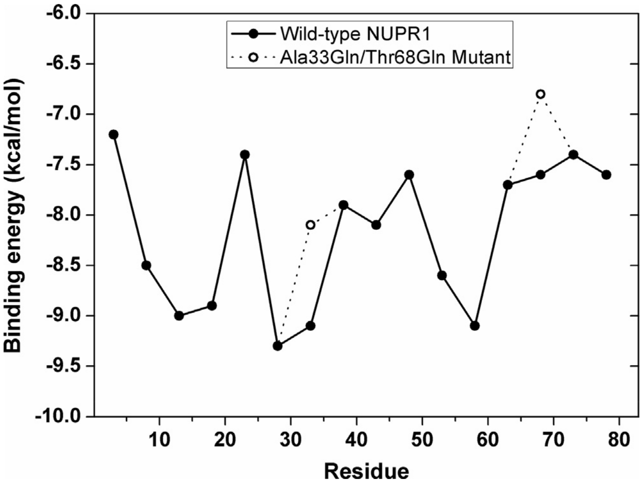

Figure 4. Predicted affinity for the binding to PADI4 of fragments of the sequence of NUPR1. The binding energy is obtained from molecular docking of seven-residue fragments performed for both wild-type NUPR1 (solid line and symbols) and the Ala33Gln/Thr68Gln protein mutant (dotted line and empty symbols).

matched that of the region around the 30 s in the interaction with the surface of PADI4, although being less favorable. In the context of a very hydrophilic and disorder-prone polypeptide chain such as NUPR1, this could be expected to result in a very dynamic and fuzzy ensemble of bound conformations of this IDP in complex with PADI4.

The most favorable docking poses obtained in simulation for the fragments of the sequence of NUPR1 were also mapped on the surface of PADI4, to identify their preferred binding locations. The results reported in Figure 5 clearly suggest the crevices at the interface of the two monomers of PADI4 as the favored region for the interaction. The docking poses were found clustered in four possible binding locations, which could be considered corresponding to two sole binding patches due to the symmetry in the structure of the PADI4 homodimer.[43] These two binding patches are at the interface between either of the two immunoglobulin-like β-structure subdomains at the N terminus, which are present in each monomer of PADI4, and the facing α -structure domain (at the C terminus) belonging to the other monomer. In particular, most of the docking poses appeared to be in contact with the immunoglobulin-like subdomains closer to the central region of PADI4. These four binding patches (or, more precisely, two couples of symmetric of patches) on the surface of PADI4 may provide a further variety of possibilities for the interaction between the two proteins.

Evidence of the interaction of NUPR1 with PADI4 in an intracellular environment

To test whether interaction between endogenous PADI4 and NUPR1 occurred within cells, we used different GBM cell lines. To perform these experiments, we used the patient-derived GBM cell lines HGUE-GB-16, HGUE-GB-18, HGUE-GB-37, HGUE-GB-39, HGUE-GB-40, HGUE-GB-42, and HGUE-GB-48.[49,50] They have been previously described to show different sensitivity/resistance profile to a variety of cancer treatments and, therefore, we hypothesized that PADI4 and NUPR1 could have different degree of association within these cell lines.[49] First, we performed IF experiments to address whether both proteins were expressed and colocalized in the same cellular compartments for the different cell lines (Figure S3). Interestingly, we found that the two proteins were highly expressed in every patient-derived cell line. Moreover, the fact that both proteins shared a nuclear staining, as shown by the colocalization with DAPI, indicates the possibility that they could interact within the nuclear compartment (Figure S3). Subsequently, we sought to confirm their interaction by using the Duolink *in situ* assay. This technique, known as PLA, resolves the binding of proteins that occurs at distances shorter than 16 Å. The green fluorescent spots, corresponding to the PLA signals, indicates that PADI4 efficiently interacted with NUPR1 within the nucleus of GBM cells (Figure 6).

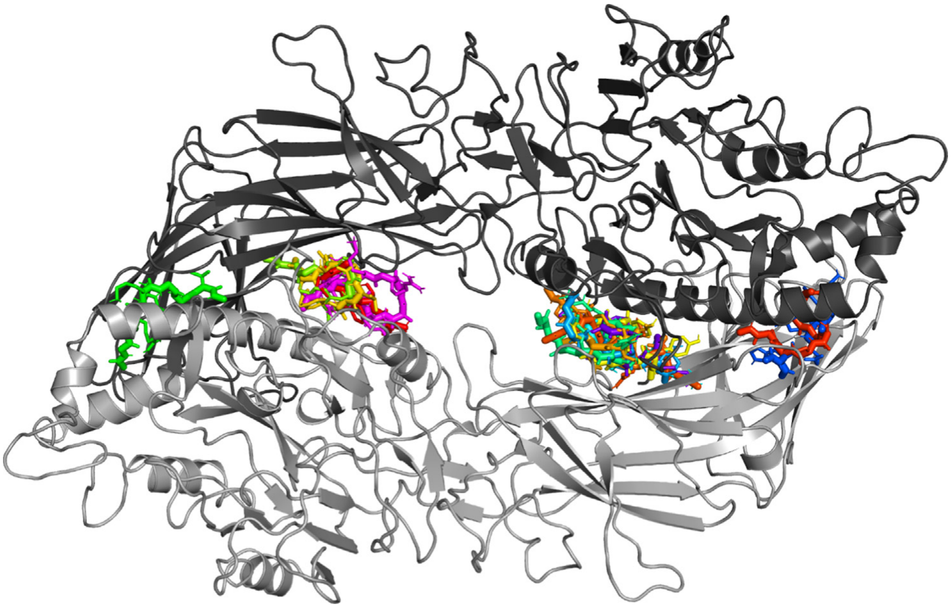

Figure 5. Predicted locations for the binding to PADI4 of fragments encompassing the sequence of NUPR1. The two monomers in the homodimer of PADI4 are represented in slightly different colors (dark and light grey). Molecular docking was performed by considering seven-residue fragments of NUPR1, overall encompassing the entire protein sequence. Fragments follow a rainbow color scheme (red → yellow → green → cyan → blue → magenta) from the N to the C terminus of NUPR1.

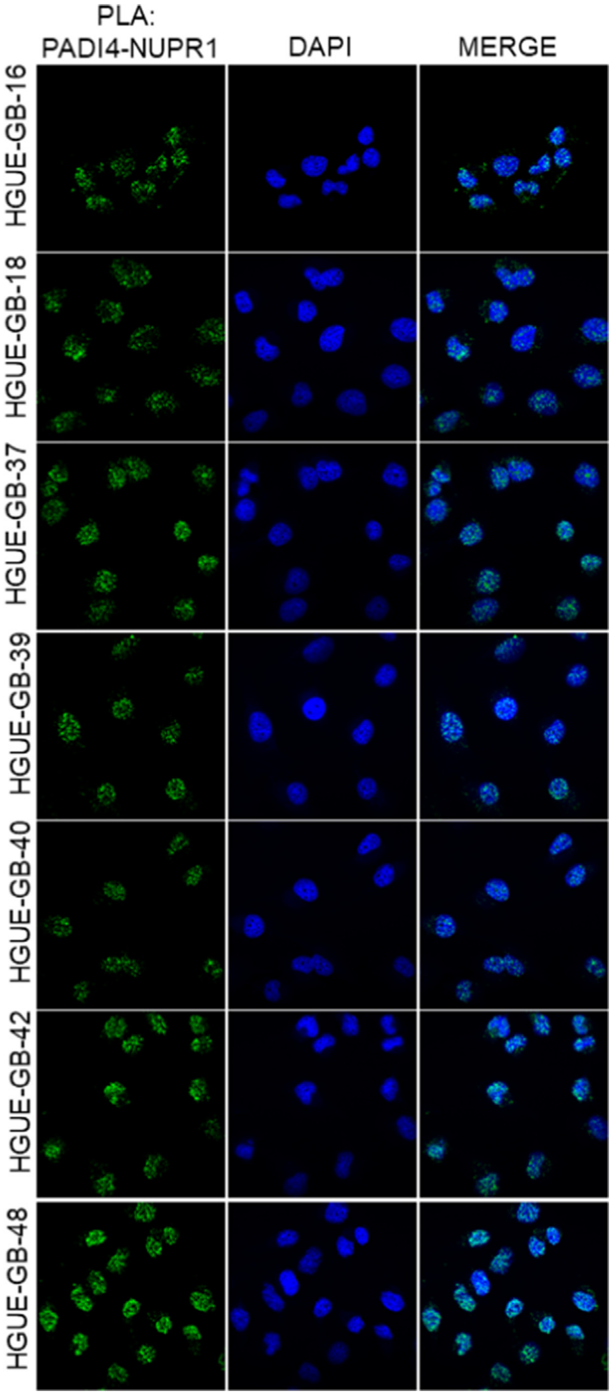

Figure 6. proximity ligation assays of PADI4 with wild-type NUPR1. Mouse anti-human PADI4 and rabbit anti-human NUPR1 were tested to reveal the interaction between the proteins in different patients-derived GBM cells.

It is important to highlight that, regardless of the patient's cell line, our results strongly indicate that PADI4 and NUPR1 are expressed, and efficiently interacted within the nuclear compartment of GBM tumor cells. As, so far, it was thought that the major role of PADI4 in the nucleus was histone citrullination, the fact that in this location it can also bind NUPR1 opens new venues to elucidate the role of both proteins in tumorigenesis.

The isoform of NUPR1, NUPR1L, also interacted with PADI4

Given that the isoform of NUPR1, i.e. NUPR1L, can interact with typical partners of NUPR1, such as prothymosin α and the C-terminal region of RING 1B,[37] we wondered whether NUPR1L could bind to PADI4, as well. As described above for NUPR1, we first performed steady-state fluorescence and far-UV CD experiments, and next we measured the affinity between NUPR1L and PADI4 by means of fluorescence titrations. In fact, we observed a variation in the intensity between the fluorescence spectrum of the complex and that obtained by the addition of the spectra of the isolated macromolecules (Figure 7 (A)), similar to the results for wild-type NUPR1 (Figure 1 (A)). On the other hand, conversely to what happened with NUPR1 (Figure 1 (B)), for NUPR1L the far-UV CD spectrum of the complex and that resulting from the addition of the spectra did show differences (Figure 7 (B)). Following the same reasoning applied above for NUPR1, these results suggest that, upon binding to PADI4, there was a certain degree of ordering in NUPR1L, which is also an IDP in isolation.[37] Fluorescence titrations of NUPR1L over PADI4, in the absence of Ca(II), led to an apparent dissociation constant of 14 ± 4 μM, which is similar, within the error, to that obtained for wild-type NUPR1 (Figure 3 (B)). Therefore, we can conclude that NUPR1L was also capable of binding to PADI4 *in vitro*.

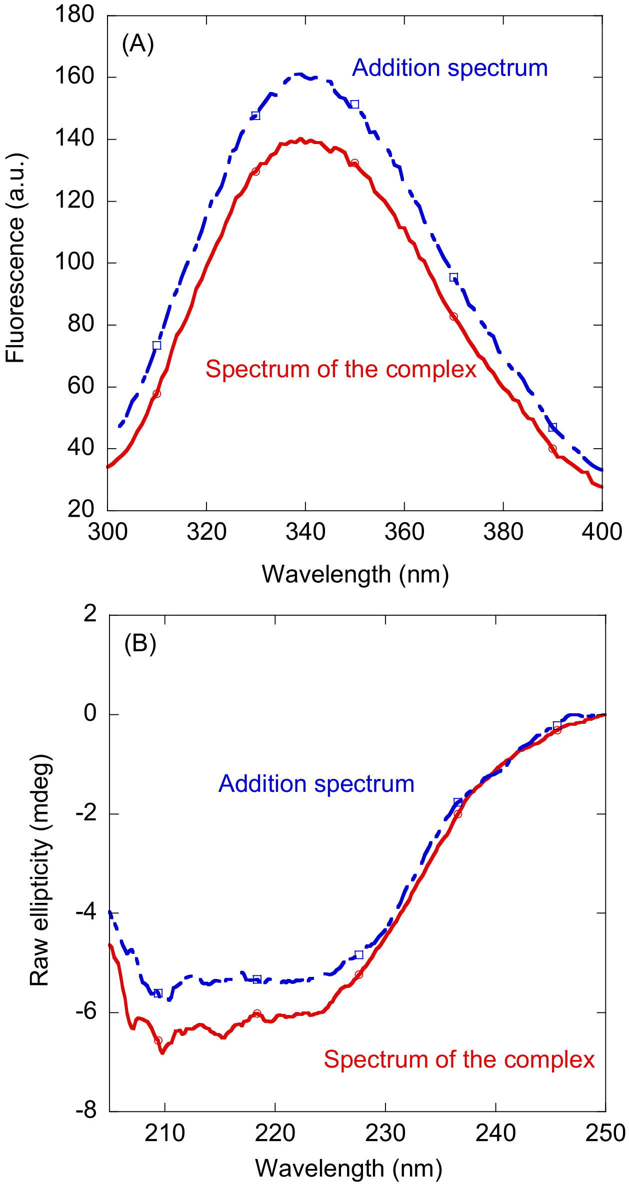

Figure 7. Binding of NUPR1L to PADI4 as monitored by spectroscopic techniques: (A) Fluorescence spectrum obtained by excitation at 280 nm of the NUPR1L/PADI4 complex, and addition spectrum obtained by the sum of the spectra of the two isolated macromolecules. (B) Far-UV CD spectrum of the NUPR1L/PADI4 complex, and addition spectrum obtained by the sum of the spectra of the two isolated macromolecules.

Discussion

NUPR1 was bound to PADI4 in vitro and in the cell

We have identified and characterized the interaction between NUPR1 and the enzyme PADI4, both being involved in stress-mediated cell responses, carcinogenesis, and cancer progression. The interaction between the two proteins was specific, as shown by two pieces of evidence: (i) the results *in cellulo* of the PLAs (Figure 4); and (ii) the findings obtained with the Thr68Gln and Ala33Gln/Thr68Gln mutants of NUPR1 *in vitro* (Figure S2). The mutations at those two specific residues decreased, or completely abolished in the case of Ala33, the interaction between NUPR1 and PADI4. The importance of residue Ala33 and of the surrounding regions of the sequence in the binding was further confirmed by the docking *in silico* of the complexes of PADI4 with wild-type NUPR1 and its mutants (Figure 4). The spectroscopic results further indicated that NUPR1 remained fuzzy in the complex formed,[42] as it happens in its other complexes either with other folded polypeptides[30–32] or with DNA.[25]

The recognition region of NUPR1 involved residues around the 30 s region in the sequence, as suggested by the NMR and protein-engineering results, and further confirmed by the docking simulations (Figures 4 and 5). The aromatic residues in this region have been previously described to intervene also in the binding to: (i) prothymosin α[33]; (ii) the C-terminal region of RING1B[30]; (iii) importin α3[26,27]; and (iv) PKP1.[31] In fact, previous molecular simulations contribute to indicate that aromatic residues in that region (Tyr30 and Tyr36) also play a role in the association to DNA[36] and in the binding of drugs designed to target NUPR1.[46–48] Not only the 30 s region of NUPR1 is a hot spot, but Thr68, as it happens in the binding with other proteins or DNA,[25–27,30,31] did also intervene in the interaction with PADI4, although it did so to a lesser extent (Figure S2). Conversely, this residue is key in the interaction with importin α3 during translocation, as its phosphorylation hampers binding to this karyopherin.[27] The fact that mutation of the sole residue Ala33 in NUPR1 can disrupt binding to another macromolecule is not unusual. A similar effect of full disruption in the binding to molecular partners by mutation of a single residue has been observed for α -synuclein[51,52] or some kinases.[53,54] In addition, our findings in this work further pinpoint that the short linear motif[55] including Ala33 was mainly responsible for the binding of NUPR1 to PADI4 (Figure 2).

Not only the intervening hot spot region, but also the measured K_d of NUPR1 for PADI4 (∼10 μM) was similar to that observed for the binding of this IDP to other proteins[25–27,30,31] and small organic compounds.[46] Such affinity is relatively small, but we believe that this low value is enough to obtain a proper control of the several regulation routes where NUPR1 intervenes,[28,29,38] achieving a high specificity despite a low affinity. Affinities in the range 1–10 μM have also been described in the formation of fuzzy complexes, involving at least an IDP that remains disordered upon binding.[42,56]

PADI4 and the NUPR1 isoform, NUPR1L, also interacted in vitro

NUPR1L is an isoform of NUPR1, and it is also an IDP, although with some evidence of residual structure. This protein is oligomeric, and capable of binding to NUPR1.[37] In contrast to what happened with NUPR1, binding of NUPR1L to PADI4 caused an ordering of the former (Figure 7 (B)), suggesting that the complex NUPR1L/PADI4 was not as disordered as that of NUPR1/PADI4. The affinity constant for PADI4 of both isoforms was similar, but it must be kept in mind that such constant for NUPR1L should include the contribution due to its self-association. Studies with other proteins capable of binding to both NUPR1L and NUPR1 have shown differences in their affinities for each isoform.[37] Conversely to what happens in the binding of NUPR1L to both prothymosin α and NUPR1,[37] it remains unclear whether its residue Trp62 was involved in the binding to PADI4, as the latter has several tryptophan residues, whose fluorescence hampers any conclusion.

Biological implications of the interaction between PADI4 and NUPR1

Although NUPR1 is an oncogene known to regulate carcinogenesis, tumorigenesis and metastasis,[38,57] it also has a suppressive function in several cancers.[38,58] On the other hand, PADI4 is activated in a large proportion of cancer tissues, probably due to citrullination of several proteins,[39,59] but it also acts as a tumor suppressor in regulating breast cancer stem cells.[60] Since both proteins can have several opposite functions (oncogene and suppression) in cancer cells, in the next paragraphs, we hypothesize how the formation of the newly-identified NUPR1/PADI4 complex, described in this work, might modulate several cell functions. Some of these hypotheses are being currently investigated in our laboratories.

PADIs catalyze the PTM of peptidyl arginine to citrulline. This citrullination reaction is a hydrolytic deamination removing the positive charge of the arginine side-chain. The human isoform PADI4 is nuclear-targeted, calcium-regulated, and it intervenes in gene regulation by citrullination of histones and in chromatin remodeling. The regions of PADI4 that are involved in the binding to NUPR1 are not yet fully experimentally identified, but based on our simulation results we predict that they are close to both the immunoglobulin-like domains and to the interface of its two monomers. It is interesting to note that the N-terminal immunoglobulin-like domains of PADI4 have been already indicated as being involved in the binding to the p53 protein[61] and of the inhibitor growth 4 (ING4), which is also citrullinated.[62] On the other hand, NUPR1 interacted with PADI4 through the hot spot comprising residues around Ala33, and with a contribution of Thr68, as shown by NMR, site-directed mutagenesis (Figure S1 (B)), and our *in silico* results (Figure 4). NUPR1 has 9 arginine residues out of 82 amino acids, at residue number 42, 45, 48, 56, 64, 75, 78, 81, and 82. Given that NUPR1 does not contain any arginine around the 30 s, which is the main interacting region with PADI4, and Arg64 and Arg75 are close to Thr68, it seems unlikely that NUPR1 is a substrate for PADI4. However, at this stage, we cannot rule out that citrullination of NUPR1 is involved in the binding between the two proteins. We hypothesize that a possible role of NUPR1/PADI4 complex formation could be the regulation of PADI4 function. PADI4 is Ca(II)-regulated, but ion concentrations required to achieve maximal PADI4 activity are 100–1000 fold higher than those observed in activated cells. On the other hand, binding of NUPR1 could modify the conformation of the PADI4 active site, through an allosteric mechanism, in a similar fashion as the binding of Ca(II) to PADI4 does. Therefore, we can speculate that PADI's calcium dependency is altered by the interaction with NUPR1. Along this hypothesis, antibodies isolated from patients with rheumatoid arthritis might bind and activate PADI4 by lowering the Ca(II) concentration required for its maximal activity.[63]

The mechanisms that regulate PADI4 function and how it works within cells remain unclear.[40,41] It is known that estrogen regulates the expression of PADI4 through both the classical and non-classical pathways.[64] It has also been reported that p53 transactivates PADI4 through a *p53*-binding site at the first intron.[15] Moreover, the significance of PADI4-mediated protein citrullination in the p53-signaling pathway has been proved by attenuating p53-mediated growth-inhibitory activity after the knockdown PADI4 expression.[17] PADI4 is involved in the repression of p53-target genes by interacting with the C-terminus of p53, as well as having other modulation effects on p53-target genes.[15,16] As PADI4 has histone-deiminase activity, it results in the negative regulation of downstream p53-target genes, and thus PADI4 functions as a p53 co-repressor. Moreover, NUPR1L is also p53-regulated, and its expression down-regulates that of the *NUPR1* gene, leading to binding to NUPR1. We suggest that the formation of the complex NUPR1/PADI4 might avoid the repression of p53 and, in addition, hampering the binding of NUPR1 by its own isoform.

In response to DNA damage, histones H3 and H4 are citrullinated by PADI4, which in turn promotes DNA fragmentation.[13] In addition, DNA damage triggers the formation of a complex between NUPR1 and the male specific lethal protein (MSL).[25,65] The NUPR1/MSL complex protects cells from death. The possibility of forming a complex NUPR1/PADI4 might hamper the activation of the two DNA-repair routes, and thus it could be a way of modulating such repair.

The role of NUPR1 in cancer progression was identified in the study of breast metastasis from breast cancer.[66] This study has shown that expression of NUPR1 allows one to discern between metastatic-potential breast cancer cells and those without such potential; that is, NUPR1 is necessary for the establishment of cells derived from breast cancer cells in a secondary organ. Citrullination of glycogen synthase kinase-3β (GSK-3β) by PADI4 induces epithelial-to-mesenchymal transition in breast cancer cells,[67] which is a key step in breast cancer cells to achieve metastasis in other organs. We suggest that the presence of NUPR1, and formation of its complex with PADI4, might hamper the citrullination of GSK-3 β,and therefore would decrease the epithelial-to-mesenchymal transition in breast cancer cells.

Altogether, then, our results demonstrate the interaction between PADI4 with NUPR1 and NUPR1L, and they might highlight the importance of this complex in tumorigenesis and shed some light in the possible regulation mechanisms of these proteins.

Materials and methods

Materials

Imidazole, Trizma base and acid, DNase, SIGMAFAST protease tablets, NaCl and Ni(II)-resin, were from Sigma (Madrid, Spain). Isopropyl-β-D-1-thiogalactopyranoside, kanamycin and ampicillin were obtained from Apollo Scientific (Stockport, UK). Dialysis tubing with a molecular weight cut-off of 3500 Da, Triton X-100, TCEP (Tris(2-carboxyethyl)phosphine) and the SDS protein marker (PAGEmark Tricolor) were from VWR (Barcelona, Spain). Amicon centrifugal devices with a molecular weight cut-off of 30 kDa or 3 kDa were from Millipore (Barcelona, Spain). The rest of the materials used were of analytical grade. Water was deionized and purified on a Millipore system.

Protein expression and purification

PADI4, NUPR1 and NUPR1L were purified as previously described.[18–20,24,25,37] Protein concentrations were determined by UV absorbance, employing an extinction coefficient at 280 nm estimated from the number of tyrosines (in particular, NUPR1 has only two tyrosine residues) and tryptophans in each protein.[68]

Fluorescence

Steady-state fluorescence. A Cary Varian spectrofluorometer (Agilent, Santa Clara, CA, USA), interfaced with a Peltier unit, was used to collect fluorescence spectra at 25 °C, by excitation at either 280 or 295 nm. The other experimental details have been described elsewhere.[69] Appropriate blank corrections corresponding to curves obtained for samples containing only buffers were made in all spectra. Following the standard protocols used in our laboratories, the samples were prepared the day before and left overnight at 5 °C; before experiments, samples were left for 1 h at 25 °C. A 1-cm path length quartz cell (Hellma, Kruibeke, Belgium) was used. Concentration of PADI4 was 2 μM (in protomer units) and those of NUPR1 or NUPR1L were 20 μM (in protomer units for the latter). Experiments were performed in 20 mM Tris buffer (pH 7.5), 5 mM TCEP, 150 mM NaCl, 10 mM EDTA and 5 % glycerol, in triplicates with newly prepared samples. Variations of results among the experiments were lower than 5 %.

Binding experiments of PADI4 with wild-type NUPR1. For the titration of wild-type NUPR1 with PADI4, increasing amounts of monomeric NUPR1, in the concentration range 0–30 μM, were added to a solution with a fixed concentration of PADI4 (2 μM, in protomer units). Experiments were carried out in the buffer described above, with the same experimental setup; experiments were also carried out in the presence of buffer, without EDTA and with 10 mM Ca(II). In all cases, the appropriate blank corrections with solutions containing only the corresponding amount of NUPR1 were applied. Spectra were corrected for inner-filter effects.[70] The titration was repeated three times, using new samples. In the three cases, the variations in the results were lower than 10 %.

The dissociation constant of the complex, K_d, was calculated by fitting the binding isotherm obtained by plotting the observed fluorescence change as a function of NUPR1 concentration to a general binding model, explicitly considering ligand depletion in solution[71,72]:

$$F = F_0 + \frac{\Delta F_{max}}{2[PADI4]_T}\left([NUPR1]_T + [PADI4]_T + K_d\right) - \sqrt{\left(\left([NUPR1]_T + [PADI4]_T + K_d\right)^2 - 4[NUPR1]_T[PADI4]_T\right)} \tag{1}$$

where F is the measured fluorescence of the solution with the fixed PADI4 concentration (2 μM, in protomer units) and a given value for NUPR1, after subtraction of the corresponding blank with the same concentration of the latter; ΔF_{max} is the largest change in the fluorescence of NUPR1 when saturation was reached, compared to the fluorescence of each isolated chain; F_0 is the fluorescence intensity when no NUPR1 was added; $[PADI4]_T$ is the constant, total concentration of PADI4 (2 μM, in protomer units); and $[NUPR1]_T$ is that of NUPR1, which was varied during the titration. Fitting to Eq. (1) was carried out by using KaleidaGraph (Synergy software, Reading, USA).

Binding experiments of PADI4 with NUPR1 mutants. For the titration of mutants with PADI4, increasing amounts of either the single mutant Thr68Gln or the double mutant Ala33Gln/Thr68Gln of NUPR1, in the concentration range 0–30 μM, were added to a solution with a fixed concentration of PADI4 (2 μM, in protomer units). Experiments were carried out as described for wild-type NUPR1, with the same experimental setup, in the presence of 10 mM EDTA.

Binding experiments of PADI4 with NUPR1L. For the titration of NUPR1L with PADI4, increasing amounts of NUPR1L species, in the concentration range 0–25 μM, were added to a solution with a fixed concentration of PADI4 (2 μM, in protomer units). Experiments were carried out in the buffer described above, with the same experimental setup, in the presence of 10 mM EDTA. In all cases, the appropriate blank corrections by using spectra obtained for solutions containing only the corresponding amount of NUPR1L were applied. Spectra were corrected for inner-filter effects.[70] The titration was repeated three times, using new samples. In the three cases, the variations in the results were lower than 10 %.

The dissociation constant of the complex, K_d, was calculated by fitting the binding isotherm obtained by plotting the observed fluorescence change as a function of NUPR1L concentration to a general binding model, explicitly considering ligand depletion in solution[71,72]:

$$F = F_0 + \frac{\Delta F_{max}}{2[PADI4]_T}\left([NUPR1L]_T + [PADI4]_T + K_d\right) - \sqrt{\left(\left([NUPR1L]_T + [PADI4]_T + K_d\right)^2 - 4[NUPR1L]_T[PADI4]_T\right)} \tag{2}$$

where the symbols in Eq. (2) have the same meaning as those in Eq. (1). However, it is important to indicate that the K_d obtained from Eq. (2) was an apparent dissociation constant, as NUPR1L is an oligomer with a self-dissociation in the order of nM.[37]

Circular dichroism (CD)

Far-UV CD spectra were collected on a Jasco J810 spectropolarimeter (Jasco, Tokyo, Japan) with a thermostated cell holder and interfaced with a Peltier unit. The instrument was periodically calibrated with (+)-10-camphorsulfonic acid. A 0.1-cm path length cell was used (Hellma, Kruibeke, Belgium). All spectra were corrected by subtracting the corresponding baseline. Concentration of each polypeptide (wild-type NUPR1, NUPR1L, or PADI4) and the buffers used were the same used for fluorescence experiments. We could not obtain meaningful data below ~200 nm, for any of the two proteins, due to the absorbance of the components of the buffer (Figure S1). Samples were prepared the day before and left overnight at 5 °C to allow them to equilibrate. Before starting the experiments, samples were further left for 1 h at 25 °C. Isothermal wavelength spectra of each isolated macromolecule (at 25 °C) and those of the corresponding complex (NUPR1/PADI4 or NUPR1L/PADI4) were acquired as an average of 6 scans, at a scan speed of 50 nm/min, with a response time of 2 s and a band-width of 1 nm.

Nuclear Magnetic Resonance (NMR)

The NMR experiments were performed on a Bruker Avance DRX-500 spectrometer (Karlsruhe, Germany) equipped with a triple resonance probe and *z*-pulse field gradients. Spectra were acquired at 25 °C and pH 7.2 (Tris, 50 mM); probe temperature was calibrated with a methanol NMR standard.[73] It is important to indicate here that the buffer employed in the NMR experiments is slightly different to that used in the far-UV CD and fluorescence experiments, to increase the signal-to-noise ratio in the spectra (which would deteriorate in the presence of high NaCl concentration, EDTA, TCEP and glycerol).

The cross-peaks in the 2D ^{1}H-^{15}N HSQC NMR spectra[74] of NUPR1 were identified by using previously determined assignments at pH 4.5.[25] We did not carry out the study of the binding between NUPR1 and PADI4 at this pH value, because the latter precipitates at acidic conditions.[18] The number of signals observed in the 2D ^{1}H-^{15}N HSQC NMR spectra at pH $\geq$ 7.0 dramatically decreased when compared to low pH due to hydrogen-exchange at physiological conditions, as it has been observed when exploring binding to other partners[30,31,75] (see also Results section).The sample containing the mixture of NUPR1 and PADI4 was prepared by using Amicon centrifugal devices of 3 kDa cut-off, where both proteins were initially mixed at dilute concentrations in buffer in 20 mM Tris (pH 7.5), 5 mM TCEP, 150 mM NaCl, 10 mM EDTA and 5 % glycerol, and then concentrated and exchanged to deuterated Tris buffer, used in NMR experiments.

Spectra were acquired in the TPPI (time proportional phase increment) mode. The concentration of ^{15}N-labeled NUPR1 was 100 μM either in isolation or in the presence of 300 μM of PADI4. The spectra were typically acquired with 2,048 complex points in the ^{1}H dimension, 60 complex points in the ^{15}N dimension, with 32 or 64 scans. Typical spectral widths for the 2D ^{1}H-^{15}N HSQC NMR spectra were 6,000 (^{1}H) and 1,500 (^{15}N) Hz. The resulting matrix of each experiment was zero-filled to double the number of original points in all dimensions, and shifted squared sine-bell apodization functions were applied before Fourier transformation. NMR data were processed and analyzed using TopSpin 1.3 (Bruker, Karlsruhe, Germany). Signal intensities in the two NMR spectra (of isolated NUPR1, and in the presence of PADI4) were measured, and in each experiment, intensities were corrected by the corresponding value of the receiver gain. Spectra were calibrated with external TSP for ^{1}H and for the indirect dimensions, as previously described.[73]

Molecular docking

Molecular docking was used to study the binding of PADI4 and NUPR1 in a simplified way, because of the relatively large size of PADI4 (a homodimer with 663 residues in each monomer) and, more importantly, the intrinsically unfolded character of NUPR1 (an 82-residue-long fully disordered sequence). The structure of PADI4 was built on the basis of the X-ray diffraction model deposited in the Protein Data Bank (PDB entry: 3APN.[43] The binding affinity towards PADI4 was predicted by considering seven-residue fragments encompassing in total the whole sequence of NUPR1, following the same protocol we adopted in other previous works.[30,31,27,76] The fragments were capped at the N- and C-terminal endings by using an acetyl and amide moiety, respectively – with the exceptions of the protein termini, where the –NH_3^+ and –COO^- groups were preserved.

The simulations were performed by using the docking engine AutoDock Vina, version 1.1.2.[77] Apolar hydrogen atoms were subsumed in the carbon atoms they are attached to, whereas polar hydrogens were explicitly considered for both the docking host protein PADI4 and the guest fragments of NUPR1. A blind exploration was carried out with an exhaustiveness twice larger with respect to the default value.[78] The search volume was centered on the PADI4 homodimer and had the size of 110 Å × 70 Å × 110 Å, which was enough to include the whole protein surface. Full flexibility due to rotations around each dihedral angle was guaranteed to the NUPR1 fragments.

Cell lines

Isolation of the seven, primary human GBM cell lines (HGUE-GB-16, HGUE-GB-18, HGUE-GB-37, HGUE-GB-39, HGUE-GB-40, HGUE-GB-42 and HGUE-GB-48) was performed from surgical washes, as reported previously.[49] GBM cells were cultured in Dulbecco's Modified Eagle's Medium: Nutrient Mixture F-12 (DMEM F-12) (Gibco, New York, USA), supplemented with 10 % (v/v) heat-inactivated fetal bovine serum (FBS) (HyClone/Cytiva, Little Chalfont, UK) and 1 % (v/v) penicillin/streptomycin mixture (Biowest, Bradenton, USA). Cells were incubated at 37 °C in a humidified 5 % CO_2 atmosphere as previously described.[49,50]

Immunofluorescence (IF)

An amount of 40,000 GBM cells were seeded in twenty-four-well plates on coverslips.[25,30] After fixation, cells were incubated with a mouse anti-PADI4 (1:200, mouse; Abcam, Cambridge, UK) primary antibody and anti-NUPR1 antibody (1:100, rabbit; homemade). After washing out the first antibody, cells were incubated with Alexa Fluor 568-labeled anti-mouse (1:500) and Alexa Fluor 488-labeled anti-rabbit (1:500) secondary antibodies (Invitrogen, Barcelona, Spain) and DAPI (4′,6-diamidino-2-phenylindole, Thermo Fisher Scientific, Valencia, Spain) was used to stain the nucleus. Image acquisition was carried out by using a confocal microscope LSM 880 (×63 lens) controlled by Zeiss Zen Black (Zeiss, Oberkochen, Germany).

proximity ligation assay (PLA)

An amount of 40,000 GBM cells of each patient were seeded in twenty-four-well plates on coverslips. Cells were assayed 24 h later. Cells were washed twice in phosphate buffer solution (PBS), fixed, washed twice again, permeabilized in PBS/0.2 % Triton X-100, and saturated with blocking solution for 30 min before immunostaining with Duolink by using PLA Technology (Merck, Madrid, Spain), following the manufacturer's protocol. Anti-PADI4 and anti-NUPR1 primary antibodies were used. Then, slides were processed for *in situ* PLA by using sequentially the Duolink In Situ Detection Reagents Green, Duolink In Situ PLA Probe Anti-Mouse MINUS, and Duolink In Situ PLA Probe Anti-Rabbit PLUS (Merck, Madrid, Spain). In these experiments, green fluorescence corresponds to the PLA-positive signal, and it indicates that the two proteins are bound to form a complex. Blue fluorescence corresponds to nuclei (so-called DAPI staining). To check the specificity of the PLA signal, negative control experiments omitting one of the primary antibodies and positive controls[25,30] were performed. Image acquisition was carried out by using the same confocal microscope described above.

Funding

This research was funded by Instituto de Salud Carlos III and European Union (ERDF/ESF, “Investing in your future”) [CP19/00095 to CdJ] [PI22/00824 to CdJ]; and Consellería de Innovación, Universidades, Ciencia y Sociedad Digital (Generalitat Valenciana) [CAICO 2021/0135 to CdJ and JLN]. SAA was recipient of a “Carolina Foundation predoctoral fellowship 2020”. SAA was supported by the Company of Biologists Ltd to travel to the laboratory of JLI and PSC (grant number DMMTF2110601). The funders had no role in the study design, data collection and analysis, decision to publish, or preparation of the manuscript.

CRediT authorship contribution statement

Salomé Araujo-Abad: Investigation, Formal analysis, Writing – review & editing. **José L. Neira:** Conceptualization, Methodology, Investigation, Formal analysis, Writing – original draft, Resources, Writing – review & editing, Funding acquisition. **Bruno Rizzuti:** Conceptualization, Methodology, Investigation, Formal analysis, Writing – original draft, Writing – review & editing. **Pilar García-Morales:** Resources, Writing – review & editing. **Camino de Juan Romero:** Conceptualization, Writing – original draft, Resources, Writing – review & editing, Funding acquisition. **Patricia Santofimia-Castaño:** Conceptualization, Methodology, Investigation, Formal analysis, Writing – original draft, Resources, Writing – review & editing, Funding acquisition. **Juan Iovanna:** Conceptualization, Methodology, Writing – review & editing, Funding acquisition.

DATA AVAILABILITY

Data will be made available on request.

DECLARATION OF COMPETING INTEREST

The authors declare that they have no known competing financial interests or personal relationships that could have appeared to influence the work reported in this paper.

Acknowledgment

BR acknowledges the kind use of computational resources of the European Magnetic Resonance Center (CERM), Sesto Fiorentino (Florence), Italy.

Appendix A. Supplementary Data

The supplementary material contains: far-UV CD spectra of isolated NUPR1 and PADI4 in 20 mM Tris buffer (pH 7.5), 5 mM TCEP, 150 mM NaCl, 10 mM EDTA and 5 % glycerol (Figure S1); fluorescence titration curves for Thr68Gln and Ala33Gln/Thr68Gln mutants of NUPR1 in the presence of PADI4 and 10 mM EDTA (Figure S2); fluorescence titration curve of wild-type NUPR1 when added to PADI4 in the presence of 10 mM Ca(II) (Figure S3); IF experiments on PADI4 with NUPR1 in several patient-derived cell lines (Figure S4). Supplementary data to this article can be found online at https://doi.org/10.1016/j.jmb.2023.168033.

Received 27 November 2022;
Accepted 21 February 2023;
Available online 27 February 2023

Keywords:
PADI4;
protein–protein interactions;
citrullination;
fluorescence;
molecular modeling

† These two authors contributed equally to this work.

Abbreviations:
CD, circular dichroism; DAPI 4′, 6-diamidino-2-phenylindole; GBM, glioblastoma; GSK-3β, glycogen synthase kinase-3β; HSQC, heteronuclear single quantum correlation; IDP, intrinsically disordered protein; IF, immunofluorescence; Impα3, human importin α3 protein; MSL, male specific lethal protein; NUPR1, nuclear protein 1; NUPR1L, nuclear protein 1-like, isoform of NUPR1; PADI, peptidyl-arginine deiminase; PBS, phosphate buffer solution; PDB, Protein Data Bank; PKP1, plakophilin 1; PLA, proximity ligation assay; PPI, protein–protein interaction; PTM, post-translational modification; UV, ultraviolet

References

1. Vossenaar, E.R., Zendman, A.J.W., van Venrooij, W.J., Pruijn, G.J.M., (2003). PAD, a growing family of citrullinating enzymes: genes, features and involvement in disease. *Bioessays* **25**, 1106–1118. https://doi.org/10.1002/bies.10357.
2. Nakashima, K., Hagiwara, T., Ishigami, A., Nagata, S., Asaga, H., Kuramoto, M., Senshu, T., Yamada, M., (1999). Molecular characterization of peptidylarginine deiminase in HL-60 cells induced by retinoic acid and 1alpha,25-dihydroxyvitamin D(3). *J. Biol. Chem.* **274**, 27786–122792. https://doi.org/10.1074/jbc274.39.27786.
3. Guerrin, M., Ishigami, A., Méchin, M.C., Nachat, R., Valmary, S., Sebbag, M., Simon, M., Senshu, T., et al., (2003). cDNA cloning, gene organization and expression analysis of human peptidylarginine deiminase type I. *Biochem. J.* **370**, 167–174. https://doi.org/10.1042/bj20020870.
4. Ishigami, A., Ohsawa, T., Asaga, H., Akiyama, K., Kuramoto, M., Maruyama, N., (2002). Human peptidylarginine deiminase type II: molecular cloning, gene organization, and expression in human skin. *Arch. Biochem. Biophys.* **407**, 25–31. https://doi.org/10.1016/s0003-9861(02)00516-7.
5. Kanno, T., Kawada, A., Yamanouchi, J., Yosida-Noro, C., Yoshiki, A., Shiraiwa, M., Kusakabe, M., Manabe, M., et al., (2000). Human peptidylarginine deiminase type III: Molecular cloning and nucleotide sequence of the cDNA, properties of the recombinant enzyme, and immunohistochemical localization in human skin. *J. Invest. Dermatol.* **115**, 813–823. https://doi.org/10.1046/j.1523-1747.2000.00131.x.
6. Chavanas, S., Méchin, M.C., Takahara, H., Kawada, A., Nachat, R., Serre, G., Simon, M., (2004). Comparative analysis of the mouse and human peptidylarginine deiminase gene clusters reveals highly conserved non-coding segments and a new human gene, PADI6. *Gene* **330**, 19–27. https://doi.org/10.1016/j.gene.2003.12.038.
7. Hriria, H., Mokrab, Y., Mizuguchi, K., (2006). The guanidino-group modifying enzymes: structural basis for their diversity and commonality. *Proteins* **64**, 1010–1023. https://doi.org/10.1002/prot.20863.
8. Dong, S., Kanno, T., Yamaki, A., Kojima, T., Shiraiwa, M., Kawada, A., Méchin, M.C., Chavanas, S., et al., (2006). NF-Y and Sp1/Sp3 are involved in the transcriptional regulation of the peptidylarginine deiminase type III gene (PADI3) in human keratinocytes. *Biochem. J.* **397**, 449–459. https://doi.org/10.1042/BJ20051939.
9. Yang, C., Dong, Z.-Z., Zhang, J., Teng, D., Luo, X., Li, D., Zhou, Y., (2021). Peptidylarginine deiminases 4 as a promising target in drug discovery. *Eur. J. Med. Chem.* **226**, https://doi.org/10.1016/j.ejmech.2021.113840 113840.
10. Slade, D.J., Horibata, S., Coonrod, S.A., Thompson, P.R., (2014). A novel role for protein arginine deiminase 4 in pluripotency: the merging role of citrullinated histone H1 in cellular programming. *Bioessays* **36**, 736–740. https://doi.org/10.1002/bies.201400057.
11. Witalison, E.E., Thompson, P.R., Hofseth, L.J., (2015). Protein arginine deiminases and associated citrullination: physiological functions and diseases associated with dysregulation. *Curr. Drug Targets* **16**, 700–710. https://doi.org/10.2174/1389450116666150202160954.
12. Wang, Y., Chen, R., Gan, Y., Ying, S., (2021). The roles of PAD2- and PAD4-mediated protein citrullination catalysis in cancers. *Int. J. Cancer* **148**, 267–276. https://doi.org/10.1002/ijc.33205.
13. Tanikawa, C., Espinosa, M., Suzuki, A., Masuda, K., Yamamoto, K., Tsuchiya, E., Ueda, K., Daigo, Y., et al., (2012). Regulation of histone modification and chromatin structure by the p53-PADI4 pathway. *Nat. Commun.* **3**, 676. https://doi.org/10.1038/ncomms1676.
14. Chang, X., Han, J., Pang, L., Zhao, Y., Yang, Y., Shen, Z., (2009). Increased PADI4 expression in blood and tissues of patients with malignant tumors. *BMC Cancer* **9**, 40. https://doi.org/10.1186/1471-2407-9-40.
15. Li, P., Yao, H., Zhang, Z., Li, M., Luo, Y., Thompson, P.R., Gilmour, D.S., Wang, Y., (2008). Regulation of p53 target gene expression by peptidylarginine deiminase 4. *Mol. Cell Biol.* **28**, 4745–4758. https://doi.org/10.1128/MCB.01747-07.
16. Li, P., Wang, D., Yao, H., Doret, P., Hao, G., Shen, Q., Qiu, H., Zhang, X., et al., (2010). Coordination of PAD4 and HDAC2 in the regulation of p53-target gene expression. *Oncogene* **29**, 3153–3162. https://doi.org/10.1038/onc.2010.51.
17. Tanikawa, C., Ueda, K., Nakagawa, H., Yoshida, N., Nakamura, Y., Matsuda, K., (2009). Regulation of protein citrullination through p53/PADI4 network in DNA damage response. *Cancer Res.* **69**, 8761–8769. https://doi.org/10.1158/0008-5472.CAN-09-2280.
18. Neira, J.L., Araujo-Abad, S., Cámara-Artigas, A., Rizzuti, B., Abián, O., Giudici, A.M., Velázquez-Campoy, A., de Juan Romero, C., (2022). Biochemical and biophysical

characterization of PADI4 supports its involvement in cancer. *Arch. Biochem. Biophys.* **717**, https://doi.org/10.1016/j.abb.2022.109125 109125.

19. Neira, J.L., Rizzuti, B., Abián, O., Araujo-Abad, S., Velázquez-Campoy, A., de Juan Romero, C., (2022). Human enzyme PADI4 binds to the nuclear carrier Importin α3. *Cells* **11**, 2166. https://doi.org/10.3390/cells11142166.
20. Neira, J.L., Rizzuti, B., Araujo-Abad, S., Abian, O., Fárez-Vidal, M.E., Velazquez-Campoy, A., de Juan Romero, C., (2022). The armadillo-repeat domain of Plakophilin 1 binds to human enzyme PADI4. *Biochim. Biophys. Acta Proteins Proteom.*. https://doi.org/10.1016/j.bbapap.2022.140868.
21. Mallo, G.V., Fiedler, F., Calvo, E.L., Ortiz, E.M., Vasseur, S., Keim, V., Morisset, J., Iovanna, J.L., (1997). Cloning and expression of the rat p8 cDNA, a new gene activated in pancreas during the acute phase of pancreatitis, pancreatic development, and regeneration, and which promotes cellular growth. *J. Biol. Chem.* **272**, 32360–32369. https://doi.org/10.1074/jbc.272.51.32360.
22. Uversky, V.N., (2013). A decade and a half of protein intrinsic disorder: biology still waits for physics. *Protein Sci.* **22**, 693–724. https://doi.org/10.1002/pro.2261.
23. Wright, P.E., Dyson, H.J., (2015). Intrinsically disordered proteins in cellular signaling and regulation. *Nat. Mol. Cell Biol.* **16**, 18–29. https://doi.org/10.1038/nrm3920.
24. Encinar, J.A., Mallo, G.V., Mizyrycki, C., Giono, L., González-Ros, J.M., Rico, M., Cánepa, E., Moreno, S., et al., (2001). Human p8 is a HMG-I/Y-like protein with DNA binding activity enhanced by phosphorylation. *J. Biol. Chem.* **276**, 2742–2751. https://doi.org/10.1074/jbc.M008594200.
25. Aguado-Llera, D., Hamidi, T., Doménech, R., Pantoja-Uceda, D., Gironella, M., Santoro, J., Velázquez-Campoy, A., Neira, J.L., et al., (2013). Deciphering the binding between Nupr1 and MSL1 and their DNA-repairing activity. *PLoS One* **8**, e78101. https://doi.org/10.1371/journal.pone.0078101.
26. Lan, W., Santofimia-Castaño, P., Swayden, M., Xia, Y., Zhou, Z., Audebert, S., Camoin, L., Huang, C., et al., (2020). ZZW-115-dependent inhibition of NUPR1 nuclear translocation sensitizes cancer cells to genotoxic agents. *JCI Insight* **5**, e138117. https://doi.org/10.1172/jci.insight.138117.
27. Neira, J.L., Rizzuti, B., Jiménez-Alesanco, A., Palomino-Schätzlein, M., Abián, O., Velázquez-Campoy, A., Iovanna, J.L., (2020). A phosphorylation-induced switch in the nuclear localization sequence of the intrinsically disordered NUPR1 hampers binding to importin. *Biomolecules* **10**, 1313. https://doi.org/10.3390/biom10091313.
28. Cano, C.E., Hamidi, T., Sandi, M.J., Iovanna, J.L., (2011). Nupr-1: the Swiss knife of cancer. *J. Cell. Physiol.* **226**, 1439–1443. https://doi.org/10.1002/jcp.22324.
29. Goruppi, S., Iovanna, J.L., (2010). Stress-inducible protein p8 is involved in several physiological and pathological processes. *J. Biol. Chem.* **285**, 1577–1581. https://doi.org/10.1074/jbc.R109.080887.
30. Santofimia-Castaño, P., Rizzuti, B., Pey, A.L., Soubeyran, P., Vidal, M., Urrutia, R., Iovanna, J.L., Neira, J.L., (2017). Intrinsically disordered chromatin protein NUPR1 binds to the C-terminal region of Polycomb RING1B. *PNAS* **114**, E6332–E6341. https://doi.org/10.1073/pnas.1619932114.
31. Santofimia-Castaño, P., Rizzuti, B., Pey, A.L., Fárez-Vidal, M.E., Iovanna, J.L., Neira, J.L., (2021). Intrinsically disordered protein NUPR1 binds to the armadillo-repeat domain of Plakophilin 1. *Int. J. Biol. Macromol.* **170**, 549–560. https://doi.org/10.1016/j.ijbiomac.2020.12.193.
32. Santofimia-Castaño, P., Huang, C., Liu, X., Xia, Y., Audebert, S., Camoin, L., Peng, L., Lomberk, G., et al., (2022). NUPR1 protects against hyperPARylation-dependent cell death. *Commun. Biol.* **5**, 732. https://doi.org/10.1038/s42003-022-03705-1.
33. Malicet, C., Giroux, V., Vasseur, S., Dagorn, J.C., Neira, J. L., Iovanna, J.L., (2006). Regulation of apoptosis by the p8/prothymosin alpha complex. *PNAS* **103**, 2671–2676. https://doi.org/10.1073/pnas.0508955103.
34. Lopez, M.B., Garcia, M.N., Grasso, D., Bintz, J., Molejon, M.I., Velez, G., Lomberk, G., Neira, J.L., et al., (2015). Functional Characterization of Nupr1L, A Novel p53-Regulated Isoform of the High-Mobility Group (HMG)-Related Protumoral Protein Nupr1. *J. Cell. Physiol.* **230**, 2936–2950. https://doi.org/10.1002/jcp.25022.
35. Neira, J.L., Rizzuti, B., Jiménez-Alesanco, A., Abián, O., Velázquez-Campoy, A., Iovanna, J.L., (2020). The paralogue of the intrinsically disordered nuclear protein 1 has a nuclear localization sequence that binds to Human Importin α3. *Int. J. Mol. Sci.* **21**, 7428. https://doi.org/10.3390/ijms21197428.
36. Urrutia, R., Velez, G., Lin, M., Lomberk, G., Neira, J.L., Iovanna, J., (2014). Evidence supporting the existence of a NUPR1-like family of helix-loop-helix chromatin proteins related to, yet distinct from, AT hook-containing HMG proteins. *J. Mol. Model.* **20**, 2357. https://doi.org/10.1007/s00894-014-2357-7.
37. Neira, J.L., López, M.B., Sevilla, P., Rizzuti, B., Cámara-Artigas, A., Vidal, M., Iovanna, J.L., (2018). The chromatin nuclear protein NUPR1L is intrinsically disordered and binds to the same proteins as its paralogue. *Biochem. J.* **475**, 2271–2291. https://doi.org/10.1042/BCJ20180365.
38. Lis, S., Costa, M., (2022). The role of NUPR1 in response to stress and cancer development. *Tox. App. Pharmacol.* **454**, https://doi.org/10.1016/j.taap.2022.116244 116244.
39. Chang, X., Fang, K., (2010). PADI4 and tumorigenesis. *Cancer Cell Int.* **10**, 7. https://doi.org/10.1186/1475-2867-10-7.
40. Fuhrmann, J., Clancy, K.W., Thompson, P.R., (2015). Chemical biology of protein arginine modifications in epigenetic regulation. *Chem. Rev.* **115**, 5413–5461. https://doi.org/10.1021/acs.chemrev.5b00003.
41. Mondal, S., Thompson, P.R., (2021). Chemical biology of protein citrullination by the protein arginine deiminases. *Cur. Opin. Strcut. Biol.* **63**, 19–27. https://doi.org/10.1016/j.cbpa.2021.01.010.
42. Miskei, M., Antal, C., Fuxreiter, M., (2017). FuzDB: Database of fuzzy complexes, a tool to develop stochastic structure-function relationships for protein complexes and higher order assemblies. *Nucleic Acids Res.* **45**, D228–D235. https://doi.org/10.1093/nar/gkw1019.
43. Horikoshi, N., Tachiwana, H., Saito, K., Osakabe, A., Sato, M., Yamada, M., Akashi, S., Nishimura, Y., et al., (2011). Structural and biochemical analyses of the human PAD4 variant encoded by a functional haplotype gene. *Acta Crystallogr.* **D67**, 112–118. https://doi.org/10.1107/S0907444910051711.

44. Rai, R.K., Tripathi, P., Sinha, N., (2009). Quantification of metabolites from two-dimensional nuclear magnetic resonance spectroscopy: Application to human urine samples. *Anal. Chem.* **81**, 10232–10238. https://doi.org/10.1021/ac902405z.
45. Pastore, A., Temussi, P.A., (2017). The emperor's new clothes: Myths and truths of in-cell NMR. *Arch. Biochem. Biophys.* **628**, 114–122. https://doi.org/10.1016/j.abb.2017.02.008.
46. Neira, J.L., Bintz, J., Arruebo, M., Rizzuti, B., Bonacci, T., Vega, S., Lanas, A., Velázquez-Campoy, A., et al., (2017). Identification of a drug targeting an intrinsically disordered protein involved in pancreatic adenocarcinoma. *Sci. Rep.* **7**, 39732. https://doi.org/10.1038/srep39732.
47. Santofimia-Castaño, P., Xia, Y., Lan, W., Zhou, Z., Huang, C., Peng, L., Soubeyran, P., Velázquez-Campoy, A., et al., (2019). Ligand-based design identifies a potent NUPR1 inhibitor exerting anticancer activity via necroptosis. *J. Clin. Inves.* **129**, 2500–2513. https://doi.org/10.1172/JCI127223.
48. Rizzuti, B., Lan, W., Santofimia-Castaño, P., Zhou, Z., Velázquez-Campoy, A., Abián, O., Peng, L., Neira, J.L., et al., (2021). Design of inhibitors of the intrinsically disordered protein NUPR1: balance between drug affinity and target function. *Biomolecules* **11**, 1453. https://doi.org/10.3390/biom11101453.
49. Ventero, M.P., Fuentes-Baile, M., Quereda, C., Perez-Valeciano, E., Alenda, C., Garcia-Morales, P., Esposito, D., Dorado, P., et al., (2019). Radiotherapy resistance acquisition in Glioblastoma. Role of SOCS1 and SOCS3. *PLoS One* **14**, e0212581. https://doi.org/10.1371/journal.pone.0212581.
50. Fuentes-Baile, M., Pérez-Valenciano, E., de Garcia-Morales, P., Juan Romero, C., Bello-Gil, D., Barbera, V. M., Rodríguez-Lescure, A., Sanz, J.M., et al., (2021). CLytA-DAAO chimeric enzyme bound to magnetic nanoparticles. A new therapeutical approach for cancer patients? *Int. J. Mol. Sci.* **22**, 1477. https://doi.org/10.3390/ijms22031477.
51. Sekhar, A., Kay, L.E., (2013). NMR paves the way for atomic level descriptions of sparsely populated, transiently formed biomolecular conformers. *PNAS* **110**, 12867–12874. https://doi.org/10.1073/pnas.1305688110.
52. Fusco, G., De Simone, A., Gopinath, T., Vostrikov, V., Vendruscolo, M., Dobson, C.M., Veglia, G., (2014). Direct observation of the three regions in α-synuclein that determine its membrane-bound behaviour. *Nat. Commun.* **5**, 3827. https://doi.org/10.1038/ncomms4827.
53. Arbesu, M., Maffei, M., Cordeiro, T.N., Teixeira, J.M.C., Pérez, Y., Bernardo, P., Roche, S., Pons, M., (2017). The unique domain forms a fuzzy intramolecular complex in SRC family kinases. *Structure* **25**, 630–640. https://doi.org/10.1016/j.str.2017.02.011.
54. Borkosky, S.S., Camporeale, G., Chemes, L.B., Risso, M., Noval, M.G., Sánchez, I.E., Alonso, L.G., De Prat Gay, G., (2017). Hidden structural codes in protein intrinsic disorder. *Biochemistry* **56**, 5560–5569. https://doi.org/10.1021/acs.biochem.7b00721.
55. Mittag, T., Kay, L.E., Forman-Kay, J.D., (2010). Protein dynamics and conformational disorder in molecular recognition. *J. Mol. Recognit.* **23**, 105–116. https://doi.org/10.1002/jmr.961.
56. Freibrger, M.L., Wolynes, P.G., Ferreiro, D.U., Fuxreiter, M., (2021). Frustration in fuzzy protein complexes leads to interaction versatility. *J. Phys. Chem.* **125**, 2513–2520. https://doi.org/10.1021/acs.jpcb.0c11068.
57. Murphy, A., Costa, M., (2020). Nuclear protein 1 imparts oncogenic potential and chemotherapeutic resistance in cancer. *Cancer Lett.* **494**, 132–141. https://doi.org/10.1016/j.canlet.2020.08.019.
58. Malicent, C., Lesavre, N., Vasseur, S., Iovanna, J.L., (2003). p8 inhibits the growth of human pancreatic cancer cells and its expression is induced through pathways involved in growth inhibition and repressed by factors promoting cell growth. *Mol. Cancer* **2**, 37. https://doi.org/10.1186/1476-4598-2-37.
59. Chang, X., Han, J., Pang, L., Zhao, Y., Yang, Y., Shan, Z., (2009). Increased PADI4 expression in blood and tissues of patient with malignant tumors. *BMC Cancer* **9**, 40. https://doi.org/10.1186/1471-2407-9-40.
60. Moshkovic, N., Ochoa, H.J., Tang, B., Yang, H.H., Yang, Y., Huang, J., Lee, M.P., Wakefield, L.M., (2020). Peptidylarginine deiminase IV regulates breast cancer stem cells vi a novel tumor cell-autonomous suppressor role. *Cancer Res.* **80**, 2125–2137. https://doi.org/10.1158/0008-5472.CAN-19-3018.
61. Li, P., Yao, H., Zhang, Z., Li, M., Luo, Y., Thompson, P.R., Glimour, D.S., Wang, Y., (2008). Regulation of p53 target gene expression by peptidyl-arginine deiminase 4. *Mol. Cell Biol.* **28**, 4745–4758. https://doi.org/10.1128/MCB.01747-07.
62. Guo, Q., Fast, W., (2011). Citrullination of inhibitor growth 4 (ING4) by peptidylarginine deminase 4 (PAD4) disrupts the interaction between ING4 and p53. *J. Biol. Chem.* **286**, 17069–17078. https://doi.org/10.1074/jbc.M111.230961.
63. Darrah, E., Giles, J.T., Ols, M.L., Bull, H.G., Andrade, F., Rosen, A., (2013). Erosive rheumatoid arthritis is associated with antibodies that activate PAD4 by increasing calcium sensitivity. *Sci. Transl. Med.* **5**, 186ra65. https://doi.org/10.1126/scitranslmed.3005370.
64. Dong, S., Zhang, Z., Takahara, H., (2007). Estrogen-enhanced peptidylarginine deiminase type IV gene (PADI4) expression in MCF-7 cells is mediated by estrogen receptor-α-promoted transfactors activator protein-1, nuclear factor-Y and Sp1. *Mol. Endocrinol.* **21**, 1617–1629. https://doi.org/10.1210/me.2006-0550.
65. Gironella, M., Malicet, C., Cano, C., Sandi, M.J., Hamidi, T., Tauil, R.M.N., Baston, M., Valaco, P., et al., (2009). p8/NUPR1 regulates DNA-repair activity after double-strand gamma irradiation-induced DNA-damage. *J. Cell. Physiol.* **221**, 594–602. https://doi.org/10.1002/jcp.21889.
66. Ree, A.H., Tvermyr, M., Engebraaten, O., Rooman, M., Røsok, O., Hovig, E., MezaZepeda, L.A., Bruland, O.S., et al., (1999). Expression of a novel factor in human breast cancer cells with metastatic potential. *Cancer Res.* **59**, 4675–4680.
67. Stadler, S.C., Vicent, C.T., Fedorov, V.D., Patsialou, A., Cherrington, B.D., Wakshlag, J.J., Mohanan, S., Zee, B.M., et al., (2013). Dysregulation of PADI4-mediated citrullination of nuclear GSK-3β activates TGF-beta signaling and induces epithelial-to-mesenchymal transition in breast cancer cells. *PNAS* **110**, 11851–11856. https://doi.org/10.1073/pnas.1308362110.
68. Gill, S.C., von Hippel, P.H., (1989). Calculation of protein extinction coefficients from amino acid sequence data. *Anal. Biochem.* **182**, 319–326. https://doi.org/10.1016/0003-2697(89)90602-7.

69. Neira, J.L., Hornos, F., Bacarizo, J., Cámara-Artigas, A., Gómez, J., (2017). The monomeric species of the regulatory domain of tyrosine hydroxylase has a low conformational stability. *Biochemistry* **55**, 3418–3431. https://doi.org/10.1021/acs.biochem.6b00135.
70. Birdsall, B., King, R.W., Wheeler, M.R., Lewis Jr., C.A., Goode, S., Dunlap, R.B., Roberts, G.C., (1983). Correction for light absorption in fluorescence studies of protein-ligand interactions. *Anal. Biochem.* **132**, 353–361. https://doi.org/10.1016/0003-2697(83)90020-9.
71. Beckett, D., (2011). Measurement and analysis of equilibrium binding titrations: a beginner's guide. *Methods Enzymol.* **488**, 1–16. https://doi.org/10.1016/B978-0-12-381268-1.00001-X.
72. Royer, C.A., Scarlatta, S.F., (2008). Fluorescence approaches to quantifying biomolecular interactions. *Methods Enzymol.* **450**, 79–106. https://doi.org/10.1016/S0076-6879(08)03405-8.
73. Cavanagh, J.F., Wayne, J., Palmer III, A.G., Skelton, N.J., (1996). Protein NMR Spectroscopy: Principles and Practice. Academic Press, San Diego.
74. Bodenhausen, G., Ruben, D., (1980). Natural abundance nitrogen-15 NMR by enhanced heteronuclear spectroscopy. *Chem. Phys. Lett.* **69**, 185–189.
75. Bonucci, A., Palomino-Schätzlein, M., Malo de Molina, P., Arbe, A., Pierattelli, R., Rizzuti, B., Iovanna, J.L., Neira, J. L., (2021). Crowding effects on the structure and dynamics of the intrinsically disordered nuclear chromatin protein NUPR1. *Front. Mol. Biosci.* **8**, https://doi.org/10.3389/fmolb.2021.684622 684622.
76. Santofimia-Castaño, P., Rizzuti, B., Abián, O., Velázquez-Campoy, A., Iovanna, J.L., Neira, J.L., (2018). Amphipathic helical peptides hamper protein-protein interactions of the intrinsically disordered chromatin nuclear protein 1 (NUPR1). *Biochim. Biophys. Acta Gen. Sub.* **1862**, 1283–1295. https://doi.org/10.1016/j.bbagen.2018.03.009.
77. Trott, O., Olson, A.J., (2010). AutoDock Vina: Improving the speed and accuracy of docking with a new scoring function, efficient optimization, and multithreading. *J. Comput. Chem.* **31**, 455–461. https://doi.org/10.1002/jcc.21334.
78. Grande, F., Rizzuti, B., Occhiuzzi, M.A., Ioele, G., Casacchia, T., Gelmini, F., Guzzi, R., Garofalo, A., et al., (2018). Identification by molecular docking of homoisoflavones from *Leopoldia comosa* as ligands of estrogen receptors. *Molecules* **23**, 894. https://doi.org/10.3390/molecules23040894.

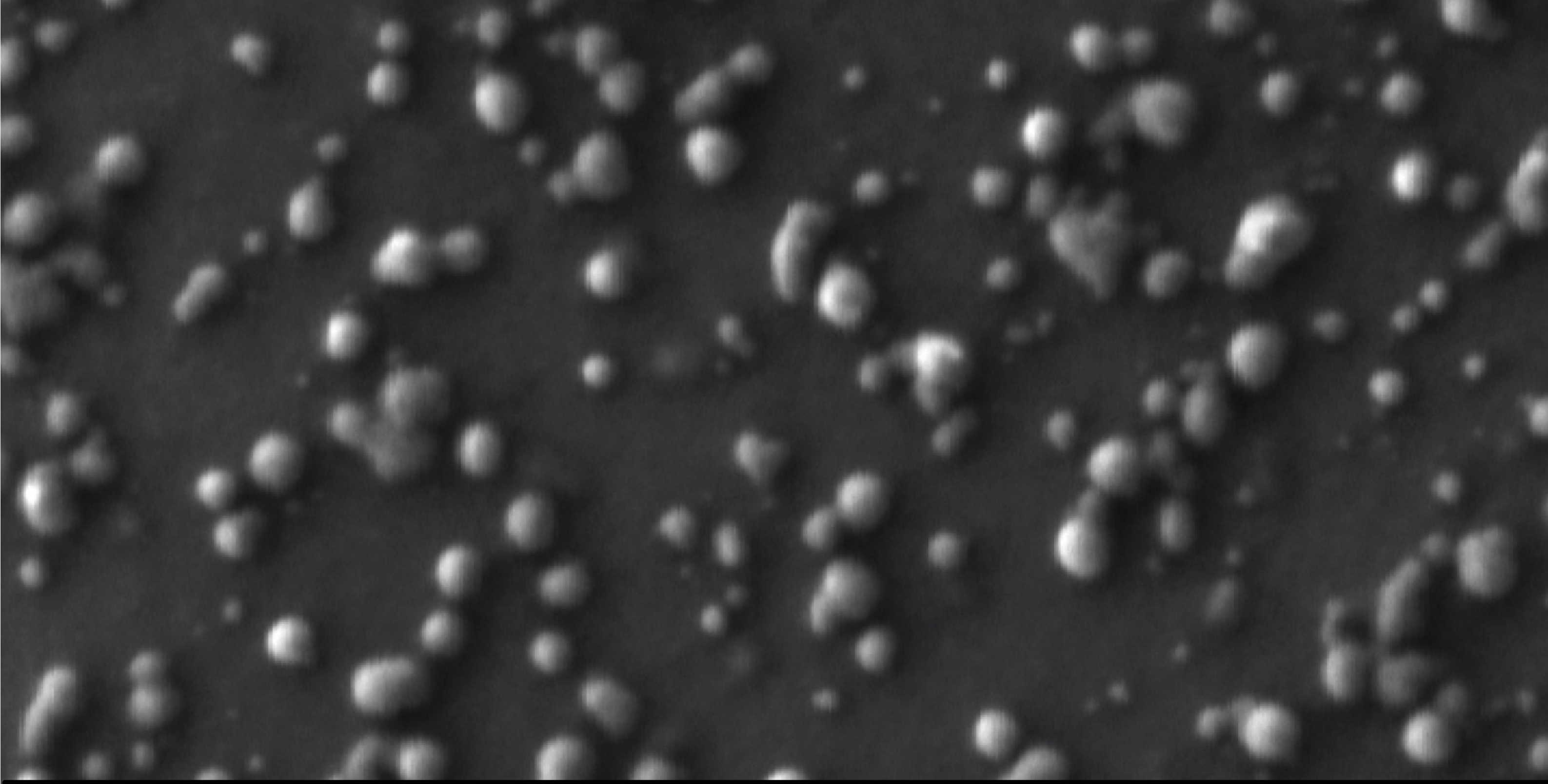

CHAPTER 7

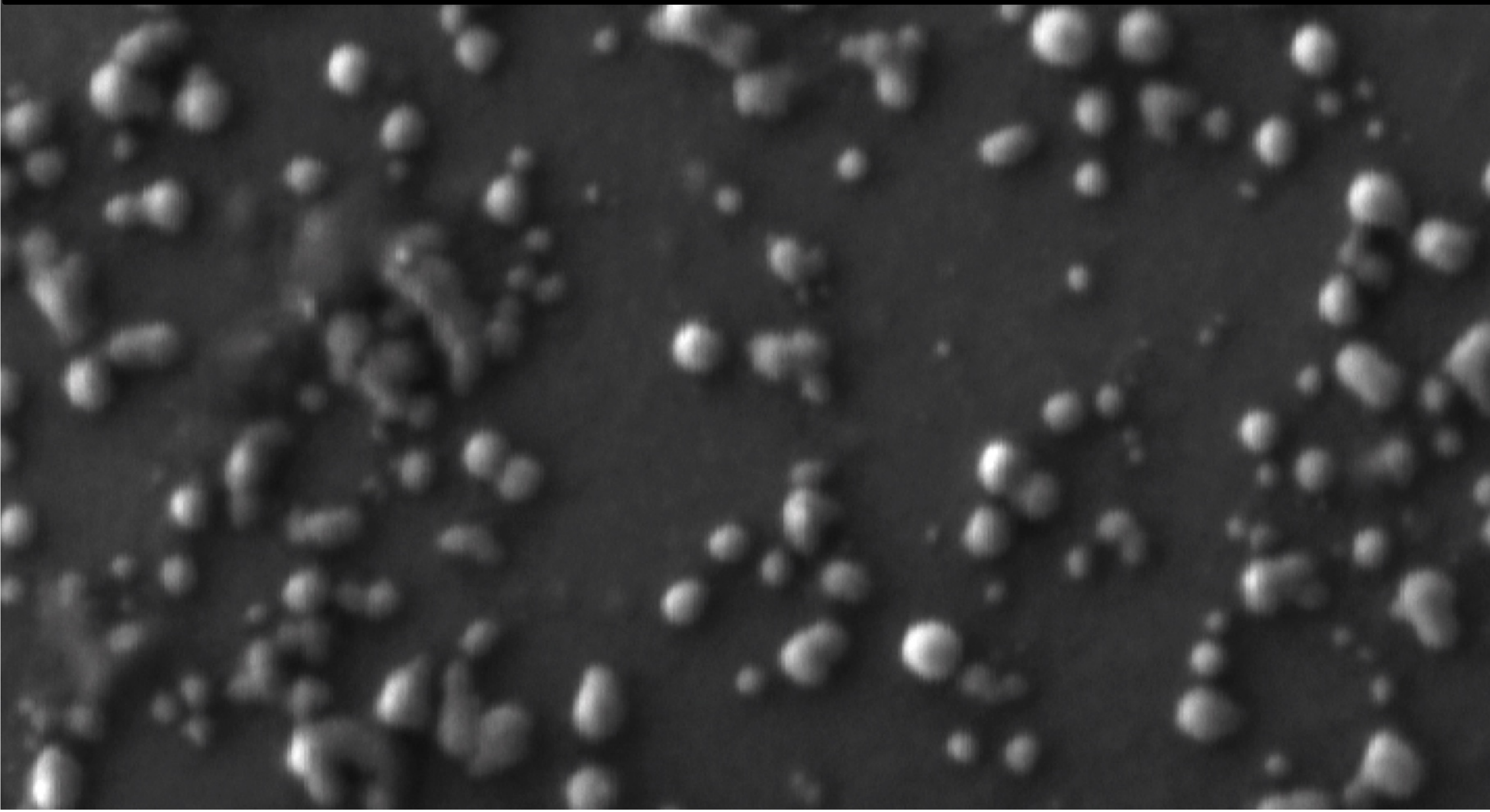

4.7 Chapter 7. The N-terminal region of MDM2 binds to human enzyme PADI4

Summary of the results

In this work, we described the interaction between PADI4 and MDM2. MDM2 (EC. 2.3.2.27) is a key protein that regulates p53 through several processes, including (i) altering p53-transcriptional activity, (ii) exporting p53 from the nucleus, and (iii) activating p53-degradation via ubiquitin-proteasome pathways. Given the relationship between MDM2, PADI4, and p53, we suggest that they could also interact in several cancer cell lines. In this study, we used *in cellulo*, *in vitro,* and *in silico* techniques to identify the interaction between PADI4 and MDM2.

In order to verify the *in cellulo* localization of the proteins, we performed IF assays using GB-42, RWP-1, and SW-480 cell lines. The results showed nuclear colocalization that was observed in all cell lines. Therefore, we used PLA to analyze the interaction between MDM2 and PADI4. As a result of PLA, we observed red dots that confirmed a positive interaction between the two proteins, which occurred in the nuclei and cytoplasm of all cell lines. We also tested the effect of GSK484 on this interaction, which resulted in a significant decrease in the nuclear PLA signal in all cell lines, suggesting that MDM2 probably binds to the active site of PADI4.

In vitro studies showed an affinity in the micromolar range, as measured by isothermal titration calorimetry (ITC), which was comparable to the measured IC_{50} of GSK484, which was ~ 20 μM. NMR experiments showed that the PADI4-binding region of N-MDM2 was mainly formed by residues Thr26, Val28, Phe91, and Lys98 [206].

Finally, we tested the effect of the PADI4 inhibitor GSK484 in combination with TMZ in a GBM cell line. The results showed that when both drugs were applied together, they had a better cytotoxic effect than when applied alone. This could improve the benefits of other drugs used for cancer treatment.

Our findings indicate binding between MDM2 and NUPR1, suggesting that this interaction may be a target for cancer therapy.

Received: 6 April 2023 | Revised: 30 June 2023 | Accepted: 4 July 2023
DOI: 10.1002/pro.4723

RESEARCH ARTICLE

New insights into cancer: MDM2 binds to the citrullinating enzyme PADI4

Salomé Araujo-Abad[1,2] | **Bruno Rizzuti**[3,4] | **Adrián Villamarin-Ortiz**[5] | **David Pantoja-Uceda**[6] | **Celia M. Moreno-Gonzalez**[1] | **Olga Abian**[3,7,8,9] | **Adrián Velazquez-Campoy**[3,7,8,9] | **José L. Neira**[1,3] | **Camino de Juan Romero**[1,10]

[1]IDIBE, Universidad Miguel Hernández, Elche, Spain
[2]Centro de Biotecnología, Universidad Nacional de Loja, Avda, Loja, Ecuador
[3]Instituto de Biocomputación y Física de Sistemas Complejos (BIFI) – Unidad mixta GBsC-CSIC-BIFI, Universidad de Zaragoza, Zaragoza, Spain
[4]CNR-NANOTEC, SS Rende (CS), Department of Physics, University of Calabria, Rende, Italy
[5]Instituto de Bioingeniería, Universidad Miguel Hernández, Elche, Spain
[6]Instituto de Química Física Rocasolano (IQFR-CSIC), Madrid, Spain
[7]Instituto de Investigación Sanitaria Aragón (IIS Aragón), Zaragoza, Spain
[8]Centro de Investigación Biomédica en Red en el Área Temática de Enfermedades Hepáticas y Digestivas (CIBERehd), Madrid, Spain
[9]Departamento de Bioquímica y Biología Molecular y Celular, Universidad de Zaragoza, Zaragoza, Spain
[10]Unidad de Investigación, Fundación para el Fomento de la Investigación Sanitaria y Biomédica de la Comunidad Valenciana (FISABIO), Hospital General Universitario de Elche, Elche, Spain

Correspondence
Camino de Juan Romero, Unidad de Investigación, Fundación para el Fomento de la Investigación Sanitaria y Biomédica de la Comunidad Valenciana (FISABIO), Hospital General Universitario de Elche, Camí de l'Almazara 11, 03203 Elche (Alicante), Spain.
Email: m.juan@umh.es

José L. Neira, IDIBE, Edificio Torregaitán, Universidad Miguel Hernández, Avda. del Ferrocarril s/n, 03202 Elche (Alicante), Spain.
Email: jlneira@umh.es

Abstract

PADI4 is one of the human isoforms of a family of enzymes implicated in the conversion of arginine to citrulline. MDM2 is an E3 ubiquitin ligase which is crucial for down-regulation of degradation of the tumor suppressor gene p53. Given the relationship between both PADI4 and MDM2 with p53-signaling pathways, we hypothesized they may interact directly, and this interaction could be relevant in the context of cancer. Here, we showed their association in the nucleus and cytosol in several cancer cell lines. Furthermore, binding was hampered in the presence of GSK484, an enzymatic PADI4 inhibitor, suggesting that MDM2 could bind to the active site of PADI4, as confirmed by *in silico* experiments. *In vitro* and *in silico* studies showed that the isolated

---

Abbreviations: BLI, biolayer interferometry; CD, circular dichroism; CSP, chemical shift perturbation; DAPI, 4′,6-diamino-2-phenylindole; DMSO, dimethyl sulfoxide; EMT, epithelial-to-mesenchymal transition; FBS, fetal bovine serum; GBM, glioblastoma; GBSA, generalized Born surface area; GSK3β, glycogen synthase kinase 3 beta; IF, immunofluorescence; ITC, isothermal titration calorimetry; MDM2, murine double minute 2 oncoprotein; MGMT, O6-methylguanine methyltransferase; MM, molecular mechanics; MTT, 3-(4,5-Dimethylthiazol-2-Yl)-2,5-diphenyltetrazolium bromide; N-MDM2, N-terminal region of MDM2 (residues 6–125 of the intact protein); NMR, nuclear magnetic resonance; PADI, peptidyl-arginine deiminase; PBS, phosphate buffered saline; PDB, Protein Data Bank; PLA, proximity ligation assay; PPI, protein–protein interaction; PTM, post-translational modification; RMSD, root mean square deviation; SAMp73, the sterile alpha motif of p73; SD, standard deviation; TA, transactivation domain; TCEP, tris(2-carboxyethyl)phosphine; TMZ, temozolomide; TSG, tumor suppressor gene; UV, ultraviolet.

Salomé Araujo-Abad and José L. Neira are contributed equally to this work.

https://doi.org/10.1002/pro.4723

Funding information
Diputación de Aragón; Generalitat Valenciana; Instituto de Salud Carlos III; Ministerio de Ciencia e Innovación; Ministerio de Economía y Competitividad; Spanish Ministry of Economy and Competitiveness and European ERDF Funds, Grant/Award Number: BFU2016-78232-P; Ministry of Science and Innovation, Grant/Award Numbers: MCIN/AEI/10.13039/501100011033/, PID2021-127296OB-I00; Instituto de Salud Carlos III co-funded by European Social Fund, Grant/Award Numbers: CP19/00095toCdJ, PI222/00824toCdJ, PI18/00394toOA; Diputación General de Aragón, Grant/Award Numbers: B25-20RtoOA, E45-20RtoAVC; Consellería de Innovación, Grant/Award Number: CAICO 2021/0135

Review Editor: Aitziber L. Cortajarena

N-terminal region of MDM2, N-MDM2, interacted with PADI4, and residues Thr26, Val28, Phe91 and Lys98 were more affected by the presence of the enzyme. Moreover, the dissociation constant between N-MDM2 and PADI4 was comparable to the IC_{50} of GSK484 from *in cellulo* experiments. The interaction between MDM2 and PADI4 might imply MDM2 citrullination, with potential therapeutic relevance for improving cancer treatment, due to the generation of new antigens.

KEYWORDS

citrullination, isothermal titration calorimetry, MDM2, molecular docking, NMR, PADI4, protein ligation assay, protein–protein interactions

1 | INTRODUCTION

PADI4 belongs to a family of peptidyl-arginine deiminases (PADI, EC 3.5.3.15) hydrolytic enzymes responsible of catalyzing citrullination, that is, the conversion of arginine to citrulline residues in a polypeptide chain, in the presence of Ca(II). This post-translational modification (PTM) is permanent, unless the protein is degraded. Such modification influences the molecular properties of the polypeptide chain and it has important roles in human disease (Gudmann et al., 2015; György et al., 2006; Ishigami & Maruyama, 2010; Yuzhalin, 2019). PADI4 is usually located in cytoplasmic granules of inflammatory cells (eosinophils, neutrophils and macrophages), mammary gland cells, stem cells, and tumor cells, where is highly expressed, either in the cytosol or in the nucleus. This protein is involved in gene transcription and immune system modulation, leading to cell inflammation and immune response (Slade et al., 2014; Wang et al., 2021; Witalison et al., 2015; Yang et al., 2021; Ying et al., 2009). In addition, an enzymatic activity increase is observed for several PADI4 haplotype mutants during the apoptosis enhanced through the mitochondrial pathway (Hung et al., 2007). Furthermore, PADI4 is involved in p53-gene expression, as well as in the expression of other p53-target genes (Li et al., 2008; Li et al., 2010; Yang et al., 2021). We have shown recently that PADI4 is expressed in glioblastoma (GBM), pancreatic adenocarcinoma and colon cancer (Neira, Araujo-Abad, et al., 2022), and it binds to other key proteins involved in cancer development, such as importin α (Neira, Rizzuti, et al., 2022) and plakophilin 1 (Neira et al., 2023). Therefore, in recent years, PADI4 has attracted the attention of the research community due to its key role in cancer progression, which affects patient survival and prognosis.

Tumor suppressor genes (TSGs) are frequently downregulated in cancer, leading to dysregulation of the pathways they control and, therefore, provide opportunities for alternative therapies (Gregory & Copple, 2022). The protein p53 is a protein produced by a well-known TSG (Lei et al., 2023). A key p53 regulator is the cellular protein MDM2 (murine double minute 2 oncoprotein) (EC. 2.3.2.27) (Momand et al., 1992; Reza Saadatzadeh et al., 2017), an E3 ubiquitin ligase encoded by the *mdm2* oncogene. MDM2 can inhibit p53 in several ways: (i) the N-terminal region of MDM2, N-MDM2 (comprising the first 125 residues), binds to the p53 N-terminal transactivation domain (residues 15–29, TA), and can alter p53-transcriptional activity; (ii) the full-length MDM2 exports p53 from the nucleus (Chen et al., 1993; Kussie et al., 1996; Momand et al., 1992); and (iii) MDM2 activates p53-degradation via ubiquitin-proteasome pathways (Kubbutat et al., 1997). The N-MDM2, which includes the well-folded p53 binding-domain (residues 25–109; McCoy et al., 2003), is composed by four α-helices (residues 32–41, 50–63, 81–86 and 96–104) and a three-stranded anti-parallel β-sheet (residues 66–68, 74–76 and 90–92) (Kussie et al., 1996; Uhrinova et al., 2005). The α-helices are the side-walls and bottom of the cavity where the TA of p53 binds, and the antiparallel β-sheet covers the binding cleft from both sides. Since p53 and MDM2 interact, as well as p53 and PADI4 (Chen et al., 1993; Kussie et al., 1996; Reza Saadatzadeh et al., 2017), we hypothesized that PADI4 and MDM2 might interact directly as well.

In this work, we hypothesized that given the relationship of MDM2 and PADI4 with p53, they could also interact directly, and indeed we identified and described the interaction between intact MDM2 and PADI4 *in cellulo* in several cancer cell lines. Importantly, in the presence of GSK484, an enzyme inhibitor of PADI4, we observed that the interaction between the two proteins was hampered. Those results indicate that the MDM2-binding region of PADI4 could be located in, or close to, its active site, or alternatively, in another region involved in a conformational change associated with an allosteric inhibition. As p53 binds MDM2 at the N-MDM2 region, we performed *in vitro* and *in silico* analyses to characterize the possible association of PADI4 through the N-MDM2. We provided evidence of this binding by a combination of experimental and simulation techniques. The *in vitro* studies showed an affinity in the micromolar range, as measured by isothermal titration calorimetry (ITC) ($K_d \sim 1$ μM), fluorescence ($K_d \sim 6$ μM) and biolayer interferometry (BLI) ($K_d \sim 2$ μM), comparable to the measured IC_{50} of GSK484 that was ~20 μM (taking into consideration that IC_{50} is not a true interaction constant depending on many experimental factors). The PADI4-binding region of N-MDM2 was mainly formed by residues Thr26, Val28, Phe91 and Lys98, as suggested by nuclear magnetic resonance (NMR) experiments. Blind docking and simulations followed by re-scoring through molecular mechanics (MM) methods further pinpointed the involvement of most of these residues of N-MDM2 in the binding, together with the critical participation of some arginine amino acids. Furthermore, the simulation results strongly supported the idea that the binding of N-MDM2 involved the active site of PADI4. Interestingly, N-MDM2 has four arginine residues (Arg29, Arg65, Arg97 and Arg105) that could be susceptible of being citrullinated by PADI4 to further modulate its binding to p53. The fact that MDM2 might be post-translationally modified opens the possibility to develop new cancer therapies based on its citrullination, or alternatively, its use in liquid biopsy for early detection and prognosis of citrullinated species or the antigens raised against them.

2 | RESULTS

2.1 | Binding of PADI4 to intact MDM2 occurred *in cellulo* in the cytosol and nucleus

To test whether interaction between endogenous PADI4 and intact MDM2 occurred within cancer cells, we used different cell lines. For GBM, we employed a previously described patient-derived cell line, HGUE-GB-42 (Ventero et al., 2019). We also used other two cell lines, SW-480, isolated from the large intestine of a Dukes C colorectal cancer patient, and RWP-1, as a model of pancreatic cancer. First, we performed immunofluorescence (IF) experiments to address whether both proteins were expressed and colocalized in the same cellular compartments for the different cell lines (Figure S1). We found that the two proteins were highly expressed in all the patient-derived cell lines. Moreover, the fact that both proteins had a nuclear staining, as shown by the colocalization with DAPI, suggested that they may interact directly within the nuclear compartment. Subsequently, we sought to confirm their interaction by using the Duolink in situ assay. The red fluorescent spots, corresponding to the Proximity ligation assay (PLA) signals, indicated that PADI4 interacted with full-length MDM2 within the nucleus and cytosol, regardless of the cancer cell type (Figures 1 and S2).

To sum up, our results indicate that PADI4 and the intact MDM2 not only co-expressed, but they interacted directly in different cell compartments of cancer cells corresponding to several tissues.

2.2 | Inhibition of PADI4 *in cellulo* resulted in a decrease of PADI4-MDM2 interaction

It has been described that the compound GSK484 is an enzymatic inhibitor of PADI proteins, but it shows a strong preference for PADI4 over the other isozymes (Lewis et al., 2015). To establish the optimal concentration at which GSK484 had an effect on the studied tumor cell lines, we performed a series of proliferation assays.

We observed that the GBM was the most sensitive cell line to the presence of GSK484, with an IC_{50} of 12.7 μM (Figure 2a), followed by the colorectal cell line, SW-480, with an IC_{50} of 19.2 μM. At 20 μM of GSK484, the highest tested concentration, the pancreatic cancer cell line, did not reach a 50% reduction in the cell proliferation. We considered that the reduction by 40% shown by RWP-1 was sufficient to affect the binding, and hence, we decided to use GSK484 at 20 μM concentration in the PLAs with PADI4 and MDM2.

We treated the cells with GSK484 for 6 and 24 h, and then, we fixed them to perform PLAs. After 6 h, we already observed a great reduction in the number of observed red dots, indicating that the interaction between PADI4 and MDM2 occurred mainly in the nucleus as shown by DAPI nuclear counterstaining (Figures 2b and S3). The reduction in the population of MDM2/PADI4

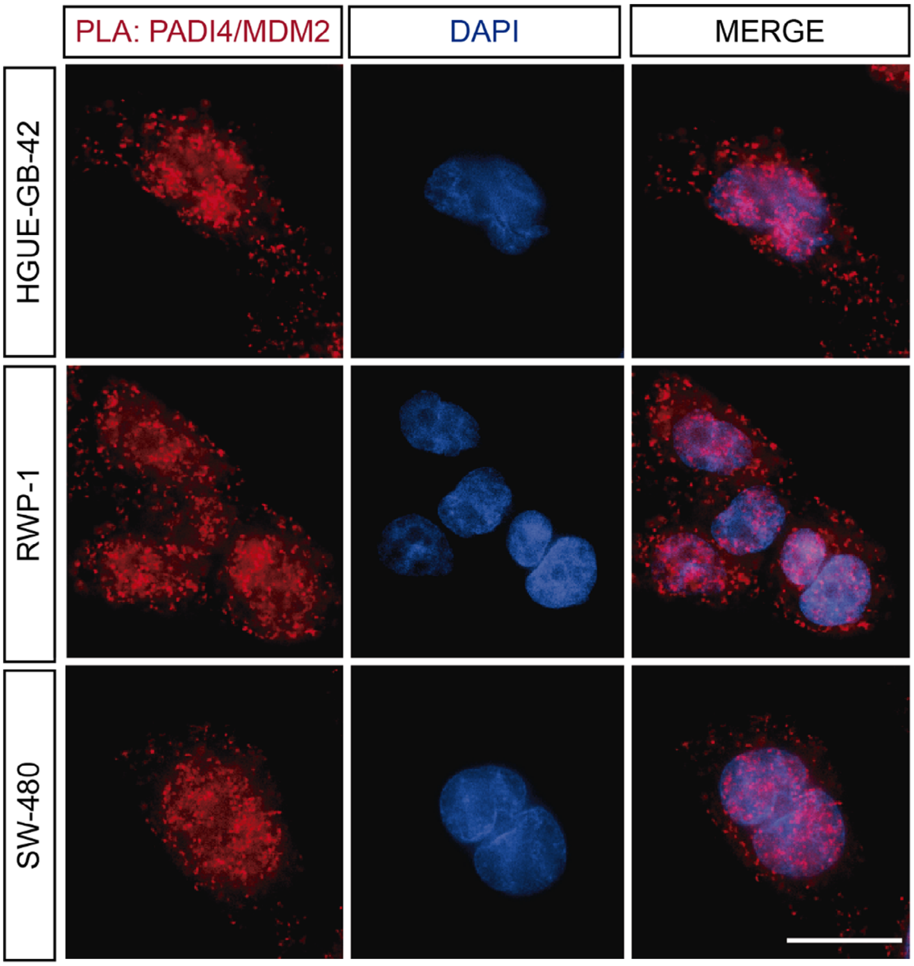

FIGURE 1 MDM2 interacted directly with PADI4 *in cellulo*. PLAs of PADI4 with MDM2 reveal the direct interaction between the two proteins in different patient-derived HGUE-GB-42, SW-480 and RWP-1 cells. A representative experiment is shown ($n = 5$). Scale bar = 20 μm.

formed complexes was even greater after the 24-h treatment with the inhibitor (GSK484), suggesting that the binding of GSK484 could prevent the binding of MDM2 with PADI4. At this stage, we cannot unambiguously conclude that PADI4 may likely competitively prevent the binding of MDM2 with PADI4 or alternatively, the presence of GSK484 could modify allosterically the MDM2-binding site of PADI4. (Figures 2b,c and S3). Interestingly, each of the tumor cell lines responded differently to GSK484 treatment. Contrary to what we would expect after the proliferation experiments, RWP-1 showed a large decrease in the amount of the MDM2/PADI4 complexes formed already at 6 h, and the number of those formed was not substantially decreased by longer treatment times. On the other hand, SW-480 did not respond until 24-h exposure to the GSK484 treatment. The number of dots *per* cell in the GBM cell line, HGUE-GB-42, decreased over time, suggesting a direct correlation between the treatment time and inhibition effect by GSK484 (Figures 2c and S3). These results agree with previous observations reporting that PADI4 inhibition results in different outcomes in multiple cancer cell lines (Yuzhalin, 2019), besides its different expression among several cell lines, as we have recently shown (Neira, Araujo-Abad, et al., 2022). Then, all in all, those findings suggest that the inhibitory effect of GSK484 may have different effects among the cell lines (Duan et al., 2016; Stadler et al., 2013; Yuzhalin et al., 2018; Zhang et al., 2021). Altogether, our experiments showed that, in the presence of GSK484, the binding between MDM2 and PADI4 was hampered (Figures 2 and S3).

2.3 | PADI4 was bound to N-MDM2 *in vitro*

The complex between MDM2 and p53 is primarily formed by the interaction between the N-terminal domain of MDM2 (N-MDM2), comprising the first 125 residues of the protein, and the TA of p53 (Joerger & Fersht, 2008; Wallace et al., 2006; Yadahalli et al., 2019). Therefore, as the *in cellulo* experiments indicated unambiguously that there was binding between intact MDM2 and PADI4, we hypothesized that MDM2 could also interact with PADI4 by using that same p53-binding region. Then, we tested whether PADI4 interacted with

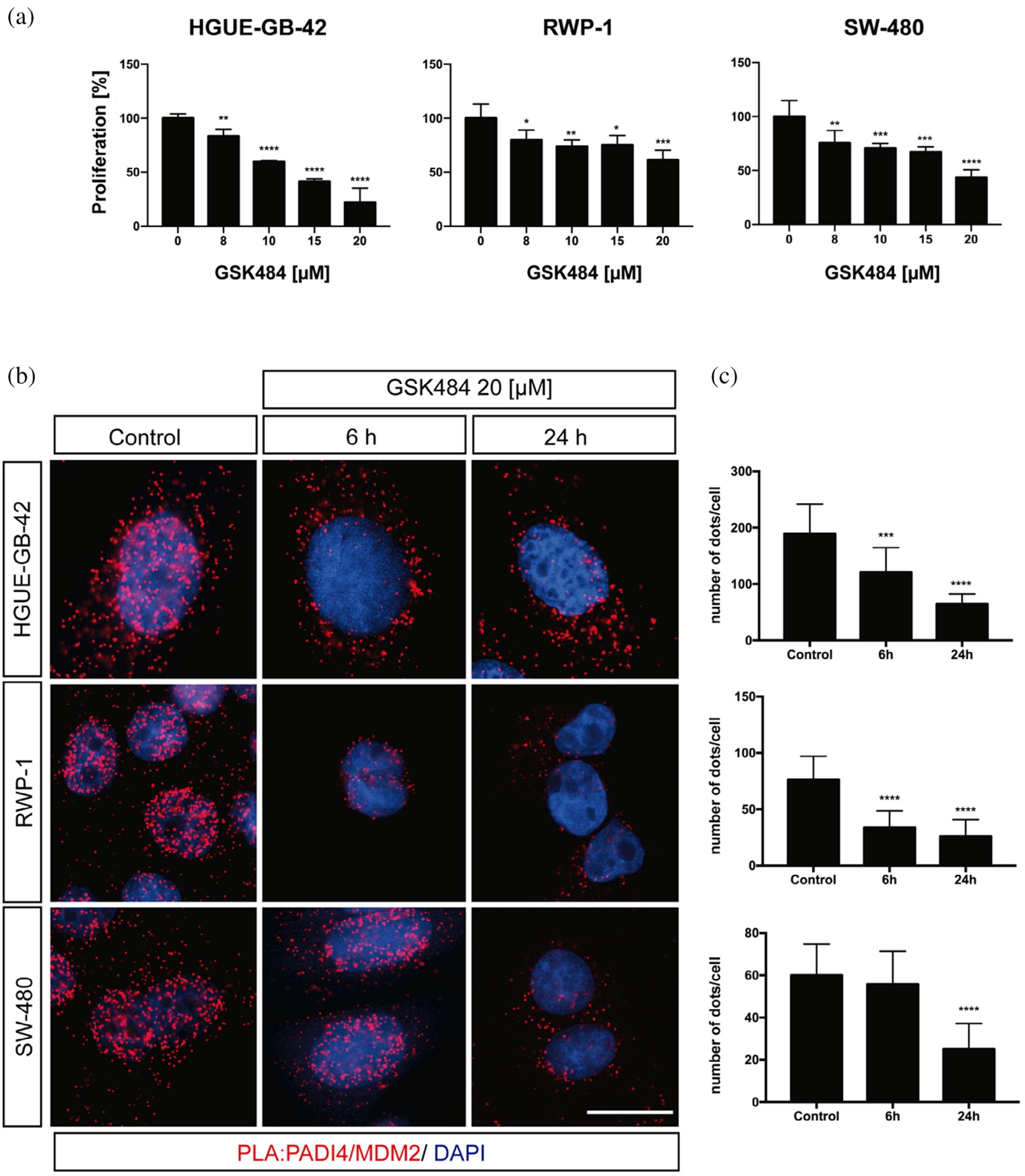

FIGURE 2 MDM2/PADI4 interaction inhibited by GSK484. (a) Proliferation cell experiments in the presence of GSK484 (at 20 μM) for the three cell lines. (b) PLA was performed in HGUE-GB-42, RWP-1 and SW-480 cells in the presence or absence of GSK484 at a concentration of 20 μM, for 6 and 24 h. Control experiments were carried out at 6 h. Scale bar = 20 mm. (c) A representative experiment is shown ($n = 5$). Each panel corresponds to the cell lines shown in B. The Fiji software was used to account for the number of red dots. Data represent mean ± SD, Student's 2-tailed unpaired t test was used, $^{*}p < 0.05$; $^{**}p < 0.01$; $^{***}p < 0.001$; $^{****}p < 0.0001$.

N-MDM2 *in vitro*, by following a two-part experimental approach. First, we used steady-state fluorescence, far-ultraviolet (UV) circular dichroism (CD) and NMR, as spectroscopic techniques to observe a possible binding and concomitant conformational changes in the macromolecules; and second, we used fluorescence, BLI and

ITC to quantitatively measure the thermodynamic parameters of such binding.

We used fluorescence to determine whether there was a change in: (i) the position of the maximum wavelength; (ii) the intensity at that wavelength; or (iii) both, when the spectrum of the complex was compared to that obtained from the addition of the separated spectra of the two isolated proteins. A variation in fluorescence intensity by excitation at 280 nm was observed when the complex of PADI4 with N-MDM2 was formed (Figure 3a, left panel), but there were no changes in the maximum wavelength of the spectrum.

Next, we carried out far-UV CD measurements, trying to confirm the fluorescence binding results. In agreement with the observations by fluorescence described above, the addition spectrum was different from that of the complex (Figure 3a, right panel). Then, we can conclude that there were changes in the secondary structure of PADI4 and/or in that of N-MDM2 when the two proteins were bound; however, we cannot rule out that the changes observed were due to displacements of some aromatic residues (or interactions involving these residues) of at least one of the proteins.

To further confirm *in vitro* the binding between the two proteins, and to elucidate the PADI4-binding region of N-MDM2, we acquired a 2D ^{1}H-^{15}N HSQC NMR spectra in isolated ^{15}N-labeled N-MDM2 and in a complex, with an excess of PADI4 (Figure 4a). The chemical shift perturbations (CSPs) (Equation (2)) of residues Thr26, Val28, Leu33, Gln44, Glu52, Glu69, Phe91, His96 and Lys98 of N-MDM2 in the presence of PADI4 were larger than the average ± standard deviation (SD) (Figure 4b). As Glu52, Glu69 and His96 have ionizable side-chains, which could be titrating at the pH of the experiments, we

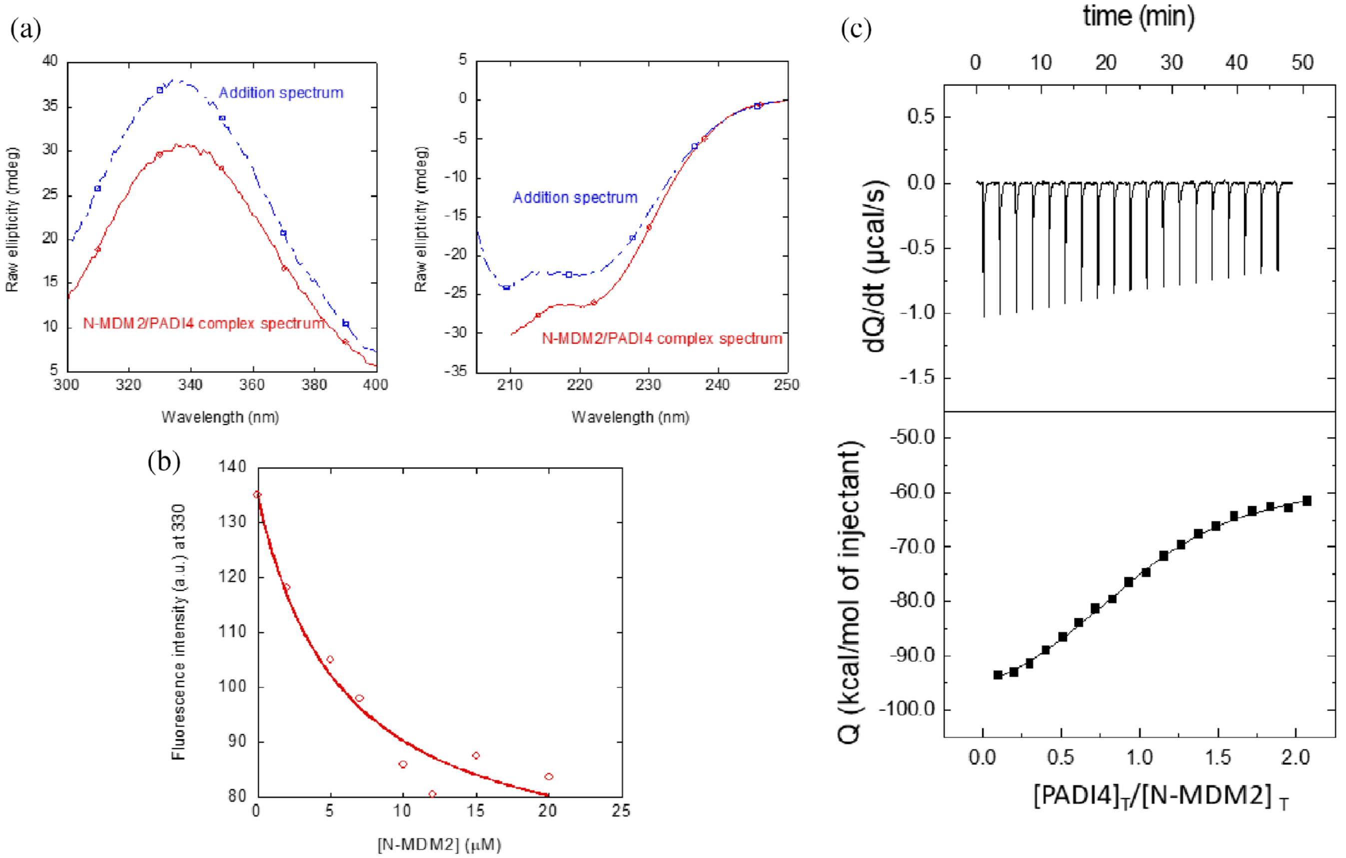

FIGURE 3 Binding of N-MDM2 to PADI4 as monitored by different biophysical probes: (a) (Right panel) Fluorescence spectrum obtained by excitation at 280 nm of the N-MDM2/PADI4 complex, and addition spectrum obtained by the sum of the spectra of the two isolated macromolecules. (Left panel) Far-UV CD spectrum of the N-MDM2/PADI4 complex, and addition spectrum obtained by the sum of the spectra of the two isolated macromolecules. (b) Titration curve monitoring the changes in the fluorescence at 315 nm when N-MDM2 was added to PADI4. The fluorescence intensity on the y-axis is the relative signal after removal of the corresponding blank. The line through the data are the fitting to Equation (1). Experiments were carried out at 25°C. (c) Calorimetric titrations for the PADI4 binding to N-MDM2. Upper panel show the thermogram (thermal power as a function of time), and lower panel show the binding isotherm (ligand-normalized heat effects per injection as a function of the molar ratio in the calorimetric cell). Continuous lines correspond to the fitting curves according to a single ligand binding site interaction model. Experiments were carried out at 25°C.

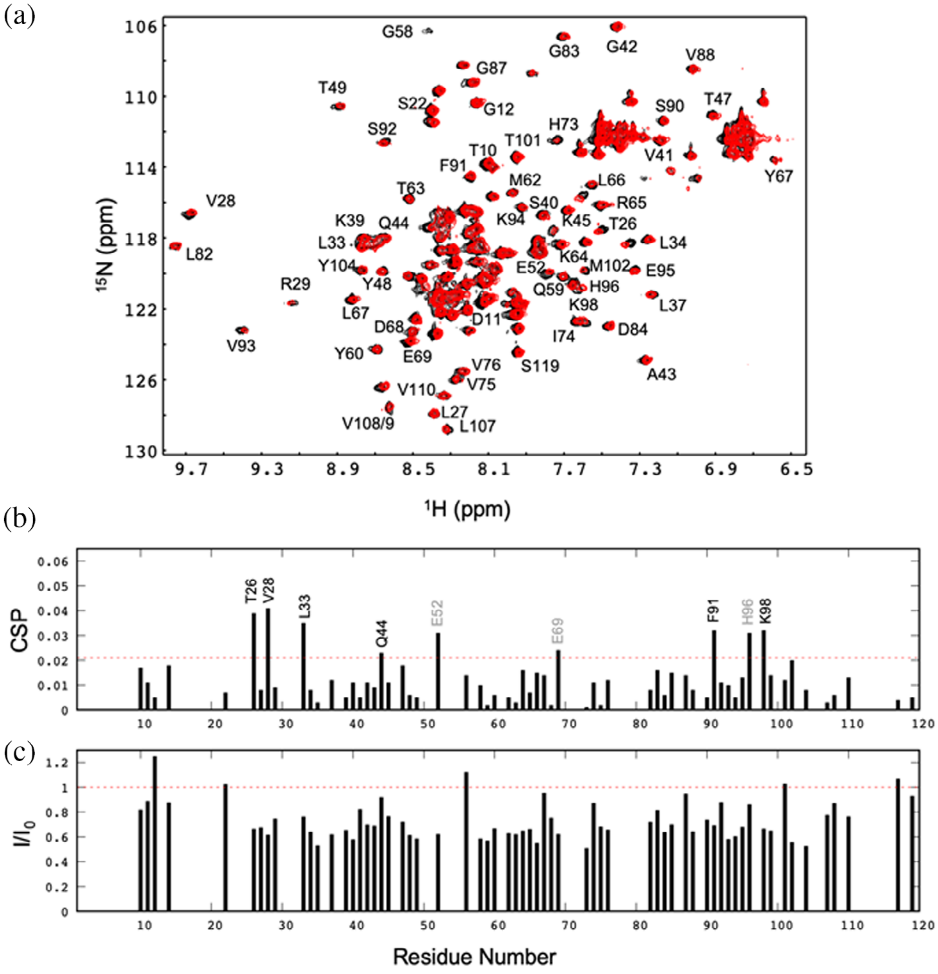

FIGURE 4 Binding of N-MDM2 to PADI4 mapped by NMR. (a) 2D ^{1}H-^{15}N HSQC NMR spectra of isolated N-MDM2 (black) and in the presence of PADI4 (red). (b) CSPs (Equation (2)) of the unambiguously assigned cross-peaks, showing no overlapping with others. The dotted line is the average value ± SD. (c) Ratio of the intensity of a cross-peak in the spectrum of the complex (red in panel a) to the intensity of the same cross-peak in the spectrum of isolated MDM2 (black in panel a). The dotted line is the average value ± SD. Experiments were carried out at 25°C.

did not consider any further these residues. The presence of such large CSPs for the rest of the residues indicates a fast equilibrium between the free and bound-N-MDM2 and, therefore, it confirms the binding to PADI4. We also point out that the fact that large CSP values are restricted to some particular residues of N-MDM2 further confirms that the association is specific, as already suggested by: (i) the ITC titration curves observed (Figure 3c); and (ii) the well-defined stoichiometry of the binding reaction. On the other hand, when mapped on the tertiary structure of N-MDM2 (Figure S4), the CSP values are scattered on several distant regions; this is suggesting that some of those variations might be due to indirect effects on the affected residues rather than a direct contact with the surface of PADI4, and/or to multiple binding modes (i.e., orientations) of N-MDM2 on the same hot-spot of PADI4. It is interesting to note that some of those residues are not far away from those involved in forming the p53-binding pocket in N-MDM2 (Kussie et al., 1996): Leu54, His96, Ile99 and Tyr100. On the other hand, we observed a general decrease in the signal intensity of any cross-peak of the spectrum of the complex (i.e., general broadening), when compared with the intensity of the corresponding cross-peak of the spectrum of isolated N-MDM2 (Figure 4c).

Since we observed changes in the fluorescence spectra upon PADI4 binding to N-MDM2, to determine the affinity constant, we carried out titrations by keeping constant the concentration of PADI4, and increasing that of N-MDM2. The results provided a K_d value of 5 ± 2 μM (Figure 3b) for the interaction between PADI4 and N-MDM2. We also used ITC to determine the thermodynamic binding parameters (Figure 3c). The results indicated that the interaction was highly exothermic (favorable enthalpic contribution and unfavorable entropic contribution to the Gibbs energy of binding), with $\Delta H = -$ 42 kcal mol^{-1}, and the K_d was 1.0 ± 0.2 μM (slightly lower than the value obtained by fluorescence). The stoichiometry of the reaction was 1.1, indicating that the dimer of PADI4 was bound to two molecules of N-MDM2.

The results from BLI (Figure 5a) yielded a value of the dissociation constant similar to that measured by ITC and fluorescence. The K_d value obtained was: 2 ± 2 μM,

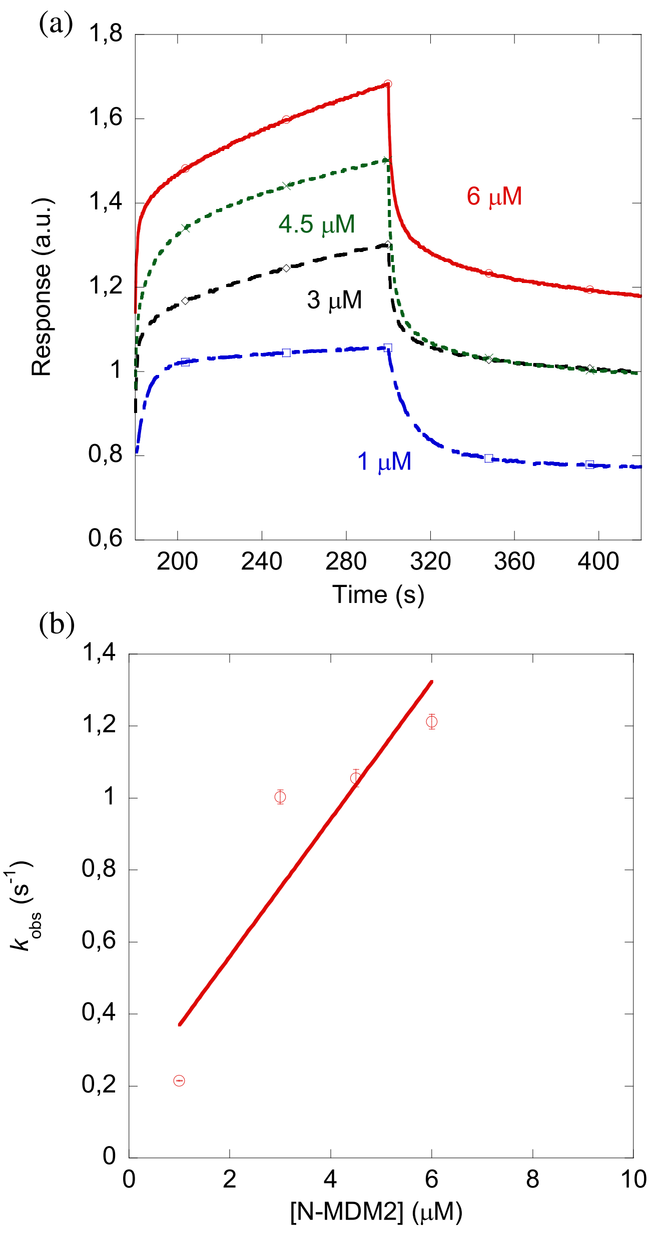

FIGURE 5 Affinity of N-MDM2 toward PADI4 from BLI assays. (a) Sensorgrams at different concentrations of N-MDM2 used in the assays for PADI4-immobilized on the sensor. (b) Pseudo-first order plot of the binding of N-MDM2 to PADI4 (Equation (6)). The error bars are errors from fitting sensorgrams to Equation (5). Experiments were carried out at 25°C.

with $k_{on} = 0.17 \pm 0.10\ \mu M^{-1}\ s^{-1}$ and $k_{off} = 0.3 \pm 0.2\ s^{-1}$ (Figure 5b). The latter value was similar to the average obtained from the fitting of dissociation curves of the sensorgrams at the different N-MDM2 concentrations.

To sum up, we conclude that N-MDM2 could bind to PADI4, with a dissociation constant in the low micromolar range through an enthalpically driven process, and therefore the binding we had observed *in cellulo* should occur through the N-terminus of the intact protein.

2.4 | Using blind docking to define the binding regions of PADI4 and N-MDM2

Protein–protein docking was used to model the essential features of the structure of the N-MDM2/PADI4 complex, and to clarify details of their respective hot-spot regions in the binding.

Some of the results of our *in vitro* and *in cellulo* experiments were used to simplify the simulations in a preliminary stage, and as a filter to sort out the predicted docking poses in a subsequent stage. To begin with, the hot-spot of MDM2 was restricted to a subset of residues of its N-terminal region N-MDM2 and, more precisely, of the well-folded p53-binding domain encompassing residues 25–109 (McCoy et al., 2003). In fact, both the N-terminal (residues 1–24) and C-terminal region (residues 110–125) of N-MDM2, flanking the p53-binding domain from either side, are unstructured in the unliganded protein species, and not solved in NMR complexes with protein partners different from PADI4 (Jae-Sun et al., 2015; Michelsen et al., 2012; Nagata et al., 2014). More importantly, the residues of N-MDM2 whose NMR signals were significantly affected by the binding to PADI4 and do not contain a titrating side-chain around pH 7.0 (Thr26, Val28, Leu33, Gln44, Phe91, and Lys98) are all included within the sequence of the p53-binding domain. Therefore, in our docking simulations we limited our study to the binding of this sole domain.

Possible conformations of the complex between PADI4 and the p53-binding domain of MDM2 were predicted on the basis of the consensus obtained from different popular docking algorithms: ClusPro (Kozakov et al., 2017), GRAMM (Katchalski-Katzir et al., 1992), HDOCK (Yan et al., 2020), ZDOCK (Pierce et al., 2014), and pyDock (Jiménez-García et al., 2013). These algorithms provide a variety of anchoring positions and orientations, which were subsequently screened up to select only eight possible binding modes (Figure 6) on the basis of some simple criteria, again solely based on our previous experimental results. As a first criterion, when two distinct docking poses obtained with the same algorithm were anchored to PADI4 in a symmetric fashion, this was considered equivalent to the prediction of a single binding mode, because the binding stoichiometry we had found by using ITC (Figure 3c) consists of two monomers of N-MDM2 bound to a sole PADI4 homodimer. For instance, the best two docking poses obtained by ClusPro were located in a similar fashion on each monomer, leading to a single prediction for the molecular complex (Figure S5). As a second criterion, any docking pose was excluded if it overlapped with its symmetrical image when the two were considered together. In fact, their

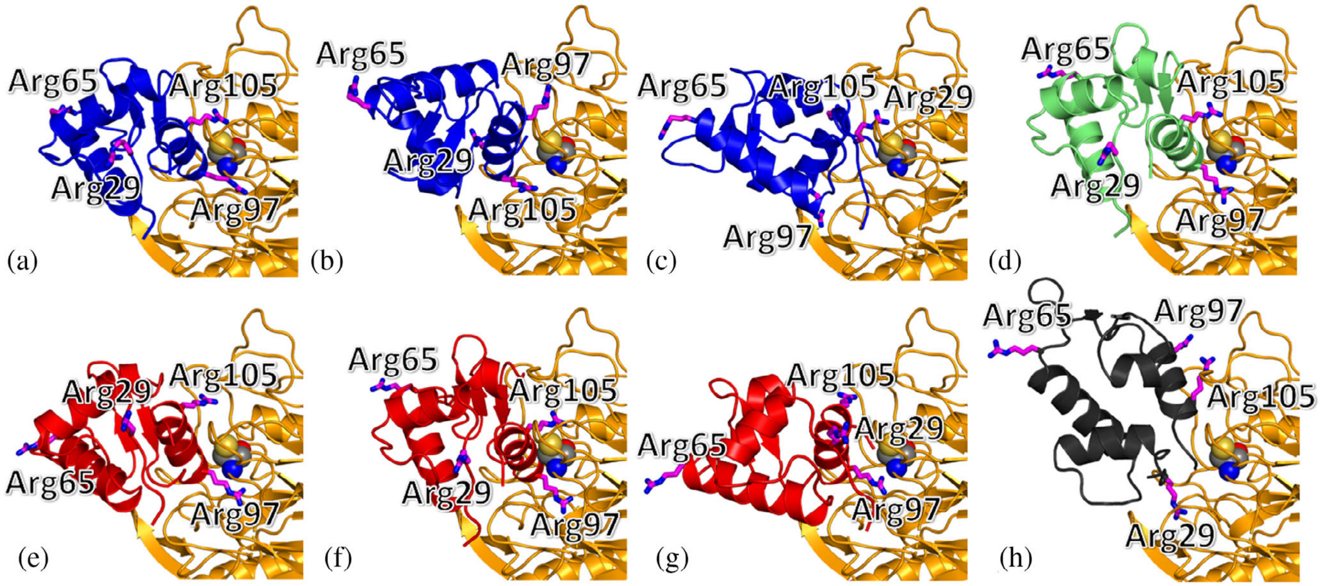

FIGURE 6 Simulated binding locations of N-MDM2 on the surface of PADI4. Structures are predicted by using molecular docking, considering the sole p53-binding domain (residues 25–109) of N-MDM2, and obtained by using (blue) ClusPro [54], (green) HDOCK (Yan et al., 2020), (red) ZDOCK (Pierce et al., 2014), and (black) pyDock (Jiménez-García et al., 2013). A detail of the hot-spot location on the surface of PADI4 (yellow) is shown, with the key catalytic residue Cys645 in van der Waals representation. (a) Pose 1 and 2 of ClusPro; (b) pose 3 and 4 of ClusPro; (c) pose 7 and 8 of ClusPro; (d) pose 3 and 4 of HDOCK; (e) pose 1 of ZDOCK; (f) pose 2 of ZDOCK; (g) pose 3 and 4 of ZDOCK; (h) pose 7 of pyDock. The Arg residues (magenta) of N-MDM2 are explicitly shown and labeled.

actual existence would be mutually exclusive and, therefore, incompatible with the binding stoichiometry expected. This condition eliminated all of the docking poses predicted by GRAMM, as well as most of the those predicted by HDOCK, with the except for a pair of symmetrical poses. As a third criterion, a maximum of three binding modes were considered for each predictor, when they were too similar to each other. This criterion is normally satisfied in the output of most docking algorithms, but it was necessary in our case to reduce the number of predictions of ZDOCK, which essentially clustered in a single conformation for each monomer of PADI4. Finally, the poses predicted by pyDock were eliminated upon visual inspection because they appeared little anchored to the surface of PADI4, with the sole exception of the best docking conformation bound to the catalytic site of PADI4.

The eight docking poses obtained at the end of the screening procedure represent alternative binding modes that may coexist (although with different statistical weights) in the thermodynamic ensemble of the PADI4/MDM2 complex, as they can interconvert in solution. The predictions of all the docking programs were further re-scored by using MM/GBSA, one of the most popular techniques to estimate the free energy of the binding of a biomolecular complex in simulation. This procedure was performed for several reasons: (i) to use a more accurate methodology to calculate the binding score of the docking poses; (ii) to compare on a common ground the results of the different docking predictors, for obtaining a single classification for all the poses; (iii) to provide a quantitative value of the affinity of the docking poses, besides their relative position in an energy ranking list; and (iv) to decompose the free energy of binding in distinct per-residue contributions.

The main results of the re-scoring procedure are summarized in Table 1. It appears clear that the best results were those obtained by using ClusPro as docking algorithm. In particular, in the highest ranked model of the complex (Figure S5), the p53-binding domain interacted closely with the catalytic residue Cys645 of PADI4 by means of the two pairs of consecutive residues Arg97-Lys98 and Tyr104-Arg105. The best docking poses found by using both HDOCK and ZDOCK, although having a binding affinity significantly less favorable compared to the top prediction of ClusPro (-55.21 and -69.66 kcal mol^{-1} vs. -112.33 kcal mol^{-1}, respectively), had a similar position and orientation (RMSD <2 Å). In contrast, pyDock was found to be less accurate than the other predictors, suggesting that the geometry of the encounter complex proposed by this algorithm has likely little specificity.

Some interesting conclusions can be drawn by analyzing the binding interface calculated for the two proteins, on the basis of the residues providing the largest contribution to the calculated binding affinity. As shown in

TABLE 1 Docking poses of the p53-binding domain of N-MDM2 to the host structure of PADI4, obtained from different predictors and ranked by using the MM/GBSA technique, with total binding affinity and per-residue contribution (in parentheses).

Docking algorithm	Pose rank	Binding affinity (kcal mol^{-1})	Best contributions to binding affinity (kcal mol^{-1})	
			PADI4	MDM2
ClusPro	1, 2	−112.33	Phe634 (−6.99), Thr635 (−5.71), Asp473 (−5.68)	Arg97 (−12.91), Tyr104 (−6.98), Arg105 (−4.96)
ClusPro	3, 4	−91.38	Phe633 (−7.47), Asp345 (−4.67), Ser402 (−4.05)	Arg97 (−6.48), Arg105 (−5.48), Thr26 (−4.82)
ClusPro	7, 8	−74.14	Gln349 (−8.25), Phe576 (−6.49), Tyr636 (−4.47)	Arg97 (−6.97), Met50 (−6.27), Thr26 (−5.74)
ZDOCK	2*	−69.66	Phe634 (−4.55), Phe633 (−4.52), Thr635 (−4.06)	Arg97 (−7.30), Tyr104 (−5.56), Val108 (−2.68)
HDOCK	3, 4	−55.21	Phe634 (−3.78), Ser312 (−3.74), Thr635 (−3.73)	Arg105 (−6.52), Arg97 (−4.71), Thr26 (−3.10)
ZDOCK	1*	−51.83	Ile313 (−4.13), Asp632 (−3.95), Glu642 (−3.63)	Arg97 (−12.7), Lys31 (−5.74), Arg105 (−4.11)
ZDOCK	3,4	−42.97	Phe634 (−5.34), Gln346 (−3.34), Asp632 (−3.30)	Arg105 (−8.06), Arg97 (−6.78), Lys31 (−3.76)
pyDock	7*	−25.78	Phe633 (−5.10), Phe634 (−4.08), Tyr636 (−3.58)	Arg29 (−5.32), Arg105 (−2.75), Leu27 (−2.62)

*Single docking pose, missing a similar symmetric pose bound to the other monomers of the homodimeric structure of PADI4.

Figure 7, the docking poses selected from all the predictors are clustered on a single position on the surface of PADI4, which is approximately centred on the catalytic site of the protein with significant accuracy. This observation is intriguing due to the relatively large surface area of PADI4, and because of the protocol of blind docking adopted in the search did not make any prior assumption on the binding pocket. The result obtained strongly suggests that the competitive binding observed in our *in cellulo* experiments (Figure 2) is not due to an allosteric effect, and that N-MDM2 targets directly the active site of PADI4 not only with a good affinity, but also with a high specificity.

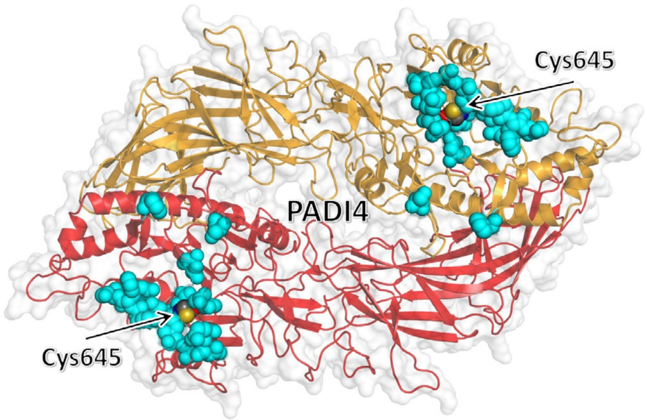

FIGURE 7 Clustering of residues of PADI4 with the most favorable affinity toward the p53-binding domain of N-MDM2. Top three residues of PADI4 with the most favorable binding affinity to each of the eight selected docking poses, as obtained by using MM/GBSA with per residue decomposition (Table 1), are shown (cyan) in van der Waals representation. The key catalytic residue Cys645 is also explicitly shown and labeled. The two chains of the homodimeric structure of PADI4 are represented in different colors.

It is also evident that in all the docking poses found there is an arginine of N-MDM2 involved as the residue contributing the most to the binding energy in the association of the two proteins (Table 1). Moreover, in most of the docking complexes a second arginine is also present among the other top residues ranked in terms of their most favorable affinity toward PADI4. Since only four arginine residues are present in the p53 domain of N-MDM2, their affinity toward the catalytic site of PADI4 on the basis of the simulation results can be ranked as follows: Arg97 $\gtrsim$ Arg105 > Arg29 > Arg65. We note that, although our simulations cannot provide evidence of the citrullination of MDM2, the direct and favorable interaction of these arginines with the active site of PADI4—both in terms of geometry (Figure 6) and affinity (Table 1)—coupled with the high reactivity of the catalytic centre of this protein strongly supports this hypothesis, especially for Arg97 and Arg105. We also stress that our simulation findings have a good agreement with the NMR results, because most of the residues with the highest contribution to the binding affinity of the complex correspond to those whose NMR signals were affected by the binding to PADI4, either exactly or shifted by 1–2 residues (Figure 4b, Table 1).

2.5 | Inhibition of PADI4 enhanced temozolomide (TMZ) effect on GBM cells

We observed a strong decrease in the population of MDM2/PADI4 complexes formed at the nucleus of the GBM cell line upon GSK484 treatment (Figure 2). It has been shown that the inhibition of MDM2 expression leads to down-regulation of O6-methylguanine methyltransferase (MGMT) enhancing tumor cell sensitivity to the main GBM treatment: the use of the oral alkylating agent TMZ (Sato et al., 2011), which methylates the DNA and triggers the death of tumor cells. Some drugs can bind to proteins that are responsible of drug resistance or, alternatively, relevant in cancer treatment. The sequential application of several drugs, used for different purposes, can have an impact on the cells at different extent; for instance, the co-administration of a PADI inhibitor and an androgen receptor signal transduction inhibitor hampered tumor growth in prostate cancer and cell proliferation (Wang et al., 2017). In that way, the use of TMZ in combination with other drugs can increase its cytotoxicity at a much lower concentration than when used in isolation (Chakravarty et al., 2021). Therefore, we speculated that the treatment of GBM tumor cells by TMZ could be also enhanced by the presence of GSK484. For this reason, we carried out a first experiment, where the concentration of the inhibitor was increased while that of TMZ was kept constant. TMZ contains a methyl group that modifies the purine DNA bases (O6-guanine; N7-guanine and N3-adenine) in cells. The addition in the first place of this drug, results in an alkylating modification, and therefore may have an impact on the cells for a possible GSK484 action on PADI4, although the exact details of the mechanism are unknown. Then, we also treated the cells firstly with a constant concentration of TMZ, followed by GSK484 increasing concentrations, to experimentally explore the effect of inhibition of PADI4 on cells whose purine bases had been previously alkylated.

To ensure that single treatments did not affect GBM cell line proliferation, we performed monotherapy experiments at low dosages with the two drugs (Figure 8a,b). First, we observed that a range of GSK484 treatment between 1 and 6 μM led to no effect in proliferation of HGUE-GB-42 cells (Figure 8a). Similarly, low dosage of TMZ ranging between 1 and 12 μM did not significantly reduce their proliferation either (Figure 8b).

To test whether the combination of both compounds had an impact on GBM proliferation, we treated the cells at a TMZ constant concentration of 6 μM, that was previously reported to have no effects (Figure 8b). That constant TMZ concentration was administered together with increasing concentrations of GSK484, at the same range of low concentrations, at which monotherapy did not alter proliferation (Figure 8a). Our experiments showed that such combined treatment of GBM cells resulted in a significant decrease of proliferation, which was highly dependent on the GSK484 concentration (Figure 8c). We also performed the reverse experiment where the cells were treated with a constant concentration of 6 μM of GSK484. Concomitantly, cells were treated with increasing concentrations of TMZ ranging from 1 to 12 μM, also resulting in a significant decrease of cell proliferation (Figure 8d). These results demonstrate the synergistic effect of the two drugs, opening the venue for new treatments based on the additive effect that PADI4 inhibition might have, in combination with other drugs approved for different types of cancers.

3 | DISCUSSION

Cancer accounts for nearly one in six deaths corresponding to around 10 million deaths in 2020 (Sung et al., 2021). To ensure more effective treatments, we need to improve not only the identification of aggressive tumors at an earlier stage, but also to increase the efficiency of therapies against current cancer targets, or alternatively to find new ones (Adashek et al., 2021). This would not only improve the quality of cancer patients lives, but would also enhance survival rates of patients for many types of cancers. Given the importance of PADI4 and MDM2 in cancer, we discuss the possible implications of this new interaction for tumor development and progression.

We observed that the inhibition of PADI4 by GSK484 enhanced the sensitivity to an oral DNA alkylating agent, TMZ, the current main GBM treatment. The combination of these two compounds had a synergistic effect that led to a decrease in GBM cell proliferation, which neither of the isolated drugs could achieve independently. These results might lead to more effective treatments to enhance the effects of other approved drugs against cancer, by using GSK484 against PADI4 in several protein routes. The observed different effects on several cancer cell lines (Section 2.1) is related to the different cross-talk routes where PADI4 can intervene. For instance, in epithelial-to-mesenchymal transition (EMT), PADI4 inhibition results in different outcomes in multiple cancer cell lines. In breast cancer, PADI4 acts through glycogen synthase kinase 3 beta GSK3β; whereas in lung cancer, the inhibition of PADI4 increases the ETS-domain

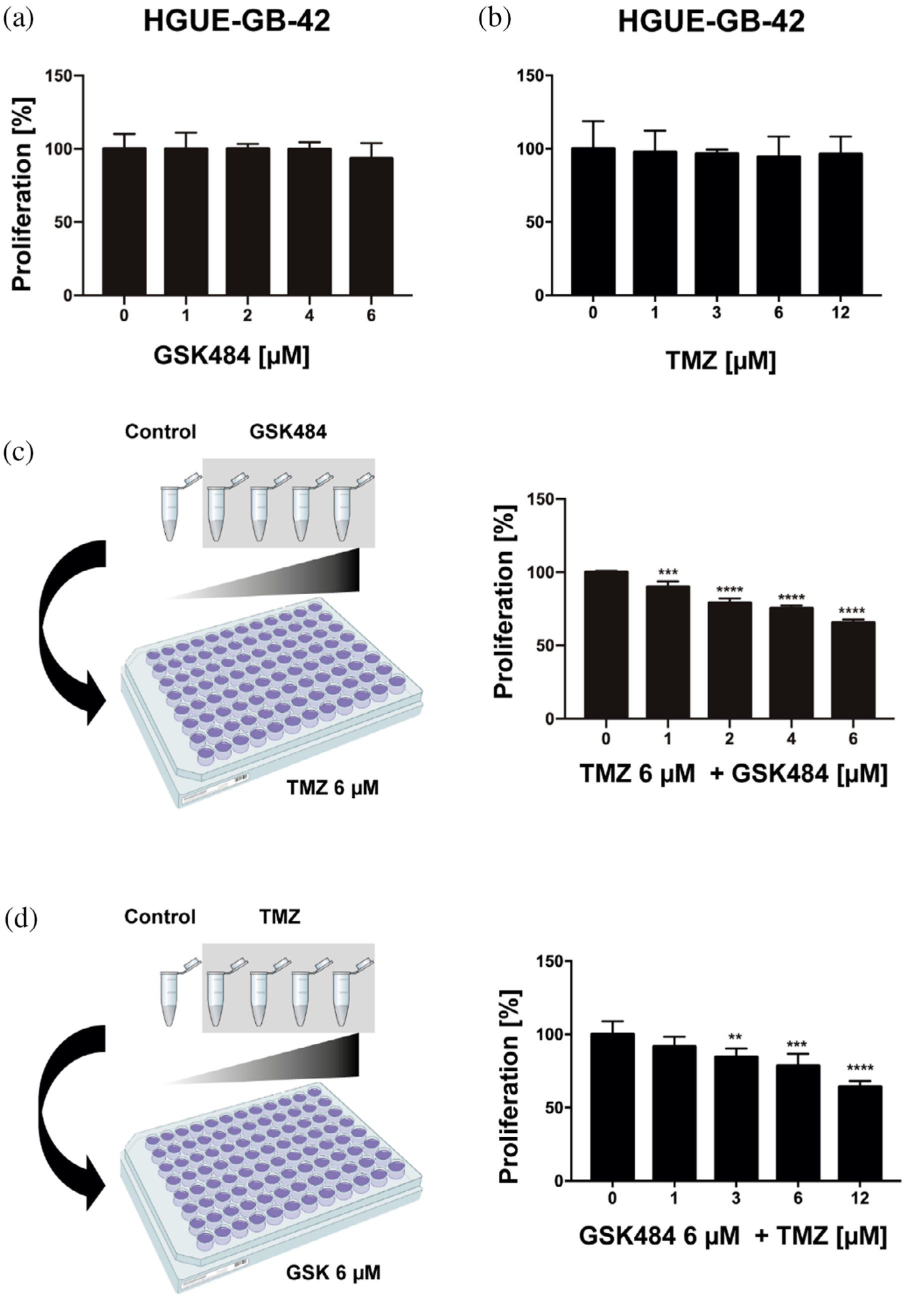

FIGURE 8 Combinatorial effect of GSK484 and TMZ. Monotherapy applied to GBM cell line HGUE-GB-42 with GSK484 (a) and TMZ (b). (c) Scheme and measurements showing the proliferation assays made keeping a constant concentration of 6 μM TMZ and increasing those of GSK484. (d) Scheme and measurements showing the proliferation assays made keeping a constant concentration of 6 μM GSK484 and increasing those of TMZ. Asterisks indicate the statistical significance of the results (**$p < 0.01$, ***$p < 0.001$, ****$p < 0.0001$).

containing protein (Elk1) expression. On the other hand, in colon cancer, citrullination of the extracellular matrix by PADI4 promotes the EMT, and therefore cancer progression (Yuzhalin et al., 2018). We do not know exactly how the combination of TMZ (acting on DNA) and GSK484 (acting on PADI4) results in a synergistic effect in the cells, but it could probably involve a combined action on several proteins along the pathway, at least one of which implies handling of modified DNA (due to the TMZ effect). We hypothesized that a direct interaction of intact MDM2 with PADI4 could take place through the N-terminal region of MDM2, the N-MDM2, which also intervenes in the interaction with the S100 proteins (van Dieck et al., 2010) and the sterile alpha motif (SAM) of p73, SAMp73 (Neira et al., 2019). The results of our *in vitro* experiments support that hypothesis clearly demonstrating the binding of N-MDM2 and PADI4. In addition, the NMR experiments indicated that the PADI4-binding region of N-MDM2 comprised Thr26, Val28, Gln44– all involved in several loops–, and Phe91 and Lys98– forming the C-terminal α-helix. These two latter residues are close, but they do not belong to the region implicated in the binding to the TA of p53; however, different protein partners (either PADI4 or p53) might elicit different changes in the structure of MDM2 to modulate functions in several cellular processes. Except for the above indicated residues, and those whose side chains could be titrating at the pH where experiments were acquired, the chemical shifts of the amide protons of residues of N-MDM2 did not change substantially in the presence of PADI4 (Figure 4a), indicating that the secondary structure of N-MDM2 was not modified dramatically upon binding to PADI4. Therefore, the observed changes in the far-UV CD spectra must occur in the backbone of PADI4, in the disordered N- and C-terminal regions of MDM2 (which are not observed in the NMR spectra), or alternatively in the orientation of some aromatic residues of any of the two proteins (Figure 3a, right panel). For instance, it has been shown that the side-chains of His96 and Tyr100 move away in the presence of TA of p53 to allocate the side-chain of Pro27 of p53. Interestingly enough, residues Ile99 and Tyr100 showed split resonances in the ^{1}H-^{15}N HSQC spectra of isolated N-MDM2, indicating a slow conformational equilibrium exchange in such region (Uhrinova et al., 2005). We hypothesize that similar changes in the side-chains of His96 and Tyr100, both close enough to Phe91 and Lys98, can occur in the presence of PADI4, explaining the variations in the far-UV CD spectra.

ITC experiments demonstrating the interaction between N-MDM2 and the intact p53 have provided a value of ~0.30 ± 0.01 μM for the dissociation constant of the complex (Schon et al., 2002; Schon et al., 2004; Yu et al., 2006). These values are comparable to the one measured between N-MDM2 and the TA of p53: 0.10 ± 0.03 μM (Kussie et al., 1996; Lai et al., 2000). Furthermore, the core region of p53 (residues 93–293) also binds to the acidic domain and part of the zinc finger domain of MDM2 with similar values of affinity (0.1–0.3 μM, depending on the MDM2 region explored) (Yu et al., 2006). All these values are within the same range determined in this work for the interaction between N-MDM2 and PADI4 (Figure 3c,d), by ITC ($K_d = 1.0 \pm 0.2$ μM). Similar, but slightly larger figures have been found when the binding between N-MDM2 and SAMp73 has been studied: 8 ± 3 μM by fluorescence, or 18 ± 6 μM by BLI (Neira et al., 2019). Thus, it seems that the affinity of N-MDM2 for any of its partners is in the low micromolar region, further pinpointing that PADI4 should be among the canonical binding proteins of intact MDM2.

A close look into the N-MDM2 region involved in binding to PADI4 further indicates which arginine residues could be the potential citrullination sites. The N-MDM2 has four arginines: Arg29, Arg65, Arg97 and Arg105. Three of them are close to residues having the largest conformational shifts: Arg29 (close to Val28), Arg97 and Arg105 (both close to Lys98). (Figure 4 B). The simulation results support the idea that some of those arginines are candidates to be citrullinated by PADI4. More specifically, they exclude access of Arg65 to the active site of PADI4; they suggest as possible, but unlikely, an interaction of Arg29; and they point out to Arg97 and Arg105 as the most likely candidates. Although molecular docking cannot demonstrate directly that the citrullination reaction will take place, there is a very favorable interaction geometry and affinity of the enzymatic site of PADI4 with Arg97, which is close to His96. However, we could not unambiguously conclude that their chemical shifts were only affected by the presence of PADI4 because of its titrating imidazole side-chain. Moreover, Arg97 is close to Ile99, which forms the pocket where Leu26 of p53 is located in the complex with such protein, and therefore, it could hamper the binding of p53, suggesting a potential role of PADI4 in the mechanism of degradation and regulation of p53 by MDM2.

There is a relationship between p53 pathways and citrullination, where PADI4 citrullinates the nuclear localization signal of ING4, preventing ING4 binding to p53 (Guo & Fast, 2011).The lack of ING4/p53 association hampers ING4-promoted-p53-acetylation and the expression of p21. Furthermore, in several PADI4-overexpressing cancer cells, the use of PADI4 inhibitors or PADI4 siRNA raised the expression of p53 target genes, resulting in apoptosis and cell cycle arrest (Yao et al., 2008). Moreover, p53 transactivates PADI4 through an intronic p53-binding site, but, the relationship with MDM2 has never been studied (Tanikawa et al., 2009). We hypothesize that MDM2 might be a non-histone substrate, which could add to the well-known list of substrates of the PADI4 enzyme, such as ING4, p300 or GSK3β (Zhu et al., 2022). MDM2 not only regulates p53 function by mediating its export from the nucleus in a manner that involves mono-ubiquitination and SUMOylation (Brooks & Gu, 2011), but it can also self-ubiquitinate. MDM2 can also be SUMOylated (Chen & Chen, 2003), phosphorylated (Li & Kurokawa, 2015), and acetylated. Then, as regulation of MDM2 takes place at multiple levels including transcriptional, post-transcription, and even by protein modification through ubiquitination, it would not be surprising that MDM2 might also be citrullinated. Taken all together, our study opens up venues for understanding the basis of molecular mechanism of cancers although, given the promiscuity of PADI4 in the interaction with several proteins, further studies are necessary to translate these findings into possible therapeutic applications.

4 | MATERIALS AND METHODS

4.1 | Materials

Imidazole, Trizma base, DNase, SIGMAFAST protease tablets, NaCl, Ni^{2+}-resin, temozolamide (TMZ), 3-(4,5-Dimethylthiazol-2-Yl)-2,5-Diphenyltetrazolium bromide (MTT), dimethyl sulfoxide (DMSO), DAPI (4′,6-diamidino-2-phenylindole) and Amicon centrifugal devices with a molecular weight cut-off of 3 or 30 kDa were from Sigma (Madrid, Spain). The β-mercaptoethanol was from BioRad (Madrid, Spain). Ampicillin and isopropyl-β-D-1-thiogalactopyranoside were obtained from Apollo Scientific (Stockport, UK). Triton X-100, Tris(2-carboxyethyl)phosphine (TCEP), dialysis tubing with a molecular weight cut-off of 3500 Da and the SDS protein marker (PAGEmark Tricolor) were from VWR (Barcelona, Spain). Thrombin and GST-resin were from GE Healthcare (Barcelona, Spain). The rest of the used materials were of analytical grade. Water was deionized and purified on a Millipore system.

4.2 | Protein expression and purification

The dimeric PADI4 (with 663 residues *per* monomer) and monomeric His-tagged N-MDM2 (residues 6–125 of the intact protein) were purified as previously described (Neira et al., 2019; Neira, Araujo-Abad, et al., 2022). The first five residues of N-MDM2 were missing due to optimization of cloning sequence. For BLI experiments, GST-tagged-N-MDM2 was produced as described (Yadahalli et al., 2019) and the GST-tag was removed by using thrombin on the same GST-column. For the ^{15}N-labeled His-tagged N-MDM2, BL21 cells were grown in M9 minimal medium supplemented with 1 g of $^{15}NH_4Cl$ *per* liter of media, and the protein was purified as that obtained in rich media. In all cases, protein concentrations were determined by UV absorbance, employing an extinction coefficient at 280 nm estimated from the number of tyrosines and tryptophans in each of these proteins (Gill & von Hippel, 1989). The construct of His-tagged N-MDM2 has eight tyrosines, that of GST-tagged-N-MDM2 has seven tyrosines and PADI4 has 10 tryptophans and 13 tyrosines *per* monomer.

4.3 | Cell lines

Isolation of the primary human GBM cell line (HGUE-GB-42) was performed from surgical washes, as reported previously (Ventero et al., 2019). Human pancreatic adenocarcinoma (RWP-1) and colorectal cancer (SW-480) cell lines were donated by Instituto Municipal de Investigaciones Médicas (IMIM, Barcelona, Spain) (Fuentes-Baile et al., 2020). The RWP-1 and SW-480 cell lines were cultured in Dulbecco's Modified Eagle's Medium: High Glucose (DEMEM-HG) (Biowest, MO, USA). The GBM cells were cultured in Dulbecco's Modified Eagle's Medium: Nutrient Mixture F-12 (DMEM F-12) (Biowest, MO, USA), supplemented with 10% (v/v) heat-inactivated fetal bovine serum (FBS) (Capricorn Scientific, Ebsdorfergrund, Germany) and 1% (v/v) penicillin/streptomycin mixture (Biowest, MO, USA). Cells were incubated at 37°C in a humidified 5% CO_2 atmosphere as previously described (Fuentes-Baile et al., 2021; Ventero et al., 2019).

4.4 | Immunofluorescence

An amount of 30,000 cells of HGUE-GB-42, SW-480 and RWP-1 cell lines were seeded into 24-well plates on coverslips. After 24 h, they were fixed with paraformaldehyde at 4% concentration and blocked with FBS/PBS (phosphate buffered saline) (1×) (50 μL/mL). Next, cells were incubated with anti-PADI4 (1:200, mouse; Abcam, Cambridge, UK) and anti-MDM2 (1:100, rabbit, Invitrogen, Barcelona, Spain) primary antibodies. After washing out the first antibody, cells were incubated with Alexa Fluor 568-labeled anti-mouse (1:500) and Alexa Fluor 488-labeled anti-rabbit (1:500) secondary antibodies (Invitrogen, Barcelona, Spain); the DAPI reagent was used to stain the nucleus. Coverslips were mounted in Prolong™ Gold Antifade Reagent (Invitrogen, Barcelona, Spain) and analyzed using a Zeiss Axioscope 5 microscope with the LED light source Colibri 3 (Carl Zeiss, Oberkochen, Germany).

4.5 | Proximity ligation assay

An amount of 30,000 cells of HGUE-GB-42, SW480 and RWP-1 cell lines were seeded in 24-well plates on coverslips to perform the experiments, either in the absence or the presence of GSK484 (at a final concentration of 20 μM). Experiments were carried out at either 6 or 24 h; control experiments were carried out with 6 h. After the corresponding time, cells were washed twice in PBS (1×), fixed, washed twice again, permeabilized in PBS, with 0.2% Triton X-100, and saturated with blocking solution for 30 min before immune-staining with Duolink by using PLA Technology (Merck, Madrid, Spain), following the manufacturer's protocol. Anti-PADI4 and anti-MDM2 primary antibodies were used. Then, slides were processed for in situ PLA by using sequentially the Duolink In Situ Detection Reagents Red, Duolink In Situ PLA Probe Anti-Mouse MINUS, and Duolink In Situ PLA Probe Anti-Rabbit PLUS (Merck, Madrid, Spain). In these experiments, red fluorescence corresponds to the PLA-positive signal, and it indicates that the two proteins are bound, forming a protein complex. Blue fluorescence corresponds to nuclei (DAPI staining). Both negative and positive control experiments, the former by omitting one of the primary antibodies, were performed. Image acquisition was carried out by using an Axio Observer Z1 inverted microscope (Carl Zeiss, Oberkochen, Germany) at ×63 magnification.

4.6 | Proliferation assays

The HGUE-GB-42, SW480 and RWP-1 cell lines were seeded in 96-well standard plates (Sarstedt, Nümbrecht, Germany) with a density of 4000 cells/well and incubated at 37°C in the presence of 5% CO_2 for 24 h. Subsequently, cells were treated with increasing concentrations of one of the drugs—either the PADI4 enzyme inhibitor (GSK484) or TMZ—for 72 h under the same conditions. Then in any of the experiments, 0.25 mg/mL of MTT were added and the samples were incubated for 3 h; afterwards, the medium was removed and 100 μL of DMSO were added. The plate was shaken at room temperature for 20 min to dissolve the formed formazan crystals. Finally, the absorbance was measured on an Eon™ Microplate Spectrophotometer (BioTeK®, Winooski, VT, USA) at 570 nm.

Experiments with HGUE-GB-42 were carried out with GSK484, in concentrations ranging between 1 and 6 μM. Similarly, dosage of TMZ with the same cell lines ranged between 1 and 12 μM. For the first series of experiments in the presence of both compounds, the concentration of TMZ was kept constant at 6 μM, whereas that of GSK484 was increased in the range described above. For the second series of experiments in the presence of both compounds, the concentration of GSK484 was kept constant at 6 μM, whereas that of TMZ was increased in the range described above.

4.7 | Fluorescence

4.7.1 | Steady-state fluorescence

Fluorescence spectra were collected on a Cary Varian spectrofluorometer (Agilent, Santa Clara, CA, USA), interfaced with a Peltier unit. Following the standard protocols used in our laboratories, the samples were prepared the day before and left overnight at 5°C; before experiments, samples were left for 1 h at 25°C. A 1-cm-pathlength quartz cell (Hellma, Kruibeke, Belgium) was used. Concentration of PADI4 was 3 μM (in protomer units), and that of N-MDM2 was 20 μM. Experiments were performed in 20 mM Tris buffer (pH 7.5), 5 mM TCEP, 150 mM NaCl and 5% glycerol. Protein samples were excited at 280 and 295 nm. The other experimental parameters have been described elsewhere (Neira et al., 2016). Appropriate blank corrections were made in all spectra. Fluorescence experiments were repeated in triplicates with newly prepared samples. Variations of results among the experiments were lower than 10%.

4.7.2 | Binding experiments with PADI4

For the titration between N-MDM2 and PADI4, increasing amounts of the monomeric N-MDM2 species, in the concentration range 0–20 μM, were added to a solution with a fixed concentration of PADI4 (2.8 μM in protomer units). The samples were prepared the day before and left overnight at 5°C; before the measurements, they were incubated for 1 h at 25°C. Experiments were carried out in the same buffer used for the steady-state experiments. The samples were excited at 280 and 295 nm, and the rest of the experimental set-up was the same described above. In all cases, the appropriate blank-corrections were made by subtracting the signal obtained with the corresponding amounts of N-MDM2 by using the software KaleidaGraph (Synergy software, Reading, PA, USA). Spectra were corrected for inner-filter effects during fluorescence excitation (Birdsall et al., 1983). The titration was repeated three times, using new samples; variations in the results were lower than 10%.

The dissociation constant of the corresponding complex, K_d, was calculated by fitting the binding isotherm constructed by plotting the observed fluorescence change as a function of N-MDM2 concentration to the general binding model, explicitly considering protein depletion due to binding (Beckett, 2011; Royer & Scarlata, 2008):

$$F = F_0 + \frac{\Delta F_{\max}}{2[PADI4]_T}\left([\mathrm{N-MDM2}]_T + [\mathrm{PADI4}]_T + K_d\right) - \sqrt{\left(\left([\mathrm{N-MDM2}]_T + [\mathrm{PADI4}]_T + K_d\right)^2 - 4[\mathrm{N-MDM2}]_T[\mathrm{PADI4}]_T\right)} \quad (1)$$

where F is the measured fluorescence at any particular concentration of N-MDM2 after subtraction of the spectrum of sample containing only the same concentration of such protein (i.e., F is the differential, or difference fluorescence); $\Delta F_{\max}$ is the largest change in the fluorescence of N-MDM2 when all polypeptide molecules were forming the complex, compared to the fluorescence of each isolated protein (at the same corresponding concentration); F_0 is the fluorescence intensity when no N-MDM2 was added; $[\text{PADi4}]_T$ is the constant, total concentration of PADI4 (2.8 μM in protomer units); and $[\text{N-MDM2}]_T$ is that of N-MDM2, which was varied during the titration. Fitting to Equation (1) was carried out by using KaleidaGraph (Synergy software, Reading, PA, USA).

4.8 | Circular dichroism

Far-UV CD spectra were collected on a Jasco J810 spectropolarimeter (Jasco, Tokyo, Japan) with a thermostated cell holder and interfaced with a Peltier unit. The instrument was periodically calibrated with (+)-10-camphorsulfonic acid. A cell of path length 0.1 cm was used (Hellma, Kruibeke, Belgium). Spectra were corrected by subtracting the corresponding baseline. Polypeptides concentrations and the buffers were the same used in the fluorescence experiments.

Isothermal spectra of each isolated macromolecule and that of the complex were acquired at 25°C as an average of 6 scans, at a scan speed of 50 nm/min, with a response time of 2 s and a band-width of 1 nm. Samples were prepared the day before and left overnight at 5°C to allow them to equilibrate. Before starting the experiments, samples were further left for 1 h at 25°C.

4.9 | Nuclear magnetic resonance

The NMR experiments were acquired in a 600 MHz (1H) Bruker AVNEO spectrometer, (Karlsruhe, Germany) equipped with a z-gradient cryoprobe. Spectra were acquired at 25°C in 20 mM Tris buffer (pH 7.5), 5 mM TCEP, 150 mM NaCl, 10 mM EDTA, and 5% glycerol with 50 μL of D_2O; probe temperature was calibrated with a methanol NMR standard (Cavanagh et al., 2007).

The cross-peaks in the 2D ^{1}H-^{15}N HSQC NMR spectra (Bodenhausen & Ruben, 1980) of N-MDM2 were identified by using previously determined assignments (BMRB number 6612) (Uhrinova et al., 2005). The sample containing the mixture of N-MDM2 and PADI4 was prepared by using Amicon centrifugal devices of 3 kDa cut-off, in which both proteins were initially mixed at diluted concentrations in the above indicated buffer, and then, concentrated in the same buffer; any possible precipitation in the Amicon devices was removed during the concentration step. For the isolated N-MDM2 the buffer was the same, with a final protein concentration of 95 μM. In the sample of the complex, the concentration of N-MDM2 was the same, and that of PADI4 was 234 μM (in protomer units). The pH of both samples (complex and isolated N-MDM2) was measured after removal from the Amicon device with an ultra-thin electrode. Spectra were processed with TopSpin 4.1.3 (Bruker, Karlsruhe, Germany).

Chemical shift perturbations (CSPs) for every cross-peak in the spectra of either isolated N-MDM2 or the complex were calculated as:

$$\text{CSP} = \left[(\Delta\delta_H)^2 + \left(\frac{\Delta\delta_N}{5} \right)^2 \right]^{1/2} \quad (2)$$

4.10 | Isothermal titration calorimetry

Calorimetric titrations for assessing the interaction of PADI4 with N-MDM2 were carried out in an automated high-sensitivity Auto-iTC200 calorimeter (MicroCal, Malvern-Panalytical, Malvern, UK). Experiments were performed at 25°C in 20 mM Tris buffer (pH 7.5), 5 mM TCEP, 150 mM NaCl and 5% glycerol at 25°C. PADI4 (100 μM in protomer units) in the injection syringe was titrated into the N-MDM2 solution (10 μM) in the calorimetric cell. A series of 19 injections with 2 μL volume, 0.5 μL/s injection speed, and 150 s time spacing was programmed while maintaining a reference power of 10 μcal/s and a stirring speed of 750 rpm. The heat effect *per* injection was calculated by integration of the thermal power raw data after baseline correction, and the interaction isotherm (ligand-normalized heat effect *per* injection as a function of the molar ratio) was analyzed by non-linear least-squares regression data analysis, applying a model that considers a single binding site to estimate the association constant, K_a; the interaction enthalpy, ΔH; and the stoichiometry of binding, n (although, in practice, the apparent stoichiometry n usually reports the fraction of active protein in the calorimetric cell). The background injection heat (usually called "dilution heat," but reflecting any unspecific phenomenon such as solute dilution, buffer neutralization, temperature equilibration or solution mechanical mixing) was accounted for by including an adjustable constant parameter in the fitting equation. Due to the presence of glycerol in solution, the background injection heat was rather large. The data analysis was conducted in Origin 7.0 (OriginLab, Northampton, MA, USA) with user-defined fitting functions.

4.11 | Biolayer interferometry

4.11.1 | Experimental design of BLI experiments

The association (k_{on}) and dissociation (k_{off}) rate constants of the binding of N-MDM2 to PADI4 were determined by using a BLItz system (ForteBio, Pall, Barcelona, Spain) (Frenzel & Willbold, 2014). The buffer used in the experiments was that recommended by the manufacturer. As PADI4 had a His-tag, it was immobilized on His-tag biosensors (Forte Bio) at 0.45 μM, and we used N-MDM2 derived from a GST-tagged protein, where the tag had been removed. Experiments were carried out at 25°C. The N-MDM2 concentrations were in the range from 1 to 9 μM during the association step. The general schemes of the protein association/dissociation reactions in the BLItz system were: 30 s of acquisition of the initial baseline with the 10 × kinetics buffer; 120 s of loading PADI4 into the biosensor; 30 s of baseline with the 10 × kinetics buffer; 120 s of association of N-MDM2 to the biosensor (which had been previously loaded with PADI4); and 120 s of dissociation of N-MDM2 from the biosensor.

4.11.2 | Fitting of the sensorgrams

Fittings of the sensorgrams was carried out by using KaleidaGraph (Synergy software, Reading, PA, USA) (Pantoja-Uceda et al., 2016). The interferometry response during the association step, $R(t)$ (measured in response units, RU), and the binding rate, $dR(t)/dt$, can be used to evaluate the kinetics of the formation of the N-MDM2/PADI4 complex, according to:

$$\frac{dR(t)}{dt} = k_{\mathrm{on}}[\mathrm{N-MDM2}](R_{\max} - R(t)) - k_{\mathrm{off}}R(t) \tag{3}$$

where $R_{\max}$ is proportional to the total concentration of biosensor-bound PADI4; and [N-MDM2] represents the corresponding concentration of N-MDM2.

In Equation (3), $R(t)$ is given by:

$$R(t) = R_{\mathrm{eq}} - R_{\mathrm{eq}}e^{(-k_{\mathrm{obs}}(t-t_0))} \tag{4}$$

where R_{eq} is the steady-state (or equilibrium) response obtained at infinite time when $dR(t)/dt = 0$, and $t_0 = 180$ s is the time at which the association step between biosensor-immobilized PADI4 and N-MDM2 in the solution started. We fitted the experimentally obtained $R(t)$ under any condition as:

$$R(t) = R_{\mathrm{eq}} - R_{\mathrm{eq}}e^{(-k_{\mathrm{obs}}(t-t_0))} - R'_{\mathrm{eq}}(t-t_0) \tag{5}$$

since we observed a slope of the signal at the largest sensorgram acquisition times. The determined k_{obs} was used for the pseudo-first order plots, where its value is given by:

$$k_{obs} = k_{on}[\mathrm{N-MDM2}] + k_{off} \tag{6}$$

The dissociation process was always fitted to a single exponential, with $R(t)$ given by:

$$R(t) = R_1\, e^{(-k_{off}(t-t_0))} \tag{7}$$

where $t_0 = 300$ s is the time at which the dissociation of N-MDM2 from the biosensor-bound PADI4 started in our experimental set-up, and R_1 is the response level when dissociation starts.

4.12 | Molecular modeling and simulation

PADI4 was built in homodimeric form as previously described (Neira, Araujo-Abad, et al., 2022), on the basis of the structure deposited in the Protein Data Bank (PDB) and obtained by x-ray diffraction (PDB entry: 3APN; Horikoshi et al., 2011).

The structure of N-MDM2 is present in numerous entries in the PDB database (>100 structures with sequence identity ≥98%), including a 24-model ensemble of the unliganded protein in solution obtained by NMR (PDB entry: 1Z1M (Uhrinova et al., 2005)) as well as bound to a large variety of molecular partners (McCoy et al., 2003). Both the N-terminal (residues 1–24) and C-terminal region (residues 110–125) of N-MDM2 are unstructured in the unliganded protein species. More importantly, they are generally not solved in the experimentally determined structure of the complexes—or absent in the protein construct used to obtain crystals. These observations suggest that the two termini of N-MDM2 do not tend to acquire a structure when the protein is engaged in a complex, and may not be essential in the binding. Therefore, for our molecular docking simulations we considered the sole well-folded N-terminal domain of N-MDM2, the so-called p53-binding domain, encompassing residues 25–109 (Marine et al., 2007).

The structure of the p53-binding domain is essentially identical (deviations of backbone atoms <1 Å) in almost all the structures of N-MDM2 reported in the PDB (McCoy et al., 2003). To avoid any potential bias due to choosing a specific experimental structure over any other, for our calculations we used the structure of the p53-binding domain obtained from the AlphaFold Protein Structure Database (Varadi et al., 2022), entry Q00987. Models of the complex between PADI4 and the p53-binding domain of MDM2 were built on the basis of the 10 most favorable conformations predicted by each of the following protein–protein docking servers: ClusPro (version 2.0) (Kozakov et al., 2017), GRAMM (current version) (Katchalski-Katzir et al., 1992), HDOCK (version 2020) (Yan et al., 2020), pyDock (current version) (Jiménez-García et al., 2013), and ZDOCK (version 3.0.2) (Pierce et al., 2014). All these algorithms were used with default parameters, and without specifying any preference or constraint on the possible binding hot-spot of the two proteins.

After the protein–protein docking stage, the poses calculated with the different predictors were sieved to eliminate those that were not consistent with our experimental findings, leading to a smaller subset that was re-scored by using a more accurate methodology to estimate the binding free energy, and evaluate its decomposition into contributions of each single residue. To this aim, MM combined with generalized Born surface area (MM/GBSA) continuum solvation was applied (Rizzuti, 2022), as implemented in the web server HawkDock (Weng et al., 2019). Interactions were calculated after an energy minimization of 5000 steps (steepest descent followed by the conjugate gradient algorithm for 2000 and 3000 cycles, respectively), using the Amber ff02 force field (Cieplak et al., 2001) and the implicit solvent $\mathrm{GB}^{\mathrm{OBC1}}$ model (Onufriev et al., 2004) with interior dielectric constant $\varepsilon_{\mathrm{in}} = 1$.

4.13 | Statistical analysis

Results in the isolated or combined therapy (GSK484 and TMZ) are always shown as the mean ± standard deviation (SD) of three independent experiments. To evaluate the normal distribution of the data, the Shapiro–Wilk statistical test was used; either the Student's *t*-test or the Mann–Whitney *U* test were used to analyze the association between variables. Differences were considered to be statistically significant with a *p*-value <0.05. Statistical analysis was performed with GraphPad Prism v7.0a software (GraphPad Software Inc., San Diego CA, USA).

AUTHOR CONTRIBUTIONS

Conceptualization: José L. Neira, Bruno Rizzuti, Camino de Juan Romero and Adrián Velazquez-Campoy. *Methodology*: Salomé Araujo-Abad, José L. Neira, Camino de Juan Romero, Bruno Rizzuti and Adrián Velazquez-Campoy. *Investigation*: José L. Neira, Salomé Araujo-Abad, Adrián Villamarin-Ortiz, David Pantoja-Uceda, Celia M. Moreno-Gonzalez, Bruno Rizzuti and Olga Abian. *Data formal analysis*: José L. Neira, Salomé Araujo-Abad, Olga Abian, Adrián Villamarin-Ortiz, David Pantoja-Uceda, Celia M. Moreno-Gonzalez, Bruno Rizzuti and Adrián Velazquez-Campoy. *Writing-original draft preparation*: Salomé Araujo-Abad, David Pantoja-Uceda, José L. Neira, Camino de Juan Romero, Bruno Rizzuti and Adrián Velazquez-Campoy. *Materials*: José L. Neira, Camino de Juan Romero, Olga Abian, Bruno Rizzuti and Adrián Velazquez-Campoy. *Writing-review and editing*: José L. Neira, Olga Abian, Camino de Juan Romero, Bruno Rizzuti and Adrián Velazquez-Campoy. *Funding acquisition*: José L. Neira, Camino de Juan Romero, Olga Abian and Adrián Velazquez-Campoy. All authors have read and agreed to the published version of the manuscript.

ACKNOWLEDGMENTS

We thank Miguel Saceda for the use of the cancer cell lines. The inverted microscope (at Bioengineering Institute of the Miguel Hernández University) used to obtain high-resolution images of our samples, was funded by the Fondo Europeo de Desarrollo Regional (FEDER)-operational program 2007/2013. We would like to thank Dr. Eduardo Fernández Jover and his team for their kindness, generosity and their technical support and expertise in the use of the microscope. We deeply thank the two anonymous reviewers for their helpful comments and suggestions.

FUNDING INFORMATION

This research was funded by Spanish Ministry of Economy and Competitiveness and European ERDF Funds (MCIU/AEI/FEDER, EU) [BFU2016-78232-P to Adrián Velazquez-Campoy]; by Ministry of Science and Innovation MCIN/AEI/10.13039/501100011033/ and "ERDF A way of Making Europe" [PID2021-127296OB-I00 to Adrián Velazquez-Campoy]; by Instituto de Salud Carlos III co-funded by European Social Fund "Investing in your future" [CP19/00095 to Camino de Juan Romero] [PI22/00824 to Camino de Juan Romero] [PI18/00394 to Olga Abian]; by Diputación General de Aragón ["Protein targets and Bioactive Compounds group" E45-20R to Adrián Velazquez-Campoy, and "Digestive Pathology Group" B25-20R to Olga Abian], and by Consellería de Innovación, Universidades, Ciencia y Sociedad Digital (Generalitat Valenciana) [CAICO 2021/0135 to Camino de Juan Romero and José L. Neira]. Salomé Araujo-Abad was recipient of a "Carolina Foundation predoctoral fellowship 2020". The funders had no role in the study design, data collection and analysis, decision to publish, or preparation of the manuscript.

CONFLICT OF INTEREST STATEMENT

The authors have no relevant financial or non-financial interest to disclosure.

DATA AVAILABILITY STATEMENT

The datasets generated during and/or analyzed during the current study are available from the corresponding authors on reasonable request.

ORCID

Adrián Velazquez-Campoy https://orcid.org/0000-0001-5702-4538
José L. Neira https://orcid.org/0000-0002-4933-0428
Camino de Juan Romero https://orcid.org/0000-0001-7890-8447

REFERENCES

Adashek JJ, Janku F, Kurzrock R. Signed in blood: circulating tumor DNA in cancer diagnosis, treatment and screening. Cancers (Basel) [Internet]. 2021;13:3600. Available from: https://pubmed.ncbi.nlm.nih.gov/34298813/

Beckett D. Measurement and analysis of equilibrium binding titrations: a beginner's guide. Methods Enzymol. 2011;488:1–6.

Birdsall B, King RW, Wheeler MR, Lewis CA, Goode SR, Dunlap RB, et al. Correction for light absorption in fluorescence studies of protein-ligand interactions. Anal Biochem. 1983;132:353–61.

Bodenhausen G, Ruben DJ. Natural abundance nitrogen-15 NMR by enhanced heteronuclear spectroscopy. Chem Phys Lett. 1980;69:185–9.

Brooks CL, Gu W. p53 regulation by ubiquitin. FEBS Lett [Internet]. 2011;585:2803–9. Available from: https://pubmed.ncbi.nlm.nih.gov/21624367/

Cavanagh J, Wayne J, Fairbrother WJ, Palmer AG III, Rance M, Skelton NJ. Protein NMR spectroscopy: principles and practice. New York: Academic Press; 2007.

Chakravarty M, Ganguli P, Murahari M, Sarkar RR, Peters GJ, Mayur YC. Study of combinatorial drug synergy of novel Acridone derivatives with Temozolomide using in-silico and in-vitro methods in the treatment of drug-resistant glioma. Front Oncol. 2021;11:640.

Chen J, Marechal V, Levine AJ. Mapping of the p53 and mdm-2 interaction domains. Mol Cell Biol. 1993;13:4107–14.

Chen L, Chen J. MDM2-ARF complex regulates p53 sumoylation. Oncogene [Internet]. 2003;22:5348–57. Available from: https://pubmed.ncbi.nlm.nih.gov/12917636/

Cieplak P, Caldwell J, Kollman P. Molecular mechanical models for organic and biological systems going beyond the atom centered two body additive approximation: aqueous solution free energies of methanol and N-methyl acetamide, nucleic acid base, and amide hydrogen bonding and chloroform/water partition coefficients of the nucleic acid bases. J Comput Chem [Internet]. 2001;22:1048–57. https://doi.org/10.1002/jcc.1065

Duan Q, Pang C, Chang N, Zhang J, Liu W. Overexpression of PAD4 suppresses drug resistance of NSCLC cell lines to gefitinib through inhibiting Elk1-mediated epithelial-mesenchymal transition. Oncol Rep [Internet]. 2016;36:551–8. https://doi.org/10.3892/or.2016.4780/abstract

Frenzel D, Willbold D. Kinetic titration series with biolayer interferometry. PloS One. 2014;9:e106882.

Fuentes-Baile M, Bello-Gil D, Pérez-Valenciano E, Sanz JM, García-Morales P, Maestro B, et al. CLyta-DAAO, free and immobilized in magnetic nanoparticles, induces cell death in human cancer cells. Biomolecules. 2020;10:222.

Fuentes-Baile M, Pérez-Valenciano E, García-Morales P, de Romero CJ, Bello-Gil D, Barberá VM, et al. Clyta-daao chimeric enzyme bound to magnetic nanoparticles. A new therapeutical approach for cancer patients? Int J Mol Sci. 2021;22:1–24.

Gill SC, von Hippel PH. Calculation of protein extinction coefficients from amino acid sequence data. Anal Biochem. 1989;182:319–26.

Gregory GL, Copple IM. Modulating the expression of tumor suppressor genes using activating oligonucleotide technologies as a therapeutic approach in cancer. Mol Ther Nucleic Acids [Internet]. 2022;31:211–23. Available from: https://pubmed.ncbi.nlm.nih.gov/36700046/

Gudmann NS, Hansen NUB, Jensen ACB, Karsdal MA, Siebuhr AS. Biological relevance of citrullinations: diagnostic, prognostic and therapeutic options. Autoimmunity. 2015;48:73–9.

Guo Q, Fast W. Citrullination of inhibitor of growth 4 (ING4) by peptidylarginine deminase 4 (PAD4) disrupts the interaction between ING4 and p53. J Biol Chem. 2011;286:17069–78.

György B, Tóth E, Tarcsa E, Falus A, Buzás EI. Citrullination: a posttranslational modification in health and disease. Int J Biochem Cell Biol. 2006;38:1662–77.

Horikoshi N, Tachiwana H, Saito K, Osakabe A, Sato M, Yamada M, et al. Structural and biochemical analyses of the human PAD4 variant encoded by a functional haplotype gene. Acta Crystallogr D Biol Crystallogr [Internet]. 2011;67:112–8. Available from: https://pubmed.ncbi.nlm.nih.gov/21245532/

Hung HC, Lin CY, Liao YF, Hsu PC, Tsay GJ, Liu GY. The functional haplotype of peptidylarginine deiminase IV (S55G, A82V and A112G) associated with susceptibility to rheumatoid arthritis dominates apoptosis of acute T leukemia Jurkat cells. Apoptosis. 2007;12:475–87.

Ishigami A, Maruyama N. Importance of research on peptidylarginine deiminase and citrullinated proteins in age-related disease. Geriatr Gerontol Int. 2010;10:S53–8.

Jae-Sun S, Ji-Hyang H, Dong-Hwa L, Kyoung-Seok R, Kwang-Hee B, Byoung CP, et al. Structural convergence of unstructured p53 family transactivation domains in MDM2 recognition. Cell Cycle [Internet]. 2015;14:533–43. Available from: https://pubmed.ncbi.nlm.nih.gov/25591003/

Jiménez-García B, Pons C, Fernández-Recio J. pyDockWEB: a web server for rigid-body protein-protein docking using electrostatics and desolvation scoring. Bioinformatics. 2013;29:1698–9.

Joerger AC, Fersht AR. Structural biology of the tumor suppressor p53. Annu Rev Biochem [Internet]. 2008;77:557–82. Available from: https://pubmed.ncbi.nlm.nih.gov/18410249/

Katchalski-Katzir E, Shariv I, Eisenstein M, Friesem AA, Aflalo C, Vakser IA. Molecular surface recognition: determination of geometric fit between proteins and their ligands by correlation techniques. Proc Natl Acad Sci [Internet]. 1992;89:2195–9. https://doi.org/10.1073/pnas.89.6.2195

Kozakov D, Hall DR, Xia B, Porter KA, Padhorny D, Yueh C, et al. The ClusPro web server for protein–protein docking. Nature Protocols. 2017;12(2):255–78. Available from: https://www.nature.com/articles/nprot.2016.169

Kubbutat MHG, Jones SN, Vousden KH. Regulation of p53 stability by Mdm2. Nature. 1997;387:299–303.

Kussie PH, Gorina S, Marechal V, Elenbaas B, Moreau J, Levine AJ, et al. Structure of the MDM2 oncoprotein bound to the p53 tumor suppressor transactivation domain. Science [Internet]. 1996;274:948–53. Available from: https://pubmed.ncbi.nlm.nih.gov/8875929/

Lai Z, Auger KR, Manubay CM, Copeland RA. Thermodynamics of p53 binding to hdm2(1–126): effects of phosphorylation and p53 peptide length. Arch Biochem Biophys. 2000;381:278–84.

Lei L, Lu Q, Ma G, Li T, Deng J, Li W. P53 protein and the diseases in central nervous system. Front Genet [Internet]. 2023;13:1051395. Available from: https://pubmed.ncbi.nlm.nih.gov/36712862/

Lewis HD, Liddle J, Coote JE, Atkinson SJ, Barker MD, Bax BD, et al. Inhibition of PAD4 activity is sufficient to disrupt mouse and human NET formation. Nat Chem Biol [Internet]. 2015;11: 191 Available from: https://www.ncbi.nlm.nih.gov/pmc/articles/PMC4397581/

Li J, Kurokawa M. Regulation of MDM2 stability after DNA damage. J Cell Physiol [Internet]. 2015;230:2318Available from: https://www.ncbi.nlm.nih.gov/pmc/articles/PMC5810548/–27.

Li P, Wang D, Yao H, Doret P, Hao G, Shen Q, et al. Coordination of PAD4 and HDAC2 in the regulation of p53-target gene expression. Oncogene. 2010;29:3153–62.

Li P, Yao H, Zhang Z, Li M, Luo Y, Thompson PR, et al. Regulation of p53 target gene expression by peptidylarginine deiminase 4. Mol Cell Biol. 2008;28:4758.

Marine JCW, Dyer MA, Jochemsen AG. MDMX: from bench to bedside. J Cell Sci [Internet]. 2007;120:371–8. Available from: https://journals.biologists.com/jcs/article/120/3/371/29795/MDMX-from-bench-to-bedside

McCoy MA, Gesell JJ, Senior MM, Wyss DF. Flexible lid to the p53-binding domain of human Mdm2: implications for p53 regulation. Proc Natl Acad Sci U S A [Internet]. 2003;100:1645–8. Available from: https://pubmed.ncbi.nlm.nih.gov/12552135/

Michelsen K, Jordan JB, Lewis J, Long AM, Yang E, Rew Y, et al. Ordering of the N-terminus of human MDM2 by small molecule inhibitors. J Am Chem Soc [Internet]. 2012;134:17059–67. Available from: https://europepmc.org/article/MED/22991965

Momand J, Zambetti GP, Olson DC, George D, Levine AJ. The mdm-2 oncogene product forms a complex with the p53 protein and inhibits p53-mediated transactivation. Cell. 1992;69:1237–45.

Nagata T, Shirakawa K, Kobayashi N, Shiheido H, Tabata N, Sakuma-Yonemura Y, et al. Structural basis for inhibition of the MDM2:p53 interaction by an optimized MDM2-binding peptide selected with mRNA display. PLoS One [Internet]. 2014;9:e109163. Available from: https://pubmed.ncbi.nlm.nih.gov/25275651/

Neira JL, Araujo-Abad S, Cámara-Artigas A, Rizzuti B, Abian O, Giudici AM, et al. Biochemical and biophysical characterization of PADI4 supports its involvement in cancer. Arch Biochem Biophys. 2022;717:109125.

Neira JL, Díaz-García C, Prieto M, Coutinho A. The C-terminal SAM domain of p73 binds to the N terminus of MDM2. Biochim Biophys Acta Gen Subj. 2019;1863:760–70.

Neira JL, Hornos F, Bacarizo J, Cámara-Artigás A, Gómez J. The monomeric species of the regulatory domain of tyrosine hydroxylase has a low conformational stability. Biochemistry. 2016;55:3418–31.

Neira JL, Rizzuti B, Abián O, Araujo-Abad S, Velázquez-Campoy A, de Juan RC. Human enzyme PADI4 binds to the nuclear carrier importin α3. Cells [Internet]. 2022;11:2166. Available from: https://pubmed.ncbi.nlm.nih.gov/35883608/

Neira JL, Rizzuti B, Araujo-Abad S, Abian O, Fárez-Vidal ME, Velazquez-Campoy A, et al. The armadillo-repeat domain of Plakophilin 1 binds to human enzyme PADI4. Biochim Biophys Acta. Proteins Proteom [Internet] Available from: https://pubmed.ncbi.nlm.nih.gov/36372391/. 2023;1871:140868.

Onufriev A, Bashford D, Case DA. Exploring protein native states and large-scale conformational changes with a modified generalized born model. Proteins. 2004;55:383–94. https://doi.org/10.1002/prot.20033

Pantoja-Uceda D, Neira JL, Saelices L, Robles-Rengel R, Florencio FJ, Muro-Pastor MI, et al. Dissecting the binding between glutamine Synthetase and its two natively unfolded protein inhibitors. Biochemistry. 2016;55:3370–82.

Pierce BG, Wiehe K, Hwang H, Kim BH, Vreven T, Weng Z. ZDOCK server: interactive docking prediction of protein-protein complexes and symmetric multimers. Bioinformatics [Internet]. 2014;30:1771–3. Available from: https://pubmed.ncbi.nlm.nih.gov/24532726/

Reza Saadatzadeh M, Elmi AN, Pandya PH, Bijangi-Vishehsaraei K, Ding J, Stamatkin CW, et al. The role of MDM2 in promoting genome stability versus instability. Int J Mol Sci. 2017;18:2216.

Rizzuti B. Molecular simulations of proteins: from simplified physical interactions to complex biological phenomena. Biochim Biophys Acta Proteins Proteom [Internet]. 2022;1870:140757. Available from: https://pubmed.ncbi.nlm.nih.gov/35051666/

Royer CA, Scarlata SF. Fluorescence approaches to quantifying biomolecular interactions. Methods Enzymol. 2008;450:79–106.

Sato A, Sunayama J, Matsuda KI, Seino S, Suzuki K, Watanabe E, et al. MEK-ERK signaling dictates DNA-repair gene MGMT expression and temozolomide resistance of stem-like glioblastoma cells via the MDM2-p53 axis. Stem Cells [Internet]. 2011;29:1942–51. Available from: https://pubmed.ncbi.nlm.nih.gov/21957016/

Schon O, Friedler A, Bycroft M, Freund SMV, Fersht AR. Molecular mechanism of the interaction between MDM2 and p53. J Mol Biol [Internet]. 2002;323:491–501. Available from: https://pubmed.ncbi.nlm.nih.gov/12381304/

Schon O, Friedler A, Freund S, Fersht AR. Binding of p53-derived ligands to MDM2 induces a variety of long range conformational changes. J Mol Biol [Internet]. 2004;336:197–202. Available from: https://pubmed.ncbi.nlm.nih.gov/14741215/

Slade DJ, Horibata S, Coonrod SA, Thompson PR. A novel role for protein arginine deiminase 4 in pluripotency: the emerging role of citrullinated histone H1 in cellular programming. Bioessays. 2014;36:736–40.

Stadler SC, Vincent CT, Fedorov VD, Patsialou A, Cherrington BD, Wakshlag JJ, et al. Dysregulation of PAD4-mediated citrullination of nuclear GSK3β activates TGF-β signaling and induces epithelialto-mesenchymal transition in breast cancer cells. Proc Natl Acad Sci U S A [Internet]. 2013;110:11851–6. https://doi.org/10.1073/pnas.1308362110

Sung H, Ferlay J, Siegel RL, Laversanne M, Soerjomataram I, Jemal A, Bray F. Global cancer statistics 2020: GLOBOCAN estimates of incidence and mortality worldwide for 36 cancers in 185 countries. CA Cancer J Clin. 2021;71:209–49.

Tanikawa C, Ueda K, Nakagawa H, Yoshida N, Nakamura Y, Matsuda K. Regulation of protein Citrullination through p53/-PADI4 network in DNA damage response. Cancer Res [Internet]. 2009;69:8761–9. Available from: https://pubmed.ncbi.nlm.nih.gov/19843866/

Uhrinova S, Uhrin D, Powers H, Watt K, Zheleva D, Fischer P, et al. Structure of free MDM2 N-terminal domain reveals conformational adjustments that accompany p53-binding. J Mol Biol. 2005;350:587–98.

van Dieck J, Lum JK, Teufel DP, Fersht AR. S100 proteins interact with the N-terminal domain of MDM2. FEBS Lett [Internet]. 2010;584:3269–74. Available from: https://pubmed.ncbi.nlm.nih.gov/20591429/

Varadi M, Anyango S, Deshpande M, Nair S, Natassia C, Yordanova G, et al. AlphaFold protein structure database: massively expanding the structural coverage of protein-sequence space with high-accuracy models. Nucleic Acids Res [Internet]. 2022;50:D439–44. Available from: https://academic.oup.com/nar/article/50/D1/D439/6430488

Ventero MP, Fuentes-Baile M, Quereda C, Perez-Valeciano E, Alenda C, Garcia-Morales P, et al. Radiotherapy resistance acquisition in glioblastoma. Role of SOCS1 and SOCS3. PLoS One. 2019;14:e0212581.

Wallace M, Worrall E, Pettersson S, Hupp TR, Ball KL. Dual-site regulation of MDM2 E3-ubiquitin ligase activity. Mol Cell. 2006;23:251–63.

Wang L, Song G, Zhang X, Feng T, Pan J, Chen W, et al. PADI2-mediated Citrullination promotes prostate cancer progression. Cancer Res [Internet]. 2017;77:5755–68. Available from: https://pubmed.ncbi.nlm.nih.gov/28819028/

Wang Y, Chen R, Gan Y, Ying S. The roles of PAD2- and PAD4-mediated protein citrullination catalysis in cancers. Int J Cancer. 2021;148:267–76.

Weng G, Wang E, Wang Z, Liu H, Zhu F, Li D, et al. HawkDock: a web server to predict and analyze the protein-protein complex based on computational docking and MM/GBSA. Nucleic Acids Res [Internet]. 2019;47:W322–30. Available from: https://pubmed.ncbi.nlm.nih.gov/31106357/

Witalison E, Thompson P, Hofseth L. Protein arginine deiminases and associated citrullination: physiological functions and diseases associated with dysregulation. Curr Drug Targets. 2015;16:700–10.

Yadahalli S, Neira JL, Johnson CM, Tan YS, Rowling PJE, Chattopadhyay A, et al. Kinetic and thermodynamic effects of phosphorylation on p53 binding to MDM2. Sci Rep [Internet]. 2019;9:693. Available from: https://pubmed.ncbi.nlm.nih.gov/30679555/

Yan Y, Tao H, He J, Huang SY. The HDOCK server for integrated protein–protein docking. Nat Protoc. 2020;15(5):1829–52. Available from: https://www.nature.com/articles/s41596-020-0312-x

Yang C, Dong ZZ, Zhang J, Teng D, Luo X, Li D, et al. Peptidylarginine deiminases 4 as a promising target in drug discovery. Eur J Med Chem. 2021;226:113840.

Yao H, Li P, Venters BJ, Zheng S, Thompson PR, Pugh BF, et al. Histone Arg modifications and p53 regulate the expression of OKL38, a mediator of apoptosis. J Biol Chem [Internet]. 2008;283:20060–8. Available from: https://pubmed.ncbi.nlm.nih.gov/18499678/

Ying S, Dong S, Kawada A, Kojima T, Chavanas S, Méchin MC, et al. Transcriptional regulation of peptidylarginine deiminase expression in human keratinocytes. J Dermatol Sci. 2009;53:2–9.

Yu GW, Rudiger S, Veprintsev D, Freund S, Fernandez-Fernandez MR, Fersht AR. The central region of HDM2 provides a second binding site for p53. Proc Natl Acad Sci U S A [Internet]. 2006;103:1227–32. https://doi.org/10.1073/pnas.0510343103

Yuzhalin AE. Citrullination in cancer. Cancer Res. 2019;79:1274–84.

Yuzhalin AE, Gordon-Weeks AN, Tognoli ML, Jones K, Markelc B, Konietzny R, et al. Colorectal cancer liver metastatic growth depends on PAD4-driven citrullination of the extracellular matrix. Nat Commun. 2018;9(1):1–5. Available from: https://www.nature.com/articles/s41467-018-07306-7

Zhang Y, Yang Y, Hu X, Wang Z, Li L, Chen P. PADs in cancer: current and future. Biochim Biophys Acta rev. Cancer Available from: https://pubmed.ncbi.nlm.nih.gov/33321174/. 2021;1875:188492.

Zhu D, Lu Y, Wang Y, Wang Y. PAD4 and its inhibitors in cancer progression and prognosis. Pharmaceutics [Internet]. 2022;14:2414 Available from: https://pubmed.ncbi.nlm.nih.gov/36365233/

SUPPORTING INFORMATION

Additional supporting information can be found online in the Supporting Information section at the end of this article.

How to cite this article: Araujo-Abad S, Rizzuti B, Villamarin-Ortiz A, Pantoja-Uceda D, Moreno-Gonzalez CM, Abian O, et al. New insights into cancer: MDM2 binds to the citrullinating enzyme PADI4. Protein Science. 2023;32(8):e4723. https://doi.org/10.1002/pro.4723

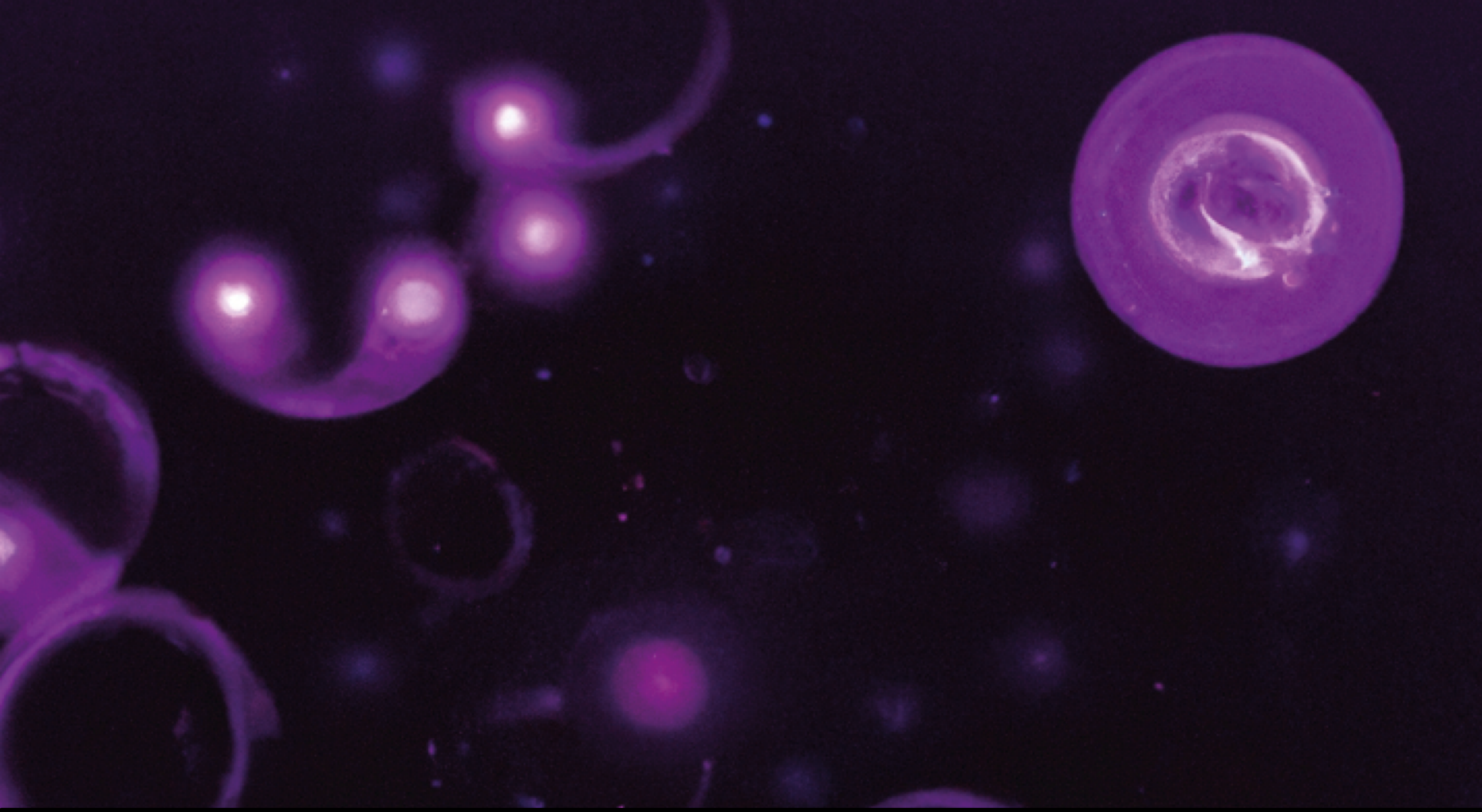

DISCUSSION

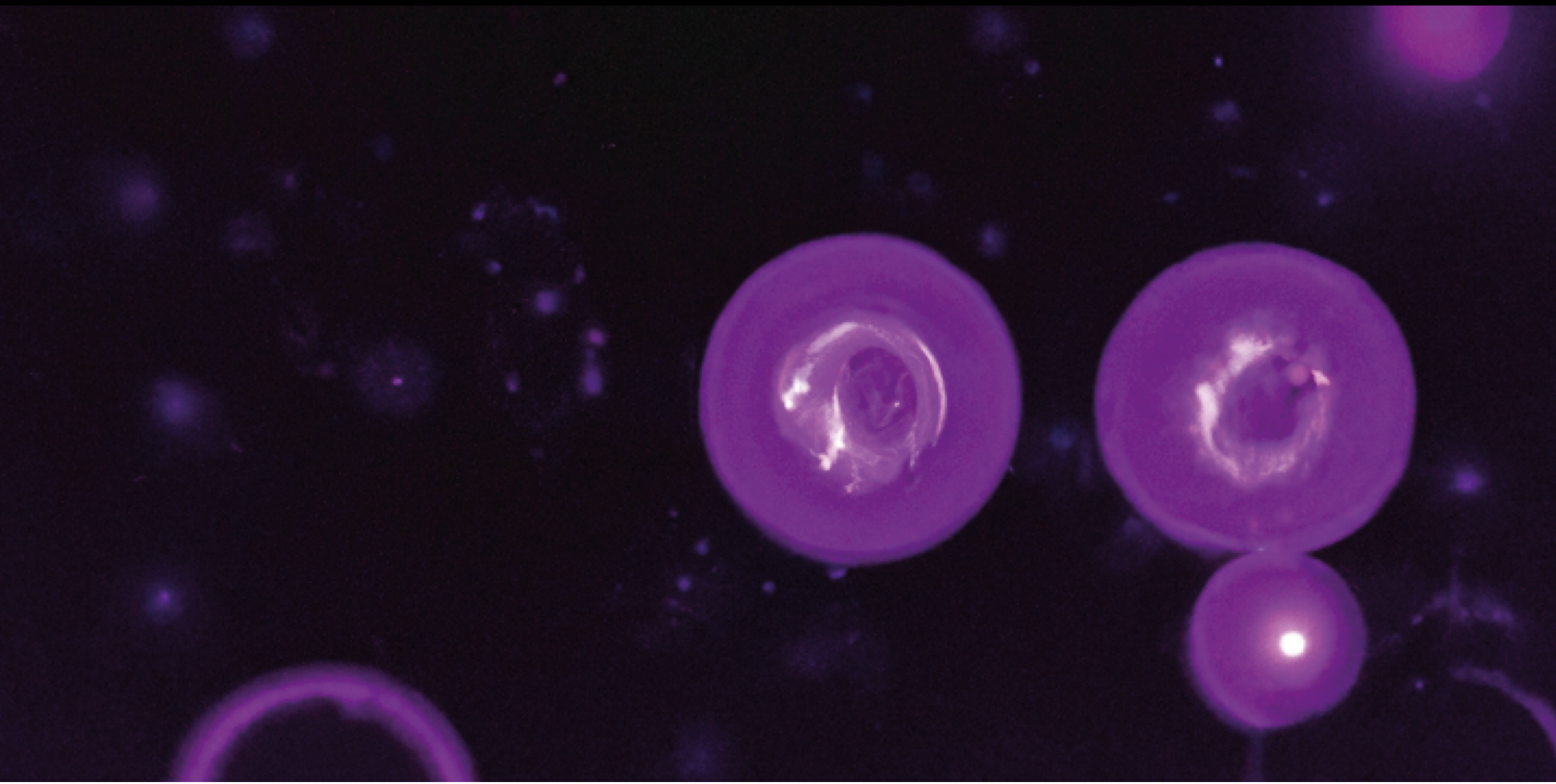

5. Discussion

Hard-to-treat cancers, such as GBM and PDAC, have the worst prognosis and do not receive curative treatment. The standard of care for both types of patients is surgery, followed by chemotherapy and radiotherapy. Therefore, the development of new strategies for more efficient treatments is urgently required. In this context, studies on small EVs have emerged. Small EVs are nanovesicles that are released from normal and abnormal cells of every type of tissue. They participate in cell-to-cell communication and are also involved in cancer progression. Moreover, small EVs can be used as drug delivery systems because they can incorporate drugs into the hydrophobic and hydrophilic compartments. In this work, we have used them to probe target specificity for their parental cells and if they are suitable for cancer treatment. Additionally, we investigated the citrullination process performed by the PADI4 protein, its implication in hard-to-treat cancer progression, and its role as a target for cancer therapy.

Small EVs as drug delivery systems: could small EVs derived from hard-to-treat cancer cells improve actual therapies?

In Chapter 2 "**Glioblastoma derived small EVs: Nanoparticles for glioma treatment**", ", we showed for the first time the isolation and characterization of GBM small EVs derived from seven patient cell lines established by Ventero *et al.* [204]. Differential ultracentrifugation was used as the isolation method, which is a standard method in the field and has been employed to isolate several cancer-derived small EVs, including colon cancer, melanoma, hepatocellular carcinoma, gastric, and breast cancer [123,149,209–211]. As there is no consensus on the use of certain markers because they are not the same for all EVs, as mentioned by MISEV 2018, we used WB to identify proteins that are normally present in small EVs and we observed that they were positive for ALIX, TSG101, and CD63 [92]. Additionally, as a control, we used α–tubulin and HSP90, which were only present in cells but not in small EVs, contrary to other findings with small EVs isolated from breast or prostate cancer cells [212,213]. Moreover, the absence of these proteins can be indicative of the purity of the isolation, as reported by other authors [209]. For morphological characterization, we used DLS and FESEM, being the size of small EVs measured by DLS between 100-150 nm. This small size correlates with the literature where authors obtained measurements for other EV types, such as prostate-derived EVs, with a similar diameter of 120-150 nm [214] or breast cancer patient-plasma-derived EVs with a diameter of 100 nm [215]. FESEM was used to visualize small EVs, which appeared round in shape, consistent with other findings [216–218].

Once the small EVs were characterized, we tested whether they were suitable for drug delivery. Methods like electroporation, transfection, and sonication can be used to load small EVs but they can damage and alter the structure of the EVs, therefore we used incubation methods in our studies [219,220]. More precisely, we loaded GB-39-derived small EVs with two chemotherapeutic drugs TMZ and EPZ015666, using direct and indirect incubation methods.

TMZ is the chemotherapeutic drug used in the Stupp protocol for GBM treatment. This protocol includes tumor resection followed by chemotherapy and radiotherapy [38,79]. High doses of this drug are used and have several side effects such as headache, fatigue, and loss of appetite among others [42–44]. TMZ is dissolved in DMSO in the majority of experiments where is used, which increases its cytotoxicity, therefore we used Milli-Q water in our experiments according to tests done by other authors [221]. Consequently, the results and the cytotoxic effects of TMZ that we have shown solely correspond to the drug. We have also tested the effect of EPZ015666, a newly developed specific PRMT5 inhibitor. PRMT5 has emerged as a target in several cancer types including GBM [48], which is upregulated in the classical GBM subtype, and its expression has also been correlated with poor patient outcomes [15]. In this work, we demonstrated for the first time not only that direct application of EPZ015666 has an effect on patient-derived GBM cell lines but also that it decreases GBM cell proliferation more than the current treatment, TMZ.

Although TMZ and EPZ015666 loaded into the small EVs by both incubation methods reduced cell proliferation when applied to cancer cells, the direct incubation method has proven to be more efficient. Along this line, HPLC measurements showed higher loading efficiency of the direct incubation method for any of the drugs. Moreover, this was the first time that the EPZ015666 measurement protocol was tested and we concluded that can be used for small EVs. HPLC analysis of the loaded GBM small EVs revealed that a very low concentration of EPZ015666 was more harmful to cancer cells than TMZ. This is probably because of the type of drugs we used and their hydrophobicity capacity, which has better interaction with the lipid bilayer of small EVs, as was reported for other compounds [222–224].

Loaded small EVs derived from GBM cell lines were used to test their effect on cell proliferation, showing a significant dose-dependent effect on GBM cells regardless of the patient they belong to. The fact that the RWP-1 cell line was also affected by GB-39 drug-loaded small EVs, but not in a dosage-dependent manner, suggests that this drug delivery system could also be used to treat secondary metastases (i.e. pancreas) [225]. Although extracranial metastases of GBM are rare, they occur in less than 2 % of patients [226,227]. Hence, these patients could also benefit from the finding that GBM-derived small EVs are also capable of affecting other tumor cells, although additional analysis is needed to further investigate this possibility. The results of this work showed that GB-39 small EVs could be loaded with 400 times less EPZ015666 and at least 200 times less TMZ without compromising efficiency. It is known that chemotherapy alone can damage healthy cells; in this sense, small EVs may constitute an alternative to reduce both, toxicity and the amount of drug being administered to a patient with the same effect as the drug alone. Then, this study provides a basis for the use of GBM small EVs as drug delivery systems for GBM treatment.

In Chapter 3 “**New therapy for pancreatic cancer based on extracellular vesicles**”, we further explore the use of small EVs as drug delivery systems for other types of cancer. We tested the effect of RWP-1 small EVs loaded with TMZ and EPZ01566, and similar to the observations in Chapter 2, we noticed a higher decrease in proliferation with these treatments than with applying the drugs alone. Additionally, we used GB-39 small EVs to treat the RWP-1 cell line to corroborate that RWP-1 small EVs were more efficient than GB-39 small EVs. These results confirmed the small EVs target specificity for their own parental cells, having a greater effect on proliferation when they are isolated from the same type of cancer cell. Other studies have reported this characteristic of small EVs in fibrosarcoma (HT1080) and cervical (HeLa) cancer cell lines [141].

There are different storing conditions for small EVs 4 ºC, -20, and -80 ºC [228]. We evaluated the stability of RWP-1 small EVs loaded with drugs at -80 ºC after two years of storage. Our study further corroborated previous observations by several authors, that consider -80 ºC as the best temperature to store small EVs for a long term [229–231]. When we performed proliferation experiments with RWP-1-derived EVs^{TMZ} and EVs^{EPZ015666} stored at temperatures below -80 ºC for two years, we only found a 4 % reduction in TMZ efficiency and a 10 % decrease in EPZ015666 efficiency compared to our previous results. These results are important because they confirm that the treatment can be maintained for a long period at a low temperature of -80 ºC. However, incorporation and stability also depend on the type of drug used.

As small EVs have tropism for their parental cells [137,141], we challenge to visualize the internalization of the RWP-1 small EVs into their parental cells. We performed an assay in living cells for 3 h and 6 h treating RWP-1 cell line with red-labeled RWP-1 small EVs loaded with TMZ. These small EVs tended to aggregate in the nucleus, and their number significantly increased after 6 h. In addition, we performed an ICC at 6 h of treatment with red-labeled RWP-1 small EVs, and showed that these small EVs were internalized in the RWP-1 cell line and aggregated around the nucleus. This internalization of small EVs into the nucleus can target specific nuclear components and molecular pathways that play a critical role in cancer progression.

We showed that TMZ and EPZ015666 were more effective at minimum concentrations when loaded into small EVs, thereby inhibiting the growth of GBM and PDAC cells *in vitro*. It is important to note that the optimal use of small EVs depends on the type of drug employed, probably because of the multiple interactions between the chemical composition of the drug and the extravesicular membrane that determine its internalization. Our results indicated that TMZ interacts with the lipid bilayer more effectively than EPZ015666.

Overall, these findings highlight the possible use of small EVs derived from RWP-1 and GB-39 as drug delivery systems to achieve better therapeutic benefits for hard-to-treat cancer patients.

PADI4 expression in different cancer cell lines: a potential new therapeutic target for cancer.

PADI proteins catalyze a PTM called citrullination, which affects the arginine residues. Citrullination facilitates cancer development through several mechanisms including cell differentiation and apoptosis. One isoform in humans, PADI4, is involved in the development of several diseases and apoptosis cascades. It has been observed that under hypoxic conditions, PADI4 expression and production of citrullinated proteins are increased in some tumor cell lines, such as GBM [232]. In Chapter 4 **"Biochemical and biophysical characterization of PADI4 supports its involvement in cancer"**, we explored the localization of PADI4 in different cancer cell lines, GBM (GB-39), colon adenocarcinoma (HT-29), and pancreatic cancer (RWP-1). We observed different intracellular localizations among different cancer cell lines, indicating the possibility that PADI4 could play different functional roles depending on the tumor type. Additionally, the WB analyses showed different protein expression levels and patterns. In PDAC, PADI4 expression was lower than in colon adenocarcinoma, and GBM showed the highest expression. In addition, protein extracts showed several PADI4 bands, indicating the possibility that PADI4 might experience alternative splicing, resulting in the generation of protein species with or without NLS, which in turn would result in variable subcellular localizations. Anti-PADI4 antibody immunostaining supported (i) PADI4 expression in the aforementioned tumors and (ii) tumor-dependent distribution.

On the other hand, p53 is believed to be the gene most frequently altered in human cancer [233]. Li *et al*. observed that p53 interacts with PADI4 in the 293T epithelial cell line [183], and our results showed that the cancer cell lines differed in p53 and PADI4 protein expression levels. In this sense, we speculate that PADI4 may have a variable impact on cell function and development depending on tumor origin because it interferes with p53 control of tumor suppressor genes during carcinogenesis [54]. In agreement with other authors, our findings also support the major role of PADI4 in cancer development in other cancer types [234]. Therefore, inhibition of citrullination mediated by PADI4 could be proposed as a target for cancer treatment.

PADI4 and its citrullination capacity are related to cancer progression, migration, and metastasis, therefore we focused on PADI4 to explore its expression in GBM and PDAC cell lines. We load the GB-39 small EVs, mentioned in Chapter 2, with a PADI4 inhibitor. In Chapter 5 "**PADI4 and its role in cancer progression**", we observed different PADI4 expression in all GBM cell lines using WB. Based on these differences, we determined whether PADI4 was inhibited by the specific inhibitor GSK484 in GBM and RWP-1 cell lines by performing antiproliferative assays. We observed different responses to GSK484 treatment depending on the cell line being GB-18, GB-39, and GB-42 cell lines the most sensitive, whereas GB-16, GB-37, and GB-48 were resistant. On the other hand, the RWP-1 cell line was partially sensitive to GSK484. Other studies with this drug demonstrated that triple-negative breast cancer cell lines such as MDA-MB-231 and BT-549 were sensitive to treatment at very low concentrations, and its apoptotic effect was increased when it was combined with IR [196]. All these results highlight the heterogeneity of this type of tumor depending on the patient, stressing the need for advancements in personalized medicine.

Consistent with our previous studies with other drugs, when loading GSK484 by direct incubation method into small EVs derived from GB-39, it was necessary a small amount of the drug to trigger an effect in GB-39, GB-42, and RWP-1 cell lines [67,137]. Moreover, it is important to mention that the antiproliferative effect of the loaded small EVs^{GSK484} was only dose-dependent in GB-39, confirming the small EVs tropism for their parental cells.

PADI4 interactome study to develop new hard-to-treat cancer therapies.

PADI4 protein has several partners, and its interaction can modulate cell function. We have previously investigated the relationship of PADI4 with plakophilin1 and integrin α3 [208,235]. In Chapter 6 "**Intrinsically disordered chromatin protein NUPR1 binds to the enzyme PADI4**", we showed the interaction between PADI4 and NUPR1, and how this interaction could be a possible target in cancer therapy. The interaction of NUPR1/PADI4 was identified in GBM cancer cells using the PLA technique, which is a sensitive method that detects the binding of proteins that occur at distances less than 16 Å. This technique is widely used to test protein-protein interactions [236,237].

PADI4 and NUPR1 are involved in cancer development, carcinogenesis, and stress-mediated cellular responses. NUPR1 is an oncogene known for its capacity to control carcinogenesis, tumorigenesis, and metastasis [238,239]. However, other authors have reported its suppressive function in Panc-1 and BxPc-3 pancreatic cells and in PC-3, DU145, and CA-HPV10 prostate cancer cells [239–241]. On the other hand, PADI4 also acts as a tumor suppressor in breast cancer cells [234]. Both proteins have different mechanisms of action in cancer cells; therefore, the NUPR1/PADI4 complex may be modulating several cell functions.

In breast cancer cells, the lack of GSK3β citrullination by PADI4 induces EMT, which is a crucial stage for breast cancer cells to spread to other organs [186]. Thus, the formation of the NUPR1/PADI4 complex might prevent GSK3β from becoming citrullinated, which would enhance the EMT in breast cancer cells. Similarly, in GBM the NUPR1/PADI4 complex could activate pathways associated with EMT, such as the TGF-β pathway, enhance the expression of genes related to cell cycle progression, and inhibit apoptosis, resulting in a more migratory and invasive phenotype of GBM cells [242]. Therefore, this protein complex could be a potential therapeutic target for GBM treatment.

Finally, in Chapter 7, **"The N-terminal region of MDM2 binds to human enzyme PADI4"**. We showed the interaction between MDM2 and PADI4 in several cancer cell lines, including GBM (GB-42), PDAC (RWP-1), and colon adenocarcinoma (SW-480), and how this binding is affected by GSK484. Binding occurred mostly in the nucleus of all cell lines, and after the application of GSK484, this binding was impeded and localized only in the cytoplasm. Therefore, since MDM2's N-terminal region also interferes with its interactions with S100 proteins [243] and the sterile alpha motif (SAM) of p73, SAMp73 [244], we suggest that the interaction of MDM2 with PADI4 could occur through this area.

Additionally, we demonstrated that treatment with GSK484 enhanced the effect of TMZ on GBM cell lines. It has been shown that suppressing MDM2 expression causes downregulation of MGMT, enhancing GBM cell sensitivity to TMZ treatment [245]. The sequential use of several drugs can affect cells in different ways. For example, in prostate cancer, the co-administration of a PADI4 inhibitor and an androgen receptor signal transduction inhibitor inhibits tumor growth and cell proliferation [246]. Thus, TMZ can increase cytotoxicity when combined with other drugs at considerably lower concentrations than when administered alone [247]. The use of GSK484 against PADI4 may result in more potent therapies to improve the benefits of other approved drugs for cancer treatment.

Our findings point out PRMT5 and PADI4 as potential new targets for hard-to-treat cancers and their specific inhibitors as potential new therapies. Our data provided evidence that small EVs derived from hard-to-treat cancer cells can be loaded with different therapeutic agents, such as TMZ, EPZ015666, and GSK484, to trigger a reduction in cell proliferation with a small amount of the drug, and therefore are suitable for cancer therapy. The study of small EVs could provide an opportunity to discover new ways to deliver drugs to specific tumor regions without comprising healthy cells. This work not only highlights the relevance of PADI4 and its citrullination capacity in cancer, but also its interactions with partners such as NUPR1 and MDM2 provide valuable insights into the mechanisms involved in cancer progression. This Thesis contributes to the understanding of personalized medical approaches for hard-to-treat cancer treatment, emphasizing the importance of targeting specific molecular pathways and using small EVs as delivery vehicles for improved therapeutic efficacy. Further research is needed along with the development of novel therapeutic strategies to improve patient outcomes.

CONCLUSIONS

6. Conclusions

1. All GBM and RWP-1 cell lines were sensitive to TMZ and partially sensitive to EPZ015666. GB-42 cell line was the most sensitive to all treatments while GB-16 was the most resistant.
2. GBM and RWP-1-derived small EVs were successfully isolated by the ultracentrifugation method. The morphological characterization by DLS and FESEM showed small EVs with a circular shape and with a diameter between 100 to 150 nm.
3. Loading TMZ and EPZ015666 in small EVs with the direct incubation method can reduce the necessary drug exposure while effectively inhibiting the growth of GBM and PDAC cells *in vitro*.
4. The amount of EPZ015666 was measured by HPLC for the first time in EVs, and the results showed that direct incubation was a better loading method for small EVs.
5. GBM-derived small EVs tend to fuse with their parent cells, which is evidenced by the dose-dependent proliferation effect observed in GBM cell lines, but not in the PDAC cell line.
6. The ability of drug-loaded GBM small EVs to also affect other cancer cells, suggests their potential application in the treatment of secondary metastasis.
7. The drug's chemical structure has relevance for the efficiency of the small EVs drug loading and the activity after long-term storage. Drug internalization, defined by the interaction with the small EVs lipid bilayer, was measured by HPLC showing that TMZ has better interaction as compared to EPZ015666 and GSK484.
8. GBM and PDAC-derived small EVs have the potential to be used as drug delivery vehicles to achieve a maximal therapeutic effect with minimal toxicity in patients' treatment.
9. PADI4 was biochemically characterized using different cancer cell lines, including GB-39 and RWP-1, suggesting that PADI4 plays a significant role in cancer progression and setting the basis to study PADI4 function.
10. The highest expression of PADI4 among all GBM cell lines was in the GB-16 cell line. GB-18 was the most sensitive line to GSK484, a PADI4 inhibitor, while RWP-1 was the most resistant cell line. GB-39 derived small EVs^{GSK484} reduced more effectively tumor cell proliferation than the drug alone.
11. PADI4 interacts with NUPR1 in GBM cell lines mainly in the nucleus, suggesting that this interaction may have implications in cancer development, and hence can be useful in cancer therapy.

12. PADI4 interaction with MDM2 can be inhibited by GSK484 treatment and the inhibition of PADI4 by GSK484 enhanced the sensitivity of GBM cells to TMZ supporting PADI4 potential role as a target for cancer therapy. These data represent a starting point to develop new GBM therapies based on the use of GSK484 in combination with other drugs that may have synergistic effects, leading to more effective treatments.

Conclusiones

1. Todas las líneas celulares GBM y RWP-1 fueron sensibles a TMZ y parcialmente sensibles a EPZ015666. La línea celular GB-42 fue la más sensible a todos los tratamientos, mientras que GB-16 fue la más resistente.
2. Las vesículas extracelulares pequeñas (EVs en inglés) derivadas de GBM y RWP-1 se aislaron exitosamente mediante el método de ultracentrifugación diferencial. La caracterización morfológica mediante DLS y FESEM mostró a las vesículas extracelulares con forma circular y con un diámetro entre 100 y 150 nm.
3. La carga de TMZ y EPZ015666 dentro de EVs con el método de incubación directa puede reducir la exposición necesaria al fármaco, a la vez que inhibe eficazmente el crecimiento de células GBM y PDAC *in vitro*.
4. La cantidad de EPZ015666 se determinó por HPLC por primera vez en vesículas extracelulares, y nuestros resultados mostraron que la incubación directa es un mejor método de carga.
5. Las EVs derivadas de GBM tienden a fusionarse preferentemente con sus células progenitoras, lo que se evidencia por el efecto de proliferación dosis dependiente observado en las líneas celulares de GBM, pero no en la línea celular de PDAC.
6. La capacidad de las EVs derivadas de GBM cargadas con fármacos para afectar a otras células cancerosas, sugiere su posible aplicación en el tratamiento de metástasis secundarias.
7. La estructura química del fármaco tiene relevancia en la eficacia de carga del fármaco en las EVs y también en su actividad tras un almacenamiento a largo plazo. La internalización del fármaco, definida por su interacción con la bicapa lipídica de las EVs, se determinó mediante HPLC mostrando que TMZ tiene una mejor interacción en comparación con EPZ015666 y GSK484.
8. Las EVs derivadas de GBM y PDAC tienen el potencial de utilizarse como vehículos de administración de fármacos para lograr un efecto terapéutico máximo con una toxicidad mínima en el tratamiento de los pacientes.
9. PADI4 se caracterizó bioquímicamente utilizando diferentes líneas celulares de cáncer, incluidas GB-39 y RWP-1, lo que sugiere que PADI4 desempeña un papel importante en la progresión del cáncer y sienta las bases para estudiar la función de PADI4.
10. La expresión más alta de PADI4 entre todas las líneas celulares de GBM fue en la línea celular GB-16. GB-18 fue la línea más sensible a GSK484, un inhibidor de PADI4, mientras que RWP-1 fue la línea celular más resistente. Las EVs derivadas de GB-39

^{GSK484} disminuyen más eficientemente la proliferación de células tumorales que el uso del fármaco solo.

11. PADI4 interactúa con NUPR1 en líneas celulares de GBM, principalmente en el núcleo, lo que sugiere que esta interacción puede tener implicaciones en el desarrollo del cáncer, y por lo tanto puede ser útil en la terapia de esta enfermedad.
12. La interacción de PADI4 con MDM2 puede ser inhibida por el tratamiento con GSK484 y la inhibición de PADI4 por GSK484 aumentó la sensibilidad de las células GBM a TMZ, apoyando el papel de PADI4 como potencial diana para la terapia del cáncer. Estos datos representan un punto de partida para desarrollar nuevas terapias contra el GBM basadas en el uso de GSK484 en combinación con otros fármacos que puedan tener efectos sinérgicos, dando lugar a tratamientos más eficaces.

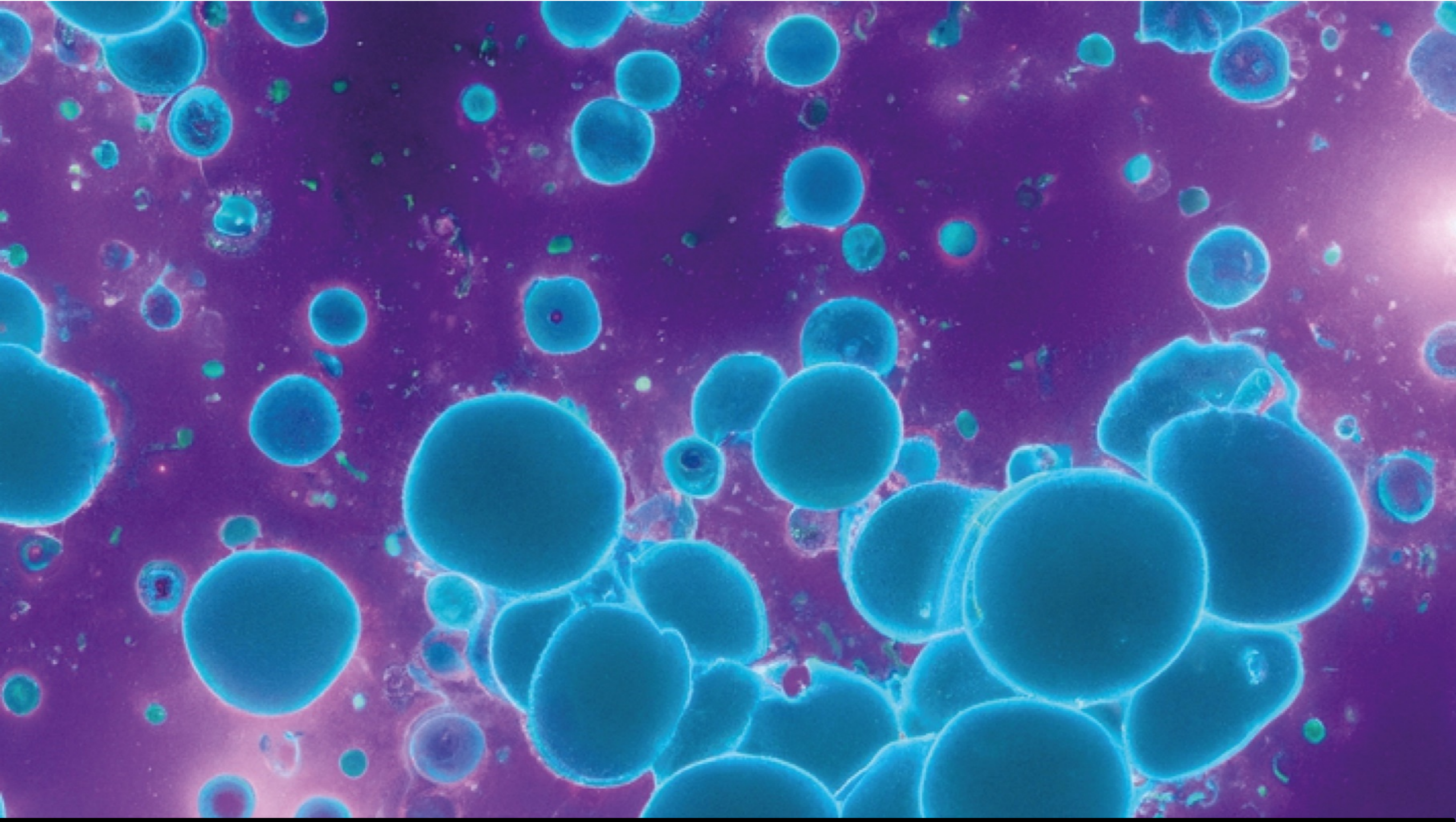

REFERENCES

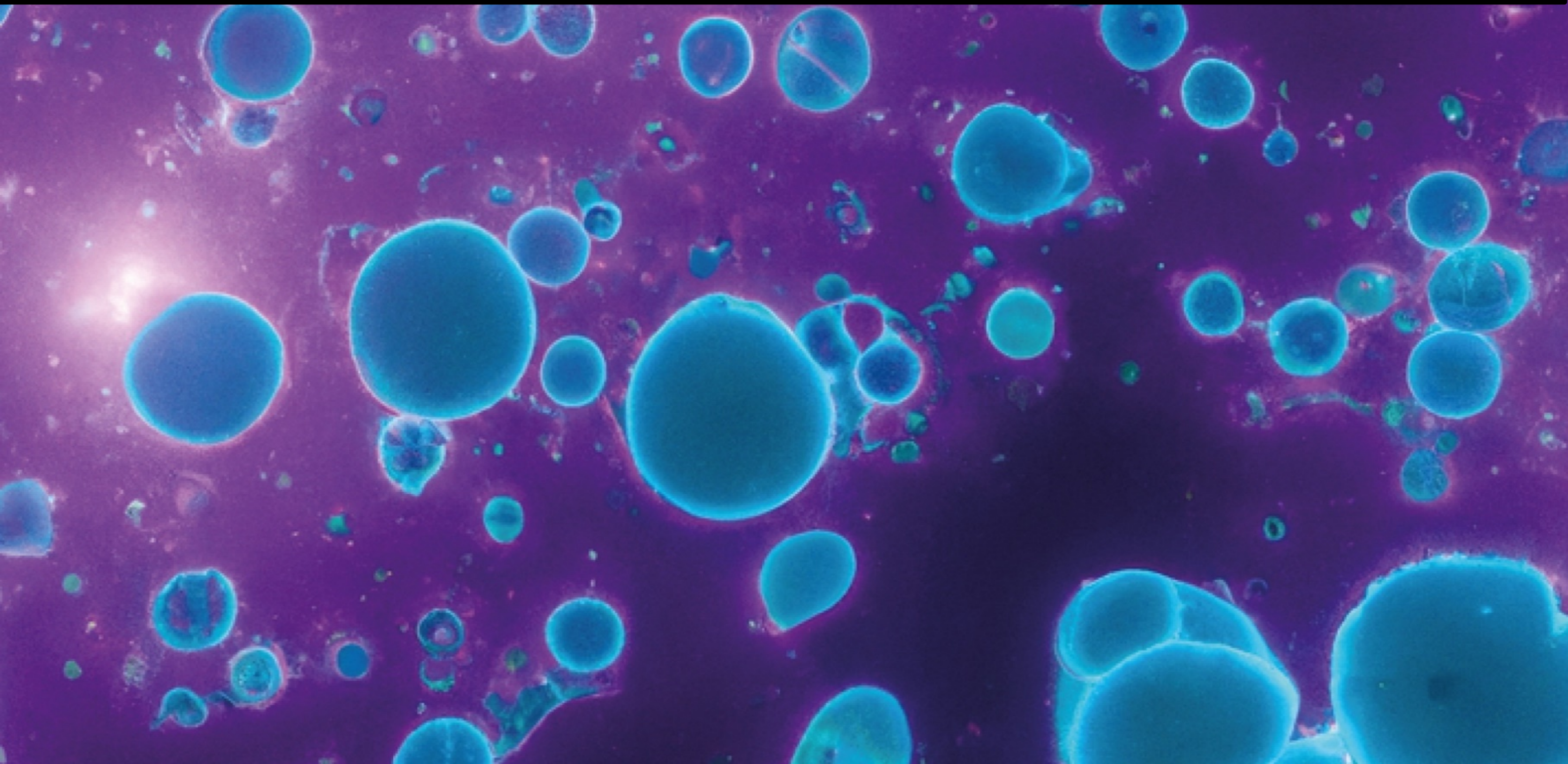

7. References

1. Willis, R.A. Pathology of Tumours. In *Pathology of tumours*; London: Butterworth & Co., 1960.
2. Truskowski, K.; Amend, S.R.; Pienta, K.J. Dormant Cancer Cells: Programmed Quiescence, Senescence, or Both? *Cancer and Metastasis Reviews 2023 42:1* **2023**, *42*, 37–47, doi:10.1007/S10555-022-10073-Z.
3. Hanahan, D.; Weinberg, R.A. Hallmarks of Cancer: The next Generation. *Cell* **2011**, *144*, 646–674, doi:10.1016/J.CELL.2011.02.013.
4. NIH Cancer Classification | SEER Training Available online: https://training.seer.cancer.gov/disease/categories/classification.html (accessed on 24 April 2023).
5. Sung, H.; Ferlay, J.; Siegel, R.L.; Laversanne, M.; Soerjomataram, I.; Jemal, A.; Bray, F. Global Cancer Statistics 2020: GLOBOCAN Estimates of Incidence and Mortality Worldwide for 36 Cancers in 185 Countries. *CA Cancer J Clin* **2021**, *71*, 209–249, doi:10.3322/CAAC.21660.
6. Global Cancer Observatory Available online: https://gco.iarc.fr/ (accessed on 27 April 2023).
7. Manegold, C. Current Advancements in Hard-to-Treat Cancers. *American Journal of Cancer* **2005**, *4*, 105–113, doi:10.2165/00024669-200504020-00004/METRICS.
8. Singh, K.; Batich, K.A.; Wen, P.Y.; Tan, A.C.; Bagley, S.J.; Lim, M.; Platten, M.; Colman, H.; Ashley, D.M.; Chang, S.M.; et al. Designing Clinical Trials for Combination Immunotherapy: A Framework for Glioblastoma. *Clinical Cancer Research* **2022**, *28*, 593, doi:10.1158/1078-0432.CCR-21-2681.
9. Artene, S.A.; Tuţă, C.; Dragoi, A.; Alexandru, O.; Stefana Oana, P.; Tache, D.E.; Dănciulescu, M.M.; Boldeanu, M.V.; Siloşi, C.A.; Dricu, A. Current and Emerging EGFR Therapies for Glioblastoma. *J Immunoassay Immunochem* **2018**, *39*, 1–11, doi:10.1080/15321819.2017.1411816.
10. Grochans, S.; Cybulska, A.M.; Simińska, D.; Korbecki, J.; Kojder, K.; Chlubek, D.; Baranowska-Bosiacka, I. Epidemiology of Glioblastoma Multiforme–Literature Review. *Cancers (Basel)* **2022**, *14*, 2412, doi:10.3390/CANCERS14102412.
11. Koshy, M.; Villano, J.L.; Dolecek, T.A.; Howard, A.; Mahmood, U.; Chmura, S.J.; Weichselbaum, R.R.; McCarthy, B.J. Improved Survival Time Trends for Glioblastoma Using the SEER 17 Population-Based Registries. *J Neurooncol* **2012**, *107*, 212, doi:10.1007/S11060-011-0738-7.
12. Louis, D.N.; Perry, A.; Wesseling, P.; Brat, D.J.; Cree, I.A.; Figarella-Branger, D.; Hawkins, C.; Ng, H.K.; Pfister, S.M.; Reifenberger, G.; et al. The 2021 WHO Classification of Tumors of the Central Nervous System: A Summary. *Neuro Oncol* **2021**, *23*, 1251, doi:10.1093/NEUONC/NOAB106.
13. Osborn, A.G.; Louis, D.N.; Poussaint, T.Y.; Linscott, L.L.; Salzman, K.L. The 2021 World Health Organization Classification of Tumors of the Central Nervous System: What Neuroradiologists Need to Know. *American Journal of Neuroradiology* **2022**, *43*, 928–937, doi:10.3174/AJNR.A7462.
14. Torp, S.H.; Solheim, O.; Skjulsvik, A.J. The WHO 2021 Classification of Central Nervous System Tumours: A Practical Update on What Neurosurgeons Need to Know—a Minireview. *Acta Neurochir (Wien)* **2022**, *164*, 2453–2464, doi:10.1007/S00701-022-05301-Y/TABLES/11.
15. Verhaak, R.G.W.; Hoadley, K.A.; Purdom, E.; Wang, V.; Qi, Y.; Wilkerson, M.D.; Miller, C.R.; Ding, L.; Golub, T.; Mesirov, J.P.; et al. Integrated Genomic Analysis Identifies Clinically Relevant Subtypes of Glioblastoma Characterized by Abnormalities in PDGFRA, IDH1, EGFR, and NF1. *Cancer Cell* **2010**, *17*, 98–110, doi:10.1016/J.CCR.2009.12.020.

16. Ellingson, B.M.; Lai, A.; Harris, R.J.; Selfridge, J.M.; Yong, W.H.; Das, K.; Pope, W.B.; Nghiemphu, P.L.; Vinters, H. V.; Liau, L.M.; et al. Probabilistic Radiographic Atlas of Glioblastoma Phenotypes. *AJNR Am J Neuroradiol* **2013**, *34*, 540, doi:10.3174/AJNR.A3253.
17. Brain Anatomy and How the Brain Works | Johns Hopkins Medicine Available online: https://www.hopkinsmedicine.org/health/conditions-and-diseases/anatomy-of-the-brain (accessed on 28 April 2023).
18. Ostrom, Q.T.; Fahmideh, M.A.; Cote, D.J.; Muskens, I.S.; Schraw, J.M.; Scheurer, M.E.; Bondy, M.L. Risk Factors for Childhood and Adult Primary Brain Tumors. *Neuro Oncol* **2019**, *21*, 1357, doi:10.1093/NEUONC/NOZ123.
19. Hansen, S.; Rasmussen, B.K.; Laursen, R.J.; Kosteljanetz, M.; Schultz, H.; Nørgård, B.M.; Guldberg, R.; Gradel, K.O. Treatment and Survival of Glioblastoma Patients in Denmark: The Danish Neuro-Oncology Registry 2009-2014. *J Neurooncol* **2018**, *139*, 479–489, doi:10.1007/S11060-018-2892-7.
20. Sun, T.; Warrington, N.M.; Luo, J.; Brooks, M.D.; Dahiya, S.; Snyder, S.C.; Sengupta, R.; Rubin, J.B. Sexually Dimorphic RB Inactivation Underlies Mesenchymal Glioblastoma Prevalence in Males. *J Clin Invest* **2014**, *124*, 4133, doi:10.1172/JCI71048.
21. Nobusawa, S.; Watanabe, T.; Kleihues, P.; Ohgaki, H. IDH1 Mutations as Molecular Signature and Predictive Factor of Secondary Glioblastomas. *Clin Cancer Res* **2009**, *15*, 6002–6007, doi:10.1158/1078-0432.CCR-09-0715.
22. Bleeker, F.E.; Atai, N.A.; Lamba, S.; Jonker, A.; Rijkeboer, D.; Bosch, K.S.; Tigchelaar, W.; Troost, D.; Van Dertop, W.P.; Bardelli, A.; et al. The Prognostic IDH1R132 Mutation Is Associated with Reduced NADP+-Dependent IDH Activity in Glioblastoma. *Acta Neuropathol* **2010**, *119*, 494, doi:10.1007/S00401-010-0645-6.
23. Jeong, D.E.; Woo, S.R.; Nam, H.; Nam, D.H.; Lee, J.H.; Joo, K.M. Preclinical and Clinical Implications of TERT Promoter Mutation in Glioblastoma Multiforme. *Oncol Lett* **2017**, *14*, 8219, doi:10.3892/OL.2017.7196.
24. Ferguson, S.D.; Xiu, J.; Weathers, S.P.; Zhou, S.; Kesari, S.; Weiss, S.E.; Verhaak, R.G.; Hohl, R.J.; Barger, G.R.; Reddy, S.K.; et al. GBM-Associated Mutations and Altered Protein Expression Are More Common in Young Patients. *Oncotarget* **2016**, *7*, 68478, doi:10.18632/ONCOTARGET.11617.
25. Fang, X.; Wei, J.; He, X.; Lian, J.; Han, D.; An, P.; Zhou, T.; Liu, S.; Wang, F.; Min, J. Quantitative Association between Body Mass Index and the Risk of Cancer: A Global Meta-Analysis of Prospective Cohort Studies. *Int J Cancer* **2018**, *143*, 1595–1603, doi:10.1002/IJC.31553.
26. Moore, S.C.; Rajaraman, P.; Dubrow, R.; Darefsky, A.S.; Koebnick, C.; Hollenbeck, A.; Schatzkin, A.; Leitzmann, M.F. Height, Body Mass Index, and Physical Activity in Relation to Glioma Risk. *Cancer Res* **2009**, *69*, 8349–8355, doi:10.1158/0008-5472.CAN-09-1669.
27. Little, R.B.; Madden, M.H.; Thompson, R.C.; Olson, J.J.; LaRocca, R. V.; Pan, E.; Browning, J.E.; Egan, K.M.; Nabors, L.B. Anthropometric Factors in Relation to Risk of Glioma. *Cancer Causes Control* **2013**, *24*, 1031, doi:10.1007/S10552-013-0178-0.
28. Simińska, D.; Korbecki, J.; Kojder, K.; Kapczuk, P.; Fabiańska, M.; Gutowska, I.; Machoy-Mokrzyńska, A.; Chlubek, D.; Baranowska-Bosiacka, I. Epidemiology of Anthropometric Factors in Glioblastoma Multiforme—Literature Review. *Brain Sci* **2021**, *11*, 1–14, doi:10.3390/BRAINSCI11010116.
29. Phillips, H.S.; Kharbanda, S.; Chen, R.; Forrest, W.F.; Soriano, R.H.; Wu, T.D.; Misra, A.; Nigro, J.M.; Colman, H.; Soroceanu, L.; et al. Molecular Subclasses of High-Grade Glioma Predict Prognosis, Delineate a Pattern of Disease Progression, and Resemble Stages in Neurogenesis. *Cancer Cell* **2006**, *9*, 157–173, doi:10.1016/J.CCR.2006.02.019.
30. Furgason, J.M.; Koncar, R.F.; Michelhaugh, S.K.; Sarkar, F.H.; Mittal, S.; Sloan, A.E.; Barnholtz-Sloan, J.S.; Bahassi, E.M. Whole Genome Sequence Analysis Links

Chromothripsis to EGFR, MDM2, MDM4, and CDK4 Amplification in Glioblastoma. *Oncoscience* **2015**, *2*, 618, doi:10.18632/ONCOSCIENCE.178.

31. Chen, R.; Smith-Cohn, M.; Cohen, A.L.; Colman, H. Glioma Subclassifications and Their Clinical Significance. *Neurotherapeutics* **2017**, *14*, 284, doi:10.1007/S13311-017-0519-X.
32. McNamara, M.G.; Sahebjam, S.; Mason, W.P. Emerging Biomarkers in Glioblastoma. *Cancers* **2013**, *5*, 1103–1119, doi:10.3390/CANCERS5031103.
33. Martini, M.; de Pascalis, I.; D'Alessandris, Q.G.; Fiorentino, V.; Pierconti, F.; Marei, H.E.S.; Ricci-Vitiani, L.; Pallini, R.; Larocca, L.M. VEGF-121 Plasma Level as Biomarker for Response to Anti-Angiogenetic Therapy in Recurrent Glioblastoma. *BMC Cancer* **2018**, *18*, doi:10.1186/S12885-018-4442-2.
34. Furgason, J.M.; Koncar, R.F.; Michelhaugh, S.K.; Sarkar, F.H.; Mittal, S.; Sloan, A.E.; Barnholtz-Sloan, J.S.; Bahassi, E.M. Whole Genome Sequence Analysis Links Chromothripsis to EGFR, MDM2, MDM4, and CDK4 Amplification in Glioblastoma. *Oncoscience* **2015**, *2*, 628, doi:10.18632/ONCOSCIENCE.178.
35. Mosrati, M.A.; Malmström, A.; Lysiak, M.; Krysztofiak, A.; Hallbeck, M.; Milos, P.; Hallbeck, A.L.; Bratthäll, C.; Strandéus, M.; Stenmark-Askmalm, M.; et al. TERT Promoter Mutations and Polymorphisms as Prognostic Factors in Primary Glioblastoma. *Oncotarget* **2015**, *6*, 16663, doi:10.18632/ONCOTARGET.4389.
36. Haynes, H.R.; Camelo-Piragua, S.; Kurian, K.M. Prognostic and Predictive Biomarkers in Adult and Pediatric Gliomas: Toward Personalized Treatment. *Front Oncol* **2014**, *4*, doi:10.3389/FONC.2014.00047.
37. Jadoon, S.S.; Ilyas, U.; Zafar, H.; Paiva-Santos, A.C.; Khan, S.; Khan, S.A.; Ahmed, T.; Rasool, Y.; Altaf, R.; Raza, F.; et al. Genomic and Epigenomic Features of Glioblastoma Multiforme and Its Biomarkers. *J Oncol* **2022**, *2022*, doi:10.1155/2022/4022960.
38. Stupp, R.; Mason, W.P.; van den Bent, M.J.; Weller, M.; Fisher, B.; Taphoorn, M.J.B.; Belanger, K.; Brandes, A.A.; Marosi, C.; Bogdahn, U.; et al. Radiotherapy plus Concomitant and Adjuvant Temozolomide for Glioblastoma. *N Engl J Med* **2005**, *352*, 987–996, doi:10.1056/NEJMOA043330.
39. Davis, M.E. Glioblastoma: Overview of Disease and Treatment. *Clin J Oncol Nurs* **2016**, *20*, S2–S8, doi:10.1188/16.CJON.S1.2-8.
40. Fang, C.; Wang, K.; Stephen, Z.R.; Mu, Q.; Kievit, F.M.; Chiu, D.T.; Press, O.W.; Zhang, M. Temozolomide Nanoparticles for Targeted Glioblastoma Therapy. *ACS Appl Mater Interfaces* **2015**, *7*, 6682, doi:10.1021/AM5092165.
41. Ostermann, S.; Csajka, C.; Buclin, T.; Leyvraz, S.; Lejeune, F.; Decosterd, L.A.; Stupp, R. Plasma and Cerebrospinal Fluid Population Pharmacokinetics of Temozolomide in Malignant Glioma Patients. *Clinical Cancer Research* **2004**, *10*, 3728–3736, doi:10.1158/1078-0432.CCR-03-0807.
42. Sengupta, S.; Marrinan, J.; Frishman, C.; Sampath, P. Impact of Temozolomide on Immune Response during Malignant Glioma Chemotherapy. *Clin Dev Immunol* **2012**, *2012*, 831090, doi:10.1155/2012/831090.
43. Chamberlain, M.C. Temozolomide: Therapeutic Limitations in the Treatment of Adult High-Grade Gliomas. *Expert Rev Neurother* **2014**, *10*, 1537–1544, doi:10.1586/ERN.10.32.
44. Trinh, V.A.; Patel, S.P.; Hwu, W.-J. The Safety of Temozolomide in the Treatment of Malignancies. *Expert Opin Drug Saf* **2009**, *8*, 493–499, doi:10.1517/14740330902918281.
45. Khan, A.; Imam, S.S.; Aqil, M.; Ahad, A.; Sultana, Y.; Ali, A.; Khan, K. Brain Targeting of Temozolomide via the Intranasal Route Using Lipid-Based Nanoparticles: Brain Pharmacokinetic and Scintigraphic Analyses. *Mol Pharm* **2016**, *13*, 3773–3782, doi:10.1021/ACS.MOLPHARMACEUT.6B00586.
46. Gullà, A.; Hideshima, T.; Bianchi, G.; Fulciniti, M.; Samur, M.K.; Qi, J.; Tai, Y.-T.; Harada, T.; Morelli, E.; Amodio, N.; et al. Protein Arginine Methyltransferase 5 (PRMT5) Has Prognostic Relevance and Is a Druggable Target in Multiple Myeloma. *Leukemia* **2018**, *32*, 1002, doi:10.1038/LEU.2017.334.

47. Stopa, N.; Krebs, J.E.; Shechter, D. The PRMT5 Arginine Methyltransferase: Many Roles in Development, Cancer and Beyond. *Cellular and molecular life sciences* **2015**, *72*, 2059, doi:10.1007/S00018-015-1847-9.
48. Vinet, M.; Suresh, S.; Maire, V.; Monchecourt, C.; Némati, F.; Lesage, L.; Pierre, F.; Ye, M.; Lescure, A.; Brisson, A.; et al. Protein Arginine Methyltransferase 5: A Novel Therapeutic Target for Triple-negative Breast Cancers. *Cancer Med* **2019**, *8*, 2428, doi:10.1002/CAM4.2114.
49. Chan-Penebre, E.; Kuplast, K.G.; Majer, C.R.; Boriack-Sjodin, P.A.; Wigle, T.J.; Johnston, L.D.; Rioux, N.; Munchhof, M.J.; Jin, L.; Jacques, S.L.; et al. A Selective Inhibitor of PRMT5 with in Vivo and in Vitro Potency in MCL Models. *Nat Chem Biol* **2015**, *11*, 432–437, doi:10.1038/nchembio.1810.
50. Aguilera-Márquez, J.D.R.; de Dios-Figueroa, G.T.; Reza-Saldivar, E.E.; Camacho-Villegas, T.A.; Canales-Aguirre, A.A.; Lugo-Fabres, P.H. Biomaterials: Emerging Systems for Study and Treatment of Glioblastoma. *Neurology perspectives* **2022**, *2*, S31–S42, doi:10.1016/J.NEUROP.2021.12.001.
51. Simon, T.; Jackson, E.; Giamas, G. Breaking through the Glioblastoma Micro-Environment via Extracellular Vesicles. *Oncogene 2020 39:23* **2020**, *39*, 4477–4490, doi:10.1038/s41388-020-1308-2.
52. Walker, S.; Busatto, S.; Pham, A.; Tian, M.; Suh, A.; Carson, K.; Quintero, A.; Lafrence, M.; Malik, H.; Santana, M.X.; et al. Extracellular Vesicle-Based Drug Delivery Systems for Cancer Treatment. *Theranostics* **2019**, *9*, 8001–8017, doi:10.7150/THNO.37097.
53. Miller, K.D.; Siegel, R.L.; Lin, C.C.; Mariotto, A.B.; Kramer, J.L.; Rowland, J.H.; Stein, K.D.; Alteri, R.; Jemal, A. Cancer Treatment and Survivorship Statistics, 2016. *CA Cancer J Clin* **2016**, *66*, 271–289, doi:10.3322/CAAC.21349.
54. Gonzalez, R. WHO Classification Available online: https://www.pathologyoutlines.com/topic/pancreaswho.html (accessed on 30 April 2023).
55. Talathi, S.S.; Zimmerman, R.; Young, M. Anatomy, Abdomen and Pelvis, Pancreas. In *StatPearls*; StatPearls Publishing, 2022.
56. Johns Hopkins Medicine Pancreatic Cancer Types Available online: https://www.hopkinsmedicine.org/health/conditions-and-diseases/pancreatic-cancer/pancreatic-cancer-types (accessed on 3 May 2023).
57. Truong, L.H.; Pauklin, S. Pancreatic Cancer Microenvironment and Cellular Composition: Current Understandings and Therapeutic Approaches. *Cancers* **2021**, *13*, 5028, doi:10.3390/CANCERS13195028.
58. Ciernikova, S.; Earl, J.; Bermejo, M.L.G.; Stevurkova, V.; Carrato, A.; Smolkova, B. Epigenetic Landscape in Pancreatic Ductal Adenocarcinoma: On the Way to Overcoming Drug Resistance? *Int J Mol Sci* **2020**, *21*, 11–17, doi:10.3390/IJMS21114091.
59. Nagendram, S.; Bhattacharya, S. Pancreatic Cancer: A Glimmer of Hope. *Trends in Urology & Men’s Health* **2023**, *14*, 5–10, doi:10.1002/TRE.904.
60. Yachida, S.; Iacobuzio-Donahue, C.A. Evolution and Dynamics of Pancreatic Cancer Progression. *Oncogene* **2013**, *32*, 5253–5260, doi:10.1038/ONC.2013.29.
61. Capasso, M.; Franceschi, M.; Rodriguez-Castro, K.I.; Crafa, P.; Cambiè, G.; Miraglia, C.; Barchi, A.; Nouvenne, A.; Leandro, G.; Meschi, T.; et al. Epidemiology and Risk Factors of Pancreatic Cancer. *Acta Biomed* **2018**, *89*, 141–146, doi:10.23750/ABM.V89I9-S.7923.
62. McGuigan, A.; Kelly, P.; Turkington, R.C.; Jones, C.; Coleman, H.G.; McCain, R.S. Pancreatic Cancer: A Review of Clinical Diagnosis, Epidemiology, Treatment and Outcomes. *World J Gastroenterol* **2018**, *24*, 4846–4861, doi:10.3748/WJG.V24.I43.4846.
63. Zheng, J.; Guinter, M.A.; Merchant, A.T.; Wirth, M.D.; Zhang, J.; Stolzenberg-Solomon, R.Z.; Steck, S.E. Dietary Patterns and Risk of Pancreatic Cancer: A Systematic Review. *Nutr Rev* **2017**, *75*, 883–908, doi:10.1093/NUTRIT/NUX038.

64. Hruban, R.H.; Canto, M.I.; Goggins, M.; Schulick, R.; Klein, A.P. Update on Familial Pancreatic Cancer. *Adv Surg* **2010**, *44*, 311, doi:10.1016/J.YASU.2010.05.011.
65. Chen, F.; Roberts, N.J.; Klein, A.P. Inherited Pancreatic Cancer. *Chin Clin Oncol* **2017**, *6*, 58, doi:10.21037/CCO.2017.12.04.
66. Del Chiaro, M.; Segersvärd, R.; Löhr, M.; Verbeke, C. Early Detection and Prevention of Pancreatic Cancer: Is It Really Possible Today? *World Journal of Gastroenterology : WJG* **2014**, *20*, 12131, doi:10.3748/WJG.V20.I34.12118.
67. Araujo-Abad, S.; Manresa-Manresa, A.; Rodríguez-Cañas, E.; Fuentes- Baile, M.; García-Morales, P.; Mallavia, R.; Saceda, M.; de Juan Romero, C. New Therapy for Pancreatic Cancer Based on Extracellular Vesicles. *Biomedicine & Pharmacotherapy* **2023**, *162*, 114657, doi:10.1016/J.BIOPHA.2023.114657.
68. Abbruzzese, J.L. Adjuvant Therapy for Surgically Resected Pancreatic Adenocarcinoma. *JAMA* **2008**, *299*, 1066–1067, doi:10.1001/JAMA.299.9.1066.
69. Casper, E.S.; Green, M.R.; Kelsen, D.P.; Heelan, R.T.; Brown, T.D.; Flombaum, C.D.; Trochanowski, B.; Tarassoff, P.G. Phase II Trial of Gemcitabine (2,2'-Difluorodeoxycytidine) in Patients with Adenocarcinoma of the Pancreas. *Invest New Drugs* **1994**, *12*, 29–34, doi:10.1007/BF00873232.
70. Carmichael, J.; Fink, U.; Russell, R.C.G.; Spittle, M.F.; Harris, A.L.; Spiessi, G.; Blatter, J. Phase II Study of Gemcitabine in Patients with Advanced Pancreatic Cancer. *Br J Cancer* **1996**, *73*, 101–105, doi:10.1038/BJC.1996.18.
71. Moore, M. Activity of Gemcitabine in Patients with Advanced Pancreatic Carcinoma A Review BACKGROUND. In Early Phase I1 Trials in Advanced Pancreatic Cancer, Gemcitabine. *Cancer* **1996**, *78*, 633–638, doi:10.1002/(SICI)1097-0142(19960801)78:3<633::AID-CNCR44>3.0.CO;2-X.
72. Conroy, T.; Hammel, P.; Hebbar, M.; Ben Abdelghani, M.; Wei, A.C.; Raoul, J.-L.; Choné, L.; Francois, E.; Artru, P.; Biagi, J.J.; et al. FOLFIRINOX or Gemcitabine as Adjuvant Therapy for Pancreatic Cancer. *N Engl J Med* **2018**, *379*, 2395–2406, doi:10.1056/NEJMOA1809775.
73. Gronchi, A.; Miah, A.B.; Dei Tos, A.P.; Abecassis, N.; Bajpai, J.; Bauer, S.; Biagini, R.; Bielack, S.; Blay, J.Y.; Bolle, S.; et al. Soft Tissue and Visceral Sarcomas: ESMO-EURACAN-GENTURIS Clinical Practice Guidelines for Diagnosis, Treatment and Follow-Up☆. *Ann Oncol* **2021**, *32*, 1348–1365, doi:10.1016/J.ANNONC.2021.07.006.
74. Casali, P.G.; Bielack, S.; Abecassis, N.; Aro, H.T.; Bauer, S.; Biagini, R.; Bonvalot, S.; Boukovinas, I.; Bovee, J.V.M.G.; Brennan, B.; et al. Bone Sarcomas: ESMO-PaedCan-EURACAN Clinical Practice Guidelines for Diagnosis, Treatment and Follow-Up. *Annals of oncology* **2018**, *29*, iv79–iv95, doi:10.1093/ANNONC/MDY310.
75. Nabors, L.B.; Portnow, J.; Ahluwalia, M.; Baehring, J.; Brem, H.; Brem, S.; Butowski, N.; Campian, J.L.; Clark, S.W.; Fabiano, A.J.; et al. Central Nervous System Cancers, Version 3.2020, NCCN Clinical Practice Guidelines in Oncology. *J Natl Compr Canc Netw* **2020**, *18*, 1537–1570, doi:10.6004/JNCCN.2020.0052.
76. von Mehren, M.; Kane, J.M.; Bui, M.M.; Choy, E.; Connelly, M.; Dry, S.; Ganjoo, K.N.; George, S.; Gonzalez, R.J.; Heslin, M.J.; et al. NCCN Guidelines Insights: Soft Tissue Sarcoma, Version 1.2021. *J Natl Compr Canc Netw* **2020**, *18*, 1605–1612, doi:10.6004/JNCCN.2020.0058.
77. Swetter, S.M.; Thompson, J.A.; Albertini, M.R.; Barker, C.A.; Baumgartner, J.; Boland, G.; Chmielowski, B.; DiMaio, D.; Durham, A.; Fields, R.C.; et al. NCCN Guidelines® Insights: Melanoma: Cutaneous, Version 2.2021. *Journal of the National Comprehensive Cancer Network* **2021**, *19*, 364–376, doi:10.6004/JNCCN.2021.0018.
78. Pavel, M.; Öberg, K.; Falconi, M.; Krenning, E.P.; Sundin, A.; Perren, A.; Berruti, A. Gastroenteropancreatic Neuroendocrine Neoplasms: ESMO Clinical Practice Guidelines for Diagnosis, Treatment and Follow-Up. *Annals of Oncology* **2020**, *31*, 844–860, doi:10.1016/J.ANNONC.2020.03.304.
79. Stupp, R.; Brada, M.; van den Bent, M.J.; Tonn, J.C.; Pentheroudakis, G. High-Grade Glioma: ESMO Clinical Practice Guidelines for Diagnosis, Treatment and Follow-Up. *Annals of Oncology* **2014**, *25*, iii93–iii101, doi:10.1093/ANNONC/MDU050.

80. Moore, M.J.; Feld, R.; Hedley, D.; Oza, A.; Siu, L.L. A Phase II Study of Temozolomide in Advanced Untreated Pancreatic Cancer. *Invest New Drugs* **1998**, *16*, 77–79, doi:10.1023/A:1006043332368.
81. Liu, X.; He, J.Z.; Mao, L.; Zhang, Y.; Cui, W.W.; Duan, S.; Jiang, A.; Gao, Y.; Sang, Y.; Huang, G. EPZ015666, a Selective Protein Arginine Methyltransferase 5 (PRMT5) Inhibitor with an Antitumour Effect in Retinoblastoma. *Exp Eye Res* **2021**, *202*, 108286, doi:10.1016/J.EXER.2020.108286.
82. Braun, C.J.; Stanciu, M.; Boutz, P.L.; Patterson, J.C.; Calligaris, D.; Higuchi, F.; Neupane, R.; Fenoglio, S.; Cahill, D.P.; Wakimoto, H.; et al. Coordinated Splicing of Regulatory Detained Introns within Oncogenic Transcripts Creates an Exploitable Vulnerability in Malignant Glioma. *Cancer Cell* **2017**, *32*, 411-426.e11, doi:10.1016/J.CCELL.2017.08.018.
83. Wei, X.; Yang, J.; Adair, S.J.; Ozturk, H.; Kuscu, C.; Lee, K.Y.; Kane, W.J.; O'Hara, P.E.; Liu, D.; Demirlenk, Y.M.; et al. Targeted CRISPR Screening Identifies PRMT5 as Synthetic Lethality Combinatorial Target with Gemcitabine in Pancreatic Cancer Cells. *Proc Natl Acad Sci U S A* **2020**, *117*, 28068–28079, doi:10.1073/PNAS.2009899117/-/DCSUPPLEMENTAL.
84. Chargaff, E.; West, R. The biological significance of the thromboplastic protein of blood. *Journal of Biological Chemistry* **1946**, *166*, 189–197, doi:10.1016/S0021-9258(17)34997-9.
85. Wolf, P. The Nature and Significance of Platelet Products in Human Plasma. *Br J Haematol* **1967**, *13*, 269–288, doi:10.1111/J.1365-2141.1967.TB08741.X.
86. Anderson, H.C. Vesicles Associated with Calcification in the Matrix of Epiphyseal Cartilage. *J Cell Biol* **1969**, *41*, 72, doi:10.1083/JCB.41.1.59.
87. Couch, Y.; Buzàs, E.I.; Vizio, D. Di; Gho, Y.S.; Harrison, P.; Hill, A.F.; Lötvall, J.; Raposo, G.; Stahl, P.D.; Théry, C.; et al. A Brief History of Nearly EV-Erything – The Rise and Rise of Extracellular Vesicles. *J Extracell Vesicles* **2021**, *10*, e12144, doi:10.1002/JEV2.12144.
88. György, B.; Szabó, T.G.; Pásztói, M.; Pál, Z.; Misják, P.; Aradi, B.; László, V.; Pállinger, É.; Pap, E.; Kittel, Á.; et al. Membrane Vesicles, Current State-of-the-Art: Emerging Role of Extracellular Vesicles. *Cellular and molecular life sciences* **2011**, *68*, 2667–2688, doi:10.1007/S00018-011-0689-3.
89. Mathieu, M.; Martin-Jaular, L.; Lavieu, G.; Théry, C. Specificities of Secretion and Uptake of Exosomes and Other Extracellular Vesicles for Cell-to-Cell Communication. *Nat Cell Biol* **2019**, *21*, 9–17, doi:10.1038/s41556-018-0250-9.
90. Johnstone, R.M.; Adam, M.; Hammond, J.R.; Orr, L.; Turbide, C. Vesicle Formation during Reticulocyte Maturation. Association of Plasma Membrane Activities with Released Vesicles (Exosomes). *Journal of Biological Chemistry* **1987**, *262*, 9412–9420, doi:10.1016/S0021-9258(18)48095-7.
91. Conde-Vancells, J.; Rodriguez-Suarez, E.; Embade, N.; Gil, D.; Matthiesen, R.; Valle, M.; Elortza, F.; Lu, S.C.; Mato, J.M.; Falcon-Perez, J.M. Characterization and Comprehensive Proteome Profiling of Exosomes Secreted by Hepatocytes. *J Proteome Res* **2008**, *7*, 5157–5166, doi:10.1021/pr8004887.
92. Théry, C.; Witwer, K.W.; Aikawa, E.; Alcaraz, M.J.; Anderson, J.D.; Andriantsitohaina, R.; Antoniou, A.; Arab, T.; Archer, F.; Atkin-Smith, G.K.; et al. Minimal Information for Studies of Extracellular Vesicles 2018 (MISEV2018): A Position Statement of the International Society for Extracellular Vesicles and Update of the MISEV2014 Guidelines. *J Extracell Vesicles* **2018**, *7*, doi:10.1080/20013078.2018.1535750.
93. Poupardin, R.; Wolf, M.; Strunk, D. Adherence to Minimal Experimental Requirements for Defining Extracellular Vesicles and Their Functions. *Adv Drug Deliv Rev* **2021**, *176*, 113872, doi:10.1016/J.ADDR.2021.113872.
94. Huang, H.; Liu, S.; Zhao, X.; Zhao, P.; Jia, Q.; Ma, H.; Lin, Q. Role of Tear Exosomes in the Spread of Herpes Simplex Virus Type 1 in Recurrent Herpes Simplex Keratitis. *Eye 2023* **2023**, 1–6, doi:10.1038/s41433-023-02473-4.

95. Sharma, S.; Rasool, H.I.; Palanisamy, V.; Mathisen, C.; Schmidt, M.; Wong, D.T.; Gimzewski, J.K. Structural-Mechanical Characterization of Nanoparticle Exosomes in Human Saliva, Using Correlative AFM, FESEM, and Force Spectroscopy. *ACS Nano* **2010**, *4*, 1921–1926, doi:10.1021/NN901824N.
96. Chopra, N.; Dutt Arya, B.; Jain, N.; Yadav, P.; Wajid, S.; Singh, S.P.; Choudhury, S. Biophysical Characterization and Drug Delivery Potential of Exosomes from Human Wharton's Jelly-Derived Mesenchymal Stem Cells. *ACS Omega* **2019**, *4*, 13143–13152, doi:10.1021/ACSOMEGA.9B01180.
97. Hurley, J.H.; Boura, E.; Carlson, L.A.; Róycki, B. Membrane Budding. *Cell* **2010**, *143*, 887, doi:10.1016/J.CELL.2010.11.030.
98. Han, Q.F.; Li, W.J.; Hu, K.S.; Gao, J.; Zhai, W.L.; Yang, J.H.; Zhang, S.J. Exosome Biogenesis: Machinery, Regulation, and Therapeutic Implications in Cancer. *Mol Cancer* **2022**, *21*, 207, doi:10.1186/S12943-022-01671-0.
99. Henne, W.M.; Buchkovich, N.J.; Emr, S.D. The ESCRT Pathway. *Dev Cell* **2011**, *21*, 77–91, doi:10.1016/J.DEVCEL.2011.05.015.
100. Tschuschke, M.; Kocherova, I.; Bryja, A.; Mozdziak, P.; Angelova Volponi, A.; Janowicz, K.; Sibiak, R.; Piotrowska-Kempisty, H.; Iżycki, D.; Bukowska, D.; et al. Inclusion Biogenesis, Methods of Isolation and Clinical Application of Human Cellular Exosomes. *J Clin Med* **2020**, *9*, 436, doi:10.3390/jcm9020436.
101. Skotland, T.; Hessvik, N.P.; Sandvig, K.; Llorente, A. Exosomal Lipid Composition and the Role of Ether Lipids and Phosphoinositides in Exosome Biology. *J Lipid Res* **2019**, *60*, 18, doi:10.1194/JLR.R084343.
102. Dawson, G. Isolation of Lipid Rafts (Detergent-Resistant Microdomains) and Comparison to Extracellular Vesicles (Exosomes). *Methods in molecular biology* **2021**, *2187*, 99–112, doi:10.1007/978-1-0716-0814-2_6.
103. Colombo, M.; Raposo, G.; Théry, C. Biogenesis, Secretion, and Intercellular Interactions of Exosomes and Other Extracellular Vesicles. *Annu Rev Cell Dev Biol* **2014**, *30*, 255–289, doi:10.1146/ANNUREV-CELLBIO-101512-122326.
104. Rani, S.; O'Brien, K.; Kelleher, F.C.; Corcoran, C.; Germano, S.; Radomski, M.W.; Crown, J.; O'Driscoll, L. Isolation of Exosomes for Subsequent MRNA, MicroRNA, and Protein Profiling. *Methods in Molecular Biology* **2011**, *784*, 181–195, doi:10.1007/978-1-61779-289-2_13.
105. Skotland, T.; Sandvig, K.; Llorente, A. Lipids in Exosomes: Current Knowledge and the Way Forward. *Prog Lipid Res* **2017**, *66*, 30–41, doi:10.1016/j.plipres.2017.03.001.
106. Wubbolts, R.; Leckie, R.S.; Veenhuizen, P.T.M.; Schwarzmann, G.; Möbius, W.; Hoernschemeyer, J.; Slot, J.W.; Geuze, H.J.; Stoorvogel, W. Proteomic and Biochemical Analyses of Human B Cell-Derived Exosomes: Potential Implications for Their Function and Multivesicular Body Formation. *Journal of Biological Chemistry* **2003**, *278*, 10963–10972, doi:10.1074/jbc.M207550200.
107. Araujo-Abad, S.; Saceda, M.; de Juan Romero, C. Biomedical Application of Small Extracellular Vesicles in Cancer Treatment. *Adv Drug Deliv Rev* **2022**, *182*, 114117, doi:10.1016/J.ADDR.2022.114117.
108. Yang, X.X.; Sun, C.; Wang, L.; Guo, X.L. New Insight into Isolation, Identification Techniques and Medical Applications of Exosomes. *Journal of Controlled Release* **2019**, *308*, 119–129, doi:10.1016/J.JCONREL.2019.07.021.
109. Andreu, Z.; Yáñez-Mó, M. Tetraspanins in Extracellular Vesicle Formation and Function. *Front Immunol* **2014**, *5*, 442, doi:10.3389/FIMMU.2014.00442.
110. Liang, Y.; Duan, L.; Lu, J.; Xia, J. Engineering Exosomes for Targeted Drug Delivery. *Theranostics* **2021**, *11*, 3195, doi:10.7150/THNO.52570.
111. Wang, W.; Zhu, N.; Yan, T.; Shi, Y.N.; Chen, J.; Zhang, C.J.; Xie, X.J.; Liao, D.F.; Qin, L. The Crosstalk: Exosomes and Lipid Metabolism. *Cell Communication and Signaling* **2020**, *18*, doi:10.1186/S12964-020-00581-2.
112. Zhu, L.; Sun, H.T.; Wang, S.; Huang, S.L.; Zheng, Y.; Wang, C.Q.; Hu, B.Y.; Qin, W.; Zou, T.T.; Fu, Y.; et al. Isolation and Characterization of Exosomes for Cancer

Research. *Journal of Hematology & Oncology 2020 13:1* **2020**, *13*, 1–24, doi:10.1186/S13045-020-00987-Y.

113. Théry, C.; Amigorena, S.; Raposo, G.; Clayton, A. Isolation and Characterization of Exosomes from Cell Culture Supernatants and Biological Fluids. *Curr Protoc Cell Biol* **2006**, *30*, 3.22.1-3.22.29, doi:10.1002/0471143030.CB0322S30.
114. Momen-Heravi, F. Isolation of Extracellular Vesicles by Ultracentrifugation. *Methods Mol Biol* **2017**, *1660*, 25–32, doi:10.1007/978-1-4939-7253-1_3.
115. Cheruvanky, A.; Zhou, H.; Pisitkun, T.; Kopp, J.B.; Knepper, M.A.; Yuen, P.S.T.; Star., R.A. Rapid Isolation of Urinary Exosomal Biomarkers Using a Nanomembrane Ultrafiltration Concentrator. *Am J Physiol Renal Physiol* **2007**, *292*, F1657, doi:10.1152/AJPRENAL.00434.2006.
116. Böing, A.N.; Pol, E. van der; Grootemaat, A.E.; Coumans, F.A.W.; Sturk, A.; Nieuwland, R. Single-Step Isolation of Extracellular Vesicles by Size-Exclusion Chromatography. *J Extracell Vesicles* **2014**, *3*, doi:10.3402/JEV.V3.23430.
117. Fitzgerald, J.; Leonard, P.; Darcy, E.; Sharma, S.; O'Kennedy, R. Immunoaffinity Chromatography: Concepts and Applications. *Methods in Molecular Biology* **2017**, *1485*, 27–51, doi:10.1007/978-1-4939-6412-3_3.
118. Rider, M.A.; Hurwitz, S.N.; Meckes, D.G. ExtraPEG: A Polyethylene Glycol-Based Method for Enrichment of Extracellular Vesicles. *Scientific Reports* **2016**, *6*, 1–14, doi:10.1038/srep23978.
119. Liga, A.; Vliegenthart, A.D.B.; Oosthuyzen, W.; Dear, J.W.; Kersaudy-Kerhoas, M. Exosome Isolation: A Microfluidic Road-Map. *Lab Chip* **2015**, *15*, 2388–2394, doi:10.1039/C5LC00240K.
120. Gupta, S.; Rawat, S.; Arora, V.; Kottarath, S.K.; Dinda, A.K.; Vaishnav, P.K.; Nayak, B.; Mohanty, S. An Improvised One-Step Sucrose Cushion Ultracentrifugation Method for Exosome Isolation from Culture Supernatants of Mesenchymal Stem Cells. *Stem Cell Res Ther* **2018**, *9*, 1–11, doi:10.1186/S13287-018-0923-0/FIGURES/6.
121. Taylor, D.D.; Zacharias, W.; Gercel-Taylor, C. Exosome Isolation for Proteomic Analyses and RNA Profiling. *Methods in Molecular Biology* **2011**, *728*, 235–246, doi:10.1007/978-1-61779-068-3_15.
122. Greening, D.W.; Xu, R.; Ji, H.; Tauro, B.J.; Simpson, R.J. A Protocol for Exosome Isolation and Characterization: Evaluation of Ultracentrifugation, Density-Gradient Separation, and Immunoaffinity Capture Methods. *Methods in Molecular Biology* **2015**, *1295*, 179–209, doi:10.1007/978-1-4939-2550-6_15.
123. Tauro, B.J.; Greening, D.W.; Mathias, R.A.; Ji, H.; Mathivanan, S.; Scott, A.M.; Simpson, R.J. Comparison of Ultracentrifugation, Density Gradient Separation, and Immunoaffinity Capture Methods for Isolating Human Colon Cancer Cell Line LIM1863-Derived Exosomes. *Methods* **2012**, *56*, 293–304, doi:10.1016/J.YMETH.2012.01.002.
124. Gámez-Valero, A.; Monguió-Tortajada, M.; Carreras-Planella, L.; Franquesa, M.; Beyer, K.; Borràs, F.E. Size-Exclusion Chromatography-Based Isolation Minimally Alters Extracellular Vesicles' Characteristics Compared to Precipitating Agents. *Sci Rep* **2016**, *6*, doi:10.1038/SREP33641.
125. He, M.; Crow, J.; Roth, M.; Zeng, Y.; Godwin, A.K. Integrated Immunoisolation and Protein Analysis of Circulating Exosomes Using Microfluidic Technology. *Lab Chip* **2014**, *14*, 3780, doi:10.1039/C4LC00662C.
126. Mashouri, L.; Yousefi, H.; Aref, A.R.; Ahadi, A.M.; Molaei, F.; Alahari, S.K. Exosomes: Composition, Biogenesis, and Mechanisms in Cancer Metastasis and Drug Resistance. *Molecular Cancer 2019 18:1* **2019**, *18*, 1–14, doi:10.1186/S12943-019-0991-5.
127. Zhang, H.G.; Grizzle, W.E. Exosomes: A Novel Pathway of Local and Distant Intercellular Communication That Facilitates the Growth and Metastasis of Neoplastic Lesions. *Am J Pathol* **2014**, *184*, 28–41, doi:10.1016/J.AJPATH.2013.09.027.
128. Cruz, L.; Romero, J.A.A.; Iglesia, R.P.; Lopes, M.H. Extracellular Vesicles: Decoding a New Language for Cellular Communication in Early Embryonic Development. *Front Cell Dev Biol* **2018**, *6*, doi:10.3389/FCELL.2018.00094.

129. Zomer, A.; Maynard, C.; Verweij, F.J.; Kamermans, A.; Schäfer, R.; Beerling, E.; Schiffelers, R.M.; De Wit, E.; Berenguer, J.; Ellenbroek, S.I.J.; et al. In Vivo Imaging Reveals Extracellular Vesicle-Mediated Phenocopying of Metastatic Behavior. *Cell* **2015**, *161*, 1046–1057, doi:10.1016/j.cell.2015.04.042.
130. Nishida, N.; Yano, H.; Nishida, T.; Kamura, T.; Kojiro, M. Angiogenesis in Cancer. *Vasc Health Risk Manag* **2006**, *2*, 219, doi:10.2147/VHRM.2006.2.3.213.
131. Katoh, M. Therapeutics Targeting Angiogenesis: Genetics and Epigenetics, Extracellular MiRNAs and Signaling Networks (Review). *Int J Mol Med* **2013**, *32*, 763–767, doi:10.3892/IJMM.2013.1444.
132. Monteforte, A.; Lam, B.; Sherman, M.B.; Henderson, K.; Sligar, A.D.; Spencer, A.; Tang, B.; Dunn, A.K.; Baker, A.B. Glioblastoma Exosomes for Therapeutic Angiogenesis in Peripheral Ischemia. *Tissue Eng Part A* **2017**, *23*, 1261, doi:10.1089/TEN.TEA.2016.0508.
133. Schmidt, L.H.; Spieker, T.; Koschmieder, S.; Humberg, J.; Jungen, D.; Bulk, E.; Hascher, A.; Wittmer, D.; Marra, A.; Hillejan, L.; et al. The Long Noncoding MALAT-1 RNA Indicates a Poor Prognosis in Non-Small Cell Lung Cancer and Induces Migration and Tumor Growth. *J Thorac Oncol* **2011**, *6*, 1984–1992, doi:10.1097/JTO.0B013E3182307EAC.
134. Pompili, S.; Vetuschi, A.; Sferra, R.; Cappariello, A. Extracellular Vesicles and Resistance to Anticancer Drugs: A Tumor Skeleton Key for Unhinging Chemotherapies. *Front Oncol* **2022**, *12*, doi:10.3389/FONC.2022.933675.
135. Safaei, R.; Larson, B.J.; Cheng, T.C.; Gibson, M.A.; Otani, S.; Naerdemann, W.; Howell, S.B. Abnormal Lysosomal Trafficking and Enhanced Exosomal Export of Cisplatin in Drug-Resistant Human Ovarian Carcinoma Cells. *Mol Cancer Ther* **2005**, *4*, 1595–1604, doi:10.1158/1535-7163.MCT-05-0102.
136. Yoshida, A.; Fujiwara, T.; Uotani, K.; Morita, T.; Kiyono, M.; Yokoo, S.; Hasei, J.; Nakata, E.; Kunisada, T.; Ozaki, T. Clinical and Functional Significance of Intracellular and Extracellular MicroRNA-25-3p in Osteosarcoma. *Acta Med Okayama* **2018**, *72*, 165–174, doi:10.18926/AMO/55857.
137. Araujo-Abad, S.; Manresa-Manresa, A.; Rodríguez-Cañas, E.; Fuentes-Baile, M.; García-Morales, P.; Mallavia, R.; Saceda, M.; De, C.; Romero, J. Glioblastoma-Derived Small Extracellular Vesicles: Nanoparticles for Glioma Treatment. *International Journal of Molecular Sciences 2023, Vol. 24, Page 5910* **2023**, *24*, 5910, doi:10.3390/IJMS24065910.
138. Barua, S.; Mitragotri, S. Challenges Associated with Penetration of Nanoparticles across Cell and Tissue Barriers: A Review of Current Status and Future Prospects. *Nano Today* **2014**, *9*, 223–243, doi:10.1016/j.nantod.2014.04.008.
139. Luan, X.; Sansanaphongpricha, K.; Myers, I.; Chen, H.; Yuan, H.; Sun, D. Engineering Exosomes as Refined Biological Nanoplatforms for Drug Delivery. *Acta Pharmacol Sin* **2017**, *38*, 754–763, doi:10.1038/aps.2017.12.
140. Batrakova, E. V.; Kim, M.S. Using Exosomes, Naturally-Equipped Nanocarriers, for Drug Delivery. *Journal of Controlled Release* **2015**, *219*, 396–405, doi:10.1016/j.jconrel.2015.07.030.
141. Qiao, L.; Hu, S.; Huang, K.; Su, T.; Li, Z.; Vandergriff, A.; Cores, J.; Dinh, P.U.; Allen, T.; Shen, D.; et al. Tumor Cell-Derived Exosomes Home to Their Cells of Origin and Can Be Used as Trojan Horses to Deliver Cancer Drugs. *Theranostics* **2020**, *10*, 3474–3487, doi:10.7150/thno.39434.
142. Dai, J.; Su, Y.; Zhong, S.; Cong, L.; Liu, B.; Yang, J.; Tao, Y.; He, Z.; Chen, C.; Jiang, Y. Exosomes: Key Players in Cancer and Potential Therapeutic Strategy. *Signal Transduct Target Ther* **2020**, *5*, 145, doi:10.1038/s41392-020-00261-0.
143. Srivastava, A.; Amreddy, N.; Babu, A.; Panneerselvam, J.; Mehta, M.; Muralidharan, R.; Chen, A.; Zhao, Y.D.; Razaq, M.; Riedinger, N.; et al. Nanosomes Carrying Doxorubicin Exhibit Potent Anticancer Activity against Human Lung Cancer Cells. *Nature* **2016**, *6*, 1–15, doi:10.1038/srep38541.

144. Lv, Q.; Cheng, L.; Lu, Y.; Zhang, X.; Wang, Y.; Deng, J.; Zhou, J.; Liu, B.; Liu, J. Thermosensitive Exosome–Liposome Hybrid Nanoparticle-Mediated Chemoimmunotherapy for Improved Treatment of Metastatic Peritoneal Cancer. *Advanced Science* **2020**, *7*, doi:10.1002/advs.202000515.

145. Kamerkar, S.; Lebleu, V.S.; Sugimoto, H.; Yang, S.; Ruivo, C.F.; Melo, S.A.; Lee, J.J.; Kalluri, R. Exosomes Facilitate Therapeutic Targeting of Oncogenic KRAS in Pancreatic Cancer. *Nature* **2017**, *546*, 498–503, doi:10.1038/nature22341.

146. Lou, G.; Chen, L.; Xia, C.; Wang, W.; Qi, J.; Li, A.; Zhao, L.; Chen, Z.; Zheng, M.; Liu, Y. MiR-199a-Modified Exosomes from Adipose Tissue-Derived Mesenchymal Stem Cells Improve Hepatocellular Carcinoma Chemosensitivity through MTOR Pathway. *Journal of Experimental and Clinical Cancer Research* **2020**, *39*, doi:10.1186/s13046-019-1512-5.

147. Haque, S.; Vaiselbuh, S.R. CD19 Chimeric Antigen Receptor-Exosome Targets CD19 Positive B-Lineage Acute Lymphocytic Leukemia and Induces Cytotoxicity. *Cancers (Basel)* **2021**, *13*, doi:10.3390/cancers13061401.

148. Pomatto, M.A.C.; Bussolati, B.; D'Antico, S.; Ghiotto, S.; Tetta, C.; Brizzi, M.F.; Camussi, G. Improved Loading of Plasma-Derived Extracellular Vesicles to Encapsulate Antitumor MiRNAs. *Mol Ther Methods Clin Dev* **2019**, *13*, 133–144, doi:10.1016/J.OMTM.2019.01.001.

149. Lv, L.H.; Wan, Y. Le; Lin, Y.; Zhang, W.; Yang, M.; Li, G.N.; Lin, H.M.; Shang, C.Z.; Chen, Y.J.; Min, J. Anticancer Drugs Cause Release of Exosomes with Heat Shock Proteins from Human Hepatocellular Carcinoma Cells That Elicit Effective Natural Killer Cell Antitumor Responses in Vitro. *J Biol Chem* **2012**, *287*, 15874–15885, doi:10.1074/JBC.M112.340588.

150. Torreggiani, E.; Roncuzzi, L.; Perut, F.; Zini, N.; Baldini, N. Multimodal Transfer of MDR by Exosomes in Human Osteosarcoma. *Int J Oncol* **2016**, *49*, 189–196, doi:10.3892/IJO.2016.3509.

151. Salarpour, S.; Forootanfar, H.; Pournamdari, M.; Ahmadi-Zeidabadi, M.; Esmaeeli, M.; Pardakhty, A. Paclitaxel Incorporated Exosomes Derived from Glioblastoma Cells: Comparative Study of Two Loading Techniques. *Daru* **2019**, *27*, 533–539, doi:10.1007/S40199-019-00280-5.

152. Liang, G.; Zhu, Y.; Ali, D.J.; Tian, T.; Xu, H.; Si, K.; Sun, B.; Chen, B.; Xiao, Z. Engineered Exosomes for Targeted Co-Delivery of MiR-21 Inhibitor and Chemotherapeutics to Reverse Drug Resistance in Colon Cancer. *J Nanobiotechnology* **2020**, *18*, 1–15, doi:10.1186/S12951-019-0563-2/FIGURES/6.

153. Kooijmans, S.A.A.; Stremersch, S.; Braeckmans, K.; De Smedt, S.C.; Hendrix, A.; Wood, M.J.A.; Schiffelers, R.M.; Raemdonck, K.; Vader, P. Electroporation-Induced SiRNA Precipitation Obscures the Efficiency of SiRNA Loading into Extracellular Vesicles. *J Control Release* **2013**, *172*, 229–238, doi:10.1016/J.JCONREL.2013.08.014.

154. Zhang, D.; Lee, H.; Zhu, Z.; Minhas, J.K.; Jin, Y. Enrichment of Selective MiRNAs in Exosomes and Delivery of Exosomal MiRNAs in Vitro and in Vivo. *Am J Physiol Lung Cell Mol Physiol* **2017**, *312*, L110–L121, doi:10.1152/AJPLUNG.00423.2016.

155. Ramanathan, S.; Douglas, S.R.; Alexander, G.M.; Shenoda, B.B.; Barrett, J.E.; Aradillas, E.; Sacan, A.; Ajit, S.K. Exosome MicroRNA Signatures in Patients with Complex Regional Pain Syndrome Undergoing Plasma Exchange. *J Transl Med* **2019**, *17*, 1–12, doi:10.1186/S12967-019-1833-3/FIGURES/6.

156. Xi, X.-M.; Xia, S.-J.; Lu, R. Drug Loading Techniques for Exosome-Based Drug Delivery Systems. *Pharmazie* **2021**, *76*, 61–67, doi:10.1691/ph.2021.0128.

157. Bosch, S.; De Beaurepaire, L.; Allard, M.; Mosser, M.; Heichette, C.; Chrétien, D.; Jegou, D.; Bach, J.M. Trehalose Prevents Aggregation of Exosomes and Cryodamage. *Scientific Reports* **2016**, *6*, 1–11, doi:10.1038/srep36162.

158. Won Lee, G.; Thangavelu, M.; Joung Choi, M.; Yeong Shin, E.; Sol Kim, H.; Seon Baek, J.; Woon Jeong, Y.; Eun Song, J.; Carlomagno, C.; Miguel Oliveira, J.; et al. Exosome Mediated Transfer of MiRNA-140 Promotes Enhanced Chondrogenic Differentiation of

Bone Marrow Stem Cells for Enhanced Cartilage Repair and Regeneration. *J Cell Biochem* **2020**, *121*, 3642–3652, doi:10.1002/JCB.29657.

159. Sancho-Albero, M.; Encabo-Berzosa, M.D.M.; Beltrán-Visiedo, M.; Fernández-Messina, L.; Sebastián, V.; Sánchez-Madrid, F.; Arruebo, M.; Santamaría, J.; Martín-Duque, P. Efficient Encapsulation of Theranostic Nanoparticles in Cell-Derived Exosomes: Leveraging the Exosomal Biogenesis Pathway to Obtain Hollow Gold Nanoparticle-Hybrids. *Nanoscale* **2019**, *11*, 18825–18836, doi:10.1039/C9NR06183E.
160. Lin, F.; Wang, R. Hemolytic Mechanism of Dioscin Proposed by Molecular Dynamics Simulations. *J Mol Model* **2010**, *16*, 107–118, doi:10.1007/S00894-009-0523-0.
161. Jeyaram, A.; Lamichhane, T.N.; Wang, S.; Zou, L.; Dahal, E.; Kronstadt, S.M.; Levy, D.; Parajuli, B.; Knudsen, D.R.; Chao, W.; et al. Enhanced Loading of Functional MiRNA Cargo via PH Gradient Modification of Extracellular Vesicles. *Mol Ther* **2020**, *28*, 975–985, doi:10.1016/J.YMTHE.2019.12.007.
162. Fuhrmann, G.; Serio, A.; Mazo, M.; Nair, R.; Stevens, M.M. Active Loading into Extracellular Vesicles Significantly Improves the Cellular Uptake and Photodynamic Effect of Porphyrins. *J Control Release* **2015**, *205*, 35–44, doi:10.1016/J.JCONREL.2014.11.029.
163. Hinestrosa, J.P.; Kurzrock, R.; Lewis, J.M.; Schork, N.J.; Schroeder, G.; Kamat, A.M.; Lowy, A.M.; Eskander, R.N.; Perrera, O.; Searson, D.; et al. Early-Stage Multi-Cancer Detection Using an Extracellular Vesicle Protein-Based Blood Test. *Communications medicine* **2022**, *2*, doi:10.1038/S43856-022-00088-6.
164. Escudier, B.; Dorval, T.; Chaput, N.; André, F.; Caby, M.P.; Novault, S.; Flament, C.; Leboulaire, C.; Borg, C.; Amigorena, S.; et al. Vaccination of Metastatic Melanoma Patients with Autologous Dendritic Cell (DC) Derived-Exosomes: Results of the First Phase 1 Clinical Trial. *J Transl Med* **2005**, *3*, 1–13, doi:10.1186/1479-5876-3-10.
165. Viaud, S.; Terme, M.; Flament, C.; Taieb, J.; André, F.; Novault, S.; Escudier, B.; Robert, C.; Caillat-Zucman, S.; Tursz, T.; et al. Dendritic Cell-Derived Exosomes Promote Natural Killer Cell Activation and Proliferation: A Role for NKG2D Ligands and IL-15Ralpha. *PLoS One* **2009**, *4*, doi:10.1371/JOURNAL.PONE.0004942.
166. Morse, M.A.; Garst, J.; Osada, T.; Khan, S.; Hobeika, A.; Clay, T.M.; Valente, N.; Shreeniwas, R.; Sutton, M.A.; Delcayre, A.; et al. A Phase I Study of Dexosome Immunotherapy in Patients with Advanced Non-Small Cell Lung Cancer. *J Transl Med* **2005**, *3*, 1–8, doi:10.1186/1479-5876-3-9.
167. Dai, S.; Wei, D.; Wu, Z.; Zhou, X.; Wei, X.; Huang, H.; Li, G. Phase I Clinical Trial of Autologous Ascites-Derived Exosomes Combined with GM-CSF for Colorectal Cancer. *Molecular Therapy* **2008**, *16*, 782–790, doi:10.1038/mt.2008.1.
168. Besse, B.; Charrier, M.; Lapierre, V.; Dansin, E.; Lantz, O.; Planchard, D.; Le Chevalier, T.; Livartoski, A.; Barlesi, F.; Laplanche, A.; et al. Dendritic Cell-Derived Exosomes as Maintenance Immunotherapy after First Line Chemotherapy in NSCLC. *Oncoimmunology* **2016**, *5*, 1071008, doi:10.1080/2162402X.2015.1071008.
169. Fuhrmann, J.; Clancy, K.W.; Thompson, P.R. Chemical Biology of Protein Arginine Modifications in Epigenetic Regulation. *Chem Rev* **2015**, *115*, 5413–5461, doi:10.1021/ACS.CHEMREV.5B00003/ASSET/IMAGES/MEDIUM/CR-2015-00003A_0038.GIF.
170. Araujo-Abad, S.; Neira, J.L.; Rizzuti, B.; García-Morales, P.; de Juan Romero, C.; Santofimia-Castaño, P.; Iovanna, J. Intrinsically Disordered Chromatin Protein NUPR1 Binds to the Enzyme PADI4. *J Mol Biol* **2023**, *435*, doi:10.1016/J.JMB.2023.168033.
171. Vossenaar, E.R.; Zendman, A.J.W.; Van Venrooij, W.J.; Pruijn, G.J.M. PAD, a Growing Family of Citrullinating Enzymes: Genes, Features and Involvement in Disease. *BioEssays* **2003**, *25*, 1106–1118, doi:10.1002/BIES.10357.
172. Mondal, S.; Thompson, P.R. Protein Arginine Deiminases (PADs): Biochemistry and Chemical Biology of Protein Citrullination. *Acc Chem Res* **2019**, *52*, 818–832, doi:10.1021/ACS.ACCOUNTS.9B00024/ASSET/IMAGES/LARGE/AR-2019-00024V_0013.JPEG.

173. Esteller, M. Epigenetics in Cancer. *N Engl J Med* **2008**, *358*, 1148–1159, doi:10.1056/NEJMRA072067.

174. Nakashima, K.; Hagiwara, T.; Yamada, M. Nuclear Localization of Peptidylarginine Deiminase V and Histone Deimination in Granulocytes. *Journal of Biological Chemistry* **2002**, *277*, 49562–49568, doi:10.1074/JBC.M208795200.

175. Jones, J.E.; Causey, C.P.; Knuckley, B.; Slack-Noyes, J.L.; Thompson, P.R. Protein Arginine Deiminase 4 (PAD4): Current Understanding and Future Therapeutic Potential. *Curr Opin Drug Discov Devel* **2009**, *12*, 627.

176. Chang, X.; Han, J.; Pang, L.; Zhao, Y.; Yang, Y.; Shen, Z. Increased PADI4 Expression in Blood and Tissues of Patients with Malignant Tumors. *BMC Cancer* **2009**, *9*, doi:10.1186/1471-2407-9-40.

177. György, B.; Tóth, E.; Tarcsa, E.; Falus, A.; Buzás, E.I. Citrullination: A Posttranslational Modification in Health and Disease. *Int J Biochem Cell Biol* **2006**, *38*, 1662–1677, doi:10.1016/J.BIOCEL.2006.03.008.

178. Neira, J.L.; Araujo-Abad, S.; Cámara-Artigas, A.; Rizzuti, B.; Abian, O.; Giudici, A.M.; Velazquez-Campoy, A.; de Juan Romero, C. Biochemical and Biophysical Characterization of PADI4 Supports Its Involvement in Cancer. *Arch Biochem Biophys* **2022**, *717*, 109125, doi:10.1016/J.ABB.2022.109125.

179. Yuzhalin, A.E. Citrullination in Cancer. *Cancer Res* **2019**, *79*, 1274–1284, doi:10.1158/0008-5472.CAN-18-2797/661345/P/CITRULLINATION-IN-CANCERCITRULLINATION-IN-CANCER.

180. Hagiwara, T.; Hidaka, Y.; Yamada, M. Deimination of Histone H2A and H4 at Arginine 3 in HL-60 Granulocytes. *Biochemistry* **2005**, *44*, 5827–5834, doi:10.1021/BI047505C/ASSET/IMAGES/MEDIUM/BI047505CU00002A.GIF.

181. Cuthbert, G.L.; Daujat, S.; Snowden, A.W.; Erdjument-Bromage, H.; Hagiwara, T.; Yamada, M.; Schneider, R.; Gregory, P.D.; Tempst, P.; Bannister, A.J.; et al. Histone Deimination Antagonizes Arginine Methylation. *Cell* **2004**, *118*, 545–553, doi:10.1016/j.cell.2004.08.020.

182. Wang, Y.; Wysocka, J.; Sayegh, J.; Lee, Y.H.; Pertin, J.R.; Leonelli, L.; Sonbuchner, L.S.; McDonald, C.H.; Cook, R.G.; Dou, Y.; et al. Human PAD4 Regulates Histone Arginine Methylation Levels via Demethylimination. *Science* **2004**, *306*, 279–283, doi:10.1126/SCIENCE.1101400.

183. Li, P.; Yao, H.; Zhang, Z.; Li, M.; Luo, Y.; Thompson, P.R.; Gilmour, D.S.; Wang, Y. Regulation of P53 Target Gene Expression by Peptidylarginine Deiminase 4. *Mol Cell Biol* **2008**, *28*, 4745–4758, doi:10.1128/MCB.01747-07.

184. Yao, H.; Li, P.; Venters, B.J.; Zheng, S.; Thompson, P.R.; Pugh, B.F.; Wang, Y. Histone Arg Modifications and P53 Regulate the Expression of OKL38, a Mediator of Apoptosis. *J Biol Chem* **2008**, *283*, 20068, doi:10.1074/JBC.M802940200.

185. Guo, Q.; Fast, W. Citrullination of Inhibitor of Growth 4 (ING4) by Peptidylarginine Deminase 4 (PAD4) Disrupts the Interaction between ING4 and P53. *J Biol Chem* **2011**, *286*, 17069–17078, doi:10.1074/JBC.M111.230961.

186. Stadler, S.C.; Vincent, C.T.; Fedorov, V.D.; Patsialou, A.; Cherrington, B.D.; Wakshlag, J.J.; Mohanan, S.; Zee, B.M.; Zhang, X.; Garcia, B.A.; et al. Dysregulation of PAD4-Mediated Citrullination of Nuclear GSK3β Activates TGF-β Signaling and Induces Epithelial-to-Mesenchymal Transition in Breast Cancer Cells. *Proc Natl Acad Sci U S A* **2013**, *110*, 11851–11856, doi:10.1073/PNAS.1308362110.

187. Roche, J. The Epithelial-to-Mesenchymal Transition in Cancer. *Cancers (Basel)* **2018**, *10*, 52, doi:10.3390/CANCERS10020052.

188. Duan, Q.; Pang, C.; Chang, N.; Zhang, J.; Liu, W. Overexpression of PAD4 Suppresses Drug Resistance of NSCLC Cell Lines to Gefitinib through Inhibiting Elk1-Mediated Epithelial-Mesenchymal Transition. *Oncol Rep* **2016**, *36*, 551–558, doi:10.3892/OR.2016.4780.

189. Yuzhalin, A.E.; Gordon-Weeks, A.N.; Tognoli, M.L.; Jones, K.; Markelc, B.; Konietzny, R.; Fischer, R.; Muth, A.; O'Neill, E.; Thompson, P.R.; et al. Colorectal Cancer Liver

Metastatic Growth Depends on PAD4-Driven Citrullination of the Extracellular Matrix. *Nature Communications 2018 9:1* **2018**, *9*, 1–15, doi:10.1038/s41467-018-07306-7.

190. Li, J.C.; Zou, X.M.; Yang, S.F.; Zhu, L.; Yang, H.; Zhang, A.G.; Zhao, T.Q.; Chen, C.Y.; Jin, J.Q.; Li, C.J. Neutrophil Extracellular Traps Participate in the Development of Cancer-Associated Thrombosis in Patients with Gastric Cancer. *World J Gastroenterol* **2022**, *28*, 3132–3149, doi:10.3748/wjg.v28.i26.3132.
191. Berger-Achituv, S.; Brinkmann, V.; Abed, U.A.; Kühn, L.I.; Ben-Ezra, J.; Elhasid, R.; Zychlinsky, A. A Proposed Role for Neutrophil Extracellular Traps in Cancer Immunoediting. *Front Immunol* **2013**, *4*, doi:10.3389/FIMMU.2013.00048.
192. Yang, C.; Wang, Z.; Li, L.; Zhang, Z.; Jin, X.; Wu, P.; Sun, S.; Pan, J.; Su, K.; Jia, F.; et al. Aged Neutrophils Form Mitochondria-Dependent Vital NETs to Promote Breast Cancer Lung Metastasis. *J Immunother Cancer* **2021**, *9*, doi:10.1136/JITC-2021-002875.
193. Khan, U.; Chowdhury, S.; Billah, M.M.; Islam, K.M.D.; Thorlacius, H.; Rahman, M. Neutrophil Extracellular Traps in Colorectal Cancer Progression and Metastasis. *Int J Mol Sci* **2021**, *22*, doi:10.3390/IJMS22147260.
194. Tohme, S.; Yazdani, H.O.; Al-Khafaji, A.B.; Chidi, A.P.; Loughran, P.; Mowen, K.; Wang, Y.; Simmons, R.L.; Huang, H.; Tsung, A. Neutrophil Extracellular Traps Promote the Development and Progression of Liver Metastases after Surgical Stress. *Cancer Res* **2016**, *76*, 1367–1380, doi:10.1158/0008-5472.CAN-15-1591.
195. Slack, J.L.; Causey, C.P.; Thompson, P.R. Protein Arginine Deiminase 4: A Target for an Epigenetic Cancer Therapy. *Cell Mol Life Sci* **2011**, *68*, 709–720, doi:10.1007/S00018-010-0480-X.
196. Wei, L.; Wang, X.; Luo, M.; Wang, H.; Chen, H.; Huang, C. The PAD4 Inhibitor GSK484 Enhances the Radiosensitivity of Triple-Negative Breast Cancer. *Hum Exp Toxicol* **2021**, *40*, 1074–1083, doi:10.1177/0960327120979028/ASSET/IMAGES/LARGE/10.1177_0960327120979028-FIG4.JPEG.
197. Knuckley, B.; Causey, C.P.; Jones, J.E.; Bhatia, M.; Dreyton, C.J.; Osborne, T.C.; Takahara, H.; Thompson, P.R. Substrate Specificity and Kinetic Studies of PADs 1, 3, and 4 Identify Potent and Selective Inhibitors of Protein Arginine Deiminase 3. *Biochemistry* **2010**, *49*, 4852–4863, doi:10.1021/BI100363T.
198. Zeng, J.; Xu, H.; Fan, P. zhi; Xie, J.; He, J.; Yu, J.; Gu, X.; Zhang, C. jie Kaempferol Blocks Neutrophil Extracellular Traps Formation and Reduces Tumour Metastasis by Inhibiting ROS-PAD4 Pathway. *J Cell Mol Med* **2020**, *24*, 7599, doi:10.1111/JCMM.15394.
199. Szabó-Taylor, K.; Ryan, B.; Osteikoetxea, X.; Szabó, T.G.; Sódar, B.; Holub, M.; Németh, A.; Pálóczi, K.; Pállinger, É.; Winyard, P.; et al. Oxidative and Other Posttranslational Modifications in Extracellular Vesicle Biology. *Semin Cell Dev Biol* **2015**, *40*, 8–16, doi:10.1016/J.SEMCDB.2015.02.012.
200. Claridge, B.; Kastaniegaard, K.; Stensballe, A.; Greening, D.W. Post-Translational and Transcriptional Dynamics–Regulating Extracellular Vesicle Biology. *Expert Rev Proteomics* **2019**, *16*, 17–31, doi:10.1080/14789450.2019.1551135.
201. Zhang, Y.; Yang, Y.; Hu, X.; Wang, Z.; Li, L.; Chen, P. PADs in Cancer: Current and Future. *Biochimica et Biophysica Acta (BBA) - Reviews on Cancer* **2021**, *1875*, 188492, doi:10.1016/J.BBCAN.2020.188492.
202. Uysal-Onganer, P.; Maclatchy, A.; Mahmoud, R.; Kraev, I.; Thompson, P.R.; Inal, J.M.; Lange, S. Peptidylarginine Deiminase Isozyme-Specific PAD2, PAD3 and PAD4 Inhibitors Differentially Modulate Extracellular Vesicle Signatures and Cell Invasion in Two Glioblastoma Multiforme Cell Lines. *International Journal of Molecular Sciences 2020, Vol. 21, Page 1495* **2020**, *21*, 1495, doi:10.3390/IJMS21041495.
203. Uysal-Onganer, P.; D'alessio, S.; Mortoglou, M.; Kraev, I.; Lange, S. Peptidylarginine Deiminase Inhibitor Application, Using Cl-Amidine, PAD2, PAD3 and PAD4 Isozyme-Specific Inhibitors in Pancreatic Cancer Cells, Reveals Roles for PAD2 and PAD3 in

Cancer Invasion and Modulation of Extracellular Vesicle Signatures. *Int J Mol Sci* **2021**, *22*, 1–26, doi:10.3390/IJMS22031396.

204. Ventero, M.P.; Fuentes-Baile, M.; Quereda, C.; Perez-Valeciano, E.; Alenda, C.; Garcia-Morales, P.; Esposito, D.; Dorado, P.; Barbera, V.M.; Saceda, M. Radiotherapy Resistance Acquisition in Glioblastoma. Role of SOCS1 and SOCS3. *PLoS One* **2019**, *14*, e0212581, doi:10.1371/journal.pone.0212581.
205. Fuentes-Baile, M.; Bello-Gil, D.; Pérez-Valenciano, E.; Sanz, J.M.; García-Morales, P.; Maestro, B.; Ventero, M.P.; Alenda, C.; Barberá, V.M.; Saceda, M. CLyta-DAAO, Free and Immobilized in Magnetic Nanoparticles, Induces Cell Death in Human Cancer Cells. *Biomolecules* **2020**, *10*, 222, doi:10.3390/biom10020222.
206. Araujo-Abad, S.; Rizzuti, B.; Villamarin-Ortiz, A.; Pantoja-Uceda, D.; Moreno-Gonzalez, C.M.; Abian, O.; Velazquez-Campoy, A.; Neira, J.L.; De Juan Romero, C. New Insights into Cancer: MDM2 Binds to the Citrullinating Enzyme PADI4. *Protein Science* **2023**, e4723, doi:10.1002/PRO.4723.
207. Araujo-Abad, S.; Fuentes-Baile, M.; Rizzuti, B.; Bazán, J.F.; Villamarin-Ortiz, A.; Saceda, M.; Fernández, E.; Vidal, M.; Abian, O.; Velazquez-Campoy, A.; et al. The Intrinsically Disordered, Epigenetic Factor RYBP Binds to the Citrullinating Enzyme PADI4 in Cancer Cells. *Int J Biol Macromol* **2023**, *246*, 125632, doi:10.1016/J.IJBIOMAC.2023.125632.
208. Neira, J.L.; Rizzuti, B.; Araujo-Abad, S.; Abian, O.; Fárez-Vidal, M.E.; Velazquez-Campoy, A.; de Juan Romero, C. The Armadillo-Repeat Domain of Plakophilin 1 Binds to Human Enzyme PADI4. *Biochim Biophys Acta Proteins Proteom* **2023**, *1871*, doi:10.1016/J.BBAPAP.2022.140868.
209. Shu, S. La; Yang, Y.; Allen, C.L.; Hurley, E.; Tung, K.H.; Minderman, H.; Wu, Y.; Ernstoff, M.S. Purity and Yield of Melanoma Exosomes Are Dependent on Isolation Method. *J Extracell Vesicles* **2020**, *9*, 1692401, doi:10.1080/20013078.2019.1692401.
210. Ding, X.Q.; Wang, Z.Y.; Xia, D.; Wang, R.X.; Pan, X.R.; Tong, J.H. Proteomic Profiling of Serum Exosomes from Patients with Metastatic Gastric Cancer. *Front Oncol* **2020**, *10*, 1113, doi:10.3389/fonc.2020.01113.
211. Maji, S.; Chaudhary, P.; Akopova, I.; Nguyen, P.M.; Hare, R.J.; Gryczynski, I.; Vishwanatha, J.K. Exosomal Annexin II Promotes Angiogenesis and Breast Cancer Metastasis. *Molecular Cancer Research* **2017**, *15*, 93–105, doi:10.1158/1541-7786.MCR-16-0163.
212. Hosseini-Beheshti, E.; Pham, S.; Adomat, H.; Li, N.; Guns, E.S.T. Exosomes as Biomarker Enriched Microvesicles: Characterization of Exosomal Proteins Derived from a Panel of Prostate Cell Lines with Distinct AR Phenotypes. *Molecular & Cellular Proteomics* **2012**, *11*, 885, doi:10.1074/MCP.M111.014845.
213. Kavanagh, E.L.; Lindsay, S.; Halasz, M.; Gubbins, L.C.; Weiner-Gorzel, K.; Guang, M.H.Z.; McGoldrick, A.; Collins, E.; Henry, M.; Blanco-Fernández, A.; et al. Protein and Chemotherapy Profiling of Extracellular Vesicles Harvested from Therapeutic Induced Senescent Triple Negative Breast Cancer Cells. *Oncogenesis 2017 6:10* **2017**, *6*, e388–e388, doi:10.1038/oncsis.2017.82.
214. Singh, A.; Fedele, C.; Lu, H.; Nevalainen, M.T.; Keen, J.H.; Languino, L.R. Exosome-Mediated Transfer of Avβ3 Integrin from Tumorigenic to Nontumorigenic Cells Promotes a Migratory Phenotype. *Molecular Cancer Research* **2016**, *14*, 1136–1146, doi:10.1158/1541-7786.MCR-16-0058.
215. Wang, X.; Zhong, W.; Bu, J.; Li, Y.; Li, R.; Nie, R.; Xiao, C.; Ma, K.; Huang, X.; Li, Y. Exosomal Protein CD82 as a Diagnostic Biomarker for Precision Medicine for Breast Cancer. *Mol Carcinog* **2019**, *58*, 674–685, doi:10.1002/mc.22960.
216. Nonaka, T.; Wong, D.T.W. Saliva-Exosomics in Cancer: Molecular Characterization of Cancer-Derived Exosomes in Saliva. *Enzymes (Essen)* **2017**, *42*, 125–151, doi:10.1016/BS.ENZ.2017.08.002.
217. Raposo, G.; Stoorvogel, W. Extracellular Vesicles: Exosomes, Microvesicles, and Friends. *Journal of Cell Biology* **2013**, *200*, 373–383, doi:10.1083/JCB.201211138.

218. Conde-Vancells, J.; Rodriguez-Suarez, E.; Embade, N.; Gil, D.; Matthiesen, R.; Valle, M.; Elortza, F.; Lu, S.C.; Mato, J.M.; Falcon-Perez, J.M. Characterization and Comprehensive Proteome Profiling of Exosomes Secreted by Hepatocytes. *J Proteome Res* **2008**, *7*, 5157–5166, doi:10.1021/PR8004887/SUPPL_FILE/PR8004887_SI_003.PDF.
219. Hood, J.L.; Scott, M.J.; Wickline, S.A. Maximizing Exosome Colloidal Stability Following Electroporation. *Anal Biochem* **2014**, *448*, 49, doi:10.1016/J.AB.2013.12.001.
220. Hung, M.E.; Leonard, J.N. Stabilization of Exosome-Targeting Peptides via Engineered Glycosylation. *Journal of Biological Chemistry* **2015**, *290*, 8166–8172, doi:10.1074/JBC.M114.621383.
221. Rubio-Camacho, M.; Encinar, J.A.; Martínez-Tomé, M.J.; Esquembre, R.; Mateo, C.R. The Interaction of Temozolomide with Blood Components Suggests the Potential Use of Human Serum Albumin as a Biomimetic Carrier for the Drug. *Biomolecules* **2020**, *10*, 1–22, doi:10.3390/BIOM10071015.
222. Yang, X.; Shi, G.; Guo, J.; Wang, C.; He, Y. Exosome-Encapsulated Antibiotic against Intracellular Infections of Methicillin-Resistant Staphylococcus Aureus. *Int J Nanomedicine* **2018**, *13*, 8095, doi:10.2147/IJN.S179380.
223. Li, X.Q.; Liu, J.T.; Fan, L.L.; Liu, Y.; Cheng, L.; Wang, F.; Yu, H.Q.; Gao, J.; Wei, W.; Wang, H.; et al. Exosomes Derived from Gefitinib-Treated EGFR-Mutant Lung Cancer Cells Alter Cisplatin Sensitivity via up-Regulating Autophagy. *Oncotarget* **2016**, *7*, 24585, doi:10.18632/ONCOTARGET.8358.
224. Sun, D.; Zhuang, X.; Xiang, X.; Liu, Y.; Zhang, S.; Liu, C.; Barnes, S.; Grizzle, W.; Miller, D.; Zhang, H.G. A Novel Nanoparticle Drug Delivery System: The Anti-Inflammatory Activity of Curcumin Is Enhanced When Encapsulated in Exosomes. *Molecular Therapy* **2010**, *18*, 1606, doi:10.1038/MT.2010.105.
225. Labuschagne, J.J.; Chetty, D. Glioblastoma Multiforme as a Secondary Malignancy Following Stereotactic Radiosurgery of a Meningioma: Case Report. *J Neurosurg* **2019**, *46*, E11, doi:10.3171/2019.3.FOCUS1948.
226. Frade Porto, N.; Delgado Fernández, J.; García Pallero, M. de los Á.; Penanes Cuesta, J.R.; Pulido Rivas, P.; Gil Simoes, R. Subcutaneous Tissue Metastasis from Glioblastoma Multiforme: A Case Report and Review of the Literature. *Neurocirugia* **2019**, *30*, 149–154, doi:10.1016/J.NEUCIR.2018.03.005.
227. Liu, J.; Shen, L.; Tang, G.; Tang, S.; Kuang, W.; Li, H.; Tian, Y.; Zhou, Q. Multiple Extracranial Metastases from Glioblastoma Multiforme: A Case and Literature Review. *J Int Med Res* **2020**, *48*, 1–10, doi:10.1177/0300060520930459.
228. Wu, J.Y.; Li, Y.J.; Hu, X. Bin; Huang, S.; Xiang, D.X. Preservation of Small Extracellular Vesicles for Functional Analysis and Therapeutic Applications: A Comparative Evaluation of Storage Conditions. *Drug Deliv* **2021**, *28*, 162–170, doi:10.1080/10717544.2020.1869866/SUPPL_FILE/IDRD_A_1869866_SM9282.DOCX.
229. Cheruvanky, A.; Zhou, H.; Pisitkun, T.; Kopp, J.B.; Knepper, M.A.; Yuen, P.S.T.; Star, R.A. Rapid Isolation of Urinary Exosomal Biomarkers Using a Nanomembrane Ultrafiltration Concentrator. *Am J Physiol Renal Physiol* **2007**, *292*, F1657, doi:10.1152/AJPRENAL.00434.2006.
230. Maroto, R.; Zhao, Y.; Jamaluddin, M.; Popov, V.L.; Wang, H.; Kalubowilage, M.; Zhang, Y.; Luisi, J.; Sun, H.; Culbertson, C.T.; et al. Impact of Storage Conditions on EV Integrity/Surface Markers and Cargos. *Life* **2022**, *12*, 697, doi:10.3390/LIFE12050697.
231. Yuan, F.; Li, Y.M.; Wang, Z. Preserving Extracellular Vesicles for Biomedical Applications: Consideration of Storage Stability before and after Isolation. *Drug Deliv* **2021**, *28*, 1501–1509, doi:10.1080/10717544.2021.1951896.
232. Sase, T.; Arito, M.; Onodera, H.; Omoteyama, K.; Kurokawa, M.S.; Kagami, Y.; Ishigami, A.; Tanaka, Y.; Kato, T. Hypoxia-Induced Production of Peptidylarginine Deiminases and Citrullinated Proteins in Malignant Glioma Cells. *Biochem Biophys Res Commun* **2017**, *482*, 50–56, doi:10.1016/J.BBRC.2016.10.154.

233. Hollstein, M.; Sidransky, D.; Vogelstein, B.; Harris, C.C. P53 Mutations in Human Cancers. *Science (1979)* **1991**, *253*, 49–53, doi:10.1126/SCIENCE.1905840.
234. Moshkovich, N.; Ochoa, H.J.; Tang, B.; Yang, H.H.; Yang, Y.; Huang, J.; Lee, M.P.; Wakefield, L.M. Peptidylarginine Deiminase IV Regulates Breast Cancer Stem Cells via a Novel Tumor Cell-Autonomous Suppressor Role. *Cancer Res* **2020**, *80*, 2125–2137, doi:10.1158/0008-5472.CAN-19-3018.
235. Neira, J.L.; Rizzuti, B.; Abián, O.; Araujo-Abad, S.; Velázquez-Campoy, A.; de Juan Romero, C. Human Enzyme PADI4 Binds to the Nuclear Carrier Importin A3. *Cells* **2022**, *11*, 2166, doi:10.3390/CELLS11142166.
236. Santofimia-Castaño, P.; Rizzuti, B.; Pey, A.L.; Fárez-Vidal, M.E.; Iovanna, J.L.; Neira, J.L. Intrinsically Disordered Protein NUPR1 Binds to the Armadillo-Repeat Domain of Plakophilin 1. *Int J Biol Macromol* **2021**, *170*, 549–560, doi:10.1016/J.IJBIOMAC.2020.12.193.
237. Santofimia-Castaño, P.; Rizzuti, B.; Pey, Á.L.; Soubeyran, P.; Vidal, M.; Urrutia, R.; Iovanna, J.L.; Neira, J.L. Intrinsically Disordered Chromatin Protein NUPR1 Binds to the C-Terminal Region of Polycomb RING1B. *Proceedings of the National Academy of Sciences* **2017**, *114*, E6332–E6341, doi:10.1073/PNAS.1619932114.
238. Murphy, A.; Costa, M. Nuclear Protein 1 Imparts Oncogenic Potential and Chemotherapeutic Resistance in Cancer. *Cancer Lett* **2020**, *494*, 132–141, doi:10.1016/J.CANLET.2020.08.019.
239. Liu, S.; Costa, M. The Role of NUPR1 in Response to Stress and Cancer Development. *Toxicol Appl Pharmacol* **2022**, *454*, 116244, doi:10.1016/J.TAAP.2022.116244.
240. Malicet, C.; Lesavre, N.; Vasseur, S.; Iovanna, J.L. P8 Inhibits the Growth of Human Pancreatic Cancer Cells and Its Expression Is Induced through Pathways Involved in Growth Inhibition and Repressed by Factors Promoting Cell Growth. *Mol Cancer* **2003**, *2*, 37, doi:10.1186/1476-4598-2-37.
241. Jiang, W.G.; Davies, G.; Martin, T.A.; Kynaston, H.; Mason, M.D.; Fodstad, O. Com-1/P8 Acts as a Putative Tumour Suppressor in Prostate Cancer. *Int J Mol Med* **2006**, *18*, 981–986, doi:10.3892/IJMM.18.5.981/HTML.
242. Hernández-Vega, A.M.; Camacho-Arroyo, I. Crosstalk between 17β-Estradiol and TGF-β Signaling Modulates Glioblastoma Progression. *Brain Sciences* **2021**, *11*, 564, doi:10.3390/BRAINSCI11050564.
243. van Dieck, J.; Lum, J.K.; Teufel, D.P.; Fersht, A.R. S100 Proteins Interact with the N-Terminal Domain of MDM2. *FEBS Lett* **2010**, *584*, 3269–3274, doi:10.1016/J.FEBSLET.2010.06.024.
244. Neira, J.L.; Díaz-García, C.; Prieto, M.; Coutinho, A. The C-Terminal SAM Domain of P73 Binds to the N Terminus of MDM2. *Biochim Biophys Acta Gen Subj* **2019**, *1863*, 760–770, doi:10.1016/J.BBAGEN.2019.01.019.
245. Sato, A.; Sunayama, J.; Matsuda, K.I.; Seino, S.; Suzuki, K.; Watanabe, E.; Tachibana, K.; Tomiyama, A.; Kayama, T.; Kitanaka, C. MEK-ERK Signaling Dictates DNA-Repair Gene MGMT Expression and Temozolomide Resistance of Stem-like Glioblastoma Cells via the MDM2-P53 Axis. *Stem Cells* **2011**, *29*, 1942–1951, doi:10.1002/STEM.753.
246. Wang, L.; Song, G.; Zhang, X.; Feng, T.; Pan, J.; Chen, W.; Yang, M.; Bai, X.; Pang, Y.; Yu, J.; et al. PADI2-Mediated Citrullination Promotes Prostate Cancer Progression. *Cancer Res* **2017**, *77*, 5755–5768, doi:10.1158/0008-5472.CAN-17-0150.
247. Chakravarty, M.; Ganguli, P.; Murahari, M.; Sarkar, R.R.; Peters, G.J.; Mayur, Y.C. Study of Combinatorial Drug Synergy of Novel Acridone Derivatives With Temozolomide Using In-Silico and in-Vitro Methods in the Treatment of Drug-Resistant Glioma. *Front Oncol* **2021**, *11*, doi:10.3389/FONC.2021.625899.

APPENDIX

Research Paper

The armadillo-repeat domain of Plakophilin 1 binds to human enzyme PADI4

José L. Neira [a,b,**], Bruno Rizzuti [b,c], Salome Araujo-Abad [a,d], Olga Abian [b,e,f,g],
María Esther Fárez-Vidal [h,i,j], Adrian Velazquez-Campoy [b,e,f,g], Camino de Juan Romero [a,k,*]

[a] IDIBE, Universidad Miguel Hernández, 03202 Elche (Alicante), Spain
[b] Institute of Biocomputation and Physics of Complex Systems – Joint Unit GBsC-CSIC-BIFI, Universidad de Zaragoza, 50018 Zaragoza, Spain
[c] CNR-NANOTEC, SS Rende (CS), Department of Physics, University of Calabria, 87036 Rende, Italy
[d] Centro de Biotecnología, Universidad Nacional de Loja, Avda. Pío Jaramillo Alvarado s/n, Loja, 110111 Loja, Ecuador
[e] Instituto de Investigación Sanitaria Aragón (IIS Aragón), Zaragoza, Spain
[f] Centro de Investigación Biomédica en Red en el Área Temática de Enfermedades Hepáticas y Digestivas (CIBERehd), 28029 Madrid, Spain
[g] Departamento de Bioquímica y Biología Molecular y Celular, Universidad de Zaragoza, 50009 Zaragoza, Spain
[h] Departamento de Bioquímica y Biología Molecular III e Inmunología, Facultad de Medicina, Universidad de Granada, 18016 Granada, Spain
[i] Instituto de Investigación Biomédica IBS, Granada, Spain
[j] Complejo Hospitalario Universitario de Granada, Universidad de Granada, 18071 Granada, Spain
[k] Unidad de Investigación, Fundación para el Fomento de la Investigación Sanitaria y Biomédica de la Comunidad Valenciana (FISABIO), Hospital General Universitario de Elche, Camí de l'Almazara 11, 03203 Elche (Alicante), Spain

---

ARTICLE INFO

Keywords:
PADI4
Protein-protein interactions
Isothermal titration calorimetry
Molecular dynamics

ABSTRACT

Plakophilin 1 (PKP1), a member of the armadillo repeat family of proteins, is a key structural component of cell-cell adhesion scaffolds, although it can also be found in other cell locations, including the cytoplasm and the nucleus. PADI4 (peptidyl-arginine deiminase 4) is one of the human isoforms of a family of enzymes engaged in the conversion of arginine to citrulline, and is present in monocytes, macrophages, granulocytes, and in several types of cancer cells. It is the only family member observed both within the nucleus and the cytoplasm under ordinary conditions. We studied the binding of the armadillo domain of PKP1 (ARM-PKP1) with PADI4, by using several biophysical methods, namely fluorescence, far-ultraviolet (far-UV) circular dichroism (CD), isothermal titration calorimetry (ITC), and molecular simulations; furthermore, binding was also tested by Western-blot (WB) analyses. Our results show that there was binding between the two proteins, with a dissociation constant in the low micromolar range (~ 1 μM). Molecular modelling provided additional information on the possible structure of the binding complex, and especially on the binding hot-spot predicted for PADI4. This is the first time that the interaction between these two proteins has been described and studied. Our findings could be of importance to understand the development of tumors, where PKP1 and PADI4 are involved. Moreover, our findings pave the way to describe the formation of neutrophil extracellular traps (NETs), whose construction is modulated by PADI4, and which mediate the proteolysis of cell-cell junctions where PKP1 intervenes.

1. Introduction

Peptidyl-arginine deiminases (PADI, EC 3.5.3.15) are enzymes catalyzing citrullination, that is the conversion of arginine residues to citrulline ones, in the presence of Ca(II). This post-translational modification (PTM) is permanent, unless the protein is degraded. PADIs have

---

Abbreviations: ARM, armadillo; ARM-PKP1, ARM-domain of PKP1 (residues 237–704 of the intact PKP1 protein); CD, circular dichroism; Impα3, human importin α3 isoform (residues 1–521); ITC, isothermal titration calorimetry; MD, molecular dynamics; NET, neutrophil extracellular trap; PADI, peptidyl-arginine deiminase or L-arginine iminohydrolase protein; PBS, phosphate buffer solution; PDB, Protein Data Bank; PKP, plakophilin; PKP1, plakophilin 1; PPI, protein-protein interaction; PTM, post-translational modification; UV, ultraviolet; WB, Western Blot.

* Corresponding author at: Unidad de Investigación, Fundación para el Fomento de la Investigación Sanitaria y Biomédica de la Comunidad Valenciana (FISABIO), Hospital General Universitario de Elche, Camí de l'Almazara 11, 03203 Elche (Alicante), Spain.

** Corresponding author at: IDIBE, Edificio Torregaitán, Universidad Miguel Hernández, Avda. del Ferrocarril s/n, 03202 Elche (Alicante), Spain.

E-mail addresses: jlneira@umh.es (J.L. Neira), m.juan@umh.es (C. de Juan Romero).

Received 11 July 2022; Received in revised form 10 October 2022; Accepted 31 October 2022

crucial roles in nerve growth, embryo development, trauma apoptosis, beginning of inflammation states, aging of tissues, epithelial terminal differentiation and transcriptional regulation of gene expression and regulation [1–8]. There are five human genes encoding PADI isoforms: PADI1, PADI2, PADI3, PADI4 and PADI6 [9–14]. Each enzyme has a pattern of expression depending on the cell and tissue, cell differentiation stage, and the physiological or pathological conditions. For instance, PADI4 is usually located in cytoplasmic granules of inflammatory cells (eosinophil, neutrophils and macrophages), mammary gland cells, stem cells, and several tumor tissues (among them, squamous cell carcinoma, pancreatic adenocarcinoma, breast cancer and lung cancer), or metastasis processes [15–18]. In addition, PADI4 is the sole isoenzyme also found in the nucleus under non-stress conditions. An increase of the enzymatic activity is also observed for several PADI4 haplotype mutants during the apoptosis occurring *via* the mitochondrial pathway [16]. Furthermore, PADI4 is involved in the p53-gene expression, and that of other p53 target-genes [15,19,20]. We have recently shown that PADI4 is a dimeric protein expressed in glioblastoma, pancreatic adenocarcinoma and colon cancer [21], and that it binds to importin α3 (Impα3), a member of the armadillo (ARM) repeat-containing family of proteins, to allow its translocation into the cell nucleus [22]. In general, the ARM motif is a 40-residue-long structure formed by a bundle of α-helices, involved in protein-protein interactions (PPIs) [23].

Proteins of the ARM repeat-containing family are also present at cell junctions. Plakophilins (PKPs) belong to such family, and they are located at cell borders in desmosomal structures [24]. PKPs are ubiquitously found in the cytoplasm and nucleus of several kinds of cells [25–27], where they intervene in signaling networks within distinct cellular compartments. There are four PKP-family members: PKP1, PKP2, PKP3 and PKP4 [24]. PKP1 acts as a modulator of mRNA translation and post-transcriptional gene expression [25,28], and it is more largely expressed in the supra-basal layers of stratified and complex epithelia [29–31]. This protein has been proposed as a valuable diagnostic biomarker, as well as a potential therapeutic target in the squamous cell carcinoma of lung [28,32–34]. The structure of the armadillo repeat domain of PKP1 (ARM-PKP1) has been solved by X-ray; it contains nine ARM motifs, and includes a large basic patch on the inner protein surface that may serve as a binding site region for its partners [35–37]. The ARM-PKP1 scaffolding is structurally identical to that observed in proteins involved in nuclear translocation (*i.e.*, the importins). We have previously shown that isolated ARM-PKP1 is a monomer in solution and it has a low conformational stability [38]. Furthermore, it interacts with another all α-helical protein, the SAM domain of p73 [39], and with an intrinsically disordered protein, NUPR1, involved in the development of pancreatic cancer [40]. Molecular simulations have allowed us to clarify at the atomic detail some key aspects in the binding of ARM-PKP1 with these proteins [39,40], as well as the dynamics and stability of PADI4 in isolation [21] and in the interaction with Impα3 [22]. Because of the binding between PADI4 and Impα3 [22], we hypothesized, based as well on their cellular localization, that PADI4 would also be capable of binding to ARM-PKP1.

In this work, we provided evidence for the binding between ARM-PKP1 and PADI4 by using biophysical and molecular biology techniques, as well as molecular simulations. All these methods provided evidence for the binding between the two proteins. The affinity of the complex was moderate ($K_d \sim 1$ μM), as measured by ITC, and it was slightly less favorable as measured by fluorescence ($K_d \sim 8$ μM). Molecular simulations confirmed as reasonable the assumption that the binding region of ARM-PKP1 was located along its basic surface patch, and predicted that the association to PADI4 was driven by a combination of electrostatic and hydrophobic interactions. As both proteins are involved in the development of several types of tumors, our findings could be of importance to understand their progress in cells.

2. Materials and methods

2.1. Materials

Imidazole, Trizma base and acid, DNase, SIGMAFAST protease tablets, NaCl, Ni^{2+}-resin, anti-PKP1 antibody and ultra-pure dioxane were from Sigma (Madrid, Spain). Isopropyl-β-D-1-thiogalactopyranoside and ampicillin were obtained from Apollo Scientific (Stockport, UK). Dialysis tubing with a molecular weight cut-off of 3500 Da, Triton X-100, TCEP (tris(2-carboxyethyl)phosphine) and the SDS protein marker (PAGEmark Tricolor) were from VWR (Barcelona, Spain). Amicon centrifugal devices with a molecular weight cut-off of 30 kDa were from Millipore (Barcelona, Spain). The rest of the used materials were of analytical grade. Water was deionized and purified on a Millipore system.

2.2. Protein expression and purification

PADI4 and ARM-PKP1 were purified as previously described [21,38]. Protein concentrations were determined by UV absorbance, employing an extinction coefficient at 280 nm estimated from the number of tyrosines and tryptophans in each protein [41].

2.3. Fluorescence

2.3.1. Steady-state fluorescence

A Cary Varian spectrofluorometer (Agilent, Santa Clara, CA, USA), interfaced with a Peltier unit, was used to collect fluorescence spectra at 25 °C, by excitation at either 280 or 295 nm. The other experimental parameters have been described elsewhere [42]. Appropriate blank corrections were made in all spectra. Following the standard protocols used in our laboratories, the samples were prepared the day before and left overnight at 5 °C; before experiments, samples were left for 1 h at 25 °C. A 1-cm-pathlength quartz cell (Hellma, Kruibeke, Belgium) was used. Concentration of PADI4 was 2.5 μM and that of ARM-PKP1 was 8 μM. Experiments were performed in 20 mM Tris buffer (pH 7.5), 5 mM TCEP, 150 mM NaCl and 5% glycerol, in triplicates with newly prepared samples. Variations of results among the experiments were lower than 5%.

2.3.2. Binding experiments with PADI4

For the titration of ARM-PKP1 with PADI4, increasing amounts of monomeric ARM-PKP1 species, in the concentration range 0–20 μM, were added to a solution with a fixed concentration of PADI4 (2 μM, in protomer units). Experiments were carried out in the buffer described above. The experimental set-up was the same described above. In all cases, the appropriate blank-corrections with solutions containing only the corresponding amount of ARM-PKP1 were applied. Spectra were corrected for inner-filter effects [43]. The titration was repeated three times, using new samples. In the three cases, the variations in the results were lower than 10%.

The dissociation constant of the complex, K_d, was calculated by fitting the binding isotherm obtained by plotting the observed fluorescence change as a function of ARM-PKP1 concentration to a general binding model, explicitly considering ligand depletion [44,45]:

$$F = F_0 + \frac{\Delta F_{max}}{2[PADI4]_T}\left([ARM - PKP1]_T + [PADI4]_T + K_d\right) - \sqrt{\left(\left([ARM - PKP1]_T + [PADI4]_T + K_d\right)^2 - 4[ARM - PKP1]_T[PADI4]_T\right)} \qquad (1)$$

where F is the measured fluorescence of the solution with the fixed PADI4 concentration (2 μM, in protomer units) and a particular ARM-PKP1 one, after subtraction of the corresponding blank with the same concentration of ARM-PKP1; $\Delta F_{\max}$ is the largest change in the fluorescence of ARM-PKP1 when all polypeptide molecules were forming the complex, compared to the fluorescence of each isolated chain; F_0 is the fluorescence intensity when no ARM-PKP1 was added; $[\mathrm{PADI4}]_\mathrm{T}$ is the constant, total concentration of PADI4 (2 μM, in protomer units); and $[\mathrm{ARM\text{-}PKP1}]_\mathrm{T}$ is that of ARM-PKP1, which was varied during the titration. Fitting to the above equation was carried out by using KaleidaGraph (Synergy software, Reading, PA, USA).

2.4. Circular dichroism (CD)

Far-UV CD spectra were collected on a Jasco J810 spectropolarimeter (Jasco, Tokyo, Japan) with a thermostated cell holder and interfaced with a Peltier unit. The instrument was periodically calibrated with (+)-10-camphorsulfonic acid. A 0.1-cm path length cell was used (Hellma, Kruibeke, Belgium). All spectra were corrected by subtracting the corresponding baseline. Concentration of each polypeptide (ARM-PKP1 or PADI4) and the buffers were the same used for fluorescence experiments (Section 2.3). Samples were prepared the day before and left overnight at 5 °C to allow them to equilibrate. Before starting the experiments, samples were further left for 1 h at 25 °C.

Isothermal wavelength spectra of each isolated macromolecule and those of the complex were acquired as an average of 6 scans, at a scan speed of 50 nm/min, with a response time of 2 s and a band-width of 1 nm.

2.5. Isothermal titration calorimetry (ITC)

Calorimetric titrations for testing the interaction of ARM-PKP1 with PADI4 were carried out in an Auto-iTC200 automated high-sensitivity calorimeter (MicroCal, Malvern-Panalytical, Malvern, UK). Experiments were performed at 25 °C in 20 mM Tris buffer (pH 7.5), 5 mM TCEP, 150 mM NaCl and 5% glycerol at 25 °C. PADI4 (100 μM) in the injection syringe was titrated into the ARM-PKP1 solution (10 μM) in the calorimetric cell. A series of 19 injections with 2 μL volume, 0.5 μL/s injection speed, and 150 s time spacing was programmed while maintaining a reference power of 10 μcal/s and a stirring speed of 750 rpm. The heat effect per injection was calculated by integration of the thermal power raw data after baseline correction, and the interaction isotherm (ligand-normalized heat effect *per* injection as a function of the molar ratio) was analyzed by non-linear least squares regression data analysis, applying a model that considers a single binding site to estimate the association constant, K_a, the interaction enthalpy, ΔH, and the stoichiometry of binding, n (although, in practice, the last parameter usually reports the fraction of active protein in the cell/syringe). The background injection heat (usually called “dilution heat”, but reflecting any unspecific phenomenon such as solute dilution, buffer neutralization, temperature equilibration, or solution mechanical mixing) was accounted for by including an adjustable constant parameter in the fit. Due to the presence of glycerol in solution, its value was rather large. The data analysis was conducted in Origin 7.0 (OriginLab, Northampton, MA, USA) with user-defined fitting functions.

2.6. Molecular modelling

The structure of ARM-PKP1 was built based on the crystallographic structure [37] deposited on the Protein Data Bank (PDB) and containing residues 244–700 (PDB ID: 1XM9). Following the protocol adopted in our previous works [39,40], two missing loops were reconstructed *in silico*, whereas the two small portions missing at both termini, compared to the protein construct used in our experimental measurements (which encompasses residues 237–704 of the intact protein), were not included. Similarly, PADI4 was built starting from the X-ray diffraction structure (PDB ID: 3APN) that reports the homodimeric protein one [46], and missing loops were reconstructed as previously described [21].

Protein-protein docking simulations were performed by using the web server ClusPro [47] version 2.0, with default options. This algorithm performs rigid body docking with an extensive sampling ($> 10^9$ structures), followed by clustering of a restricted number of conformations (~ 1000) having the most favorable score, and energy minimization to remove steric clashes up to yield the final set of selected predictions [48]. The best docking poses of ARM-PKP1, which were obtained by assuming an electrostatic-favored binding on the surface of PADI4, were subsequently refined in molecular simulations under full hydration conditions.

2.7. Molecular dynamics (MD) simulation

MD simulations were performed by using the simulation package GROMACS [49]. The force field Amber ff99SB-ILDN force field [50] was used, in combination with the water model TIP3P [51]. The two proteins, either in complex or each in the unbound state, were placed in a rhombic dodecahedron box minimum distance of 1 nm from any edge, and periodic boundary conditions were applied. Due to the different net charge of the two proteins, the systems were neutralized by adding either Na^+ (10 ions for the complex of PADI4 with two bound ARM-PKP1 monomers, and 14 for PADI4 alone) or Cl^- counterions (2 ions for ARM-PKP1 alone).

The protocol followed for the MD runs was the same we previously adopted for simulating ARM-PKP1 in complex with another protein [39], and PADI4 alone [21]. Preparation of the system was standard [[52,53], and included energy minimization, annealing, equilibration, and data production at isobaric-isothermal conditions for 20 ns. A Parrinello-Rahman [54] and Bussi-Donadio-Parrinello [55] coupling was adopted to control pressure and temperature, respectively. Electrostatic interactions were calculated by using a Particle Mesh Ewald scheme [56], and van der Waals interactions were truncated by using a Verlet scheme with a cut-off of 1 nm. Constraints were applied to hydrogen atoms by using the LINCS algorithm [57], allowing a time step of 2 fs in the integration of the equations of motion.

In the data analysis, atomic deviations and fluctuations of protein residues were calculated after removing the roto-translation motions through a least square fit on the C^α atoms of the starting structure.

2.8. Western blot (WB)

Different concentration rates of PADI4 and ARM-PKP1 (3:1,2:1,1:1,1:2, 1:3) in a total volume of 18 μL were mixed with 5 μL of NuPAGE® (Invitrogen, Barcelona, Spain). The components of the mixtures were separated by SDS-PAGE using gels at 10% acrylamide concentration into a Nitrocellulose membrane (Bio-Rad Laboratories Inc., California, USA). The membranes were incubated for 2 days with 1 μM of ARM-PKP1, then washed 3 times for 7 min with 1× PBS 0.1% Tween20 buffer, blocked for 1 h with 5% (*w/v*) milk in 1× PBS 0.1% Tween20 buffer, and finally incubated overnight at 4 °C with primary antibody: anti-PKP1 (rabbit, 1:6000; Sigma-Aldrich, Madrid, Spain), followed by a 1 h incubation at room temperature with ECL™ anti-rabbit IgG, Horseradish Peroxidase linker (GE Healthcare, UK). The membranes were visualized with ECL™ Prime Western blotting detection reagent (Amersham™, Barcelona, Spain) in a ChemiDoc Bio-Rad instrument.

3. Results

3.1. PADI4 was observed to bind PKP1

To test whether PADI4 interacted with ARM-PKP1 *in vitro*, we followed a three-part experimental approach. First, we used steady-state fluorescence and CD, as spectroscopic techniques capable of detecting a possible binding and concomitant conformational changes in the macromolecules; second, we used WB analyses to confirm the PPI; and finally, we used fluorescence and ITC to quantitatively measure the thermodynamic parameters of such binding.

We used fluorescence to determine whether there was a change in: (i) the value of the maximum wavelength in the emission spectrum; (ii) the fluorescence intensity observed at that maximum wavelength; or (iii) both the physical parameters, when the spectrum of the complex was compared to that obtained from the addition of those of the two isolated proteins. A variation in fluorescence intensity by excitation at 280 nm was observed when the complex of PADI4 with ARM-PKP1 was formed (Fig. 1 A), but there were no changes in the maximum wavelength of the spectrum; similar variations were observed by excitation at 295 nm.

Next, we carried out far-UV CD measurements, with the aim of further supporting the results obtained by fluorescence. The far-UV addition spectrum was slightly different from that of the complex (Fig. 1 B). The small differences could be either attributed to a relatively large number of aromatic residues involved in the binding or, less likely, to changes in the secondary structure of PADI4 and/or in that of ARM-PKP1 when the two proteins were bound.

To further confirm the binding of ARM-PKP1 to PADI4, we performed a series of *in vitro* experiments by using WB, to detect PPIs with the recombinant, purified proteins. We used a mixture of PADI4 and ARM-PKP1 in a gel, by testing several concentration rates (PADI4/ARM-PKP1 3:1, 2:1, 1:1, 1:2, and 1:3) that correspond to values in the range between 20 and 6 μM, considering PADI4 as the prey protein. The two proteins in the SDS gels were transferred to a nitrocellulose membrane and incubated for 2 days with ARM-PKP1 as bait protein. Finally, we washed and revealed the membrane with an antibody against ARM-PKP1. The results showed an increase in the signal of ARM-PKP1 (MW ~ 52 kDa) binding to PADI4 (MW ~ 74 kDa) according to the size and amount of loaded protein (Fig. 2). The Ponceau staining showed two bands corresponding to the isolated proteins, with molecular weights slightly lower than expected (Fig. 2 top), and a faint band at ~120 kDa at the two highest concentration rates (PADI4/ARM-PKP1 3:1 and 1:3). On the other hand (Fig. 2 bottom), we could detect in the WB analyses the bait protein (ARM-PKP1) on two spots, when: (i) the complex was formed (at ~120 kDa, visible as a wide band at the PADI4/ARM-PKP1 1:3 concentration, the highest explored); and (ii) the isolated ARM-PKP1 was present (at any of the PADI4/ARM-PKP1 concentration rates).

Finally, we carried out titrations to quantitatively measure the binding affinity of the two proteins, by keeping constant the concentration of PADI4 and increasing the concentration of ARM-PKP1. The results indicate (Fig. 3 A) that the K_d was 8.0 ± 2 μM. We also used ITC to determine the thermodynamic binding parameters (Fig. 3 B). The interaction was markedly exothermic (that is, had a favorable enthalpic contribution and unfavorable entropic contribution to the Gibbs energy of binding), with $\Delta H = -36$ kcal mol^{-1}, and the K_d was 1.4 ± 0.2 μM, which was lower than that obtained by fluorescence. The stoichiometry of the reaction was 1:1, indicating that the dimer of PADI4 had a tendency to coordinate two molecules of ARM-PKP1.

To sum up, we conclude that there was evidence that PADI4 could bind to ARM-PKP1; however, we cannot rule out that a more complex interaction may be taking place *in vivo,* where other molecular partners could also be involved.

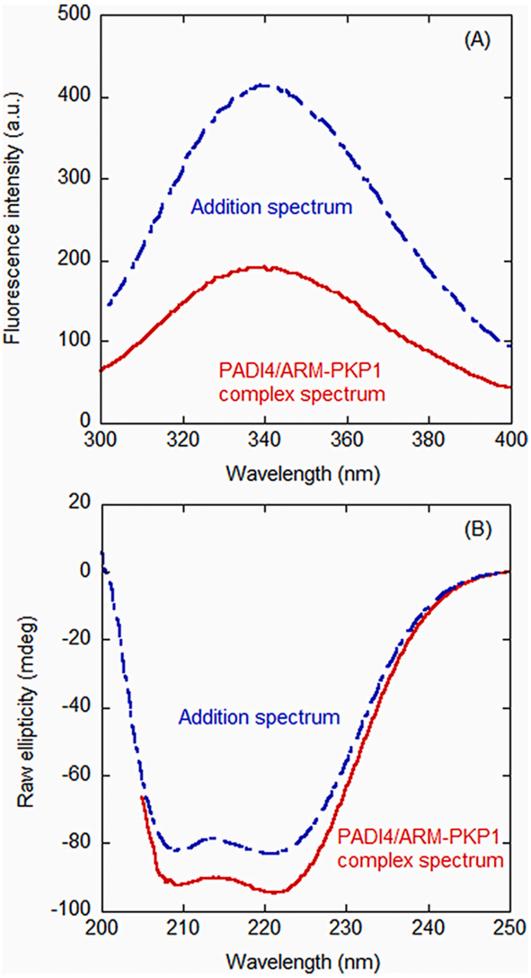

Fig. 1. Binding of ARM-PKP1 to PADI4 as monitored by spectroscopic techniques: (A) Fluorescence spectrum obtained by excitation at 280 nm of the PADI4/ARM-PKP1 complex, and addition spectrum obtained by the sum of the spectra of the two isolated macromolecules. (B) Far-UV CD spectrum of the PADI4/ARM-PKP1 complex, and addition spectrum obtained by the sum of the spectra of the two isolated macromolecules. All experiments were performed at 25 °C.

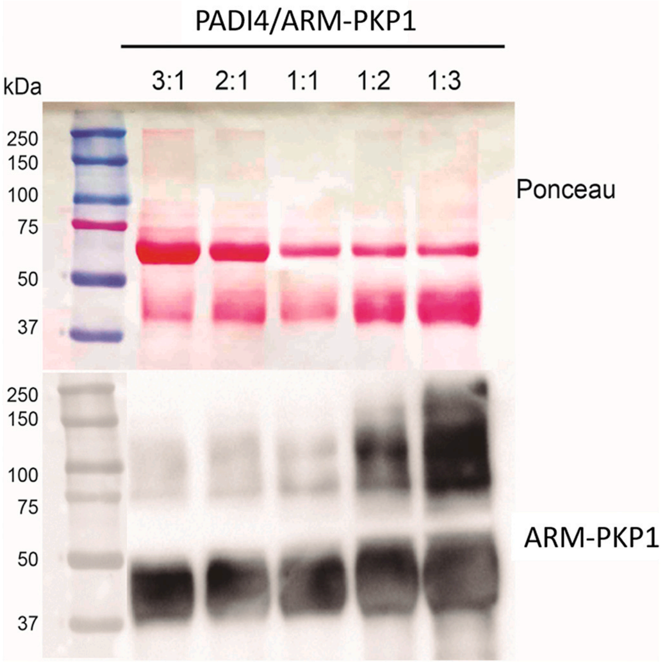

Fig. 2. Binding of ARM-PKP1 to PADI4 as monitored by Western blot analyses: (Top) Polyacrylamide gels were loaded with several concentrations of PADI4 as visualized with Ponceau staining. (Bottom) Nitrocellulose membranes incubated with ARM-PKP1, washed and revealed with the corresponding antibody against such protein.

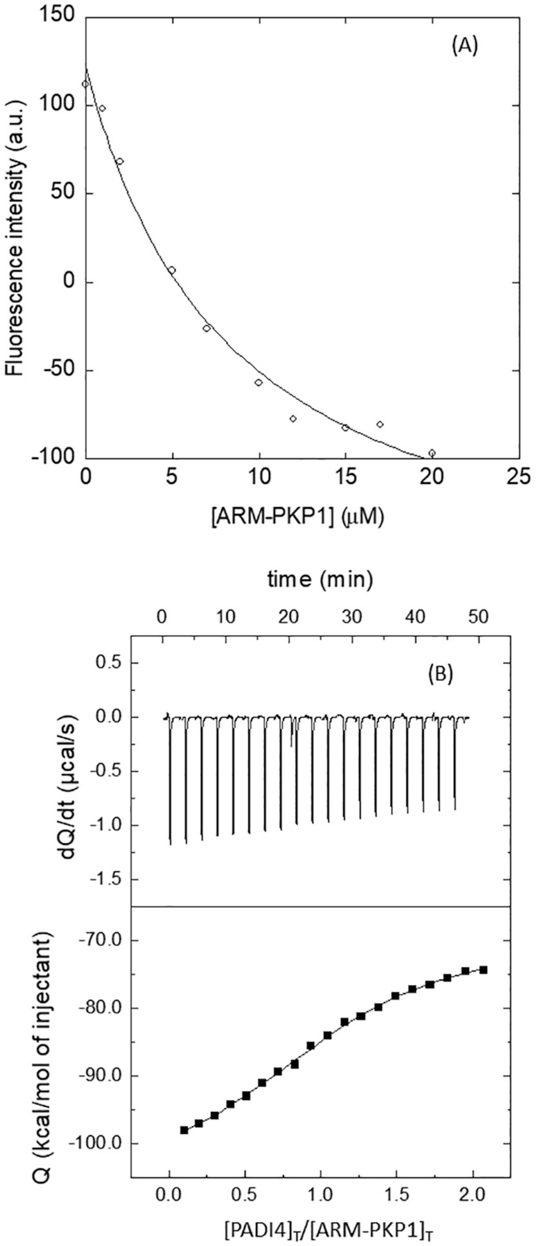

Fig. 3. Binding of ARM-PKP1 to PADI4 as monitored by biophysical techniques: (A) Titration curve monitoring the changes in the fluorescence at 315 nm when ARM-PKP1 was added to PADI4. The fluorescence intensity is the relative signal after removal of the corresponding blank. The line through the data is the fitting to Eq. (1). (B) Calorimetric titrations for the PADI4 binding to ARM-PKP1. Upper panels show the thermograms (thermal power as a function of time) and lower panels show the binding isotherms (ligand-normalized heat effects per injection as a function of the molar ratio in the calorimetric cell). Continuous lines correspond to the fitting curves according to an interaction model with a single ligand binding site. All experiments were carried out at 25 °C.

3.2. Structural prediction of the complex PADI4/ARM-PKP1

Molecular simulations were performed to obtain further details on the interaction between PADI4 and ARM-PKP1 at the atomic level. Due to the large size of both molecules (PADI4 is a homodimer with 663 residues for each monomer, for a total of 1326 residues; whereas ARM-PKP1 has 468 residues, which were slightly reduced to 457 in the construct used in our simulations, encompassing residues 244–700 of the intact protein), protein-protein docking was selected as the most accurate theoretical methodology currently available for providing a prediction of the binding complex [58].

Several tools are available to this aim, including a few online prediction servers [47,59,60]. Even for a large complex, such as that between PADI4 and ARM-PKP1, these algorithms probe a high number of potential conformations and may suggest a wide range of possibilities (up to ~100 candidate poses ranked) that need to be subsequently screened by using some reasonable criteria. We based our selection in a simple, but strict assumption: the interface of the two proteins in the complex should include the well-known binding site of ARM-PKP1, which is located within the innermost surface in the sagittal plane of this protein [37,38]. This condition indirectly implies that electrostatic interactions should be one of the main driving forces in the binding, because the hot-spot of ARM-PKP1 consists of a large patch of basic residues [37]. Our experimental findings are in line with such assumption, not only since PADI4 is an acidic protein, but also because this explains in a rather straightforward way the large favorable enthalpic contribution that dominates the Gibbs energy of binding of the complex, as obtained by ITC measurements.

Based on these preliminary considerations, we selected the protein-protein docking algorithm ClusPro as our best choice [47,48], over other available docking programs we had tested such as HDOCK [59] and ZDOCK [60]. In fact, ClusPro algorithm provides different alternatives for the docking of two proteins, depending on the prior knowledge of the forces that are expected to drive the formation of the complex, and includes a so-called ‘electrostatic-favored’ option. The results obtained by using ClusPro are shown in Fig. 4. Although this represents the best prediction obtained based on the above mentioned ‘electrostatic-favored’ option, it is worth to point out that we do not consider this outcome to be biased, for several reasons. First, this was the sole prediction satisfying our assumption on the involvement of the binding site of ARM-PKP1 that could be obtained by using any of the available choices on the force expected to drive the binding, and not only the ‘electrostatic-favored’ one. Second, it was found in a blind docking experiment, although in principle ClusPro also provides other options [47] to influence the results by indicating specific residues that are more likely to be involved in the binding – or, in contrast, that have a propensity to remain accessible to the solvent. And third, the results obtained actually correspond to the first two most favorable docking poses obtained for ARM-PKP1 interacting with the host surface; thus, they correctly reproduce the expected stoichiometry (two ARM-PKP1 monomers *per* PADI4 dimer) and symmetry (the binding poses on the two chains of PADI4 are almost identical, despite the intrinsic randomness in the search process leading to each distinct docking pose), again without the need to introduce any specific bias.

We also performed a detailed analysis of the binding interface of the two proteins in the complex (Table 1), with a special focus on the hot-spot region of PADI4 – since the one of ARM-PKP1 was already assumed to be its basic binding patch, by our assumption above. We discovered that the main binding region of PADI4 is located in the small and partly-structured subdomain 313–347 [46], which slightly protrudes from its surface. This interacting region possesses a high number of acidic residues, and therefore has a strong Coulombic interaction with the innermost region of ARM-PKP1. The interface of PADI4 also includes the adjacent and almost unstructured region 375–392, as well as the more peripheral region encompassing residues 155–176. We observed a patch of four solvent-exposed phenylalanine residues (Phe314, Phe319, Phe379, and Phe389) on the surface of PADI4 that play an important support role in the binding, by forming close hydrophobic contacts (< 5 Å) with aromatic residues of ARM-PKP1. In contrast, the region 155–176 of PADI4 provides an anchoring for the binding that is essentially electrostatic, due to the large number of acidic residues therein included, and with little non-polar interactions. Overall, the large number of aromatic residues involved in the binding interface (thirteen aromatic residues in the contact interface are within a reciprocal distance of 7.5 Å) could contribute to explain the variations that we

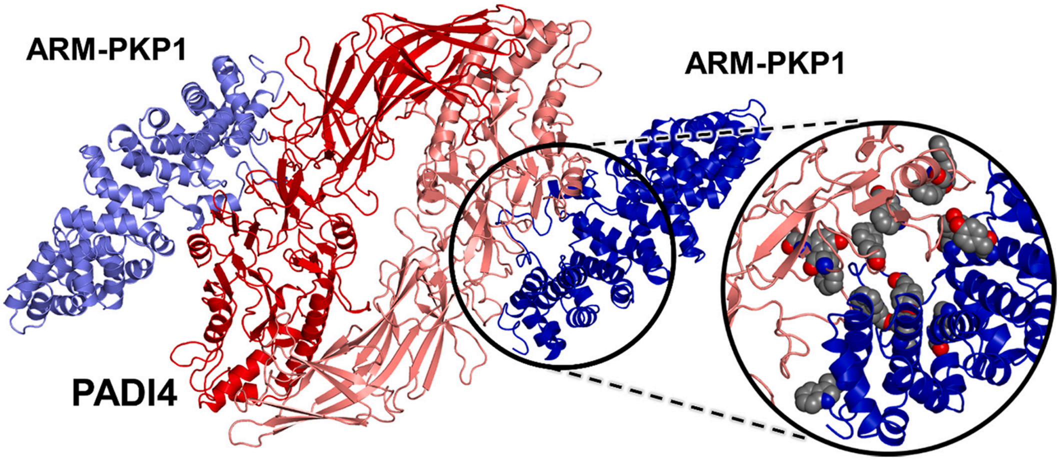

Fig. 4. Modelling of the binding complex of PADI4 and ARM-PKP1. Prediction based on the docking algorithm ClusPro [47], by assuming that the main binding region of ARM-PKP1 with molecular partners, formed by a patch of basic residues, is the hot-spot interface with PADI4 – or, equivalently, that the binding is electrostatic-favored. The bound monomers of ARM-PKP1 are the two most favorable docking poses. (Inset) Aromatic residues at the binding interface of the two proteins, shown in all-atom van der Waals representation.

Table 1
Hot-spot regions of PADI4 in the binding with ARM-PKP1, with acidic and aromatic residues involved (cut-off distance <5 Å, or < 7.5 Å for those in parentheses). The corresponding aromatic residues of ARM-PKP1 involved are also indicated.

PADI4			ARM-PKP1
Hot-spot regions	Acidic residues	Aromatic residues	Aromatic residues
155–176	Asp155, Asp157, Glu160, Asp165, Glu167, Asp173, Asp176	–	Trp691
313–347	Glu315, Glu317, Glu339, Glu340, Glu341, Asp344	Phe314$^{(a)}$, Phe319$^{(b)}$, (Trp347)	Tyr463$^{(a,b)}$, Tyr478, (His604)
375–392	Glu378	Phe379$^{(c)}$, Phe389$^{(d)}$, (Tyr391)	Tyr484$^{(c)}$, Phe493$^{(d)}$, (Tyr642)

(a,b,c,d): Residues forming direct hydrophobic contacts with each others.

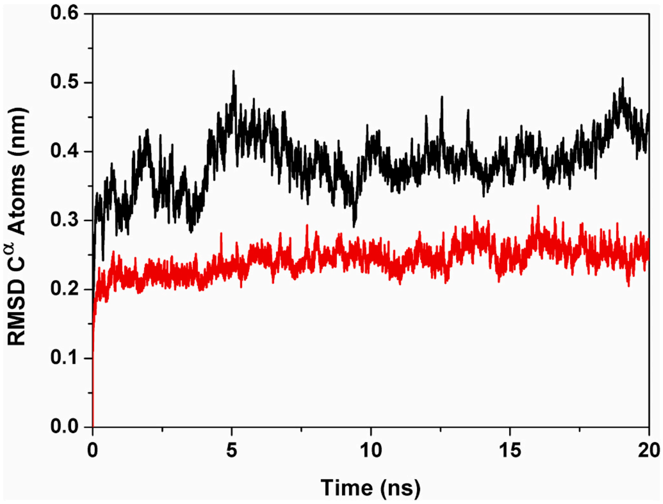

Fig. 5. Equilibration in MD simulation of PADI4 and ARM-PKP1 in their complex. Root mean square deviation (RMSD) of atomic positions of C$^{\alpha}$ atoms of the two proteins as a function of the simulation time.

experimentally observed in the CD spectra upon the association of the two proteins, when compared to the addition spectrum (Fig. 1 B).

Finally, we also refined the PADI4/ARM-PKP1 complex by using classical MD simulations in full hydration conditions. Both proteins in the complex equilibrate their structures in a few nanoseconds, with higher atomic root mean square deviations (RMSDs) for PADI4 due to a larger number of disordered regions compared to ARM-PKP1 (Fig. 5). Conformational changes (Fig. 6) were dominated by atomic deviations of loop regions from the crystallographic position, more than by fluctuations due to the inner flexibility of the two macromolecules. However, no essential modifications could be observed in the contact regions of PADI4 and ARM-PKP1 on the timescale sampled (20 ns) with respect to the docking prediction provided by ClusPro, except for small rearrangements due to accommodation of residues. We also did not observe any changes in the secondary or tertiary structure of the two proteins and, therefore, we excluded this as a possible reason for the changes observed in the CD spectra upon the binding of the two proteins (and then, those differences must be due to the large number of aromatic residues involved in the contact interface, see above). The stability of the PADI4/ARM-PKP1 docking complex in MD simulations was not unexpected, as it is a further indication of the reliability of the docking prediction.

4. Discussion and conclusion

The discovery of the interaction between ARM-PKP1 and PADI4 was prompted by an initial hypothesis. We have recently shown that PADI4 binds to Impα3, a protein involved in the nuclear translocation machinery [22]; since Impα3 has an ARM scaffold, structurally very similar to that of ARM-PKP1, we conjectured that PADI4 should bind ARM-PKP1, as well. To test the hypothesis of a well-defined complex between the two proteins, we carried out several *in vitro* and *in silico* experiments.

The binding interface of ARM-PKP1 is the basic patch on its molecular surface, as assumed in our molecular simulations. This polypeptide patch was proposed to be the main binding region of PKP1 with other molecular partners [39,40]. This is especially reasonable in the case of PADI4, which is a protein with a high content of acidic residues [21]. On such assumption, the binding interface of PADI4 predicted in our docking simulations corresponds to the subdomain 313–347, with the support of two other nearby and slightly smaller regions, *i.e.* the polypeptide patches 155–176 and 375–392.

The measured K_d of PADI4/ARM-PKP1 complex (1.4 μM) is

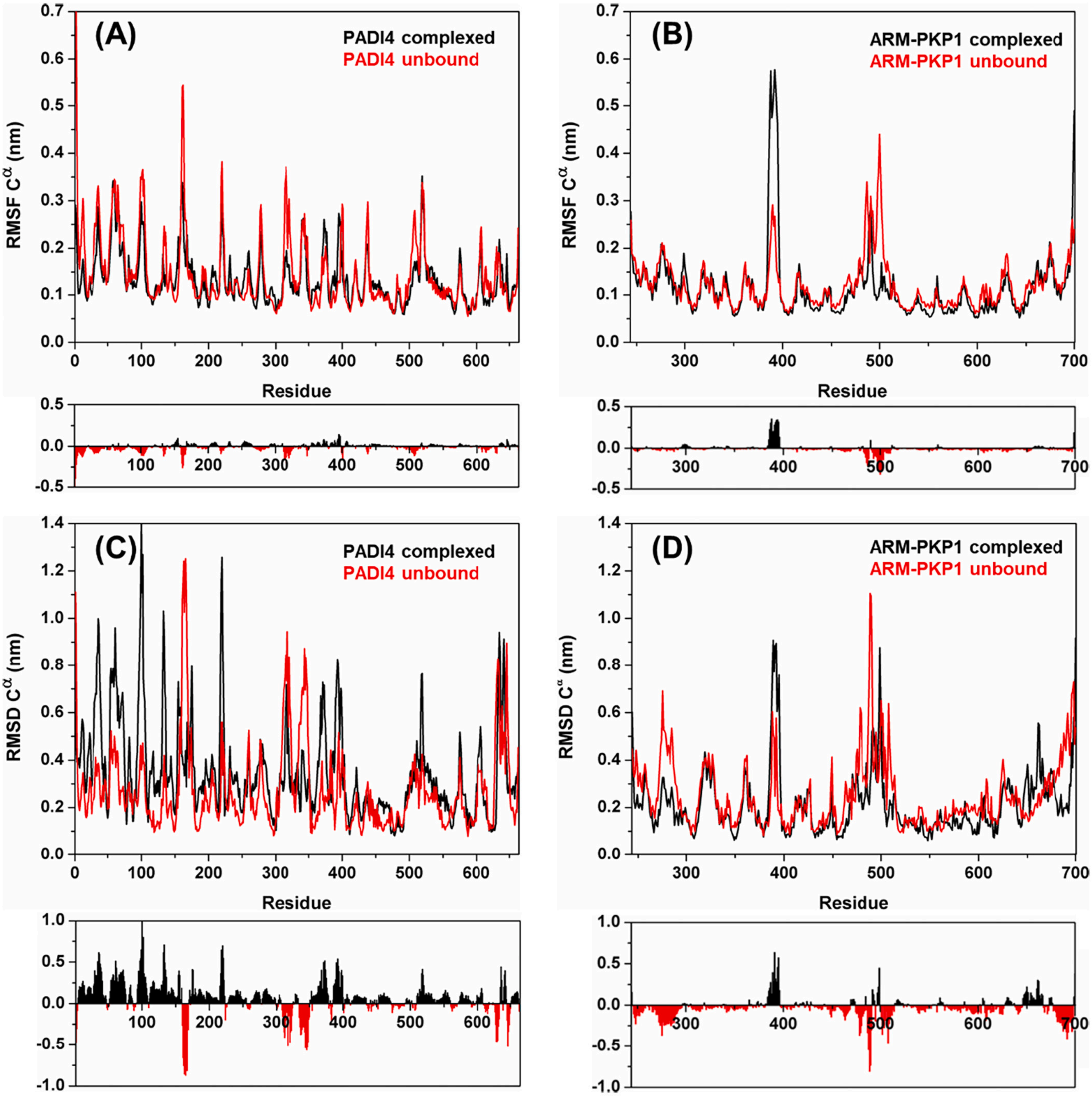

Fig. 6. Conformational flexibility and rearrangements in MD simulation of PADI4 and ARM-PKP1 in their complex. (A-B) Root mean square fluctuation (RMSF), and (C—D) root mean square deviation (RMSD) of atomic positions of C$^{\alpha}$ atoms of PADI4 and ARM-PKP1, as a function of the residue number, for each protein in the complex (black) and unbound state (red). Differences between the two curves are evidenced in the panel below each graph (unlabeled axes have the same quantity and units). Values are calculated for a single chain and monomer of PADI4 and ARM-PKP1, respectively. (For interpretation of the references to colour in this figure legend, the reader is referred to the web version of this article.)

comparable to that observed for ARM-PKP1 in complexes with an intrinsically disordered protein, such as NUPR1, *in cellulo* (~ 10 mM) [40] or, alternatively, with a well-folded protein such as the sterile alpha domain of p73 (~ 5 mM) [39]. These dissociation constants, despite their low value, might be enough to drive a proper regulation in several pathways where ARM-PKP1 could intervene, determining a high specificity in spite of a low affinity. In the case of the PADI4/ARM-PKP1 complex, the affinity can be rationalized as being influenced by a complex network of electrostatic interactions. We observed an overall negative entropy of binding; as hydrophobic and electrostatic interactions would be accompanied by positive entropy, then other contributions (such as conformational change, disorder-to-order or exchange of other solutes with the bulk solution) should be associated to the large negative entropy [61]. On the other hand, it is also true that the presence of glycerol in the buffer may alter the affinity and the enthalpy, as observed in other PPIs; in fact, it has been observed that glycerol makes the enthalpy more negative. Our molecular simulations indicate also a supporting contribution of hydrophobic interactions, especially by a cluster of several phenylalanine residues located on the binding interface of PADI4. It is important to indicate that we are hypothesizing that some of the twenty-eight arginine residues in the ARM-PKP1 sequence could be citrullinated by PADI4, but that, in addition, PADI4 could as well bind to such protein to hamper interactions with another molecules, without any PTM involved, as it happens with p53 and PADI4, where the immunoglobulin-like domains of the latter at its N-terminal region, far away from its active site, are involved [62].

PKP1 is in the nucleus [27,63], where it is associated with mRNA ribonuclein particles and ribosomal proteins [26], and its altered expression is a frequent and critical event in several cancers [26,64,65], indicating that it has key roles in proliferation, differentiation, and cell migration. Interestingly enough, nuclear localization signals have not been found in PKP1 sequence [66]. Although it is thought that the amino-terminal region is involved in its nuclear localization, it has not been ruled out that nuclear translocation of PKP1 could involve binding as a cargo to another protein which is being translocated [66,67]. In addition, PKP1 also forms desmosomes, protein complexes key to maintain cell-cell adhesion and integrity of tissues, together with transmembrane cadherins and desmoplakin [29]. PKP1 plays an important role in migration and Ca(II)-dependent stability of desmosomes. In healthy tissues, desmosomes adopt a Ca(II)-independent state (also called "hyper-adhesion") [68–70] whereas during wound healing and tissue regeneration, desmosomes lead to weaker intercellular adhesion through becoming Ca(II)-dependent and allowing tissue regeneration [69,70]. Neutrophil extracellular traps (NETs) are web-like scaffolds formed by DNA extruded from neutrophils in response to either bacterial infection or inflammation. Formation of NETs is modulated by the presence of Ca(II) ions and PADI4 [71,72], as well as by the activation of the PI3K pathways [73], which are also controlled, in some tumors, by an excess of PKP1 [74]. In fact, PI3K/AKT pathway regulates PKP1 (and none of the other PKPs), by inducing a cascade of kinases that ends in PKP1 phosphorylation, resulting in a lower cell adhesion [68–70]. In turn, NETs mediate the proteolysis of endothelial cadherin [75]. Along these lines, we suggest that PADI4 could: (i) regulate the PKP1 function, hampering interactions with other desmosomal proteins or helping in nuclear translocation by forming a complex with PADI4; and, (ii) concomitantly, trigger the formation of NETs.

There is a need for a better knowledge to describe the role of non-junctional forms of PKP1, with special attention to the interaction partners and its mission in the diverse pathways it is involved to. Our findings shed light on one of those interactions, opening the venue for new mechanistic studies based in the interaction PADI4/ARM-PKP1. We advocate future research in this field as essential to increase our knowledge on the role of these proteins in a physiologically relevant context.

Authors' contributions

Conceptualization, JLN, BR, CdJ and AVC; methodology, JLN, CdJ, BR and AVC; investigation, JLN, SAA, BR and OA; data formal analysis, JLN, SAA, OA, BR and AVC; writing-original draft preparation, JLN, CdJ, BR and AVC; materials, JLN, MEFV, CdJ, OA and AVC; writing-review and editing, JLN, OA, CdJ, MEFV, BR and AVC; funding acquisition, JLN, CdJ, OA and AVC.

Declaration of Competing Interest

The authors declare that they have no known competing financial interests or personal relationships that could have appeared to influence the work reported in this paper.

Data availability

Data will be made available on request.

Acknowledgements

This research was funded by Spanish Ministry of Economy and Competitiveness and European ERDF Funds (MCIU/AEI/FEDER, EU) [RTI2018–097991-B-I00 to JLN, BFU2016–78232-P to AVC, CP19/00095 to CdJ]; Fondo de Investigaciones Sanitarias from Instituto de Salud Carlos III, and European Union (ERDF/ESF, "Investing in your future") [PI18/00394 to OA and PI22/00824 to CdJ]; PAIDI program, Group BIO309. Junta de Andalucía, and Fondo de Investigaciones Sanitarias from Instituto de Salud Carlos III [PI10/00198 to EFV]; Diputación General de Aragón ["Protein targets and Bioactive Compounds group" E45-20R to AVC, and "Digestive Pathology Group" B25-20R to OA]; and Comunidad Valenciana [CAICO 2021/0135 to CdJ and JLN] SAA was recipient of a "Carolina Foundation predoctoral fellowship 2020". The funders had no role in the study design, data collection and analysis, decision to publish, or preparation of the manuscript. BR acknowledges the kind use of computational resources of the European Magnetic Resonance Center (CERM), Sesto Fiorentino (Florence), Italy. We thank two anonymous reviewers for their comments and suggestions. We thank Prof. Daniel Otzen for handling the manuscript.

References

[1] G.L. Cuthbert, S. Daujat, A.W. Snowden, H. Erdjument-Bromage, T. Hagiwara, M. Yamada, R. Schneider, P.D. Gregory, P. Tempst, A.J. Bannister, T. Kouzarides, Histone deimination antagonizes arginine methylation, Cell. 118 (2004) 545–553, https://doi.org/10.1016/j.cell.2004.08.020.

[2] H. Asaga, M. Yamada, T. Senshu, Selective deimination of vimentin in calcium ionophore-induced apoptosis of mouse peritoneal macrophages, Biochem. Biophys. Res. Commun. 243 (1998) 641–646, https://doi.org/10.1006/bbrc.1998.8148.

[3] C. Assohou-Luty, R. Raijmakers, W.E. Benckhuijsen, J. Stammen-Vogelzangs, A. De Ru, P.A. Van Veelen, K.L.M.C. Franken, J.W. Drijfhout, G.J.M. Pruijn, The human peptidylarginine deiminases type 2 and type 4 have distinct substrate specificities, Biochim. Biophys. Acta 2014 (1844) 829–836, https://doi.org/10.1016/j.bbapap.2014.02.019.

[4] T. Senshu, K. Akiyama, A. Ishigami, K. Nomura, Studies on specificity of peptidylarginine deiminase reactions using an immunochemical probe that recognizes an enzymatically deiminated partial sequence of mouse keratin K1, J. Dermatol. Sci. 21 (1999) 113–126, https://doi.org/10.1016/S0923-1811(99)00026-2.

[5] K. Kizawa, H. Takahara, H. Troxler, P. Kleinert, U. Mochida, C.W. Heizmann, Specific citrullination causes assembly of a globular S100A3 homotetramer: a putative Ca^{2+} modulator matures human hair cuticle, J. Biol. Chem. 283 (2008) 5004–5013, https://doi.org/10.1074/jbc.M709357200.

[6] Y. Wang, J. Wysocka, J. Sayegh, Y.H. Lee, J.R. Pertin, L. Leonelli, L.S. Sonbuchner, C.H. McDonald, R.G. Cook, Y. Dou, R.G. Roeder, S. Clarke, M.R. Stallcup, C.D. Allis, S.A. Coonrod, Human PAD4 regulates histone arginine methylation levels via demethylimination, Science 306 (2004) 279–283, https://doi.org/10.1126/science.1101400.

[7] A. Ishigami, N. Maruyama, Importance of research on peptidylarginine deiminase and citrullinated proteins in age-related disease, Geriatr Gerontol Int 10 (2010) S53–S58, https://doi.org/10.1111/j.1447-0594.2010.00593.x.

[8] J. Fuhrmann, K.W. Clancy, P.R. Thompson, Chemical biology of protein arginine modifications in epigenetic regulation, Chem. Rev. 115 (2015) 5413–5461, https://doi.org/10.1021/acs.chemrev.5b00003.

[9] M. Guerrin, A. Ishigami, M.C. Méchin, R. Nachat, S. Valmary, M. Sebbag, M. Simon, T. Senshu, G. Serre, cDNA cloning, gene organization and expression analysis of human peptidylarginine deiminase type I, Biochem. J. 370 (2003) 167–174, https://doi.org/10.1042/bj20020870.

[10] A. Ishigami, T. Ohsawa, H. Asaga, K. Akiyama, M. Kuramoto, N. Maruyama, Human peptidylarginine deiminase type II: molecular cloning, gene organization, and expression in human skin, Arch. Biochem. Biophys. 407 (2002) 25–31, https://doi.org/10.1016/s0003-9861(02)00516-7.

[11] T. Kanno, A. Kawada, J. Yamanouchi, C. Yosida-Noro, A. Yoshiki, M. Shiraiwa, M. Kusakabe, M. Manabe, T. Tezuka, H. Takahara, Human peptidylarginine deiminase type III: molecular cloning and nucleotide sequence of the cDNA, properties of the recombinant enzyme, and immunohistochemical localization in human skin, J. Invest. Dermatol. 115 (2000) 813–823, https://doi.org/10.1046/j.1523-1747.2000.00131.x.

[12] S. Chavanas, M.C. Méchin, H. Takahara, A. Kawada, R. Nachat, G. Serre, M. Simon, Comparative analysis of the mouse and human peptidylarginine deiminase gene clusters reveals highly conserved non-coding segments and a new human gene, PADI6, Gene. 330 (2004) 19–27, https://doi.org/10.1016/j.gene.2003.12.038.

[13] K. Nakashima, T. Hagiwara, A. Ishigami, S. Nagata, H. Asaga, M. Kuramotot, T. Senshu, M. Yamada, Molecular characterization of peptidylarginine deiminase in HL-60 cells induced by retinoic acid and 1α,25-dihydroxyvitamin D3, J. Biol. Chem. 274 (1999) 27786–27792, https://doi.org/10.1074/jbc.274.39.27786.

[14] S. Dong, T. Kanno, A. Yamaki, T. Kojima, M. Shiraiwa, A. Kawada, M.C. Méchin, S. Chavanas, G. Serre, M. Simon, H. Takahara, NF-Y and Sp1/Sp3 are involved in

the transcriptional regulation of the peptidylarginine deiminase type III gene (PADI3) in human keratinocytes, Biochem. J. 397 (2006) 449–459, https://doi.org/10.1042/BJ20051939.

[15] C. Yang, Z.-Z. Dong, J. Zhang, D. Teng, X. Luo, D. Li, Y. Zhou, Peptidylarginine deiminases 4 as a promising target in drug discovery, Eur. J. Med. Chem. 226 (2021), 113840, https://doi.org/10.1016/j.ejmech.2021.113840.

[16] D.J. Slade, S. Horibata, S.A. Coonrod, P.R. Thompson, A novel role for protein arginine deiminase 4 in pluripotency: the merging role of citrullinated histone H1 in cellular programming, Bioessays 36 (2014) 736–740, https://doi.org/10.1002/bies.201400057.

[17] E.E. Witalison, P.R. Thompson, L.J. Hofseth, Protein arginine deiminases and associated citrullination: physiological functions and diseases associated with dysregulation, Curr. Drug Targets 16 (2015) 700–710, https://doi.org/10.2174/1389450116666150202160954.

[18] Y. Wang, R. Chen, Y. Gan, S. Ying, The roles of PAD2- and PAD4-mediated protein citrullination catalysis in cancers, Int. J. Cancer 148 (2021) 267–276, https://doi.org/10.1002/ijc.33205.

[19] P. Li, H. Yao, Z. Zhang, M. Li, Y. Luo, P.R. Thompson, D.S. Gilmour, Y. Wang, Regulation of p53 target gene expression by peptidylarginine deiminase 4, Mol. Cell. Biol. 28 (2008) 4745–4758, https://doi.org/10.1128/MCB.01747-07.

[20] P. Li, D. Wang, H. Yao, P. Doret, G. Hao, Q. Shen, H. Qiu, X. Zhang, Y. Wang, G. Chen, Y. Wang, Coordination of PAD4 and HDAC2 in the regulation of p53-target gene expression, Oncogene 29 (2010) 3153–3162, https://doi.org/10.1038/onc.2010.51.

[21] J.L. Neira, S. Araujo-Abad, A. Cámara-Artigas, B. Rizzuti, O. Abián, A.M. Giudici, A. Velázquez-Campoy, C. de Juan Romero, Biochemical and biophysical characterization of PADI4 supports its involvement in cancer, Arch. Biochem. Biophys. 717 (2022), 109125, https://doi.org/10.1016/j.abb.2022.109125.

[22] J.L. Neira, B. Rizzuti, O. Abián, S. Araujo-Abad, A. Velázquez-Campoy, C. de Juan Romero, Human enzyme PADI4 binds to the nuclear carrier importin α3, Cells (2022), https://doi.org/10.3390/cells11142166.

[23] G.A. Petsko, D. Ringe, Protein Structure and Function, Blackwell, Oxford, 2003.

[24] S. Bonné, B. Gilbert, M. Hatzfeld, X. Chen, K.J. Green, F. van Roy, Defining desmosomal plakophilin-3 interactions, J. Cell Biol. 161 (2003) 403–416, https://doi.org/10.1083/jcb.200303036.

[25] S. Bonné, J. van Hengel, F. Nollet, P. Kools, F. van Roy, Plakophilin-3, a novel armadillo-like protein present in nuclei and desmosomes of epithelial cells, J. Cell Sci. 112 (1999) 2265–2276, https://doi.org/10.1242/jcs.112.14.2265.

[26] R. Fischer-Keso, S. Bruninger, S. Hofmann, M. Henn, T. Röhrig, P. Ströbel, G. Stoecklin, I. Hofmann, Plakophilins 1 and 3 bind to FXR1 and thereby influence the mRNA stability of desmosomal proteins, Mol. Cell. Biol. 34 (2014) 4244–4256, https://doi.org/10.1128/MCB.00766-14.

[27] I. Hofmann, M. Casella, M. Schnölzer, T. Schelechter, H. Spring, W.W. Franke, Identification of the junctional plaque protein plakophilin 3 in cytoplasmic particles containing RNA-binding proteins and the recruitment of plakophilins 1 and 3 to stress granules, Mol. Biol. Cell 17 (2006) 1388–1398, https://doi.org/10.1091/mbc.e05-08-0708.

[28] J. Martín-Padrón, L. Boyero, M.I. Rodriguez, A. Andrades, I. Díaz-Cano, P. Peinado, C. Baliñas-Gavira, J.C. Alvarez-Pérez, I.F. Coira, M.E. Fárez-Vidal, P.P. Medina, Plakophilin 1 enhances MYC translation, promoting squamous cell lung cancer, Oncogene 39 (2020) 5479–5493, https://doi.org/10.1038/s41388-019-1129-3.

[29] M. Hatzfeld, Plakophilins: multifunctional proteins or just regulators of desmosomal adhesion? Biochim. Biophys. Acta, Mol. Cell Res. 1773 (2007) 69–77, https://doi.org/10.1016/j.bbamcr.2006.04.009.

[30] H.P. Kapprell, K. Owaribe, W.W. Franke, Identification of a basic protein of Mr 75,000 as an accessory desmosomal plaque protein in stratified and complex epithelia, J. Cell Biol. 106 (1988) 1679–1691, https://doi.org/10.1083/jcb.106.5.1679.

[31] A.E. Bass-Zubek, L.M. Godsel, M. Delmar, K.J. Green, Plakophilins: multifunctional scaffolds for adhesion and signaling, Curr. Opin. Cell Biol. 21 (2009) 708–716, https://doi.org/10.1016/j.ceb.2009.07.002.

[32] A. Sánchez-Palencia, M. Gómez-Morales, J.A. Gómez-Capilla, V. Pedraza, L. Boyero, R. Rosell, M.E. Fárez-Vidal, Gene expression profiling reveals novel biomarkers in nonsmall cell lung cancer, Int. J. Cancer 129 (2011) 355–364, https://doi.org/10.1002/ijc.25704.

[33] M. Gómez-Morales, M. Cámara-Pulido, M.T. Miranda-León, A. Sánchez-Palencia, L. Boyero, J.A. Gómez-Capilla, M.E. Fárez-Vidal, Differential immunohistochemical localization of desmosomal plaque-related proteins in non-small cell lung cancer, Histopathology 63 (2013) 103–113, https://doi.org/10.1111/his.12126.

[34] I. Galindo, M. Gómez-Morales, I. Díaz-Cano, A. Andrades, M. Caba-Molina, M. T. Miranda-León, P.P. Medina, J. Martín-Padrón, M.E. Fárez-Vidal, The value of desmosomal plaque-related markers to distinguish squamous cell carcinoma and adenocarcinoma of the lung, Ups. J. Med. Sci. 125 (2020) 19–29, https://doi.org/10.1080/03009734.2019.1692101.

[35] M. Peifer, S. Berg, A.B. Reynolds, A repeating amino acid motif shared by proteins with diverse cellular roles, Cell 76 (1994) 789–791, https://doi.org/10.1016/0092-8674(94)90353-0.

[36] M.A. Andrade, C. Petosa, S.I. O'Donoghue, C.W. Muller, P. Bork, Comparison of ARM and HEAT protein repeats, J. Mol. Biol. 309 (2001) 1–18, https://doi.org/10.1006/jmbi.2001.4624.

[37] H.-J. Choi, W.I. Weis, Structure of the Armadillo repeat domain of plakophilin 1, J. Mol. Biol. 346 (2005) 367–376, https://doi.org/10.1016/j.jmb.2004.11.048.

[38] A.M. Giudici, J.G. Hernández-Cifre, A. Cámara-Artigas, F. Hornos, S. Martínez-Rodríguez, J.C. Alvarez-Pérez, I. Díaz-Cano, M.E. Fárez-Vidal, J.L. Neira, The isolated armadillo-repeat domain of Plakophilin 1 is a monomer in solution with a low conformational stability, J. Struct. Biol. 211 (2020), 107569, https://doi.org/10.1016/j.jsb.2020.107569.

[39] J.L. Neira, B. Rizzuti, D. Ortega-Alarcón, A.M. Giudici, O. Abián, M.E. Fárez-Vidal, A. Velázquez-Campoy, The armadillo-repeat domain of plakophilin 1 binds to the C-terminal sterile alpha motif (SAM) of p73, Biochim. Biophys. Acta Gen. Subj. 1865 (2021), 129914, https://doi.org/10.1016/j.bbagen.2021.129914.

[40] P. Santofimia-Castaño, B. Rizzuti, A.L. Pey, M.E. Fárez-Vidal, J.L. Iovanna, J. L. Neira, Intrinsically disordered protein NUPR1 binds to the armadillo-repeat domain of plakophilin 1, Int. J. Biol. Macromol. 170 (2021) 549–560, https://doi.org/10.1016/j.ijbiomac.2020.12.193.

[41] S.C. Gill, P.H. von Hippel, Calculation of protein extinction coefficients from amino acid sequence data, Anal. Biochem. 182 (1989) 319–326, https://doi.org/10.1016/0003-2697(89)90602-7.

[42] J.L. Neira, F. Hornos, J. Bacarizo, A. Cámara-Artigas, J. Gómez, The monomeric species of the regulatory domain of tyrosine hydroxylase has a low conformational stability, Biochemistry 55 (2017) 3418–3431, https://doi.org/10.1021/acs.biochem.6b00135.

[43] B. Birdsall, R.W. King, M.R. Wheeler, C.A.Jr. Lewis, S. Goode, R.B. Dunlap, G. C. Roberts, Correction for light absorption in fluorescence studies of protein-ligand interactions, Anal. Biochem. 132 (1983) 353–361, https://doi.org/10.1016/0003-2697(83)90020-9.

[44] D. Beckett, Measurement and analysis of equilibrium binding titrations: a beginner's guide, Methods Enzymol. 488 (2011) 1–16, https://doi.org/10.1016/B978-0-12-381268-1.00001-X.

[45] C.A. Royer, S.F. Scarlatta, Fluorescence approaches to quantifying biomolecular interactions, Methods Enzymol. 450 (2008) 79–106, https://doi.org/10.1016/S0076-6879(08)03405-8.

[46] N. Horikoshi, H. Tachiwana, K. Saito, A. Osakabe, M. Sato, M. Yamada, S. Akashi, Y. Nishimura, W. Kagawa, H. Kurumizaka, Structural and biochemical analyses of the human PAD4 variant encoded by a functional haplotype gene, Acta Crystallogr. D67 (2011) 112–118, https://doi.org/10.1107/S0907444910051711.

[47] D. Kozakov, D.R. Hall, B. Xia, K.A. Porter, D. Padhorny, C. Yueh, D. Beglo, S. Vajda, The ClusPro web server for protein-protein docking, Nat. Protoc. 12 (2017) 255–278, https://doi.org/10.1038/nprot.2016.169.

[48] S. Vajda, C. Yueh, D. Beglov, T. Bohnuud, S.E. Mottarella, B. Xia, D.R. Hall, D. Kozakov, New additions to the ClusPro server motivated by CAPRI, Proteins 85 (2017) 435–444, https://doi.org/10.1002/prot.25219.

[49] M.J. Abraham, T. Murtola, R. Schulz, S. Pall, J.C. Smith, B. Hess, E. Lindahl, GROMACS: high performance molecular simulations through multi-level parallelism from laptops to supercomputers, Software (2015) 19–25, https://doi.org/10.1016/j.softx.2015.06.001.

[50] K. Lindorff-Larsen, S. Piana, K. Palmo, P. Maragakis, J.L. Klepeis, R.O. Dror, D. E. Shaw, Improved side-chain torsion potentials for the Amber ff99SB protein force field, Proteins 78 (2010) 1950–1958, https://doi.org/10.1002/prot.22711.

[51] L. Jorgensen, J. Chandrasekhar, J.D. Madura, R.W. Impey, M.L. Klein, Comparison of simple potential functions for simulating liquid water, J. Chem. Phys. 79 (1983) 926–935, https://doi.org/10.1063/1.445869.

[52] A. Guglielmelli, B. Rizzuti, R. Guzzi, Stereoselective and domain-specific effects of ibuprofen on the thermal stability of human serum albumin, Eur. J. Pharm. Sci. 112 (2018) 122–131, https://doi.org/10.1016/j.ejps.2017.11.013.

[53] J.L. Neira, B. Rizzuti, J.L. Iovanna, Determinants of the pKa values of ionizable residues in an intrinsically disordered protein, Arch. Biochem. Biophys. 598 (2016) 18–27, https://doi.org/10.1016/j.abb.2016.03.034.

[54] M. Parrinello, A. Rahman, Polymorphic transitions in single crystals: a new molecular dynamics method, J. Appl. Phys. 52 (1981) 7182–7190, https://doi.org/10.1063/1.328693.

[55] G. Bussi, D. Donadio, M. Parrinello, Canonical sampling through velocity rescaling, J. Chem. Phys. 126 (2007), 014101, https://doi.org/10.1063/1.2408420.

[56] U. Essmann, L. Perera, M.L. Berkowitz, T. Darden, H. Lee, L.G. Pedersen, A smooth particle mesh Ewald method, J. Chem. Phys. 103 (1995) 8577–8593, https://doi.org/10.1063/1.470117.

[57] B. Hess, P-LINCS: a parallel linear constraint solver for molecular simulation, J. Chem. Theory Comput. 4 (2008) 116–122, https://doi.org/10.1021/ct700200b.

[58] B. Rizzuti, F. Grande, Virtual screening in drug discovery: A precious tool for a still-demanding challenge, in: Protein Homeostasis Diseases, Elsevier BV, Amsterdam, The Netherlands, 2020, pp. 309–327, https://doi.org/10.1016/B978-0-12-819132-3.00014-2.

[59] Y. Yan, H. Tao, J. He, S.-Y. Huang, The HDOCK server for integrated protein-protein docking, Nat. Protoc. 15 (2020) 1829–1852, https://doi.org/10.1038/s41596-020-0312-x.

[60] B.G. Pierce, K. Wiehe, H. Hwang, B.H. Kim, T. Vreven, Z. Weng, ZDOCK server: interactive docking prediction of protein-protein complexes and symmetric multimers, Bioinformatics 30 (2014) 1771–1773, https://doi.org/10.1093/bioinformatics/btu097.

[61] J. Iwahara, A. Esadze, L. Zandarashvili, Physicochemical properties of ion pairs of biological macromolecules, Biomolecules 5 (2015) 2435–2463, https://doi.org/10.3390/biom5042435.

[62] P. Li, H. Yao, Z. Zhang, M. Li, Y. Luo, P.R. Thompson, D.S. Glimour, Y. Wang, Regulation of p53 target gene expression by peptidylarginine deiminase 4, Mol. Cell. Biol. 28 (2008) 4745–4758, https://doi.org/10.1128/MCB.01747-07.

[63] T. Sobolik-Delmaire, R. Reddy, A. Pashaj, B.J. Roberts, J.K. Wall III, Plakophilin-1 localizes to the nucleus and interacts with single-stranded DNA, J. Invest. Dermatol. 130 (2010) 2638–2646, https://doi.org/10.1038/jid.2010.191.

[64] C. Yang, R. Fischer-Keso, T. Schelechter, P. Ströbel, A. Marx, I. Hofmann, Plakophilin 1-deficient cells upregulate SPOCK1: implications for prostate cancer

progression, Tumour Biol. 36 (2015) 9567–9577, https://doi.org/10.1007/s13277-015-3628-3.

[65] T. Sobolik-Delmaire, D. Katafiasz, S.A. Keim, M.G. Mahoney, J.K. Wahl III, Decreased plakophilin-1 expression promotes increased motility in head and neck squamous cell carcinoma cells, Cell Commun. Adhes. 14 (2003) 99–109, https://doi.org/10.1080/15419060701463082.

[66] M. Hatzfeld, A muclear function for Plakophilin-1 in the DNA damage response? J. Invest. Dermatol. 130 (2010) 2538–2540, https://doi.org/10.1038/jid.2010.258.

[67] M. Hatzfeld, C. Haffner, K. Schulze, U. Vinzens, The function of plakophilin 1 in desmosome assembly and actin filament organization, J. Cell Biol. 149 (2000) 209–222, https://doi.org/10.1083/jcb.149.1.209.

[68] D.R. Garrod, M.Y. Berika, W.F. Bardsley, D. Holmes, L. Tabernero, Hyper-adhesion in desmosomes: its regulation in wound healing and possible relationship to cadherin crystal structure, J. Cell Sci. 118 (2005) 5743–5754, https://doi.org/10.1242/jcs.02700.

[69] T.E. Kimura, A.J. Merritt, F.R. Lock, J.J. Eckert, T.P. Fleming, D.R. Garrod, Desmosomal adhesiveness is developmentally regulated in the mouse embryo and modulated during trophectoderm migration, Dev. Biol. 369 (2012) 286–297, https://doi.org/10.1016/j.ydbio.2012.06.025.

[70] S. Wallis, S. Lloyd, I. Wise, G. Ireland, T.P. Fleming, D. Garrod, The alpha isoform of protein kinase C is involved in signaling the response of desmosomes to wounding in cultured epithelial cells, Mol. Biol. Cell 11 (2000) 1077–1092, https://doi.org/10.1091/mbc.11.3.1077.

[71] P. Li, M. Li, M.R. Lindberg, M.J. Kennett, N. Xiong, Y. Wang, PAD4 is essential for antibacterial innate immunity mediated by neutrophil extracellular traps, J. Exp. Med. 207 (2010) 1853–1862, https://doi.org/10.1084/jem.20100239.

[72] A.K. Gupta, S. Giaglis, P. Hassler, S. Hahan, Efficient neutrophil extracellular trap induction requires mobilization of both intracellular and extracellular calcium pools and is modulated by cyclosporine a, PLoS One 9 (2014), e97088, https://doi.org/10.1371/journal.pone.0097088.

[73] S.S. Lavpie, E. Dumas, B. Vulesevic, P.-E. Neagoe, M. White, M.G. Sirois, Synthesis of human neutrophil extracellular traps contributes to angiopoietin-mediated in vitro proinflammatory and proangiogenic activities, J. Immunol. 200 (2018) 3801–3813, https://doi.org/10.4049/jimmunol.1701203.

[74] K. Li, R. Wu, M. Zhou, H. Thong, K.Q. Luo, Desmosomal proteins of DSC2 and PKP1 promote cancer cells survival and metastasis by increasing cluster formation in circulatory system, Sci. Adv. 7 (2021) 7265, https://doi.org/10.1126/sciadv.abg7265.

[75] E. Pieterse, N. Rother, M. Garsen, J.M. Hofstra, S.C. Satchell, M. Hoffmann, M. A. Loeven, H.K. Knaapen, O.W.H. van der Heijden, J.H.M. Berden, L.B. Hilbrands, J. van der Vlag, Neutrophil extracellular traps drive endothelial-to-mesenchymal transition, Aterioscler. Thromb. Vasc. Biol. 37 (2017) 1371–1379, https://doi.org/10.1161/ATVBAHA.117.309002.

cells

MDPI

Article

Human Enzyme PADI4 Binds to the Nuclear Carrier Importin α3

José L. Neira [1,2,*], Bruno Rizzuti [2,3,*], Olga Abián [2,4,5,6], Salomé Araujo-Abad [1,7], Adrián Velázquez-Campoy [2,4,5,6] and Camino de Juan Romero [1,8]

[1] Instituto de Investigación, Desarrollo e Innovación en Biotecnología Sanitaria de Elche, Universidad Miguel Hernández, 03202 Elche, Spain; lourdes.araujo@goumh.umh.es (S.A.-A.); m.juan@umh.es (C.d.J.R.)
[2] Instituto de Biocomputación y Física de Sistemas Complejos–Unidad mixta GBsC-CSIC-BIFI, Universidad de Zaragoza, 50018 Zaragoza, Spain; oabifra@unizar.es (O.A.); adrianvc@unizar.es (A.V.-C.)
[3] CNR-NANOTEC, SS Rende (CS), Department of Physics, University of Calabria, 87036 Rende, Italy
[4] Instituto de Investigación Sanitaria Aragón (IIS Aragón), 50009 Zaragoza, Spain
[5] Centro de Investigación Biomédica en Red en el Área Temática de Enfermedades Hepáticas y Digestivas (CIBERehd), 28029 Madrid, Spain
[6] Departamento de Bioquímica y Biología Molecular y Celular, Universidad de Zaragoza, 50009 Zaragoza, Spain
[7] Centro de Biotecnología, Universidad Nacional de Loja, Avda. Pío Jaramillo Alvarado s/n, Loja 110111, Ecuador
[8] Unidad de Investigación, Fundación para el Fomento de la Investigación Sanitaria y Biomédica de la Comunidad Valenciana (FISABIO), Hospital General Universitario de Elche, Camí de l'Almazara 11, 03203 Elche, Spain
* Correspondence: jlneira@umh.es (J.L.N.); bruno.rizzuti@cnr.it (B.R.)

Abstract: PADI4 is a peptidyl-arginine deiminase (PADI) involved in the conversion of arginine to citrulline. PADI4 is present in macrophages, monocytes, granulocytes, and several cancer cells. It is the only PADI family member observed within both the nucleus and the cytoplasm. PADI4 has a predicted nuclear localization sequence (NLS) comprising residues Pro56 to Ser83, to allow for nuclear translocation. Recent predictors also suggest that the region Arg495 to Ile526 is a possible NLS. To understand how PADI4 is involved in cancer, we studied the ability of intact PADI4 to bind importin α3 (Impα3), a nuclear transport factor that plays tumor-promoting roles in several cancers, and its truncated species (ΔImpα3) without the importin-binding domain (IBB), by using fluorescence, circular dichroism (CD), and isothermal titration calorimetry (ITC). Furthermore, the binding of two peptides, encompassing the first and the second NLS regions, was also studied using the same methods and molecular docking simulations. PADI4 interacted with both importin species, with affinity constants of ~1–5 μM. The isolated peptides also interacted with both importins. The molecular simulations predict that the anchoring of both peptides takes place in the major binding site of Impα3 for the NLS of cargo proteins. These findings suggest that both NLS regions were essentially responsible for the binding of PADI4 to the two importin species. Our data are discussed within the framework of a cell mechanism of nuclear transport that is crucial in cancer.

Keywords: PADI4; nuclear localization signal; binding; calorimetry; fluorescence; molecular docking; cancer

check for updates

Citation: Neira, J.L.; Rizzuti, B.; Abián, O.; Araujo-Abad, S.; Velázquez-Campoy, A.; de Juan Romero, C. Human Enzyme PADI4 Binds to the Nuclear Carrier Importin α3. *Cells* **2022**, *11*, 2166. https://doi.org/10.3390/cells11142166

Academic Editor: Ursula Stochaj

Received: 23 May 2022
Accepted: 8 July 2022
Published: 11 July 2022

1. Introduction

Deamination, or citrullination, is a post-translational modification (PTM) catalyzed by L-arginine iminohydrolases (PADIs), also known as peptidyl-arginine deiminases (EC 3.5.3.15). PADIs have key roles in nerve growth, development of embryos, trauma apoptosis, aging in tissues, epithelial terminal differentiation, and transcriptional regulation of gene expression [1–8]. Moreover, several maladies such as rheumatoid arthritis, Alzheimer's disease, psoriasis, multiple sclerosis, and many types of cancers are associated with the increased presence of PADIs and their citrullinated targets [7,9–11].

PADI1, PADI2, PADI3, PADI4, and PADI6 are the five human isozymes [12–18], each having a tissue-specific expression. An increase of enzyme activity is observed for several PADI4 haplotype mutants during the apoptosis enhanced through the mitochondrial pathway [19]. Furthermore, PADI4 is involved in the expression of p53 target genes, as well as in the gene expression of p53 [20,21].

PADI4, as well as PAD2 under some conditions, has been detected in both the cytoplasm and the nucleus [22–24], but the remaining isoforms are found in the cytoplasm. Because some of the PADI4 functions are carried out inside the nucleus, the protein must be translocated through the nuclear pore complex (NPC). PADI4 is involved in the citrullination of histones H1, H2A, H3, and H4, where a competitive inhibition between histone methylation and citrullination takes place, resulting in cancer development and progression [25]. Furthermore, citrullination also competes with histone deacetylation to regulate cancer growth and evolution [25]. Lastly, within the nucleus, p53 binds to histone deacetylase 2 and PADI4 through distinct domains, thus regulating PADI4-mediated histone citrullination. All these functions are carried out inside the nucleus and, therefore, require prior translocation of PADI4.

Nuclear translocation generally occurs through importins, together with other auxiliary proteins [26,27]. The classical nuclear import pathway is triggered by the recognition of a nuclear localization signal (NLS) polypeptide patch in the cargo by importin α [26]. The different types of NLSs, their ways of anchoring to their target, and their structures in isolation or when bound to transport factors have been extensively reviewed [28]. The cargo–importin α complex then binds to importin β, and the so-formed complex of the three proteins moves through the NPC. Importin α is a modular protein with several α-helix repeat armadillo (ARM) units [26,27]. It has two domains: (i) a 60-residue-long importin β-binding (IBB) domain, located at the N-terminal region, which is used for binding to importin β before transport through the NPC, and (ii) an NLS-binding motif formed by 10 ARM units, located at the C-terminus [29]. In the absence of importin β, the IBB domain, which mimics an NLS, occupies the ARM regions implicated in NLS recognition [29]. This intramolecular interaction has an auto-inhibitory function [29]. Variations in the nuclear transport through the importin route are important events regulating gene expression, signal transduction, and cell-cycle regulation; therefore, they can play a key role in cancer development and cell transformation [30–32]. As an example, abnormal overexpression of importin α1 has been observed in hepatocellular carcinoma [33]. Aberrant nuclear translocation is one of the hallmark features of cancer [32], also making the proteins at play in such a translocation process potential therapeutic cancer targets.

Because of the importance of the nuclear translocation in PADI4 functions, we decided to study its interaction with human importin α3 (Impα3), also called KPNA4, and with its truncated species lacking the IBB domain (ΔImpα3). Impα3 has been reported to be associated with multiple cancers (such as glioblastoma, prostate cancer, hepatocellular carcinoma, lung cancer, and ovarian cancer). Impα3 promotes tumor proliferation by facilitating several cancer-related processes [32,34–38]. We considered Impα3 as a target for PADI4 because (i) it is largely conserved among different species [39], and (ii) it has increased flexibility compared with other importins, as concluded by the structural B-factors from X-ray data; this feature confers this importin isoform a greater ability to interact with various cargos [40]. From an experimental point of view, Impα3 can also be easily expressed and purified for in vitro structural and binding studies [40–42]. In addition, Impα3 can be considered a model protein to investigate how the NLS sequence of the cargo can affect the thermodynamic parameters in the binding process, and we have already carried out several studies of the binding of Impα3 with other NLSs which can be used as a comparison [41–43]. Lastly, by studying both importin species (with and without the IBB), we could explore whether the absence of the IBB domain affects the binding of the peptide encompassing the NLS region, as studied in the case of other NLSs of several proteins (see [41–43] and references therein).

In our experiments, we firstly explored the binding between intact PADI4 and either Impα3 or ΔImpα3. Next, we described the binding of the two predicted NLS regions of PADI4 (NLS1-PADI4 and NLS2-PADI4) to the two importin species. Fluorescence, CD, and ITC confirmed that the binding took place between the intact PADI4 and the two importin species. On the other hand, we found that the two peptides corresponding to the isolated NLS1-PADI4 and NLS2-PADI4 sequences, which were mainly disordered in solution, were capable of binding to both importin species, as tested by fluorescence, ITC, and BLI. Moreover, molecular docking simulations suggested that the core regions of NLS1-PADI4 and NLS2-PADI4 were responsible for the binding, and they were both capable of anchoring to the major binding site for the NLSs of cargo proteins to Impα3. Taken together, our in vitro and in silico results suggest that PADI4 requires Impα3 to be translocated into the nucleus, and this interaction is mediated by two possible regions located at either terminus of the cargo protein. Given the importance of PADI4 in the development of tumor cells and the involvement of importins in such processes, our results can provide a molecular description of the basic binding mechanism that may lead to cancer progression.

2. Materials and Methods

2.1. Materials

The same materials used in this study have been described previously [41–43].

2.2. Protein Expression and Purification

PADI4, Impα3, and ΔImpα3 were purified as previously described [24,41–43]. The concentrations of the proteins were calculated by UV absorbance, using an extinction coefficient at 280 nm; this parameter was estimated from the number of tyrosines and tryptophans in each of these proteins [44]. In the remainder of the paper, PADI4 protein concentrations are expressed as protomer concentrations.

2.3. Prediction and Synthesis of the NLS Regions of PADI4

The NLS regions for the PADI4 sequence were predicted using the web server cNLS Mapper [45,46], available at http://nls-mapper.iab.keio.ac.jp (accessed 8 December 2021). The results pointed out the occurrence of two possible NLS regions. The one with the lowest score (5.3, in arbitrary units), hereafter indicated as NLS1, overlapped with that already predicted as the canonical NLS region [47], with the sequence P^{56}PAKKKSTGSSTWPLDPGVE-VTLTMKVASGS^{86} (according to the numbering of the intact PADI4). The predicted region with the highest score (6.1) had the sequence R^{495}SCYKLFQEQQNEGHGEALLFEGIKKKK-QQKI^{526}, which was indicated as NLS2. These two regions were synthesized as isolated peptides NLS1-PADI4 (residues Ala58–Ser86) and NLS2-PADI4 (residues Tyr498–Ile526), both slightly shorter than the predicted NLS regions to avoid potential complications due the presence of some residues (Pro56/Pro57 for NLS1 and Cys497 for NLS2) at one of their termini. The peptides were also acetylated and amidated at the N- and C-termini, respectively, to avoid fraying effects. The two peptides NLS1-PADI4 and NLS2-PADI4 were produced by Genscript (Leiden, Netherlands) and NZYtech (Lisbon, Portugal), respectively, with a purity larger than 95%. Peptide concentrations were determined from the absorbance of either Tyr498 (NLS2-PADI4) or Trp68 (NLS1-PADI4) [44].

2.4. Fluorescence

2.4.1. Steady-State Fluorescence

Spectra were collected on a Cary Varian spectrofluorometer (Agilent, Santa Clara, CA, USA), interfaced with a Peltier unit. Following the standard protocols used in our laboratories, the samples were prepared the day before and left overnight at 5 °C; before experiments, samples were left for 1 h at 25 °C, where experiments were acquired. A

1 cm pathlength quartz cell (Hellma, Kruibeke, Belgium) was used. The concentration of PADI4 or NLS1/2-PADI4 peptides was 20 μM, and that of each importin species was 2 μM. Samples containing the corresponding isolated peptides, the isolated PADI4, the isolated corresponding importin species, and the corresponding mixtures (at the concentrations indicated above) were prepared. Experiments were performed with samples in 50 mM sodium phosphate buffer, pH 7.0. Fluorescence experiments were repeated in triplicates with newly prepared samples. Variations of results among the experiments were lower than 5%.

Polypeptide samples were excited either at 280 or 295 nm (although NLS2-PADI4 has only a single tyrosine). The other experimental parameters used in the experiments have been described elsewhere [48]. Appropriate blank corrections were made in all spectra.

2.4.2. Binding Experiments with PADI4

For the titration between either Impα3 or ΔImpα3 and intact PADI4, increasing amounts of the corresponding importin species, in the concentration range 0–25 μM, were added to a solution with a fixed concentration of intact PADI4 (3 μM). Experiments were carried out in 20 mM Tris buffer (pH 7.5), 5 mM TCEP, 150 mM NaCl, and 5% glycerol at 25 °C (the storage buffer of PADI4). The experimental setup was the same as in the steady-state fluorescence experiments. Blank corrections containing the amount of each importin species were subtracted. Inner-filter effects were corrected [49]. Each titration (Impα3 with PADI4 or ΔImpα3 with PADI4) was repeated three times, using new samples. In the three cases, the variations in the results were lower than 10%.

Handling and preparation of samples were the same described in Section 2.4.1. The dissociation constant of the corresponding complex, K_d, was calculated by fitting the binding isotherm to the general binding model, explicitly considering ligand depletion [50,51].

$$F = F_0 + \frac{\Delta F_{max}}{2[PADI4]_T}\left(\left[Imp\alpha 3_{species}\right]_T + [PADI4]_T + K_d\right) - \\ \sqrt{\left(\left(\left[Imp\alpha 3_{species}\right]_T + [PADI4]_T + K_d\right)^2 - 4\left[Imp\alpha 3_{species}\right]_T [PADI4]_T\right)}, \tag{1}$$

where F is the measured fluorescence at any particular concentration of importin species after subtraction of the matching blank concentration of importin species, ΔF_{max} is the largest change in the fluorescence of importin species when all polypeptide molecules were bound, compared to the fluorescence of each unbound chain, F_0 is the fluorescence intensity when no importin species were added, $[PADI4]_T$ is the constant, total concentration of PADI4 (3 μM), and $[Imp\alpha 3_{species}]_T$ is that of either Impα3 or ΔImpα3, which was varied during the titration. Fitting to Equation (1) was carried out using KaleidaGraph (Synergy software, Reading, PA, USA).

2.4.3. Binding Experiments with NLS1/2-PADI4

For the titration between either Impα3 or ΔImpα3 and NLS1/2-PADI4, increasing amounts of the corresponding peptide, in the concentration range 0–20 μM, were added to a solution with a fixed concentration of either Impα3 or ΔImpα3 (3 μM). Experiments were carried out in the same buffer used for the titration of the intact PADI4 at 25 °C. The experimental setup was the same as in the steady-state fluorescence experiments. Blank corrections were subtracted in all cases. Spectra were corrected for inner-filter effects during fluorescence excitation [49]. Each titration (Impα3 with NLS1/2-PADI4 or ΔImpα3 with NLS1/2-PADI4) was repeated three times, using newly prepared samples. In the three cases, the variations in the results were lower than 10%.

Handling and preparation of samples were the same described in Section 2.4.1. The dissociation constant for each complex, K_d, was calculated by fitting the binding isotherm constructed to the general binding model, explicitly considering ligand depletion [50,51].

$$\begin{aligned} F = F_0 + \frac{\Delta F_{max}}{2\left[Imp\alpha3_{species}\right]_T}&\left(\left[Imp\alpha3_{species}\right]_T + [NLS1/2_{PADI4}]_T + K_d\right) \\ &-\sqrt{\Big((\left[Imp\alpha3_{species}\right]_T + [NLS1/2_{PADI4}]_T + K_d)^2 - 4\left[Imp\alpha3_{species}\right]_T[NLS1/2_{PADI4}]_T\Big)}, \end{aligned} \quad (2)$$

where F is the measured fluorescence at any particular concentration of the corresponding peptide after subtraction of the matching blank concentration of NLS1/2-PADI4, ΔF_{max} is the largest change in the fluorescence of the corresponding peptide when all polypeptide molecules were forming the complex, compared to the fluorescence of each isolated chain, F_0 is the fluorescence intensity when no NLS1/2-PADI4 was added, $[\text{NLS1/2}_{\text{PADI4}}]_T$ is the total concentration of the corresponding peptide, which was varied during the titration, and $[Imp\alpha3_{species}]_T$ is that of either Impα3 or ΔImpα3, which was kept constant during the titration. Fitting to Equation (2) was carried out using KaleidaGraph (Synergy software, Reading, PA, USA).

2.5. Circular Dichroism (CD)

Far-UV CD spectra were collected on a Jasco J810 spectropolarimeter (Jasco, Tokyo, Japan) interfaced with a Peltier unit. The instrument was periodically calibrated with (+)-10-camphorsulfonic acid. A cell of path length 0.1 cm was used (Hellma, Kruibeke, Belgium). All spectra were corrected by subtracting the corresponding baseline. Concentration of each polypeptide (importin species and either NLS1/2-PADI4 or PADI4) and the buffers were the same used in the fluorescence experiments (Section 2.4).

Isothermal wavelength spectra of each isolated macromolecule and that of the complex were acquired as an average of six scans, at a scan speed of 50 nm/min, with a response time of 2 s and a bandwidth of 1 nm. Handling and preparation of samples were the same described in Section 2.4.1.

2.6. Nuclear Magnetic Resonance (NMR) Spectroscopy

The NMR spectra were acquired at 10 °C on a Bruker Avance 500 MHz spectrometer (Bruker GmbH, Karlsruhe, Germany), equipped with a triple resonance probe and z-pulse field gradients. Spectra were processed with Bruker TopSpin 2.1 (Bruker GmbH, Karlsruhe, Germany). All NMR experiments with NLS1/2-PADI4 peptides were carried out in 100 mM sodium phosphate buffer (not corrected for isotope effects), pH 7.0. Spectra were calibrated with TSP, by considering pH-dependent changes of its chemical shifts [52]; probe temperature was calibrated with pure methanol [52].

2.6.1. 1D-^{1}H-NMR Spectra

A total of 48 scans were acquired with 16 K acquisition points for the homonuclear 1D-^{1}H-NMR spectra of each isolated peptide at a concentration of 1.2 mM. The water signal was suppressed with the WATERGATE sequence [53]. The spectra were processed by using TopSpin 2.1 with an exponential window, after zero-filling.

2.6.2. Translational Diffusion NMR (DOSY)

The NLS1/2-PADI4 concentration in DOSY experiments was 100 μM, and 128 scans were acquired, where the gradient strength was varied linearly. Details on the experimental conditions and fitting of the resulting curves have been described elsewhere [48]. A final concentration of 1% of dioxane, with an assumed hydrodynamic radius, R_h, of 2.12 Å [54], was added to the solution.

2.6.3. 2D-^{1}H-NMR Spectra

Two-dimensional spectra of NLS2-PADI4 (at 1.2 mM) were acquired in each dimension in phase-sensitive mode by using the time-proportional phase incrementation technique [55] and a spectral width of 5500 Hz. Standard TOCSY (mixing time of 80 ms) [56] and NOESY experiments (a mixing time of 250 ms) [56–58], with the WATERGATE sequence [53], as well as experimental, processing, and assigning details, were the same used in acquiring, processing, and analyzing the spectra of other NLSs [41–43]. The chemical shift values of H_{α} protons in random-coil regions were obtained from tabulated data, corrected by neighboring residue effects [59–61].

2.7. Isothermal Titration Calorimetry (ITC)

Calorimetric titrations for testing the interaction of PADI4, as well as for the interaction of NLS1/2-PADI4 peptides, with both importins, Impα3 and ΔImpα3, were carried out in an Auto-iTC200 automated high-sensitivity calorimeter (MicroCal, Malvern-Panalytical, Malvern, UK). Experiments were performed in 20 mM Tris buffer (pH 7.5), 5 mM TCEP, 150 mM NaCl, and 5% glycerol at 25 °C. PADI4 or the peptide solution (100 µM) in the injection syringe was titrated into the importin solution (10 µM) in the calorimetric cell. The remaining experimental and processing details have been described previously [41–43]. Due to the presence of glycerol in solution, background injection (included as an adjustable parameter in data fitting) was rather large. The data analysis was conducted in Origin 7.0 (OriginLab, Northampton, MA, USA) with user-defined fitting functions.

2.8. Biolayer Inteferometry (BLI)

2.8.1. Experimental Design

The association (k_{on}) and dissociation (k_{off}) rate constants of the binding of NLS1/2-PADI4 peptides to Impα3 or ΔImpα3 were determined using a BLItz system (ForteBio, Pall, Barcelona, Spain) [62]. The buffer used in the experiments was that recommended by the manufacturer. Since Impα3 and ΔImpα3 had a His-tag, they were immobilized on His-tag biosensors (Forte Bio) at 0.3 µM. The peptide concentrations were in the range from 1 to 7 µM during the association step. The general scheme of the protein association/dissociation reactions in the BLItz system for NLS1/2-PADI4 with Impα3 and ΔImpα3 immobilized on the biosensor was similar to that described previously [63].

2.8.2. Fitting of the Sensorgrams

Fittings of the sensorgrams was carried out using KaleidaGraph (Synergy software, Reading, PA, USA) [63]. The interferometry response during the association step, *R(t)* (measured in response units, RU), and the binding rate, $dR(t)/dt$, can be used to evaluate the kinetics of the formation of the Impα3/ΔImpα3–NLS1/2-PADI4 complex, according to

$$\frac{dR}{dt} = k_{on}[NLS1/2_{PADI4}](R_{max} - R(t)) - k_{off}R(t), \tag{3}$$

where R_{max} is proportional to the total concentration of biosensor-bound importin species, and [NLS1/2PADI4] represents the concentration of the corresponding NLS1/2-PADI4 peptide.

In Equation (3), *R(t)* is given by

$$R(t) = R_{eq} - R_{eq}e^{(-k_{obs}\ (t-t_0))}, \tag{4}$$

where R_{eq} is the steady-state (or equilibrium) response obtained at infinite time, when $dR(t)/dt = 0$, and $t_0 = 180$ s is the time at which the association step between biosensor-immobilized Impα3/ΔImpα3 and NLS1/2-PADI4 in the solution started. We fitted the experimentally obtained $R(t)$ under any condition as

$$R(t) = R_{eq} - R_{eq}e^{(-k_{obs}\ (t-t_0))} - R'_{eq}e^{(-k'_{obs2}\ (t-t_0))}, \tag{5}$$

since an F statistical analysis test of the kinetic constants obtained with a fitting to Equations (4) or (5) was always better in the latter, two-exponential case (at 95% confidence level). With Equation (5), we are assuming that the equilibrium response at infinite time (that is, R_{eq}) is reached with the fastest exponential. The largest-amplitude exponential had a concentration-dependent kinetic rate, and it was used for the pseudo-first-order plots, where the value of k_{obs} is given by

$$k_{obs} = k_{on}\,[NLS1/2_{PADI4}] + k_{off}. \tag{6}$$

The kinetic rate from the second exponential (with a total amplitude smaller than 5%, in all cases, and slower than the other phase) in Equation (5) remained constant at all the peptide concentrations explored.

The dissociation process was always fitted to a single exponential, with *R(t)* given by

$$R(t) = R_1\, e^{(-k_{off}(t-t_0))}, \tag{7}$$

where t_0 = 300 is the time at which the dissociation of the peptide from the biosensor-bound Impα3/ΔImpα3 started in our experimental setup, and R_1 is the response level when dissociation starts.

2.9. Molecular Docking

Molecular simulations were performed using the docking software AutoDock Vina (version 1.1.2) [64], following a methodology we already employed for the virtual screening of other NLS peptides binding to Impα3 [41–43]. The protein was modeled in the IBB-depleted form on the basis of the Protein Data Bank (PDB) entry 5XZX [65], which reports the crystallographic complex with the NLS of the Ran-binding protein 3 anchored within the major binding site of Impα3. Further simulations were performed with the protein modelled on the basis of PDB entry 5X8N [66], which reports the complex of Impα1 with the NLS of the Epstein–Barr virus EBNA-LP protein bound within the same site. The ligand and the crystallographic waters were not considered as being part of the docking host in the simulations. The search region in the docking calculations (size: 50 Å × 90 Å × 90 Å) was centered on the protein and comprised its entire volume. All simulation runs were performed with very high exhaustiveness, 32 times larger than the default value [67].

The two NLS1/2-PADI4 peptides have a number of degrees of freedom that is too large (>100 rotatable dihedral angles) to be investigated in single docking experiments. Thus, the sequence of both peptides was divided into seven-residue fragments, each having five residues in common with the adjacent one and shifted by two residues. The fragments were capped by inserting a methyl group at both their N- and C-termini, except the last fragment for which the –NH_2 terminal moiety was maintained. This modeling was adopted to avoid potential artefacts due to the introduction of polar hydrogens at the extremities of a fragment, which do not exist in the main chain of the peptides and of the native protein. The use of NLS fragments reduced the average number of degrees of freedom within the limit (≤32 rotatable dihedral angles) considered reliable for a successful use of AutoDock Vina [64]. The binding score assigned to each peptide residue was the average of the affinities obtained for all the seven-residue fragments that contained that specific amino acid.

The procedure described above was strictly followed for the peptide corresponding to NLS1-PADI4 (sequence: A^{58}KKKSTGSSTWPLDPGVEVTLTMKVAS^{84}), to obtain the eleven fragments A^{58}KKKSTG^{64}, K^{60}KSTGSS^{66}, … , L^{78}TMKVAS^{84}. For the NLS2-PADI4 (sequence: Y^{498}KLFQEQQNEGHGEALLFEGIKKKKQQKI^{526}), to more accurately investigate the binding features in correspondence with the N-terminal aromatic residue Tyr498 and Phe501, the simulations were extended by also considering the adjacent region L^{490}LASPRSC^{497}, which is part of the PADI4 sequence but not of the peptide used in our experiments. As a consequence, the binding of the 16 fragments L^{490}LASPRS^{496}, A^{492}SPRSCY^{498}, … , K^{520}KKQQKI^{526} was simulated. Therefore, our simulations are expected to reproduce more closely the binding to Impα3 of the predicted NLS2-PADI4 region of the native protein, rather than the binding of the isolated peptide in solution.

2.10. Western Blot

Different dilutions (40, 20, 10, and 5 µM) of PADI4 were mixed with 5 µL of NuPAGE® (Invitrogen, Barcelona, Spain). They were separated by SDS-PAGE using 10% gels and transferred to a nitrocellulose membrane (Bio-Rad Laboratories Inc, CA, USA). Separated membranes were incubated with 1 µM Impα3, for 2 days, and then the membranes were washed three times for periods of 7 min with 1× phosphate buffer solution (PBS), 0.1% Tween-20 buffer. Next, the membranes were blocked for 1 h with 5% (w/v) milk in 1× PBS, 0.1% Tween-20 buffer. Finally, they were incubated overnight at 4 °C with primary antibody anti-KPNA4 (rabbit, 1:800, Quimigen, Madrid, Spain), followed by 1 h incubation at room temperature with ECL TM anti-rabbit IgG, horseradish peroxidase linker (GE Healthcare, Chalfont St Giles, UK). The membranes were visualized with ECL TM Prime Western blotting detection reagent (Amersham TM) in a ChemiDoc Bio-Rad instrument.

2.11. Size Exclusion Chromatography (SEC)

Size exclusion chromatography experiments were carried out as described [48] on an AKTA FPLC using a calibrated analytical Superdex 75 10/30 HR FPLC column (GE Healthcare, Barcelona, Spain) with both peptides in the following concentration ranges: 50–400 µM of protomer concentration for NLS1-PADI4 and 200–400 µM for NLS2-PADI4 peptide. The elution volumes were obtained from analyses with UNICORN software (GE Healthcare, Barcelona, Spain) from three different measurements. The void volume (7.54 ± 0.06 mL) was determined from blue dextran, and the bed volume (18.98 ± 0.03 mL) was determined from conductivity measurements in a Tris elution buffer (20 mM, pH 7.6, and 250 mM NaCl). Samples were eluted at a rate of 1 mL/min and continuously monitored with an online detector at a wavelength of 280 nm. Analyses were carried out as described [48]. The column was calibrated with the standard set of low-molecular-weight (GE Healthcare, Barcelona, Spain) globular proteins; as a comparison, ribonuclease A, with a molecular weight of 13.7 kDa, eluted at 13.3 mL in such a column.

3. Results

3.1. PADI4 Was Bound to Impα3 and ΔImpα3

To test whether PADI4 interacted with Impα3 and ΔImpα3 (i.e., the Impα3 truncated species lacking the IBB domain) in vitro, we followed a two-part experimental approach. Firstly, we used steady-state fluorescence and CD as spectroscopic techniques to observe a possible binding and concomitant conformational changes in the macromolecules; secondly, we used fluorescence and ITC to quantitatively measure the thermodynamic parameters of such binding.

We used fluorescence to determine whether there was a change in (i) the position of the maximum wavelength, (ii) in the fluorescence intensity at that wavelength, or (iii) in both, when the spectrum of the complex was compared to that obtained from the addition of the separated spectra of the two isolated proteins. In the presence of Impα3, we observed a variation in the fluorescence intensity (after excitation at 280 nm) (Figure 1A), but there were no changes in the maximum wavelength of the spectrum. After excitation at 295 nm, similar variations were observed upon complex formation with Impα3. Furthermore, variations between the two spectra (i.e., the addition spectrum and that of the complex) were observed by excitation at both wavelengths (280 and 295 nm) when using ΔImpα3 to form the complex with PADI4 (Figure S1A). However, the variations were smaller than those observed when monitoring the binding to Impα3.

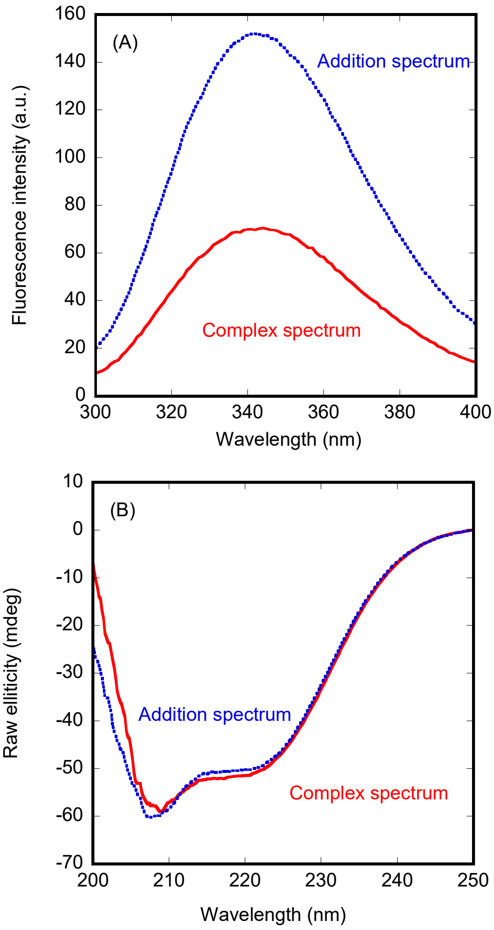

Figure 1. Binding of Impα3 to PADI4 as monitored by spectroscopic probes. (**A**) The spectrum of PADI4/Impα3 complex after excitation at 280 nm, and the addition spectrum obtained by the sum of those of the two separated macromolecules. (**B**) Far-UV CD spectrum of the PADI4/Impα3 complex, and the addition spectrum. All experiments were performed at 25 °C.

Next, we carried out far-UV CD measurements, trying to confirm the fluorescence binding results. In contrast to the observations for Impα3 described above, the addition spectrum was not very different from that of the complex (Figure 1B). A similar behavior was observed for ΔImpα3 (data not shown). Therefore, we can conclude that there were no large changes in the secondary structures of PADI4 or in those of the importin species when the two proteins were bound.

Since we observed changes in the fluorescence spectrum upon binding of PADI4 to Impα3 or ΔImpα3, we carried out titrations by keeping constant the concentration of PADI4 and increasing the concentration of the importin species. The results indicate (Figure 2A) that, for Impα3, the K_d was 3.9 ± 0.8 μM, whereas, for ΔImpα3 (Figure S1B), the K_d was 6 ± 1 μM, which are values quite comparable, within the fitting error.

We also used ITC to determine the thermodynamic binding parameters to both importin species (Figure 2B, Table 1). The result indicated that the interaction of both importins with PADI4 was highly exothermic (favorable enthalpic contribution and unfavorable entropic contribution to the Gibbs energy of binding). For Impα3, the K_d was 4.8 ± 0.9 μM (which is similar to that obtained by fluorescence; see above), whereas, for ΔImpα3, the K_d was 1.3.

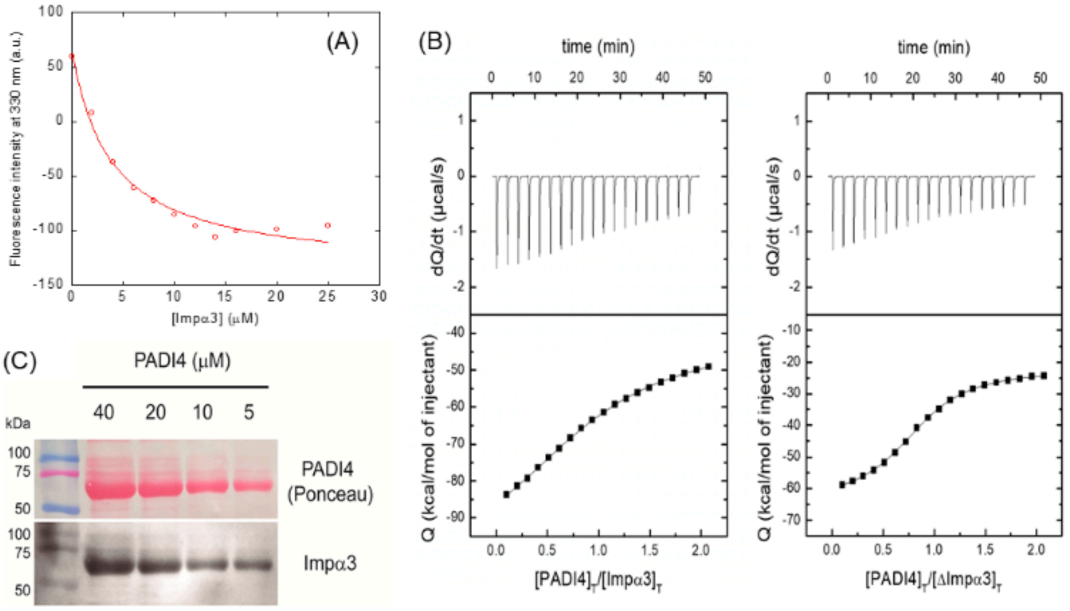

Figure 2. Binding of Impα3 to PADI4 as monitored by biophysical probes and Western blot analyses. (**A**) Titration curve monitoring the changes in the fluorescence at 330 nm when Impα3 was added to PADI4. The fluorescence intensity on the *y*-axis is the relative signal after removal of the corresponding blank. The line through the data is fitted to Equation (1). Experiments were carried out at 25 °C. (**B**) Calorimetric titrations for the PADI4 binding to (**left**) Impα3 and (**right**) ΔImpα3. Upper panels show the thermograms (thermal power as a function of time), and lower panels show the binding isotherms (ligand-normalized heat effects per injection as a function of the molar ratio in the calorimetric cell). Continuous lines correspond to the fitting curves according to a single ligand binding site interaction model. Experiments were carried out at 25 °C. (**C**) Polyacrylamide gels were loaded with several concentrations of PADI4 as visualized with Ponceau staining. Nitrocellulose membranes were later incubated with Impα3 to see the binding, washed, and revealed with the corresponding antibody against Impα3.

Table 1. Thermodynamic parameters of binding of PADI4 to the different macromolecules [a].

		K_a (10^5 M^{-1})	K_d (μM)	Δ*H* (kcal/mol)	ΔG (kcal/mol)	-TΔS (kcal/mol)	n
PADI4	Impα3	2.1 (1.7, 2.5)	4.8 (4.0, 5.9)	−65.5 (−72.0, −60.5)	−7.3	−58.2	0.97 (0.94, 1.00)
	ΔImpα3	7.8 (7.3, 8.5)	1.3 (1.2, 1.4)	−38.4 (−39.5, 37.2)	−8.0	−30.4	0.84 (0.83, 0.85)
NLS1	Impα3	2.3 (1.6, 3.0)	4.3 (3.3, 6.3)	−21.3 (−25.3, −18.8)	−7.3	−14.0	1.24 (1.15, 1.37)
	ΔImpα3	6.5 (4.9, 8.3)	1.5 (1.2, 2.0)	−8.7 (−9.6, −8.0)	−7.9	−0.8	1.22 (1.16, 1.29)
NLS2	Impα3	0.43 (0.31, 0.57)	23 (18, 32)	−35.7 (−39.8, −31.1)	−6.3	−29.4	1.08 (0.98, 1.20)
	ΔImpα3	2.3 (1.5, 3.2)	4.3 (3.2, 6.7)	−11.2 (−13.7, −9.8)	−7.3	−3.9	1.10 (1.02, 1.23)

[a] The uncertainty in the estimation of the binding parameters is reported as the confidence interval at a statistical significance of 95%, shown in parentheses below each parameter [68]. Association constant, K_a; dissociation constant, K_d; binding enthalpy, Δ*H*; binding stoichiometry (or percentage of binding-competent protein), n.

To further confirm the binding of intact Impα3 to PADI4, we performed a series of in vitro experiments, using WBs, to detect protein–protein interactions with the recombinant, purified proteins. We used PADI4 as the prey protein and loaded at several concentrations (40 to 5 μM) in a gel. The proteins were transferred to a nitrocellulose membrane and incubated for 2 days with Impα3 (KPNA4) as bait protein. Subsequently, we washed and revealed the membrane with an antibody against Impα3. The results showed a decreasing signal of Impα3 binding to PADI4 according to the size and amount of loaded protein (Figure 2C). That is, the bait protein (Impα3) was detected on spots in the membrane where the prey protein (PADI4) was located, confirming that the two proteins formed a complex.

To sum up, we conclude that PADI4 could bind to each of the two importin species, with similar affinity constants. Moreover, our experiments confirmed the direct in vitro binding of Impα3–PADI4; however, we cannot rule out that a more complex interaction may be taking place in vivo where other partners could also be involved.

3.2. *Conformational Features of the Isolated NLSs of PADI4*

Since there was binding between PADI4 and both importin species, we wondered whether its two isolated NLS regions, predicted using the webserver cNLS Mapper, were also capable of binding to both importins. Earlier X-ray studies [47] and the results of other predictors of NLS sites (such as PSORT II, available at http://psort.hgc.jp/form2.html, accessed on 8 December 2021) only identified the first region, NLS1, whose sequence is P^{56}PAKKKSTGSSTWPLDPGVEVTLTMKVASGS^{86}; this region was also predicted to be an NLS using our reference NLS predictor, cNLS Mapper. However, the latter webserver also predicted another region, NLS2, corresponding to the sequence R^{495}SCYKLFQEQQNEGHGEALLFEGIKKKKQQKI^{526} (with a score of 6.1, compared to a score of 5.7 for NLS1). Therefore, we had two distinct NLS predictions, and we decided to test the ability of the two corresponding isolated peptides, NLS1/2-PADI4 (see Section 2.3. for their sequences), to bind both importin species in solution. Before testing such ability, we carried out a biophysical and structural characterization of the isolated peptides in solution.

3.2.1. Isolated NLS1-PADI4 Was Oligomeric and Disordered in Solution

The fluorescence spectrum of NLS1-PADI4 had a maximum at ~350 nm due to the emission of its sole tryptophan, Trp68 (Figure 3A). The far-UV CD spectrum of isolated NLS1-PADI4 showed an intense band between 202 and 215 nm (Figure 3B), indicating that the peptide did not possess only a random-coil conformation. We deconvolved the CD spectrum using the k2D software on the DICHROWEB website [69–71]; the deconvolution yielded 9% α-helix, 37% β-sheet, and 54% random coil. The deconvolution using Contin or Selcon3 yielded similar results, with percentages of α-helix between 10% and 13%, of β-sheets between 20% and 24%, of β-turns between 15% and 21%, and of random coils between 45% and 52%. Therefore, all the predictors indicate that NLS1-PADI4 was mainly disordered, but with a relevant fraction of β-sheets. It could be suspected that, because of the presence of two proline residues in the central region of the polypeptide chain (Pro69 and Pro72), the peptide might also adopt a fraction of poly-proline II conformation; however, the far-UV CD spectrum (Figure 3B) lacked the positive band around 225 nm, which is a feature of this type of conformation [72]. The disordered character of NLS1-PADI4 was further confirmed by the 1D-^{1}H-NMR spectrum (Figure 3C), with all the amide protons between 8.0 and 8.6 ppm, whereas the alkyl protons were clustered between 0.8 and 1.0 ppm. Furthermore, the indole proton of Trp68 appeared at 10.2 ppm, along with two signals due to the presence of a slow *cis–trans* isomerization equilibrium of the following residue Pro69 (Figure 3C). For those kinds of protons, all such values are typical of disordered polypeptide chains [59].

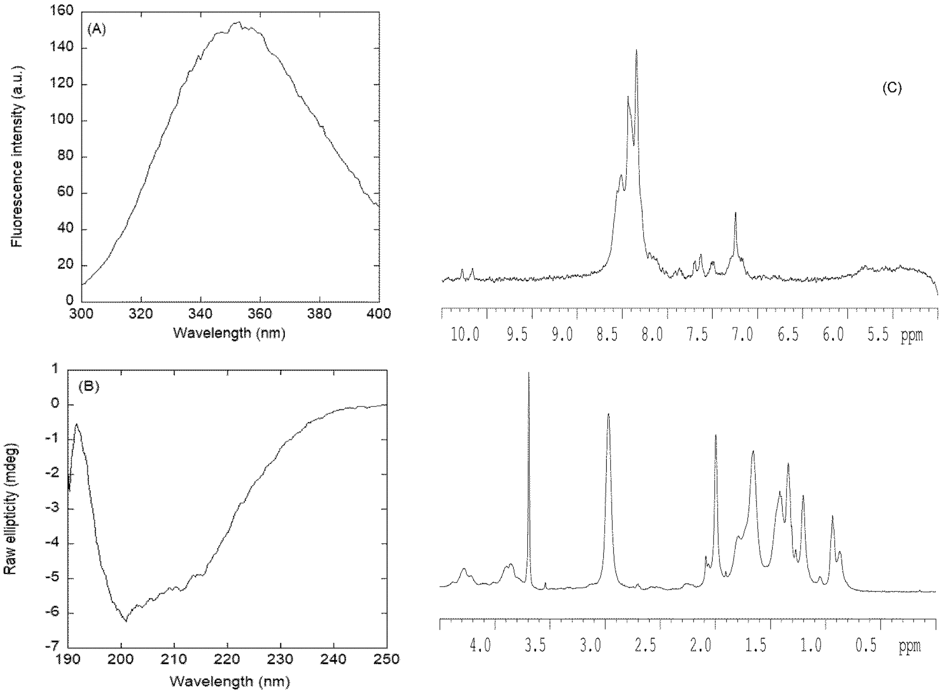

Figure 3. Conformational features of isolated NLS1-PADI4 in solution. (**A**) Fluorescence spectrum of NLS1-PADI4 in 20 mM Tris buffer (pH 7.5), 5 mM TCEP, 150 mM NaCl, and 5% glycerol at 25 °C. (**B**) Far-UV CD spectrum of NLS1-PADI4 at 25 °C in sodium phosphate buffer (50 mM, pH 7.5). (**C**) 1D-^{1}H-NMR spectrum of isolated NLS1-PADI4 at 10 °C and pH 7.0 (100 mM, sodium phosphate buffer).

We also determined the hydrodynamic radius of the peptide in solution. First, the fitting of the measurement of the intensity of the methyl groups to a single exponential from the DOSY yielded a value of D and an estimated R_h, obtained from the comparison with the D of dioxane ($6.8 \pm 0.3 \times 10^{-6}$ cm^2·s^{-1}), of $8.8 \pm 0.8 \times 10^{-7}$ cm^2·s^{-1} and 17 ± 2 Å, respectively. This value of R_h was slightly larger than that theoretically expected for a random-coil polypeptide [73] with such a molecular weight (2819.27 Da), i.e., 14.3 Å. This result suggests the presence of oligomeric species in solution. We could further confirm this hypothesis on the basis of two pieces of evidence. First, two-exponential fitting of the decay of the methyl intensity yielded a D of $4 \pm 1 \times 10^{-7}$ cm^2·s^{-1}, corresponding to an estimated R_h of 34 ± 6 Å, thus indicating the presence of a self-associated species; the second exponential led to the same D value, previously described with the fitting to a single exponential. According to the same expression used to calculate the R_h (R_h = 0.027 MW$^{1/2}$, where R_h is assumed to be in nm and MW represents the mass in Da [73]), we can estimate the molecular weight for those species in solution as 16,421.9 Da, which suggests the presence of a hexameric species (considering an MW of 2819.27 Da for the monomer). Second, attempts to obtain a good TOCSY spectrum (by varying the length of the different mixing, spin-lock sequences used) to assign the resonances of NLS1-PADI4 failed; this result is indicative of polypeptide chains with a short relaxation time, such as those associated with an oligomer with a large molecular weight [59]. Chromatograms of a solution containing NLS1-PADI4 resulted in a peak with strong tailing centered at 14.82 mL (Figure S2). This resulted in a Stokes radius, according to the weight-average partition coefficients relationships [48], of 10.7 Å. The strong tailing is indicative of equilibria among several species with different molecular weights.

To conclude, the canonical NLS1-PADI4 species was disordered and had a tendency to self-associate at physiological pH.

3.2.2. Isolated NLS2-PADI4 Was Monomeric and Disordered in Solution

The fluorescence spectrum of NLS2-PADI4 had a maximum at 308 nm due to the emission of its sole tyrosine, Tyr498 (Figure 4A). The far-UV CD spectrum of isolated NLS2-PADI4 showed an intense minimum at ~202 nm (Figure 4B), indicating that the peptide possessed mostly a random-coil conformation; the spectrum was completely different from that obtained for NLS1-PADI4, although we cannot rule out that the absorbance of the sole Trp68 in the NLS1-PADI4 spectrum in the interval 210–220 nm [74–76] could alter its shape. We tried to deconvolve the far-UV CD spectrum of NLS2-PADI4 by using the k2D software on the DICHROWEB website [69–71]; the deconvolution yielded a fraction of 5% α-helix, 40% β-sheet, and 55% random coil. Deconvolution results obtained using Contin and Selcon3 yielded fractions of 7% to 9% for α-helices, 15% to 18% for β-sheets, 7% to 13% for β-turns, and 64% for random coils. Therefore, the percentages of the structure obtained in the deconvolution of far-UV CD spectrum for NLS2-PADI4 were similar to those obtained for NLS1-PADI4 (see Section 3.2.1), and NLS2-PADI4 was mainly disordered, with a high percentage of transient β-sheets. The disordered characteristic of NLS2-PADI4 was further confirmed by the 1D-^{1}H-NMR spectrum (Figure 4C), with all the amide protons between 8.0 and 8.6 ppm, whereas the methyl protons were clustered between 0.8 and 1.0 ppm. In both cases, these values are observed in disordered chains [59].

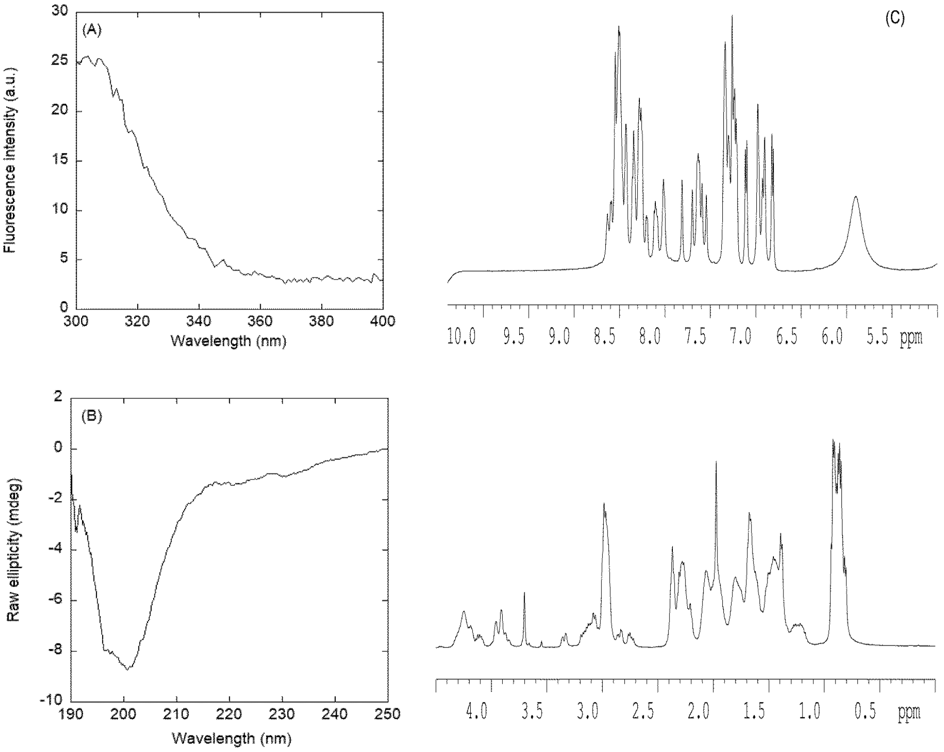

Figure 4. Conformational features of isolated NLS2-PADI4 in solution. (**A**) Fluorescence spectrum of NLS2-PADI4 in 20 mM Tris buffer (pH 7.5), 5 mM TCEP, 150 mM NaCl, and 5% glycerol at 25 °C. (**B**) Far-UV CD spectrum of NLS2-PADI4 at 25 °C in sodium phosphate buffer (50 mM, pH 7.5). (**C**) 1D-^{1}H-NMR spectrum of isolated NLS2-PADI4 at 10 °C and pH 7.0 (100 mM, sodium phosphate buffer).

On the other hand, the peptide was monomeric, as concluded from the value of D measured by the DOSY experiment and the estimated R_h (obtained from the comparison with the D of dioxane): $9.6 \pm 0.3 \times 10^{-7}$ cm$^2 \cdot$s^{-1} and 15.1 ± 0.8 Å, respectively. This value of R_h was similar to that obtained theoretically for a random-coil polypeptide [59] with a corresponding molecular weight (3501.98 Da), i.e., 15 ± 2 Å. The SEC experiments for NLS2-PADI4 yielded an elution peak at 15.15 mL (Figure S2). As the molecular weight of

NLS1-PADI4 was slightly larger than that of NLS2-PADI4, but it eluted at larger elution volumes, the actual molecular weight of the NLS1-PADI4 species loaded in the column (even taking into account of the dilution effect of the bed volume) must correspond to an oligomeric species. The elution volume of NLS2-PADI4 resulted in a Stokes radius of 9.64 Å, lower than that of NLS1-PADI4 (see previous section).

To further confirm the mainly disordered nature of NLS2-PADI4, we also carried out homonuclear 2D-^{1}H-NMR experiments (Table ST1); in this case, we were able to obtain good TOCSY spectra to allow us to assign the resonances. However, we could not fully assign them due to the large number of lysine, glutamine, and glutamic acid residues. NLS2-PADI4 was mainly disordered in solution, as suggested by different evidence, further confirming the results from far-UV CD (Figure 4B) and 1D-^{1}H-NMR spectra (Figure 4C). Firstly, the conformational shifts ($\Delta\delta$) of H_α protons [59–61] for those unambiguously assigned amino acids were within the commonly accepted range for random-coil peptides ($\Delta\delta \leq 0.1$ ppm) (Table ST1). Secondly, no long- or medium-range NOEs were observed in the spectra, but only consecutive ones (i.e., αN (I, i+1) and βN (i, i+1)) were observed in the polypeptide patches fully assigned.

Taken together, all the experimental techniques concurred that the isolated NLS2-PADI4 was monomeric and disordered in aqueous solution.

3.3. Isolated NLS1/2-PADI4 Could Bind to Each of the Importin Species

Next, we wondered whether the isolated NLS1/2-PADI4 peptides were capable of binding to both importins (Impα3 and ΔImpα3), and, if so, we wanted to measure their binding affinity for each of them. We followed the same procedure used for intact PADI4; that is, first we tried to detect binding by using fluorescence and far-UV CD, and then we tried to measure such binding quantitatively using fluorescence, ITC, and BLI.

Fluorescence experiments showed that there were no large changes in the spectra upon addition of NLS2-PADI4 to Impα3/ΔImpα3, but there were large ones upon addition of NLS1-PADI4 to each of the importin species, probably because of the presence of Trp68 in the latter peptide (Figure 5A and Figure S3A). Furthermore, the far-UV CD spectrum of the complex and that obtained by the addition of the two isolated spectra showed no changes for NLS2-PADI4 (Figure 5B), but there were large changes for NLS1-PADI4 with both importins (Figure S3B). As the peptide had a smaller size than that of the two importins, these results suggest that the secondary conformational preferences of NLS1-PADI4 changed dramatically in the presence of any of the two importins. We could not rule out that the structure of the importins changed as well, although this is unlikely for a well-folded protein with an organized and repetitive ARM structure. Furthermore, the tertiary environment around one of the tryptophans of the importins and/or Trp68 from NLS1-PADI4 changed when both macromolecules were present in solution. On the other hand, the absence of changes in the far-UV CD spectra when NLS2-PADI4 was present in solution could mean that (i) neither NLS2-PADI4 nor importin species changed their secondary structures upon binding, or (ii) CD did not report any conformational change in the polypeptide chains (i.e., CD was spectroscopically silent). However, the lack of variations in the CD spectra did not rule out the possibility that the binding took place, as we used other biophysical probes to test it. In fact, we attempted to determine the binding affinity of both peptides for each importin species using (i) ITC, (ii) BLI, and (iii) the small changes observed in fluorescence intensity for NLS2-PADI4 and the large ones for NLS1-PADI4.

The calorimetric titrations with both peptides revealed that both polypeptide chains were capable of binding to both importins, Impα3 and ΔImpα3, with a favorable enthalpic contribution and an unfavorable entropic contribution to the Gibbs energy of binding, with NLS2 showing a more exothermic binding (Figure 6, Table 1). In both cases, we observed a single binding reaction, in contrast to what was found for other NLS peptides, where two transitions were observed and explained as due to the simultaneous binding to the major and minor binding sites of importin [77]. For NLS1-PADI4, the K_d values were 4.4 ± 4 μM for Impα3 and 1.5 ± 1 μM for ΔImpα3; for NLS2-PADI4, the K_d values were 23 ± 10 μM for Impα3 and 4.3 ± 4 μM for ΔImpα3. Thus, NLS1-PADI4 showed a slightly higher affinity, compared to NLS2-PADI4, for both importins, and ΔImpα3 showed a slightly higher affinity, compared to Impα3, for NLS1/2-PADI4.

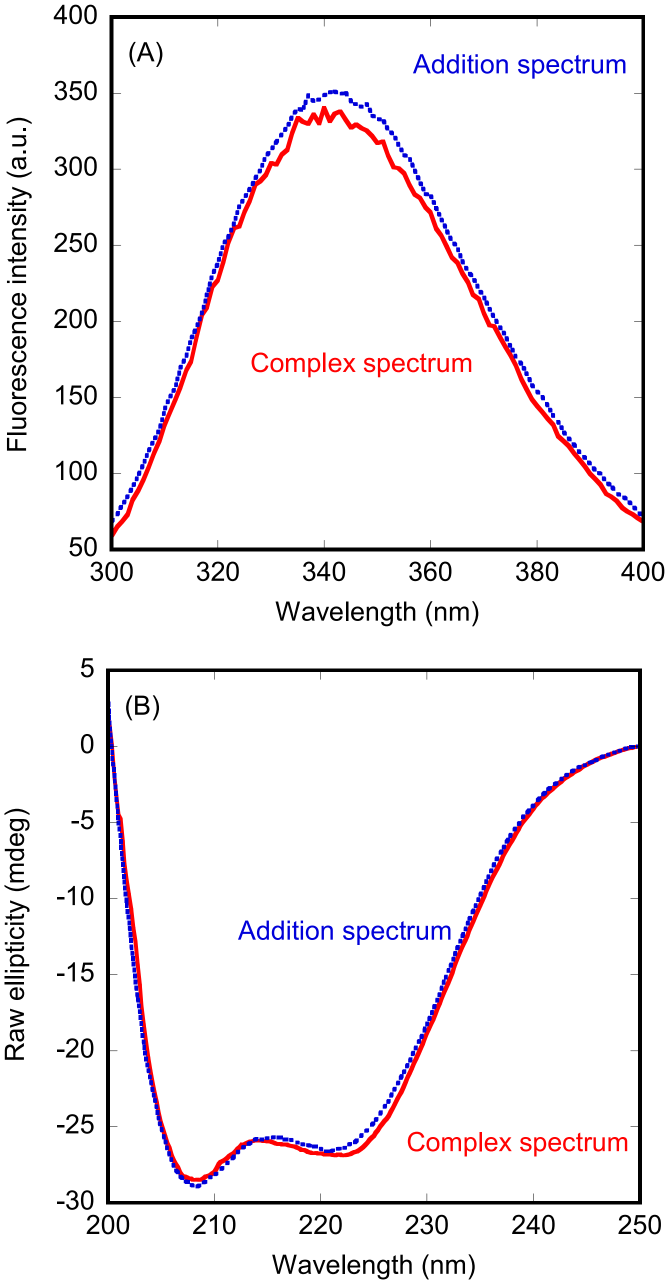

Figure 5. Binding of importin species to NLS2-PADI4 as monitored by spectroscopic probes. (**A**) Fluorescence spectrum of the complex ΔImpα3/NLS2-PADI4 and that obtained by the addition of the spectra of the two isolated molecules. (**B**) Far-UV CD spectrum of the complex Impα3/NLS2-PADI4 and that obtained by the addition of the spectra of the two isolated molecules. Experiments were carried out at 25 °C.

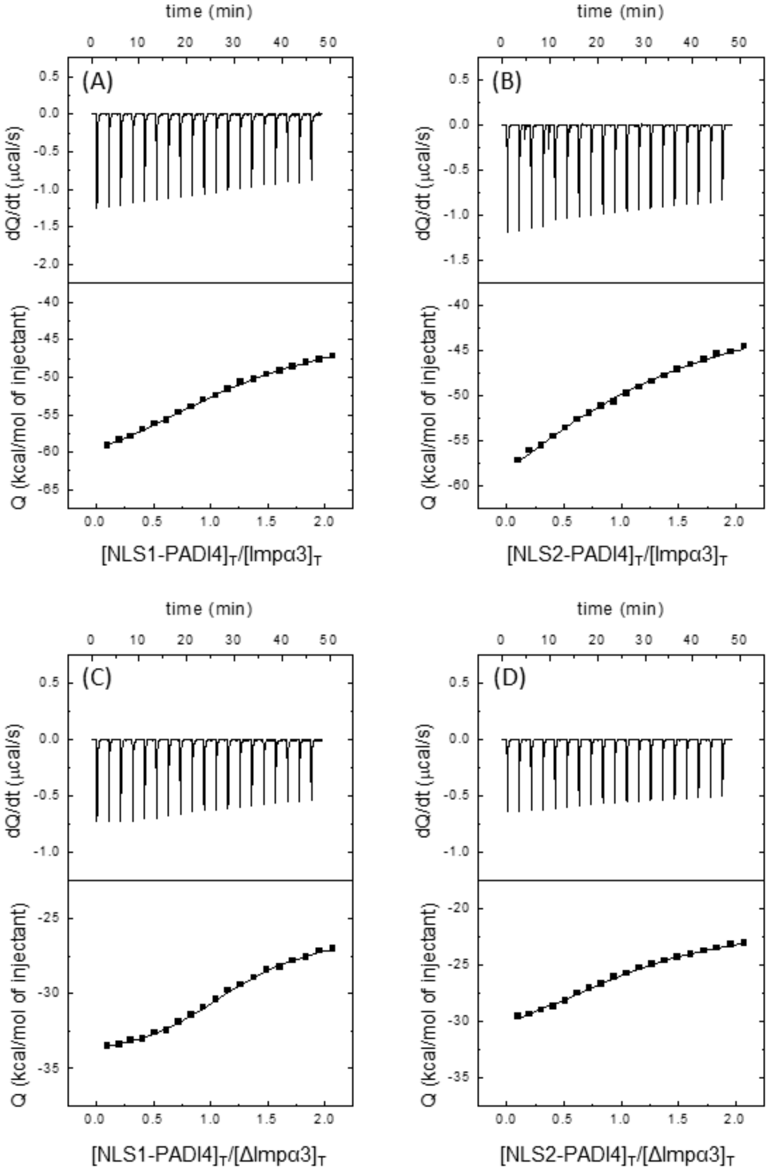

Figure 6. Binding of importin species to NLS1-PADI4 and NLS2-PADI4 as monitored by ITC. Calorimetric titrations for the NLS peptides binding to importin species. Impα3 interacting with (**A**) NLS1-PADI4 and (**B**) NLS2-PADI4, and ΔImpα3 interacting with (**C**) NLS1-PADI4 and (**D**) NLS2-PADI4. Upper panels show the thermograms (thermal power as a function of time), and lower panels show the binding isotherms (ligand-normalized heat effects per injection as a function of the molar ratio in the calorimetric cell). Continuous lines correspond to the fitting curves according to a single ligand binding site interaction model. Experiments were carried out at 25 °C.

The results from BLI (Figure S4) yielded values of the dissociation constants different from those measured for ITC. For NLS1-PADI4, the K_d values were 18 ± 4 μM (for Impα3), with k_{on} = 0.0037 ± 0.0002 $\mu M^{-1} \cdot s^{-1}$ and k_{off} = 0.0685 ± 0.0007 s^{-1} (Figure 7A), and 4 ± 1 μM (for ΔImpα3), with k_{on} = 0.011 ± 0.002 $\mu M^{-1} \cdot s^{-1}$ and k_{off} = 0.046 ± 0.005 s^{-1} (Figure 7B). On the other hand, for NLS2-PADI4, the values of the dissociation constants and kinetic rates were 99 ± 10 μM (for Impα3), with k_{on} = 0.003 ± 0.002 $\mu M^{-1} \cdot s^{-1}$ and k_{off} = 0.32 ± 0.01 s^{-1} (Figure 8A), and 12 ± 4 μM (for ΔImpα3), with k_{on} = 0.020 ± 0.003 $\mu M^{-1} \cdot s^{-1}$ and k_{off} = 0.23 ± 0.01 s^{-1}. Therefore, from the kinetic point of view, we can conclude that (i) both peptides had an affinity for ΔImpα3 higher than that for Impα3 (i.e., the dissociation equilibrium constant for ΔImpα3 was smaller than for Impα3), in agreement with the ITC experiments, (ii) NLS1-PADI4 showed always a higher affinity than NLS2-PADI4 for any of the importin species, in agreement with the ITC experiments, (iii) the values of the k_{on} rates for both peptides were one order of magnitude lower for Impα3 than for ΔImpα3, indicating that the association of both peptides to the latter importin species was faster, and (iv) the values of the dissociation rates from both importin species, k_{off}, were smaller (one order of magnitude) for NLS1-PADI4 than for NLS2-PADI4. Taken altogether, we can conclude that the binding reaction was modulated by the nature of the importin species (with or without the IBB) and each particular NLS region. Although the values for the dissociation constant determined by ITC and BLI might seem somewhat different, the relative differences (that is, the respective fold changes) for the two importin species and for the two NLS peptides were similar.

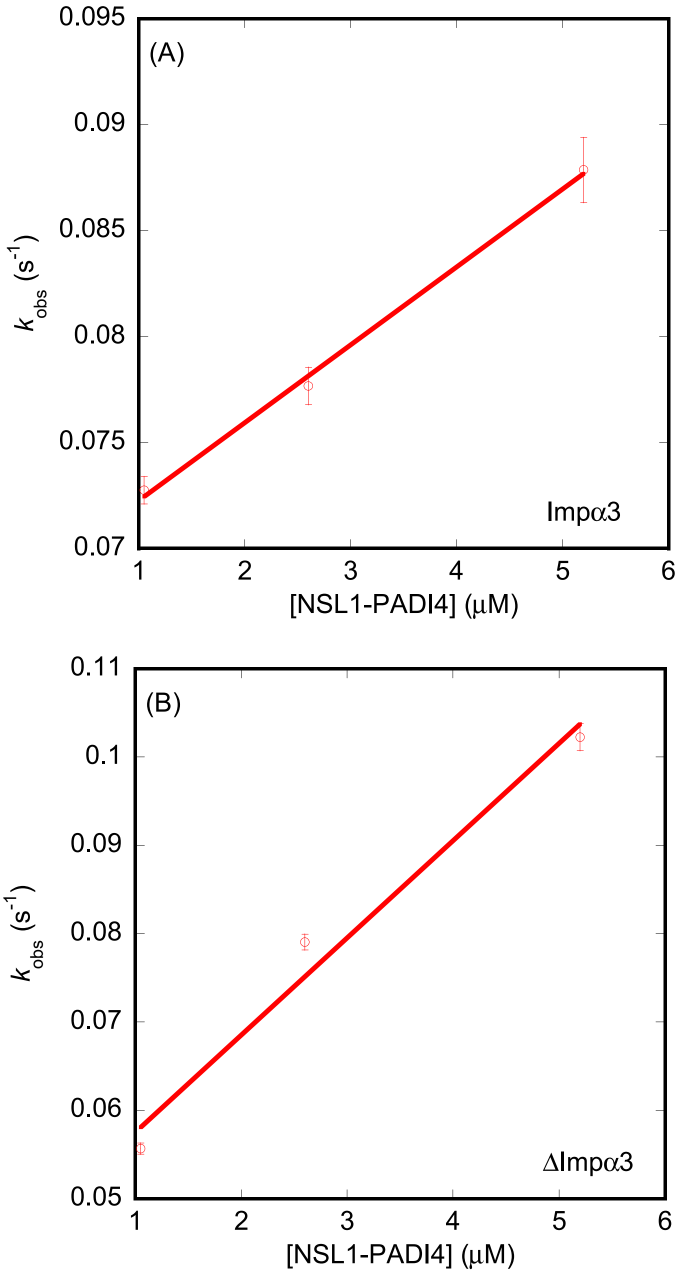

Figure 7. Binding of importin species to NLS1-PADI4 as monitored by BLI. (**A**) Pseudo-first-order plot of the binding of the peptide to Impα3 (Equation (6)). (**B**) Pseudo-first-order plot of the binding of the peptide to ΔImpα3 (Equation (6)). The error bars in both panels are fitting errors to the exponentials of the sensorgrams. Experiments were carried out at 25 °C.

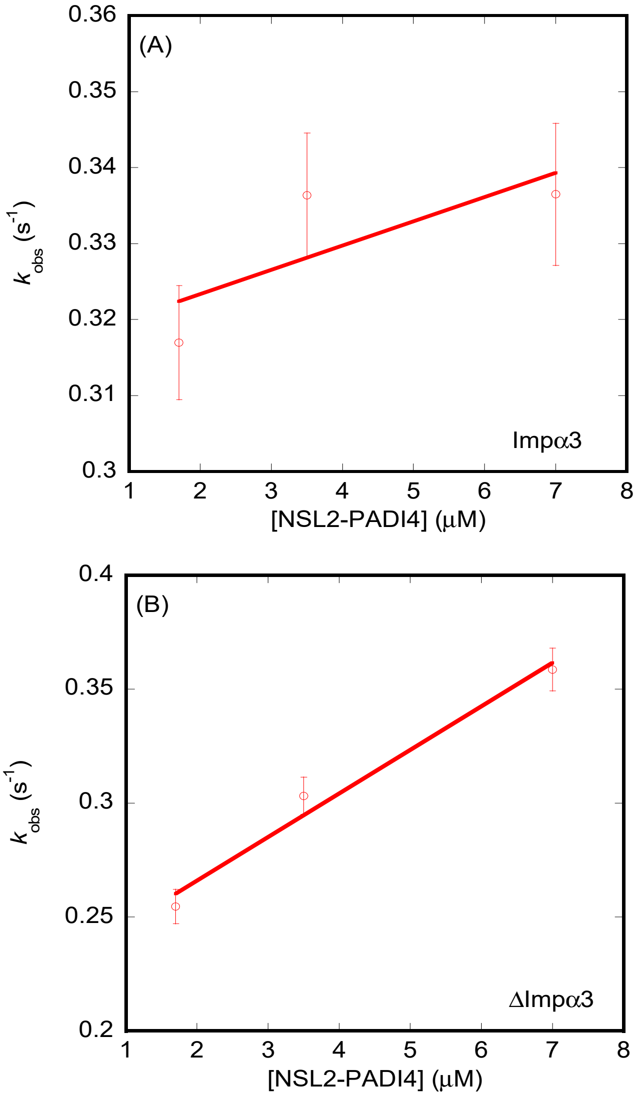

Figure 8. Binding of importin species to NLS2-PADI4 as monitored by BLI. (**A**) Pseudo-first-order plot of the binding of the peptide to Impα3 (Equation (6)). (**B**) Pseudo-first-order plot of the binding of the peptide to ΔImpα3 (Equation (6)). The error bars in both panels are fitting errors to the exponentials of the sensorgrams. Experiments were carried out at 25 °C.

The changes observed by fluorescence, even though they were small (see above), provided values of the dissociation constants very similar for both importin species when bound to NLS2-PADI, i.e., 4 ± 2 μM (for Impα3) and 4 ± 1 μM (for ΔImpα3) (Figure 9A). These values were smaller than those obtained by BLI for the same peptides, indicating that the binding process probably followed a non-two-state mechanism. Conversely, although the fluorescence changes for NLS1-PADI4 were far larger than for NLS2-PADI4, we could not monitor a reasonable titration curve within the constraints given by the experimental error (Figure 9B).

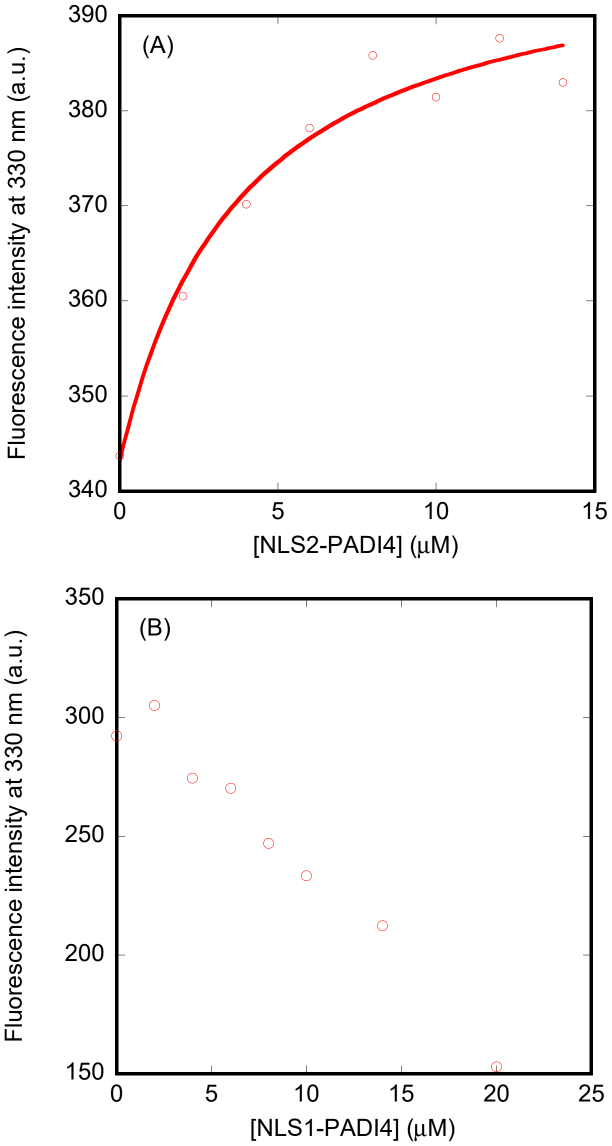

Figure 9. Binding of importin species to NLS1- and NLS2-PADI4 as monitored by fluorescence: (**A**) Titration curve monitoring the changes of fluorescence at 330 nm when NLS2-PADI4 was added to ΔImpα3. The fluorescence intensity on the *y*-axis is the relative fluorescence intensity after removal of the corresponding blank. The line through the data is fitted to Equation (2). (**B**) Titration curve monitoring the changes in the fluorescence at 330 nm when NLS1-PADI4 was added to Impα3. The fluorescence intensity on the *y*-axis is the relative fluorescence intensity after removal of the corresponding blank. All experiments were carried out at 25 °C.

3.4. NLS1/2-PADI4 Could Bind to the Major NLS Binding Site of Impα3

The binding of the two predicted NLS regions of PADI4 to Impα3 was screened in detail using molecular docking. This simulation technique does not take into account the protein dynamics and, therefore, is not sensitive to the presence or absence of the IBB domain. For this reason, the importin was modeled in the sole IBB-depleted form (ΔImpα3), and results were assumed to be approximately valid for both importin species. Furthermore, molecular docking cannot accurately treat the binding of the whole NLS1-PADI4 or NLS2-PADI4 peptide to Impα3, because the peptides possess too many degrees of freedom (105 and 136 rotatable dihedral angles for NLS1-PADI4 and NLS2-PADI4, respectively). Nevertheless, both the major and the minor NLS-binding sites of Impα3 are too small to accommodate all the residues included in the two peptides (27 and 29 residues for NLS1-

PADI4 and NLS2-PADI4, respectively); therefore, the core binding region of both peptides is expected to be much shorter. As an example, in the case of the crystallographic complex between Impα3 and the NLS sequence of the Ran-binding protein 3 [65], the anchoring sequence constituting the binding interface was significantly shorter. For this reason, according to a screening protocol we already successfully employed in other cases [78–81], the docking was performed by considering seven-residue fragments of the two peptides. Each of these fragments differed by a shift of two consecutive residues with respect to the following one, and the whole set of fragments covered the whole sequence of the two NLS peptides.

The binding affinities calculated for the two peptides are shown in Figure 10, with the energy value for each peptide residue corresponding to the average of the binding scores of all fragments that contained that residue. The binding score for the peptide NLS1-PADI4 (Figure 10A) had a minimum in the curve at about −8.0 kcal/mol, and the affinity of this region was more favorable by >1 kcal/mol compared to the other regions of the same NLS1-PADI4. This energy value is slightly more favorable compared to the range (from −7.9 to −7.2 kcal/mol) we found in analogous docking experiments between Impα3 and nine- or eight-residue-long fragments of the NLSs of two intrinsically disordered proteins, NUPR1 and its paralog NUPR1L, for which the binding was also experimentally confirmed [41,42]. Thus, the docking simulations suggested a favorable binding affinity in the low micromolar range. The core binding region of the NLS1-PADI4 included the key protein residue Trp68 and encompassed residues 66–72, confirming our initial assumption that a restricted seven-residue region drives the binding of the whole 27-residue peptide.

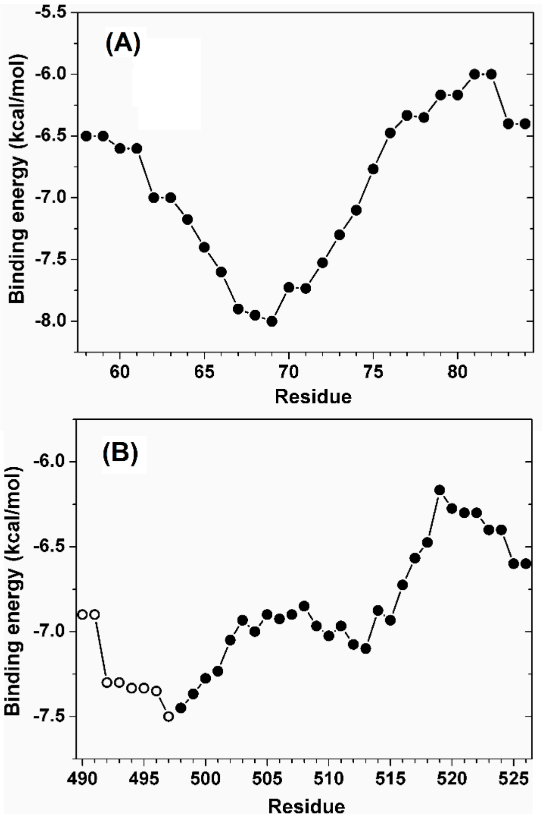

Figure 10. Affinity of the two NLS regions of PADI4 toward Impα3 estimated in molecular docking simulations. (**A**) Peptide NLS1-PADI4, encompassing residues 58–84. (**B**) The second NLS2 region of PADI4, including the N-terminal residues 490–497 (open symbols) and the peptide NLS2-PADI4 encompassing residues 498–526 (solid symbols). The affinity was calculated for seven-residue fragments, and values reported for each residue are the average over all simulation runs including that residue.

For NLS2-PADI4, the curve did not show a clear minimum in the binding energy when the sole peptide was considered (Figure 10B, solid symbols). This observation suggested the necessity to extend the exploration beyond the N-terminal region of this peptide. It is also important to note that the estimation of the binding score is less accurate for residues belonging to the two main chain termini, because they were obtained from averages of a lower number of docking experiments compared to the values obtained for amino acids far away from the termini. As an example, the binding contribution of the aromatic residue Tyr498 in this region, in the absence of other information, could only be assumed as equal to the docking score calculated for the fragment $\mathrm{Y}^{498}\mathrm{KLFQEQ}^{504}$, if the sole NLS2-PADI4 sequence were to be considered. For this reason, a longer portion of the sequence of PADI4 including eight more residues (490–497) was explored in our simulations (Figure 10B, open symbols). Thus, the results are representative of the binding of a larger region of PADI4 sequence (residues 490–526), more than representing the sole NLS2-PADI4 peptide (residues 498–526). The overall curve showed an energy minimum at about −7.5 kcal/mol, a value only slightly less favorable compared to the one obtained for NLS1-PADI4, predicting that the two NLS regions of PADI4 should bind Impα3 with a similar affinity. The core binding region in the case of NLS2-PADI4 encompassed the amino acids 495–501 and confirmed the involvement of the key residue Tyr498 and a few other adjacent amino acids, all belonging to the seven-residue fragment located at the N-terminal region of the NLS2-PADI4 peptide.

The analysis of the docking results was also extended to detail the binding location of both NLS regions of PADI4 on the surface of Impα3. The best binding modes of all the seven-residue fragments of the two peptides are reported in Figure 11. These docking poses were all found in correspondence with the ARM repeats 2–4 of Impα3, which correspond to the major protein binding site for NLS of cargo proteins [82,83]. The fact that only the major binding site of Impα3 was involved is further supported by the fact that a single binding reaction was observed in the ITC experiments (Figure 6), conversely to what was observed for other peptides encompassing classical bipartite NLSs [77]. A moderate affinity of a larger variety of adjacent fragments toward the same target site could be useful in the first steps of the binding recognition process, although the sole two fragments expected to anchor in that position at the end of the association process are the core binding regions of PADI4 previously detected (residues 66–72 and 495–501), due to their more favorable binding affinity compared to the other fragments. A further comparison with the NLS of the Ran-binding protein 3, whose conformation in the complex with Impα3 is known at atomic detail in crystallography [65], shows that the two core binding regions of the NLS peptides of PADI4 are capable of anchoring in a similar way in the same location (as shown in Figure 11), with cation–π interactions between the aromatic residues from the corresponding NLS and positively charged residues from Impα3. Similar types of interactions have been observed in some atypical NLS when bound to importin at the minor binding site [84]. The binding interface of Impα3 also encompassed a restricted number of residues, with Trp184 and Trp231 forming van der Waals interactions that maintain an anchoring with PADI4.

We also report that similar results were obtained using, as a template to build Impα3, the structure extracted from the complex between Impα1 and the NLS of the EBNA-LP protein [66], which is the reference structure we previously used in other studies [41–43]. The predicted affinity curves (Figure S5) had, in general, a different shape compared to those found using Impα3 extracted from the complex with the Ran-binding protein 3; nevertheless, the binding energy at the minima were similar (variations were ≤0.5 kcal/mol), and the position of such minima differed by at most three residues along the NLS sequence of PADI4. Furthermore, even in this case, all the poses (Figure S6) were found in correspondence with the major binding site for cargo proteins, and they overlapped with the crystallographic position of the NLS. It is also evident (Figures 11 and S6) that the core region of both crystallographic NLSs considered, as well as the two most favorable binders among the seven-residue-long fragments of the NLSs of PADI4, essentially overlapped.

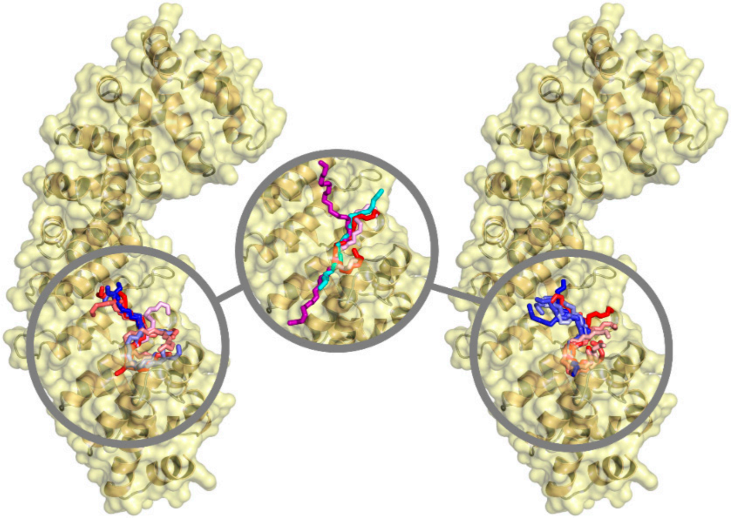

Figure 11. Binding location of seven residue long fragments of the two NLS regions of PADI4 on the surface of Impα3 observed in simulations. (**Left**) conformations of peptide NLS1, and (**right**) peptide NLS2 region. Fragments follow the color scheme red → magenta → blue, going from the N to the C terminus of the two NLS peptides. (Center) comparison among the fragments with the most favorable binding affinity of (magenta) NLS1-PADI4 and (red) NLS2-PADI4, and (cyan) crystallographic pose [66] of the NLS of the Ran-binding protein 3 (purple) and the Epstein–Barr virus EBNA-LP protein (cyan) bound to the major binding sites of Impα3 and Impα1, respectively. For clarity, the sole backbone chain is shown for all the sequences.

4. Discussion

PADI4 is a key enzyme for the conversion of arginine to citrulline, an important PTM, and the only member of PADI family observed in both the nucleus and the cytoplasm under ordinary physiological conditions. Thus, the nuclear translocation of this protein is of special interest in cancer, and this work represents a first step to investigate this process. Our results revealed that PADI4 was capable of binding to Impα3, a nuclear carrier of the importin family, and its IBB domain-depleted species, ΔImpα3. Moreover, we showed that the use of the NLS predictor cNLS Mapper returned two potential NLS regions in PADI4, approximately located at the two termini of its polypeptide chain: (i) from Pro56 to Ser83, and (ii) from Arg495 to Ile526. Whereas the first region was already suspected to be an NLS of PADI4 using earlier NLS predictors and on the basis of the crystallographic structure of the protein [47], the latter constitutes a novelty. Both regions are solvent-exposed in the folded structure of PADI4 and, therefore, available to bind Impα3 with no impediment (Figure S7). Thus, we characterized the conformational propensities of the peptides corresponding to the isolated fragments of the two regions, and we measured their binding affinity for a specific importin, Impα3, for which we had already measured the affinity toward other cargos [41–43]. According to our in vitro measurements, both isolated regions were responsible for PADI4 binding to Impα3, as further confirmed by the molecular docking results (Figures 10 and 11). The first region, from Pro56 to Ser83 (NLS1-PADI4), could not be classified as a classical monopartite NLS [28], as the core binding region comprises residues Thr67–Gly73. It has been suggested [22], on the basis of transfected cells and deletion mutants of PADI4 containing the region 45–74, that the Lys59–Lys60–Lys61 region might be important for nuclear translocation of PADI4. Our simulation studies indicate that, although such a region is involved in binding to Impα3, the core polypeptide patch is around the two central prolines flanked in the sequence by a tryptophan residue. Other examples of NLS regions that involve aromatic residues in their sequences have also been previously reported in the literature [28]. The second region, Arg495 to Ile526 (NLS2-PADI4), could not either be classified as a classical monopartite sequence, encompassing the core region of Tyr498–Gln504. As it happens with other proteins that are importin-dependent for their nuclear translocation, tryptophan residues of Impα3 and ΔImpα3 seemed to intervene in the binding, as we were able to follow the fluorescence titrations at 280 or 295 nm (Figure 9), and these findings were validated by our molecular docking calculations (Figure 10).

The main conclusions from our simulations can be summarized as follows: firstly, the whole sequence of both investigated NLS sequences of PADI4 has a distinct preference to interact with Impα3 in correspondence with the major NLS-binding site of this karyopherin. Secondly, in both cases, the core binding region of the NLS sequences corresponds to short fragments of about seven residues, corresponding to the central region of NLS1-PADI4 (residues 66–72) and the N-terminal region of NLS2-PADI4 (residues 495–501). Thirdly, in both cases, these core binding regions of the NLS peptides are located in correspondence with aromatic residues of PADI4, i.e., Trp68 and Tyr498 for, respectively, NLS1-PADI4 and NLS2-PADI4, acquiring a disordered conformation when bound. Fourthly, the binding patch on the carrier Impα3 is similarly small, albeit consisting of a surface region on the tertiary structure of the protein that is not restricted to a single portion of the protein sequence. Fifthly, the binding residues of Impα3 also include two aromatic amino acids, i.e., Trp184 and Trp231. Lastly, the binding energy between the two protein interfaces that drives the formation of the complex is between -7.5 and -8.0 kcal/mol, comparable to the values found in both simulations and experiments for the binding of other NLS polypeptides to Impα3 [41,42], and consistent with our in vitro experiments with NLS1/2-PADI4. In fact, according to ITC experiments, the binding of NLS1-PADI4 and NLS2-PADI4 to ΔImpα3 was characterized by Gibbs energy changes of -7.9 kcal/mol, and -7.3 kcal/mol, respectively. Moreover, it is not unusual that atypical and poorly basic NLSs, as those described here for PADI4, have aromatic residues involved in binding to importin (see, for instance, [28] and references therein).

We also demonstrated that both isolated NLS1/2-PADI4 peptides were disordered, and that at least NLS2-PADI4 did not have any propensity to acquire helix- or turn-like conformations, although we could not rule out the presence of local kinks around the two prolines in the sequence of NLS1-PADI4 (Pro69 and Pro72). The predicted hotspot of the importins for the association of both NLS1/2-PADI4 peptides is the major binding site for the NLSs of cargo proteins (Figure 11), as shown by the in silico experiments. Thus, we can conclude that NLS1/2-PADI4 behaved similarly to any other NLS regions belonging to a well-folded protein [29,40,85,86] or to IDPs [41–43].

Since PADI4 is a Ca(II)-dependent enzyme, it could be thought that the binding detected in this work might be affected by the presence of the ion. However, the presence of Ca(II) does not alter the monomer–dimer equilibrium of the enzyme [24,87]. Furthermore, the structural changes occurring in the presence of Ca(II) are mainly located at the C-terminus, where the active site is [47], and the two NLSs regions described here are far away from those regions where the changes in the presence of Ca(II) were detected (Ile313–Ile320, Pro338–Met348, Pro371–Pro387, Pro396–Gly403, Phe633–His644, and Ala351–Ala359) [47]. Lastly, the presence of Ca(II) was shown only to stabilize the presence of an unfolded intermediate either by using urea or temperature [24,88]. Therefore, the presence of Ca(II) can be safely assumed to not affect binding of PADI4 to Impα3 or its truncated species, although further studies will be necessary to dissect this point.

Previous studies with other NLSs of IDPs [41–43,82] or, alternatively, of folded proteins [29,40,83] suggest an inhibitory action of the IBB, which hampers binding of the NLS of the corresponding cargo protein into the major NLS-binding region of Impα3. Since ITC is considered the gold-standard for determining binding thermodynamic parameters, we focused on the dissociation constants measured by this technique. In this respect, we observed a slightly higher affinity of binding to NLS1/2-PADI4 for ΔImpα3 compared to Impα3, in agreement with the findings obtained for other NLS peptides assayed before [41–43]. The same conclusion about the values of the affinity constants of the two peptides for both importin species could be obtained from BLI experiments. Keeping in mind that the binding of the peptides might be a non-two-state process, we could observe that the apparent dissociation constants for Impα3 were always larger (i.e., lower affinity) than those for ΔImpα3. This difference between the two importin species may be due to the fact that the 60-residue-long IBB is competing with the NLS for the NLS-anchoring region. From a kinetic point of view, we observed that the binding of both peptides was faster to ΔImpα3, probably due to the absence of IBB and an associated kinetic barrier, as it is not necessary to displace that domain from the importin to allow access to the NLS binding site. As there are two NLSs in the same protein, we can speculate that either region can be used during nuclear translocation through NPC, allowing for a stronger cooperative binding. Alternatively, they can be used indistinctly, depending on the environmental conditions; hence, PADI4 can modulate its binding to the importin under different circumstances. Lastly, the fact that the dissociation constants were different for the two NLS suggests that the binding behavior of the cargo protein–Impα3 complex seems to be modulated by subtle details within the sequence of each particular NLS. These findings would open the avenue to selectively hamper nuclear translocation and might lead to the development of new molecular anticancer therapies.

5. Conclusions

PADI4 is found in both the nucleus and the cytoplasm, and it is present in several types of cancer tissues and various cells of the human innate immune system. This protein has two predicted NLS regions in its sequence, which can be recognized by importins for nuclear translocation. In this work, we demonstrated that PADI4 was capable of binding to both Impα3 and its IBB-depleted species, with a slightly higher affinity when the IBB domain was not present. As both PADI4 and importin appear to be overexpressed in some cancer types, and PADI4 must be transported within the nucleus to citrullinate histones and start de-condensation, the use of drugs hampering the binding of this enzyme to importin could provide a therapeutic approach to stop cancer progression. We also proved that the NLS regions of PADI4 were both capable of binding this nuclear carrier, and we suggested that a restricted core sequence provided an anchoring to the major NLS binding site for cargo proteins of Impα3. The results expand our knowledge on the molecular properties of PADI4, as well as support upcoming studies on the functional role of this protein.

Supplementary Materials: The following supporting information can be downloaded at https://www.mdpi.com/article/10.3390/cells11142166/s1: Figure S1. Binding to PADI4 of ΔImpα3 monitored by fluorescence; Figure S2. SEC chromatograms of NLS1/2-PADI4 in 20 mM Tris (pH 7.6) and 250 mM NaCl; Figure S3. The binding of both importin species to NLS1-PADI4 monitored by different spectroscopic probes; Figure S4. The binding as monitored by BLI (sensorgrams) of the NLS1-PADI4 and NLS2-PADI4 peptides; Figure S5. Affinity of the two NLSs of PADI4 predicted in docking simulations performed using a different template for Impα3; Figure S6. Binding location of seven -residue long fragments of the two NLSs of PADI4 predicted using a different template for Impα3; Figure S7. Location of the NLS regions Pro56–Ser83 and Arg495–Ile526 in the folded structure of PADI4; Table ST1. A reference list, and a table containing the ^{1}H-NMR assignments of NLS2-PADI4.

Author Contributions: Conceptualization, J.L.N., B.R., C.d.J.R. and A.V.-C.; methodology, J.L.N., C.d.J.R., B.R. and A.V.-C.; investigation, J.L.N., S.A.-A., B.R. and O.A.; data formal analysis, J.L.N., S.A.-A., O.A., B.R. and A.V.-C.; writing—original draft preparation, J.L.N., C.d.J.R., B.R. and A.V.-C.; writing—review and editing, J.L.N., O.A., C.d.J.R., B.R. and A.V.-C.; funding acquisition, J.L.N., C.d.J.R., O.A. and A.V.-C. All authors have read and agreed to the published version of the manuscript.

Funding: This research was funded by the Spanish Ministry of Economy and Competitiveness and European ERDF Funds (MCIU/AEI/FEDER, EU) (RTI2018-097991-B-I00 to J.L.N., BFU2016-78232-P to A.V.-C., and CP19/00095 to C.d.J.R.), the; Fondo de Investigaciones Sanitarias from Instituto de Salud Carlos III, and European Union (ERDF/ESF, "Investing in your future") (PI18/00394 to O.A.), and the Diputación General de Aragón ("Protein targets and Bioactive Compounds group" E45-20R to A.V.-C., and "Digestive Pathology Group" B25-20R to O.A.). S.A.-A. was the recipient of a "Carolina Foundation predoctoral fellowship 2020". The funders had no role in the study design, data collection and analysis, decision to publish, or preparation of the manuscript.

Institutional Review Board Statement: Not applicable.

Informed Consent Statement: Not applicable.

Data Availability Statement: The data and the vectors used are available from the corresponding authors upon reasonable request.

Acknowledgments: B.R. acknowledges the kind use of computational resources of the European Magnetic Resonance Center (CERM), Sesto Fiorentino (Florence), Italy.

Conflicts of Interest: The authors declare no conflict of interest.

References

1. Cuthbert, G.L.; Daujat, S.; Snowden, A.W.; Erdjument-Bromage, H.; Hagiwara, T.; Yamada, M.; Schneider, R.; Gregory, P.D.; Tempst, P.; Bannister, A.J.; et al. Histone deimination antagonizes arginine methylation. *Cell* **2004**, *118*, 545–553. [CrossRef] [PubMed]
2. Asaga, H.; Yamada, M.; Senshu, T. Selective deimination of vimentin in calcium ionophore-induced apoptosis of mouse peritoneal macrophages. *Biochem. Biophys. Res. Commun.* **1998**, *243*, 641–646. [CrossRef] [PubMed]
3. Assohou-Luty, C.; Raijmakers, R.; Benckhuijsen, W.E.; Stammen-Vogelzangs, J.; De Ru, A.; Van Veelen, P.A.; Franken, K.L.M.C.; Drijfhout, J.W.; Pruijn, G.J.M. The human peptidylarginine deiminases type 2 and type 4 have distinct substrate specificities. *Biochim. Biophys. Acta* **2014**, *1844*, 829–836. [CrossRef] [PubMed]
4. Senshu, T.; Akiyama, K.; Ishigami, A.; Nomura, K. Studies on specificity of peptidylarginine deiminase reactions using an immunochemical probe that recognizes an enzymatically deiminated partial sequence of mouse keratin K1. *J. Dermatol. Sci.* **1999**, *21*, 113–126. [CrossRef]
5. Kizawa, K.; Takahara, H.; Troxler, H.; Kleinert, P.; Mochida, U.; Heizmann, C.W. Specific citrullination causes assembly of a globular S100A3 homotetramer: A putative Ca^{2+} modulator matures human hair cuticle. *J. Biol. Chem.* **2008**, *283*, 5004–5013. [CrossRef]
6. Wang, Y.; Wysocka, J.; Sayegh, J.; Lee, Y.H.; Pertin, J.R.; Leonelli, L.; Sonbuchner, L.S.; McDonald, C.H.; Cook, R.G.; Dou, Y.; et al. Human PAD4 regulates histone arginine methylation levels via demethylimination. *Science* **2004**, *306*, 279–283. [CrossRef] [PubMed]
7. Ishigami, A.; Maruyama, N. Importance of research on peptidylarginine deiminase and citrullinated proteins in age-related disease. *Geriatr. Gerontol. Int.* **2010**, *10*, S53–S58. [CrossRef]
8. Klose, R.J.; Zhang, Y. Regulation of histone methylation by demethylimination and demethylation. *Nat. Rev. Mol. Cell Biol.* **2007**, *8*, 307–318. [CrossRef]
9. György, B.; Tóth, E.; Tarcsa, E.; Falus, A.; Buzás, E.I. Citrullination: A posttranslational modification in health and disease. *Int. J. Biochem. Cell Biol.* **2006**, *38*, 1662–1677. [CrossRef]
10. Anzilotti, C.; Pratesi, F.; Tommasi, C.; Migliorini, P. Peptidylarginine deiminase 4 and citrullination in health and disease. *Autoimmun. Rev.* **2010**, *9*, 158–160. [CrossRef]
11. Wang, L.L.; Song, Y.P.; Mi, J.H.; Ding, M.L. Peptidyl arginine deiminase 4 and its potential role in Alzheimer's disease. *Med. Hypotheses* **2021**, *146*, 110466. [CrossRef] [PubMed]
12. Guerrin, M.; Ishigami, A.; Méchin, M.C.; Nachat, R.; Valmary, S.; Sebbag, M.; Simon, M.; Senshu, T.; Serre, G. cDNA cloning, gene organization and expression analysis of human peptidylarginine deiminase type I. *Biochem. J.* **2003**, *370*, 174. [CrossRef] [PubMed]
13. Ishigami, A.; Ohsawa, T.; Asaga, H.; Akiyama, K.; Kuramoto, M.; Maruyama, N. Human peptidylarginine deiminase type II: Molecular cloning, gene organization, and expression in human skin. *Arch. Biochem. Biophys.* **2002**, *407*, 25–31. [CrossRef]
14. Kanno, T.; Kawada, A.; Yamanouchi, J.; Yosida-Noro, C.; Yoshiki, A.; Shiraiwa, M.; Kusakabe, M.; Manabe, M.; Tezuka, T.; Takahara, H. Human peptidylarginine deiminase type III: Molecular cloning and nucleotide sequence of the cDNA, properties of the recombinant enzyme, and immunohistochemical localization in human skin. *J. Investig. Dermatol.* **2000**, *115*, 813–823. [CrossRef] [PubMed]
15. Chavanas, S.; Méchin, M.C.; Takahara, H.; Kawada, A.; Nachat, R.; Serre, G.; Simon, M. Comparative analysis of the mouse and human peptidylarginine deiminase gene clusters reveals highly conserved non-coding segments and a new human gene, PADI6. *Gene* **2004**, *330*, 19–27. [CrossRef]
16. Nakashima, K.; Hagiwara, T.; Ishigami, A.; Nagata, S.; Asaga, H.; Kuramotot, M.; Senshu, T.; Yamada, M. Molecular characterization of peptidylarginine deiminase in HL-60 cells induced by retinoic acid and 1α,25-dihydroxyvitamin D3. *J. Biol. Chem.* **1999**, *274*, 27786–27792. [CrossRef]
17. Dong, S.; Kanno, T.; Yamaki, A.; Kojima, T.; Shiraiwa, M.; Kawada, A.; Méchin, M.C.; Chavanas, S.; Serre, G.; Simon, M.; et al. NF-Y and Sp1/Sp3 are involved in the transcriptional regulation of the peptidylarginine deiminase type III gene (PADI3) in human keratinocytes. *Biochem. J.* **2006**, *397*, 449–459. [CrossRef]
18. Chavanas, S.; Adoue, V.; Méchin, M.C.; Ying, S.; Dong, S.; Duplan, H.; Charveron, M.; Takahara, H.; Serre, G.; Simon, M. Long-range enhancer associated with chromatin looping allows AP-1 regulation of the peptidylarginine deiminase 3 gene in differentiated keratinocyte. *PLoS ONE* **2008**, *3*, e3408. [CrossRef]

19. Hung, H.C.; Lin, C.Y.; Liao, Y.F.; Hsu, P.C.; Tsay, G.J.; Liu, G.Y. The functional haplotype of peptidylarginine deiminase IV (S55G, A82V and A112G) associated with susceptibility to rheumatoid arthritis dominates apoptosis of acute T leukemia Jurkat cells. *Apoptosis* **2007**, *12*, 475–487. [CrossRef]
20. Li, P.; Yao, H.; Zhang, Z.; Li, M.; Luo, Y.; Thompson, P.R.; Gilmour, D.S.; Wang, Y. Regulation of p53 target gene expression by peptidylarginine deiminase 4. *Mol. Cell. Biol.* **2008**, *28*, 4745–4758. [CrossRef]
21. Li, P.; Wang, D.; Yao, H.; Doret, P.; Hao, G.; Shen, Q.; Qiu, H.; Zhang, X.; Wang, Y.; Chen, G.; et al. Coordination of PAD4 and HDAC2 in the regulation of p53-target gene expression. *Oncogene* **2010**, *29*, 3153–3162. [CrossRef] [PubMed]
22. Nakashima, K.; Hagiwara, T.; Yamada, M. Nuclear localization of peptidylarginine deiminase V and histone deimination in granulocytes. *J. Biol. Chem.* **2002**, *277*, 49562–49568. [CrossRef] [PubMed]
23. Jones, J.E.; Causey, C.P.; Knuckley, B.; Slack-Noyes, J.L.; Thompson, P.R. Protein arginine deiminase 4 (PAD4): Current understanding and future therapeutic potential. *Curr. Opin. Drug Discov. Dev.* **2009**, *12*, 627.
24. Neira, J.L.; Araujo-Abad, S.; Cámara-Artigas, A.; Rizzuti, B.; Abián, O.; Giudici, A.M.; Velázquez-Campoy, A.; de Juan Romero, C. Biochemical and Biophysical characterization of PADI4 supports its involvement in cancer. *Arch. Biochem. Biophys.* **2022**, *717*, 109125. [CrossRef] [PubMed]
25. Wang, Y.; Chen, R.; Gan, Y.; Ying, S. The roles of PAD2- and PAD4-mediated protein citrullination catalysis in cancers. *Int. J. Cancer* **2021**, *148*, 267–276. [CrossRef]
26. Stewart, M. Molecular mechanism of the nuclear protein import cycle. *Nat. Rev. Mol. Cell. Biol.* **2007**, *8*, 195–208. [CrossRef] [PubMed]
27. Bednenko, J.; Cingolani, G.; Gerace, L. Nucleo-cytoplasmic transport navigating the channel. *Traffic* **2003**, *4*, 127–135. [CrossRef]
28. Christie, M.; Chang, C.-W.; Róna, G.; Smith, K.M.; Stewart, A.G.; Takeda, A.A.S.; Fontes, M.R.M.; Stewart, M.; Vértessy, B.G.; Foorwood, J.K.; et al. Structural biology and regulation of protein import into the nucleus. *J. Mol. Biol.* **2016**, *428*, 2060–2090. [CrossRef]
29. Kobe, B. Autoinhibition by an internal nuclear localization signal revealed by the crystal structure of mammalian importin α. *Nat. Struct. Biol.* **1999**, *6*, 388–397. [CrossRef]
30. Zaidi, S.K.; Young, D.W.; Javed, A.; Pratap, J.; Mortecino, M.; van Wijnen, A.; Lian, J.B.; Stein, J.L.; Stein, G.S. Nuclear microenvironments in biological control and cancer. *Nat. Rev. Cancer* **2007**, *7*, 454–463. [CrossRef]
31. Fukasawa, K. Oncogenes and tumour suppressors take on centrosomes. *Nat. Rev. Cancer* **2007**, *7*, 911–924. [CrossRef] [PubMed]
32. Chahine, M.N.; Pierce, G.N. Therapeutic targeting of nuclear protein import in pathological cell conditions. *Pharmacol. Rev.* **2009**, *61*, 358–372. [CrossRef] [PubMed]
33. Yoshitake, K.; Tanaka, S.; Mogushi, K.; Aihara, A.; Murakata, A.; Matsumura, S.; Mitsunori, Y.; Yasen, M.; Ban, D.; Noguchi, N.; et al. Importin a1 as a novel prognostic target for hepatocellular carcinoma. *Ann. Surg. Oncol.* **2011**, *18*, 2093–2103. [CrossRef] [PubMed]
34. Wang, H.; Tao, T.; Yan, W.; Feng, Y.; Wang, Y.; Cai, J.; You, Y.; Jiang, T.; Jiang, C. Upregulation of miR-181s reverses mesenchymal transition by targeting KPNA4 in glioblastoma. *Sci. Rep.* **2015**, *5*, 13072. [CrossRef] [PubMed]
35. Yang, J.; Lu, C.; Wei, J.; Guo, Y.; Liu, W.; Luo, L.; Fish, G.; Li, L. Inhibition of KPNA4 attenuates prostate cancer metastasis. *Oncogene* **2017**, *36*, 2868–2878. [CrossRef]
36. Xu, M.; Liang, H.; Li, K.; Zhu, S.; Yao, Z.; Xu, R.; Lin, N. Value of KPNA4 as a diagnostic and prognostic biomarker for hepatocellular carcinoma. *Aging* **2021**, *13*, 5263–5283. [CrossRef]
37. Li, X.; Yu, M.; Yang, C. YY1-mediated overexpression of long noncoding RNA MCM3AP-AS1 accelerates angiogenesis and progression in lung cancer by targeting miR-340-5p/KPNA4 axis. *J. Cell. Biochem.* **2020**, *121*, 2258–2267. [CrossRef]
38. Wang, D.; Cui, Y.; Xu, A.; Zhao, L.; Li, P. MiR-596 activated by EP300 controls the tumorigenesis in epithelial ovarian cancer by declining BRD4 and KPNA4. *Cancer Cell. Int.* **2020**, *20*, 447. [CrossRef]
39. Thiele, S.; Stanelle-Bertram, S.; Beck, S.; Kouassi, N.M.; Zickler, M.; Müller, M.; Tuku, B.; Resa-Infante, P.; van Riel, D.; Alawi, M.; et al. Cellular Importin-α3 expression dynamics in the lung regulate antiviral response pathways against influenza A virus infection. *Cell Rep.* **2020**, *31*, 107549. [CrossRef]
40. Smith, K.M.; Tsimbalyuk, S.; Edwards, M.G.; Cross, E.M.; Batra, J.; Soares da Costa, T.P.; Aragao, D.; Basler, C.F.; Forwood, J.K. Structural basis for importin alpha 3 specificity of W proteins in Hendra and Nipah viruses. *Nat. Commun.* **2018**, *9*, 3703. [CrossRef]
41. Neira, J.L.; Rizzuti, B.; Jiménez-Alesanco, A.; Abián, O.; Velázquez-Campoy, A.; Iovanna, J.L. The paralogue of the intrinsically disordered Nuclear Protein 1 has a nuclear localization sequence that binds to human importin α3. *Int. J. Mol. Sci.* **2020**, *21*, 7428. [CrossRef] [PubMed]
42. Neira, J.L.; Rizzuti, B.; Jiménez-Alesanco, A.; Palomino-Schätzlein, M.; Abián, O.; Velázquez-Campoy, A.; Iovanna, J.L. A phosphorylation-induced switch in the nuclear localization sequence of the intrinsically disordered NUPR1 hampers binding to importin. *Biomolecules* **2020**, *10*, 1313. [CrossRef] [PubMed]
43. Neira, J.L.; Jiménez-Alesanco, A.; Rizzuti, B.; Velázquez-Campoy, A. The nuclear localization sequence of the epigenetic factor RYBP binds to human importin α3. *Biochim. Biophys. Acta Proteins Proteom.* **2021**, *1869*, 140670. [CrossRef]
44. Gill, S.C.; von Hippel, P.H. Calculation of protein extinction coefficients from amino acid sequence data. *Anal. Biochem.* **1989**, *182*, 319–326. [CrossRef]

45. Kosugi, S.; Hasebe, M.; Tomita, M.; Yanagawa, H. Systematic identification of yeast cell cycle-dependent nucleocytoplasmic shuttling proteins by prediction of composite motifs. *Proc. Natl. Acad. Sci. USA* **2009**, *106*, 10171–10176. [CrossRef]
46. Kosugi, S.; Hasebe, M.; Matsumura, N.; Takashima, H.; Miyamoto-Sato, E.; Tomita, M.; Yanagawa, H. Six classes of nuclear localization signals specific to different binding grooves of importin α. *J. Biol. Chem.* **2009**, *284*, 478–485. [CrossRef] [PubMed]
47. Arita, K.; Hashimoto, H.; Shimizu, T.; Nakashima, K.; Yamada, M.; Sato, M. Structural basis for Ca^{2+}-induced activation of human PAD4. *Nat. Struct. Mol. Biol.* **2004**, *11*, 777–783. [CrossRef] [PubMed]
48. Neira, J.L.; Hornos, F.; Bacarizo, J.; Cámara-Artigas, A.; Gómez, J. The monomeric species of the regulatory domain of tyrosine hydroxylase has a low conformational stability. *Biochemistry* **2017**, *55*, 3418–3431. [CrossRef]
49. Birdsall, B.; King, R.W.; Wheeler, M.R.; Lewis, C.A., Jr.; Goode, S.; Dunlap, R.B.; Roberts, G.C. Correction for light absorption in fluorescence studies of protein-ligand interactions. *Anal. Biochem.* **1983**, *132*, 353–361. [CrossRef]
50. Beckett, D. Measurement and analysis of equilibrium binding titrations: A beginner's guide. *Methods Enzymol.* **2011**, *488*, 1–16. [CrossRef]
51. Royer, C.A.; Scarlatta, S.F. Fluorescence approaches to quantifying biomolecular interactions. *Methods Enzymol.* **2008**, *450*, 79–106. [CrossRef] [PubMed]
52. Cavanagh, J.; Fairbrother, W.J.; Palmer, A.G.; Skelton, N.J. *Protein NMR Spectroscopy: Principles and Practice*; Academic Press: New York, NY, USA, 1996.
53. Piotto, M.; Saudek, V.; Sklenar, V. Gradient-tailored excitation for single-quantum NMR spectroscopy of aqueous solutions. *J. Biomol. NMR* **1992**, *2*, 661–675. [CrossRef] [PubMed]
54. Wilkins, D.K.; Grimshaw, S.B.; Receveur, V.; Dobson, C.M.; Jones, J.A.; Smith, L.J. Hydrodynamic radii of native and denatured proteins measured by pulse field gradient NMR technique. *Biochemistry* **1999**, *38*, 16424–16431. [CrossRef]
55. Marion, M.; Wüthrich, K. Application of phase sensitive two-dimensional correlated spectroscopy (COSY) for measurements of 1H-1H spin-spin coupling constants in proteins. *Biochem. Biophys. Res. Commun.* **1983**, *11*, 967–975. [CrossRef]
56. Bax, A.; Davis, D.G. MLEV-17-based two-dimensional homonuclear magnetization transfer spectroscopy. *J. Magn. Reson.* **1985**, *65*, 355–360. [CrossRef]
57. Kumar, A.; Ernst, R.R.; Wüthrich, K. A two-dimensional nuclear Overhauser enhancement (2D NOE) experiment for the elucidation of complete proton-proton cross-relaxation networks in biological macromolecules. *Biochem. Biophys. Res. Commun.* **1980**, *95*, 1–6. [CrossRef]
58. Cavanagh, J.; Rance, M. Suppression of cross-relaxation effects in TOCSY spectra via a modified DIPSI-2 mixing sequence. *J. Magn. Reson.* **1992**, *96*, 670–678. [CrossRef]
59. Wüthrich, K. *NMR of Proteins and Nucleic Acids*; John Wiley and Sons: New York, NY, USA, 1986.
60. Kjaergaard, M.; Brander, S.; Poulsen, F.M. Random coil chemical shifts for intrinsically disordered proteins: Effects of temperature and pH. *J. Biomol. NMR* **2011**, *49*, 139–149. [CrossRef]
61. Kjaergaard, M.; Poulsen, F.M. Sequence correction of random coil chemical shifts: Correlation between neighbour correction factors and changes in the Ramachandran distribution. *J. Biomol. NMR* **2011**, *50*, 157–165. [CrossRef]
62. Frenzel, D.; Willbolds, D. Kinetic titration series with biolayer interferometry. *PLoS ONE* **2014**, *9*, e106882. [CrossRef]
63. Pantoja-Uceda, D.; Neira, J.L.; Saelices, L.; Robles-Rengel, R.; Florencio, F.J.; Muro-Pastor, M.I.; Santoro, J. Dissecting the binding between glutamine synthetase and its two natively unfolded protein inhibitors. *Biochemistry* **2016**, *55*, 3370–3382. [CrossRef] [PubMed]
64. Trott, O.; Olson, A.J. AutoDock Vina: Improving the speed and accuracy of docking with a new scoring function, efficient optimization, and multithreading. *J. Comput. Chem.* **2010**, *31*, 455–461. [CrossRef] [PubMed]
65. Koyama, M.; Matsuura, Y. Crystal structure of importin-alpha 3 bound to the nuclear localization signal of Ran-binding protein 3. *Biochem. Biophys. Res Commun.* **2017**, *491*, 609–613. [CrossRef]
66. Nakada, R.; Matsuura, Y. Crystal structure of importin-α bound to the nuclear localization signal of Epstein-Barr virus EBNA-LP protein. *Protein Sci.* **2017**, *26*, 1231–1235. [CrossRef]
67. Grande, F.; Rizzuti, B.; Occhiuzzi, M.A.; Ioele, G.; Casacchia, T.; Gelmini, F.; Guzzi, R.; Garofalo, A.; Statti, B. Identification by molecular docking of homoisoflavones from *Leopoldia comosa* as ligands of estrogen receptors. *Molecules* **2018**, *23*, 894. [CrossRef]
68. Paketurytė, V.; Petrauskas, V.; Zubrienė, A.; Abian, O.; Bastos, M.; Chen, W.Y.; Moreno, M.J.; Krainer, G.; Linkuvienė, V.; Sedivy, A.; et al. Uncertainty in protein-ligand binding constants: Asymmetric confidence intervals versus standard errors. *Eur. Biophys. J.* **2021**, *50*, 661–670. [CrossRef]
69. Lobley, A.; Whitmore, L.; Wallace, B.A. DICHROWEB: An interactive website for the analysis of protein secondary structure from circular dichroism spectra. *Bioinformatics* **2002**, *18*, 211–212. [CrossRef]
70. Whitmore, L.; Wallace, B.A. DICHROWEB an online server for protein secondary structure analyses from circular dichroism spectroscopic data. *Nucleic Acids Res.* **2004**, *32*, W668–W673. [CrossRef] [PubMed]
71. Whitmore, L.; Wallace, B.A. Protein secondary structure analyses from circular dichroism spectroscopy: Methods and reference databases. *Biopolymers* **2008**, *89*, 392–400. [CrossRef]
72. Shi, Z.; Woody, R.W.; Kallenbach, N.R. Is poly-proline II a major backbone conformation in unfolded proteins? *Adv. Protein Chem.* **2002**, *62*, 163–240. [CrossRef]

73. Danielsson, J.; Jarvet, J.; Damberg, P.; Gräslund, A. Translational diffusion measured by PFG-NMR on full length and fragments of the Alzheimer Aβ(1–40) peptide. Determination of hydrodynamic radii of random coil peptides of varying length. *Magn. Reson. Chem.* **2002**, *40*, S89–S97. [CrossRef]
74. Kelly, S.M.; Jess, T.J.; Price, N.C. How to study proteins by circular dichroism. *Biochim. Biophys. Acta Proteins Proteom* **2005**, *1751*, 119–139. [CrossRef] [PubMed]
75. Kelly, S.M.; Price, N.C. The use of circular dichroism in the investigation of protein structure and function. *Curr. Protein Pept. Sci.* **2000**, *1*, 349–384. [CrossRef] [PubMed]
76. Woody, R.W. Circular dichroism. *Methods Enzymol.* **1995**, *246*, 34–71. [CrossRef] [PubMed]
77. De Barros, A.C.; Takeda, A.A.S.; Dreyer, T.R.; Velázquez-Campoy, A.; Kobe, B.; Fontes, M.R.M. DNA mismatch repair proteins MLH1 and PMS2 can be imported to the nucleus by a classical nuclear import pathway. *Biochimie* **2018**, *146*, 87–96. [CrossRef]
78. Santofimia-Castaño, P.; Rizzuti, B.; Pey, A.L.; Soubeyran, P.; Vidal, M.; Urrutia, R.; Iovanna, J.L.; Neira, J.L. Intrinsically disordered chromatin protein NUPR1 binds to the C-terminal region of Polycomb RING1B. *Proc. Natl. Acad. Sci. USA* **2017**, *114*, E6332–E6341. [CrossRef]
79. Santofimia-Castaño, P.; Rizzuti, B.; Abián, O.; Velázquez-Campoy, A.; Iovanna, J.L.; Neira, J.L. Amphipathic helical peptides hamper protein-protein interactions of the intrinsically disordered chromatin nuclear protein 1 (NUPR1). *Biochim. Biophys. Acta Gen. Subj.* **2018**, *1862*, 1283–1295. [CrossRef]
80. Santofimia-Castaño, P.; Xia, Y.; Lan, W.; Zhou, Z.; Huang, C.; Peng, L.; Soubeyran, P.; Velázquez-Campoy, A.; Abián, O.; Rizzuti, B.; et al. Ligand-based design identifies a potent NUPR1 inhibitor exerting anticancer activity via necroptosis. *J. Clin. Investig.* **2019**, *129*, 2500–2513. [CrossRef]
81. Rizzuti, B.; Lan, W.; Santofimia-Castaño, P.; Zhou, Z.; Velázquez-Campoy, A.; Abián, O.; Peng, L.; Neira, J.L.; Xia, Y.; Iovanna, J.L. Design of inhibitors of the intrinsically disordered protein NUPR1: Balance between drug affinity and target function. *Biomolecules* **2021**, *11*, 1453. [CrossRef]
82. Lan, W.; Santofimia-Castaño, P.; Swayden, M.; Xia, Y.; Zhou, Z.; Audebert, S.; Camoin, L.; Huang, C.; Peng, L.; Jiménez-Alesanco, A.; et al. ZZW-115-dependent inhibition of NUPR1 nuclear translocation sensitizes cancer cells to genotoxic agents. *JCI Insight* **2020**, *5*, 138117. [CrossRef]
83. Miyatake, H.; Sanjoh, A.; Unzai, S.; Matsuda, G.; Tatsumi, Y.; Miyamoto, Y.; Dohmae, N.; Aida, Y. Crystal structure of human Importin α1 (Rch1) revealing a potential autoinhibition mode involving homodimerization. *PLoS ONE* **2015**, *10*, e0115995. [CrossRef] [PubMed]
84. Chang, C.-W.; Counago, R.M.; Williams, S.J.; Boden, M.; Kobe, B. Distinctive conformation of minor site-specific nuclear localization signals bound to importin-alpha. *Traffic* **2013**, *14*, 1144–1154. [CrossRef] [PubMed]
85. Miyamoto, Y.; Loveland, K.L.; Yoneda, Y. Nuclear importin α and its physiological importance. *Commun. Integr. Biol.* **2012**, *5*, 220–222. [CrossRef] [PubMed]
86. Goldfarb, D.S.; Corbett, A.H.; Mason, D.A.; Harreman, M.T.; Adam, S.A. Importin α: A multipurpose nuclear-transport receptor. *Trends Cell Biol.* **2004**, *14*, 505–514. [CrossRef] [PubMed]
87. Liu, Y.-L.; Chiang, Y.-H.; Liu, G.-Y.; Hung, H.-C. Functional role of dimerization of human peptidylarginine deiminase 4 (PAD4). *PLoS ONE* **2011**, *6*, e21314. [CrossRef]
88. Liu, Y.-L.; Lee, C.-Y.; Huang, Y.-N.; Chen, H.-Y.; Liu, G.-Y.; Hung, H.-C. Probing the roles of calcium binding sites during the folding of human peptidylarginine deiminase 4. *Sci Rep.* **2017**, *7*, 2429. [CrossRef]